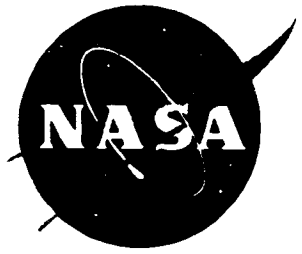

NASA Contractor Report 4661
Part 1

Space Environmental Effects on Spacecraft: LEO Materials Selection Guide

Edward M. Silverman

Contract NAS1-19291
Prepared for Langley Research Center

August 1995

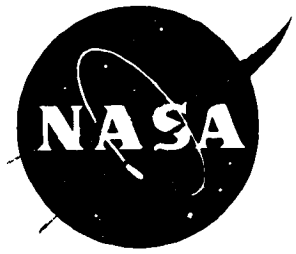

NASA Contractor Report 4661
Part 1

Space Environmental Effects on Spacecraft: LEO Materials Selection Guide

Edward M. Silverman
TRW Space & Electronics Group • Redondo Beach, California

National Aeronautics and Space Administration
Langley Research Center • Hampton, Virginia 23681-0001

Prepared for Langley Research Center
under Contract NAS1-19291

August 1995

Printed copies available from the following:

NASA Center for AeroSpace Information
800 Elkridge Landing Road
Linthicum Heights, MD 21090-2934
(301) 621-0390

National Technical Information Service (NTIS)
5285 Port Royal Road
Springfield, VA 22161-2171
(703) 487-4650

FOREWORD

This report describes the work accomplished under the "Mission Systems Operations Analysis of NASA Space Station Freedom Advanced Concepts (MSOA) contract NAS1-19291, Task 12 (April 1993 through March 1995). Sponsorship for this program was provided by National Aeronautics and Space Administration, Langley Research Center, Hampton, Virginia.

Ms. Joan G. Funk and Dr. Stephen S. Tompkins were the NASA Task Technical Monitors. The following aerospace personnel provided critical support throughout the program:

Brian Blakkolb	TRW Space & Electronics Group
Dennis Rhoads	TRW Space & Electronics Group
Dr. Robert Stillwell	TRW Space & Electronics Group
Dr. Gary Pippin	Boeing Defense & Space Group
Harry Dursch	Boeing Defense & Space Group
Dr. Hank Babel	McDonnell Douglas
Dr. Alan Tribble	Rockwell International

ABBREVIATIONS, ACRONYMS, AND SYMBOLS

Å	Angstrom
Al	Aluminum
AL	Anomalously Large
AO	Atomic Oxygen
A*p*	Geomagnetic Activity Index (daily)
a*p*	Geomagnetic Activity Iindex (3-hourly)
AR	Anti-reflectance
ASTM	American Society for Testing Materials
AXAF	Advanced X-Ray Astrophysics Facility
BOL	Beginning of Life
BRDF	Bi-directional Reflection Distribution Function
C	Centigrade
CAA	Chromic Acid Anodize
CERES	Cloud and the Earth's Radiant Energy System
CLEO	Circular Low Earth Orbit
CN	Cumulative Number
cm	Centimeter
CTE	Coefficient of Thermal Expansion
CVCM	Collectible Volatile Condensable Material
DHW	Double Halfwave
DoD	Department of Defense
DSP	Defense Support Program
DSCS	Defense Satellite Communications System
EDAC	Error detection and correction
EECC	Environmental Exposure Control Canister
EIS	Experiment Initiate System
EMI	Electromagnetic Interference
EPDM	Ethylene Propylene Diene Monomer
ESCA	Electron Spectroscopy for Chemical Analysis
ESD	Electro Static Discharge
ESH	Equivalent Sun Hours
EO	Electro-optical
EOS	Earth Orbiting Satellite
EOL	End-of-Life
EPDS	Experiment Power & Data System
ESA	European Space Agency
EURECA	European Retrievable Carrier
EUV	Extreme ultraviolet

eV	Electron Volt
$F_{10.7}$	10.7 Centimeter Solar Radio Noise Flux
°F	Fahrenheit
FEP	Fluorinated Ethylene Propylene
FEWS	Follow-on Early Warning Satellite
FRECOPA	FREnch COoperative Passive Payload
FTIR	Fourier Transform Infrared
g	gram
GCR	Galactic Cosmic Ray
GEO	Geosynchronous Orbit
GeV	Ggaelectron Volt
Ghz	Gigahertz
GPS	Global Positioning System
GSFC	Goddard Space Flight Center
HEO	Highly Elliptical Orbit
HSLA	High Strength Low Alloy
HVI	Hypervelocity Impact
Hz	Hertz
IBEX	Ion Beam Textured and Coated Surfaces Experiment
IDE	Interplanetary Dust Experiment
IR	Infrared
Isc	Short-Circuit Current
ITO	Indium-Tin Oxide
I-V	Current-Voltage
JPL	Jet Propulsion Laboratory
JSC	Johnson Space Center
K	Kelvin
KeV	Kiloelectron volt
kg	Kilogram
kHz	KiloHertz
km	Kilometer
KSC	Kennedy Space Center
LaRC	Langley Research Center
LMSC	Lockheed Missiles & Space Company
LDEF	Long Duration Exposure Facility
LEO	low Earth orbit
LeRC	Lewis Research Center

LSI	Large-scale integration
m	Meter
MEO	Medium Earth Orbit
MeV	Megaelectron Volt
Mhz	Megahertz
MIL-STD	Military Standard
MLI	Multilayer Insulation
MDSSC	McDonnell Douglas Space Systems Company
mm	Millimeter
M/OD	Micrometeoroids/Orbital Debris
MSFC	Marshall Space Flight Center
MTM	Magnetic Tape Module
mV	Millivolt
MW	Megawatt
NASA	National Aeronautics and Space Administration
nm	Nanometer
OCLI	Optical Coating Laboratory, Inc.
OSO-H	Orbiting Solar Observatory
OSR	Optical Solar Reflector
PL	Phillips Laboratory
Pmp	Maximum Power Point
PTFE	Polytetrafluoroethylene
QCM	Quartz Crystal Microbalances
RCC	Removable Cassette Container
R_e	Earth radii
rf	Radio Frequency
RMS	Remote Manipulator System
SAEF-2	Spacecraft Assembly and Encapsulation Facility - 2
SAMPLE	Solar Array Materials Passive LDEF Exposure
sec	Second
SEM	Scanning Electron Microscopy
SEU	Single Event Upset
SEL	Single Event Latchup
SIG	Special Investigation Group
SMM	Solar Maximum Mission
SPENV	Space Environment
SAA	Sulfuric Acid Anodize
SSF	Space Station Freedom

SSM	Second Surface Mirror
SSN	Sunspot Number
TCSE	Thermal Control Surfaces Experiment
TML	Total Mass Loss
TOMS	Total Ozone Mapping System
TRMM	Tropical Rainfall Measuring Mission
UHCRE	High Resolution Study of Ultra-Heavy Cosmic Ray Nuclei
ULE	Ultra Low Expansion
UV	Ultraviolet
UTIAS	University of Toronto Institute for Aerospace Studies
UTRC	United Technologies Research Center
VDA	Vapor Deposited Aluminum
VLSID	Very Large-Scale Integrated Device
Voc	Open Circuit Voltage
ZOT	Zinc Orthotitanate
α	absorptivity
ε	emissivity
μ	micron, micrometer
λ	wavelengths

TABLE OF CONTENTS

PART 1

PART 2*

*Published under separate cover.

1. INTRODUCTION

1.1 SCOPE OF MATERIALS SELECTION GUIDE

1.1.1 Objectives

The main objective of this "Space Environmental Effects on Spacecraft: LEO Materials Selection Guide" is to provide a decision tool to spacecraft designers for their use in the design of low Earth orbit spacecraft and structures. This guide provides critical performance properties on the major spacecraft materials and spacecraft subsystems that have been exposed to the space environment. Spacecraft materials include metals, polymers, advanced composites, white and black paints, thermal control blankets, adhesives, and lubricants. Spacecraft subsystems include optical components, solar cells, batteries, and electronics.

The information found within this guide is a compilation of LEO space flight experiment results as well as ground simulation LEO space experiments results. Data have been compiled from short-term space flight experiments (e.g., 40 hours) that include Space Shuttle flights (e.g., STS-5, STS-8, STS-46) and from retrieved satellites of longer mission durations (e.g., Long Duration Exposure Facility, Solar Maximum Mission). Major space environment effects include atomic oxygen, ultraviolet radiation, micrometeoroids and debris, and contamination. Understanding of the environmental parameters has been expanded to include synergistic effects that were not widely known outside the research laboratories. For example, atomic oxygen flux and ultraviolet radiation interact in the degradation of silver/Teflon materials.

Hence, this guide identifies the critical space environmental effect parameters that will affect the performance of materials and components in the LEO space environment, e.g., dimensional changes resulting from composites' moisture outgassing, surface optical performance property changes due to AO/UV exposures, mechanical property degradation of composites due to AO-induced surface erosion. This knowledge is needed by designers for materials selection decisions and spacecraft components design considering the particular orbital mission.

Finally, this guide compares the space environmental effects on materials between the short-term and long-term flight experiments. Where applicable, predictions are provided that a spacecraft designer can use to determine the effects of the space environment on material properties for longer mission durations.

1.1.2 Design Data

The aim of this guide is to assist the spacecraft design engineer by providing materials performance properties relevant to spacecraft design. Performance properties are provided for the major spacecraft material classes. For example, a basic material property for polymers and advanced composites is the (AO) reaction efficiency, which is defined as the volume loss per oxygen atom (cm^3/AO). The reaction efficiency characterizes the rate of material recession in the presence of the AO flux. The total mass loss is generally in linear proportion to the total AO fluence. For some materials, such as FEP Teflon film, the relationship is nonlinear due to anticipated AO/UV synergistic interactions. Other performance properties for spacecraft design include thermo-optical properties (e.g., solar absorptance, thermal emittance) and dimensional changes due to outgassing and thermal cycling effects. Where appropriate, rules of thumbs governing the relationships between the low Earth orbit space environment and the attendant material/system effects (e.g., linear reactivity of polymers with atomic oxygen fluence, 1% change in absorptance coefficient per 100 Å molecular film deposition) are identified.

The information within the guide can be classified in terms of its relevance in the design process. In terms of decreasing design utility the following three categories are identified:

- Engineering design values typically used in the design of LEO spacecraft structures. These data are based on at least a statistical number of samples with error of margins. Examples of thi type of design information include the surface recession of silver Teflon as a function of atomic oxygen fluence and mission duration, the end-of-life absorptance values of thermal control paints, and dimensional changes in spacecraft structures due to moisture desorption.

- Comparative information for material selection and conducting material tradeoff analysis. Examples of this type of information, which can be found throughout the design guide, include selection of thermal control materials for radiators and blankets and protective coatings for structural components and solar arrays.

- Finally, information that establish the flight heritage of materials (e.g., accept/reject criteria for risk-adverse program managers) are available. Examples of this type of information include the use of lubricants, rubber seals, and adhesives.

In addition to providing a design tool that identifies materials suitable for use in the natural space environment, this guide can also be used to avoid materials that are likely to be vulnerable to one or more of the natural space environment components. Hence, this guide also identifies

gaps in present day knowledge of space environment effects on promising materials (e.g., photochemical deposition of contamination) so that these gaps can be filled in a timely manner.

1.1.3 Organization of Materials Selection Guide

The organization of the materials selection guide is based on major material groups with cross references to the relevant space environment degradation factors (i.e., atomic oxygen, radiation, micrometeoroid and debris) and where appropriate to the relevant spacecraft subsystems.[a] Hence, this guide presents the data and experience learned from the materials flight experiments in one volume.

The guide is divided into the following fourteen chapters:

Chapter One presents a brief overview of the space environment from near Earth to geosynchronous-altitude, and its potential effects on materials. Most of the information on the space environment in this chapter are from the references, "Introduction to the Space Environment,"[1] NASA TM 4527,[2] and a TRW internal document.[3] Emphasis is placed on understanding the potential effects of the different space environment components on the spacecraft. This information is important in understanding the observations in the space flight and ground simulation experiments and in extrapolating the results to spacecraft designs for other orbits. This chapter also presents a summary of the major LEO space flight experiments, including their objectives and space environment exposure conditions.

Chapter Two provides a more detailed discussion of the LEO space environment effects on materials as well as design guidelines for evaluating and selecting materials. The chapter is categorized by the major environment components and effects, such as atomic oxygen, ultraviolet radiation, micrometeoroid and debris impact, thermal cycling, vacuum-induced outgassing, contamination, and environmental synergistic effects.

Chapter Three provides a detailed discussion of space effects on advanced composites materials.

Chapter Four provides a detailed discussion of space effects on polymer materials.

---

[a] Based on an questionnaire sent to experts in the space environmental effects on materials community, it was apparent that the design guide should be categorized along major materials groups and cross-referenced to the space environment degradation factors. The survey also identified the types of information that would be most useful from a designer's perspective. In order of importance these are: flight heritage; ground simulation experiments; followed by cost and manufacturability.

Chapter Five provides a detailed discussion of space effects on adhesives.

Chapter Six provides a detailed discussion of space effects on metals.

Chapter Seven provides a detailed discussion of space effects on ceramics.

Chapter Eight provides a limited discussion of space effects on protective coatings materials for polymers.

Chapter Nine provides a detailed discussion of space effects on lubricants, greases, and seals.

Chapter Ten provides a detailed discussion of space effects on thermal control materials, including white and black paints, thermal control blankets, aluminum surface coatings, and optical solar reflectors.

Chapter Eleven provides a detailed discussion of space effects on power systems.

Chapter Twelve provides a detailed discussion of space effects on optical components.

Chapter Thirteen provides a discussic of past flight experiments results on the space environment effects on electronic systems.

Chapter Fourteen provides examples of applying the information contained within this design guide for designing components and conducting materials tradeoff studies for future spacecraft missions (e.g., International Space Station Alpha, TRMM, CERES).

1.1.4 Space Environmental Effects Data Bases

This guide identifies design considerations for materials and critical space environmental effects parameters that affect the performance of materials exposed to the space environment. Hence, this guide expands the various data base systems that are already available to the spacecraft materials and design engineers, while extracting information from these same data bases. These data base systems augment this guide with space environmental effects information (e.g., outgassing characteristics) as well as materials and processes information. A short description for some of the data base systems are provided below.

MAPTIS. The Materials and Processes Technical Information System (MAPTIS) is a NASA-sponsored, automated storage, retrieval and display data base system. It provides comprehensive materials and processes information. It also contains a comprehensive data base covering the materials results from LDEF. MAPTIS uses an Oracle Corporation's Relational Data Base Management System and can be accessed via a modem and a 1-800 phone number or via Telnet. A user and operations guide for the MAPTIS is available.[4]

M/VISION®. The **M/VISION®** version of the LDEF Materials Data Base requires the user to have more sophisticated hardware and software, allowing the user to manipulate and analyze the data. Once the **M/VISION®** version of the data base is transferred to the user's local machine, the data base requires only local access by the user and is available to any local networked X device. The user can incorporate in-house data or data from other sources into the data base. The **M/VISION®** version of the LDEF Materials Data Base are available at no charge.

Boeing Mini-Data Bases. The Boeing Defense and Space Group, under contract to the SSIG and MSIG, has developed a series of data bases containing results from LDEF. These data bases were developed to provide the user community with early access to LDEF data. The data bases were developed for use with PC and Mac versions of the Claris Corporation's Filemaker Pro software. Filemaker Pro is a flat file data base which allows the user to retrieve multiple data types such as tabular data, test, graphs, diagrams, and/or picture files. The data bases' simple interface allows for easy use by novice users.

The mini-data bases cover optical materials, silverized Teflon thermal blankets, treated aluminum hardware and thermal control paints that flown on or as part of LDEF, and the LDEF environments. The Optical Materials Data Base is a compilation of the results on the optical materials flown on LDEF and was originally developed by the SSIG. The Silverized Teflon Thermal Blankets Data Base covers the results from the silverized Teflon thermal blankets utilized

on LDEF. The Treated Aluminum Hardware Data Base is a compilation of data from the various types of aluminum hardware flown on LDEF including different alloys, surface conditions, etc. The Thermal Control Paints Data Base contains information on the wide variety of paints flown on LDEF. The LDEF Environments Data Base contains information on the environment that LDEF was exposed to, including thermal profiles, solar UV irradiation, and AO exposure levels.

LDEF Archive System. The Long Duration Exposure Facility (LDEF) Archive System is designed to provide spacecraft designers and space environment researchers single point access to all available resources from LDEF. These include data, micrographs, photographs, technical reports, papers, hardware and test specimens, as well as technical expertise.

The LDEF Archive System is comprised of two parts. The first part is the physical contents of the archive, including space flight and ground control hardware, documentation, data, photographs and publications. The second part is the electronic on-line system. It is available to users via the Internet. It contains data files, both numerical and graphical image files, micrograph and photograph image files, technical report abstracts and full text files. The elements of both components of the LDEF Archive System, physical and electronic, are categorized as follows: project/mission documentation; experiment documentation; hardware; data/analysis; photographs; and publication. Data are categorized according to environments and effects: ionizing radiation; meteoroids and debris; contamination; thermal and solar; materials and processes; and systems.

The LDEF Archive is a distributed system, and both physical and electronic segments are maintained at a host of locations. The LDEF On-line Archive System has been established on a UNIX workstation at NASA LaRC, and it is accessible via Internet. The LDEF Archive System's capability to reach out to other data systems is achieved through the use of an Internet information service referred to as the World Wide Web (WWW), which uses hypertext, text that may be expanded to provide links to other text. The LDEF Archive utilizes Mosaic from the National Center for Supercomputing Applications (NCSA) as the WWW client, although other WWW browsers are available.

Other Data Bases. Two special investigation groups data bases are accessible directly from the LDEF Archive System by using the capabilities of the Mosaic browser and the Wide World Web (WWW) server. These are the Meteoroids and Debris Special Investigation Group Data Base at NASA JSC, and the LDEF Materials Data Base at NASA MSFC. The Technical University of Munich has developed hypermedia data bases using NCSA Mosaic. They include data, micrographs, photographs, publications and other items relative to LDEF experiments AO187-1, AO187-2, AO201 and S1003. These data bases are accessible through the LDEF

Archive System. Also as part of Materials and Systems SIG activities, Aerospace Corporation's M0003 Deintegration Data Base is available for use with Fourth Dimension and Paradox software.

1.1.5 Publication Resources

The information reported in the guide is a compilation of both the space flight experimental results and the ground-simulation space environmental effects experiments published by major government and industry organizations as well as by individual experimenters. Important data resources for this guide are listed below, as well as being referenced in the text.

Space Flight Experiments

J. Visentine, ed., "Atomic Oxygen Effects Measurements for Shuttle Missions STS-8 and 41-G," vols. I-III, NASA Technical Memorandum 100459, September 1988.

Satellite Servicing Project Goddard Space Flight Center, "Proceedings of the SMRM Degradation Study Workshop," NASA-TM-89274, May 1985.

L.A. Teichman and B.A. Stein, compilers, "NASA/SDIO Space Environmental Effects Workshop, NASA CP 3035, 1988.

J.W. Haffner et al, "Natural Environmental Effects on SDI Spacecraft Surface Materials," Rockwell International, Report No. AFGL-TR-89-0084, Air Force Geophysical Laboratory, May 20, 1989.

A.C. Tribble, R. Lukins, and E. Watts, "Low Earth Orbit Thermal Control Coatings Exposure Flight Tests: A Comparison of U.S. and Russian Results," NASA Contract NAS1-19243, Task 16, Rockwell International Space Systems Division, August 1994.

S.Y. Chung et al., "Flight- and Ground-Test Correlation Study of BMDO SDS Materials: Phase I Report," JPL Publication 93-31, 1993.

LDEF Flight Experiments

A.S. Levine, ed., "LDEF First Post-Retrieval Symposium," NASA CP-3134, 1991.

A.S. Levine, ed., "LDEF Second Post-Retrieval Symposium," NASA CP-3194, 1993.

A.S. Levine, ed., "LDEF Third Post-Retrieval Symposium," in press.

B.A. Stein and P.R. Young, eds., "LDEF Materials Workshop '91, NASA CP-3162, 1992.

A.F. Whitaker, ed., "LDEF Materials Results for Spacecraft Applications," NASA CP-3257, 1994.

H. Dursch, ed., "Analysis of Systems Hardware Flown on LDEF-Results of the Systems Special Investigation Group," NASA Contractor Report 189628, Contract NAS-19247, April, 1992.

H.W. Dursch, B.K. Keough, and H.G. Pippin, "Evaluation of Seals and Lubricants Used on the Long Duration Exposure Facility," NASA CR 4604, June 1994.

H.A. Smith, K.M. Nelson, D. Eash, and H.G. Pippin, "Analysis of Selected Materials Flown on Interior Locations of the Long Duration Exposure Facility, NASA CR 4586, April 1994.

W.L. Plagemann, "Space Environmental Effects on the Integrity of Chromic Acid Anodized Coatings, NASA CR 191468, May 1993.

J.L. Golden, "Results of Examination of LDEF Polyurethane Thermal Control Coatings," NASA CR 4617, July 1994.

D. R. Wilkes and L.L. Hummer, "Thermal Control Surfaces Experiment Initial Flight Data Analysis," Final Report, AZ Technology Report No. 90-1-100-2, June 1991.

P. George, H.W. Dursch, and H.G. Pippin, "Composite Materials Flown on the Long Duration Exposure Facility, NASA CR–4657, April 1995.

H.G. Pippin and R.J. Bourassa, "Performance of Metals Flown on the Long Duration Exposure Facility, NASA CR–4662, April 1995.

H.G. Pippin, "Analysis of Silverized Teflon Thermal Control Material Flown on the Long Duration Exposure Facility, NASA CR–4663, April 1995.

H.W. Dursch, B.K. Keough, and H.G. Pippin, "Evaluation of Adhesive Materials Used on the Long Duration Exposure Facility," NASA CR–4646, March 1995.

H.G. Pippin and J.R. Gillis, "Analysis of Materials Flown on the Long Duration Exposure Facility: Summary of Results of the Materials Special Investigation Group," NASA CR–4664, April 1995.

Space Environment

T.F. Tascione, "Introduction to the Space Environment," Orbit Book Company, Malabar, Florida, 1988.

B. J. Anderson, Ed., R.E. Smith, Compiler, "Natural Orbital Environment Guidelines for Use in Aerospace Vehicle Development," NASA TM 4527, June 1994.

LDEF Data Bases

J.G. Funk, J.W. Strickland, and J.M. Davis, "Materials and Processes Technical Information System (MAPTIS)," LDEF Second Post-Retrieval Symposium, NASA CP-3194, 1993, pp. 1201-1222.

G. Bohnhoff-Hlavacek, "Data Bases for LDEF Results," LDEF Second Post-Retrieval Symposium, NASA CP-3194, 1993, pp. 1223-1234.

Micrometeoroid and Debris Effects

T. See et al., "Meteoroid and Debris Impact Features Documented on the Long Duration Exposure Facility," NASA JSC Publication #84, JSC #24608, August 1990.

M.J. Meshishnek et al., "Long Duration Exposure Facility Experiment M0003 Meteoroid and Debris Survey," LDEF Second Post-Retrieval Symposium, NASA CP 3194, 1993, pp. 357-415.

M. Allbrooks and D. Atkinson, "The Magnitude of Impact Damage on LDEF Materials," NASA Contractor Report CR 188258, July 1992.

Atomic Oxygen Effects

J. Visentine, ed., "Atomic Oxygen Effects Measurements for Shuttle Missions STS-8 and 41-G," NASA Technical Memorandum 100459, vols. I-III, September 1988.

J.T. Visentine and A.F. Whitaker, "Material Selection Guidelines to Limit Atomic Oxygen Effects on Spacecraft Surfaces," NASA TM-100351, February 1989.

L.J. Leger, "Oxygen Atom Reaction with Shuttle Materials at Orbital Altitudes - Data and Experiment Status," AIAA Paper 83-0073, Jan. 1983.

D.E. Brinza, ed., "Proceedings of the NASA Workshop on Atomic Oxygen Effects, JPL Publication 87-14, November 1986.

Optical Components

W.T. Kemp et al., "Long Duration Exposure Facility Space Optics Handbook," Air Force Document PL-TN-93-1067, September 1993, pp. 6-12 to 6-14.

M.D. Blue, "Degradation of Optical Materials in Space," NASA Contract Number NAS1-14654, April 1993.

1.1.6 Future Research

As environment effects are obviously very much material and application dependent (e.g., mission orbit, duration) knowledge of the operating space environments is important in drawing conclusions on the environmental effects on materials and in predicting spacecraft subsystem performance. Hence, it would be useful to the designers to integrate the expanding data base of environment effects on spacecraft material properties with environment computation models into a user-friendly software package that asks a few questions at the beginning (e.g., mission specific parameters) and gives a report on the predicted material design properties at the end of the mission lifetime for a specific mission orbit.

In the past five years Maxwell Laboratories, Inc., funded by NASA Lewis, developed and compiled models of environments and of environment interactions on spacecraft components that can be used to extend the laboratory and flight data to new orbits and missions. Over 100 environment models (e.g., orbit generation, neutral environment, debris flux, solar radiation spectrum, nozzle effluents outgassing densities) have been incorporated into an integrated assessment tool called the Environment WorkBench (EWB), representing one quantitative design tool useful to spacecraft designers. Hence, EWB is an intelligent, knowledge-based, desktop, integrated analysis tool that is programmed to integrate environment, system definition, and effects models together to display to the designer the mission lifetime effects of selected environment parameters on spacecraft design features. Although EWB provides the architecture for modeling the complex environmental interactions of a material on a spacecraft, in many cases, the models have not been validated with high quality material data.

A FY95-96 research effort will extend and leverage the results of the current LEO Materials Selection Guide by enhancing the EWB with a material property effects module containing recently developed material properties and space environment and material effects design rules. Data base integration of the relationships between the low-Earth orbit space environment and the attendant material/system effects (i.e., the materials effects module) with existing orbital and environmental models will provide a highly effective tool in the design of specific spacecraft operating in LEO.

1.2 SPACE ENVIRONMENTS

1.2.1 Orbital Definit.

The relative impact of any of the space environment effects on materials depends on the type of mission the spacecraft has to perform (e.g., communication, defense, Earth observing) and more important, the orbit in which the spacecraft is placed. Figure 1-1 shows the variations in the space environment as a function of orbit altitude. Low Earth orbit (LEO) extends up to 1000 km. Mid Earth orbit (MEO) is above 1000 km and extends up to 35,000 km. Geosynchronous orbit (GEO) is ~35,000 km and higher.

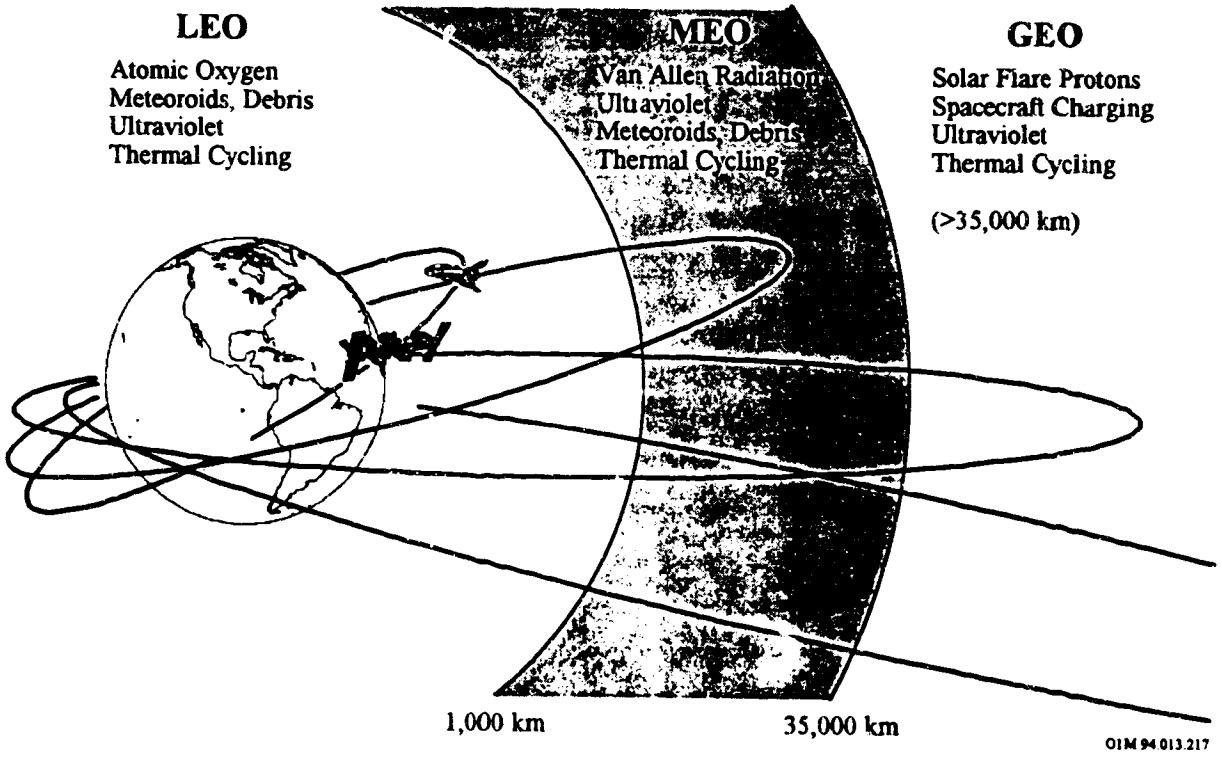

Figure 1- 1. Variation of Space Environments with Altitude

The relative impact of the space environment effects on the ability of a spacecraft to perform its mission is ranked and listed in Table 1-1.[5] This ranking ranges from an impact of 0 (the effects can be ignored) to an impact of 10 (the effects will negate the mission. The effects considered are negating, shortening, or reducing the effectiveness of the mission, as well as permanent (design changes) or transient (upsets) spacecraft changes. Each effect is further subdivided into "will" and "may" categories.

Table 1-2 lists the relative impact of each space environment effect on materials for the different altitudes. The entries range from 9 (the effects of neutral gases, i.e., atomic oxygen exposure on low Earth orbit spacecraft) to 0 (the effects of gravity fields, magnetic fields, the ionosphere, and neutral gases on GEO spacecraft). Also included are the ratings for several spacecrafts at the different altitudes in which they operate (e.g., International Space Station Alpha, EOS, TRMM, GPS, DSCS).

Table 1-1. Relative Ranking of the Space Environment Impact on Mission

Impact	Significance
10	Effects produced will negate the mission
9	Effects produced may negate the mission
8	Effects produced will shorten the mission
7	Effects produced may shorten the mission
6	Effects produced will reduce mission effectiveness
5	Effects produced may reduce mission effectiveness
4	Effects produced will require design changes
3	Effects produced may require design changes
2	Effects produced will cause upsets
1	Effects produced may cause upsets
0	Effects produced can be ignored

Table 1-2. Relative Impact of the Space Environment Effects on Materials for Different Orbits and Satellites

Spacecraft Environment	LEO[1] Low Incl.	LEO High Incl.	MEO[2]	GEO[3]	Int'l Space Station 500 km 51.6° incl	EOS 500 km 28.5° incl	TRMM 600 km 28.5° incl	GPS 20,000km 55° incl	DSCS GEO Classified
Direct Sunlight	4[4]	4	4	4	4	4	4	4	4
Gravity Field	3	3	3	0	3	3	3	0	0
Magnetic Field	3	3	3	0	3	3	3	0	0
Van Allen Belts	0-5	2-5	8-5	1	2-5	2-5	2-5	5	1
Solar flare Particles	0	4	3	5	4	0	0	3	5
Galactic Cosmic Rays	0	4	3	5	4	0	0	3	5
Debris Objects	7	7	3-0	3	7	7	7	0	3
Micrometeoroids	3	3	3	3	3	3	3	3	3
Ionosphere	3	3	1	0	3	3	3	0	0
Hot Plasma	0	3	0	5	0	0	0	3	5
Neutral Gases	9-7	9-7	3-0	0	9-7	9-7	9-7	0	0

(1) Low Earth orbit (LEO) extends up to 1000 km.
(2) Mid Earth orbit (MEO) is above 1000 km and extends up to 35,000 km.
(3) Geosynchronous orbit (GEO) is ~35,000 km and higher.
(4) This ranking, from an imact of 0 (the effects can be ignored) to an impact of 10 (the effects will negate the mission)

1.2.2 Terrestrial Space

This region of space extends from the base of the ionosphere (see below) at about 60 km above the surface of the Earth to the boundary of the magnetosphere beyond which interplanetary space is unaffected by the Earth. This distance is about 95,000 km above the surface of the Earth (16 radii of the Earth (R_E)) in the sunward direction and several times this in the anti-sunward direction. This region is loosely referred to as the magnetosphere, although more strictly speaking, this term means the major part of terrestrial space into which the Earth's magnetic field extends. The morphology is roughly axisymmetric within 4 R_E of the Earth's center, but at greater distances it becomes very unsymmetric, with a long tail extending in the anti-sunward direction. The principal regions and their interacting phenomena are described below.

1.2.2.1 Gravity Field

The Earth's gravity field may require spacecraft design changes if the gradient torques impose appreciable requirements on the mechanisms that control the spacecraft attitude (small rocket thrusters, momentum wheels, control moment gyros, magnetic torque rods, etc.). Since these gradient torques decrease inversely with the cube of the distance from the center of the Earth, such design changes are more significant for low and medium-altitude spacecraft.

1.2.2.2 Magnetic Field

The gravitational field results from the mass of the solid Earth and reflects the distribution of that mass. It traps the neutral atmosphere, constrains its motion, and influences the motions of meteoroids and debris. However, it has little effect on the rest of terrestrial space because electrical forces are so much stronger. The magnetic field has two sources: (1) currents inside the Earth that produce about 99 percent of the field at the surface and (2) currents in the magnetosphere. The latter becomes relatively more important beyond a few Earth radii because the internal field decreases as the inverse distance cubed from the Earth's center.

For many purposes, the Earth's field may be regarded as a dipole tilted 11.7° from the rotation axis and offset from the geometric center of the Earth by 430 km in the direction of southeast Asia. Many phenomena are related to magnetic latitude which, as a result of the tilt, is 11.7° greater than geographic latitude in the longitude of eastern North America and 11.7° less on the opposite side of the world. The offset puts the surface of the Earth, or a circular orbit, at a higher altitude with respect to the geomagnetic field in the region of the South Atlantic of the coast of Brazil than it is elsewhere. This region is called the South Atlantic Anomaly. Since both

the tilt and the offset are changing slowly, the South Atlantic Anomaly is drifting slowly to the west.

The Earth's magnetic field provides the mechanism that traps charged particles within specific regions, called the Van Allen belts, about the equator. The trapping regions (both electrons and protons) extend from the geomagnetic equator to about ±50° geomagnetic, but the trapping altitude structure is not discrete. Instead, the trapped particles extend over a range of altitudes with areas of slightly higher average concentration defining the traditional radiation belts. The . .diation belts are approximately azimuthally symmetric, except near the South Atlantic anomaly. The magnetic field strength is lower than normal over the South Atlantic due to the offset of the dipole field geometry (see above), and therefore, the radiation belts reach their lowest altitudes in this area. The impact of such particles on space missions is discussed below.

The Earth's magnetic field will produce torques on current loops and ferromagnetic materials. As with the gravity field, these effects may require design changes in the altitude control systems of LEO and MEO spacecraft.

1.2.3 Neutral Atmosphere

The Earth's neutral atmosphere is vertically differentiated by composition, density, and temperature. Figure 1-2 (ref. 1) shows the temperature gradients[b] of the various atmospheric levels and Figure 1-3[6] shows the major atmospheric constituents at varying altitude levels. For space vehicle operations, the neutral atmosphere is significant because (1) even at its low density, it produces torques and drags on the vehicle: (2) the density height profile of the atmosphere above 100 km altitude modulates the flux of trapped radiation encountered and the orbital debris; and (3) the atomic oxygen both erodes and chemically changes those surfaces which are exposed to it.

1.2.3.1 Atmospheric Temperatures

The region of the Earth's atmosphere lying between about 90 and 500 km is known as the thermosphere, while that region lying above 500 km is known as the exosphere. The temperature in the lower thermosphere increases rapidly with increasing altitude from a minimum at 90 km towards a value dependent on the level of solar activity (see Figure 1-2). Eventually it becomes altitude independent at upper thermospheric altitudes. The heterosphere is primarily heated by the thermospheric gases (i.e., atomic oxygen), which absorbs solar extreme ultraviolet (EUV) with wavelength of 1000 to 2000 Å. At the lowest thermospheric altitudes, the absorption of ultraviolet (UV) radiation is also important. An additional heat source for the thermosphere is the interaction of the Earth's magnetic field at very great distances (several Earth radii), in the region known as the magnetopause, with the solar wind. The solar wind is a stream of high speed plasma emanating from the Sun. This interaction causes energetic particles to penetrate down into the lower thermosphere at high geographic latitudes and directly heat the thermospheric gas. These energetic particles are also responsible for the aurora seen at these high latitudes.

---

[b] This is kinetic temperature, not sensible temperature.

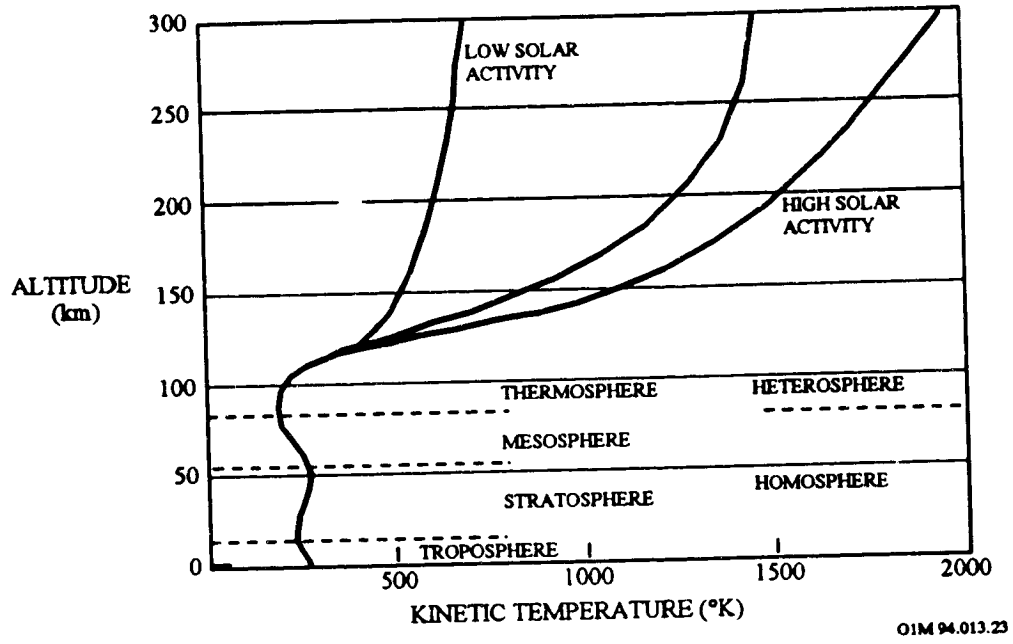

Figure 1- 2. Temperature Gradients of the Atmosphere

1.2.3.2 Atmospheric Constituents

The homosphere, which makes up the lower 50 km of the atmosphere, is composed of ~78% molecular nitrogen, ~21% molecular oxygen, and ~1% argon, with variable concentrations of such gases as carbon dioxide and water vapor. Within this region the atmosphere is well mixed by turbulence, so that the composition of the atmosphere does not vary with altitude. The heterosphere, which extends upward to 500 km, is composed of molecular nitrogen, molecular oxygen, atomic oxygen, argon, helium, and atomic hydrogen. Within this region, diffusion becomes so rapid that the altitude variation of the various species becomes dependent on molecular mass, with the result that composition varies with altitude. Thus, the number densities of the heavier thermospheric species (N_2 and O_2) decrease with increasing altitude much faster than those of the lighter species (H and He). This means that the heavier molecular species predominate in the lower heterosphere, while the lighter atomic species predominate in the upper heterosphere. A typical altitude profile for the individual constituents is shown in Figure 1-3.

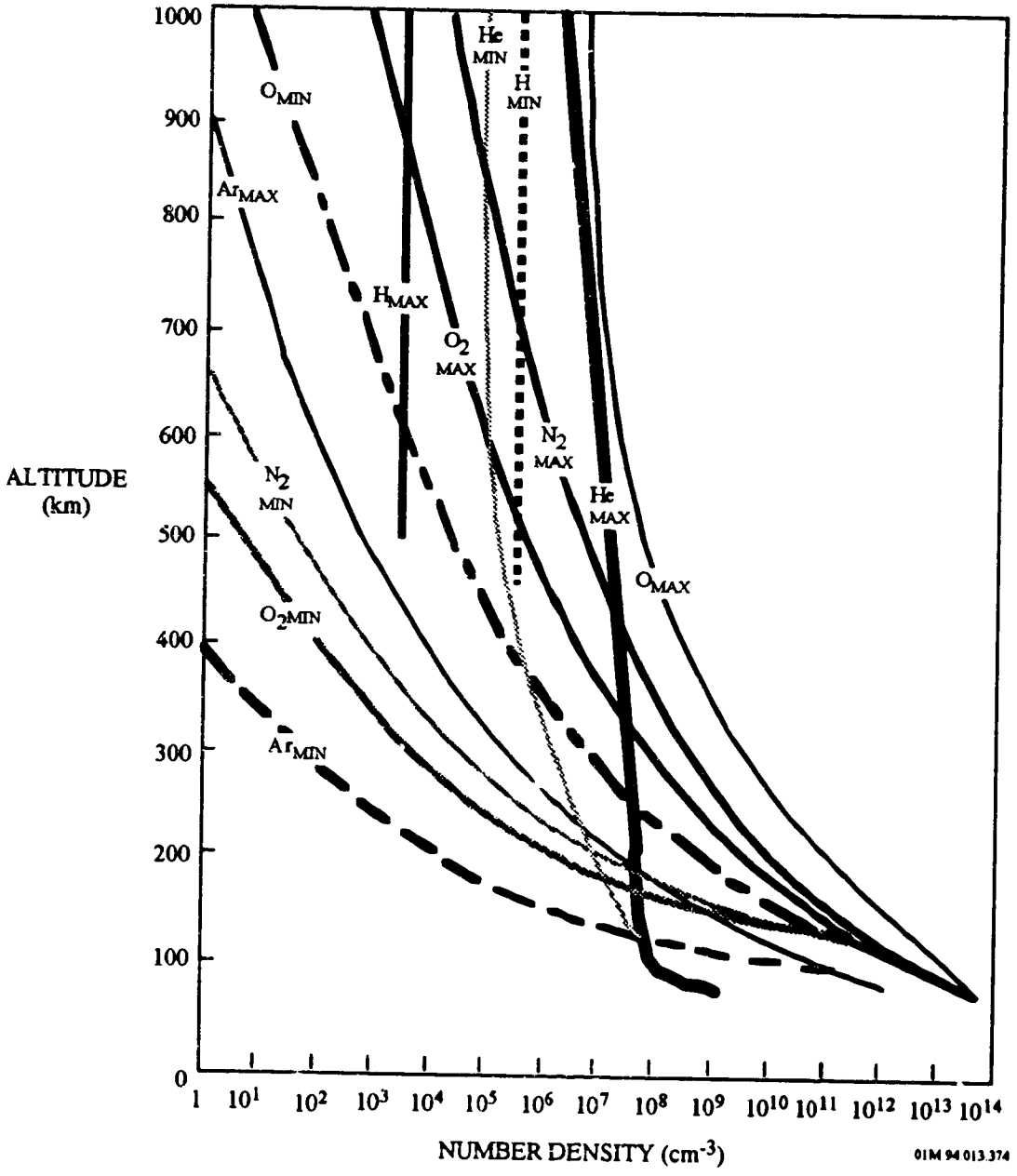

Figure 1- 3. Number Density of Atmospheric Constituents versus Altitude

1.2.3.3 Atmospheric Variations

The atmospheric density at high altitudes changes in response to many factors including local time, latitude, altitude, and level of solar activity and geometric activity. The short wavelength solar electromagnetic radiation (EUV and UV) changes substantially with the overall level of solar activity (i.e., sunspot number), and this variability translate into a variation of energy available to the thermosphere.[c] The result is that the thermospheric density, especially at orbital altitudes, is strongly dependent on the level of solar activity. The amount of solar radiation depends on the 27 day rotation period of the Sun and the 22 year solar cycle. Of the total solar energy absorbed in the atmosphere, about one-third is used to heat the ambient neutral particle, nearly half is radiated away as atmospheric ultraviolet airglow, and the remainder is available for atomic oxygen chemistry (above 80 km solar ultraviolet radiation is efficient in the photodissociation of molecular oxygen into atomic oxygen).

Atmospheric density variations are also related with geomagnetic activity. When a geomagnetic storm occurs, large numbers of charged particles are dumped from the magnetosphere into the high latitude atmosphere. These particles ionize and heat the high latitude atmosphere by collisions, with the heating first observed several hours (1 to 10) after the geomagnetic disturbance begins. The effects of geomagnetic heating extend from at least 300 km to over 1000 km and may persist for 8 to 12 hours following the end of the magnetic disturbance.

1.2.3.4 Solar and Geomagnetic Indices

Various surrogate indices are used to quantitatively assess the levels of solar activity. One of these is the 10.7 cm (2800 Mhz) solar radio noise flux, designated $F_{10.7}$. Although it is the EUV radiation that heats the thermosphere, it cannot be measured at the ground. The $F_{10.7}$ can be measured from the ground, and it also correlates quite well with the EUV radiation

An index that is used as a measure of episodic type solar activity is the planetary geomagnetic activity index a_p. It is based on magnetic field fluctuation data reported every 3 h at 12 stations between geomagnetic latitudes 48° and 63° and selected for good longitudinal coverage. Although it is the high latitude ionospheric current fluctuations that drive the magnetic field fluctuations as observed at these stations, it is not the magnetic field fluctuations which are driving the thermosphere. Therefore, the correlations between observed density changes and the a_p index

---

[c] Little EUV radiation reaches the ground, and direct EUV flux observations have been made only rarely. However, one can infer the value of the variable EUV flux based on the 2800 MHz solar radio flux (better known as the 10.7 centimeter flux) because EUV and 2800 MHz fluxes show a fairly good correlation.

are not always good. The daily planetary geomagnetic index, A_p, is the average of the eight 3-hourly a_p values for that particular day.

Figures 1-4 and 1-5 (ref. 2) show the maximum, mean, and minimum values for $F_{10.7}$ and A_p throughout a mean 22-year solar cycle.[7] The $F_{10.7}$ data are derived from sunspot records for the period 1749 to 1947 with direct $F_{10.7}$ measurements thereafter. The standard deviation about the mean length is 1.23 years in the historical record. Max and min are the historical extremes for each point in the cycle and have been determined after the data have been 13-month smoothed and constrained to the mean duration cycle. The exact level of solar activity cannot be predicted very accurately, although the phase within the 22-year period can be established. The A_p values are derived in a similar fashion based on a data record that goes back to 1932.

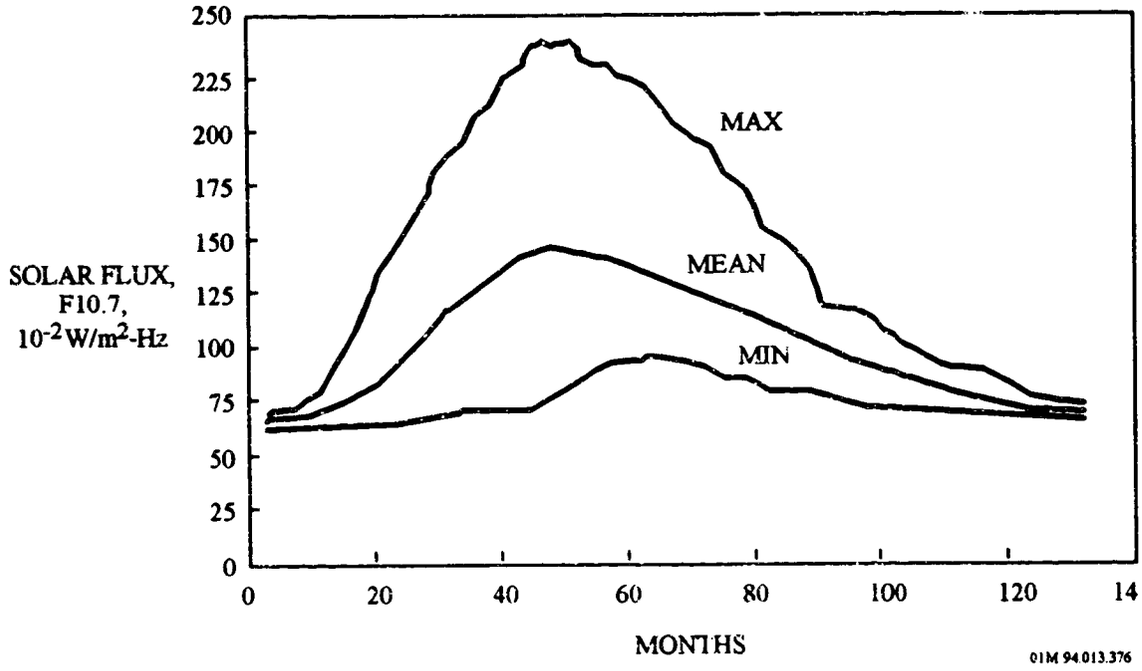

Figure 1- 4. $F_{10.7}$ Values Over the Mean Solar Cycle

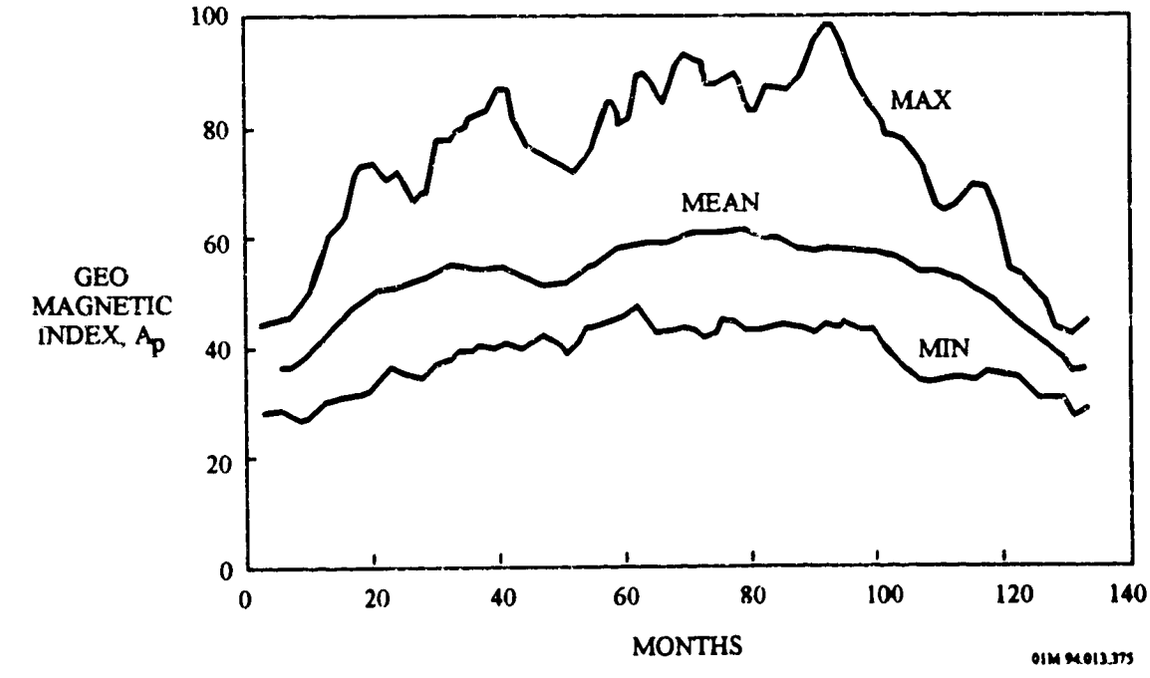

Figure 1- 5. Geomagnetic Activity Index (A_p) Over the Mean Solar Cycle.

1.2.3.5 Spacecraft-Neutral Atmosphere Interactions

Neutral gases, especially atomic oxygen will primarily affect LEO spacecraft. The erosion effects of atomic oxygen may shorten the duration of a LEO spacecraft mission, so careful choices of surface ram-facing materials is definitely required. Until more is known about the glow phenomenon, which can blind an optical sensor, LEO spacecraft may not be able to perform its mission. Hence, the effects of neutral gases (above and beyond the known drag and torques produced) on the long-term erosion rates in materials must be considered as potentially mission-threatening for LEO spacecraft.

1.2.4 Electromagnetic Radiation

1.2.4.1 Solar Electromagnetic Radiation

The wavelength range of solar ultraviolet (UV) radiation present in LEO is between approximately 0.1 and 0.4 μm which is a small portion of the solar irradiance curve shown in Figure 1-6.[8] The total energy provided by radiation in this wavelength range is approximately 8% of the solar constant, where the solar constant is defined as the total energy provided by the sun over all wavelengths up 1000 μm and is equal to 136.7 mW/cm^2.

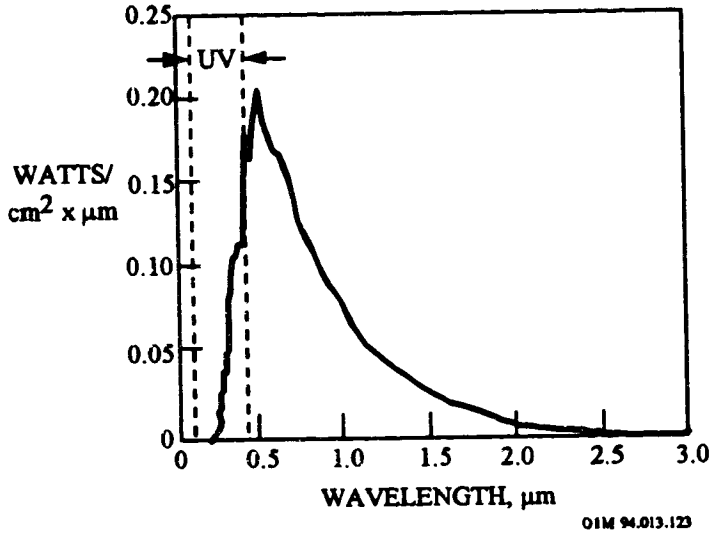

Figure 1- 6. Solar Spectrum At Air Mass Zero

1.2.4.2 Spacecraft-UV Radiation Interactions

The UV portion (0.1 μm < λ < 0.4 μm) of the electromagnetic spectrum is of particular importance in determining the effects of solar radiation on material properties. This ultraviolet radiation is energetic enough to cause the breaking of organic bonds as shown in Figure 1-7 (ref. 8). Although the solar radiation below 0.2 μm represents less than 0.001% of the solar constant, its presence may promote breakage of important organic structural bonds, such as C-C and C-O, and functional groups.

Solar ultraviolet irradiation can lead to crosslinking of polymer surfaces which may lead to embrittlement and possibly to surface cracking. UV radiation has also been shown to degrade mechanical properties of polymeric materials as is shown in the degradation in the tensile strength of Mylar. Because atomic oxygen is present in LEO, it is expected that the reaction intermediates

from the photon absorption will react with reaction intermediates from the oxidation process. This photo-oxidation can lead to discoloration and reduced transparency of some polymers. Chemical changes in the molecule as a result of these reactions may also lead to the formation of polar groups which may affect electrical properties.[9]

A high value of solar transmittance ($\alpha \leq 0.09$; see page 10-115) in the wavelength range between 0.3 and 0.6 μm is necessary for polymer use as second surface reflectors (e.g., metallic-coated Teflon (FEP) tapes) in thermal control applications. Ultraviolet radiation degradation of this transmittance may result in decreased efficiency of the thermal control surface. As shown by the LDEF results, the effects of sunlight (including UV) on all spacecraft will require careful selection of exposed materials to avoid those materials that change their α_s/ε ratios, optical transparencies or reflectivities, and other properties that affect the thermal behavior of the spacecraft. The abilities of optical transmitters or receivers (sensors) to function can be affected. These material selections are considered to be design changes required by the environment (sunlight in this case).

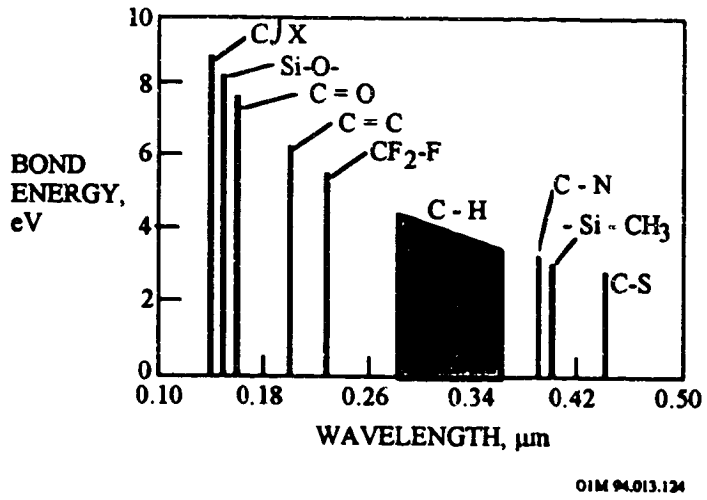

Figure 1- 7. Wavelength Requirement to Break Various Polymeric Material Bonds.

1.2.5 Penetrating Charged Particles

Penetrating charged particles, often referred to as charged-particle radiation, presents a significant challenge to the design and operation of a spacecraft. This is because many of the particles have sufficient energy to penetrate metal and to produce significant levels of ionization inside the spacecraft. It will also affect electronics by causing bit flips in digital microelectronic circuits (referred to as single event upsets (SEUs). In addition, ionizing radiation will affect the propagation of light through optical materials by altering their optical properties.

It is convenient to divide the natural radiation in near Earth space (up to geosynchronous orbit) into two primary components: cosmic radiation and radiation produced by trapped particles (e.g., Van Allen belts). Both of these components are influenced by solar activity and the Earth's magnetic field. Trapped radiation particles are accelerated from thermal, low-energy plasma by processes inside the magnetosphere and occur only within terrestrial space. Cosmic rays exist in interplanetary space and, therefore, enter terrestrial space from outside. Within terrestrial space, the motion of both kinds of charged particles is controlled by the geomagnetic field. Their relative contributions to radiation hazards are most easily understood when considered separately.

1.2.5.2 Trapped Radiation

Trapped radiation or van Allen radiation consists of both electrons and protons. The range of energies is rather large and is centered in the tens of keV for electrons and MeV for protons. The Earth's magnetic field provides the mechanism which traps charged particles within specific regions, called the van Allen belts, about the equator. The trapping regions (both electrons and prtons) extend from the geomagnetic equator to about ±50° geomagentic. The approximate radiation belt distributions for protons and electrons in a meridional plane are shown in Figures 1-8 and 1-9, respectively (ref. 1). The verty steep inner gradient is controlled by the exact altitude dependence of the neutral atmospheric density which varies with solar activity. The atmosphere is more extended (higher density at a given altitude) when the Sun is active. Thus, at 500 km, the trapped proton flux is greater when the Sun is quiet.

The general shape of the van Allen belts follows the shape of the geomagnetic field, except near the South Atlantic anomaly where the magnetic field strength is lower than normal over the South Atlantic because of the dipole field geometry. Hence, the radiation belts reach their lowest altitudes in this area. This means that the most intense radiation is encountered in the South Atlantic Anomaly.

Energetic protons trapped in the inner Van Allen belt are the major source of radiation for Earth orbiting spacecraft above 500 km, particularly in the South Atlantic anomaly region. The amount of radiation varies with latitude and longitude (the inner belt extends to about 45° latitude). The inner belt proton population is also susceptible to solar-induced variations. Population density varies out of phase with the 22 year solar cycle, so that the inner belt is most inflated during solar minimum. This variation in particle population produces a factor of two variation in radiation dose rate during the solar cycle for low orbiting spacecraft.

The outer Van Allen belt contains both electrons and protons. However, the electrons have much higher number densities and are responsible for most of the radiation dose within this region. The outer belt is asymmetric, with the nightside being elongated and the dayside flattened. Generally, particle energy and outer boundary location vary with the 22 year cycle. During solar maximum, the outer boundary of the electron belt is closer to the Earth and contains higher energy particles. At solar minimum, the outer boundary moves outward and contains fewer energetic electrons. Outer belt electron densities undergo order of magnitude changes over time scales of weeks. These short-term variations can produce significant radiation dose variations and are related to the level of geophysical activity. During, or shortly after, very active periods, the outer belt is inflated with high energy electrons which increase the radiation substantially. Diurnal variations in radiation dose inside a spacecraft (in high-altitude circular orbits) can occur when the trajectory crosses the asymmetric outer electron belt.

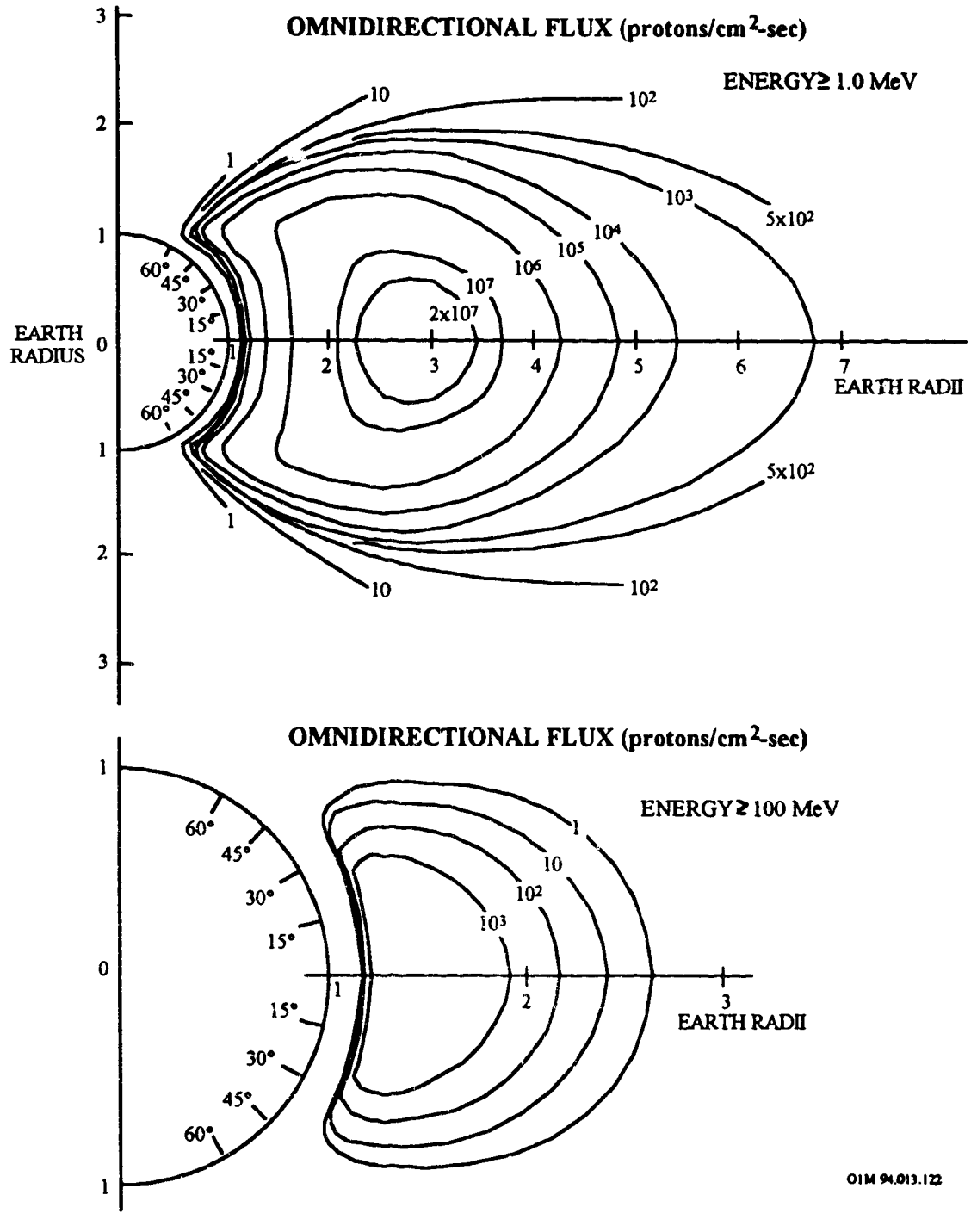

Note:

1 Earth radius = 1 RE = 6370 km; Geostationary orbits are at 6.6 Earth radii.

Figure 1- 8. Distribution of Trapped Protons With Energy Greater than 1 MeV and 100 MeV.

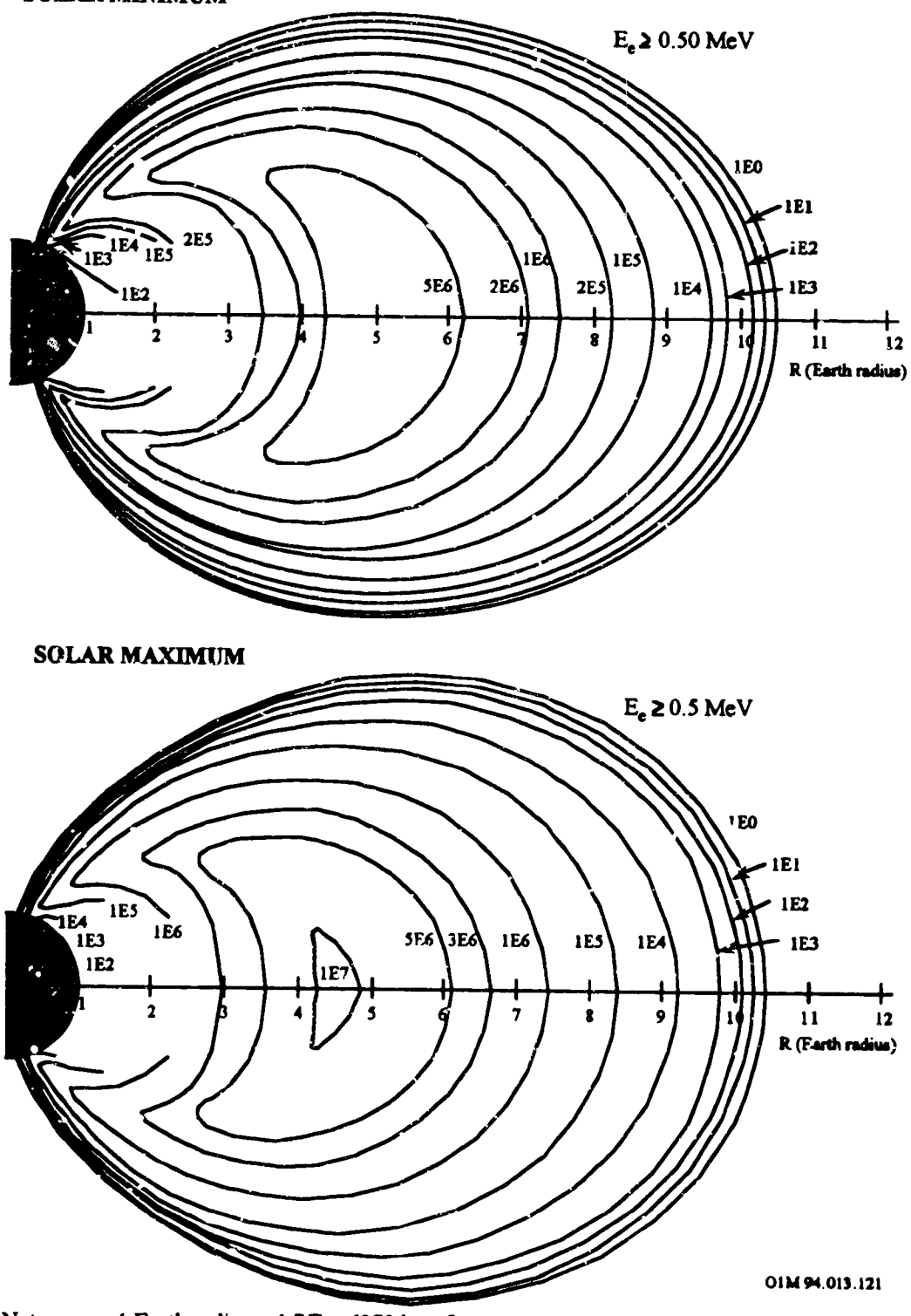

Note: 1 Earth radius = 1 RE = 6370 km; Geostationary orbits are at 6.6 Earth radii.

Note: The notation "E" refers to the power of ten: 1E4 = 1×10^4 cm^{-2} sec^{-1}, etc.

Figure 1- 9. Distribution of Trapped Electrons During Solar Minimum and Maximum with Energy Greater Than 0.5 MeV.

1.2.5.2 Cosmic Rays

Cosmic rays applies to electrons, protons, and the nuclei of all elements. The source of cosmic rays is either galactic or solar. Galactic cosmic rays (GCRs) originate outside the solar system and permeate our galaxy. Solar particle events, in contrast, originate in the Sun and are produced in solar flares. They are lower in energy than GCRs (1 MeV to 1 GeV/nucleon) and are mostly protons and alpha particles.

1.2.5.2.1 Galactic Cosmic Rays

GCRs consist of the nuclei of the elements plus about 2 percent which are electrons. Their energies cover the range from below 10 MeV per particle to above 10^{16} MeV per particle. Emitted by distant stars and even more distant galaxies, they diffuse through space and arrive at Earth from all directions. Hence, GCRs consist of the nuclei of the elements from hydrogen through iron in roughly the same proportions as are found in the solar system, but with the heavier nuclei more abundant in the cosmic rays. Figure 1-10 gives the relative abundances and energy spectra of GCRs of interest (ref. 2). In spite of their small number, the heavy elements are very important due to their densely ionizing tracks. They are responsible for many effects in detectors and microelectroncis. From Figure 1-10, it can be seen that the flux of each nuclear specie decreases rapidly with increasing energy. The lowest energies are observed outside the magnetosphere, where the flux is limited by magnetic fields carried by the solar wind. The energies observed and the flux at these energies vary ivnersely with the solar cycle (see below).

Spatial variations in GCR flux (and therefore GCR related radiation) are produced by variations in source location, the Earth's magnetic field, atmospheric shielding, and with increasing altitude. Particle flux is also larger over the polar regions where "open" geomagnetic field lines allow easier access. The Earth's magnetic field deflects incoming cosmic rays (solar and galactic) to a degree which depends on the energy of the particles, preventing those with lower energies from penetrating deep into the magnetosphere. The most important temporal variation influx is associated with the 22 year solar cycle. During solar maximum, when the interplanetary magnetic field strength is greatest, cosmic ray particles are scattered away from the Earth. This produces a GCR flux minimum. Conversely, GCR flux is largest during solar minimum. The 22 year solar cycle produces a factor of three or more variations in the cosmic ray dose at a geosynchronous orbit. Low-altitude, low-inclination orbits would experience smaller dose variations due to the strong shielding produced by the combined effects of the atmosphere and geomagnetic field.

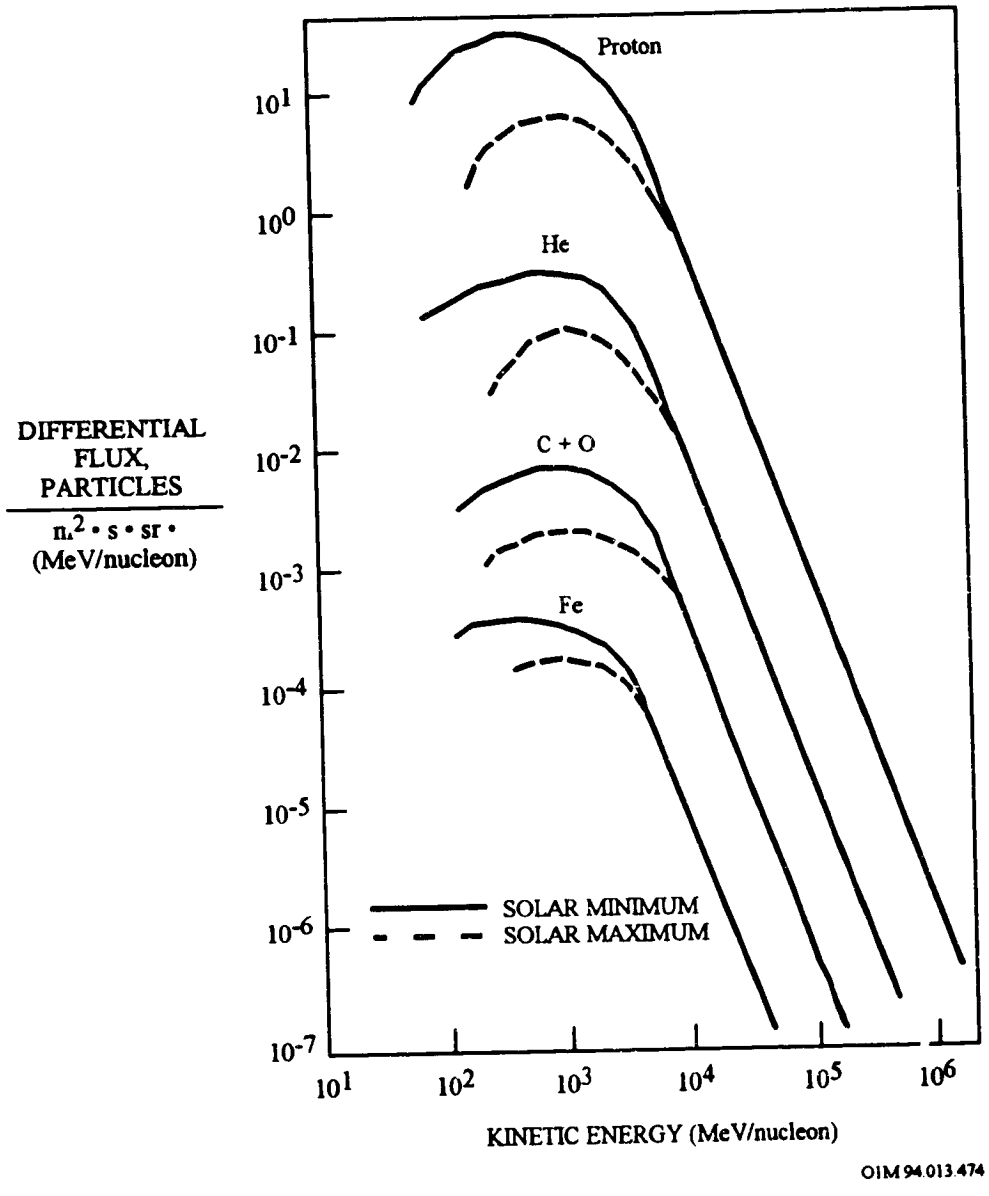

Figure 1- 10. Differential Energy Spectra for GCRs Outside the Magnetosphere at Maximum and Minimum Solar Activity

1.2.5.2.2 Solar Particle Events

Solar particle events, also referred to as solar cosmic rays (SCRs) or solar particle events, represent the most variable component of natural space radiation. Solar cosmic rays are mostly composed of protons and other heavy nuclei (e.g., alpha particles) accelerated to energies between 10 MeV and 1000 MeV during very large solar flares (occurring several times in a solar cycle). These particles can be responsible for a large (e.g., thousand fold) increase in the

radiation dose over short periods of time. Similar to the other energetic particles, SCRs produce ionizing radiation when they interact with atoms (shielding).

Solar particle events show a correlation with the 22 year solar cycle. Figure 1-11 shows a history of solar proton events over two solar cycles (ref. 2). The largest events normally occur in the months following sunspot maximum. Usually, a few very large flares dominate the total particle fluence for the entire solar cycle. Solar polar events are less likely to occur during solar cycle minima. Within the Earth's magnetosphere, the protons reach LEO most freely in the polar regions at magnetic latitudes above 63° because the magnetic energetic cutoff goes to near zero at higher latitudes.

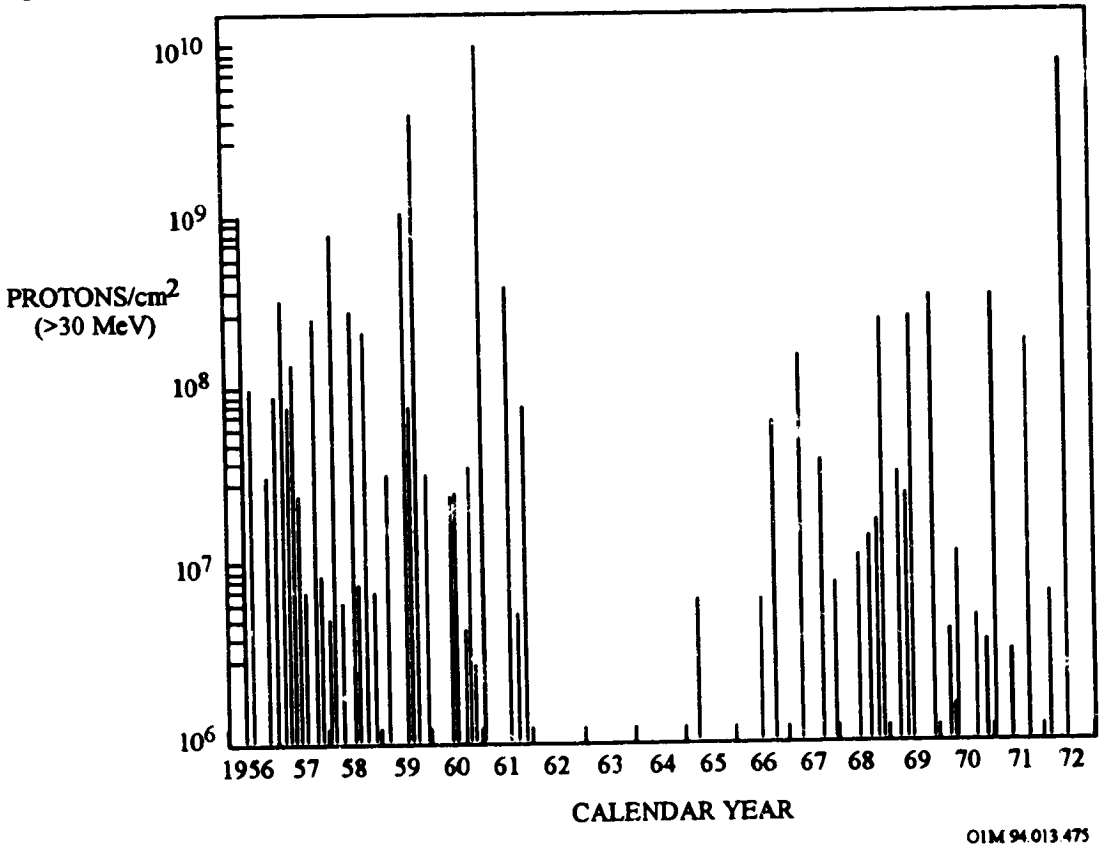

Figure 1- 11. Event-Integrated Proton Fluxes Above 30 MeV for the Major Solar Events of the 19th and 20th Solar Cycles

1.2.5.3 Spacecraft-Charged Particles Interactions

1.2.5.3.1 Trapped Radiation

The Earth's Van Allen belts have their greatest intensity at MEO altitudes, so their effects will be greatest on MEO spacecraft. Specifically, the mission duration will be shortened for a spacecraft in MEO because it is not practical to shield its semiconductor electronics sufficiently to prevent it.

For LEO and GEO spacecraft the mission effectiveness may be reduced due to the necessity of selecting only radiation-hard electronic components, providing a considerable mass of radiation shielding for those electronics, and selecting only surface materials which retain their thermal and optical properties after large (>10^8 rads) charged particles doses. The LEO spacecraft will have to cope with electronics upsets caused by charged particles while the GEO spacecraft may have to select radiation-hard surface materials (the penetrating, high energy Van Allen particles only extend to an altitude of $\leq$ 5,000 km, while the low energy Van Allen belt particles are significant up to and beyond geosynchronous altitude). Figure 1-12 presents the average integrated electron fluxes for the geosynchronous, sun-synchronous, and Molniya missions orbits (ref. 3). The average integrated proton fluxes for the synchronous and Molniya mission orbits are give in Figure 1-13 (ref. 3). Some trapped protons exist in the outer Van Allen belt but have an insignificant effect on satellites in geosynchronous orbits.

In calculating total dose in LEO, it will be found that trapped protons contribute nearly the entire amount with three exceptions:

- At the lowest altitudes (below about 300 km), the contribution from trapped particles becomes so small that galactic cosmic rays (GCRs) make the largest contribution;
- For very thin shields (<0.3 g/cm^2), trapped electrons are more important than trapped protons; and
- At high inclination orbits, GCRs (e.g., solar flare event particles) dominate over trapped radiations (see below).

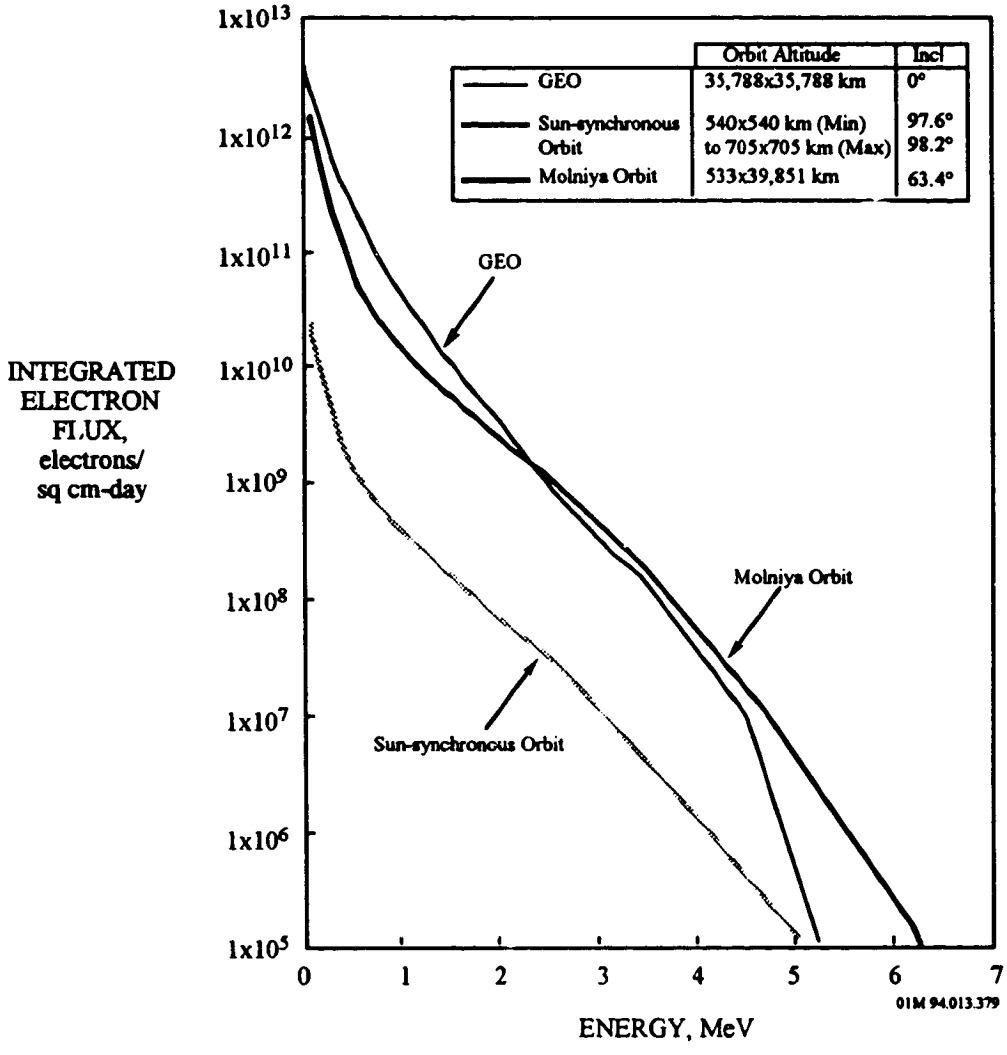

Figure 1- 12. Average Integrated Electron Flux

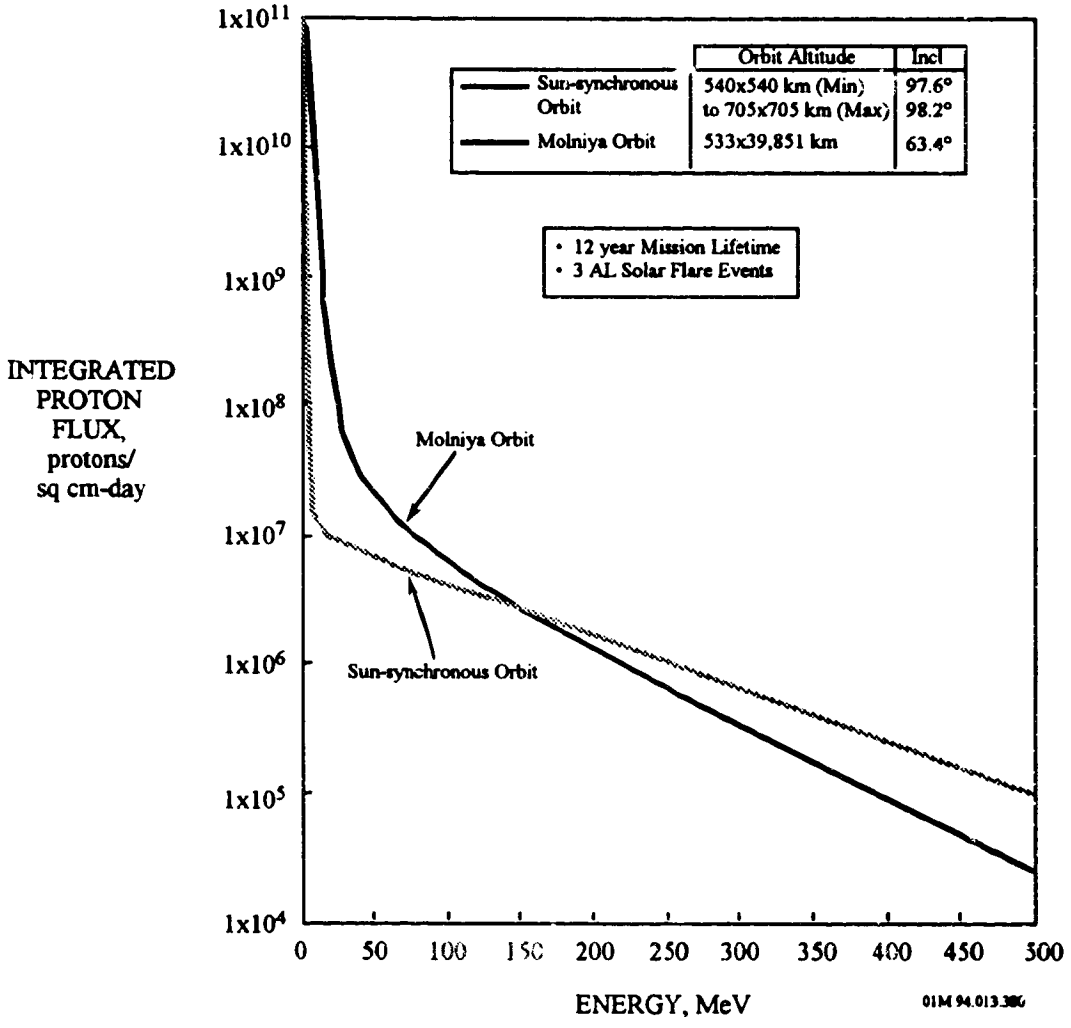

Figure 1- 13. Average Integrated Proton Flux

1.2.5.3.2 Galactic Cosmic Radiation

Due to its extremely high energy, GCRs is very penetrating, and spacecraft shielding is not very effective in reducing the radiation dose. Although the contribution from GCRs to the total dose in rads inside a spacecraft is typically less than 15 percent for most geocentric orbits, these nuclei are responsible for such effects as "SEUs" and "latch-up" in microcircuits (large-scale integrated (LSI) and very large-scale integrated devices (VLSIDS)). Along with the trapped radiation-belt protons, the nuclei are also responsible for the induced radioactivity in most materials in orbit. Noise induced directly by ionization in sensitive devices such as charge-coupled devices (CCDs) and via Cherenkov and fluorescence radiation in photomultiplier tubes are other effects of GCRs that must frequently be considered. The designer should also consider the possible effects of GCRs on materials as well as the probability of production of secondary particles and their effects.

1.2.5.3.3 Solar Particle Events

For a fixed altitude, spacecraft can experience different levels of radiation depending on orbit trajectory. Equatorial orbiting spacecraft will experience lower proton fluence (and therefore a lower radiation dose) than a polar orbiting satellite at similar altitudes. In general, solar particle radiation is a significant hazard for orbits passing above 50° latitude from LEO altitudes to above a few Earth radii (1 Earth radius = 6378 km = 3960 miles). Within the Earth's magnetosphere, the protons reach LEO most freely in the polar regions at magnetic latitudes above about 63° because the magnetic energetic cutoff goes to near zero at higher latitudes.[d] Hence, equatorial orbiting spacecraft will experience lower particle fluence (and therefore a lower radiation dose) than a polar orbiting satellite at similar altitudes. However, in some cases severe magnetic storms allow for large penetration below 50° latitude. Solar cosmic rays emitted during a large solar flare present the greatest uncertainty and the greatest threat to manned spacecraft in regions beyond the protection of the Earth's atmosphere.

---

[d] The Earth's magnetic field deflects incoming cosmic rays (solar and galactic) to a degree which depends on the energy of the particles, preventing those with lower energies from penetrating deep into the magnetosphere.

Hence, solar flare charged particles are a high-altitude and/or high latitude environment that will primarily affect only spacecraft at geosynchronous altitude or spacecraft at LEO altitude at polar inclination, except in rare cases where they extend to low latitudes. Figure 1-14 presents the integrated solar flare proton fluence for one anomalously larege (AL) event for the geosynchronous, sun-synchronous and Molniya orbits (ref. 3). These particles are sufficiently penetrating making it impractical to shield all of them out, and those that do reach the spacecraft electronic components and circuits can cause upsets and total-dose degradation (the galactic cosmic rays will be the major cause of upsets for these high-altitude/high-latitude spacecraft). These upsets and total dose effects may be sufficiently numerous and severe to reduce the mission effectiveness of spacecraft at geosynchronous or high latitude missions.

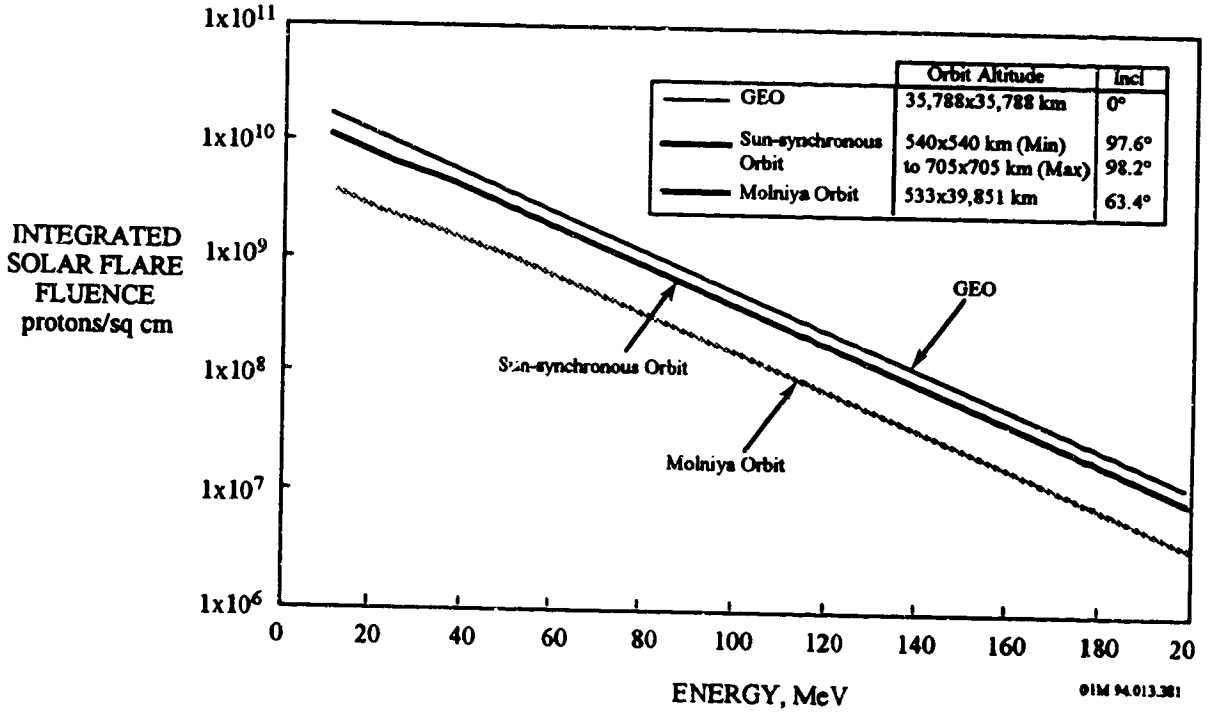

Figure 1- 14. Integrated Solar Flare Fluence, One Anomalously Large Event

1.2.6 Plasma Environment

A plasma is a quasi-neutral gas of charged and neutral particles that exhibits collective behavior. The particles' movements are controlled to a great extent by the Earth's magnetic field and the solar wind, but their collective behavior and movement generate electric and magnetic fields that, in turn, affect the particle's motion and the motion of other charged particles far away.[e]

At roughly 80 km altitude, there is a division between the lower turbulent neutral gas mixture region where all the meteorological processes occur and the upper region where solar irradiation produces a partially ionized plasma composed of O, N_2, O_2, He, H, O^+, H^+, He^+, NO^+, O_2^+, N_2^+, and electrons. This upper region is electrically neutral, with the most abundant neutral being O and the most abundant ion being O^+ up to about 1000 km altitude where H^+ and He^+ become dominant.

The plasma environment may be conceptually divided into three regions: the ionosphere, which is contained within the magnetosphere; the magnetosphere; and the solar wind, as shown in Figure 1-15 (ref. 1). The ionosphere is characterized by its low temperature and high density relative to the other regions, as well as its predominantly O^+ composition. Frequently, this region is considered to extend to about 1000 km, the altitude where the ion density begins to exceed the neutral density. Alternately, an arbitrary density criterion of 10^9 m^{-3} places the ionopause at a few thousand kilometers altitude in the polar regions and at a few tens of thousands of kilometers in the equatorial regions. At low altitudes, the temperatures of these plasmas are typically 300 K to 3500 K (0.05 to 0.3 eV) except in the polar auroral regions. In the auroral regions, an intense, energetic electron flux often precipitates from the plasma sheet. The high altitude plasma is much more energetic; typically 10^5 K (10 eV) for ions and 1 to $5x10^5$ K (10 to 50 eV) for electrons in the solar wind, ~$3x10^7$ K (3 kiloelectron volts (keV)) for electrons and ~$1x10^8$ K (10 keV) for ions in the magnetospheric plasma sheet. However, the dynamics of the intervening region are such that temperatures can sometimes be 1 to 2 orders of magnitude higher. Contact of this energetic plasma with the atmosphere produces the aurora.

---

[e] A plasma is usually defined as an electrically neutral, ionized gas. A gas can be both ionized and electrically neutral at the same time, provided there are as many free electrons in the gas as there are net positive charges on the positive gas ions.

The boundaries between the other regions are termed the "geopause," where the terrestrial plasma is replaced by the solar wind plasma leaking into the magnetosphere, and the "magnetopause" where the geomagnetic field is replaced by the interplanetary or solar wind magnetic field. The magnetopause ranges from 6 to 10 Earth radii in the sunward directions to hundreds of Earth radii in the antisunward direction.

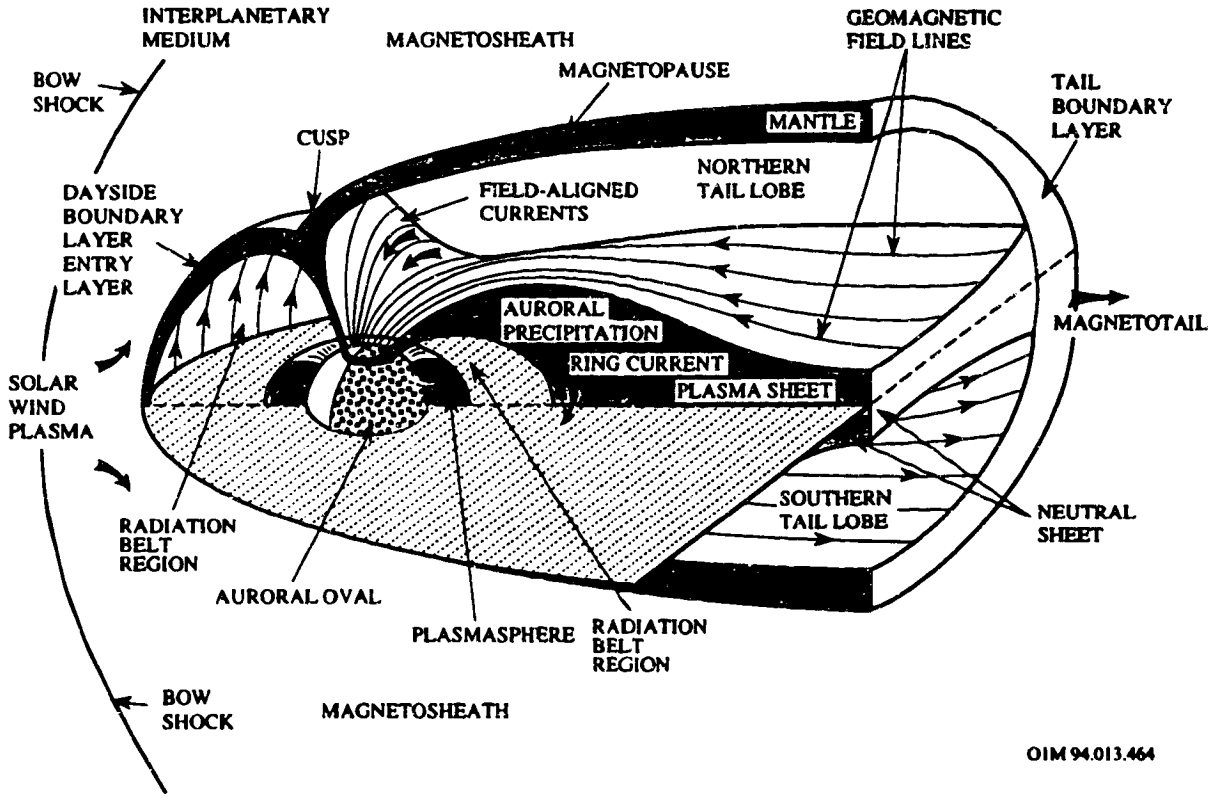

Figure 1- 15. Cross Section of the Magnetosphere

1.2.6.1 Ionospheric Plasma

The ionospheric plasma is generated principally by photoionization of the Earth's ambient neutral atmosphere and by magnetospheric particles interacting with the thermosphere in the 100 to 200 km altitude region. The transport of the plasma is controlled by the geomagnetic field. Within the ionosphere, the recombination of the ions and electrons proceeds slowly (due to low gas densities) so that fairly high concentrations of free electrons persist even throughout the night. In practice, the ionosphere has a lower limit of 50 to 70 km and no distinct upper limit, although 2000 km is somewhat arbitrarily set as the upper limit for most application purposes.

The vertical structure of the ionosphere is changing continuously. It varies from day to night, with the seasons of the year, and with latitude. Furthermore, it is sensitive to enhanced periods of short-wavelength solar radiation accompanying solar activity. In spite of all this, the essential features of the ionosphere are usually identifiable, except during periods of unusually intense geomagnetic disturbances. The different ionospheric vertical layers are shown in Figure 1-16 (ref. 1). In order of increasing altitude and increasing electron concentration, these layers are called D, E, F1, and F2. Figure 1-16 also shows how typical daytime and nighttime vertical electron density profiles change over the course of the sunspot cycle (profiles apply for midlatitudes only). Above the maximum electron density of the F2-region, the electron density decrease monotonically out to several Earth radii. Not only does the overall electron density decrease at night (no production, only electron losses), but the F1- and D-layers disappear soon after sunset.

The Earth's ionosphere may cause design changes if exposed electrical conductors at potentials > 100 volts are present. Since the density of the ionosphere is greatest at low altitudes, these effect will be significant only for the LEO spacecraft. The MEO spacecraft may experience upsets if exposed high-voltage conductors cause discharges due to the presence of the ionosphere.

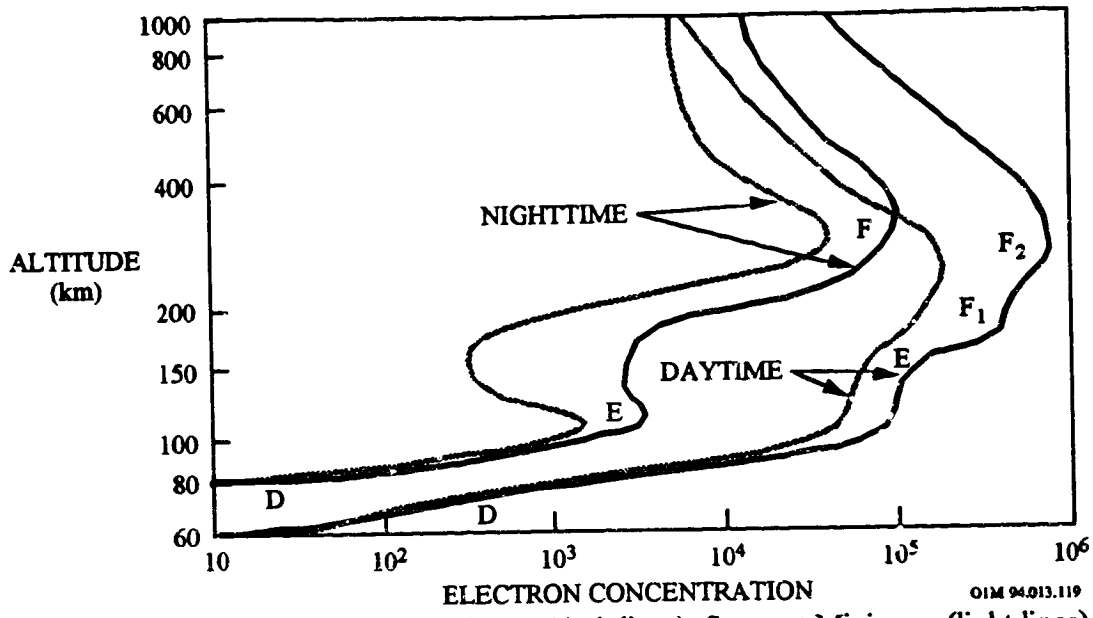

Note: Sunspot Maximum (dark lines); Sunspot Minimum (light lines)

Figure 1- 16. Typical Midlatitude Daytime and Nighttime Electron Density Profiles for Sunspot Maximum and Minimum

1.2.6.2 Auroral Oval Plasma

As mentioned previously, the aurora is primarily produced by high-energy charged particles precipitating into the atmosphere along magnetic field lines. One result of these fluxes is the increase of local plasma density by factors of up to 100 over regions of tens of kilometers in latitudinal dimension and hundred or thousands of kilometers in longitudinal dimension in the auroral regions (60° to 70° magnetic latitude).

1.2.6.3 Geosynchronous Altitude Plasma

The geosynchronous altitude plasma environment is very complex and dynamic. The fluxes in GEO can be quite energetic and are highly variable with magnetic activity especially during geomagnetic substorms. The values given in Table 1-3 are an estimate of the 90th percentile worst charging case environment assuming a Maxwellian representation of the environment.

Table 1-3. Worst-Case Plasma Environment in Geosynchronous Earth Orbit.

Characteristics	Value
Electron number density, n_e m^{-3}	1.12×10^6
Electron temperature, T_e, eV	$1.2\ 10 \times 10^4$
Ion number density, n_i m^{-3}	2.36×10^5
Ion temperature, T_i, eV	2.95×10^4

1.2.6.3 Spacecraft-Plasma Interactions

1.2.6.3.1 Spacecraft Charging

Spacecraft charging is defined as those phenomena associated with the buildup of charge on exposed external surfaces of spacecraft. A body immersed in a plasma (i.e., an electrically neutral, ionized gas) will become negatively charged due to the fact that the electrons, which have a much smaller mass than the positive ions, have a much greater velocity than the ions and impact the body at a higher rate than the ions. As a result, spacecraft surfaces tend to accumulate negative charge. Consequently, a spacecraft accumulates electric charge from the plasma in order to establish electrical equilibrium with the plasma, which is the spacecraft charging process. Equilibrium requires that no net current be collected by the vehicle. Both the plasma properties and the spacecraft design and operating characteristics influence the process.

Plasma interactions can be quite complicated, and there are significant differences between a space vehicle's interactions with the relatively cold, dense plasma of the ionosphere or the plasmaphere (10^2 to 10^4 particles per cm^3), the hot tenuous (below 1 particle per cm^3) plasma at very high orbits, and interactions in the auroral regions where the higher energy plasma characteristic of higher altitudes penetrates to LEO.

Spacecraft charging is vehicle as well as orbit dependent. A spherical satellite with a homogenous, conducting surface would probably not experience significant charging-related problems because the vehicle's potential would be uniformly high. The utility of such a design is, of course, extremely limited. Nonetheless, vehicle design is an important consideration.

Two different mechanisms are thought to combine with vehicle design to generate spacecraft surface charging. Photoelectric effect and plasma bombardment are common terms for these effects.

Illumination of the vehicle skin by photons knocks loose electrons. As these electrons are freed from the spacecraft (photoemission), the skin develops a relative positive charge. The electrons may form a negative plasma cloud or sheath near the vehicle skin. If the entire surface of the spacecraft were a homogeneous conductor, this charge buildup would generate a current flow to spread the charge evenly over the vehicle. Since most spacecraft exteriors have solar panels, probes, lenses, etc., there is a marked difference in conductivity across the surface. The result is differential charging of the sunlit surface with respect to the unlighted portions of the vehicle. Even in the best designed spacecraft, depressions or holes in the vehicle may be

constantly shaded. This means that even spin-stabilized satellites are subject to photoelectric charging.

The success of plasma bombardment, which is associated with geomagnetic disturbances and substorms, in charging a spacecraft is structure dependent. A vehicle immersed in a hot (energetic) plasma is constantly colliding with charged particles. The extent and severity of surface charging depends, to a large extent, on spacecraft structure and design. Electrons with energies above a few KeV are capable of penetrating 1 micron or more into a dielectric. Consequently, they stick to the spacecraft skin, causing a negative charge buildup. Hoes or cavities in the front end of a vehicle (relative to its direction of flight) may actually scoop up energetic particles and accelerate this charging process.

1.2.6.3.2 LEO Altitude Spacecraft Charging

At low latitudes in LEO, the plasma is relatively dense and of low energy, so equilibrium is established within a few volts negative of the reference plasma potential. At these altitudes (within a region called the "plasmasphere" which extends up to about 5 Earth radii), the plasma has a dense "cold" component which can supply sufficient ions or electrons to maintain the potential on a body close to the potential of the plasma. Thus, charging of passive surfaces is usually not a problem in this regime. However, for active surfaces, e.g., solar arrays and structure tied electrically to them, arcing and related significant effects can occur, depending upon the grounding scheme and the magnitude of the spacecraft-imposed voltages.

1.2.6.3.3 Geosynchronous Altitude Spacecraft Charging

The geosynchronous altitude plasma environment is very complex and dynamic. Hence, geostationary vehicles are thought to be most susceptible to charging for two reasons. First, they are close to the magnetopause where the fluxes in GEO can be quite energetic and are highly variable with magnetic activity especially during geomagnetic substorms. These events occur several times a day, even on quiet days, and may produce a ten-fold enhancement of ion density and a thousand-fold jump in electron density at geosynchronous orbit. Second, the ambient plasma density at 6.6 R_E is low (below 1 particle per cm3). This means that, unlike low orbit vehicles, the ambient atmosphere is incapable of "bleeding off" or neutralizing small charges before a discharge can occur.

In GEO, thermal current densities can be three orders of magnitude less than in LEO, so that photoelectron emission from surfaces can play a significant role in balancing currents to a

spacecraft. Photoemission can charge a body to tens of volts positive with respect to the plasma. However, geomagnetic substorms heat plasma in the tail of the magnetosphere (and perhaps in the auroral regions) and inject the hot plasma into the region near geosynchronous altitudes. The hot plasma, with very high velocity electrons at substantial densities, can charge the body to high negative potentials in the absence of sunlight. Hence, sun/shade effects become important to the point that potentials as large as several kilovolts can develop between sunlit and shaded surfaces (depending on geometry and materials properties).

Since electrostatic discharges caused by hot plasma have damaged spacecraft (Intelsat III & IV, DSCS-II, and DSP), design changes have been required with reduced mission effectiveness being a possible consequence.

1.2.6.3.4 Low Earth Polar Spacecraft Charging

In polar LEO the important transient and energetic fluxes occur in the auroral zone. These particles are not very penetrating but may be significant for charging at altitudes above 250 km. Spacecraft passing through the auroral zone can be charged to large negative potentials by energetic electrons precipitating from the magnetosphere. This is because large surface potentials are required to retard this flux and allow equilibrium (no net current) to be achieved. Also, in this region, conditions occur in the wake of large structures, or they may occur naturally so that the entire vehicle is involved, where the low energy plasma density is depleted. This makes it ineffective in balancing the current from the high energy electron flux, and the charging process is enhanced. This is similar to the situation in GEO where the plasma is very energetic but tenuous.

1.2.7 Micrometeoroid and Orbital Debris

The microparticle environment encountered by a spacecraft in low and medium Earth orbit is defined by two sources: man-made debris from space activity since October 1957, and naturally occurring micrometeoroids.

1.2.7.1 Micrometeoroids

Meteoroids are solid particles moving in interplanetary space and originate from both cometary and asteroidal sources. The cometary meteoroids are made primarily of a conglomeration of ice particles with small amounts of higher density minerals mixed with the ice. This gives them a relative density of ~0.5 g/cm^3. The asteroidal particles are primarily of higher density minerals with densities that can go as high as ~8 g/cm^3. Meteoroids have been detected with sizes as small as 0.4 microns and as large as several meters in diameter. Because of their velocity, density, and mass, meteoroids can cause damage to vehicles operating in space. However, the primary threat of meteoroids in the near-Earth space environment is from particles ranging from 50 μm to 1 mm in diameter. The very small meteoritic particles (less than 1 μm in diameter) are primarily from beta meteoroids. These are meteoroids which are accelerated by radiation pressure outward from the sun. Collision velocities can vary widely and depend upon the constant orbital velocity of the Earth, the spacecraft orbital velocity, the impactor velocity, and the direction of impact. The collision velocities for meteoroids range from about 3 to 72 km/s with an average velocity of 19 km/s. Zook and Erickson have provided data that give the distribution of meteoroid velocities seen by spacecraft.[10,11,12,13]

1.2.7.2 Orbital Debris

Orbital debris refers to man-made particles orbiting the Earth, which is a continuous changing environment. Within about 2000 km above the Earth's surface there is an estimated 3,000,000 kg of man-made orbiting objects. These objects are in mostly high inclination orbits and sweep past one another at an average speed of 10 km/sec. These particles are a result of standard launch and spacecraft operations as well as rocket and satellite breakups. Launch and spacecraft operations place both large particles (i.e., greater than 1 cm diameter such as sateliite shrouds, lens covers, and dropped tools) and small particles (i.e., ~10 μm diameter solid rocket exhaust) in orbit. Exposure of satellites and spent rocket bodies to the space environments (i.e., UV, AO, thermal cycling, radiation, and impact) also creates small particles, less than 1 mm diameter, due to materials' degradation and erosion. After shutdown, spent spacecraft and rocket bodies are allowed to remain in orbit as very large (i.e., great than 1 m diameter) pieces of orbital debris. In

addition, both operational and spent spacecraft and rocket bodies are susceptible to intentional and accidental breakups, either due to explosions or hypervelocity impacts. These breakups create orbital debris of all sizes.

Collision velocities can vary widely and depend upon the constant orbital velocity of the Earth, the spacecraft orbital velocity, the impactor velocity, and the direction of impact. The collision velocities for space debris particles range from about 3 to 15 km/s, with average values of 10 to 13 km/s. The distribution of velocities has been given by Kessler.[14] With regard to the mean density of the debris, the present recommendation is that for particles smaller than 0.5 cm the mean density is 4.0 g/cm^3. This is based on the fact that most of such small particles consists of either small alumina particles (e.g., from propellants) or the debris from paint and pigments, which are usually comprised of such materials as titania and zinc oxide. For larger particles greater than 0.5 cm the density is initially about 2.8 g/cm^3 (representing aluminum) but becomes a decreasing factor of the size of the particle (i.e., $\rho = 2.8/d^{0.74}$). The basic explanation for this is that the particles are not solid bodies but rather portions of structures which, therefore, act as if partially hollow and pseudo-porous.

The distribution of mass and relative velocity is sufficient to cause the orbital debris environment to be more hazardous than the meteoroid environment to most spacecraft operating in Earth orbit below 2000 km. Mathematical modeling of this distribution of orbital debris predicts that collisional fragmentation will cause the amount of mass in the 1 cm and smaller size range to grow at twice the rate as the accumulation of total mass in Earth orbit. Over the past 10 years, this accumulation has increased at an average rate of 5 percent per year, indicating that the small sizes should be expected to increase at 10 percent per year.

1.2.7.3 Microparticle Fluence Models

The microparticle environment is described in terms of two separate models, one for the man-made debris, and the second one for the naturally occurring micrometeoroids. The phenomenology numerically computed models are provided by B.G. Cour-Palais for micrometeoroids and by D. Kessler and R.C. Reynolds for space debris. The models are outlined in NASA SP-8013, and NASA-TM-100471 with recent, 1990, data, provided in a recent Phillips Laboratory briefing by Kessler, respectively. Cour-Palais et al.[15] provides a good general model of the near-Earth meteoroid environment. Eberhard Grun's 1985 model[16] provides a good update to the Cour-Palais model by including the beta meteoroid environment. The Kessler debris model[17] was developed in 1987 and has been widely adopted and used by the U.S. Department of Defense, NASA, and the European Space Agency (ESA).

The existing Kessler debris model assumes that the particles are all in circular orbits and, therefore, have a common speed with that of any spacecraft which is also in a circular orbit at the same altitude. This logic immediately implies that hits can only be in the plane which is parallel to the Earth's surface. Therefore, only the ram and sides can be hit and there will be no hits on either the SPACE end, the EARTH end, or the TRAIL end. The debris model predicts that the number of hits per area, per time are functions of altitude, the 22 year solar cycle, orbit inclination, particle size, and time. A growth model has been assumed which has two components - one component due to continued launches and a second component due to fragmentation resulting from explosions and collisions between the various pieces within orbit. An important point to note is that for debris altitudes greater than 700 km there is only a simple growth factor, since the influence of the atmosphere is negligible. However, as altitude decreased below 700 km the effect of the atmosphere becomes increasingly important and there is a cyclic component to the history which is due to the solar cycle behavior and the consequential atmospheric heating effect.

For micrometeoroids, it should be noted that the Earth passes through many "tubes" of micrometeoroid orbits during its annual orbit. For short mission times of less than 1 year, it would be necessary to correctly track exactly which of the micrometeoroid orbits have been intercepted by the Earth. However, for a multiyear mission, where collisions occur with a large number of micrometeoroid orbits, the assumption is that the micrometeoroids are coming in towards the Earth from all possible directions and, therefore, the system appears to be geocentric on average.

Figure 1-17 shows the predicted meteoroid and man-made debris impact fluxes with varying particle size (ref. 14).

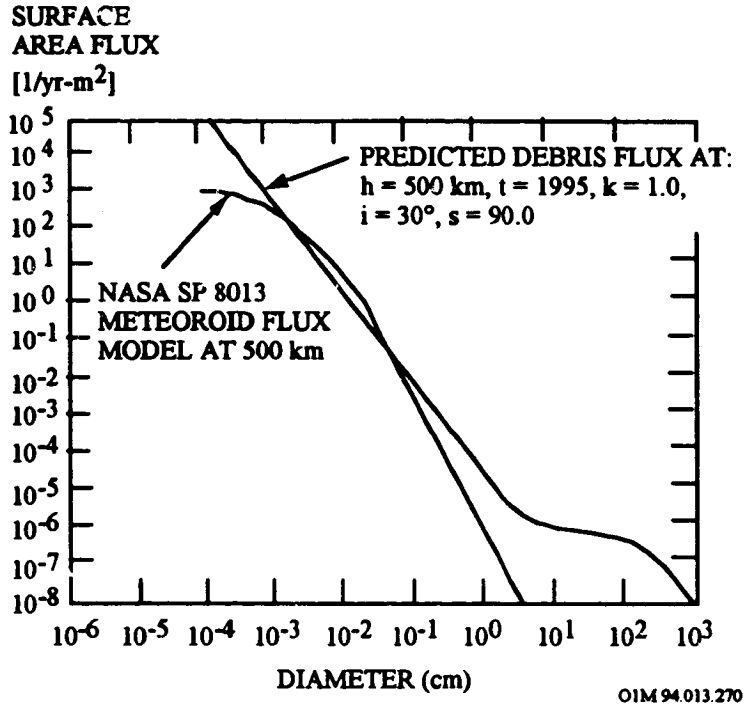

Figure 1- 17. Predicted Meteoroid and Man-Made Debris Impact Fluxes at 500 km with Varying Particle Size

In general, the LEO debris environment flux surpasses the LEO meteoroid environment flux for particles larger than ~1 mm in diameter. In this size regime the debris is composed primarily of particles from orbiting spacecraft which have broken apart. These particles are irregular in shape. They may also be of much higher densities (e.g., stainless steel and tantalum) but the average density is that of aluminum. The LEO debris environment also contains more particles in the size regime less than ~50 μm in diameter than does the meteoroid environment. In this population regime, the particles which are ~10 μm in diameter are primarily aluminum oxide from solid rocket motors, whereas the other particles in this range are primarily paint pigments, both averaging ~4 g/cm^3 density. For a circular orbit at 500 km altitude and 28.5° inclination (the inclination and altitude of the proposed Space Station), the average relative impact velocity of orbital debris is about 10 km/s. However, this relative velocity can range from almost 0 to ~19 km/s for particles in highly elliptical orbits. Since the majority of impacts occur at oblique angles, the relative normal incidence impact velocity averages ~8 to 10 km/s.[18]

The meteoroid environment impinging on a spacecraft in orbit around the Earth shows a tendency to impact about twice as much on the satellite's leading edge (which is moving in the velocity, or ram direction) as on the trailing, or wake, edge. Orbital debris, on the other hand, is much more focused towards the leading sides of the spacecraft, with the exception that particles

in elliptical orbits have higher fluences at ~45° either side of the ram direction.[19] With orbital debris, approximately 1/10th to 1/20th of the number of particles hit the trailing edge compared to the leading edge surfaces.

Generally, the meteoroid environment is modeled as unchanging over both time and spacecraft inclination whereas the orbital debris environment is modeled as highly changing both over time and with spacecraft inclination. The higher inclinations possess a much higher population of debris particles. The debris environment is considered to be increasing with time, with the small particle population increasing faster (at a compound rate of ~2% per year) than the population of the much larger trackable particle (which increase at a linear rate of ~5% per year).[20] Both the meteoroid and debris environments increase with altitude, although the current models of the debris environment show the flux decreasing at altitudes above ~1000 km. This may change as the elliptical orbits of the debris are included in future models.

The debris object flux is an important and growing problem at low altitudes, and is not negligible at geosynchronous altitudes. A single debris object impact can destroy a spacecraft, so a large spacecraft at low altitudes can only expect to operate for a calculable time before its probability of being hit exceeds a specified limit. Thus, the LEO spacecraft should be designed to survive small object hits. The MEO spacecraft should also be designed so it can withstand hits by small objects or not contribute additional debris objects (i.e., avoid surface materials that shatter upon impact). The same effects may be observed at geosynchronous orbit so similar design changes should be considered.

The flux and size distribution of micrometeoroids is almost independent of altitude, so design changes to limit the effects of abrasion (by $<10^{-6}$ g micrometeoroids) and punctures (by $>10^{-6}$ g micrometeoroids) may be necessary for all spacecraft.

1.2.7.4 Spacecraft-Micrometeoroid/Debris Interactions

Impact damage can degrade the performance of exposed spacecraft materials and, in some cases, destroy a satellite's ability to perform or complete its mission. For both micrometeoroids and debris, the particles can range in size from sub-microns to many centimeters. Both components display a power law of number versus size, with the smaller particles being far more numerous than the larger ones.

The different phenomena observed with hypervelocity impacts in materials depend on several factors: the impact velocity; the relative sizes of the impactor and target; and the material properties of the target. The physical response of any target to a micrometeoroid and debris impact depends on the material, induced stress level, material temperature, number of projectiles and the system configuration. These phenomena may be enhanced by subsequent exposure of underlying layers to the UV, atomic oxygen, charged particles, and thermal cycling. This subsequent exposure can modify a material and thus enhance cracking and delamination regions. Also, material embrittlement, erosion and other property degradation can occur to either the surface or exposed underlying material. For example, AO can creep under locally delaminated regions causing greater damage, or previously protected materials may become exposed to UV through small cracks or fissures. In short, the synergistic environment can lead to accelerated damage rates and a significant increase in the damage zone.

A more detail discussion on the effects of micrometeoroid and debris impact on materials and optical components is presented in Chapter 2, Sections 2.3.6. and 2.3.7.

1.2.8 Thermal Environment

1.2.8.1 General Discussion

A vehicle in LEO will receive radiant thermal energy from three primary sources: the incoming solar radiation (described by the solar constant), reflected solar energy (Earth albedo energy), and outgoing longwave radiation emitted by the Earth and atmosphere. Portions of this energy will be reflected by the vehicle, and the vehicle radiates energy into the cold sink of space at 3 K. Spacecraft surfaces will tend toward a temperature which balances these energy fluxes with any energy produced internally within the vehicle. A similar thermal balance process applies to the Earth itself. In contrast, a vehicle in GEO will not be affected by the albedo and emitted radiation.

LEO and GEO experience different eclipse periods. A spacecraft in LEO moves in and out of eclipse once every orbit, as often as every 90 minutes. A spacecraft in GEO remains in continuous sunlight during most of the year. Twice per year, during the spring and autumn, it is in eclipse once a day for about 45 days. These differences in orbital characteristics impose different requirements on the design of the thermal control system.

1.2.8.2 Spacecraft-Thermal Interactions

The energy absorbed by a spacecraft depends on the thermal characteristics and area of its outer surface, its orientation to the source of thermal radiation, and the characteristics of that source. Geometric considerations determine in part how much energy is absorbed on the outer surface due to area size and spacecraft orientation. However, radiation source characteristics and thermal surface properties are interrelated and require some amplification.

External radiation sources of importance are the sun, albedo (planetary reflection), and Earth emission. The intensity of solar radiation - parallel sun rays are assumed at these distances - varies with the distance from the sun according to the inverse square law. The intensity also varies spectrally, i.e., according to the wavelength spectrum, with approximate distribution of energy as follows:

- Ultraviolet (wavelength less than 0.38 micrometers): 7%
- visible (wavelength between 0.38 and 0.76 micrometers): 45.5%
- Infrared (wavelength greater than 0.76 micrometers): 47.5%

The Earth's albedo is almost diffuse, which means that from any fixed point on Earth, the intensity of reflected radiation is almost uniformly distributed out from that point and is not

dependent upon the angle of incident radiation. The Earth's albedo is not a fixed value but varies considerably with local conditions such as cloud cover. The spectral distribution is approximately the same as the source (the sun).

The Earth emission, on the other hand, is based on an apparent "black body" temperature of the Earth and its atmosphere (A black body emits the maximum amount or radiant energy at a given temperature and wavelength.) A temperature of 450°R is commonly assumed, with the emission considered to be diffuse.

The spectral distribution of the energy source is particularly important in spacecraft thermal design since spacecraft coating sand surfaces are spectrally responsive to the radiation source. A black coating absorbs almost all of the impinging solar energy and has a flat spectral response, i.e., the same response to all wavelengths. A second surface mirror, on the other hand, reflects most of the solar radiation and shows a marked change over the spectrum, except for a flat response in the solar band. Other coatings, in general, have surface characteristics that vary between those of black bodies and second surface. (A more detailed discussion on thermal control systems can be found in Chapter 10).

The solar absorptance of spacecraft materials will, in general, increase over the lifetime of a mission - the longer the mission, the larger the increase. The magnitude of this increase cannot be precisely determined, but must nevertheless be considered in all spacecraft thermal design. Absorptance changes can be induced by the ultraviolet spectrum of solar radiation, by energetic particles, by contamination from materials outgassing during the various mission phases, and by other factors such as high temperatures and the vacuum of space.

1.3 SPACECRAFT SUBSYSTEMS

In selecting surface materials for spacecraft applications, the functions of the exposed components which are fabricated from these materials must be considered. While many components can do their jobs in the interior of the spacecraft, other components (by the nature of their functions) must be exposed. These necessarily exposed components include radio frequency (RF) antennas, optical sensor windows and/or mirrors, thermal control radiators, propulsion and attitude control rocket nozzles and solar cells. These exposed components are the eyes, ears, and arms (or legs) of the spacecraft.

Table 1-4 lists the spacecraft subsystems, the exposed spacecraft components, their functions, the critical material properties necessary to perform these functions, and some of the materials often used. For example, electrical conductivity is the critical property for RF antennas, therefore aluminum, copper, or silver (often as plating) are used. Materials transparent to infrared wavelengths are used for navigation Earth sensors and infrared (IR) laser communication transmitters and receivers. Selenium, germanium, and cesium iodide are often used in these applications. In addition, mirrors to collect infrared or visible optical radiations are used for communication, navigation, or surveillance purposes. Polished aluminum, nickel, silver, and osmium make good mirror surfaces.

Table 1-4. Spacecraft Subsystems, Exposed Components, and Materials

Subsystem	Component	Critical Property	Candidate Materials
Communication	RF Antenna	Electrical Conductivity	Al, Cu, Ag
Sensors	Optical Window Optical Mirrors	Optical Transparency (IR) Optical Reflectivity	Se, Ge, CsI Al, Ni, Ag
Thermal Control	Radiators Thermal Blankets Heat Pipes	α/ε Ratio	White Paints Black Paints
Attitude Control	Rocket Nozzle	High Temperature Strength	Mo, Ta, W,C
Power	Solar Cells Batteries Optical Windows	Efficiency at Temperature Optical Transparency (Visible)	Si, GaAs, InP LiF, SiO_2
Avionics	Electronic Devices		
Structures	Bus Structure Deployable Booms Gimbals	Strength Stiffness	Polymeric composites Metals, Ceramics

Thermal control involves keeping the interior of the spacecraft within acceptable temperature limits (typically 0°C to 50°C for electronics, but since hydrazine freezes at ~3°C temperature limits of 10°C to 50°C are often specified). Since radiation is the only passive heat transfer mechanism to and from the spacecraft, white and black paints are often used. White paints have a low solar absorption α_s (typically < 0.2) coupled with a high emissivity ε (typically 0.8), while black paints have high values (0.9) for both solar absorption and thermal emissivity. Bare metals usually have an α_s/ε ratio of ~1.

Propulsion (almost always) and altitude control (often) is accomplished by mass-expelling rockets. The nozzles of these rockets, which must be exposed, are made of high-temperature metals. These refractory metals are typically alloys of molybdenum, columbium (niobium), tantalum, and tungsten. The interior of rocket nozzles are often lined with a form of carbon that can withstand the extreme pressures and temperatures involved.

Solar cells are the usual source of spacecraft electrical power, with solar cells being relatively exposed. Solar cells are typically silicon, gallium arsenide (new) or indium phosphide (experimental). Silicon dioxide (SiO_2) is used to protect solar cells from low-energy proton damage, often being in turn protected by a quarter-wavelength-thick LiF anti reflection coating. Thus, the LiF is the only material in the solar cell stack really exposed to the ambient environment, with the SiO_2 cover slide and the Si solar cell being behind it. Even if solar concentrators (mirrors or lenses) are used, the solar cells will be protected this way.

1.4 FLIGHT EXPERIMENTS

More than 1000 materials have been evaluated during several space shuttle flight experiments and recovered satellites (e.g., LDEF, Solar Maximum Mission, MIR). A summary of the comparative altitude, exposure time and the atomic oxygen fluence level is provided in Table 1-5.

Table 1-5. Flight Experiments and Recovered Satellites Mission Summary

Flight	Altitude (Inclin.)	Exposure Time	Atomic Oxygen Fluence atoms/cm^2 (Attitude)
STS - 5	222 km (28.5°)	44 hours	1 x 10^{20} (VAR)
STS - 8	222 km (28.5°)	41.75 hours	3.5 x 10^{20} (ram)
STS - 41G	225 km (57.0°)	38 hours	3 x 10^{20} (ram)
STS-46 EOIM-3	230 km (28.5°)	42.25 hours	2.0 - 2.5 x 10^{20} (ram)
STS-46 LCDE	425[a] - 230 km (28.5°)	41 - 58.55 hours[a]	2.0 - 2.7 x 10^{20} (ram)
Solar Max	574 - 491 km (28.5°)	50 months	2 x 10^{21} (VAR)
COMES/MIR	425 - 350 km (51.6°)	13 months 2 days	1 2x10^{18} - 5.8x10^{20}
LDEF	479 - 324 km (28.5°)	69 months	10^3 - 9.0x10^{21} (wake to ram)
EURECA	515 km	10 months	TBD

(a) 16.55 hours at 425 km during EURECA deployment

1.4.1 Long Duration Exposure Facility (LDEF)

1.4.1.1 Mission Information

The Space Shuttle STS 41-C deployed the Long Duration Exposure Facility (LDEF) carrying 57 different experiments on April 6, 1984 for a planned 10 month to 1 year mission. The LDEF spacecraft flew in a 28.5 degree inclination circular orbit with an altitude in the range from 324 to 479 km (175 to 258.5 nautical miles). It was gravity-gradient stabilized and oriented so that one side always pointed along the velocity vector. The LDEF was a 12-sided, 4.3-m (14-ft) diameter, 9.1-m (30-ft) long aluminum open frame. The structure was configured with 72 equal-size rectangular openings on the sides (six on each side) and 14 openings on the ends (six on the Earth-facing end, and eight on the space-facing end) for mounting experiment trays. The LDEF total weight with experiments was approximately 9,720 kg (21,400 lbs). LDEF exposed a total surface area of about 130 m^2 for 69 months.[21]

The orientation of the spacecraft with respect to the Earth during its 5.8 years flight is shown in Figure 1-18. The location of a specific experiment is described by referencing a row (1-12) and a column (A-F) as shown in Figure 1-18. Values of key parameters of the low Earth orbit environment which LDEF encountered are listed in Table 1-6. The remarkable flight attitude stability of LDEF (within less than 1° of movement in yaw, pitch, or roll) enables specific analyses of various individual and combined effects of LEO environmental parameters on identical materials and systems on the same space vehicle.

The LDEF experiments ranged from the study of the LEO environment to determining the effect of long-term space exposure on tomato seeds. Most of the experiments were passive with the majority of the data resulting from post-flight analysis. Because of schedule changes and the loss of the Space Shuttle Challenger, LDEF was not retrieved until January 12, 1990 after spending 69 months in orbit. During these 69 months, LDEF completed 32,422 orbits of Earth and traveled almost 750,000,000 nautical miles. Post-flight analysis of the LDEF generated a wealth of data on the interaction of materials and system with the LEO environment. These data have been presented at three post-retrieval symposiums[22,23,24] and two materials workshops,[25,26] and integrated into several data bases.[27,28]

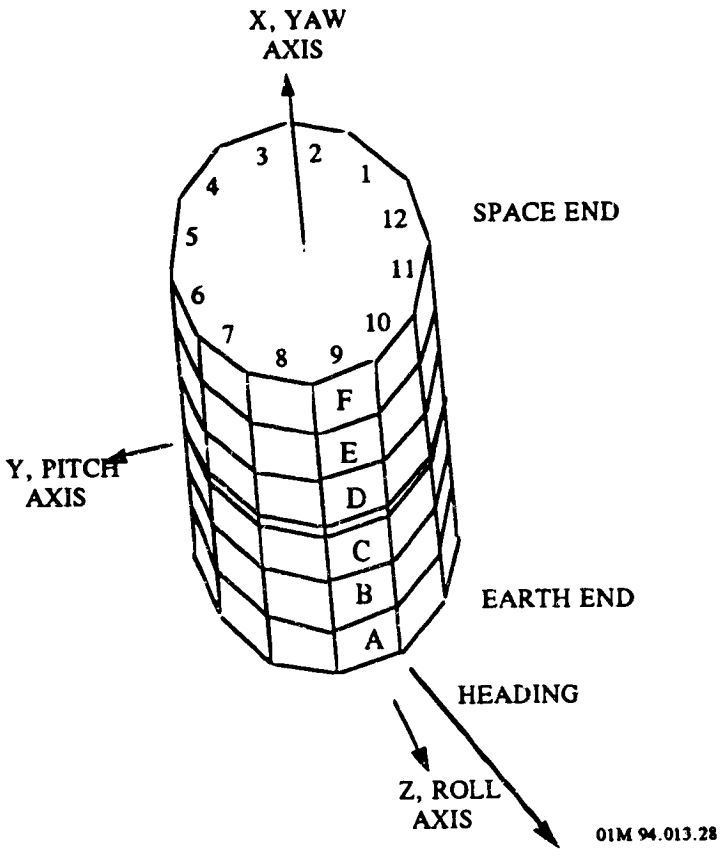

Figure 1- 18. LDEF Orientation

Table 1-6. LDEF Exposure Conditions

Environment	Conditions
High Vacuum	10^{-6} to 10^{-7} torr
UV Radiation	100-400 nm 4,500 to 14,500 equivalent sun hours
Electron and Proton Radiation	~2.5 x 10^5 rads surface fluence
Atomic Oxygen	~10^3 to 9.02 x 10^{21} atoms/cm^2 (wake- to ram-facing)
Meteoroid and Debris Impacts	>36000 particles from ~0.1 mm to ~2.5 mm High fluence on ram-facing surfaces
Cosmic Radiation	~6 rads ~20 tracks Thorium and Uranium
Thermal Cycling	~34,000 cycles -29°C (-20°F) to 71°C (160°F), ±11°C (±20°F)

Figures 1-19[29] and 1-20[30] summarize the results of calculations of atomic oxygen (AO) fluence and equivalent sun hours of UV radiation, respectively, at the end of the mission on each LDEF tray location. Examination of these figures reveals the many combinations of AO/UV exposure conditions available on LDEF, attributable to the remarkable attitude stability during the 5.8-year flight. Figure 1-19 shows that the highest AO fluence was 9.02×10^{21} atoms/cm^2 on the LDEF leading edge, about 8.1° from row 9 (towards row 10). Experiment trays on the side rows experienced different AO fluences because of the 8° ram vector angle. The Earth and space end AO fluences were more than one order of magnitude lower than the ram fluence. The lowest AO fluence on LDEF was 2.66×10^3 atoms/cm^2 between rows 3 and 4. During the LDEF flight, the total fluence for rows 2 through 4 was in the same order of magnitude as the lowest fluence listed in Figure 1-19. However, during the retrieval mission, after LDEF was safely clamped in the shuttle payload bay, LDEF rows 1 through 3 (which faced out of the bay) were inadvertently subjected to atomic oxygen at the retrieval altitude for approximately 15 minutes. This inadvertent exposure raised the AO fluence from the 10^3 to the 10^{17} atoms/cm^2 order-of-magnitude for the experiment trays on those rows.

Figure 1-20 shows the cumulative equivalent sun hours exposure of total direct solar and earth reflected radiation as a function of LDEF row position. The high vacuum ultraviolet (VUV) fluences were 14,500 equivalent sun hours (esh) on LDEF space-end experiment trays, with intermediate values of 11,100 to 11,200 esh on leading and trailing edge trays and 6,400 to 6,800 esh on side trays. The lowest VUV fluence was 4,500 esh, received by the Earth-end trays.

The results from LDEF show that past atomic oxygen fluence models do not account for atomic oxygen impingement rates at grazing angles to the spacecraft (see Figure 1-21), and therefore do not include the thermal molecular velocity contribution. Because of the Maxwellian distribution of the atomic oxygen molecular velocity, the atomic oxygen flux on a surface is not simply the atomic oxygen density times the magnitude of the flow velocity times the cosine of the angle between the flow velocity and the surface normal. Hence, LDEF surfaces parallel to the ram direction and also surfaces with incident angles slightly greater than 90 degrees received some atomic oxygen. Using a modified AO fluence model to account for the thermal velocity distribution of the atomic oxygen atoms in LEO, Figure 1-22 shows the higher AO fluences at AO incidence angles to LDEF from 95° to 110° in comparison with that predicated with the MSIS-86 model that excludes the thermal molecular velocity.[31]

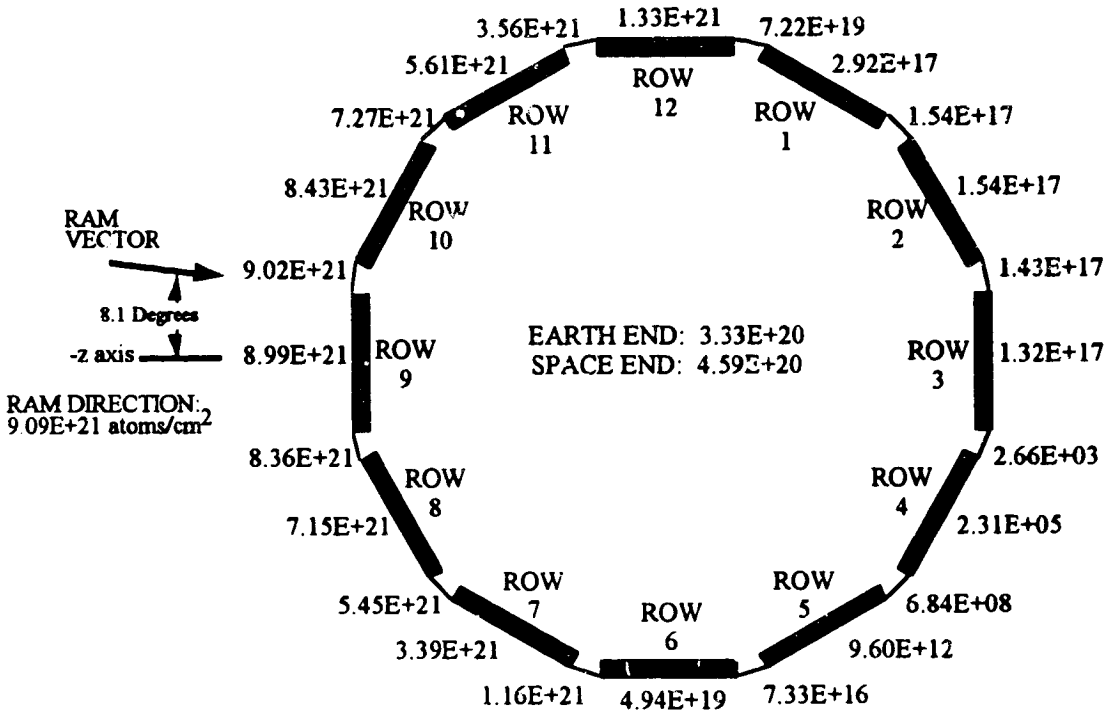

Atomic Oxygen Fluences (atoms/cm^2) at End of Mission, Including Exposure During Retrieval OIM 94 013 038

Figure 1- 19. Atomic Oxygen Fluence for Each LDEF Tray Location

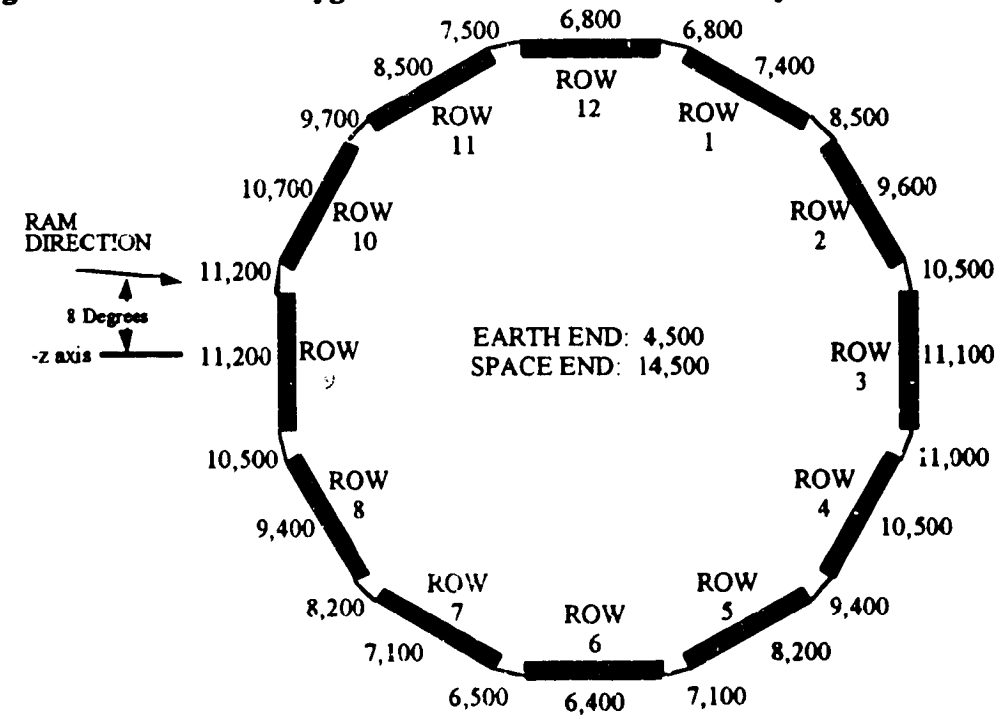

Cumulative Equivalent Sun Hours Exposure at End of Mission OIM 94 013 039

Figure 1- 20. Equivalent Sun Hours at End of Mission for Each LDEF Tray Location

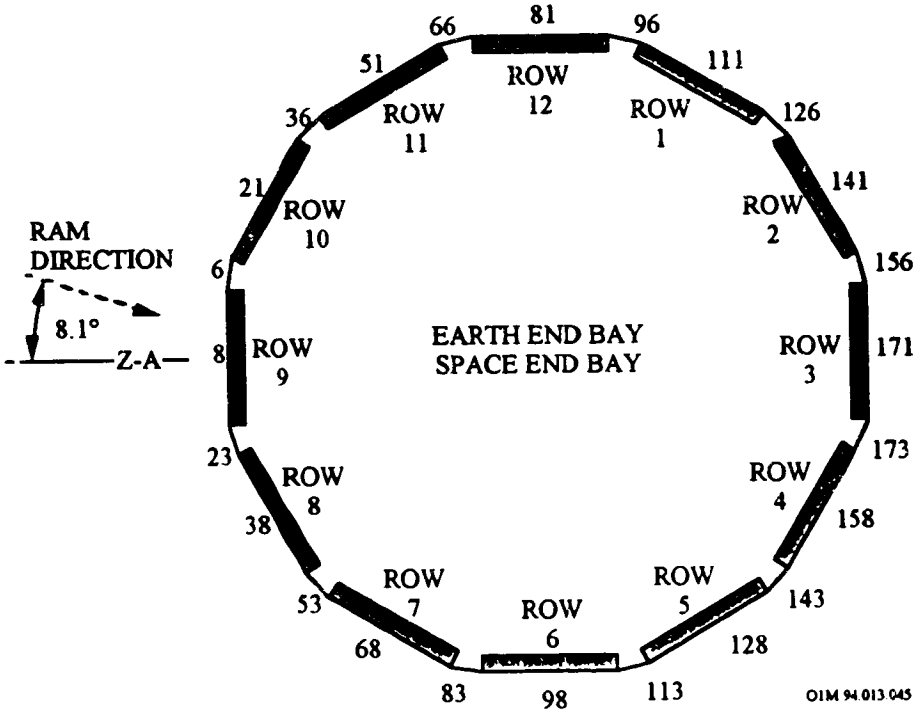

Figure 1- 21. Incidence Angles for LDEF Tray and Longeron Location.

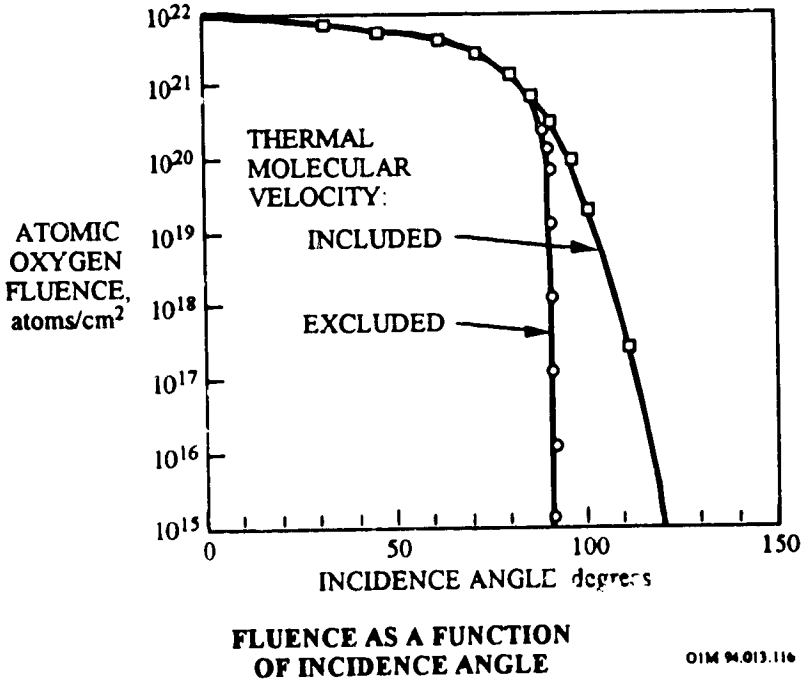

Figure 1- 22. Effect of Thermal Molecular Velocity on Atomic Oxygen Fluence.

1.4.1.2 Thermal Environment

The thermal control of the LDEF was totally passive by design, thus relying on internal radiation heat transfer, heat conduction paths, and the external surface coatings (α/ε) for facility temperature control. Over 90% of the interior structure and tray surfaces were coated with Chemglaze Z306 high emissivity black paint (ε=.90) to minimize any circumferential thermal gradients and to maximize the radiation heat transfer across the facility. To minimize conduction heat transfer from the structure, the experiment trays were attached to the LDEF structure by eight 2-in x 5-in aluminum clamps along the tray perimeter. The tray mounting scheme minimizes the contact conduction area through which heat can be transferred between the facility and the experiment trays. The passive thermal control of the LDEF results in a variation in the experiment's structure boundary temperature due to the orbiting nature of the spacecraft.

A thermal analysis of LDEF's flight experiments was conducted by Berrios et al.[32,33] Three heat sources were considered for the thermal analysis of the LDEF experiments: the solar irradiation; the Earth reflected solar irradiation (albedo); and the Earth emitted energy (planetary infrared). LDEF lacked any internally generated heat resulting from electronics or heaters. Figure 1-23 defines the LDEF principal sources of heat. The angle β is defined as the angle between the spacecraft's orbit plane and the Sun's illumination rays and its minimum and maximum amplitudes are calculated by adding the declination of the Earth's equator (±23.5°) with the inclination of the spacecraft's orbit plane (±28.5°). The Thermal Radiation Analyzer System (TRASYS) computer code[34] was employed to calculate the albedo, solar, and planetary incident heat fluxes. A TRASYS model of the LDEF spacecraft was constructed which represented a 12 side polygon closed on both ends. Program inputs consisted of the LDEF spacecraft orientation, orbit β angle, and altitude. Transient orbital heat fluxes were calculated for 10° beta angle increments within the range from -52° to +52°. The mission incident surface fluxes were calculated by time averaging the orbital heat flux over one complete orbit and tabulating the average flux versus orbit β angle, as summarized in Table 1-7. The results show that for the row 6 location, the peak heat flux occurred at a β angle of -52° and the minimum heat flux is at a β of +52°.

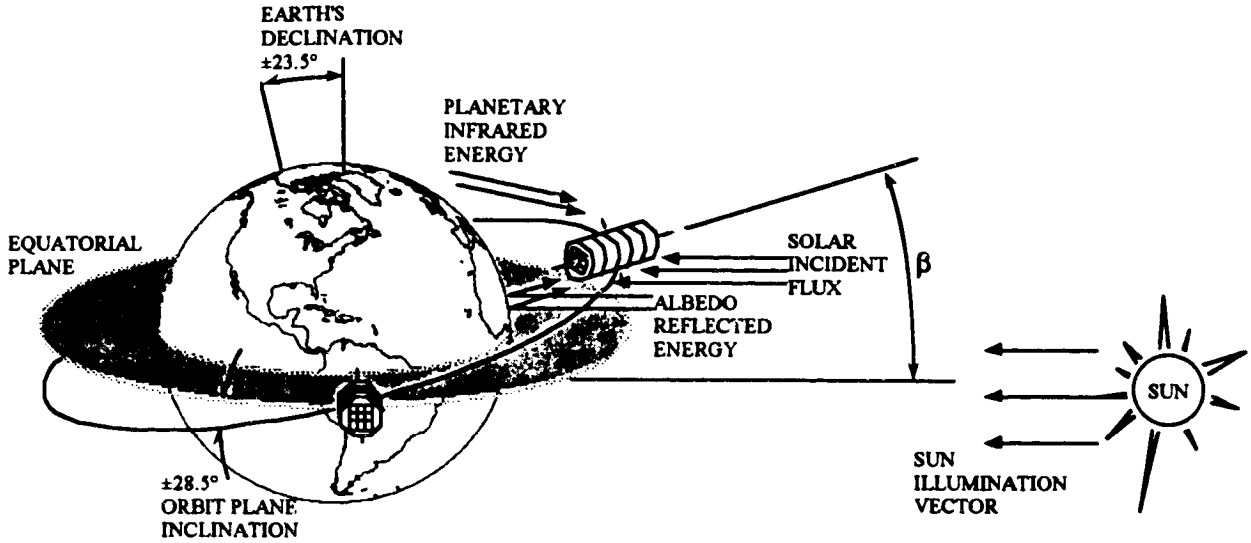

Beta Angle:

β = Angle between the plane of the orbit and the sun illumination vector

Range = -52 < β > ±52°, calculated by adding the declination of the Earth (±23.5°) to the inclination of the orbit plane (±28.5°)

Principal Heating Sources in Space:

Solar Incident Flux = Heat due to the direct illumination from the sun (Watts/M ^{2})

Albedo = Heat due to the portion of the solar incident energy reflected from the planet on to the LDEF (23%-32% from this type of orbit, Watts/M ^{2})

Planetary = Heat emitted from the planet (Watts/M ^{2})

OIM 94.013.125

Figure 1- 23. LDEF Principal Heating Sources

Table 1-7. LDEF Average Incident Heat Flux (Solar + Albedo)
BTU/Hr-Ft^2 by Beta Angle

Row	-52	-40	-30	-20	-10	0	10	20	30	40	52
1	6.03	7.99	9.37	10.47	23.86	43.76	68.27	98.82	141.04	182.52	234.22
2	6.38	19.54	35.49	51.88	67.19	83.99	99.09	112.30	125.46	138.73	162.39
3	53.69	69.99	81.70	91.34	98.79	103.88	106.94	107.54	105.96	102.14	95.95
4	116.22	115.85	114.58	111.62	106.70	99.38	90.54	79.48	66.76	52.48	33.48
5	191.95	149.94	127.50	108.49	90.03	71.67	53.83	36.49	20.34	7.96	6.06
6	245.39	190.93	147.40	103.11	57.70	27.90	11.17	10.37	9.27	7.89	5.90
7	234.92	183.04	141.58	99.36	68.72	44.11	20.91	10.47	9.37	7.99	6.01
8	163.42	139.81	126.43	113.22	99.21	84.47	68.62	52.37	35.81	19.79	6.47
9	96.72	103.04	106.87	108.55	107.89	104.84	99.59	92.07	82.29	70.61	53.92
10	33.65	51.93	67.30	80.10	91.26	100.32	107.55	112.51	115.39	116.79	116.70
11	6.08	7.97	20.46	36.77	54.25	72.32	90.71	109.28	128.30	150.81	192.24
12	5.93	7.89	9.27	10.37	11.17	28.08	58.02	103.40	147.61	191.19	245.15
Space	84.82	105.56	119.34	129.49	135.71	137.80	135.71	129.49	119.34	105.56	84.82
Earth	39.82	42.10	44.28	46.14	47.34	47.79	47.34	46.14	44.28	42.10	39.82

Actual internal flight temperatures were recorded at intervals of approximately 112 minutes for the first 390 days of LDEF's mission. Temperatures were taken using five copper-constantant thermocouples, one suspended radiometer, and two thermistors were used for reference measurements. The actual recorded temperature range for all seven locations was from a low of 39°F to the maximum of 134°F. Table 1-8 compares the measured flight temperatures with the post-flight calculated temperatures.[35,36] Also included are the design temperataures which were maintained throughout the mission. The calculated temperatures and thermal gradients derived from the thermal model calculations were found to be accurate with the flight temperature data from LDEF.

Table 1-8. Comparison of LDEF Temperature Ranges

LDEF Location	Measured °C (°F)	Post-Flight Calculated °C (°F)	Design Limits °C (°F)
Internal Average Temperature	11 - 32 (52 - 89)	14 - 32 (58 - 89)	-12 - 50 (10 - 120)
Structure North/South (Rows 6/12)	2 - 57 (35 - 134)	4 - 58 (39 - 136)	-23 - 65 (-10 - 150)
Structure East/West (Rows 3/9)	N/A	12 - 38 (53 - 100)	-23 - 65 (-10 - 150)
Earth End Structure	14 - 39 (56 - 103)	14 - 40 (57 - 104)	-12 - 57 (10 - 135)
Space End Structure	16 - 32 (60 - 90)	18 - 36 (64 - 96)	-12 - 57 (10 - 135)

1.4.1.3 Ionizing Radiation

LDEF was well-instrumented with ionizing radiation dosimeters, including thermoluminescent dosimeters (TLD's), plastic nuclear track detectors (PNTD's), and a variety of metal foil samples for measuring nuclear activation products. In addition, the induced radioactivity produced in various spacecraft components provided information on the radiation exposure. The estimated radiation fluence exposure in the LDEF orbit provided input into transport calculations codes (e.g., High Energy Transport Code) to develop scaling relations for predicting the radiation environment for other missions (e.g., Space Station, Space Observatories) and to assess the accuracy of current models.

Because the LDEF orbit altitude was well below the Earth's Van Allen radiation belts, except at the small region of the belt that is generally referred to as the South Atlantic Anomaly, the LDEF and the onboard experiments were exposed to only modest levels of ionizing radiation. The penetrating ionizing radiation that the LDEF did received resulted primarily from protons trapped in the South Atlantic Anomaly Region of the Van Allen belts, and to a much lesser degree, galactic protons and albedo neutrons and protons emanating from the Earth's atmosphere due to galactic cosmic rays bombardment. Table 1-9 summarized the energy range for the different sources. Figure 1-24 shows the cumulative ionizing radiation of these penetrating particles striking LDEF. The predicted trapped proton integral fluence for the LDEF is presented in Figure 1-25.

Figure 1-26 shows the depth dependence of proton and neutron fluences over all energies produced by trapped proton, galactic proton, albedo proton, and albedo neutron environments during the LDEF mission time.[37] The spatial dependence of the results are in terms of the areal density depth in aluminum from 0 to 100g/cm^2. To roughly relate these thicknesses to LDEF, the spacecraft diameter is 32 g/cm^2, and the length is 68 g/cm^2. (This is based on an average density obtained from the overall dimensions of 14 ft. diameter x 30 ft. long, a spacecraft structure weight of 8,000 lb., and a weight of 13,400 lb. for the experiments.)

Table 1-9. LDEF Sources of Ionizing Radiation[38]

Source	Minimum Incidence Energy	Maximum Incidence Energy	Fluence cm^{-2}	Range of Angular Distribution
Trapped Protons	15 MeV	600 MeV	4.3×10^9	4π
Galactic Protons	3.2 GeV	100 GeV	2.8×10^7	2π
Albedo Protons	15 MeV	3.5 GeV	2.3×10^7	4π
Albedo Neutrons	1 keV	3.0 GeV	7.4×10^7	1.3π

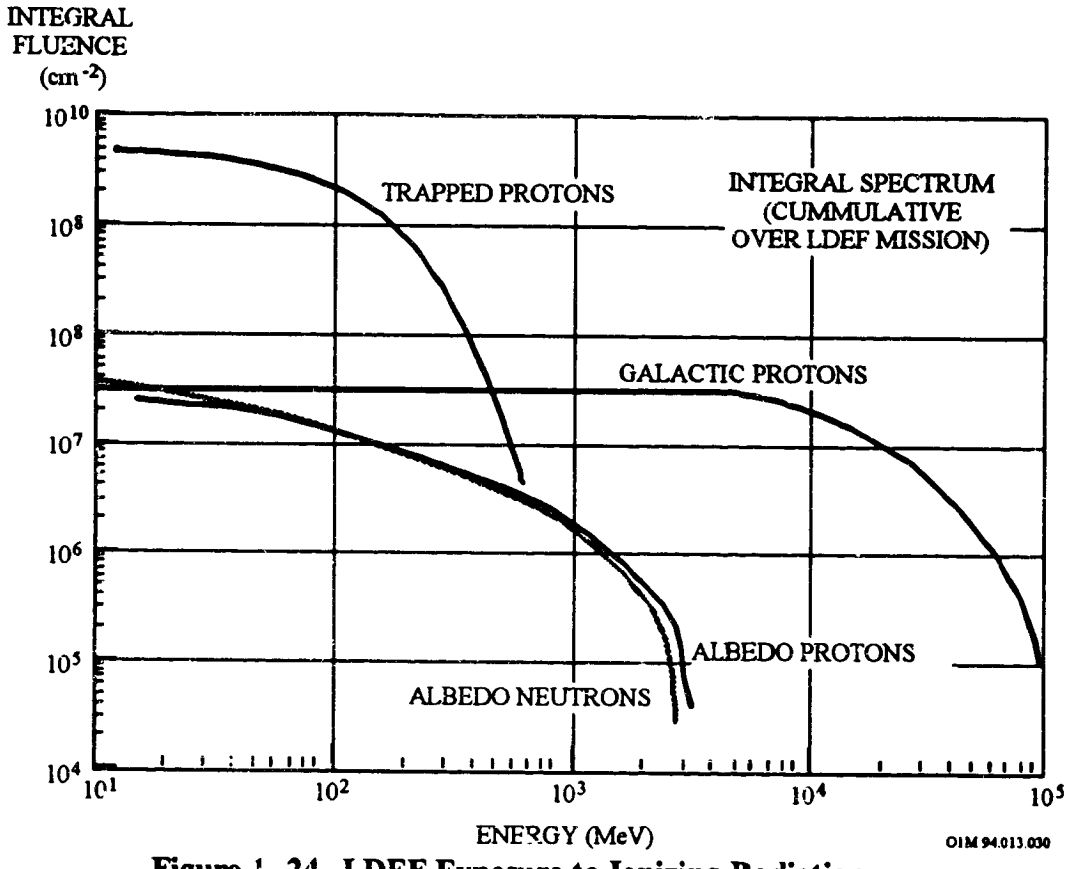

Figure 1- 24. LDEF Exposure to Ionizing Radiation

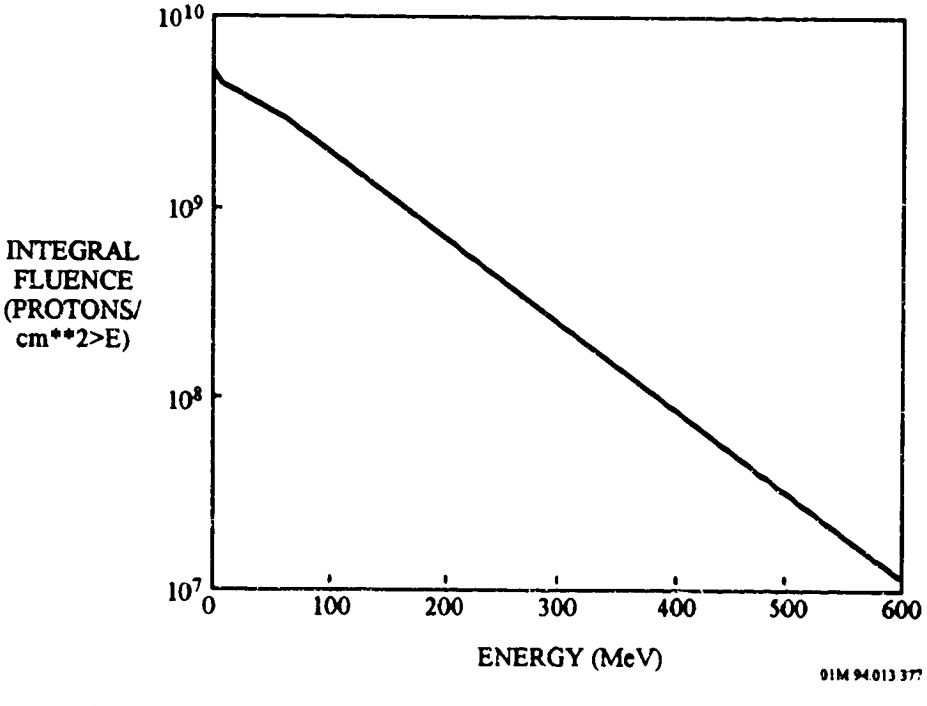

Figure 1- 25. Predicted Integral Fluence of Trapped Protons Striking LDEF Surfaces

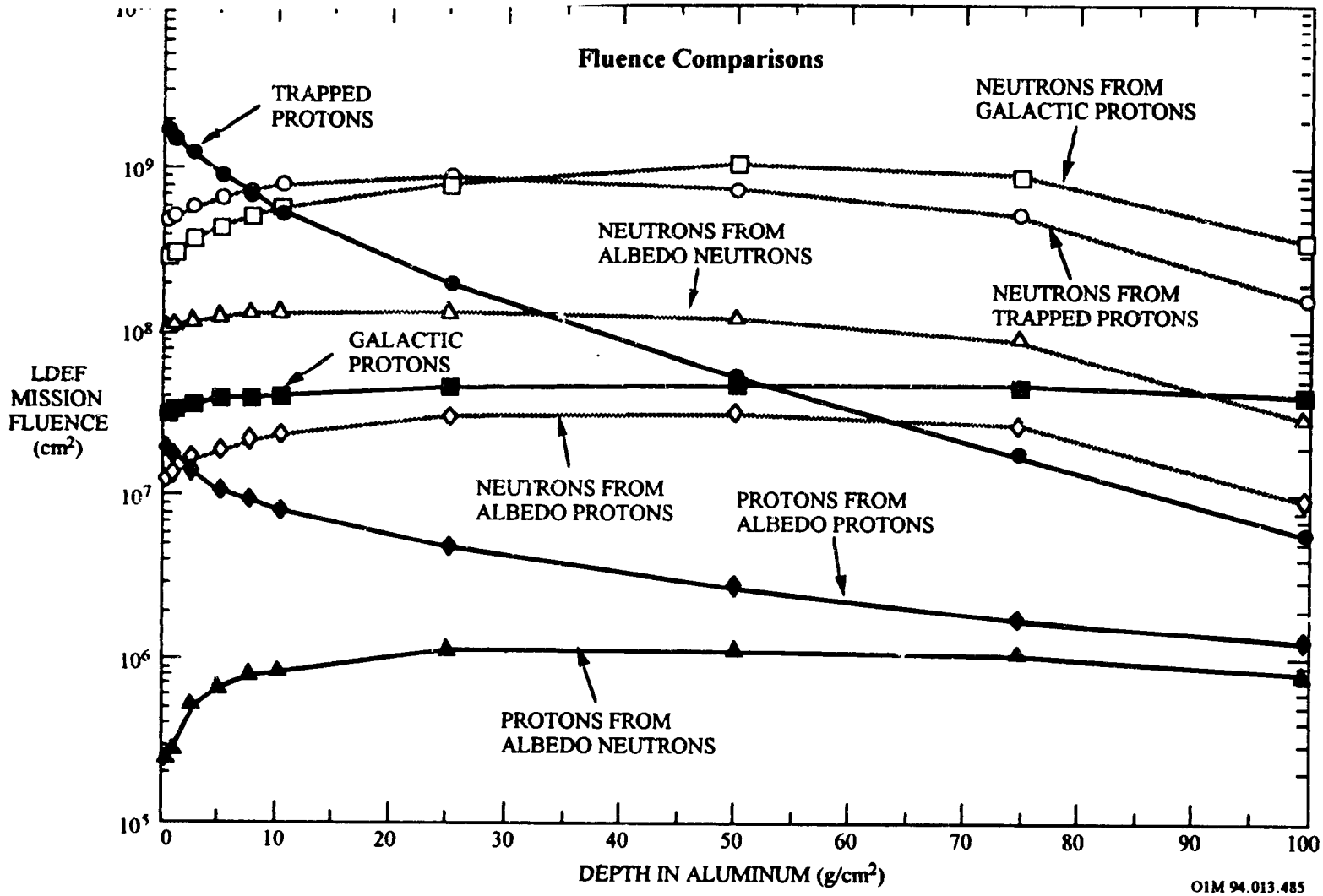

Figure 1-26. Depth Dependence of Proton and Neutron Fluences During LDEF

The geomagnetically trapped electrons are of low energy and produced effects only very near the spacecraft surface. The predicted integral fluence of trapped electrons striking the LDEF surface varied from $1x10^6$ to $1x10^{12}$ electrons/cm^2 at energies between 0.1 and 3.7 MeV. The trapped electrons are of such low energy that they contribute significantly to the dose only at small penetration depths (≤ 0.5 g/cm^2) and do not contribute at all to radionuclide production. The integral fluence of the trapped electrons on the LDEF is presented in Figure 1-27.

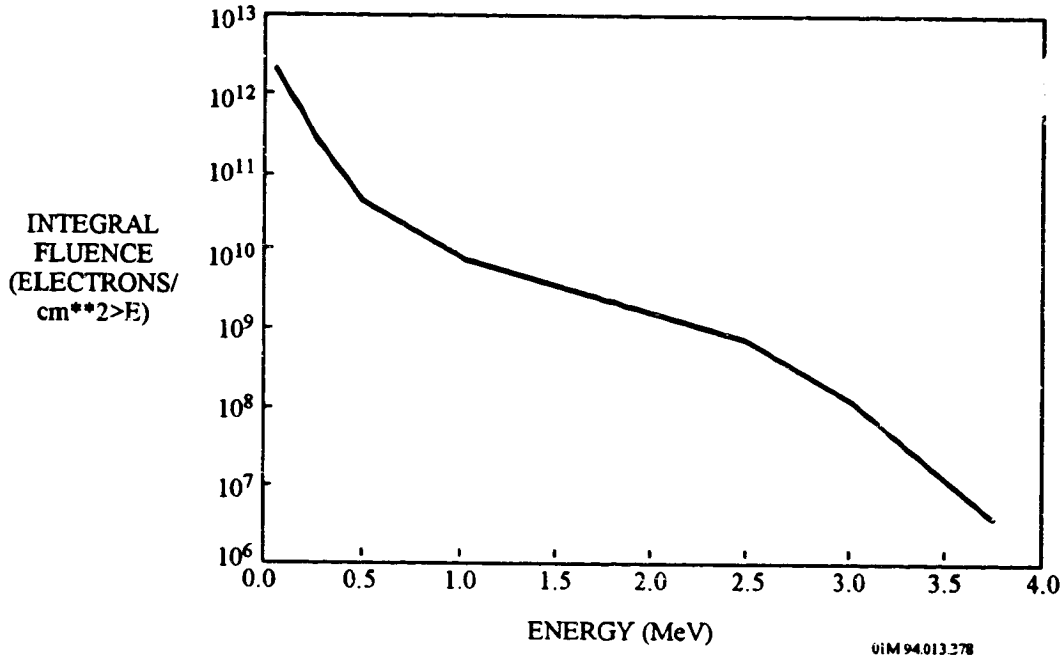

Figure 1- 27. Predicted Integral Fluence of Trapped Electrons Striking LDEF Surfaces

1.4.1.4 Micrometeoroid and Debris

LDEF provided a huge collection of impact data that cover a wide size range of impact craters from below 0.01 mm (10 μm) to 5.25 mm. The LDEF Meteoroid and Debris Special Investigation Group (M&D SIG) has catalogued all meteoroid and space debris impacts on LDEF. All exposed surfaces including the experimental trays and all of the exterior surfaces have been optically scanned for impact features. Target materials range from the aluminum 6061-T6 frame components to glasses and ceramics, composites, polymers, electronic materials, and paints. Large area surfaces that were studied included the experiment power and data system (EPDS) sunshields, the environment exposure control canister (EECC) sunshields, and the M0003 signal conditioning unit (SCU) covers. The EPDS sunshields are aluminum panels painted with A-276 white thermal control paint, the EECC sunshields are chromic acid-anodized aluminum, and the SCU covers are aluminum painted with S13G/LO white thermal control paint. The data have been reduced to the form of impact fluences (hits per unit area, or the integral of the crater production rates) versus crater diameter for various surface orientations. Detailed results of this investigation can be found in several references by See et al.,[39,40] M.E. Zolensky et al.,[41] M.J. Meshishnek el al.,[42] M. Allbrooks and D. Atkinson,[43] C. Coombs et al.,[44] A. Watts el al.,[45] and J.M. Zwiener and M.M. Finckenor.[46]

Overall, 34,336 impacts were found on the LDEF surfaces, of which ~4000 of these impact images have been stored on laser disc.[f] The largest impact crater was 5.25 mm in diameter. Distribution of impact according to surface types are summarized in Table 1-10.[47]

Table 1-10. Distribution of Impact Features on LDEF

Size (mm)	Bolts, Shims Clamps	Tray Flanges	Experimental Surfaces	LDEF Frame	Thermal Blankets	Totals
<0.3	NA	NA	158	NA	2831[1]	3069
>0.3	NA	NA	172	NA	625[2]	797
<0.5	1318	1923	14171	5171	NA	27385
>0.5	161	419	2106	432	NA	3118
Totals	1479	2342	16687	5603	3456	34336

1. Count is incomplete; the <0.3 mm diameter features from F02, C05, C06 and D07 not included.
2. Count is incomplete; the > and =0.3 mm diameter features from F02 are not included..

[f] The total number of impact features has increased with the discovery of numerous smaller impacts and the continued analysis of the approximately one-fourth of the experiment trays designed for meteoroid/debris investigation. However, these smaller impacts have no significant damage to material surfaces which could affect the design of spacecraft and selection of spacecraft materials.

Impact data were evaluated for impact craters having diameters from 0.1 mm to less than 3 mm in order to determine the flux as a function of crater diameters versus the angle from the velocity vector. A summary of the crater impact data of diameter ≥ 0.1 mm reported in each row by surface type is provided in Table 1-11.[48] The count column lists the total number of craters, the area column lists the area (square meters) used to calculate flux values. The flux column provides the reduced counts of impact craters per square meter per year, for each type of surface. The angle "Beta" is the angle from the velocity vector (or ram) to the normal to each row. Note that Beta increases with increasing row number in a positive value up to 180 degrees. Negative values mean the direction is decreasing with row number up to a -180 degrees. As an example, row 9 is -8 degrees.[49]

Table 1-11. Crater Impact of Diameter ≥ 0.1 mm

Row No.	Experiments & Trays			LDEF Structure			Thermal Panels			
	Count	Area m^2	Flux	Count	Area m^2	Flux	Count	Area m^2	Flux	Angle Beta
1	622	6.58	16.43	112	1.22	15.95	46	0.316	25.33	+122°
2	126	6.58	3.33	68	1.22	9.68	36	0.316	19.83	+142°
3	399	6.58	10.54	74	1.22	10.54	10	0.316	5.49	+172°
4	311	6.58	8.22	96	1.22	13.67	15	0.316	8.26	+158°
5	846	6.58	22.36	184	1.22	26.20	29	0.316	15.97	+128°
6	915	6.58	24.15	442	1.22	62.94	12	0.316	6.60	-98°
7	2108	6.58	55.71	572	1.22	81.46	170	0.315	93.62	-68°
8	3289	6.58	86.92	939	1.22	133.72	175	0.316	95.37	-38°
9	3077	6.58	81.40	924	1.22	131.59	246	0.316	117.53	-8°
10	3118	6.58	82.40	652	1.22	92.85	204	0.316	112.34	+22°
11	2435	6.58	64.35	493	1.22	70.21	168	0.316	92.52	+52°
12	1620	6.58	42.81	321	1.22	45.71	132	0.316	72.56	+82°
Space End	112	5.966	3.26	79	—	—	165	4.65	6.16	-90°
Earth End	1095	5.966	31.92	649	—	—	1200	4.55	44.82	-90°

Approximately 10 times more impact craters occurred on the leading edge (ram) of LDEF compared to the trailing edge (e.g., compare Rows 9 and 3). Apparent flux variations occurred within the same row for different materials. Flux values derived from impacts on experiment surfaces are normally lower than those from the structure or thermal panels. Each experiment was composed of a variety of different materials. Impacts on some surfaces exhibited excellent contrast making identification for counting fairly easy, while other materials, such as composites, exhibited very poor contrast making it much more difficult to identify impacts. The LDEF structure and thermal panels had smaller exposed areas than the experiment surfaces, but each consisted of the same type material and coating resulting in a more reliable and consistent count. During the 5.75 year mission LDEF experienced a maximum of approximately 140 significant impact craters/m^2/yr.

Some of the most salient findings concerning the separate meteoroid and debris impact populations, and their directionalities, that have been derived from LDEF investigations are summarized below.

Micrometeoroid versus Debris Impacts. Both orbital debris and meteoroids impacted LDEF. Separation of the two populations is determined by the composition of the residue, if any, in the impact craters. Most spacecraft debris particles consist of aluminum fragments of spacecraft structures, of aluminum oxide from the burning of solid rocket fuel, or of paint particles (shown by the elements zinc, titanium, and aluminum, whose oxides commonly provide the white pigments in thermal paints). Below 50 microns in diameter, orbital debris appeared to dominate the crater populations on leading-edge LDEF surfaces. For impact craters smaller than about 100 microns in diameter, orbital debris impacts started to become more numerous than meteoroid impacts on aluminum surfaces at about 50 degrees from the leading edge.[50]

Temporal Variations of Impacts. The Interplanetary Dust Experiment (IDE) on LDEF discovered the temporal nonuniformity in the impact rates.[51] This active meteoroid experiment electrically recorded when each impact occurred that penetrated one of many MOS detectors placed around LDEF. This experiment recorded over 15,000 impacts that penetrated either 0.4 mm or 1.0 mm thick dielectric layers of MOS capacitors. The IDE data has shown that LDEF encountered significant amounts of orbital debris in the form of small particles concentrated in clouds or rings, where the impact rate would greatly increase for a few minutes on every orbit IDE also detected, "beta meteoroids", which are dust grains that are leaving the solar system on hyperbolic orbits to become interstella grains, and their apparent flux should be at a maximum when a sensor faces toward the Sun. The beta's were best, and most clearly, detected by rearward-facing IDE sensors when they faced the Sun.

Spatial Density Dependency of Impacts. The spatial density of impact craters is much greater on surfaces close to the leading edge of LDEF than it is on surfaces near, or at, the trailing edge. Directional dependence of meteoroid/debris impacts as a function of the angle from the velocity vector can be seen from the count and flux data listed in Table 1-11, which is plotted graphically in Figure 1-28. D. Humes has shown the significant dependence of meteoroid/orbital debris flux vs. angle from velocity vector as derived from model calculations and from the LDEF experiment S0001 data.[52] Note that the flux data for the structure surfaces is skewed from velocity vector zero degree reference. This skewing resulted from assuming the longerons pointed in the same direction as the rows, and combining their count data with that for the intercostals (which do face in the same direction as each row). The offset in angle is 15 degrees would restore part of the symmetry. Leading edge-to-trailing edge ratios of spatial densities of

craters depended on crater size and ranged from about 10 for craters smaller than about 50 microns in diameter[53] to about 20 for impact craters larger than about 500 micron in diameter.[54,55]

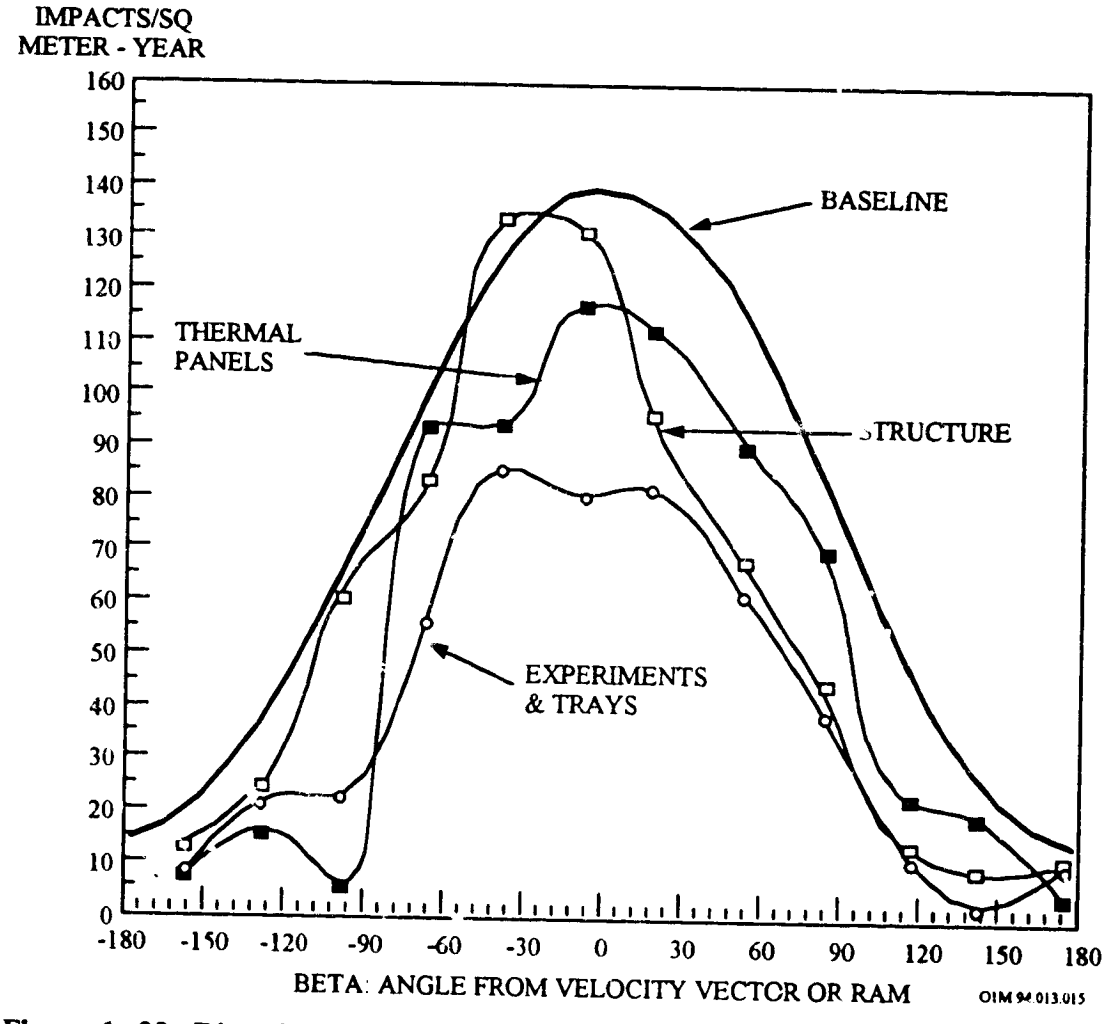

Figure 1- 28. Directional Dependence of Meteoroid/Space Debris Impact Craters.

A simple function, defined as the "baseline," encompasses all of these curves as a worst case value. A simple relationship for the total number of impacts is approximated by the following equation which is also plotted in Figure 1-28.

$$\text{Flux } f(\text{Beta}) = a + b \cos^2(\text{Beta}/2)$$

where: $a = 15$

$b = 125$

Beta = degrees from velocity vector or ram direction.

Size Dependency of Impact Craters. A relationship between total number of impacts per crater diameter was determined by summing all of the impacts on LDEF for each crater diameter.

C 2

Table 1-12 lists impacts summed on each row for diameters between 0.1 mm up to 2.5 mm. This count includes impacts on experiments, trays, clamps, structures, and thermal panels. The total count for each diameter was summed for all rows and plotted in Figure 1-29. This size distribution can be approximated by the following relationship given by the following equation which is plotted in Figure 1-29.

$$\text{Ln}(d) = C1 + (C2 * N)$$

where:

N	=	number of impacts craters
Ln	=	natural logarithm
d	=	diameter of crater in mm.
C1	=	+8.693612
C2	=	-3.532209

This approximation permits an estimation of the actual number of impacts below 0 5 mm where incomplete counting occurred. A summation was made using this relation for all diameters between 0.1 mm and 3.0 mm. The total sum was used to normalize the size distribution data into a fractional distribution.

Table 1-12. Impact Crater Size Distribution

Total Number of Impact Craters Per Row and Per Diameter

Diam (mm) Row #	0≤.1	0.5	0.6	0.7	0.8	0.9	1.0	1.1	1.2	1.3	1.4	1.5	1.6	1.7	1.8	1.9	2.0	2.1	2.2	2.3	2.4	≥2.5
1	10	32	34	25	25	13	15	5	0	1	2	0	0	0	0	0	0	1	0	1	0	0
2	25	25	7	10	12		3	2	1	1	1	0	0	0	1	0	0	0	0	0	0	0
3	22	9	13	9	10	4	3	2	2	1	0	2	1	0	2	1	1	0	0	0	0	1
4	29	20	11	5	7	2	2	6	2	0	0	1	0	0	0	0	0	0	0	0	0	0
5	29	29	21	13	15	5	4	4	2	0	1	3	1	1	0	0	0	0	0	0	0	0
6	68	45	43	33	19	16	15	5	2	4	2	3	2	0	0	0	0	0	0	0	0	0
7	65	106	72	61	32	28	15	11	3	8	2	4	2	1	0	2	0	0	2	1	0	1
8	85	132	97	75	42	29	22	9	13	13	5	6	1	1	0	1	0	0	0	1	0	4
9	100	125	95	75	51	24	22	27	15	9	10	8	6	1	5	0	0	1	0	1	0	7
10	124	149	107	79	51	24	30	20	15	11	4	7	5	1	5	2	7	4	1	2	0	6
11	66	106	83	109	55	22	22	9	12	7	3	3	6	2	2	0	0	1	0	1	1	5
12	65	51	46	54	33	11	18	4	9	1	2	4	2	2	1	0	0	0	2	0	0	3
Totals	688	829	629	548	352	178	171	104	76	56	32	41	26	9	16	6	8	6	5	7	1	27

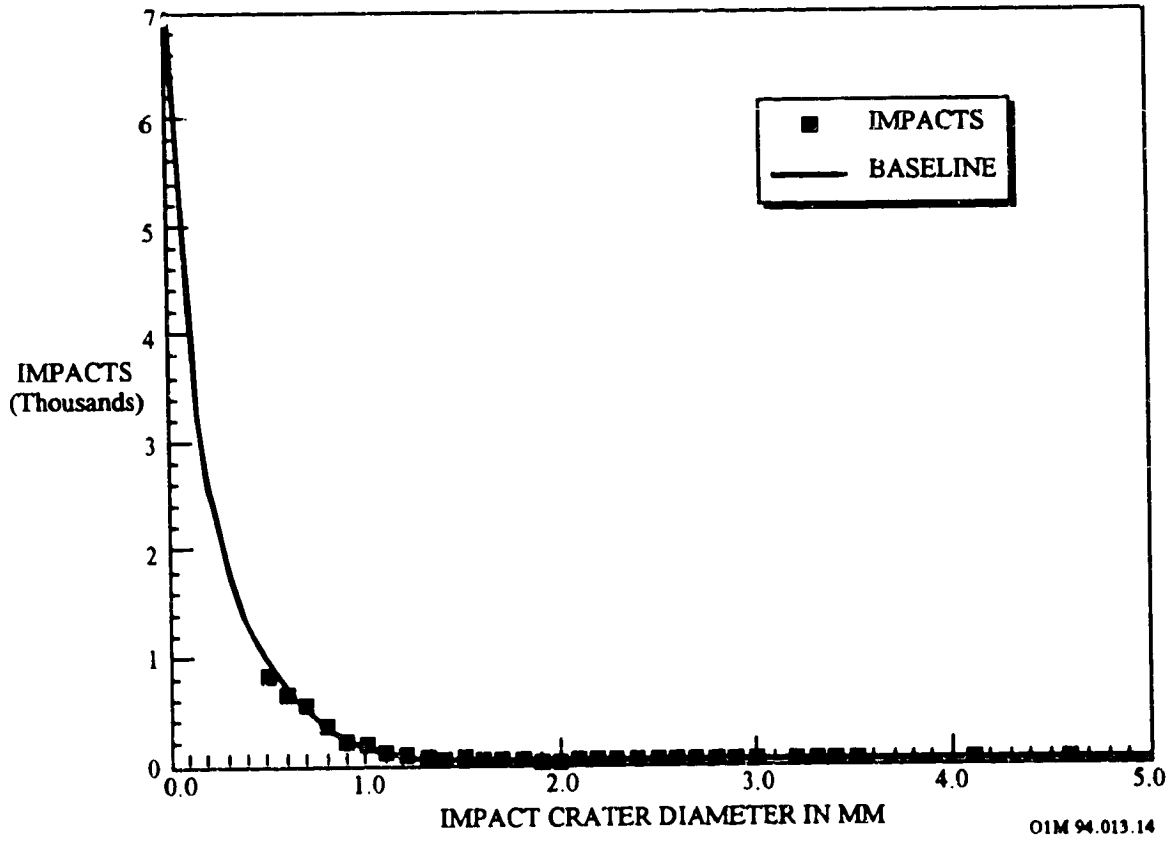

Figure 1- 29. Size Dependence of Impact Craters.

1.4.1.5 Contamination Effects

Most of the particulate contaminants present in orbit were deposited on the surface of LDEF during ground exposure or during the launch.[56] The particles were characteristic of fabrication, assembly, and integration activities, with some of the distributions suggesting launch redistribution or cross contamination. Particulate contaminants effect systems both mechanically and optically. Particles optically obscure, scatter, refract, diffract, and reflect light. They may also become infrared emitters when heated by solar radiation. Scatter, refraction, diffraction, and reflection all change the path of a ray of light. The effect is to introduce unwanted energy causing a decrease in the signal-to-noise ratio in an optical system, thereby decreasing the device's sensitivity. The cleanliness level of LDEF when it entered orbit was approximately a MIL-STD 1246B Level 1000 for particles smaller than 250 micrometers or a Level 2000 for particles smaller than 750 micrometers.

The amount of molecular contaminants in the form of nonvolatile residues averaged over the surface of LDEF at launch has been estimated at about 2.5 $\mu gm/cm^2$. This corresponds to a MIL-STD 1246B Level C. This may have been sufficient to degrade some systems, but its effects were largely hidden by the far greater amount of outgassing materials deposited on the surface of LDEF during orbit.

In orbit, additional particulate contaminants accumulated as a result of impacts with meteoroids and space debris. These contaminants tended to be deposited very close to the impact, with concentration dropping off with the square of the distance from the impact, as would be expected. Impacts with surfaces projecting radial from the surface of LDEF, such as tray edges or bolt heads, resulted in the greatest amount of material being deposited on the surface of LDEF. The concentration of such debris could be very detrimental to optical systems within a few inches of the impact.

The most detrimental contamination event in orbit was the outgassing and redeposition of molecular contaminants on the surface of LDEF. The brown discoloration caused by a contaminating molecular film on the surface of LDEF was evident through the windows of the Space Shuttle Columbia as it approached LDEF. This brown film was widely dispersed over the trailing rows of LDEF and at the space and Earth ends. Closer examination in Spacecraft Assembly and Encapsulation Facility (SAEF-2) following recovery permitted a much more detailed analysis of the film and its distribution. Large areas of the exterior surface were covered with a film a few hundred nanometers thick. In some areas it was as much as a few hundred micrometers thick and completely opaque. Analysis of the film indicated it was a polymer

consisting of a combination of silicones and hydrocarbons. The ram facing trays appeared clean but surface elemental analysis of ram surfaces indicated a silica residue remaining from atomic oxygen attack of the brown film. An infrared analysis of the film and possible sources indicated that two systems had sufficient mass to be major contributors to the film; the thermal control paints and the silicone adhesives used with both fasteners (to enable fastener assemblies to survive vibration testing without a decrease in installation torques) and the bonding of velcro to LDEF and/or experimenter hardware.

The local thermal loading caused by the molecular film created a variety of detrimental effects. The film was a relatively effective absorber and resulted in significant heating of some surfaces. The delamination of thin films in optics and metal-plated composite surfaces has been attributed to the combination of poor coefficient of thermal expansion matching between the delaminating surfaces and the thermal cycling extremes due to the presence of this contaminating film. The film increased the thermal loading over many areas of the satellite b it seemed to have relatively little effect on the anodized aluminum surfaces of the tray clamps. The ratio of absorptance to emissivity for the tray clamps was about 2.27 for both leading and trailing edge clamps A276 white thermal control paint buttons on many of the clamps did, however, experience a change. Paint buttons on the leading rows had an α/ε ratio of approximately 0.32 while those on the trailing edge were about 0.63. The brown discoloration on trailing edge buttons was largely due to the modification of the top organic layer of the paint as a result of ultraviolet exposure.

A decrease in the transmission through some optics was noted and has been attributed to the molecular film. A change in some of the wavelength characteristics of coated optics was noted and has been attributed to the effect of an added contaminant thin film. Elemental analysis of the surface of some of these optics on the ram side of LDEF indicated a silica residue was present from the atomic-oxygen-degraded molecular film. Other optical effects included selective reflection due to submicron droplet size, decreased signal-to-noise ratio broadband, and increased background in the infrared.

The recovery operation redistributed LDEF contaminants that were presumably stable in orbit. These contaminants included thin metal foils the remained after the organic film on which they had been vapor deposited had been removed by the atomic oxygen exposure. Fragments of partially eroded polymers were also widely distributed. Paint pigments, ash from a variety of composites, fragments of thick molecular film deposits, and both glass fibers and graphite fibers freed from atomic oxygen eroded composite materials completed the compliment of redistributed LDEF materials. Materials from the Space Shuttle were also transported to the surface of LDEF.

The materials from the Space Shuttle included liquid droplets containing hydrocarbons as well as solid particles, and glass from tile material and from the bay liner. This redistribution of contaminants existed through the final removal of LDEF from the Shuttle Bay.

The exposure to contaminants continued during the deintegration in SAEF-2. Automatic airborne particle count data indicated a controlled class 100,000 clean room environment in SAEF-2, but pollens, natural minerals, clothing fiber, paper fiber, etc., accumulated on the surface of LDEF during its exposure.

In summary, the systems most susceptible to contamination were thermal control surfaces as shown in Figure 1-30.[57] The systems most likely to be a source of contamination were thermal control paints, silicone adhesives, polymeric films, and carbon-based sheet materials.

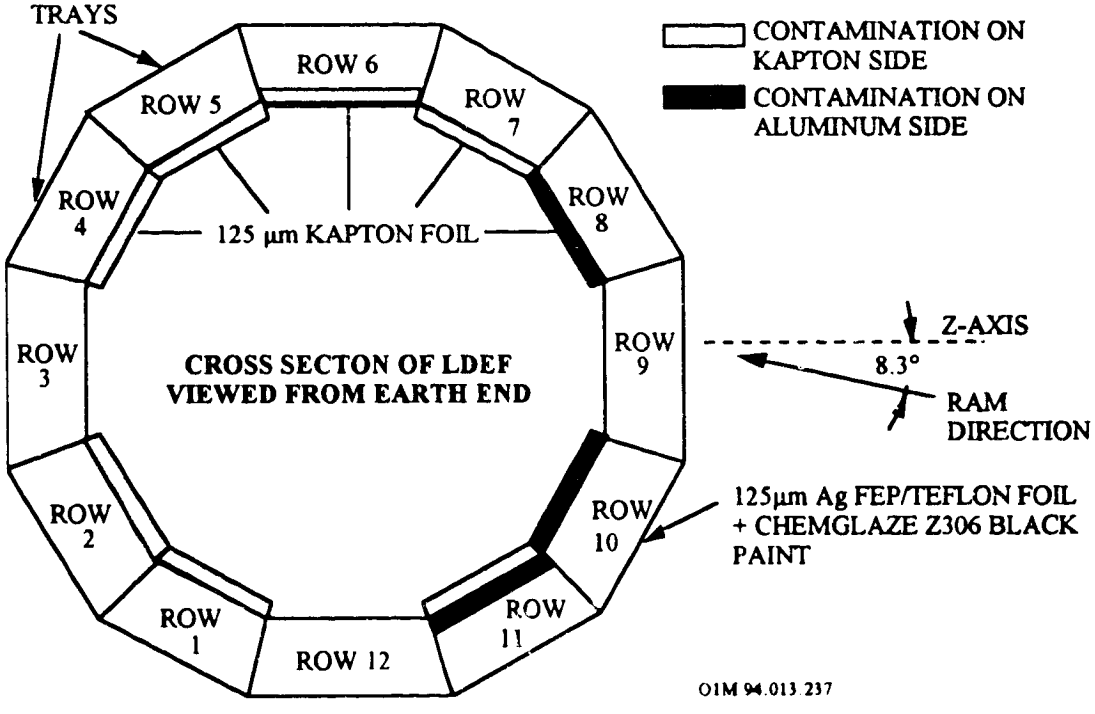

Figure 1- 30. Contaminated Thermal Surfaces on LDEF

1.4.1.6 Vacuum Exposure

Neglecting the contribution from LDEF-generated contamination, the molecular density adjacent to individual LDEF surfaces at any given time was dependent on the LDEF orbital altitude, the solar activity, and the orientation of the surface with respect to the LDEF velocity vector. The density increased as the altitude decreased and as the solar activity increased. The density also built up adjacent to leading surfaces as a result of ram effects, and it diminished adjacent to trailing surfaces as a result of wake shielding effects.[58]

The ambient molecular density along the LDEF orbit was lowest early in the mission while the LDEF orbital altitude was above 250 nautical miles and the solar activity was near minimum. The predominant molecular species were atomic oxygen (approximately 1.86×10^7 molecules per cubic centimeter) and nitrogen (second in abundance with a density several orders of magnitude lower than the atomic oxygen).

The ambient molecular density along the LDEF orbit was highest (approximately 6.58×10^8 molecules per cubic centimeter) late in the mission when the orbital altitude had decayed to approximately 179 nautical miles and the solar activity had increased to near-record highs. The predominant molecular species at that time was still atomic oxygen (5.42×10^8 molecules per cubic centimeter) and nitrogen was still second in abundance (1.06×10^8 molecules per cubic centimeter).

The ram effects made the molecular density adjacent to surfaces on the leading side of the LDEF approximately an order of magnitude higher than the ambient density. The wake shielding effects reduced the molecular density adjacent to surfaces on the trailing side of LDEF more than an order of magnitude. The molecular densities presented above were calculated using the model described in the Smithsonian Astrophysical Observatory Special Report 375.

1.4.1.7 Gravity/Accelerations

The LDEF experiments were exposed to very low accelerations during the mission since the facility was passively stabilized and there were no systems on board to generate vibrations or shocks. The acceleration level at the center of the LDEF remained less than 1E-7 g's throughout the mission.[59]

1.4.2 The COMES Experiment on Mir

The experiment COMES was installed outside of the MIR space station during an extravehicular activity. On January 11, 1990, the COMES experiment unit was refolded during an extravehicular activity of cosmonauts after having spent 392 days (13 months and 2 days) in space outside of the MIR; then it was stored aboard the station until February 19, 1990, at which date it was returned to Earth.[60] During the flight, the MIR station followed an orbit located between 350 and 425 km in altitude, inclined at 51.6°.

The COMES experiment consisted of four panels which were deployed by a cosmonaut in space outside of MIR with the possibility of exposing samples on both sides, conventionally identified as "V" and "R", to vacuum, O-atoms and UV radiation for 1.1 year. Table 1-13 summarizes the exposure conditions for the COMES experiment. Differentiation of the effects of UV-radiation and oxygen atoms was possible due to the differences in exposure conditions and the use of transparent filters protecting some on the samples.

Table 1-13. Space Environment Exposure Conditions for the COMES Experiment

	COMES-MIR	
	FACE V	**FACE R**
Oxygen atoms cm^{-2}	$1.2x10^{18}$ to $7.5x10^{19}$ (1)	$3.5x10^{20}$ to $5.8x10^{20}$ (2)
Solar UV (esh)	2850(2)	1900(2)
Temp. Cold case (°C)	-60 to -70	-60 to -70
Temp. Hot case (°C)	+10 to +30	+50 to +60

(1) Estimated from data of experiment calorimeter
(2) Estimated from AO reactivity erosion of Kapton (3.0×10^{-24} cm^3atom^{-1})and Terphane (PET) (3.0×10^{-24} cm^3atom^{-1}) samples

A description of the V and R modules are provided below.

V Side. A total of 113 samples (20 x 20 mm squares or circles of 25 mm in diameter) had their central areas exposed to the space environment, without mechanical stress (20 mm in diameter). Among them, 8 groups consisting of 4 identical samples of the same material were used to distinguish the effects of different space environment constituents.

- Exposure to all of the parameters (UV, atomic oxygen, vacuum, temperature).

- Exposure behind a 1 mm thick silica filter transmitting solar radiation with a wavelength greater than 190 nm (thus including most of the solar ultraviolet radiation).

- Exposure behind a 1 mm thick optical filter only transmitting wavelengths greater than 360 nm.

- Exposure behind a metal disk, painted white and protecting the sample against the effects of atomic oxygen and UV radiation.

In addition, six samples of polymeric films were exposed to the space environment while maintained under traction by a spring and six samples of composite materials with an organic matrix underwent bending stress.

R Side. Thirty-two samples were exposed without mechanical stress.

As the Russian team of the experiment had not provided much information on the altitude of the station during exposure of the COMES experiment, it is difficult to ascertain exactly the amount of sunlight received by each side of the experimental unit. However, after analysis of the data from the "Microcalorimeter" experiment, also mounted on the COMES panels, it may be estimated that the V side received a solar UV dose of 2850 esh and the R side 1900 esh. For the same reasons, it was not possible to calculate, by means of the MSIS-86 environment model, the fluence of oxygen atoms accumulated by each of the two sides of COMES during the mission. Nor was it possible to determine whether the oxygen atoms had been received more for a particular inclination to the surfaces. On the basis of the erosion measured on samples of Kapton polyimide and Terphane polyethylene terephtalate arranged over the surface, it may be estimated that the fluences received were probably between 3.6×10^{20} and 5.9×10^{20} atoms/cm^2 on the R side, and between 3.7×10^{18} and 7.3×10^{19} atoms/cm^2 on the V side. It should however be pointed out that; (a) whereas the fluences appear to be rather uniform on R, this is probably not the case on V, (b) these values have probably been underestimated, since a strong contamination, in particular by silicones, was detected on the samples on both sides; this must have protected the surfaces, at least partially, against atomic oxygen. The temperature estimates of the sample-holders on COMES, determined using thermal modeling, indicated that, in the case of the hottest exposure, the average temperature of the sample holders on the V side is probably of the order of +10 to -30°C and that of the R side of the order of +50 to +60°C; in the case of the coldest exposure (experiment unit in the shade of the station), the temperature was determined for both sides to be between -60 and -70°C.

1.4.3 The Removable Cassette Container Experiment (RCC-1) on Mir

The Removable Cassette Container experiment, (RCC-1), which was flown on the Mir Orbital Station from 11 January 1990 to 26 April 1991, evaluated several thermal control coating materials. During the flight the Mir was in LEO with an apogee in the range 380 - 430 km, perigee in the range 360 - 390 km, and an inclination of 51.6 degrees. The results confirmed that zinc oxide and zinc oxide orthotitanate white thermal control paints in metasilicate binders are the most stable upon exposure to the space environment.[61]

The RCC-1 experiment took place during the solar maximum. In contrast, the LDEF was launched just before solar minimum and remained in orbit until just before solar maximum. The RCC-1 solar exposure is estimated at no more than 20 - 25 equivalent solar days, 480 - 600 hours, at least one full order of magnitude less than the LDEF. The sun exposure is a significant measure of a materials stability in that photons having energy in the range 5 - 10 eV, the solar UV, are capable of severing molecular bonds and altering materials properties.

The integrated fluence of AO to the RCC-1 was estimated at 5.36×10^{22} cm^{-2}, which is based on a total exposure time of 188 days, a mean value of cos α of 0.051, and a $F_{10.7}$ value of 267.5. This AO fluence exceeds the exposure of any LDEF surfaces by at least a factor of five. However, using the AO density values predicted by the MSIS model at $F_{10.7} = 200$ would reduce the AO fluence by more than a factor of 5, whcih would bring the RCC-1 fluence into general agreement with the exposure seen by rows 9 and 10 on LDEF.

Because of its low altitude, the RCC-1 was below most of the trapped radiation belts save for the region referred to as the South Atlantic Anaomaly. As with LDEF, this phenomena provided most of the ionizing radiation that the RCC-1 was exposed to as the Earth's magnetic field effectively screened the majority of the solar protons and galactic cosmic rays. Figure 1-31 compares the proton and electron belt fluence predictions for the LDEF and RCC-1 experiments. Note that even though the RCC-1 mission was significantly shorter than that of the LDEF its fluence is greater because of its higher orbital inclination. The LDEF radiation dose values are on the order of 3×10^4 rads whereas the radiation dose absorbed by the RCC-1 samples was estimated at 8×10^5 rads, which includes 2.7×10^5 rad of trapped protons and 5.3×10^5 rad of trapped electrons.

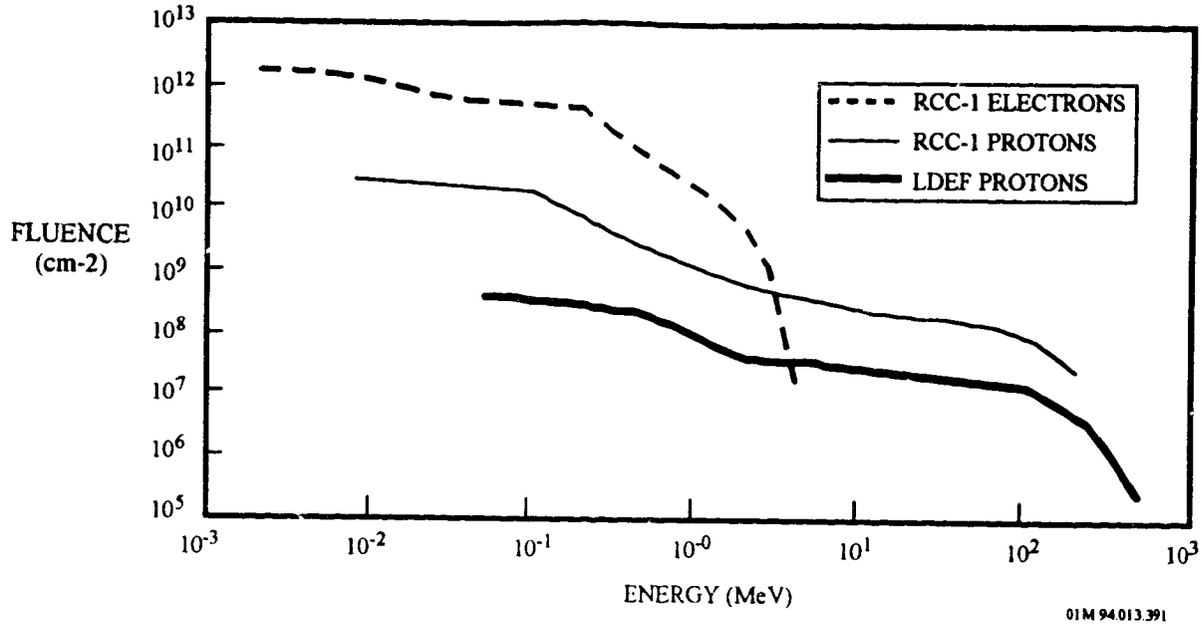

Figure 1- 31. Proton and Electron Belt Fluence Predictions for the LDEF and RCC-1 Experiments

Table 1-14 compares the LDEF and RCC-1 orbital exposure conditions. As shown, the RCC-1 AO fluence is approximately equal to that seen by rows 9 - 10 of LDEF when determined using U.S. models. The RCC-1 UV exposure is only about 1/20th of rows 9 and 10 of LDEF and the RCC-1 radiation dose is a factor of 25 higher. As a result, the RCC-1 experiment would not be expected to witness UV degradation in materials if the time scale associated with the degradation process were longer than ~500 hours. Conversely, the RCC-1 materials would be more susceptible to radiation damage. However, since these levels of radiation are not close to the usable limits for most materials, the main difference will be the UV exposure value.

Table 1-14. Comparison of the RCC-1 and the LDEF Environmental Exposure Conditions

Space Environment	LDEF		RCC-1	
	Row 9	Row 10	Russian Models	U.S. Models
UV esh	11,200	10,700	~600	
AO Fluence 10^{21} atoms cm^{-2}	8.99	8.43	53.6	~10
Dose, krad	30	30	800	

1.4.4 Solar Maximum Mission

The Solar Maximum Mission (SMM) spacecraft, built at the Goddard Space Flight Center, was launched in February 1980 with solar flare research its primary objective.[62] Launched near the peak of the 22-year solar cycle, the SMM was put in a 310 nautical miles, nearly circular orbit with 28.5° inclination. The spacecraft's longitudinal axis was pointing at the Sun in a 3-axis stabilized mode, so that the seven instruments aboard the spacecraft could monitor the activities of the Sun. Some of the instruments required very fine pointing accuracy and stability to obtain high-resolution data. During the initial period, the pointing accuracy of the SMM was better than 2 arc-sec with stability less than 1 arc-sec.

The Solar Max spacecraft was the first spacecraft designed to be serviced and repaired in space by the Space Shuttle crew. The Solar Maximum Repair Mission (SMRM) was performed during STS flight 41-C in April 1984, which also was the LDEF deployment mission. By this time the SMM orbit altitude had decayed to 265 nautical miles. After replacement of faulty equipment, the SMM was checked out and deployed to provide more data near the Sun's least active solar flare period. The Orbiter landed two days later on April 14, 1984.

Laboratory analyses were performed on materials retrieved from the Solar Max thermal control system, as well as on various impact particles that were embedded in the thermal control materials. The materials analyzed were aluminized Kapton and Mylar, and Dacron netting from the multilayer insulation (MLI) blankets, and silver Teflon used on a thermal radiator and as trim on louver assemblies. MLI is used to thermally insulate various spacecraft components. The portions of the MLI returned to Earth were primarily from the blankets used to insulate the Modular Attitude Control System (MACS) module and the Main Electronics Box of the Coronagraph/Polarimeter. Materials from the blankets included aluminized Kapton used as the top layer of the MLI as well as the other layers of the MLI, such as aluminized Kapton or aluminized Mylar separated by Dacron netting. Silver Teflon, used on spacecraft components to increase the thermal radiation performance of exposed surfaces, was removed from the thermal louver assembly of the MACS.

Kapton films (0.005-in) exhibited up to a 40% loss of thickness as a result of exposure to approximately 2×10^{21} atoms/cm^2 during 50 months on-orbit. Silver/Teflon material exhibited obvious degradation, especially in regions exposed both to AO and solar radiation. A summary of these analyses can be found within the appropriate sections of this guide.

1.4.4 The Effects of Oxygen Interaction with Materials (EOIM) Experiments

1.4.4.1 STS-5 EOIM Experiments

The STS-5 EOIM experiment, flown in November 1982, exposed a rather limited set of materials to an estimated AO fluence of nearly 10^{20} atoms/cm^2. Results from this early experiment have been summarized by Leger, et al. in AIAA Paper 83-2361 (1983),[63] and will be discussed in later sections.

1.4.4.2 STS-8 EOIM Experiments

A flight experiment was performed on STS-8 (August 1983) mission to measure reaction of surfaces with atomic oxygen in the low Earth orbital environment. The objectives of the STS-8 mission were (1) to obtain a larger quantitative reaction rate data base in comparison to the STS-5 mission, (2) to confirm reaction rate temperature dependence, (3) to determine whether mass transfer from surface to surface occurs as a result of the interaction, (4) to evaluate solar radiation effects on reaction rate, and (5) to determine the importance of atmospheric electrically charged species on reaction rate.

The basic experimental approach consisted of exposing samples to the LEO environment and then returning them for ground-based laboratory analysis. More than 360 samples were supplied and analyzed by the participating organizations. Most of these samples were exposed in disc form (2.54 cm diameter); however, film strips, woven cables, and fabrics were also used.

The STS-8 exposure provided the largest atomic oxygen fluence of any experiment to date. The high fluence was achieved by lowering the vehicle altitude to 225 km and maintaining the payload bay pointing into the velocity vector, nose to the Earth, for a total of 41.75 hour during three exposure periods of approximately 14 hr each. This attitude provided 86 percent of all the mission atomic oxygen fluence; therefore, essentially all of the impingement was normal to the exposure surfaces for the first time. It can be assumed that the remaining fluence (14 percent) was provided under conditions which resulted in an atomic oxygen beam sweeping relative to the sample surface. Using atmospheric density as derived from the mass spectrometer and incoherent scatter (MSIS) model for the specific mission flight period, total atomic exposure fluence was 3.5×10^{20} atoms/cm^2.

A detailed review of several key investigations for these experiments was compiled by James Visentine (NASA/JSC) in the three-volume NASA Technical Memorandum 100459.[64] A more complete description of AO related research (flight experiments, chemical mechanisms, ground simulations, etc.) may be found in the "Proceedings of the NASA workshop on Atomic Oxygen Effects" (JPL Publication 87-14), edited by D.E. Brinza.[65]

1.4.4.3 STS-41-G EOIM Experiments

Experimental packages flown on Space Shuttle mission STS-41G was designed to investigate the effect of atomic oxygen in low Earth orbit on metallizations, silicone coatings, FEP Teflon, and polymeric-based spacecraft materials.[66,67] Materials were configured into 2.54 cm diameter (1-in diameter) disc-type specimens or into thin foils. These materials specimens were attached directly to the lower arm boom of the Space Shuttle remote manipulator system and positioned normal to and in the direction of flight for a total of approximately 38 hours of equivalent normal exposure at 225-km altitude to obtain a total atomic oxygen fluence (mass spectrometer and incoherent scatter model calculations for a ram surface at 120 nm) of 2.45×10^{20} atoms/cm^2.

1.4.4.4 STS-46 EOIM-3 Experiments

The STS-46 shuttle mission was launched on July 31, 1992 and landed on August 8 at Kennedy Space Center, Fla. The STS-46 contained three payloads with material exposures to the space environment. These included the Evaluation of Oxygen Interaction with Materials III (EOIM), the Long Duration Candidate Exposure (LDCE) experiments (see section 1.5.5), and the Consortium for Material Development in Space Complex Autonomous payload (Concap) experiments that studied materials processing in addition to investigating samples for exposure to atomic oxygen. Another primary payload on STS-46 was the European Space Agency (ESA) EURECA-1 (see Section 1.5.6).

The NASA Evaluation of Oxygen Interactions with Materials (EOIM) experiments are an evolutionary series of investigations based on limited duration exposure of materials to substantial fluences of atomic oxygen in the low Earth orbital environment. These low altitude shuttle-borne experiments are able to subject test materials to AO fluences equivalent to several months or even years of exposure at higher orbital altitudes. For example, EOIM-III bombarded materials with approximately 2.5×10^{20} oxygen atoms per cm^2 during a 42-hour period. This is nearly the same fluence encountered by the Long Duration Exposure Facility (LDEF) after its first year on orbit.

Key observations in prior flight experiments were that material recession was essentially proportional to AO fluence, which allows the establishment of material-specific "reaction efficiency" parameters, the development of textured surfaces similar to the erosion morphologies witnessed in directed-beam sputtering targets, and changes in the chemical composition of exposed surfaces due to oxidation. Reaction efficiency parameters allow an estimation of the recession in a given mission to be made for a material by multiplication with the anticipated mission AO fluence. Table 1-15 provides a few representative reaction efficiencies determined in prior EOIM experiments.

Table 1-15. Atomic Oxygen Reaction Efficiencies for Several Materials

Material	Reaction Efficiency ($x10^{-24}$ cm^3/atom)
Kapton	3.0
Tedlar	3.2
Mylar	3.4
Polyethylene	3.7
Carbon/Epoxies: T300/5208 1034C	 2.6 2.1
Carbon (various forms)	0.5-1.3
FEP Teflon (EOIM)	<0.05
FEP Teflon (LDEF)	0.25
Silicones: RTV-560 DC6-1104	 0.02* 0.02*

* Units of mg/cm^2, loss assumed to occur in early part of exposure on STS-8 mission

The discrepancy in reaction efficiencies of the fluorocarbon FEP in LDEF and EOIM exposures is attributed to the synergistic interaction of the solar vacuum ultraviolet radiation and AO on LDEF which dramatically increases the susceptibility of fluorocarbons to AO attack. Silicones are known to form a self-protective SiO_x glass-like film which resists AO attack. For this reason, the EOIM experiments are quite sensitive to contamination, especially from silicone or fluorocarbon oils, greases, and release agents. Special attention is required to prevent contamination effects from invalidating test results.

1.4.5 LCDE (Limited Duration Space Environment Candidate Materials Exposure) Experiments

The Long Duration Candidate Exposure (LDCE) experiments on STS-46 consisted of three separate payload elements identified as LDCE-1, LDCE-2 and LDCE-3. The three assemblies held an aggregate total of 356 specimens. The LDCE-1 and -2 sample holder trays were each mounted inside the top of a Complex Autonomous Payload (CAP) canister that was equipped with a Motorized Door Assembly (MDA). The MDA was only open during those specific periods of the mission when the payload bay was pointed toward the direction of travel in orbit (the velocity vector). In other times and when water dumps, thruster firings and Orbiter operations that may cause contamination occurred, the MDA was closed. This restricted the exposure of the samples to ram atomic oxygen (samples facing the velocity vector) and limited contamination. LDCE-1 and -2 were mounted on the port side of the Orbiter cargo bay.

The LDCE-3 sample tray was mounted on top of Concap II. This was one of the two CAP payloads mounted on the starboard side of Bay 13. The LDCE-3 sample tray and its specimens were continuously exposed throughout the mission. This provided comparative data for limited ram as received by samples on LDCE-1 and -2 vs. extensive exposure to all phases and activities during STS-46 flight as represented by LDCE-3.

In order to expose the material specimens to atomic oxygen at the planned 124 nautical miles altitude, the Space Shuttle Orbiter was oriented with the payload bay towards the velocity vector. The MDA doors were opened on LDCE-1 and -2. A total of 43 hours of direct exposure was obtained. Upon completion of the exposure the doors were closed. Other than opening and closing of the MDA's, the LDCE payload operations were completely passive. The effect of low Earth orbit environment on LDCE materials was based on post-flight analysis of the specimens. Table 1-16 summarizes the exposure conditions.

Table 1-16. Space Exposure Conditions for LDCE Experiments

Altitude	231/124 nautical miles (circular orbit)
Duration: LDCE-1, -2	41 hours at 124 nm (230 km)
Duration: LDCE-3	42 hours of ram at 124 nm (230 km) 16.55 hours of ram at 231 nm (425 km) during EURECA operations
Total Fluence	LDCE-1,-2: 2×10^{20} atoms/cm^2 LDCE-3: 2.7×10^{20} atoms/cm^2

1.4.6 Lockheed Space Flight Experiment

This Lockheed Space Flight Experiment investigated the material stability of four polymer materials in a relatively high fluence atomic oxygen environment of approximately 2.0×10^{22} atoms/cm^2, accumulated over at least 100 days.[68] The materials investigated included: (1) 0.052 mm aluminized Kapton; (2) aluminized Kapton with a 0.0076 mm coating of siloxane (IITRI RTV 602/LO dimethyl silicone; (3) 0.0254 mm aluminized FEP Teflon; and (4) 0.127 mm carbon-filled PTFE impregnated fiberglass. The flight data results confirmed that there are two mechanisms of degradation in process in the LEO environment: (1) a fast surface oxidation; and (2) a slower, diffusion limited bulk oxidation. The results support a non-linear fluence dependence for the degradation effects on certain materials (i.e., Teflon). Both laboratory and flight experimental data verified the stability of a siloxane coating in order to achieve protection of reactive substrates in the LEO oxygen environment.

1.4.7 European Retrievable Carrier (EURECA)

The European Space Agency (ESA) EURECA-1 was a primary payload on STS-46 which was launched on July 31, 1992 and returned on August 8. After deployment EURECA ascended to its operational orbit of 515 km using its own propulsion system. EURECA is a retrievable, reusable satellite built by the ESA and designed to be maintained during its long-term mission by ground controllers at ESA's Space Operations Center in Darmstadt, Germany. After 9 month EURECA was moved to a lower orbit for retrieval by another Shuttle in late April 1993. Aboard EURECA-1 were 15 experiments devoted to researching the fields of material science, life sciences and radiobiology, all of which required a controlled microgravity environment.

REFERENCES

[1] T.F. Tascione, "Introduction to the Space Environment " Orbit Book Company, Malabar, Florida, 1988.

[2] B. J. Anderson, Ed., R.E. Smith, Compiler, "Natural Orbital Environment Guidelines for Use in Aerospace Vehicle Development," NASA TM 4527, June 1994.

[3] TRW internal report.

[4] User and Operations Guide for the Marshall Space Flight Center Materials and Processes Technical Information System (MAPTIS), available from NASA-MSFC, Mail Code EH02, Huntsville, AL 35812, January 1992.

[5] J.W. Haffner et al, "Natural Environmental Effects on SDI Spacecraft Surface Materials," Rockwell International, Report No. AFGL-TR-89-0084, Air Force Geophysical Laboratory, May 20, 1989.

[6] J.T. Visentine and A. Whitaker, "Material Selection Guidelines to Limit Atomic Oxygen Effects on Spacecraft Surfaces," NASA TM 100351, February 1989.

[7] G.D. Badhwar and P.M. O'Neill, "Time Lag of Twenty Two Z Modulation," Proceedings of the 23rd International Cosmic-Ray Conference, SH 6, 21, Calgary, 1993.

[8] W.S. Slemp, "Ultraviolet Radiation Effects," NASA/SDIO Space Environmental Effects Workshop, NASA CP 3035, Part 2, 1989, pp.425-446.

[9] A.C. Somersall and J.E. Guillet, "Modeling of Photodegradation in Solar Cell Modules of Substrate and Superstrate Design Made with Ethylene-Vinyl Acetate as Pottant Material," NASA Contract NAS7-100, 1983.

[10] H.A. Zook, "Deriving the Velocity Distribution of Meteoroids From the Measured Meteoroid Impact Directionality on the Various LDEF Surfaces," LDEF First Post-Retrieval Symposium, NASA CP 3134, 1992, pp. 569-579.

[11] H.A. Zook, "Flux Versus Direction of Impacts on LDEF by Meteoroids and Orbital Debris," Lunar and Planetary Science XXI, 1990.

[12] H.A. Zook, "The Velocity Distribution and Angular Directionality of Meteoroids that Impact on an Earth-Orbiting Satellite," Lunar and Planetary Science Conference XVII Abstracts, 1987, pp. 1138-1139.

[13] J.E. Erickson, "Velocity Distribution of Sporadic Photographic Meteors," Journal of Geophyscial Research, vol. 7, no. 12, 1968, pp. 3721-3726.

[14] D.J. Kessler, R.C. Reynolds, and P.D. Anz-Meador, "Orbital Debris Environment for Spacecraft Designed to Operate in Low Earth Orbit," NASA-TM 100471, September, 1988.

[15] B.G. Cour-Palais et al., "Meteoroid Environment Model - 1969 (Near Earth to Lunar Surface)," NASA SP-8013, March 1969.

[16] E. Grun et al., "Collision Balance of the Meteoritic Complex." Icarus, Vol. 62, 1985.

[17] D.J. Kessler et al., "Orbital Debris Environment for Spacecraft Designed to Operate in Low-Earth Orbit," NASA TM 100471, September 1988.

[18] A. Watts et al, "LDEF Penetration Assessment Final Report," Final Report, Contract F3361-90-C-5903, Task 0008, June 1992.

[19] D.J. Kessler, "Origin of Orbital Debris Impacts on LDEF Trailing Surfaces," LDEF Second Post-Retrieval Symposium," NASA CP-3194, 1993, pp. 585-594.

[20] D.J. Kessler et al., "Orbital Debris Environment for Spacecraft Designed to Operate in Low-Earth Orbit," NASA TM-100471, September 1988.

[21] L.G. Clark, W.H. Kinard, D.J. Carter,Jr., and J.L. Jones, Jr. (Editors), "The Long Duration Exposure Facility (LDEF)," NASA SP-473, 1984.

[22] A.S. Levine, editor, "LDEF First Post-Retrieval Symposium," NASA CP-3134, 1991.

[23] A.S. Levine, editor, "LDEF Second Post-Retrieval Symposium," NASA CP-3194, 1993.

[24] A.S. Levine, editor, "LDEF Third Post-Retrieval Symposium," in press.

[25] B.A. Stein and P.R. Young, editors, "LDEF Materials Workshop '91," NASA CP-3162, 1992.

[26] A.F. Whitaker, editor, "LDEF Materials Results for Spacecraft Applications," NASA CP-3257, 1994.

[27] J.G. Funk, J.W. Strickland, and J.M. Davis, "Materials and Processes Technical Information System (MAPTIS)," LDEF Second Post-Retrieval Symposium, NASA CP-3194, 1993, pp. 1201-1222.

[28] G. Bohnhoff-Hlavacek, "Data Bases for LDEF Results," NASA CP-3194, pp. 1223-1234.

[29] R.J. Bourassa and J.R. Gillis, "Atomic Oxygen Exposure of LDEF Experiment Trays," Long Duration Exposure Facility Materials Special Investigation Group--LDEF

Supporting Data, NASA Contract NAS1-19247, Boeing Defense and Space Group, March 1992.

[30] R.J. Bourassa, J.R. Gillis, and K.W. Rousslang, "Atomic Oxygen and Ultraviolet Radiation Mission Total Exposures for LDEF Experiments," LDEF First Post-Retrieval Symposium, NASA CP-3134, 1991, pp. 643-661.

[31] R.J. Bourassa and J.R. Gillis, "Atomic Oxygen Flux and Fluence Calculation for Long Duration Exposure Facility," NASA Contract NAS1-18224, Task 12, Boeing Defense and Space Group, January 1991.

[32] W.M. Berrios and T.R. Sampair, "Long Duration Exposure Facility Post-Flight Thermal Analysis," NASA TM-104208 Parts 1 and 2, January 1992.

[33] W.M. Berrios, "Use of the Long Duration Exposure Facility's Thermal Measurement System for the Verification of Thermal Models," LDEF First Post-Retrieval Symposium, 1991, NASA CP-3134, pp. 69-83.

[34] Thermal Radiation Analysis System (TRASYS), User's Manual, NAS9-15832, June 1983.

[35] W.M. Berrios, "Long Duration Exposure Facility Post Flight Thermal Analysis - Orbital/Thermal Environment Data Package, NASA Langley Research Center, Hampton, VA, October 3, 1990.

[36] W.M. Berrios, "Use of LDEF's Thermal Measurement System for the Verification of Thermal Models," LDEF First Post-Retrieval Conference, NASA CP-3134, 1992, pp. 69-83.

[37] E.V. Benton and W. Heinrich, "Ionizing Radiation Exposure of LDEF", Department of Physics, University of San Francisco, USF-TR-77, August 1990.

[38] T.W. Armstrong and B.L. Colborn, "Scoping Estimates of the LDEF Satellite Induced Radioactivity", Contract No. NAS8-38427 for NASA Marshall Space Flight Center, Science Applications International Corporation, September, 1990.

[39] T.H. See et al., "Meteoroid and Debris Impact Features Documented on the Long Duration Exposure Facility - A Preliminary Report," NASA JSC #24608, August 1990.

[40] T.H. See et al., "Continued Investigation of LDEF's Structural Frame and Thermal Blankets by the Meteoroid & Debris special Investigation Group," LDEF Second Post-Retrieval Symposium, NASA CP 3194, 1993, pp. 313-324.

[41] M.E. Zolensky et al., "Interim Report of the Meteoroid and Debris Special Investigation Group," LDEF Second Post-Retrieval Symposium, NASA CP 3194, 1993, pp. 277-302.

[42] M.J. Meshishnek et al., "Long Duration Exposure Facility (LDEF) Experiment M0003 Meteoroid and Debris Survey," LDEF Second Post-Retrieval Symposium, NASA CP 3194, 1993, pp.357-415.

[43] M. Allbrooks and D. Atkinson, "The Magnitude of Impact Damage on LDEF Materials," NASA Contractor Report NCR 188258, July 1992.

[44] C. Coombs et al., "LDEF Data: Comparisons with Existing Models," NASA Contractor Report NAS9-17900, July 1992.

[45] A. Watts et al., "Dimensional Scaling for Impact Cratering and Perforation," POD Associates, Inc., subcontract report to Lockheed Egnineering and Sciences Company, March 1993.

[46] J.M. Zwiener and M.M. Finckenor, "Micrometeoroid/Space Debris Effects on Materials," LDEF Materials Results for Spacecraft Applications Conference, NASA CP-3257, 1994, pp. 258-280.

[47] T.H. See et al., "Meteoroid and Debris Impact Features Documented on the Long Duration Exposure Facility - A Preliminary Report," NASA JSC #24608, August 1990.

[48] J.M. Zwiener and M.M. Finckenor, "Micrometeoroid/Space Debris Effects on Materials," LDEF Materials Results for Spacecraft Applications Conference, NASA CP-3257, 1994, pp. 258-280.

[49] A. Banks and L. Begauer, "LDEF Yaw and Pitch Angle Estimates," LDEF Materials Workshop '91, NASA CP-3162, 1992, pp. 71-93.

[50] F. Horz et al., "Preliminary Analysis of LDEF Instrument AO187-1: Chemistry of Micrometeoroids Experiment," LDEF First Post-Retrieval Symposium, NASA CP-3134, pp. 487-501.

[51] S.F. Singer et al., "First Spatio-Temporal Results from the LDEF Interplanetary Dust Experiment," Adv. Space Res., vol. 11, No. 12, pp. 115-122.

[52] D.H. Humes, "Large Craters on the Meteoroid and Space Debris Impact Experiment," LDEF First Post-Retrieval Symposium, NASA CP-3134, 1991, p. 399-418.

[53] J.A.M. McDonnell and T.J. Stevenson, "Hypervelocity Impact Microfoil Perforations in the LEO Space Environment (LDEF MAP A0023 Experiment)," LDEF First Post-Retrieval Symposium, NASA CP-3134, 1991, pp. 443-457.

[54] D.H. Humes, "Large Craters on the Meteoroid and Space Debris Impact Experiment," LDEF First Post-Retrieval Symposium, NASA CP-3134, 1991, p. 399-418.

[55] T.H. See et al., "Meteoroid and Debris Special Investigation Group Preliminary Results: Size-Frequency Distribution and Spatial Density of Large Impact Features on LDEF," LDEF First Post-Retrieval Symposium, NASA CP-3134, 1991, pp. 477-486.

[56] H. Dursch, editor, "Analysis of Systems Hardware Flown on LDEF--Results of the Systems Special Investigation Group," NASA Contractor Report 189628, Contract NAS-19247, April, 1992.

[57] F. Levadou, M. Froggatt, M. Rott, and E. Schneider, "Preliminary Investigations into UHCRE Thermal Control Materials," LDEF First Post-Retrieval Symposium, NASA CP 3134, 1991, pp .899-918.

[58] W.H. Kinard and G.D. Martin, "Long Duration Exposure Facility (LDEF) Space Environments Ov :rview," LDEF First Post Retrieval Symposium, NASA CP 3134, 1991, pp. 49-60.

[59] W.H. Kinard and G.D. Martin, "Long Duration Exposure Facility (LDEF) Space Environments Overview," LDEF First Post Retrieval Symposium, NASA CP 3134, 1991, pp. 49-60.

[60] J.C. Guillaumon and A. Paillous, "Spacecraft Materials: Comparison Between Flight Results Obtained on LDEF and MIR," LDEF Materials Results for Spacecraft Applications, NASA CP-3257, 1994, pp. 485-498.

[61] A.C. Tribble, R. Lukins, and E. Watts, "Low Earth Orbit Thermal Control Coatings Exposure Flight Tests: A Comparison of U.S. and Russian Results," NASA Contract NAS1-19243, Task 16, Rockwell International Space Systems Division, August 1994.

[62] Satellite Servicing Project Goddard Space Flight Center, "Proceedings of the SMRM Degradation Study Workshop," NASA-TM-89274, pp. 1-32.

[63] L.J. Leger, I.K. Spiker, J.F. Kuminecz, T.J. Ballentine, and J.T. Visentine, "STS-5 LEO Effects Experiment - Background Description and Thin Film Results," AIAA Paper 83-2631-CP, AIAA Shuttle Environment and Operations Meeting, Washington, D.C., October - November, 1983.

[64] J. Visentine, ed., "Atomic Oxygen Effects Measurements for Shuttle Missions STS-8 and 41-G," vols. I-III, NASA Technical Memorandum 100459, September 1988.

[65] D.E. Brinza, ed., Proceedings of the NASA Workshop on Atomic Oxygen Effects," JPL Publication 87-14.

[66] A.F. Whitaker, J.A. Burka, J.E. Coston, I. Dalins, S.A. Little, and R.F. DeHaye, "Protective Coatings for Atomic Oxygen Susceptible Spacecraft Materials - STS-41G

Results," AIAA Paper 85-7017, Presented at the Shuttle Environment and Operations II Conference, November 1985.

[67] D.G. Zimcik and C.R. Maag, "Results of Apparent Atomic Oxygen Reactions with Spacecraft Materials During Shuttle Flight STS-41G," AIAA Paper 85-7020, presented at the AIAA Shuttle Environment and Operations II Conference, 1985.

[68] P.W. Knopf, R.J. Martin, R.E. Damman, and M. McCargo, "Correlation of Laboratory and Flight Data for the Effects of Atomic Oxygen on Polymeric Materials," AIAA 20th Thermophysics Conference, Williamsburg, VA, June 19-21, 1985.

2. SPACECRAFT DESIGN CONSIDERATIONS FOR THE SPACE ENVIRONMENT 2-1

2. SPACECRAFT DESIGN CONSIDERATIONS FOR THE SPACE ENVIRONMENT

Each of the natural space environments acts on materials in a distinct way, with some materials being more vulnerable than others. This section presents an overview of these effects and the types of materials which are especially sensitive to each environment.

2.1 ATOMIC OXYGEN EFFECTS

2.1.1 Introduction

The major gas in LEO is atomic oxygen, which erodes organic materials and some oxides of other materials on the ram side of the spacecraft. Materials being considered for spacecraft and commercial satellites need to be reviewed for susceptibility to atomic oxygen interactions which produce surface erosion or degradation in optical and thermal properties that may result in failure of spacecraft systems to achieve mission goals. As the degree of surface degradation is directly proportional to atomic oxygen fluence (total integrated flux), and fluence, in turn, is determined by such parameters as spacecraft altitude, attitude, orbital inclination, mission duration and solar activity conditions, materials deemed acceptable for one application may not be acceptable for other applications. Consequently, rather than listing materials acceptable for spacecraft systems under varied sets of operational circumstances, this section will:

1. Establish guidelines to aid spacecraft designers in materials selection
2. Provide a nomograph for estimating atomic oxygen fluence and, consequently, the degree of surface erosion the spacecraft material will experience over its lifetime.

2.1.2 Atomic Oxygen Effects on Surface Recession

2.1.2.1 Material Atomic Oxygen Reaction Efficiency Data

Most of the data related to the behavior of materials in the atomic oxygen environment were obtained from Space Shuttle flight experiments. These flights provided limited exposure of materials typically used in spacecraft construction to both sweeping impingement and atmospheric ram conditions.[1,2,3,4,5,6,7,8,9,10,11] The altitudes selected for these experiments (220 and 300 km) and the duration of exposure time (40 hours) produced high levels of fluence (1.0×10^{20} to 3.5×10^{20} atoms/cm^2) which are typical for future spacecraft operating at higher altitudes (500 to 600 km) during nominal solar activity conditions for periods of one year or more.

LDEF clearly demonstrated in long-term flight that LEO atomic oxygen will erode all polymeric materials that are flown, which includes all those commonly used on spacecraft for thermal and electrical insulation, as paint vehicles, and as composite matrices. Rates of erosion vary in different materials and appear to change with length of exposure for some polymers. Thus, results of short-term LEO-exposure test[12] may not provide data which can readily be extrapolated to predict long-term erosion rates. Fortunately, this erosion was found to be completely preventable with even extremely thin coatings of metals such as aluminum and oxides such as silica; many such coatings also adhered well to the polymer or composite substrate specimen surfaces in spite of thermal cycling during each orbit.

Material samples exposed under the conditions described above (e.g., Space Shuttle and LDEF flights) were studied post-flight for property changes. Since the exposures resulted in significant loss of material (organic specimens experienced thickness losses as much as 12 μm or ~0.5 mil), mass change measurements of the flight samples provided an excellent assessment of material reactivity in the environment. Most of the data obtained are reported in terms of a reactivity parameter that quantifies the susceptibility of a material to erosion by atomic oxygen, known as the "erosion yield" or the "reaction efficiency" (R_e). This parameter is defined as

$$R_e = \frac{\text{Volume of Material Lost}}{\text{Total No. of Incident O Atoms}} \quad (\text{cm}^3/\text{atom})$$

R_e can be calculated using the relation:

$$R_e = \frac{\Delta m/\rho}{\phi t\, A}$$

where
- Δm = mass loss (g)
- ρ = material density (g/cm^3)
- ϕ = incident AO Flux (atoms/cm^2-s)
- t = exposure time (s)
- A = exposed surface area (cm^2)

Note that $\phi t = F$, where F is the total fluence of oxygen atoms, which is obtained from atmospheric models, spacecraft velocity, and exposure history. Consequently, the reaction efficiencies derived from previous Space Shuttle flights (see below) can used in computing surface recession for materials subject to the orbital environment by the following equation:

$$\Delta x = F_T \times R_e$$

where F_T is accumulated fluence, R_e is reaction efficiency, and Δx is surface recession.

Hence, the property reaction efficiency can also be defined as thickness of material lost normalized to total oxygen fluence.

Table 2-1 presents a classification of the reaction efficiency data.[13] A general assessment of the deleterious effects on spacecraft surfaces are as follows:

1. Unfilled organic materials containing only C, H, O, N, and S react with approximately the same reaction efficiency (2 to 4 x 10^{-24} cm^3/atom).

2. Prefluorinated carbon-based polymers and silicones have lower reaction efficiencies by a factor of ten or more than organics.

3. Filled or composite materials have reaction efficiencies that are strongly dependent upon the characteristics of the fillers.

4. Metals, except for silver and osmium, do not show macroscopic changes. Microscopic changes have, however, been observed and should be investigated for systems very sensitive to surface properties. Silver and osmium react rapidly and are generally considered unacceptable for use in uncoated applications.

5. Magnesium fluoride and oxides in various forms show good stability.

6. Copper forms a protective oxide which adversely affects optical and thermal properties.

Table 2- 1. Classification of AO Reaction Efficiencies (10^{-24} cm^3/atom) Data

0.01-0.1	.1-.9	1.0-1.9	2-4	>4
Al_2O_3 (<0.025)	Polysiloxane/ Kapton (0.3)	Various forms of Carbon (0.5-1.3)	Kapton H Polyimide (3.0)	Silver
Al/Kapton (0.1)	Siloxane /Polyimide (0.3)	Epoxies (1.7)	Polycarbonate Resin	
Diamond (0.021)	Polysilane/ Polyimide (0.3)	Polystyrene	Polyester	
ITO/aluminized Kapton (0.01)	401-C10 (flat black)	Polybenzimidazole	Polysulphone	
SiOx/aluminized Kapton (0.01)	Z-306 (flat black)	Kevlar/Epoxy	Mylar	
Al_2O_3, 700Å on Kapton H (<0.02)		LDEF Carbon/Epoxy (~1.0)	Polyethylene	
Silicones	Apiezon Grease		Tedlar, clear (3.2)	
Fluorpolymers	Tedlar (white)		Z-302(glossy black)	
Teflon FEP	Osmium (bulk)		STS Carbon/Epoxy (2.1-2.6)	
MgF_2 on Glass				
Mo (0.006)				
S Glass/Epoxy (0.14)				

The major limitation of the current reaction rate data base is that atomic oxygen fluence to which the recession rates are normalized are not precisely known. Atomic oxygen number densities used to compute fluence for previous space flight missions were obtained using thermospheric models to predict atmospheric constituent concentrations as functions of altitude, time of year, Earth latitude and longitude, local solar time, and solar activity conditions. Typically, errors of as much as 25 percent or more can be expected for the density estimations, and since they are used to compute fluence, these errors also appear in the surface recession rates for satellite materials. To improve the database, ambient density measurements need to be made simultaneously with recession measurements during future flight experiments.

A summary of data obtained from space flight experiments conducted to date are shown quantitatively in Tables 2-2 to 2-6.

Table 2- 2. AO Reaction Efficiencies of Polymeric Materials in Low Earth Orbit

Material	Reaction Efficiency, $x10^{-24}$ cm^3/atom	Flight Experiment	Reference
Fluoropolymers:			
• FEP Kapton	0.03		14
• Kapton F	<0.05		15
• Teflon, FEP	0.037		16
• Teflon, FEP	<0.05		17
• Teflon, TFE	<0.05		15,17
• Teflon, FEP and TFE	0.0 and 0.2	STS-5	18 ,19
• Teflon, FEP and TFE	0.1	STS-5	18
• Teflon	0.109		14
• Teflon	0.5	STS-5	18
• Teflon	0.03	STS-5	18
• Teflon	<0.03		20
Mylar	3.4	STS-5	17
Mylar	2.3	STS-5	18,19
Mylar	3.9	STS-5	18,19,20
Mylar	1.5 to 3.9		18
Mylar A	3.7		14
Mylar A	3.4		15,21
Mylar A	3.6		15
Mylar D	3.0		15
Mylar D	2.9		21
Mylar with Antiox	Heavily attacked		22
Polybenzimidazole	1.5	STS-5	17,23
Polycarbonate	6.0		24
Polycarbonate resin	2.9		25
Polyester-7% Polysilane/93% Polyimide	0.6		17
Polyester	Heavily attacked	STS-5	17,22
Polyester with Antioxidant	Heavily attacked	STS-5	17,22
Polyethylene	3.7		17,18,21, 26
Polyethylene	3.3		14,15
Polyimides			
• Kapton (black)	1.4 to 2.2	STS-5	18,27
• Kapton (TV blanket)	2.0	STS-5	18
• Kapton (TV blanket)	2.04		19
• Kapton (OSS -1 blanket)	2.55	STS-5	18
• Kapton (OSS -1 blanket)	2.5	STS-5	18
• Kapton H	3.0	STS-5	15,17,18,19,20,28
• Kapton H	2.4	STS-5	18,19
• Kapton H	2.7	STS-5	14,18
• Kapton H	1.5 to 2.8	STS-5	18
• Kapton H	2.0		14
• Kapton H	3.1		14
• Kapton (uncoated)	.1 and .06	STS-8	29
Polymethylmethacrylate	3.1		26
25% Polysiloxane/45% Polyimide	0.3	STS-5	17
7% Polysilane/93% Polyimide	0.6	STS-5	17
25% Polysiloxane	0.3		20
Polystyrene-Polyimide	1.7		17,20,26
Polysulfone	2.4	STS-5	17,26
Polyvinylidene fluoride	0.6		20
Siloxane polyimide (25% Sx)	0.3		23
Siloxane polyimide (7%)	0.6		23

Table 2- 3. AO Reaction Efficiencies of Thermal Control Materials in Low Earth Orbit

Material	Reaction Efficiency, $x10^{-24}$ cm^3/atom	Flight Experiment	Reference
Black paint Z306	0.3-0.4[a]	STS-8	30
White paint A276	0.3-0.4[a]	STS-8	30
Black paint Z302	2.03[a]	STS-8	30
Teflon, TFE	<0.05	STS-5	17
Teflon, FEP	<0.05	STS-5	15,17
TiO_2, (1000 Å)	0.0067		16
Tedlar (clear)	1.3	STS-5	18
Tedlar (clear)	3.2	STS-8	14,15
Tedlar (white)	.4 and .6		18
Tedlar (white)	0.05	STS-5	18
Tedlar (white)	0.29	LDEF	31

(a)Units of mg/cm^2 for STS-8 mission. Loss is assumed to occur in early part of exposure; therefore, no assessment of efficiency can be made.

Table 2- 4. AO Reaction Efficiencies of Composites in Low Earth Orbit

Material	Reaction Efficiency, $x10^{-24}$ cm^3/atom	Flight Experiment	Reference
T300 Carbon/1034C Epoxy	2.1	STS-5	17
T300 Carbon/5208 Epoxy	2.6	STS-5	17
Epoxy	1.7	STS-5	17,26
Carbon (various forms)	0.5-1.3	STS-5	17
Carbon	1.2		20,23,24,32
T300/934 Epoxy	0.99	LDEF	33
T300/934 Epoxy	1.35	LDEF	34
T300/934 Epoxy	1.25	LDEF	35
AS-4/3501-6 Epoxy	0.8	LDEF	33
C6000/PMR-15 Polyimide	0.9	LDEF	33
HMS/934 Epoxy	1.0	LDEF	36
P75S/934 Epoxy	1.0	LDEF	35

Table 2- 5. AO Reaction Efficiencies of Lubricants and Coatings in Low Earth Orbit

Material	Reaction Efficiency, $x10^{-24}$ cm^3/atom	Flight Experiment	Reference
Silicones			
• DC1-2577	0.055		21
• DC1-2755-coated Kapton	0.05	STS-5	18
• DC1-2775-coated Kapton	< .5	STS-5	18
• DC6-1104	0.515		37
• Grease 60 mm	Intact, but oxidized		38
• RTV-615 (black, conductive)	0.0		32
• RTV-615 (clear)	0.0625		16
• RTV-560	0.02[a]		34
• DC6-1104	0.02[a]		34
• T-650	0.02[a]		34
• DC1-2577	0.02[a]		39
• RTV-670	0.0		31
• RTV-S695	1.48		40
• RTV-3145	0.128		31
Apiezon grease 2 mm	>0.625		16
Al_2O_3	<0.025		41
SiO_2 (650 Å) on Kapton H	< .0008		28
SiO_2 (650 Å) with ≤4% PTFE	< .0008		28
SiO_x/Kapton (aluminized)	0.01	STS-8	29

(a)Units of mg/cm^2 for STS-8 mission. Loss is assumed to occur in early part of exposure; therefore, no assessment of efficiency can be made.

Table 2- 6. AO Reaction Efficiencies of Selected Metals in Low Earth Orbit

Material	Reaction Efficiency, $x10^{-24}$ cm^3/atom	Flight Experiment	Reference
Aluminum (150 Å)	0		31
Chromium (123 Å)	partially eroded		42
Copper (bulk)	0		25
Copper (1,000 Å) on sapphire	0.007		26
Copper (1,000 Å)	0.0064		37
Gold (bulk)	0		25
Gold	appears resistant		22
Iridium Film	0.0007		25
Lead	0		30,31
Magnesium	0		30,31
Molybdenum (1,000 Å)	0.0056		28
Molybdenum (1,000 Å)	0.006		18,26
Molybdenum	0		30,31
Nichrome (100Å)	0		31
Nickel film	0		25
Nickel	0		24,30
Niobium film	0		25,31
Osmium	0.026	STS-5	17
Osmium	heavily attacked		32
Osmium (bulk)	0.314		25
Platinum	0		30,31
Platinum	appears resistant		32
Platinum film	0		25
Silver	10.5	STS-5	16
Tantalum	appears resistant		32
Tungsten	0		24,30

2.1.2.2 Surface Recession Predictions

As discussed earlier, the amount of surface recession for a material of known reactivity is directly proportional to atomic oxygen fluence, or the total number of atoms impinging on each square centimeter surface area during the duration of the intended mission. Fluence, in turn, is dependent on such parameters as spacecraft altitude, surface attitude relative to the spacecraft velocity vector, orbit inclination, duration of exposure, and solar activity conditions during the lifetime of the spacecraft (as atomic oxygen is produced by the photodissociation of molecular oxygen initiated by the absorption of solar near-ultraviolet radiation, its concentration is known to change as sun spot activity varies during the 11-year solar cycle).

To aid the spacecraft designers in estimating the atomic oxygen fluence effects on specific surfaces under question, a parametric study was performed to evaluate the effects of altitude, inclination, and solar activity on atomic oxygen fluence,[43] and its attendent changes in surface recession. Altitudes and inclinations selected for this study ranged from 150 to 900 km and from 0 to 89°, respectively. Solar activity parameters used in the computations represented low, medium, and high activity conditions. In addition, as fluence is also strongly influenced by surface orientation, seven surfaces were selected for analysis as these parameters were varied. These surface orientations included three E surfaces (ram and oblique effects), two I surfaces (solar and antisolar), and two B surfaces (deep-space and Earth-viewing).* The results of this analysis comprise a generalized description of the manner in which changes in surface orientation, altitude, inclination, and solar activity affect total accumulated fluence.

Fluence as a function of altitude for various solar activities and surface orientations is shown in Figure 2-1 (ref. 43). Atomic oxygen number densities used to compute fluence were obtained from the MSIS-83 thermospheric model,[44] which predicts atmospheric constituent concentrations as functions of input parameters such as altitude, time of year, latitude, longitude, local solar time, and solar activity conditions. The solar flux index ($F_{10.7}$ number) for each year the spacecraft is exposed to the LEO environment was obtained by using Figure 2-2, which shows solar activity predictions for solar cycle 22, the current cycle which began in 1988.[45] To provide conservative estimates of accumulated fluence, 2σ variations over the long-range statistical averages of the solar activity indicators were used as inputs to the MSIS-83 model.[46]

---

* An E surface represents a body coordinate system fixed to the spacecraft that flies in a local vertical-local horizontal (LVLH) flight mode; an I surface is a solar inertial coordinate system that rotates in two degrees of freedom to maintain Sun-pointing attitudes; and a B surface is a space-viewing coordinate system that rotates in a single degree of freedom to provide radiator attitudes for deep-space heat rejection.

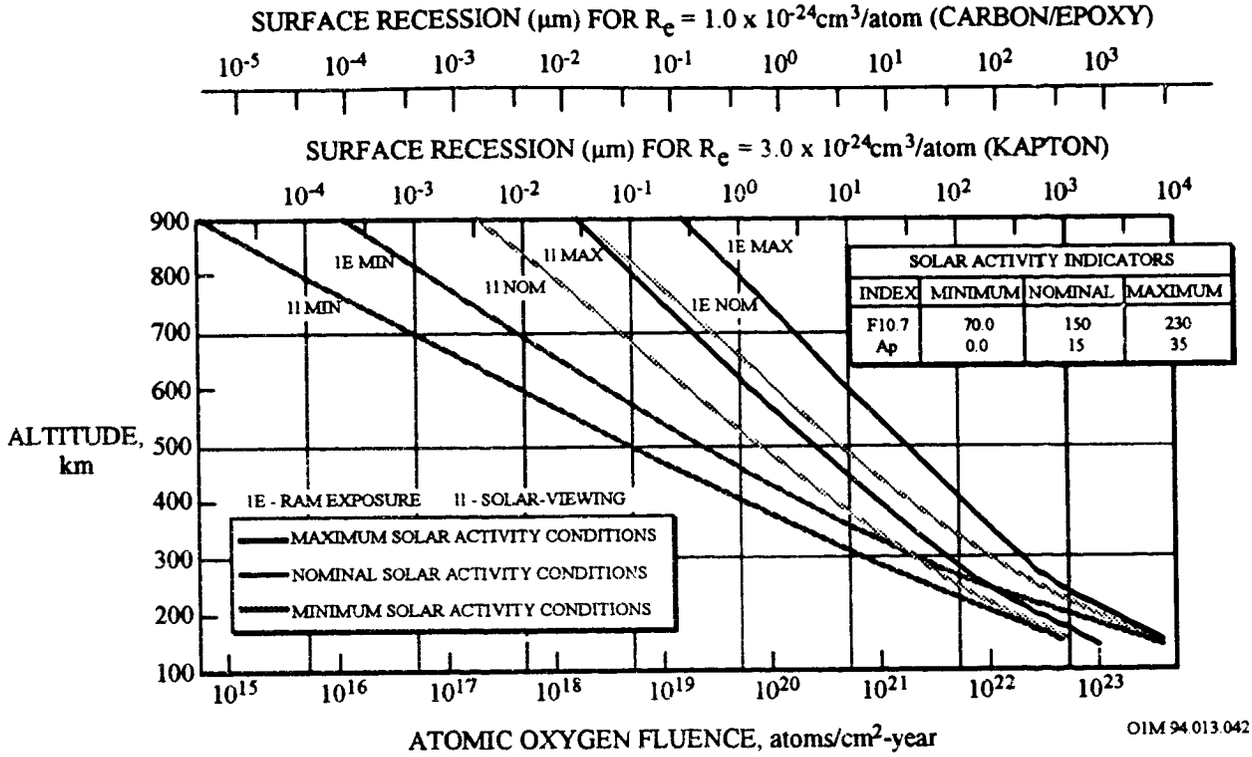

Figure 2- 1. AO Fluence Nomograph for Predicting Surface Recession

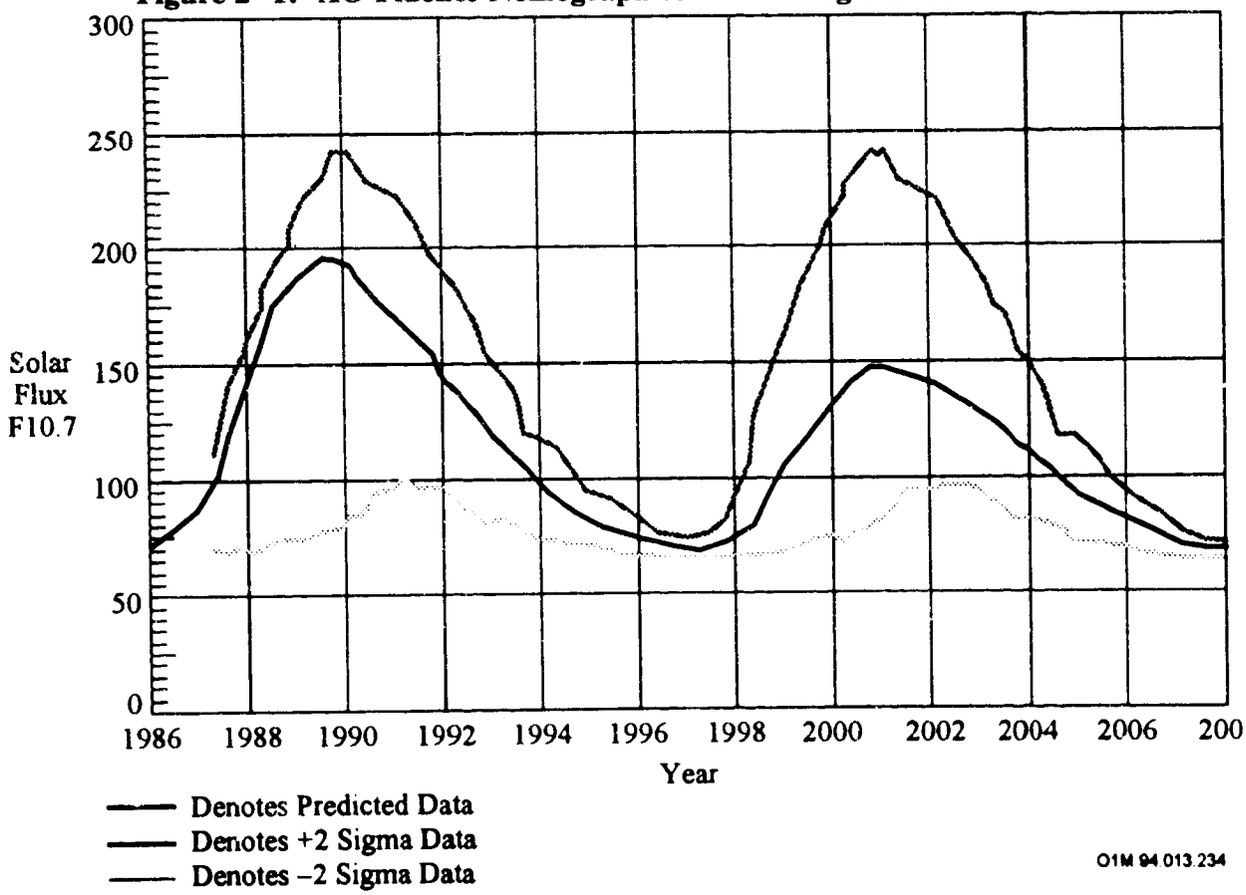

Figure 2- 2. Long Range Estimate of 10.7 cm Solar Flux Cycles 22 and 23.

Figure 2-1 serves as a nomograph for calculating the amount of surface erosion in microns (μm; 10^{-4} mm) for a material with $R_e = 3.0 \times 10^{-24}$ cm^3/atom (e.g., Kapton) or for a less reactive material with $R_e = 1.0 \times 10^{-24}$ cm^3/atom (e.g., carbon/epoxy composite) for the given solar activity conditions (the 10.7 cm solar flux index, $F_{10.7}$, and the geomagnetic index, A_p). During nominal activity ($F_{10.7}$=150; A_p=15), the fluence on ram-oriented surfaces increased from 3.1×10^{18} to 4.4×10^{23} atoms/cm^2 per year as the altitude is reduced from 900 to 150 km. As expected, the fluence increases with increasing solar activity. For example, at a nominal altitude of 500 km (Space Station), the yearly fluence on these surfaces increases from 4.6×10^{19} to 2.2×10^{21} atoms/cm^2 as solar activity increases from minimal ($F_{10.7}$=70; A_p=0) to maximum ($F_{10.7}$=230; A_p=35).

Fluence is also strongly influenced by surface orientation as shown in Figure 2-3 (ref. 45). For example, the fluence for surface 1L (ram conditions) situated in a circular orbit of 500 km during nominal solar activity is 7.4×10^{21} atoms/cm^2 per year. In comparison, B surfaces subjected to windward conditions at solar noon and I surfaces that are antisolar viewing undergo yearly fluences of 3.3×10^{20} and 2.7×10^{20} atoms/cm^2, respectively, or 45% and 36% of ram exposure. On the other hand, solar-viewing I surfaces and leeward B surfaces accumulate less fluence, 1.5×10^{20} and 1.4×10^{20} atoms/cm^2, respectively. This difference can be explained using Figure 2-3. Solar heating effects produce a slight bulge in number density at approximately 40° east of solar noon. The former surfaces fly through this bulge and the latter surfaces are protected from it because of wake effects. During the night exposure, the relative orientations of these surfaces are protected from it because of wake effects. During the night exposure, the relative orientations of these surfaces are reversed, but since the nighttime number density is lower (4.2×10^7 as compared to 1.4×10^8 atoms/cm^2), the reverse sides undergo less flux, or lower fluence.

The results of inclination changes are shown in Figure 2-4 (ref. 45). During spring and fall equinoxes, the density bulge produced by solar heating lies along the Equator and decreases at high latitudes. During the summer solstice (June 22), this bulge is 23.5° above the equatorial plane and orbits near this location are characterized by higher fluences.

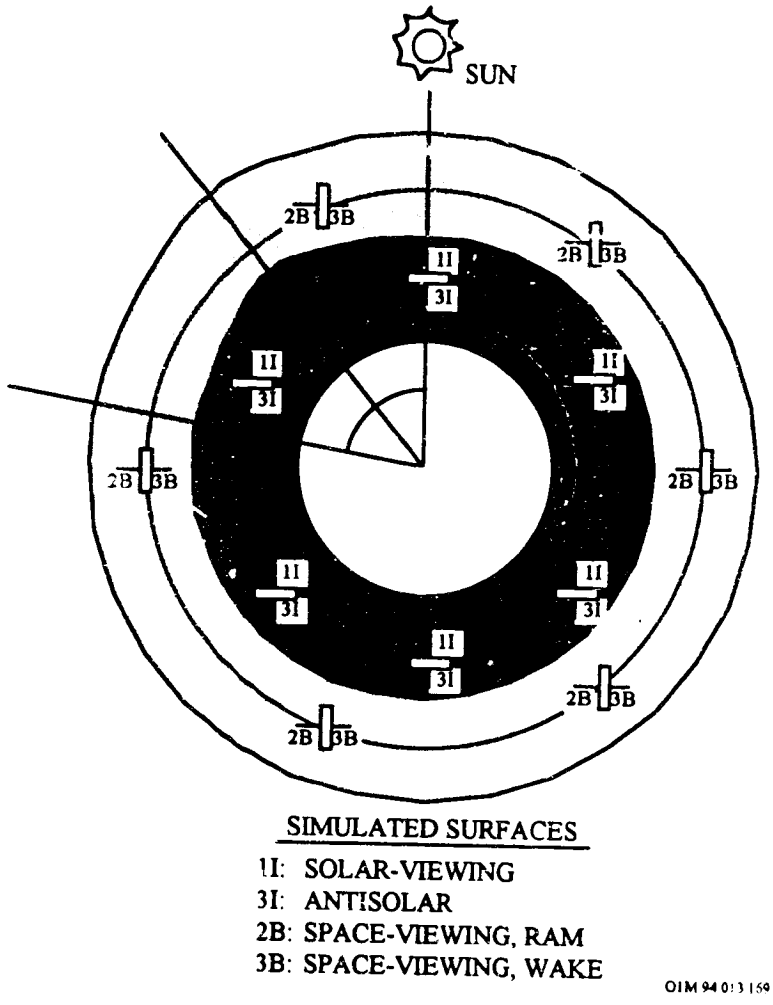

Figure 2- 3. Surface Orientations Relative to Atomic Oxygen Density Variations at Solar Noon.

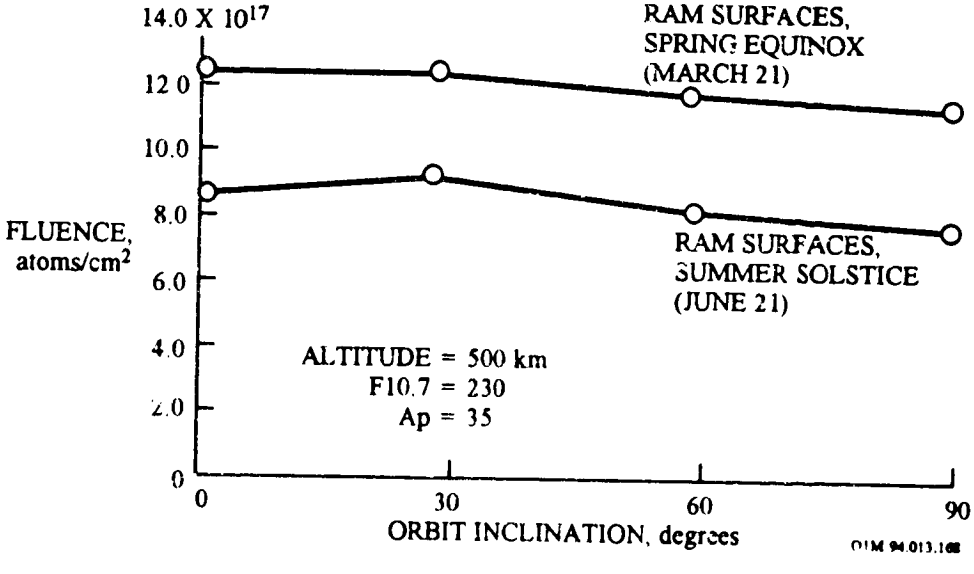

Figure 2- 4. Seasonal and Inclinational Effects on Fluence (three orbits).

Surface recession predictions as a function of atomic oxygen fluence can be determined from the nomograph of Figure 2-1 by using the following procedures (ref. 45):

1. Estimate the solar flux index ($F_{10.7}$ number) for each year the spacecraft is exposed to the LEO environment by using Figure 2-4, which shows solar activity predictions for solar cycle 22, the current cycle which began in 1988.

2. Select spacecraft attitude and orbital altitude of the surface in question.

3. Using the above information, read from the lower nomograph scale the amount of fluence per year for each year the spacecraft is in operation. To obtain an estimate of the amount of surface recession on a per year basis for the material under consideration, multiply these fluence values by the material reactivity values shown in Tables 2-2 to Table 2-6. These calculations yield the amount of surface recession (in centimeters) for each year the spacecraft is exposed to orbital conditions.

   NOTE: If the material is highly reactive, such as Kapton ($R_e = 3.0 \times 10^{-24}$ cm^3/atom), an estimate of surface erosion on a per year basis may be obtained directly from the upper horizontal scale of the nomograph.

4. Sum the values of (1) fluence per year, and (2) surface recession per year calculated in Step 3 over the lifetime of the spacecraft. These quantities represent a good estimate for the total fluence and total surface recession that each surface in question will experience during the lifetime of the mission.

2.1.2.3 Example

Assume a spacecraft is designed to operate at an altitude of 500 km and is launched into an orbit with an inclination of 28.5°. Also assume the spacecraft is gravity-gradient stabilized, is delivered to orbit during 1990, and has an intended operational lifetime of one year. The amount of surface recession on ram-oriented Kapton surface is determined from the nomograph as follows:

1. From Figure 2-4, a launch date of 1990 represents maximum solar activity conditions ($F_{10.7} = 230$).

2. From the nomograph of Figure 2-1, curve "1EMAX" represents ram exposure for these altitude conditions. Reading across the altitude scale of 500 km, the fluence and surface recession are 2×10^{21} atoms/cm^2 year and 60 μm/year, respectively. Thus, a highly reactive material such as Kapton with a thickness of 127 μm (5.0 mil) will lose 60 μm ($\Delta x = F_T \times R_e$: 2×10^{21} atoms/cm^2 x 3.0×10^{-24} cm^3/atom = 6.0×10^{-3} cm), or 47 percent, of its thickness during the time the spacecraft is in operation. Using the data in Tables 2-2 to 2-6, if the material is a fluoropolymer, such as Teflon ($R_e < 0.05 \times 10^{-24}$ cm^3/atom), the thickness loss will be 1.0 μm (0.4 mil), or 1/60th the amount predicted for Kapton. From LDEF the predicted R_e for Teflon is 3.64×10^{-25}

cm^3/atom (see page 10-129) in which case the thickness loss would be 7.3 μm ($\Delta x = F_T \times R_e$: 2×10^{21} atoms/cm^2 x 3.64×10^{-25} cm^3/atom = 7.28×10^{-4} cm).

3. If the surface in question is solar inertial, such as solar array panel, curve "1IMAX" on the nomograph represents one side exposure for solar inertial surfaces during the time this spacecraft is intended to operate. Under these conditions, the fluence and surface erosion would be 3 x 10^{20} atoms/cm^2 year and 10 μm/year, respectively. For two-sided exposure, this would represent a thickness loss of 20 μm and if the solar array substrate is 127 μm in thickness, 16 percent of the Kapton material would be eroded away during the operational period of the spacecraft. Coating the Kapton with SiOx or ITO would reduce this erosion rate by a factor of 300 (see Table 2-1) and would result in a thickness loss of only ~0.06 μm. Thus, materials unsuited for these applications can be protected from the LEO environment by coating them with materials having low reactivity rates.

Figure 2-5 shows the surface erosion or thickness loss in mils per year of spacecraft operation for Kapton as well as for other materials with different reaction efficiency values.[47]

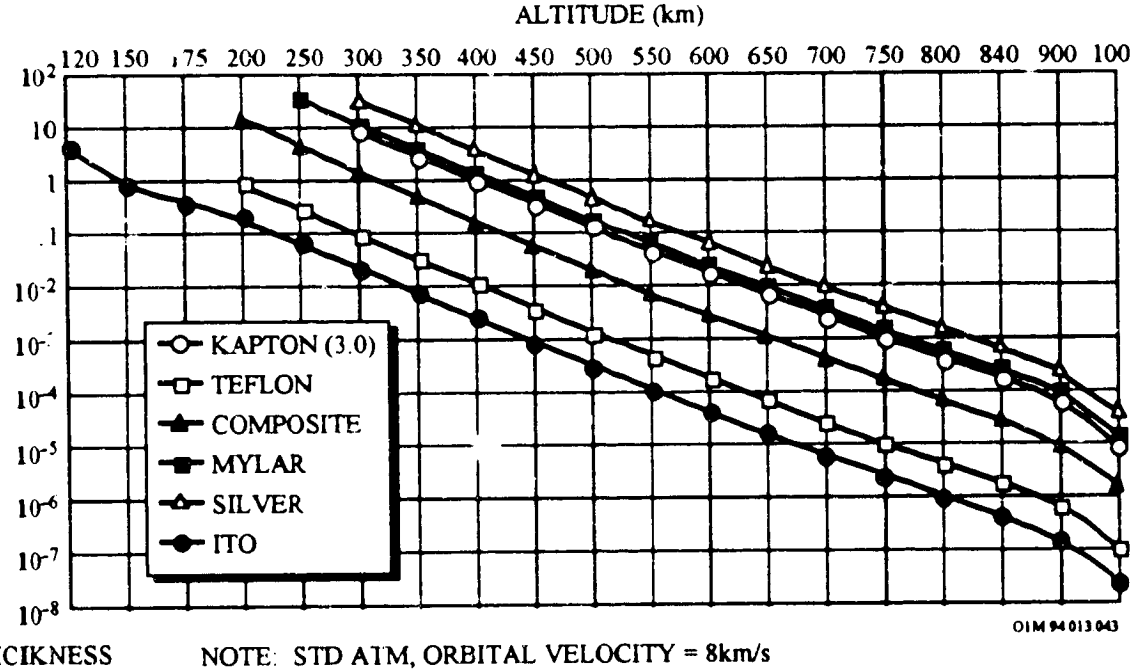

Note: Multiply by 25.4 to obtain thickness loss in μm.

Figure 2- 5. Nomogram for Atomic Oxygen-Induced Surface Erosion for Solar Inertial Facing Surfaces

2.1.2.4 Screening Techniques

Materials considered for spacecraft construction need to be evaluated by spacecraft designers for susceptibility to atomic oxygen interactions. The above mentioned techniques can be used to predict the amount of surface erosion that would be experienced by surfaces in question during an intended mission. If the amount of surface degradation is considered unacceptable, sensitive materials can be coated with low atomic oxygen reactivity materials, such as silicone oxide, aluminum oxide, RTV silicone, etc. (See Chapter 8 - Protective Coatings), or they can be substituted for materials with similar properties, but which are less reactive in an atomic oxygen environment. Table 2-7 summarizes the atomic oxygen effects on materials.

Table 2- 7. Atomic Oxygen Effects on Materials

Material	Atomic Oxygen Effects
Composites	Erosion from carbon fiber composites can be predicted from carbon reactivity. Glass fiber composites become self protecting.
Paints	Diffuse paints erode non-linearly.
Polymers	Unfilled polymers react linearly with atomic oxygen.
Metals	Reaction is non-linear and strongly dependent on temperature, stress and microstructure; accommodation on the order of less than 10 atoms per 10^4 incident.
Glassy Ceramics	Densification accompanied by a decrease of less than a few hundred angstroms results from space exposure.

2.1.3 Atomic Oxygen Effects on Optical Properties

All materials which form volatile oxides upon atomic oxygen bombardment have been found to develop a microscopic surface texture composed of left-standing fibrils or cones. This texture tends to have an influence on the optical properties of materials, causing a significant increase in diffuse reflectance. Table 2-8 delineates the changes in solar absorptance and thermal emittance of materials exposed to low-Earth orbital atomic oxygen.

Table 2- 8. Effect of LEO Atomic Oxygen on Optical Properties of Materials

Material	Change in Optical Properties Due to Atomic Oxygen			Reference
	Solar Absorptance	Emittance	Reflectance	
Ag/FEP	0.006	0.0	-----	48
Al/Al_2O_3	-.006	0.0	-----	52
$AlMgF_2$	-----	-----	0.0	41
Al_2O_3/Al (He)	0.0	-----	0.0	33
Al_2O_3/Al (Le)	-.005	0.0	-----	52
Aluminized FEP Teflon, second surface mirror (0.025 mm thick)	-.006	0.0	-----	52
Al Kapton	.05	-.19	-----	49
Al Kapton	.048	.018	-----	39
Aluminized Kapton, second surface mirror, uncoated (0.052 mm thick)	-.062	-.007	-----	39
Aluminum (150Å)	-.23	-.59	-----	53
Aluminum (chromic acid oxidized)	0.0	0.0	0.0	41
Black, carbon-filled PTEE impregnated fiberglass (0.127 mm thick)	0.0	0.0	0.0	33
Black Cr on Cr on Mo	-.16	-.05	-----	53
Black Ir on Mo	-----	-----	[a].20	50
Black Rh on Mo (matte)	-----	-----	-.75	54
Black Rh on Mo (specular	-----	-----	-.25	54
Bostic 463-14	-----	-----	-.50	54
Chemglaze A276 (w/modifiers)	.01	0.0	-----	55
Chemglaze A276 (white)	.006 t .016	.02	-----	42
Chemglaze Z004	.005	.03	-.039	41,33
Chemglaze Z302 (glossy, black)	.01	0.0	-----	55
Chromium (123Å)	.011	-----	-.01	37
FEP Teflon with silver undercoat	0.0	0.0	0.0	33
GE-PD-224	.006	0.0	-----	-----
GSFC (green)	0.0	0.0	-----	51 ,55
Indium tin oxide coated Kapton H with aluminized backing	-.002	-----	-----	40
ITO ring	.006	.004	-----	39
ITO (S) Sheldahl, black/Kapton (sputtered)	.006	.004	-----	39
ITO (VD) Sheldahl, black/Kapton (vacuum deposited)	.01	0.0		55
Ir foil on Al	0.0	0.0	-----	55
KSAT glass	-----	-----	0.0	54
Kapton with aluminized backing	-----	-----	[b]-.051 to .01	54
Kapton H (aluminized)	.048	.018	-----	39
Mo (polished)	.041	-----	-.051	54
Nickel	-----	-----	0.0	52
Ni/SiO_2	.005	0.0	-----	52
Polyurethane A-276	-.004	0.0	-----	52
Polyurethane A276 glossy white	.023	-----	.01	40
Polyurethane A276 with 0.5 mil 01650 overcoat	.002	-----	.2	40
Rh foil on Al	.002	-----	-.3	40
	-----	-----	0.0	54

[a]More reflective as a result of the exposed Mo substrate.

[b]Low absolute reflectance (-0.5 to 1 percent).

Table 2- 8. Effect of LEO Atomic Oxygen on Optical Properties of Materials (Continued)

Material	Change in Optical Properties Due to Atomic Oxygen			Reference
	Solar Absorptance	Emittance	Reflectance	
S13 - GLO	-.005	0.0	----	52
SiO_2 (650 A on Kapton H)	0.0	0.0	0.0	33
SiO_x	.039	-.002	-----	39
Silicate MS-74	0.01	0.0	-----	52 ,42
Silicone (black, Conductive)	0.0	-.005	-----	42
Silicone RTV-602/Z302	.004	-----	-----	----
Silicone RTV-650 + TiO_2	.001	-.01	-----	42
Silicone RTV-670	-.004	-----	.001	41
Silicone S1023	-.022	-.02	-----	53
Siloxane coating, RTV 602/on aluminized Kapton second surface mirror substrate (0.008 mm thick coating) (0.052mm thick Kapton)	0.0	0.0	-----	53
Ti/"tiodized" alloy	-----	-----	[c]-.25	54
Ti/"tiodized" CP	-----	-----	[d]-.40	54
Urethane (black, conductive)	.042	.55	-----	42
Urethane inhib A-276	0.0	.01	-----	42
YB-71	.004	0.0	-----	52
Z302 glossy black	.043	-----	-4.3	40
Z302 with MN41-1104-0 overcoat	-.002	-----	-----	54
Z302 with OI 651 overcoat	0.0	-----	-----	58
Z302 with OI 650 overcoat	-.001	-----	.1	40
Z302 with RTV-602	-.004	-----	-----	40
Z302 with RTV-670	-.004	-----	.4	40
Z306	.022	0.0	-----	52
Z306 (flat black)	.028	-----	-----	40
Z873, glossy yellow with MN41-1104-0 overcoat	.011	-----	-----	58
Z853, yellow	-.034	-----	-----	40
401 - C10 flat black	.005	-----	-----	40

[c]Contrast in different spectra between STS-8 and control. Possible aging effects on controls.
[d]Aging effects similar in STS-8 and control. No exposure effect.

2.2 ULTRAVIOLET (UV) RADIATION/SOLAR EXPOSURE EFFECTS

2.2.1 Introduction

The Sun's extreme ultraviolet (EUV) and UV output varies in a pattern similar to sunspot number (SSN), and this variability translates into a variation of energy available to the thermosphere. The resulting variation of exospheric temperature, in turn, produces a solar cycle variation of atmospheric density. Since little EUV radiation reaches the ground, direct EUV flux observations have been made only rarely. However, one can infer the value based on solar radio flux measurements at 2800 MHz because EUV and 2800-MHz fluxes have shown a fairly good correlation. The 2800-MHz flux is better known as the 10.7-cm flux (or $F_{10.7}$). Although the correlation is not exact (and varies from one sunspot cycle to the next), the patterns are similar enough to be useful.

The wavelength range of solar ultraviolet radiation present in LEO is between approximately 0.1 and 0.4 μm, which is a small portion of the solar irradiance curve shown in Figure 2-6.[55] The total energy provided by radiation in this wavelength range is approximately 8% of the solar constant, where the solar constant is defined as the total energy provided by the Sun over all wavelengths up 1000 μm and is equal to 136.7 mW/cm^2.

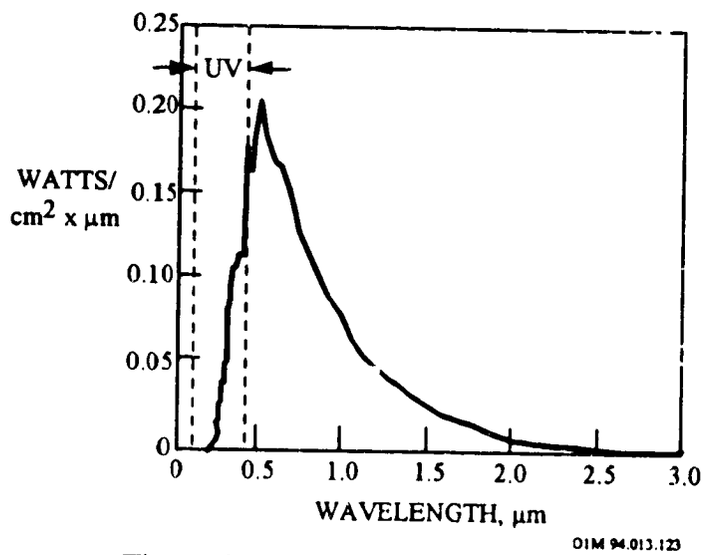

Figure 2- 6. Solar Spectrum At Air Mass Zero

The UV spectrum is divided into three parts - the vacuum or extreme UV below 200 nm (0.2 μm), the far UV from 200 nm to 300 nm, and the near UV from 300 nm to 400 nm. This UV radiation is energetic enough to cause the breaking of organic bonds as shown in Figure 2-7 (ref. 55). Although the solar radiation below 0.2 μm represents less than 0.001% of the solar constant,

its presence may promote breakage of important organic structural bonds, such as C=C and C=O and functional groups.

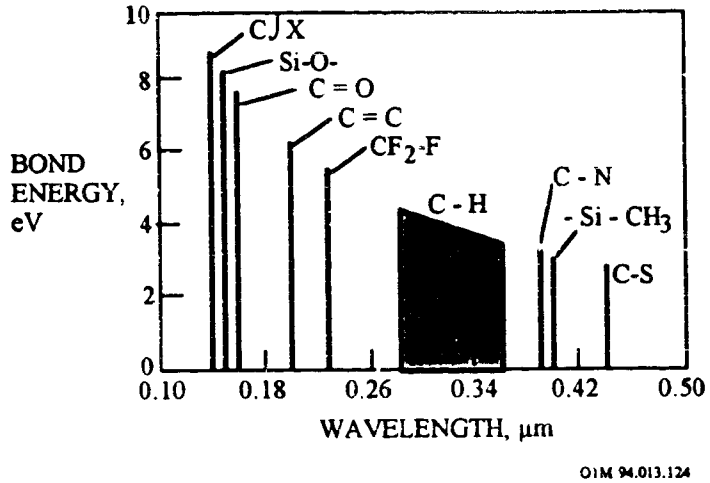

Figure 2- 7. Wavelength Requirement to Break Various Polymeric Material Bonds.

Because atomic oxygen is present in LEO, it is expected that the reaction intermediates from the photon absorption will react with reaction intermediates from the oxidation process. This photo-oxidation can lead to discoloration and reduced transparency of some polymers. Chemical changes in the molecule as a result of these reactions may also lead to the formation of polar groups which may affect electrical properties.[56]

2.2.2 Optical Properties Changes

Most of the major research emphasis has been on changes in optical properties of polymer films. LDEF revealed a larger increase in the α_s of S13G/LO white compared to Teflon film. This is attributed to the radiation vulnerability of the silicone binder of the S13G/LO white paint. The silicone is a hydrocarbon organic, and its chemical bonds are known to have lower binding energies than those of the fluorocarbon bonds of Teflon (see Figure 2-7). Thus, it is probably reasonable to ascribe the difference between the $\Delta\alpha_s$ of the S13G/LO white paint and that of Teflon to radiation damage. Laboratory experiments have been performed to determine the effects of UV radiation on the optical properties of various types of polyimides.[57] In terms of ultraviolet radiation degradation mechanism, the most stable polyimide materials were those which contained both oxygen and -$C(CF_3)_2$ bonds, and the poorest performers were those which contained sulfur atoms within the polymer molecular structure.

Comparative flight and laboratory data on solar absorptance, $\Delta\alpha_s$, changes as a function of equivalent solar hours for a zinc oxide-potassium silicate coating Z-93 are shown in Figure 2-8 (ref. 55).

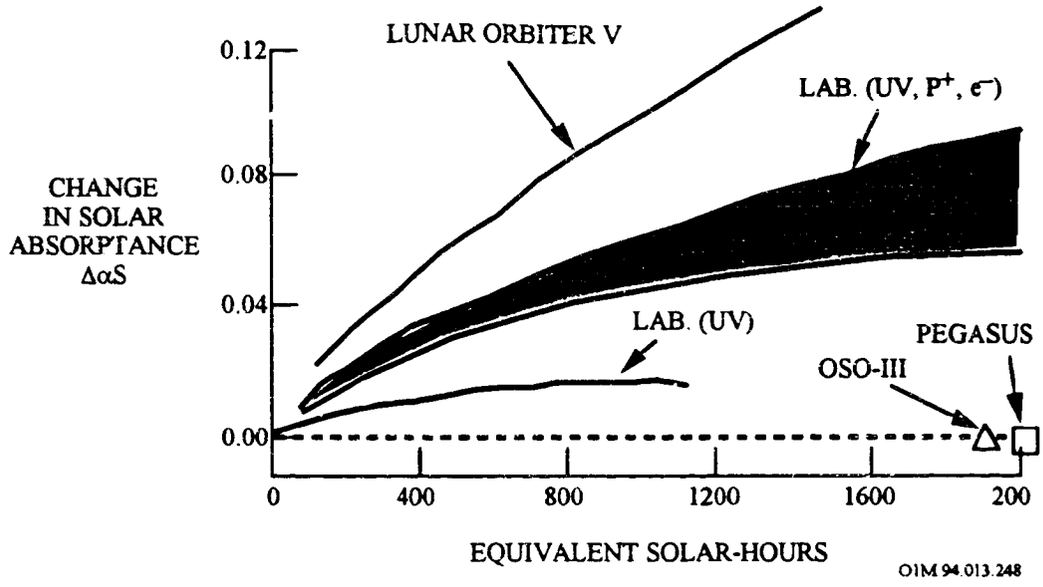

Figure 2- 8. Comparison of Flight and Laboratory Data on Z-93 Coating

The combined UV and solar wind plasma experienced on Lunar Orbiter V was under-simulated in the laboratory. The UV degradation experience by OSO-III and Pegasus was over-simulated in the laboratory test. Laboratory $\Delta\alpha_s$ was generated using a short arc xenon UV source and a 3 keV solar wind proton source with thermal electrons for charge neutralization.[b]

[b] Comparison of the spectral irradiance of a xenon short-arc lamp with a quartz envelope to the solar irradiance at air ma zero clearly shows that xenon has a good UV solar match from approximately 0.2 to 0.7 micrometers, but is much mo intense in the infrared region. This IR radiation leads to over heating of test specimens when accelerated exposure attempted. Acceleration factors of only 3X are possible without substantially overheating the test specimens.

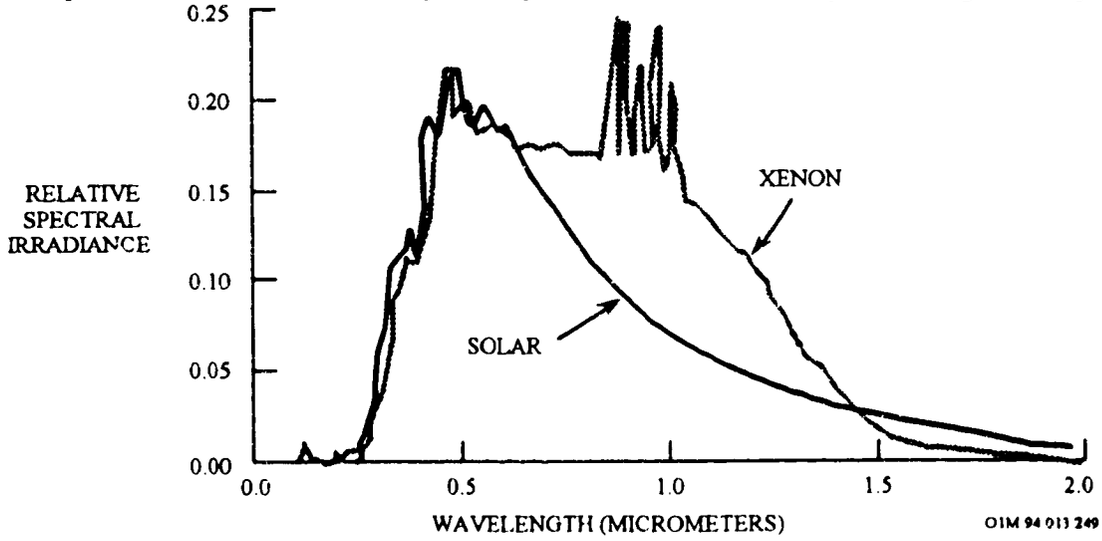

Figure 2-9 illustrates the change in spectral reflectance due to UV exposure in vacuum for a zinc-oxide, pigmented silicone paint S-13 (ref. 55). The figure also illustrates that upon introduction of air (oxygen) into the vacuum system, bleaching occurs which eliminates the UV degradation to this coating. More or less complete recovery of degradations caused by irradiation in a vacuum were noted when several white paints were returned to the air.

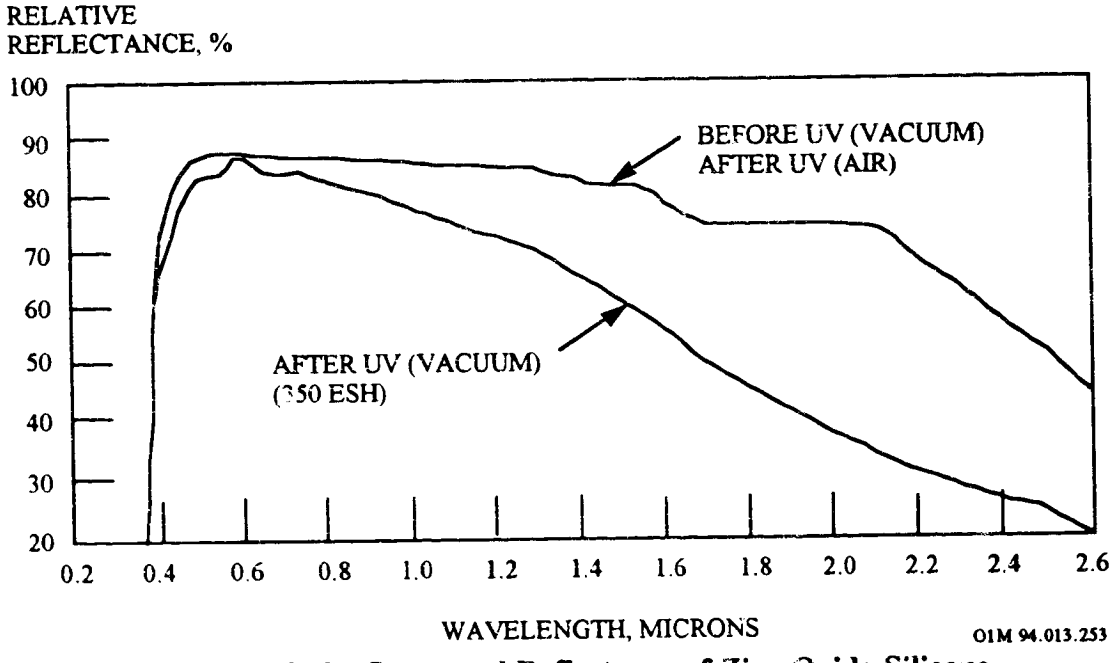

Figure 2- 9. Structural Reflectance of Zinc Oxide-Silicone

Figure 2-10 shows the in-air recovery of the white paints PSB and SG11FD after combined irradiation with UV and particles in vacuum.[58] This bleaching of white paints has led to the need for in situ testing of spacecraft coatings.

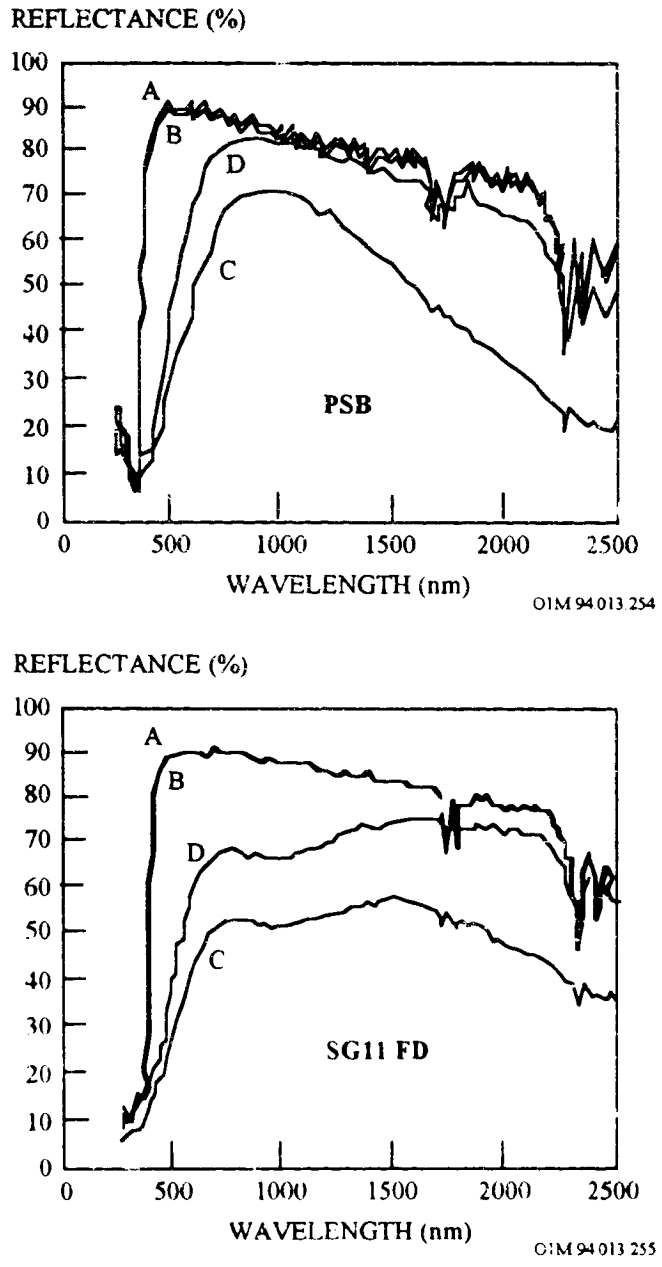

(A) in air, before irradiation,
(B) in vacuum, before irradiation,
(C) in vacuum, after combined irradiation with UV (6250 esh), electrons (2.5×10^{15} electrons cm^{-2} s^{-1} of 400 keV) and protons (5×10^{15} protons cm^{-2} s^{-1} of 45 keV, 5×10^{14} protons cm^{-2} s^{-1} of 240 keV),
(D) after 5 days in air, post-irradiation.

Figure 2- 10. In Air Recovery of the White Paints PSB and SG11 FD After Combined Irradiation with UV and Particles in Vacuum.

A high value of solar transmittance ($\alpha \leq 0.09$; see page 10-130) in the wavelength range between 0.3 and 0.6 μm is necessary for polymer used as second surface reflectors (e.g., metallic-coated Teflon tapes). UV radiation degradation of this transmittance may result in decreased efficiency of the thermal control surface. The thermal control performance of Ag/FEP in the LEO environment has generally been stable unless erosion of the Teflon on the leading edge by AO erosion occurs, which can obviously result in emissivity changes. As was observed on LDEF, 80 to 90 percent of the 127 μm (5-mil) silver Teflon surfaces showed minimal degradation compared to typical values of 0.05 to 0.07 for unflown silver Teflon [59] In the remaining area, the α had increased to values ranging from 0.28 to 0.4, but in these regions, the silver Teflon either had been visibly contaminated or had exposure on both sides of the film, resulting in severe degradation of the Inconel and silver metallization layers.

Comparison of the space environment effects on silver Teflon blankets with other flight experience of different altitudes and mission duration is summarized in Table 2-9 (ref. 59). The Solar Max repair mission, conducted on STS-41-C after the deployment of LDEF in 1984, returned 127 μm silver Teflon surfaces that had been in orbit from February 1980 until April 1984 at altitudes that decreased from 574 to 491 km. Post-flight measurements of solar absorptance were made in many areas with values of 0.06 to 0.11 representing 80 to 90 percent of the area.[60] Among other spacecraft flown at altitudes less than 1,000 km, specimens on both OSO-H[61] and ML-101[62] experiments showed rapid changes of about 0.02-in absorptance during the first month in orbit, followed by very slow, small changes over the following months and years. A likely cause of the early changes was contamination due to rapid outgassing and initial venting of the spacecraft. The more recent shuttle flights were too short in duration to cause large changes in silver Teflon.[63]

Table 2- 9. Flight Experience with Metalized Teflon

Altitude (Inclination)	Spacecraft	Thermal Property Changes
235,639 x 201,599 km (17°)	IMP-H	$\Delta\alpha_s \geq 0.07$ over 12,000 esh
237,056 x 370 - 1600 km (29°)	IMP-1	Large $\Delta\alpha_s$ over time
43,288 x 27,578 km (7.9°)	P78-2 (SCATHA)	$\Delta\alpha_s > 0.2$ over 10 years (~27,800 esh)
778 x 737 km (98°)	ML-101	$\Delta\alpha_s < 0.02$ initial; then low $\Delta\alpha_s$ over time
574 - 491 km (28.5°)	Solar Max	$\Delta\alpha_s \leq 0.04$ typical; some areas 0.28 to 0.4 (~4 years)
560 x 327 km (33°)	OSO-H	Rapid $\Delta\alpha_s / \varepsilon$ ~0.02, then constant (~8000 esh)
480 - 330 km (28.5°)	LDEF	$\Delta\alpha_s \leq 0.01$ typical: some areas >0.24 (~5.8 years)
270 km (28.5°)	STS-41G (EOIM-II)	Slight changes (< 100 esh)
220 km (28.5°)	STS-8 (EOIM-I)	Slight changes (< 100 esh)

As shown by the LDEF results, the effects of sunlight (including UV) on all spacecraft will require careful selection of exposed materials to avoid those materials that change their α_s/ε ratios, optical transparencies or reflectivities, and other properties that affect the thermal behavior of the spacecraft. The abilities of optical transmitters or receivers (sensors) to function can be affected. These material selections are considered to be design changes required by the environment (sunlight in this case).

2.2.3 Mechanical Properties Degradation

UV radiation has also been shown to degrade mechanical properties of polymeric materials as is shown in the degradation in the tensile strength of Mylar. Figure 2-11 illustrates the effect of ground-simulated UV radiation on the performance of protected and unprotected Mylar. Solar ultraviolet irradiation can lead to crosslinking of polymer surfaces which may lead to embrittlement and possibly to surface cracking.[64]

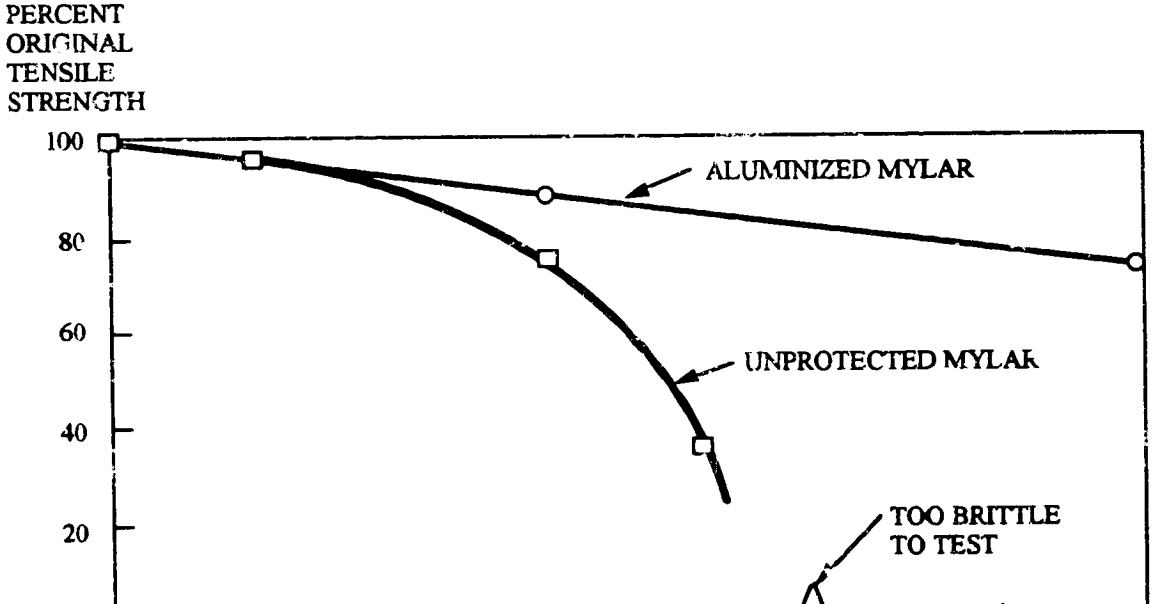

Figure 2- 11. Effect of Ground Simulated UV on the Tensile Strength of Mylar

Mechanical property changes that occurred in 127 μm (5-mil) silver/Teflon on LDEF are indicated by the property data summarized in Table 2-10 and Figure 2-12.[65] Teflon on LDEF trailing edge (i.e , rows 1 to 6; where AO fluence was low), was embrittled due to solar exposure, decreasing the percent elongation to failure by about 20 percent and the ultimate tensile strength by about one-third relative to controls (see also Figure 2-12). Teflon from the leading edge (i.e., rows with high AO fluence), was still flexible with percent-elongation to failure values only slightly decreased relative to controls. The implication is that for one group of blankets erosion of the UV-affected surface layer by AO resulted in no degradation of the film strength (based on the remaining cross-sectional area, after erosion), while for the other group (i e., low AO fluence), the changes in the chemical structure and embrittlement due to the effects of long-term solar ultraviolet radiation

has occurred in the bulk of the FEP. The leading-edge mechanical properties are not significantly different, although thinning of the Teflon would ultimately lead to reduced mechanical properties.

Table 2- 10. Mechanical Properties Changes of Teflon with Exposure on LDEF

Teflon from Blankets	% Elongation to Failure (±40%)	Ultimate Tensile Strength, N/mm^2 (±3 N/mm^2)
Trailing Edge, Rows 1 to 6		
Exposed	230	14
Masked	300	21
Leading Edge, Rows 7 to 11		
Exposed	290	19
Masked	310	20

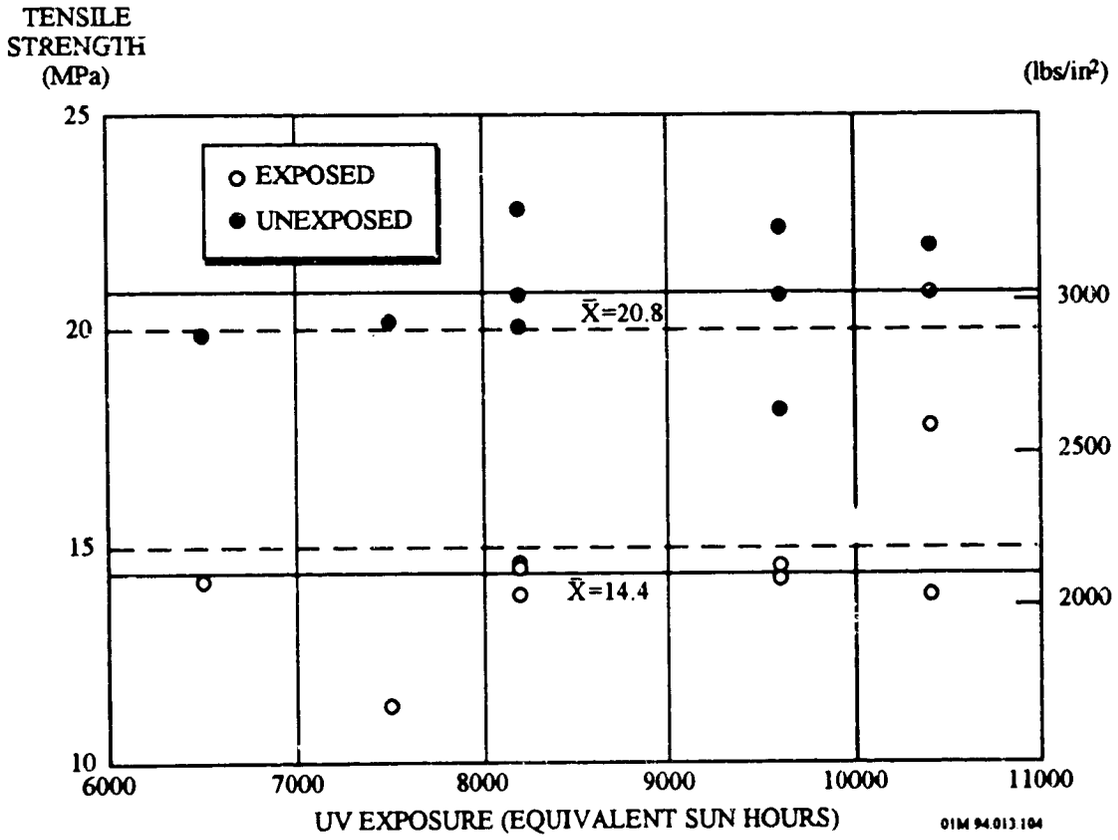

Figure 2- 12. UV Effects on the Tensile Strength of Teflon Specimens from Rows 1-6.

2.3 MICROMETEOROID AND DEBRIS IMPACT

2.3.1 Introduction

Hypervelocity impact features are produced by collisions between space debris particles or dust and small meteoroids with spacecraft surfaces. A significant amount of work has been performed by the LDEF Meteoroid and Debris Special Investigation Group and other LDEF experimenters in documenting, analyzing, and modeling the vast number of hypervelocity impacts that occurred on LDEF.[66] Impact damage is becoming importance because future satellites are being designed for ever-longer mission times (e.g., 5 to 10 years), and the debris environment is steadily worsening. This section introduce to the system designers and engineers an awareness of the extent of damage which can be caused by impacts onto different types of spacecraft materials. In addition, program managers should have a better understanding of the need to thoroughly assess this damage. With increased awareness and improved understanding, spacecraft can be designed which will have improved reliability, survivability, and performance, even during long missions.

2.2.2 Impact Fluence Models

The microparticle environment is described in terms of two separate models, one for the man-made debris, and the second one for the naturally occurring micrometeoroids. The phenomenology numerically computed models are provided by B.G. Cour-Palais[67] for micrometeoroids and by D. Kessler[68] and R.C. Reynolds for space debris. These micrometeoroids and debris models are outlined in NASA SP-8013 and in NASA-TM-100471, respectively. Recent 1990 micrometeoroids data are provided in a Phillips Laboratory briefing by Kessler. Cour-Palais et al. provides a general model of the near-Earth micrometeoroid environment. Eberhard Grun's 1985 model[69] provides an update to the Cour-Palais model by including the beta meteoroid environment. The Kessler debris model, developed in 1987, has been widely adopted and used by the U.S. Department of Defense, NASA, and the European Space Agency (ESA)

2.2.3 Comparison of Fluence Models to LDEF Results

The environment models continue to be updated with the addition of LDEF data. With these updates, predictions have been done for the LDEF satellite using the most recent version of the Kessler debris model. Some selected results are shown in Figures 2-13 and 2-14.[70] In general, the existing models fit the experimental data within a factor of two to three of the actual data from LDEF. Note that the true LDEF ram surface was accidentally set at 8° to the intended orientation (toward the North).

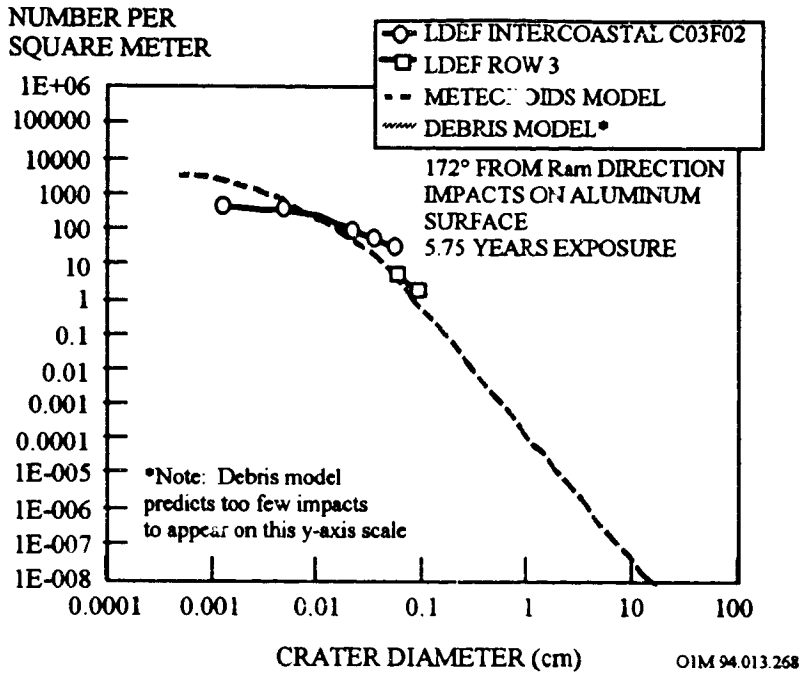

Figure 2- 13. Comparison of Crater Diameters to Number of Craters per Square Meter: Comparison of LDEF Data to Model Predictions for 172° From Ram.

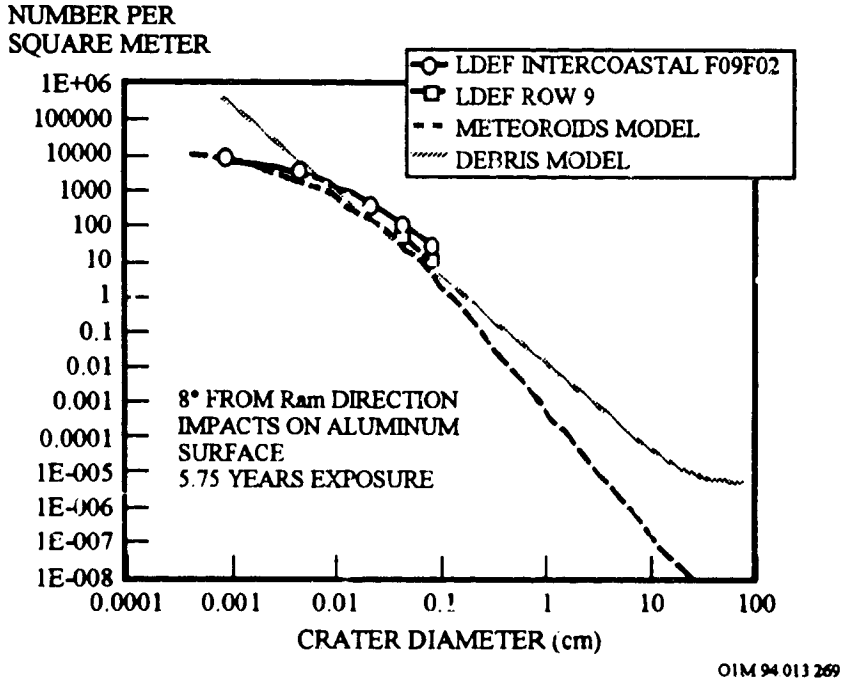

Figure 2- 14. Comparison of Crater Diameters to Number of Craters per Square Meter: Comparison of LDEF Data to Model Predictions for 8° From Ram.

Comparison of the survey of the meteoroid and space debris impacts on the various LDEF experiments to curves derived from the Kessler debris model and the Cour-Palais micrometeoroid model indicates that these models over predict small impacts (<100 micron) and may under predict large impacts (>1000 micron) while having fair to good agreement for the intermediate impacts.[71] The impact LDEF data are based primarily on crater counts, especially in the aluminum structure of LDEF (longerons and intercostals). It is observed that for the smallest particles the crater count asymptotes, whereas the Kessler debris model predicts a steady increase with decreasing particle size. This effect may be due to the anodized coating on the aluminum. This alumina coating is both tougher and of higher density than the metal. Consequently, the craters will be smaller than in the metal and may artificially cause the roll-off. Other data, available from the Interplanetary Dust Experiment (IDE) on LDEF, also provide information for the smaller particles. These data indicate a higher flux than the aluminum crater count. It should also be noted that the IDE data are for mean flux rates, whereas the actual time dependent IDE data show dynamic variations in flux rates ranging from 0 to 1000 times the mean flux rate. The IDE data also indicate that the many orbital particles are in elliptical orbits (again not predicted in the models) and that these particles are in clouds, thus causing the dynamic flux rate variations.

Using the Kessler model, the predicted number of penetrations, N_h/m^2, and the actually observed number of holes in the thermal blankets covering the Ultra High Cosmic Rays (UHCR) experiment AO178 on LDEF were compared to model predictions, and the results are shown in Table 2-11.[72]

Table 2- 11. Comparison of Predicted and Observed Number of Holes on LDEF Thermal Blankets.

Row	Predicted, N_h/m^2	Observed, N_h/m^2
1	93.4	85
2	33.3	32.5
4	18.7	29
5	48.2	31.3
6	125	70
7	203	195.5
8	264	232
10	280	350.7
11	247	237

2.3.4 LDEF-Derived Model for Predicting Micrometeoroid/Debris Impacts

The micrometeoroid/debris observed on the LDEF was transformed into a nomogram format useful for estimating the total number of hits that could be expected on a space structure as a function of time in orbit, angular location relative to ram and exposed surface area. The nomogram can then be applied to determine the total cumulative damage that could be expected over a 30-year lifetime in space for an exposed structure.

From the individual LDEF experiment trays, counts of micrometeoroid/debris crater impacts were compiled utilizing the data from T. See et al.[73] Humes has shown the significant dependence of meteoroid/orbital debris flux vs. angle from velocity vector as derived from model calculations and from the LDEF experiment S0001 data.[74] A summary of the crater impact data of diameter $\geq$ 0.1 mm reported for each type of surface in each row is provided in Table 2-12.[75] The count column lists the total number of craters. Area column lists the area (square meters) used to calculate flux values. Flux column provides the reduced counts of impact craters per square meter per year, for each type of surface. The angle "Beta" is the angle from the velocity vector (or ram) to the normal to each row. Note that Beta increases with increasing row number in a positive value up to 180 degrees. Negative values mean the direction is decreasing with row number up to a -180 degrees. As an example, row 9 is a minus 8 degrees.[76]

Directional dependence of meteoroid/debris impacts as a function of the angle from the velocity vector can be seen from the count and flux data. Apparent flux variations occurred within the same row for different materials. Flux values derived from impacts on experiment surfaces are normally lower than those from the structure or thermal panels. Each experiment was composed of a variety of different materials. Impacts on some surfaces exhibited excellent contrast making identification for counting fairly easy, while other materials, such as composites, exhibited very poor contrast making it much more difficult to identify impacts. The LDEF structure and thermal panels had smaller exposed areas than the experiment surfaces, but each consisted of the same type material and coating resulting in a more reliable and consistent count.

Table 2- 12. Crater Impact Data

Row No.	Experiments & Trays			LDEF Structure			Thermal Panels			
	Count	Area m^2	Flux	Count	Area m^2	Flux	Count	Area m^2	Flux	Angle Beta
1	622	6.58	16.43	112	1.22	15.95	46	0.316	25.33	+122°
2	126	6.58	3.33	68	1.22	9.68	36	0.316	19.83	+142°
3	399	6.58	10.54	74	1.22	10.54	10	0.316	5.49	+172°
4	311	6.58	8.22	96	1.22	13.67	15	0.316	8.26	+158°
5	846	6.58	22.36	184	1.22	26.20	29	0.316	15.97	+128°
6	915	6.58	24.15	442	1.22	62.94	12	0.316	6.60	-98°
7	2108	6.58	55.71	572	1.22	81.46	170	0.316	93.62	-68°
8	3289	6.58	86.92	939	1.22	133.72	175	0.316	96.37	-38°
9	3077	6.58	81.40	924	1.22	131.59	246	0.316	117.53	-8°
10	3118	6.58	82.40	652	1.22	92.85	204	0.316	112.34	+22°
11	2435	6.58	64.35	493	1.22	70.21	168	0.316	92.52	+52°
12	1620	6.58	42.81	321	1.22	45.71	132	0.316	72.56	+82°
Space End	112	5.966	3.26	79	—	—	165	4.65	6.16	-90°
Earth End	1095	5.966	31.92	649	—	—	1200	4.65	44.82	-90°

All of the flux data listed in Table 2-12, is plotted graphically in Figure 2-15.[77] The data was summarized for each longitudinal panel to yield an angular (θ) distribution of total impacts around LDEF after 5.75 years in low Earth orbit. Figure 2-15 presents two distributions based on the "total" reported hits that were recorded by unaided visual observation, and those hits which were ≥ 0.5 mm in size. It should be noted that the data shown are strictly valid only at $\theta = O°, \pm 30°, \pm 60°, 90°, \pm 120°, \pm 150°, 180°$, and the curves cannot be integrated to give a total number of impacts. This curve has not been corrected for the 8° yaw angle of LDEF.

Based on the number distribution presented in Figure 2-15, it is possible to construct a general purpose nomogram which permits a user to estimate the total number of impacts on a satellite or component (at the LDEF nominal altitude and inclination) for any value of time in orbit, angular location around the satellite or space structure (constrained by $\theta_n = n \times 30°$ where n=0,1,2 ...12, corresponding to a 12-sided polygon model of the satellite or component), and exposed area. For example, Figure 2-16 presents the nomogram for LDEF based on a longitudinal panel area of ~10 m^2, assuming a nominal impact fluence of 300 impacts/m^2 (ref. Tennyson and Manuelpillai, 1993). The example panel shown in Figure 2-16 corresponds to θ=30°. Thus the intersection of θ-30° and the LDEF time in orbit axis (~5.75 years) yields an impact fluence of ~300 impacts/m^2. Following up along this constant fluence curve until one intersects the desired panel area (10 m^2), one can then translate horizontally across the graph to the "Number of Impacts" ordinate. For this example, one obtains N = 3100 which agrees with the number plotted in Figure 2-15.

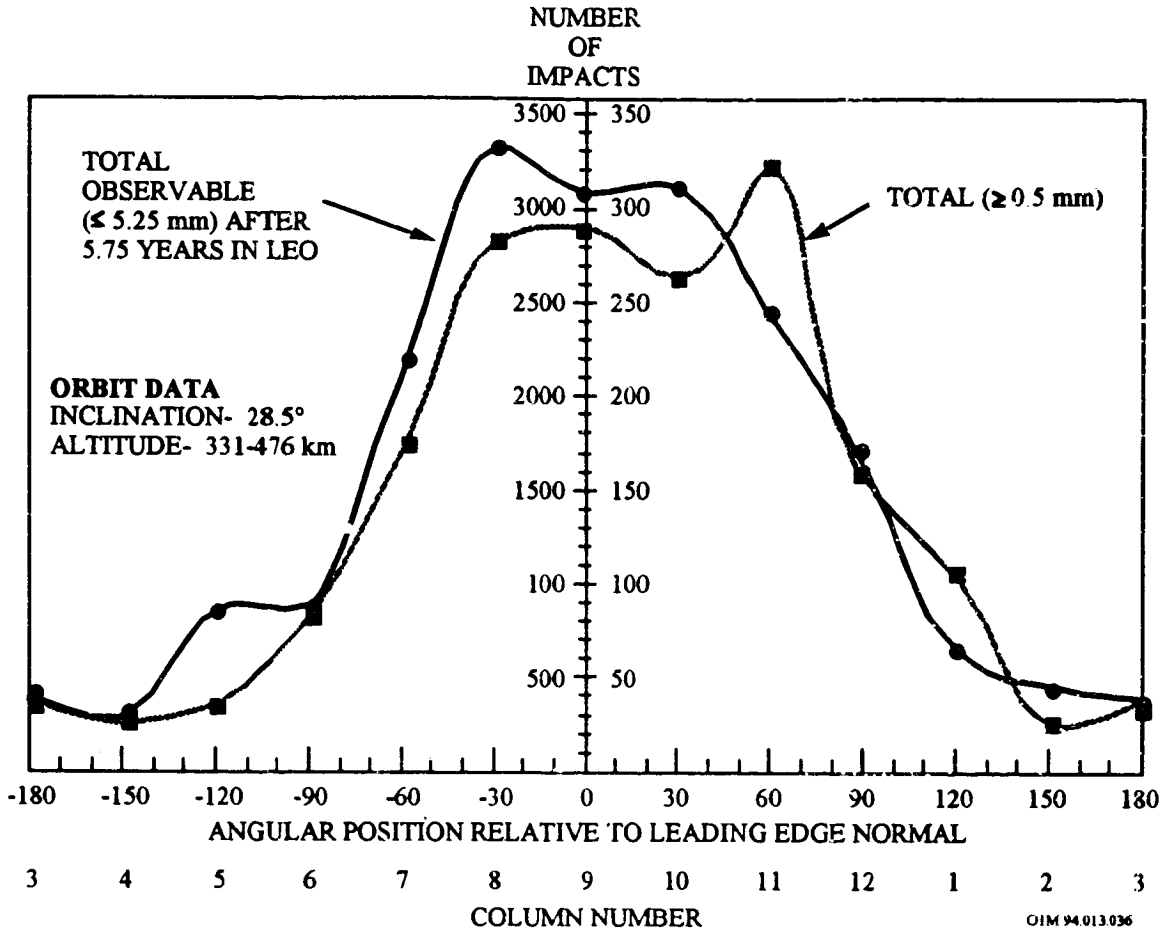

Figure 2- 15. Circumferential Distribution of Micrometeoroid/Debris Impacts on LDEF

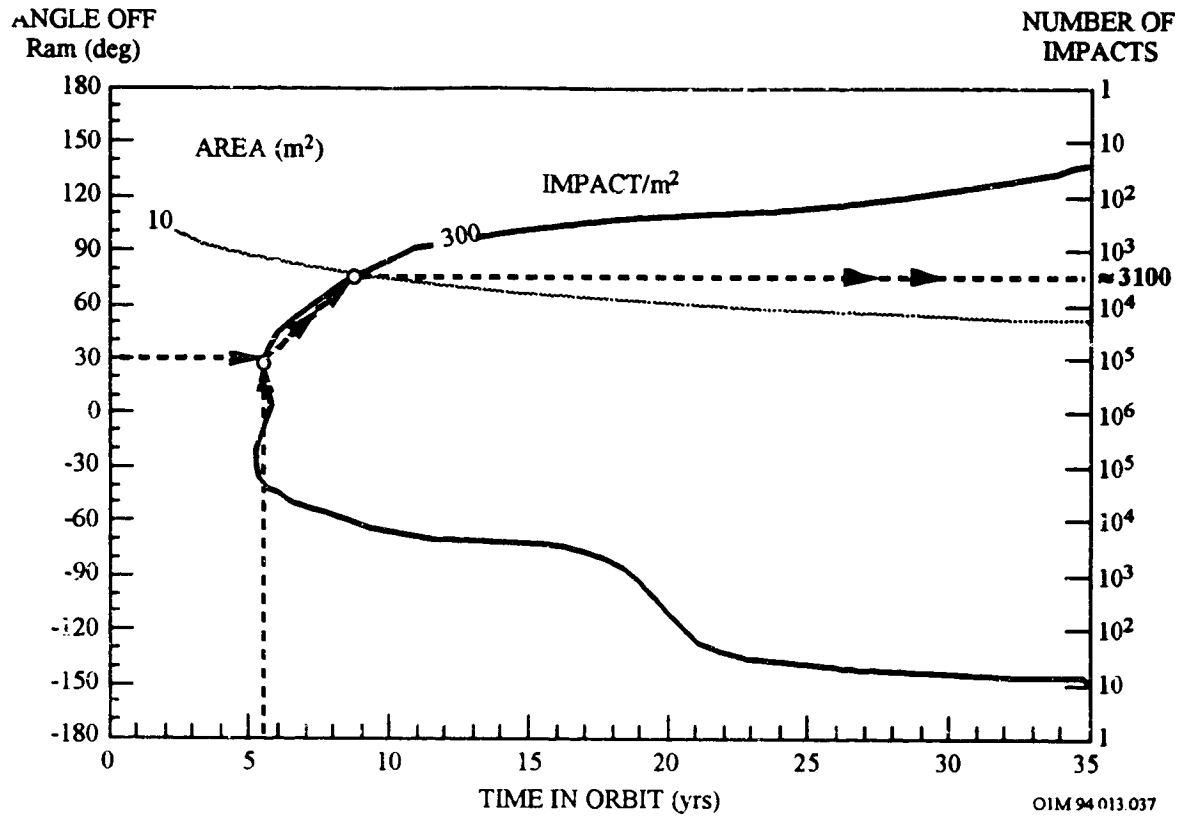

Figure 2- 16. LDEF Micrometeoroid/Debris Nomogram

Using the LDEF data from Figure 2-15, knowing panel areas and total time in orbit, one can construct a general purpose nomogram for varying areas of exposure and impact fluence levels as shown in Figure 2-17 (ref. Tennyson and Manuelpillai, 1993). Once again it must be stressed that these curves can only be used to estimate the total number of impacts at discrete angles defined by $\theta_n = n \times 30^\circ$, n = 0, 1, 2, ..., 12, and are strictly valid for an LDEF average altitude of ~463 km and inclination of 28.5°. Later it will be shown how to correct these numbers for different altitudes and orbital inclinations.

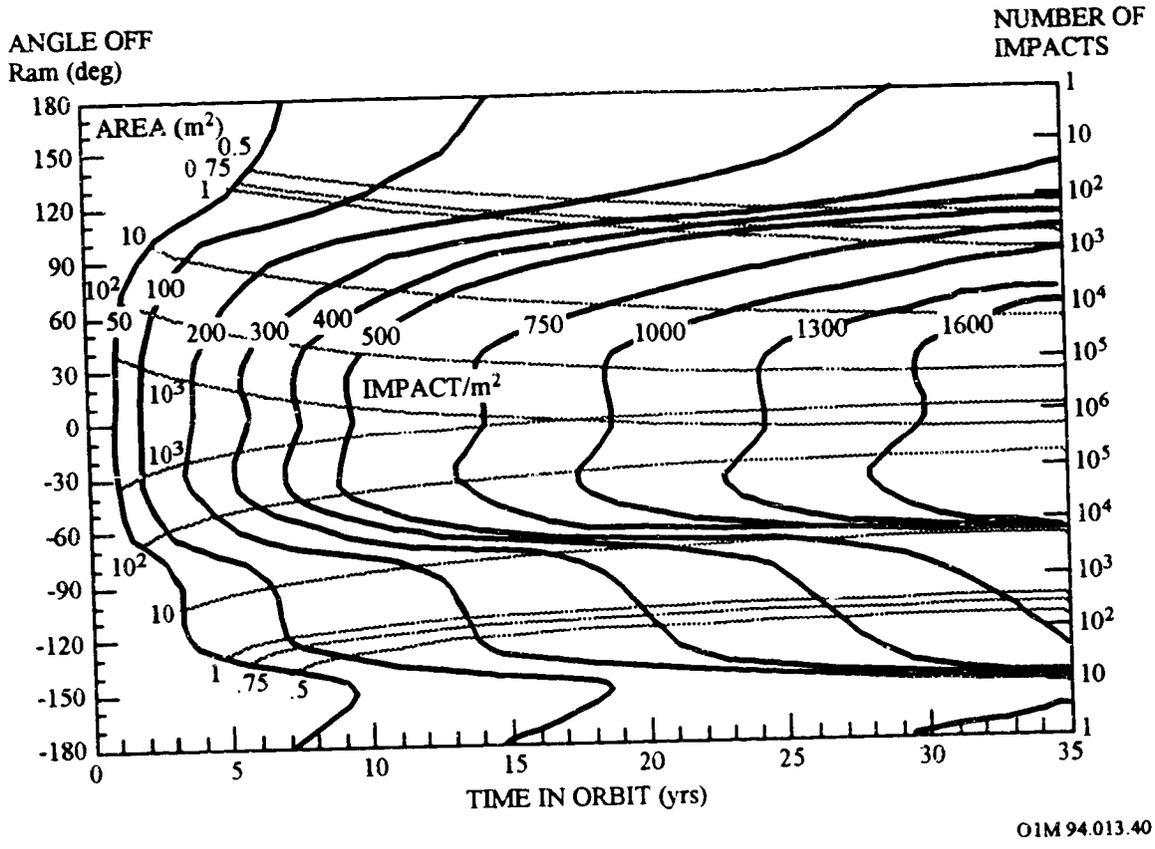

Figure 2- 17. Nomogram for Estimating Total Number of Micrometeoroid/Debris Impacts for Arbitrary Exposed Surface Areas as a Function of Angle Off Ram, and Time in Orbit.

As an example on how to use the nomogram and the 12-sided polygon model to calculate the number of impacts on a structure, consider the case of a circular cylinder, 0.5 m in diameter, 10 m long, after 30 years in low Earth orbit. The following results were obtained on the total number of hits on each panel (Nn) for n = 1, 2, ..., 12 together with the average impact separation distance (Dn), assuming a uniform distribution.

(i) Panel Area (A)

$c = 2R \sin \phi$

For the 12-sided polygon $\phi = 15^\circ$

therefore, $c = 0.13$ m and $A = 1.3$ m^2

(ii) Nn distribution from Figure 2-15 (30 years)

θ^0_n	N_n (est.)	D_n^* (cms)
0	2070	2.5
30	2070	2.5
60	1680	2.8
90	1100	3.4
120	450	5.4
150	325	6.3
180	290	6.7
-30	2260	2.4
-60	1680	2.8
-90	615	4.6
-120	550	4.9
-150	225	7.6

* = average impact feature separation distance on panel, assuming uniform distribution.

Although the particle flux LDEF was not strictly uniform in time, averaging over long periods of time (of the order of many months) is a reasonable approximation.

2.2.5 Micrometeoroid and Debris Impacts on the Solar Max Mission Satellite

Thermal blankets and louvers, exposed to space environment for 50 months in low-Earth orbit, were retrieved by Shuttle astronauts during Solar Max repair mission STS-41C. These louvers and blankets have been inspected by means of scanning electron microscopy in order to determine fluxes and origins of the impacting projectiles. The aluminum louvers were penetrated by 64 impacts, which made holes ranging from 180 micrometers to 820 micrometers in diameter. Most of these holes were made by micrometeorites as identified by chemical analysis of projectile residue associated with each hole. Seven holes were made by small particles of orbital debris.

Figure 2-18[78] shows the overall flux of holes and craters on the aluminum louvers over the size range from 10 micrometers to 1 millimeter. For the size region dominated by holes, the micrometeorite curve is clearly higher than the orbital debris curve. The transition region between holes and craters is clearly shown in the region around 200 micrometers. While not shown on this figure, chemical data indicate that a high proportion of the smaller craters are formed by debris projectiles rather than micrometeorites. Therefore, the flux curves must cross over, probably in the crater region between 50 and 100 micrometers. Hence, small projectiles (approximately those which make less than 50 micrometers crater diameters on aluminum) are dominated by orbital debris (mainly paint pigments with lessor aluminum oxide solid rocket exhaust), and the narrow region between projectiles making holes or craters in aluminum from about 0.1 mm (100 μm) to possibly 1 cm is dominated by natural meteoroids.

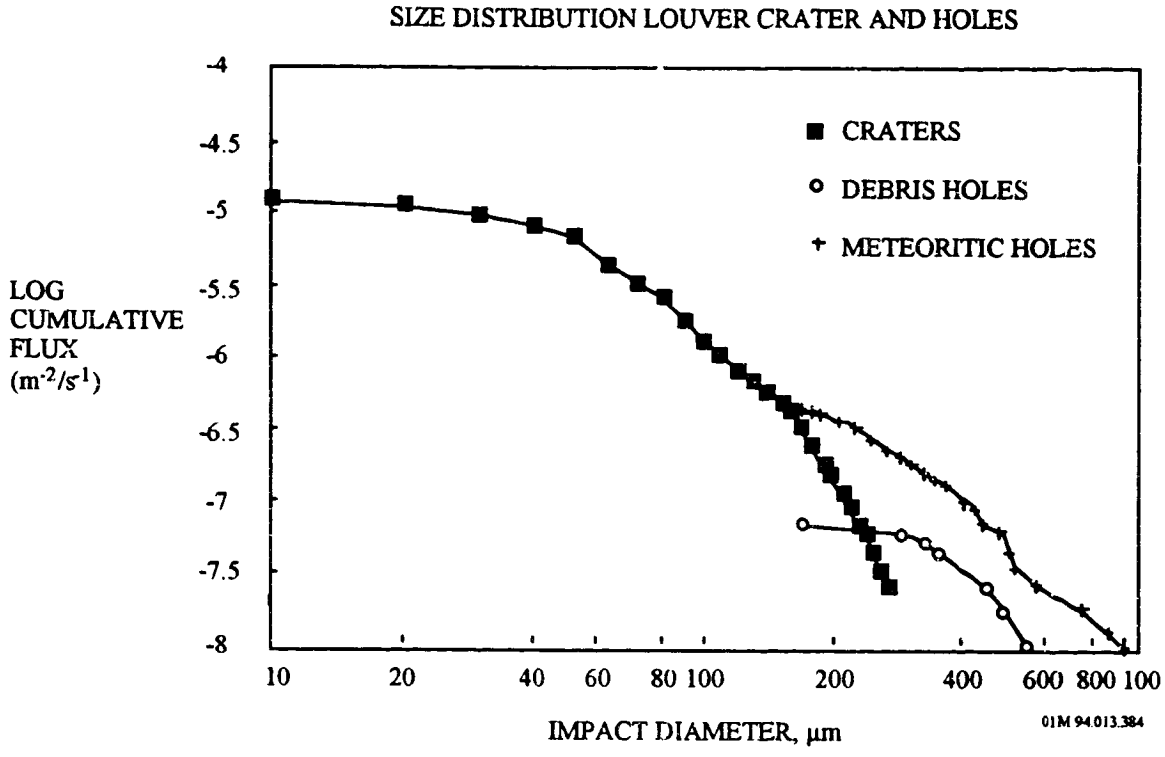

Figure 2- 18. Size Distribution of Craters and Holes on the Solar Max Mission Aluminum Louver

Orbital debris holes clearly are a minority of the population in the 200 micrometers to 1 millimeter region. However, that is somewhat misleading. Orbital debris particles have a mean velocity relative to a satellite in low-Earth orbit of about 10 km/sec, but micrometeorites have a mean velocity of about 20 km/sec relative to the satellite. Therefore, debris particles of equal mass and density as micrometeorites are likely to make smaller holes or even craters rather than holes. Consequently, the difference between the abundance of micrometeorite holes and orbital debris holes does not accurately reflect the difference in flux between these two populations; the fluxes are more nearly equal than is indicated by the hole data.

2.2.6 Deficiencies of the Microparticle Models

Many deficiencies should be applied to the existing models which define the microparticle space flux environment. The Kessler model (ref. 68) has several major downfalls.

1. It does not currently account for particles in elliptical orbits, which may total 20-30 times the amount currently trackable by USSPACECOM, and which pose a substantial threat to satellites at much higher altitudes than 1000 km. The present assumption that all debris orbits are purely circular automatically forbids any collision on either the Space-end or the Earth-end. In reality, many orbits must be slightly elliptical (due to random collisions and explosions). LDEF data demonstrates that such orbits exist since several impacts of debris have been unambiguously identified on the Trail surface (at least 15 percent of the total crater count).

   Efforts are underway to update the Kessler model for debris to allow for inclusion of noncircular debris orbits. The purpose is to allow assessment of the effects of elliptical debris orbits on any other satellite orbit, since the present Kessler analysis does not allow such facts to be determined. Results for a satellite in a different orbit, namely an altitude of 1600 km and inclination of 60° reveal larger impact velocities of up to 8.5 km/s compare to impact velocities of 5.0 km/s for LDEF. Thus, high-inclination, high-altitude orbits are most susceptible to debris.[79]

2. It cannot account for the highly dynamic nature of the debris environment which was detected by the IDE (Interplanetary Dust Experiment) on LDEF. An alternate model which will handle both the dynamics of the environment as well as the elliptical orbits is in development at the Jet Propulsion Laboratory by Dr. Neal Divine.[80]

With regard to the natural environment of micrometeoroids, the biggest downfall concerns the assumption that the particles are apparently geocentric. In reality, this will only be approximately true for long lived missions; particularly those that include a large number of satellite orbits together with a large number of precessions of the spacecraft orbital plane. Furthermore, it should be noted that in attempting to correlate the observations on LDEF versus the model predictions for the environment, the answers are sensitive to assumptions with regard to crater sizes versus particle sizes.

Examination of the LDEF data reveals an interesting bias in the impact flux:[81] the peak flux is not symmetrically distributed about the ram direction in the plane parallel to the Earth's surface (i.e., the two sides are not equal as expected). This effect cannot be readily explained for man-made debris since the interception of a circular spacecraft orbit with a circular debris orbit must necessarily involve two collisions per orbit (except for the rare condition of "kissing" orbits at apogee or perigee). These two states symmetry about the ram axis, thereby causing the ram direction to experience the greatest number of hits.

One probable explanation lies with the micrometeoroids. In reality each interception of a micrometeoroid orbit "tube" with the Earth always results in the flux being "one-sided" with respect to the Earth's orbit. Either the flux is "inward bound" towards the Sun, or it is "outward bound" from the Sun. Further, the flux appears to be monodirectional at the instant of interception. Thus, the true "Earth-shielding" is really simple ecliptic geometric shadowing for LEO (i.e., not the subtended solid angle of the Earth seen by the spacecraft). Thus, a spacecraft in LEO could be shielded from the particles for almost a complete half orbit if the plane of its orbit is close to that of the orbit of the micrometeoroids. The result can be a bias such that one half of the spacecraft experiences the impacts while the other half sees none. The half will include surfaces ranging from the ram through space round to the trail, with one side receiving more impacts than the corresponding other side, and the exact surfaces involved will depend on the local plane of the spacecraft orbit relative to that of the micrometeoroids. Note that the LDEF inclination of 28.5° together with the Earth's axial tilt of 23.5° meant that, with orbital precession, the plane of LDEF's orbit oscillated between 5° and 52° relative to the ecliptic. There were about 38 complete orbital precessions during LDEF's lifetime (precession rate of about 6.5° per day) and about 32,000 complete orbits.

One of the main disagreements within the models, which is still being defined today using the LDEF data and analysis, is the percentage of the environment which is cometary as compared to asteroidal. This affects both the velocity distribution and the expected impact phenomena (i.e., cratering depth or penetration diameter) for the meteoroids.[82] Another discrepancy within the models is their assumption of the meteoroid environment's isotropic distribution. The LDEF analysis was the first evidence that the total environment is non-isotropic and highly dynamic.

2.3.7 Micrometeoroid and Debris Impact Damage Behavior

2.3.7.1 Penetration and Crater Formation

When a hypervelocity particle impacts a surface it either creates a crater or perforates the surface (also referred to as the target). For targets that are thick relative to impactor sizes, craters will be formed that generally have lips resulting from plastic flow to molten spatter. However, for very thin targets, such as foils, which are much smaller than the impactor diameter, perforations occur resulting in a hole only slightly larger than the impactor diameter. Secondary or collateral damage can occur from the impactor remnants and the punched-out section. For high-velocity impacts, both the target foil and the impactor are vaporized. However, for lower velocities, the impactor and foil can remain molten or solid, and collateral damage is possible.

Large particles can penetrate through protective wall surfaces. With a relative impact velocity of 10 km/s, a piece of aluminum debris which is ~0.7 mm in diameter can penetrate through a typical 2.5 mm (1000 mil) thick aluminum satellite wall. During its 5.75 year exposure, LDEF saw 1 impact of this size per 7 m^2 of area exposed in the ram direction. In addition to this, LDEF experienced ~1 impact/m^2, on the ram-exposed surfaces, which could have penetrated a typical 1.5 mm (60 mil) thick aluminum electronics box wall.[83] While these impacts can be extremely damaging to internal components, electronics, batteries, motors and mechanism, they are relatively rare.

While particles greater than 1 mm can penetrate typical satellite skins and cause catastrophic damage, the more common smaller particles mostly cause a gradual degradation of a satellite surfaces, including thermal control paints, thermal blankets, coatings to provide protection against atomic oxygen (AO) or ultraviolet light (UV), solar cells and optics. Many satellite surfaces employ coatings which range from sub-micron (e.g., optics) to mils (e.g., thermal control, AO and UV protection, and solar cell covers). At impact speeds of 5 - 20 km/s particles can penetrate materials (either punching holes or causing craters with associated radial (star) cracks for brittle materials), and can cause damage regions which are considerably larger than the incoming particle. Consequently, the thermal paint coatings can be locally disrupted even by particles as small as 1 to 100 μm, and the areal number density (hits per square meter) can easily exceed 1000/m^2 for a multi-year mission. Hence, tens of thousands to even millions of these impacts may occur per square meter of typical surfaces which are exposed throughout the mission lifetime of the satellite.

2.2.7.2 Spallation

In addition to crater formation, surrounding areas can experience spallation, undercutting, cracking or delamination of an attached layer. These damage effects can lead to reduced structural strength, thermal and optical property degradation and erosion of underlying materials. Brittle materials, such as glasses or ceramics, often have chonchoidal surface spalls and cracks, and may have star cracks propagating radially from the crater. Layered targets, such as coated substrates, often exhibit delamination around or near the crater. Averaging over all impacts, the ratio of crater size to impactor size is about 5. For local spall regions, the spall radius to impactor radius ratio is about 20. Star cracks, when formed, can extend outward over 100 times the impactor diameter.

For coatings, the shock waves from the impact can cause coatings to spall. The amount of coating removed during impact is dependent upon the bond strength and type of coating. Impact crater spall data are very limited, even on LDEF samples after almost 6 years in orbit. Since, most flight samples were about 1 inch in diameter, a flux rate of 140 impact craters per year results in only 0.07 impacts per year on a one inch disc. This explains why very few impacts occurred on the experiment sample coatings. Of course large areas of LDEF such as silver Teflon, provided a large database for determining spall or effective damage area. To obtain better spall data for the paint coatings, including Z-93 (white ceramic binder type paint) and S13G/LO (white silicone binder type paint), a series of hypervelocity impacts were performed by Auburn University.[84]

Typical spall to crater ratios for thermal control coatings derived from flight and ground tests are summarized in Table 2-13. In general, spall-to-crater diameter ratio was greater for the LDEF exposed sample material. Ground simulation impact spall for a S13G/LO coating compared favorably to an impact on LDEF experiment M0003. In comparison, impacts on conversion coatings such as chromic acid anodize (CAA) did not produce any apparent spall. An example is the CAA sample from LDEF experiment S0069.

Table 2- 13. Spall Diameter to Crater Diameter Ratio

Coating Material	Ratio of Spall to Crater Diameter	
	LDEF Flight Samples	Ground Test Samples
S13G/LO	3	1.5 to 3.0
YB-71	4 to 8	5 to 8
Z-93	na	5.5 to 8
Ag/FEP	2 to 6	na
CAA	1	1

2.2.7.3 Penetration Analysis

To calculate the number of penetrating holes that a satellite surface can expect to experience during a mission a design or damage equation is used that gives the ballistic limit for given target thickness and impact parameters. The number of holes (punctures) is calculated by using the following equation which was derived for single metal plates (thin plate formula):[85]

$$t = 0.57m^{0.352}\rho^{0.167}\upsilon^{0.875} \qquad \text{(I)}$$

where
- t = threshold thickness for penetration (cm)
- m = mass of projectile (g)
- ρ = density of projectile (g/cm^3)
- υ = impact velocity of projectile (km/sec)

A puncture occurs whenever the threshold thickness for an impacting particle with given mass, density and velocity exceeds the shielding thickness of the surface under consideration.

The ability of micrometeoroids to puncture single sheets of hard aluminum or stainless steel is indicated in Figure 2-19.[86] The thicknesses are large ($\geq$ 1 cm) for meteoroids of mass $\geq 10^{-2}$ g. However, these total thicknesses can be reduced by up to a factor of 5 by using the bumper concept. A single sheet of thickness $\geq t/30$ located a distance $\geq 5t$ in front of a sheet of thickness $\geq t/6$ will stop the same particle that a single sheet of thickness t can. This concept requires that the incident particle have a velocity of at least 3 km/sec, preferably $\geq$ 5 km/sec. (Meteoroids have an average velocity of ~20 km/sec near the Earth.)

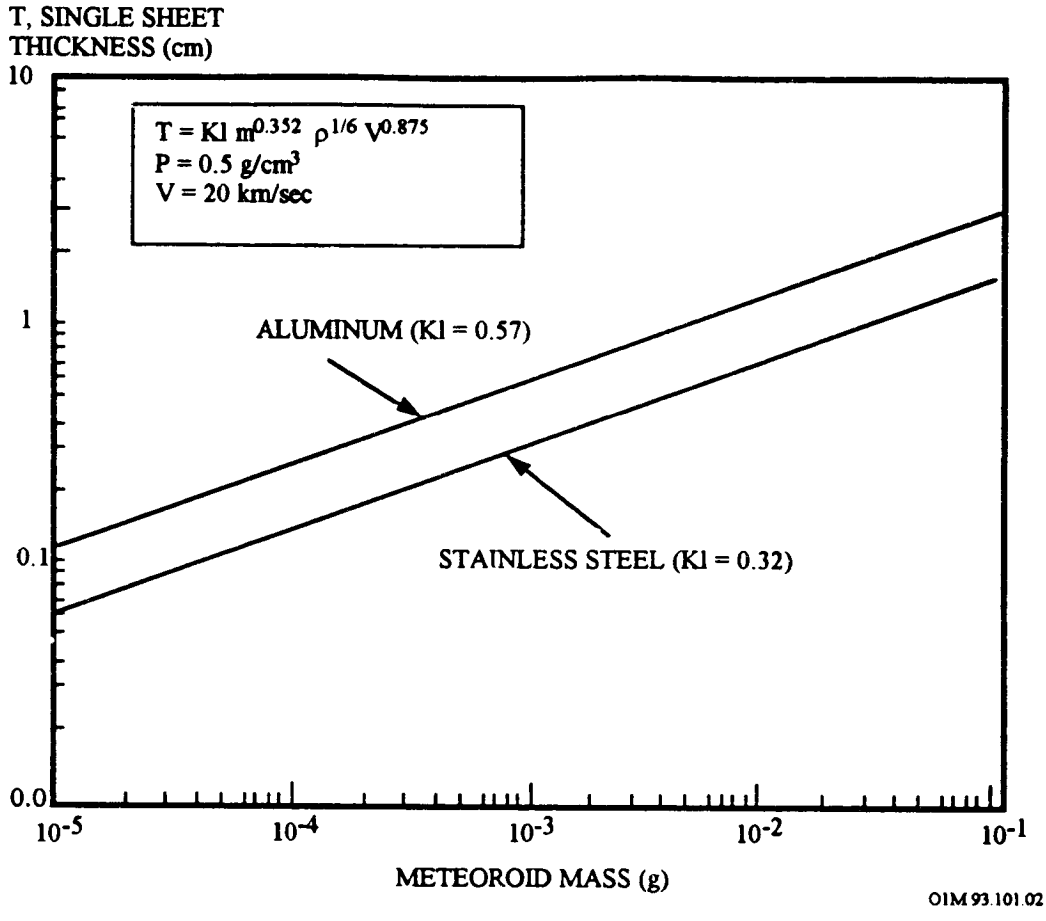

Figure 2- 19. Single Sheet Thicknesses of Al and SS Necessary to Stop Meteoroids

The probability of sustaining a puncture by a micrometeoroid increases linearly with the product of area and time. Figure 2-20 shows the probability of a single sheet of hard aluminum being punctured in 10 years as functions of total project area and aluminum thickness (ref. Haffner et al., 1989). To a first approximation, these curves are independent of altitude. Of course, the puncture probabilities remain unchanged if the single sheet of aluminum (thickness t) is replaced by two sheets of t/30 and t/6 (the bumper concept) provided the separation distance is at least 5t.

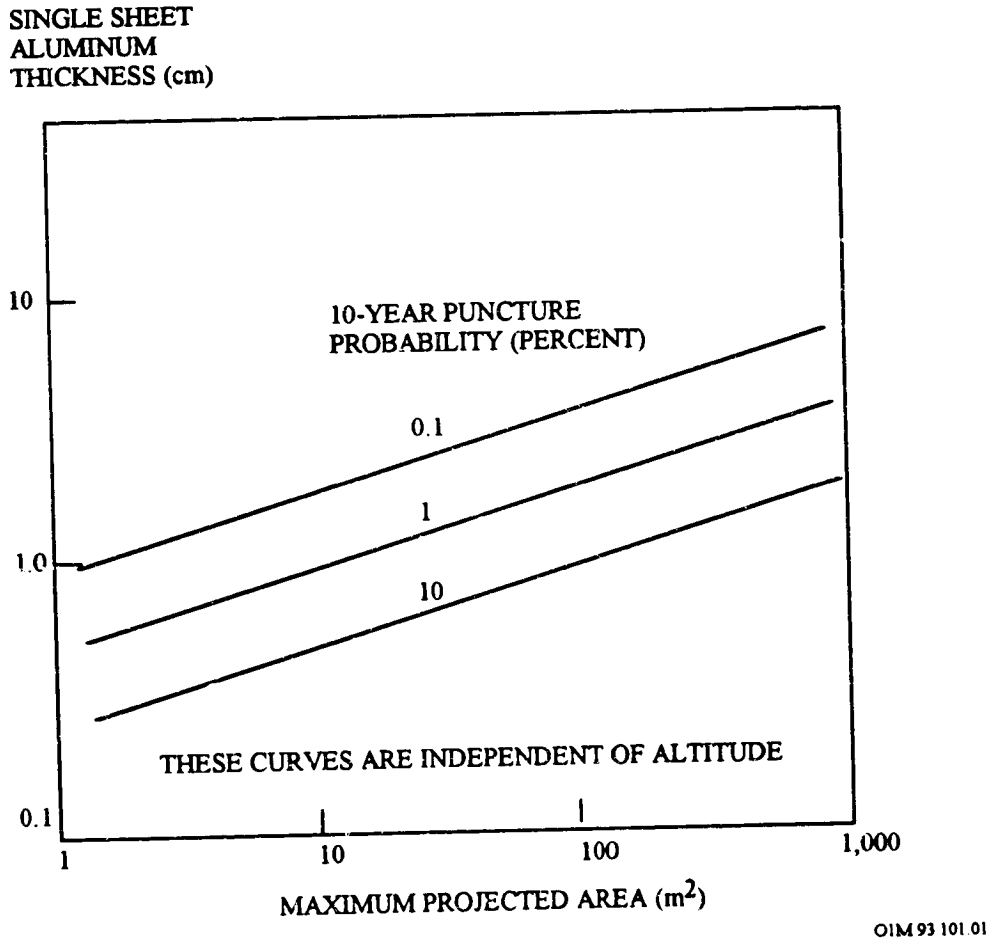

Figure 2- 20. Aluminum Thickness to Limit Meteoroid Punctures

The situation for debris objects is similar to that for micrometeoroids except for the altitude dependence. The single-sheet thicknesses necessary to stop debris objects are comparable to those to stop micrometeoroids of the same mass as shown in Figure 2-21 (ref. Haffner et al., 1989). However, the meteoroid threat is present at all altitudes; the debris object threat is primarily located at altitudes < 2000 km (with a small secondary threat near GEO).

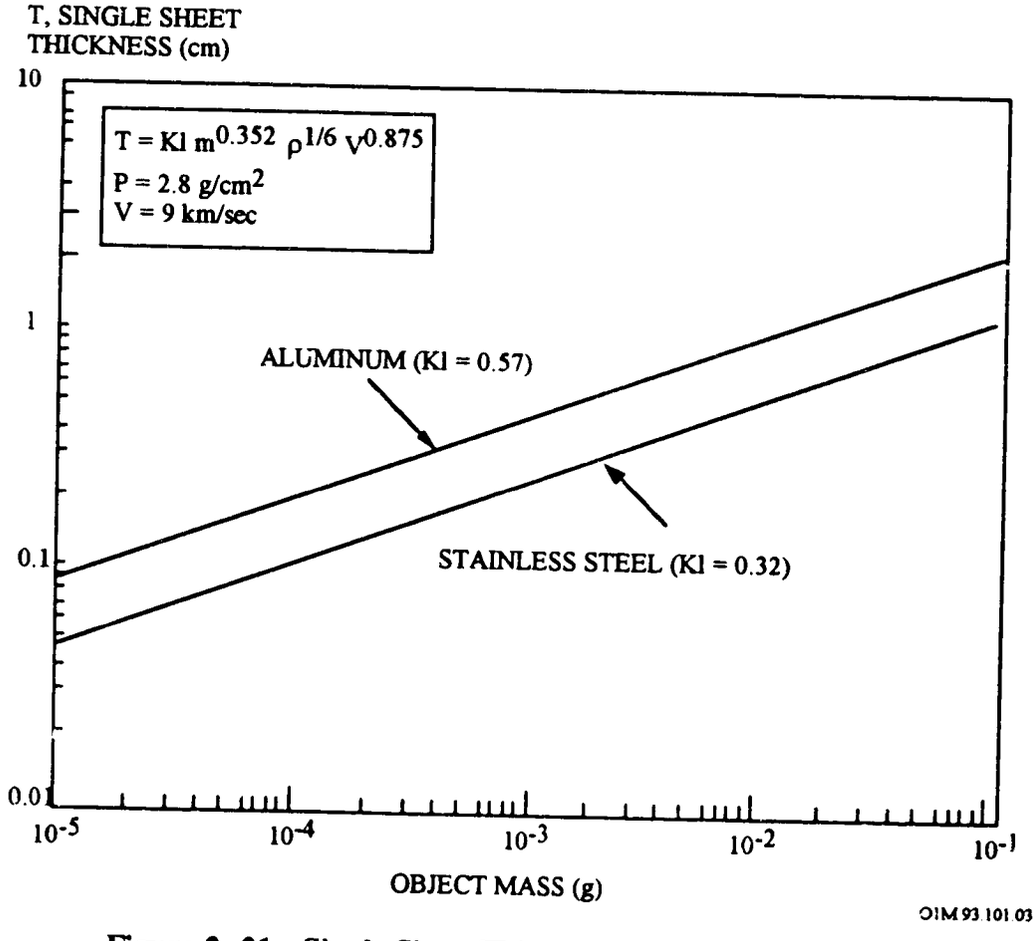

Figure 2- 21. Single Sheet Thicknesses to Stop Debris Objects

Use of equation (I) for thermal blankets implies several approximations and uncertainties. This equation was derived for normal impact directions. Impacts from both meteoroids and space debris particles, however, will generally not occur under normal direction. In that case the velocity entering into the equation can either be taken as the total impact velocity, assuming that over a wide range of angles the penetration capability is independent of the impact angle, or the normal component of the velocity can be used. The given equation is strictly valid only for aluminum. Different procedures have been suggested to modify the equation or to derive an equivalent thickness for materials other than metals and for compounds.[87] The McDonnell equation for perforation predictions, at least for symmetric Al/Al conditions is:

$$T = 1.023 d_p^{1.056} (\rho_p/\rho_t)^{0.476} (\sigma_{Al}/\sigma_t)^{0.134} \upsilon^{0.664} \qquad \text{(II)}$$

where

T is the wall thickness (cm)
d_p is the particle diameter (cm)
densities (ρ) refer to particle or target (g/cm^3)
σ values are the yield strengths of Al or the target (MPa), and
υ is the normal impact speed (km/sec)

2.3.8 Micrometeoroid and Debris Effects on Materials

Impact damage can degrade the performance of exposed spacecraft materials and, in some cases, destroy a satellite's ability to perform or complete its mission. Large particles can penetrate through protective wall surfaces. For example, with a relative impact velocity of 10 km/s, a piece of aluminum debris which is ~0.7 mm in diameter can penetrate through a typical 2.5 mm (100 mil) thick aluminum satellite wall. During its 5.75 year exposure, LDEF saw 1 impact of this size per 7 m^2 of area exposed in the ram direction. In addition to this, LDEF experienced ~1 impact/m^2 on the ram-exposed surfaces which could have penetrated a typical 1.5 mm (60 mil) thick aluminum electronics box wall (ref. 83). While these impacts are relatively rare, the frequency of impacts is expected to increase due to the continuing growth in the debris populations.

LDEF-flown materials provided examples of typical impact cratering and penetration in the various structural materials. Since LDEF was designed to withstand multiple launches, along with multiple retrieval and landing loads, its structure was made from heavy (for satellites) aluminum I-beams. A few experiment structures (e.g., electronics boxes) which were carried by LDEF had aluminum wall thicknesses (i.e., 2-2.5 mm (80-100 mils)), while other experiments carried samples of carbon/epoxy composites. In general, the overall average effects of the micrometeoroid/debris impacts on most of the spacecraft surfaces were not significant even for extended periods. This is true only for small, non-penetrating, high probability impacts causing craters in the 0.1 to 3 mm range. However, even at this minimal average impact, up to 140 impacts/yr/m^2 can be expected and must be planned for and considered in spacecraft designs requiring long periods of exposure in the low Earth orbital environment.

For very stable materials where a few percent change in overall properties is critical, then the impact and spalling can be important. For example, if the overall average emittance of a radiator must be stable for 30 years (change < 2%), then the effects of the meteoroid/space debris must be included in life prediction. Zwiener and Finckenor discusses the potential effects of micrometeoroid/space debris effects on the radiative properties of thermal control materials (ref. 75).

Localized damage, if it occurs in the wrong place can cause severe degradation. Electrical properties of solar cells appear to be minimally affected by micrometeoroid/space debris impacts as reported by Young and Trumble.[88] Cracking of the cover glass and even penetrations only had a local effect. Although the overall effect of impacts on solar cells is small, impacts that severe connections can cause lost of those cells. Hence, a high level of damage by impacts would cause significant loss in solar cell array outputs.

Finally, the type of impacts experienced on the LDEF will normally not cause penetration of optical surfaces, such as lenses and mirrors, but they can create scatter sites for light as reported by Kemp et al. (Ref. 79).

Below are examples of the types of damage various surfaces caused by these impacts.

2.3.8.1 Metals

In general, impacts into metals form craters which have diameters averaging about 5 times the impact diameter. Figure 2-22 provides a schematic diagram of damage morphology and diameter measurements for multi-cratering impacts into metals.[89] If the crater lips are included, the damage region across the highest point is ~7 times the impact diameter, while the total region out to the extremes of the crater lips can be ~10 times the impact diameter. The exact size of the crater is a function of impact diameter, impact speed, and relative ratio of impact density to target density. These craters are of concern because they can prevent impacted mechanisms from operating and can cause failure in highly stressed materials.

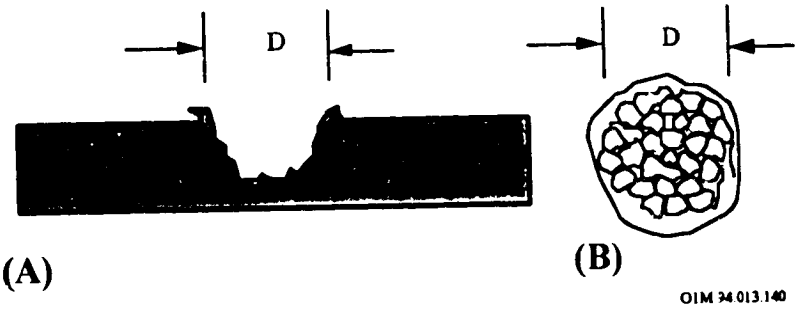

Figure 2- 22. Schematic of Impact Damage into Metals.

Large particles can penetrate through protective wall surfaces. With a relative impact velocity of 10 km/s, a piece of aluminum debris which is ~0.7 mm in diameter can penetrate through a typical 2.5 mm (100 mil) thick aluminum satellite wall. During its 5.75 year exposure, LDEF saw 1 impact of this size per 7 m^2 of area exposed in the ram direction. In addition to this, LDEF experienced ~1 impact/m^2, on the ram-exposed surfaces, which could have penetrated a typical 1.5 mm (60 mil) thick aluminum electronics box wall (ref. 83). While these impacts can be extremely damaging to internal components, electronics, batteries, motors and mechanisms, they are relatively rare.

2.3.8.2 Composites

While not large in number, LDEF had composite structural material samples on board and was able to show some of the effects of impacts and penetrations through these materials.[90,91] A schematic diagram of the damage morphology and diameter measurements for impacts of composites is shown in Figure 2-23 (ref. 89). The penetrations typically have jagged edges and contain broken fibers. For the more brittle composite structural materials, the damage is rarely a simple crater. Rather, significant in-depth damage can occur and may be anisotropic, following the structure of fibers. For complete penetrations, the rear surface damage area is frequently larger than the entry hole area. This impact damage is of concern because the breaking of the fibers, cracking of the matrix, and removal of part of the matrix via the spallation process could cause failure in highly stressed components. This could also lead to further breakdown of the composite material during subsequent exposure to other space environments such as atomic oxygen (surface erosion) or ultraviolet light (embrittlement).

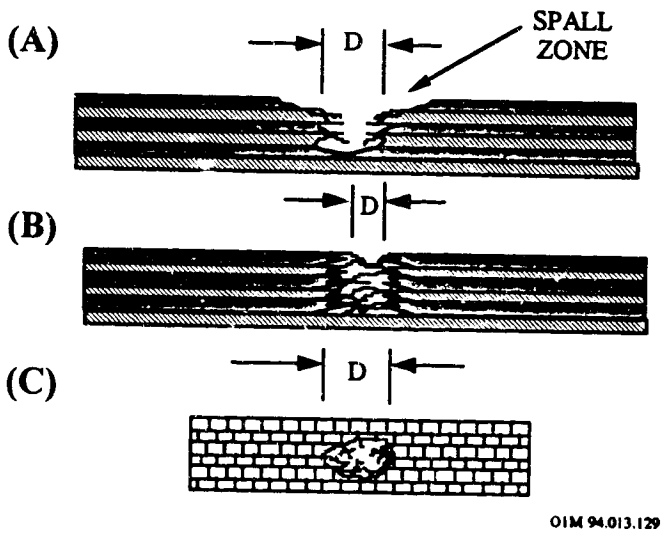

(A) Cross-sectional view of feature with surrounding spall zone
(B) Feature with a larger damage zone, beneath the composite surface, than is visually seen at the original material surface
(C) Top view of a feature in a composite surface.

Figure 2- 23. Schematic Diagram of Damage Morphology and Diameter Measurements For Impacts of Composites

Aramid fiber composite failed in a "brush or broom" mode surrounding the impact damage region (ref. 91).

Several small impacts were also found on fiberglass/epoxy samples covered with aluminized thermal control tape. No debonding of the tape was observed. Peel tests of the thermal control tape were not perceptibly affected by the impacts (ref. 75).

In general, no catastrophic failure was observed from impacts, though impact compromise of composite surfaces can allow AO to erode the substrate, creating delaminations and interply cracking.

2.3.8.3 Thermal Control Systems

2.3.8.3.1 Thermal Control Blankets

Figure 2-24 is a schematic of the damage morphology and diameter measurements for impacts into thermal control blankets and laminated materials (ref. 89). This represents the typical damage for silver Teflon blankets (Sheldahl G411500) with a back surface coating of Chemglaze Z306 black paint (e.g., LDEF A0178 thermal control blanket). Since these materials are thin laminated layers, the impacts cause delamination of layers to many times the diameter of the crater or penetration.[92]

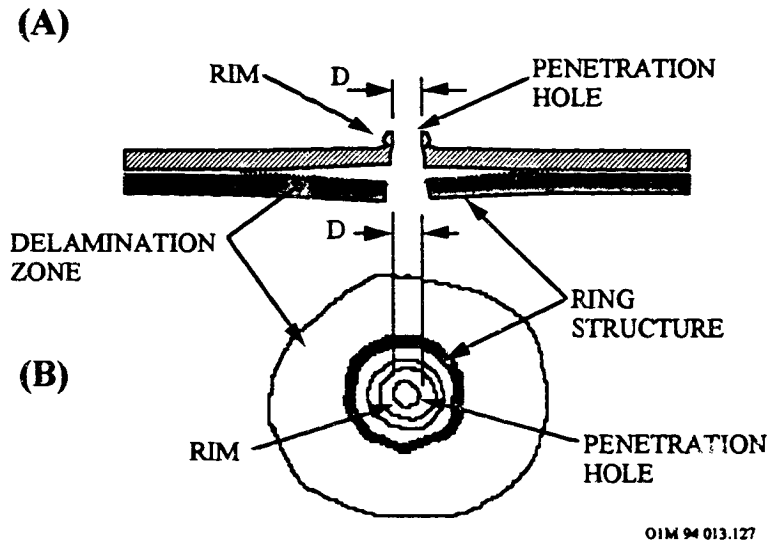

(A) Cross-sectional view depicting the delamination of the Teflon layer from the underlying silver/Inconel/paint surface

(B) Top view showing the extent of the delamination zone and the presence of the "rings" generally found in association with these features.

Figure 2- 24. Schematic Diagram of Damage Morphology and Diameter Measurements for Impacts into Thermal Control Blankets and Laminated Materials

Thermal control materials on LDEF demonstrated the greatest synergisms with other environments (i.e., AO and UV). These synergisms further expanded the damage areas caused by impacts. For example, impacts on the blankets lead to many penetration through the Teflon, allowing access of AO to the silver layer. Instead of being reflective (as on pre-flight) the entire blanket is very milky in color due to exposures to atomic oxygen. This is caused by the high amount of light scattering from the newly textured AO eroded surface of the Teflon. The ring structure growing around the smaller impact penetration is due to AO degradation (i.e., discoloration) of the silver, forming a silver oxide area.

Examination of the damage in multi-layer insulation (MLI) thermal control blankets show the extent of damage caused by the synergism of the space environment. The top surface of the metalized Mylar MLI on the leading edge of LDEF was completely eroded, exposing the interior surfaces to UV light, AO and thermal cycling. Due to exposure to these environments, the aluminum layers tended to break up into small pieces creating a shower of fine particles which went into orbit around the Earth in conjunction with LDEF. This created a type of atmosphere of fine particulates which completely surrounded LDEF and became an extreme contamination source for the entire satellite.

An even worse situation was created by the degradation of the aluminized Kapton which covered LDEF Experiment A0054. The aluminized Kapton that flew on the trailing edge at LDEF Bay B04 was essentially unchanged from pre-flight. Conversely, the Kapton on the leading edge at LDEF Bay D10 was completely eroded, leaving behind an approximately 1000 Å thick aluminum layer. This layer continued to generate particles that flaked off even after the retrieval of LDEF and became the primary source of large particle contamination for the entire satellite, even throughout LDEF's deintegration.

2.3.8.3.2 Thermal Control Paints

Impacts into thermal control materials often display a different type of damage, typically with a greater damage area, than impacts into metals. Figure 2-25 shows a schematic diagram of damage morphology and diameter measurements for impacts into thermal control paints (ref. 89). LDEF's thermal control paints showed several very interesting types of impact-related phenomena and provided the first examples of the ring phenomena as shown in Figure 2-25. The rings on these painted surfaces were typically circular and indicated a shock wave phenomena, which can cause the coatings to spall. Typical spall to crater ratios for thermal control coatings derived from flight and ground tests were summarized in Table 2-13 (see page 2-41). It is now theorized that the rings are caused by a Rayleigh wave propagation through the surface. If so, the sizes of the rings are dependent on both the thickness of the paint and the amount of erosion which had occurred in the paint prior to the time of the impact event.

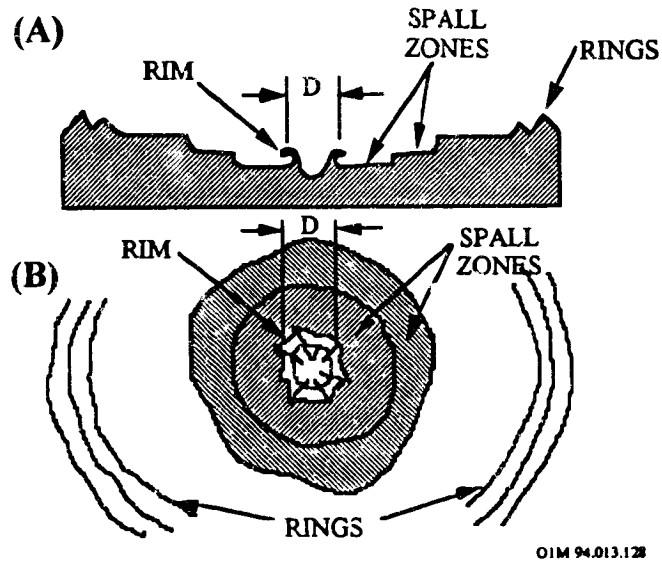

(A) Cross-sectional view
(B) Top view

Figure 2- 25. Schematic Diagram of Damage Morphology and Diameter Measurements for Impact into Thermal Control Paints.

As in the thermal control blankets, the total damage areas in the painted surfaces were always much greater than the damage areas due to simple cratering. This is of concern since the affected areas, which on LDEF approached 3% of the total painted surface areas, may have significant changes in absorptivity and emissivity, thus changing the radiative properties of the paints (see next section). In addition, the spallation and delamination areas reduce the thermal conduction effectiveness of the materials. Since these types of impact phenomena are expected in any coated materials, especially those susceptible to AO and UV, understanding these effects is particularly important for heat pipe and radiator systems.

2.3.8.3.3 Effect of Hypervelocity Impacts on Thermal Radiative Properties

This section by Zwiener and Finckneor (ref. 75) provides information to the spacecraft designers for evaluating the overall quantitative effect of meteoroid/space debris impacts on the thermal radiative properties of materials. The analysis is based on calculating the overall surface damage effects from impacts to large surface areas from the impact flux (the flux in terms of crater diameters versus the angle from the velocity vector).

A relationship between total number of impacts per crater diameter is required in order to determine the total damage area based on the impact flux. This relationship was determined by summing all of the impacts on LDEF for each crater diameter. Table 2-14 lists impacts summed on each row for diameters between 0.1 mm to 2.5 mm. This count includes impacts on experiments, trays, clamps, structures, and thermal panels. The total count for each diameter was summed for all rows and plotted in Figure 2-26. This size distribution can be approximated by the following relationship which is plotted in Figure 2-26.

$$\text{Ln}(d) = C1 + (C2 * N)$$

where:

N	=	number of impacts craters
Ln	=	natural logarithm
d	=	diameter of crater in mm.
C1	=	+8.693612
C2	=	-3.532209

This approximation permits an estimation of the actual number of impacts below 0.5 mm where incomplete counting occurred. A summation was made using this relation for all diameters between 0.1 mm and 3.0 mm. The total sum was used to normalize the size distribution data into a fractional distribution.

Table 2- 14. Impact Crater Size Distribution

Total Number of Impact Craters Per Row and Per Diameter

Diam (mm) Row #	≤.1	0.5	0.6	0.7	0.8	0.9	1.0	1.1	1.2	1.3	1.4	1.5	1.6	.17	1.8	1.9	2.0	2.1	2.2	2.3	2.4	≥2.5
1	10	32	34	25	25	13	15	5	0	1	2	0	0	0	0	0	0	1	0	1	0	0
2	25	25	7	10	12		3	2	1	1	1	0	0	0	1	0	0	0	0	0	0	0
3	22	9	13	9	10	4	3	2	2	1	0	2	1	0	2	1	1	0	0	0	0	1
4	29	20	11	5	7	2	2	6	2	0	0	1	0	0	0	0	0	0	0	0	0	0
5	29	29	21	13	15	5	4	4	2	0	1	3	1	1	0	0	0	0	0	0	0	0
6	68	45	43	33	19	16	15	5	2	4	2	3	2	0	0	0	0	0	0	0	0	0
7	65	106	72	61	32	28	15	11	3	8	2	4	2	1	0	2	0	0	2	1	0	1
8	85	132	97	75	42	29	22	9	13	13	5	6	1	1	0	1	0	0	0	1	0	4
9	100	125	95	75	51	24	22	27	15	9	10	8	6	1	5	0	0	1	0	1	0	7
10	124	149	107	79	51	24	30	20	15	11	4	7	5	1	5	2	7	4	1	2	0	6
11	66	106	83	109	55	22	22	9	12	7	3	3	6	2	2	0	0	1	0	1	1	5
12	65	51	46	54	33	11	18	4	9	1	2	4	2	2	1	0	0	0	2	0	0	3
Totals	688	829	629	548	352	178	171	104	76	56	32	41	26	9	16	6	8	6	5	7	1	27

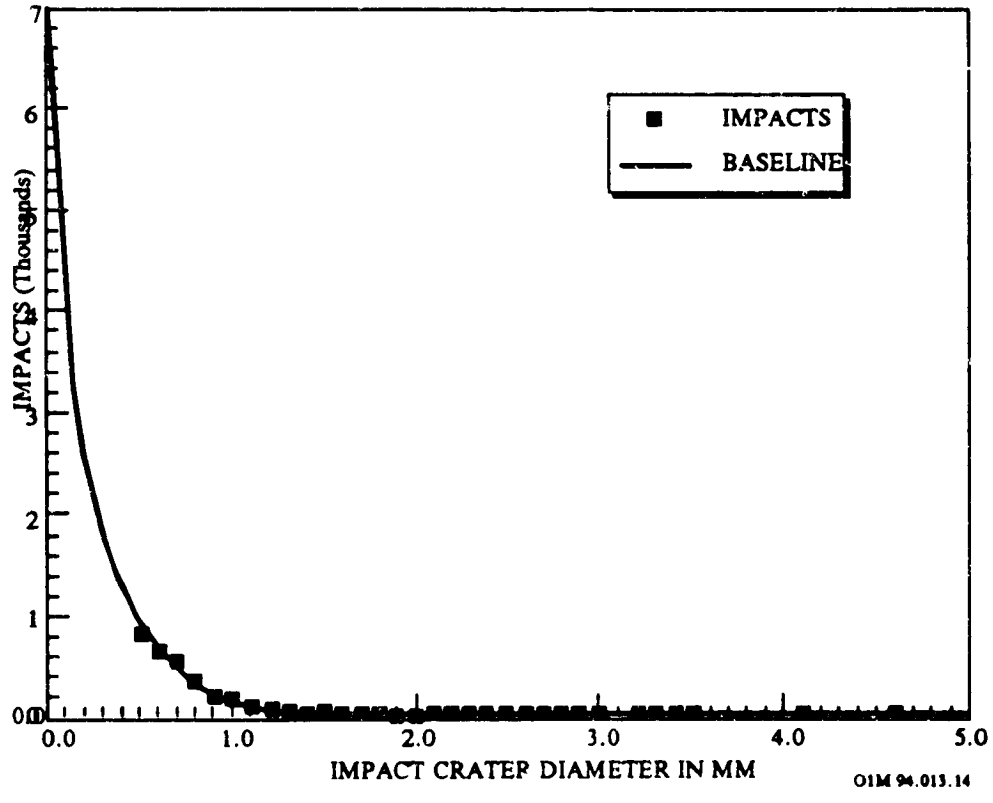

Figure 2- 26. Size Dependence of Impact Craters

Other information required in order to calculate the overall optical effects of multiple impact craters is the ratio of crater diameter to coating spall diameter. Dependent upon the bond strength and type of coating different amounts of coating will be removed during impact. The shock waves from the impact can cause coatings to spall. Typical spall to crater ratios for thermal control coatings derived from flight and ground tests were summarized in Table 2-13 (see page 2-40).

Since the flux levels as a function of Beta angle, crater size distribution, and spall/crater ratio are known, the change in effective (average) thermal radiative properties can be calculated with respect to time using the following equation:

$$A_s\,(\text{Beta}) = A_o - \left[D_{a,e} * F_a * T_{yr}\right]$$

where:	A_s (Beta, time)	=	effective or average value of solar absorptance or emittance at each Beta angle
	A_o	=	solar absorptance or emittance of original coating
	$D_{a,e}$	=	difference between coating and substrate absorptance or emittance
	F_a	=	fraction of damaged surface area per year
	T_{yr}	=	number of years exposed

The fraction of damaged surface area (F_a) is derived by summing for each angle "Beta" the product of flux, size distribution, and spall area, for crater diameters from 0.1 mm to 3.0 mm. For convenience a selection of values for "F_a" are provided in Table 2-15. These values for F_a can be used with the above equation to predict long term optical property changes from impact craters. The values provided in Table 2-15 are actually the total area in square millimeters of substrate exposed from the impact per square meter (see Figure 2-27), and subsequently include a multiplication factor of 10^{-6}, as indicated in Table 2-15. Values in Table 2-15 are listed for spall-to-crater diameter ratios ranging from 1 to 15, and for selected Beta angles in the range from 0 through 180 degrees.

Changes to the thermal radiative properties of several thermal control paint coatings (e.g., Z93, S13G/LO), chromic acid anodized aluminum, and silver Teflon blankets due to meteoroid/debris impacts for up to 30 years in orbit are provided in Chapter 10. Results indicate that the surface damage from micrometeoroid/space debris does not significantly effect the overall surface optical thermal physical properties. Of course, the damage around impact craters radically alter the local optical properties.

Table 2- 15. Fraction of Damaged Surface per Year (F_a).

Values for $F_a \times 10^{-6}$ as a function of Beta Angle								
D_s/D_c	0°	10°	30°	60°	90°	120°	150°	180°
1	21.07	20.93	19.81	16.37	11.66	6.96	3.52	2.26
2	84.28	83.71	79.24	65.47	46.65	27.84	14.07	9.03
3	189.63	188.34	178.29	147.30	104.97	62.65	31.66	20.32
4	337.12	334.83	316.96	261.87	186.62	111.37	56.28	36.12
5	526.75	523.18	495.24	409.17	291.59	174.01	87.94	56.44
6	758.52	753.37	713.15	589.21	419.89	250.58	126.64	81.27
7	1032.43	1025.43	970.68	801.97	571.52	341.07	172.37	110.62
8	1348.47	1339.33	1267.82	1047.48	746.48	445.48	225.13	144.48
9	1706.66	1695.09	1604.59	1325.71	944.76	563.81	284.93	182.86
10	2106.99	2092.70	1980.97	1636.68	1166.37	696.06	351.77	225.75
11	2549.46	2532.17	2396.98	1980.39	1411.31	842.23	425.64	273.16
12	3034.07	3013.49	2852.60	2356.82	1679.57	1002.33	506.55	325.08
13	3560.82	3536.66	3347.84	2765.99	1971.17	1176.34	594.49	381.52
14	4129.70	4101.69	3882.71	3207.89	2286.09	1364.34	689.47	442.47
15	4740.73	4708.58	4457.19	3682.53	2624.34	1566.13	791.48	507.74

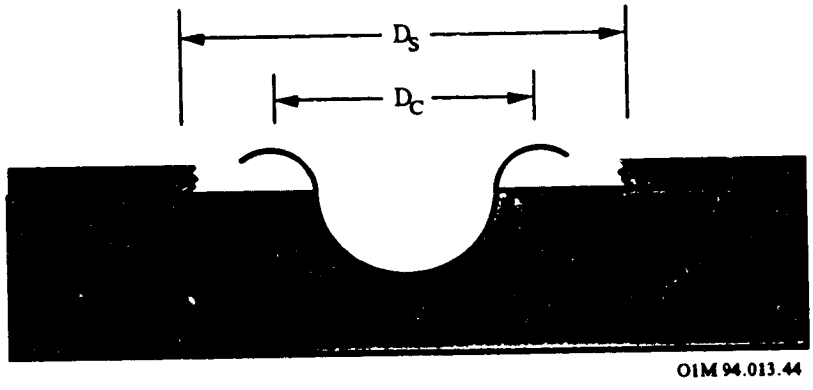

Figure 2- 27. Definition of Spall Diameter and Crater Diameter

2.3.9 Micrometeoroid and Debris Effects on Optical Components

2.3.9.1 Damage Morphology

Optics components are typically brittle materials. Under impact, brittle materials show a different type of damage than metals and ductile materials. Figure 2-28 shows a schematic of the damage morphology of these materials (ref. 89). Brittle materials often show a central crater, usually filled with finely crushed material, and exhibit little or no crater lips. These craters are usually surrounded by conchoidal fracture areas, which act as spallation zones. Finally, there are typically 2 to 4 (occasionally more) cracks which run outward from the impact site for 10 or more crater diameters.

Impacts into windows (optical substrates) and reflective metallic mirrors have been studied for many years. Basically, it has been found that the transmissivity and reflectivity are unaffected by the impacts. However, scatter dramatically increases. Unfortunately, impact-caused scatter has not been studied significantly since most imaging optics in the past have looked directly toward the Earth and thus had little threat of being impacted. In addition, impacts into reflective optics with dielectric coatings have not been studied. The reflectivity of these latter optics may be affected since the coatings which provide the reflectivity are removed in the vicinity of the impacts. Additionally, the amount of coating material removed by an impact may be much larger than in ductile materials due to delamination of the coatings from the substrate and from each other.

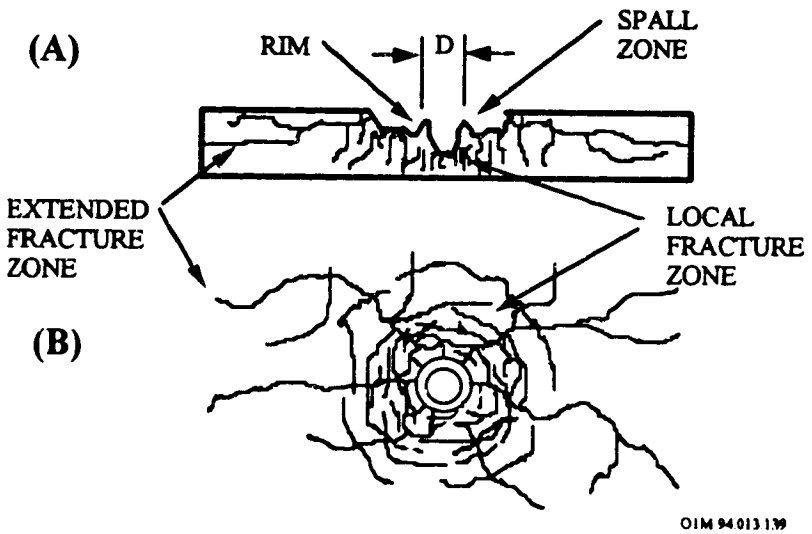

Figure 2- 28. Schematic Diagram of Damage Morphology and Diameter Measurements for Impacts into Optics and Power System Components

2.3.9.2 Reflectivity/Transmission Effects

The anticipated effects of impact damage on optics include:

- a reduction in reflectivity (for mirrors);
- a reduction in transmission (for lenses and/or windows); and
- an increase in optical scatter (for both mirrors and lenses/windows).

Experiments by Mirtich,[93,94] whereby metallic mirrors were impacted by small particles, demonstrated that reflectivity gradually decreased as the total surface impact energy density increased (i.e., ergs/cm^2 of the particle kinetic energy). Since the crater surfaces remain reflective, the decrease in reflectivity is probably related to the surface roughening which gradually produces the equivalent effect of producing a "light-trapping" baffle-like surface. However, calculations of the corresponding energy flux expected for the micrometeoroids and space debris for even 10 year missions in LEO suggest this effect to be small. Reports by Mirtich of data from space flown mirrors with missions up to 20 years (e.g., the SERT and OSO satellites) indicate very small reductions in reflectivity (less than 1 percent) in agreement with the predictions. (Note that these mirrors are non-recovered: the data are via telemetry and consist of emission/absorption in-situ measurements). Thus, changes in reflectivity (or transmission) are expected to be small. The major problem is increases in optical scatter.

2.3.9.3 Optical BRDF Scatter Effects

Optical scatter produces three effects:

1. A reduction in light throughput;
2. A reduction in resolution; and
3. A reduction in signal to noise due to background "light-up."

This can occur either due to light from bright sources (other than the required target) within the field of view, or can occur for bright sources nominally outside of the field of view if the light is redirected into the optical train path. Of these three effects, item 3 is usually the greatest concern.

Several analytical procedures are available for calculating the optical scatter due to impact damage. The most accurate procedure for calculating optical scatter is to use the Mie scatter theory (ref. 79). Mie scatter logic has been incorporated recently into the SPENV code to

automatically integrate over the impactor/crater size distributions. The detailed analysis makes use of studies done by Lowell D. Lamb at the University of Arizona, whose Ph.D. thesis concerns IR scattering for small particles on substrates.[95] The Mie calculations incorporate the optical constants for the material and, thus, can handle both highly reflective and poorly reflective conditions. The results of the calculations give values of BRDF versus off-specular angle. The BRDF data can be integrated over the 2π solid angle to give the corresponding total integrated scatter (TIS).

Variation in BRDF as a function the angle from ram has been computed for the specific case of LDEF (ref. 79). The data, shown in Figure 2-29, are given for the micrometeoroids and debris independently and are plotted as a function of the angular position from ram (0°) in the plane parallel to the Earth's surface (i.e., ram, sides, and trail). On the left vertical axis are also plotted the scatter for the space and Earth facing surfaces. In all cases each surface was assumed to have a full 2π view for impacts (i.e., no local telescope tube shielding).

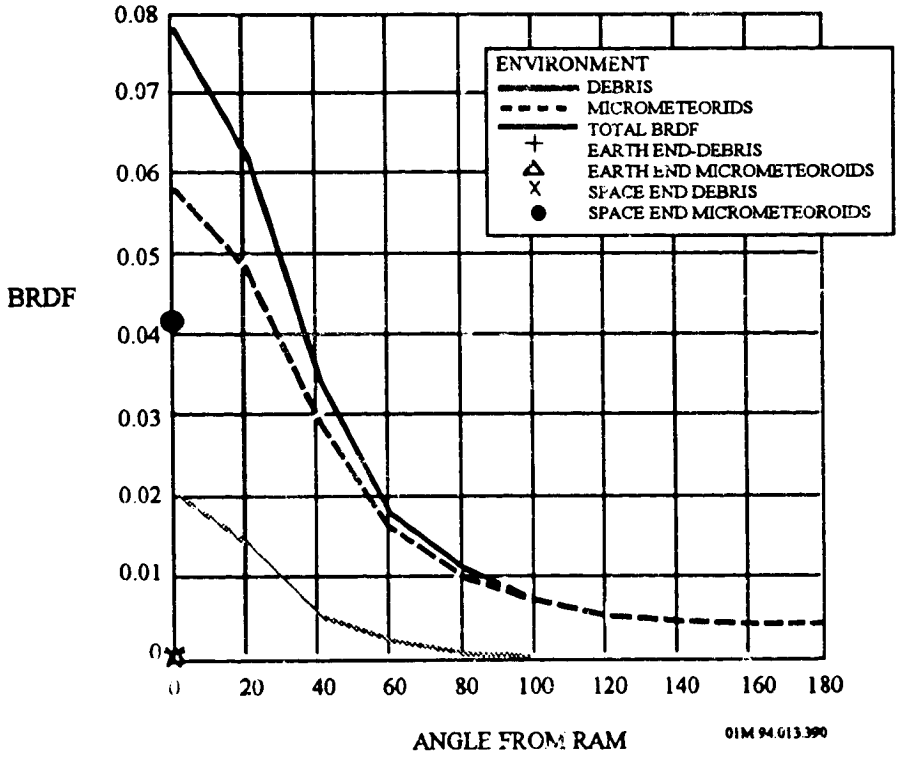

Figure 2- 29. Variation in BRDF with Angle from Ram on LDEF

For LDEF the predictions show that the micrometeoroids contribute the most to the overall scatter. The data also clearly indicate the very small degree of optical scatter for the Earth looking surface. The scatter value for the space looking surface is about 4.2×10^{-2} (per steradian). The

data demonstrate that for angles greater than about ±35° from ram the scatter is always less than for the space end, while for angles less than this the scatter is worse for the near-ram surfaces and peaks on that surface with a value of about 7.8×10^{-2}.

A parametric series of peak BRDF optical scatter predictions have been done for a series of orbits ranging from 400 km to 2000 km altitude and with inclinations of 0, 30, and 60° (ref. 79). For all these cases the mission time periods are 1996 to 2002, and the assumed operational wavelength is 5.0 mm (BRDF varies with the inverse square of the wavelength), and the optic is assumed to have an area of 100 cm^2. Figures 2-30 through 2-33 show the predictions as functions of altitude and inclination for nonshielded optics. As the altitude increases, the debris scatter increases rapidly up to the 800 - 1000 km range (where debris dominates toward the ram), and then gradually decreases for higher altitudes. However, there is a local peak in the debris at about 1500 km. The debris-induced scatter is always worse for the higher inclinations. The scatter due to micrometeoroids is independent of orbit inclination and slowly increases with altitude (below 2000 km). The space surface suffers from a constant degree of scattering independent of both inclination and altitude. There is a very large range of predicted peak BRDF values, from a high of 0.56 (800 km, 60°, ram) to a low of 0.072 (400 km, 0°, ram).

Figure 2-34 shows the predictions for some options which include telescope shrouds, for the cases of 30, 60 and 80° of "exclusion angle" for an orbit at 1600 km and 60° inclination. The "exclusion angle" is the angle measured from the surface of the optic which prevents direct impacts on the optic due to the telescope wall. For a circular optic of 100 cm^2, the diameter is 11.28 cm (4.44 inch). Thus, for exclusion angles of 30, 60, 80° the telescope wall must have a length of 6.51, 19.54, and 64 cm, respectively. Note the odd trend of the data as the exclusion angle increases. While the micrometeoroid-induced scatter merely decreases monotonically versus this angle, the debris-induced scatter is observed to drop rapidly from the ram and to display a local peak at about 20° off-ram.

As can be seen, the use of telescope shrouding can dramatically reduce the scatter predictions provided a sufficiently large exclusion angle is involved. For a 30° exclusion angle, the ram BRDF is only reduced from 0.24 to 0.20; for a 60° exclusion angle the reduction is from 0.24 to 0.013; while for an 80° exclusion angle the reduction is from 0.24 to 9×10^{-5} (at 20° off-ram), all for the same orbit of 600 km altitude and 60° inclination. However, the use of a large exclusion angle implies a reduced field of regard for the optic. Hence, to overcome the latter, it would be necessary to maneuver the entire telescope tube. Systems which rely on pan-tilt mirrors cannot use large exclusion angles, else the field of view would include looking "at" the telescope tube itself.

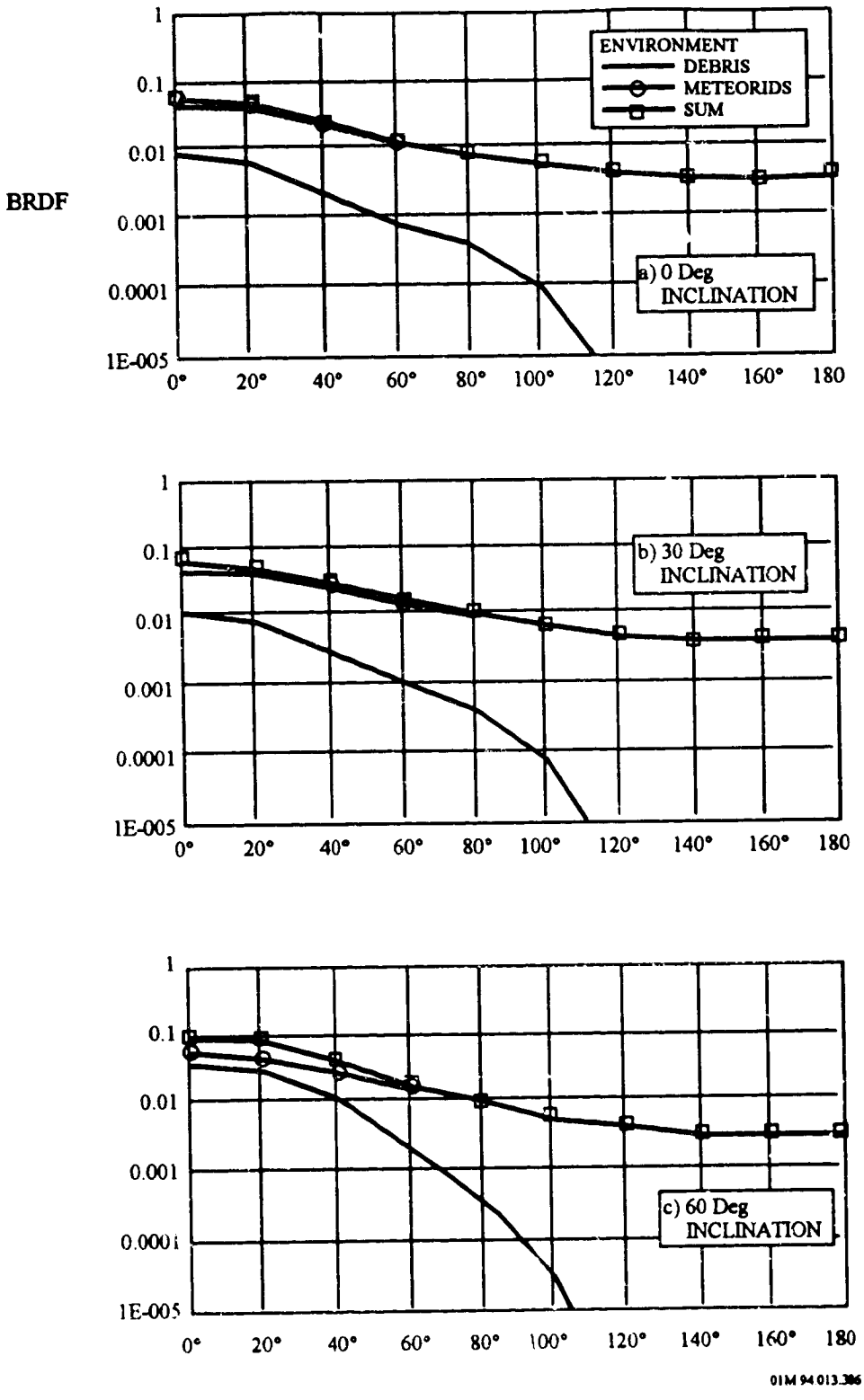

Figure 2- 30. Variation in BRDF with Angle from Ram at 400 km: (a) 0° - Inclination; (b) 30° - Inclination; (c) 60° - Inclination.

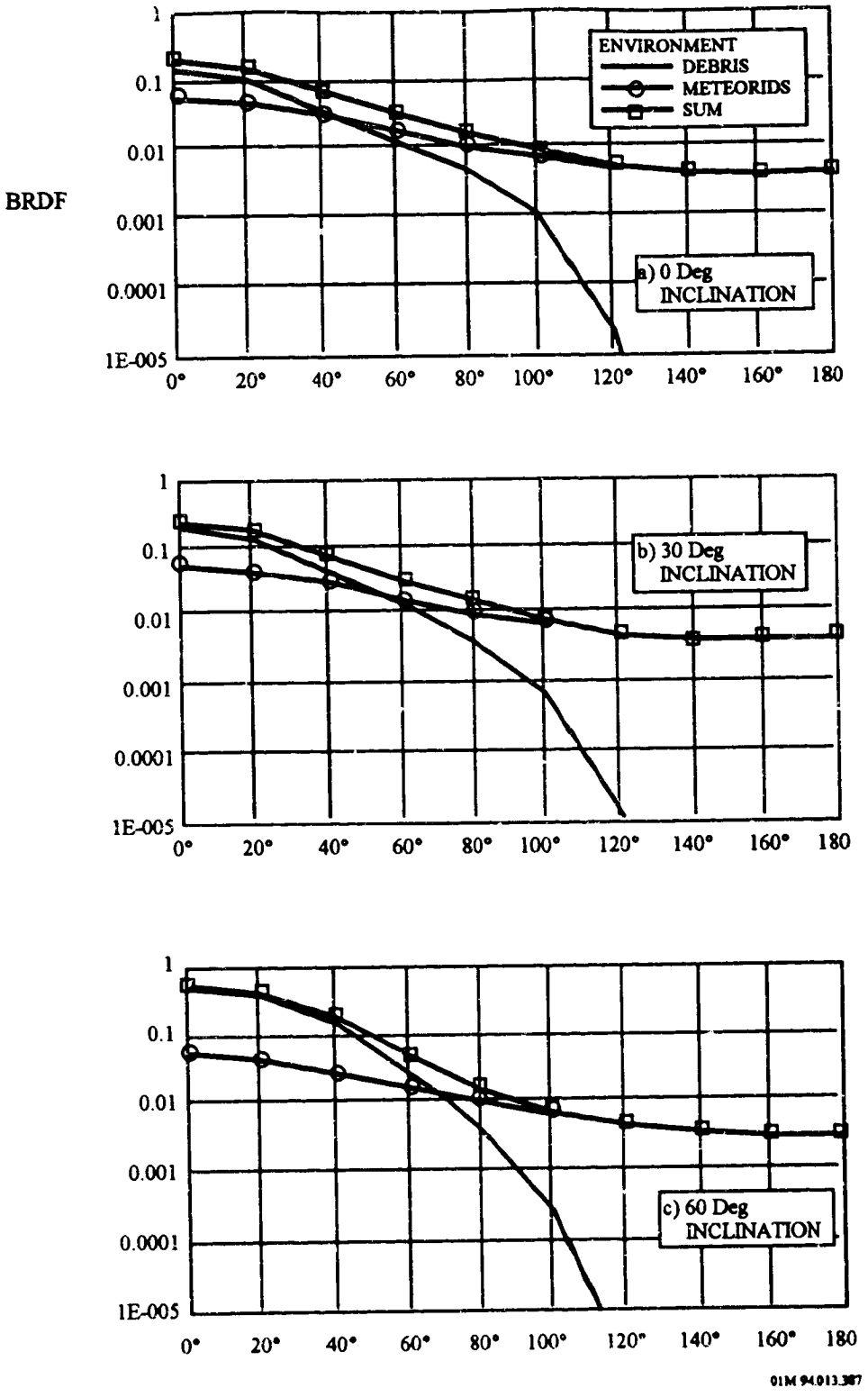

Figure 2- 31. Variation in BRDF with Angle from Ram at 800 km: (a) 0° - Inclination; (b) 30° - Inclination; (c) 60° - Inclination.

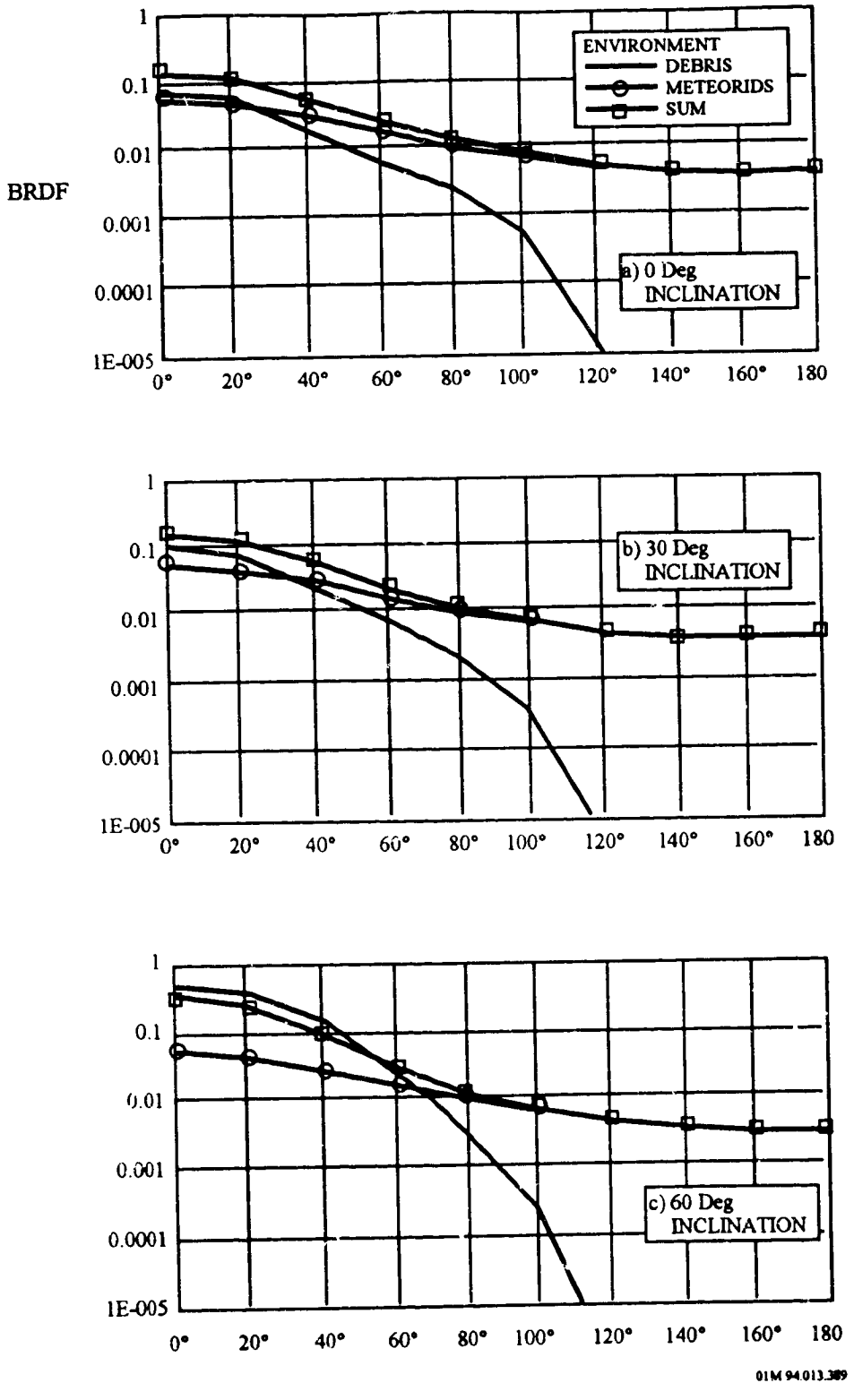

Figure 2- 32. Variation in BRDF with Angle from Ram at 1000 km: (a) 0° - Inclination; (b) 30° - Inclination; (c) 60° - Inclination.

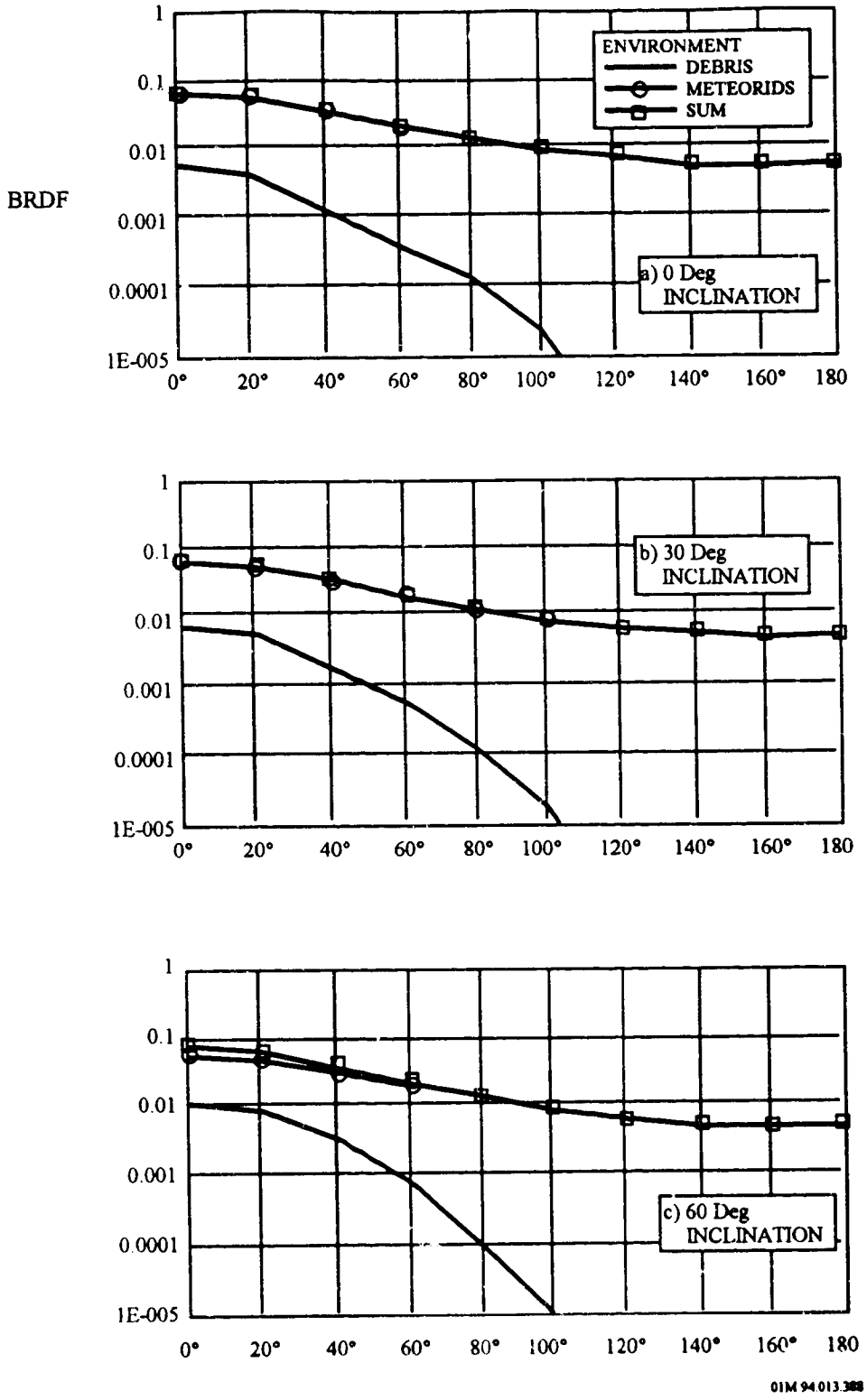

Figure 2- 33. Variation in BRDF with Angle from Ram at 1600 km: (a) 0° - Inclination; (b) 30° - Inclination; (c) 60° - Inclination.

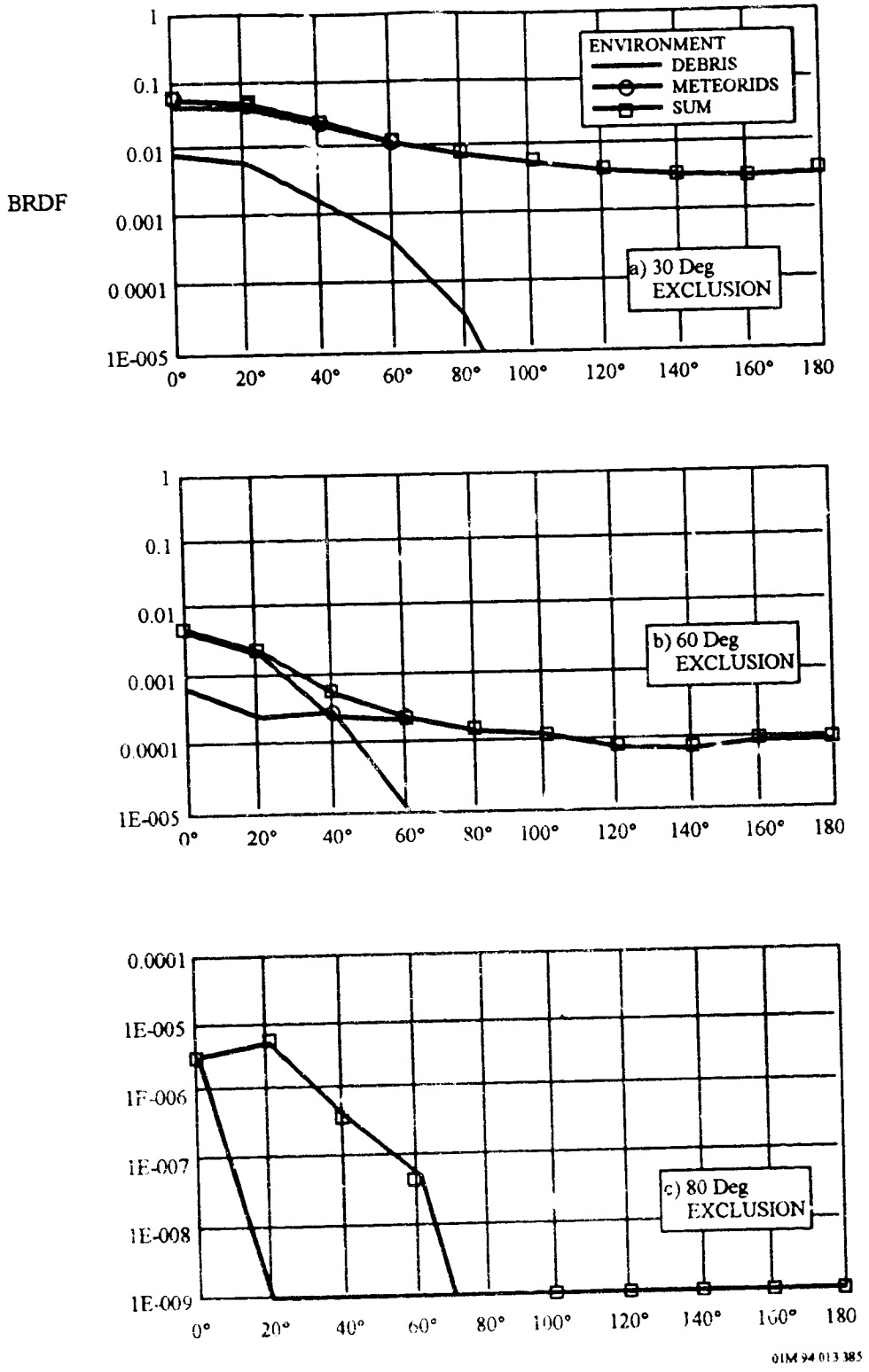

Figure 2- 34. Variation in BRDF with Angle from Ram at 1600 km and 60° Inclination: (a) 30° Telescope Exclusion Angle; (b) 60° Telescope Exclusion Angle; (c) 80° Telescope Exclusion Angle.

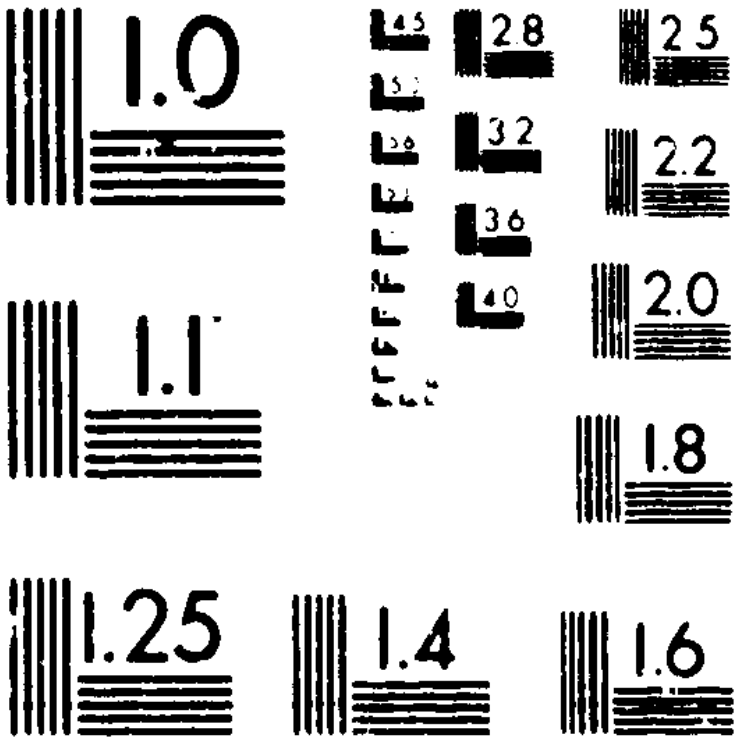

The use of "exclusion angles" in this manner addresses only the case of direct impacts on an optic. However, it is possible to have indirect hits. For example, an impactor could hit the inside of the telescope tube (including a baffle) and cause secondary ejecta to hit the optic. Likewise, for a thin-walled tube an impactor could completely perforate the wall and again generate ejecta. If the "target" material is one which produces copious secondary debris, then it is possible for this debris to again cause at least a contamination problem on the optic (this debris is mostly of low velocity and thus unlikely to cause much in the way of actual crater damage). However, most targets do not produce such debris: rather they merely throw of material in the "normal" manner of impact cratering. In the latter case the resulting blow-off is usually of smaller sizes than the original impactor, although the total mass is larger than the impactor. As scatter increases with the fourth power of the particle diameter, for a given mass, the scatter will be low provided the mean particle size is much smaller than the original impactor. Hence, for a given mass of blow-off the scatter decreases as the number of individual particles involved increases. Thus, under most circumstances, it is anticipated that secondary ejecta optical scattering is less important than that due to the (initial) direct impacts.

2.3.9.4 Summary of Micrometeoroid and Debris Effects on Optics

The following are recommended guidelines from B. Kemp (ref. 79) for designers to consider in reducing the effects of micrometeoroid and debris effects on the degree of scatter for optical components.

- The the major effect of micrometeoroid and debris impacts on optics is to produce an increase in scatter, but only minor changes in reflectivity and/or transmission. The scatter increases as the impact crater sizes increase and as the areal density of impacts increases. The effect is nonlinear with the size of the optic. The larger the optic the more likely a large crater will occur resulting in more induced scatter for the large optic. Also the increase in scatter is nonlinear with mission time. As time increases, the probability of an impact by a larger particle also increases, which causes the optical scatter to increase in a supralinear manner. The scatter is dominated by crater formation rather than by crack generation. Soft targets (e.g., metals and plastics) will produce the largest craters. Hard targets (glasses and ceramics) produce smaller pure craters; however, these craters are frequently surrounded by larger surface spalls giving the effect of larger shallow craters. Multilayer optics can also suffer from delamination effects around the impact sites, which produce large local changes in reflectivity or transmission and scatter.

- The degree of scatter depends on the orbit (altitude, inclination and time) and on the pointing direction, Ram is usually the worst direction to point while Earth is usually the best (safest) direction

- The use of telescope shrouding can significantly reduce the scatter provided the angle for entry of particles is small. This is at the expense of the optical field of regard.

2.3.10 Micrometeoroid and Debris Effects on Solar Power System Components

Similar to optics, solar power system components, such as solar cell cover glass, are typically brittle materials. Under impact, brittle materials show a different type of damage than metals and ductile materials. The LDEF flight experiments observed the fracture damage of meteoroid/debris impact on the solar cell cover glass. As is typical of other glasses, there is a central crater filled with very finely shattered material, and surrounded by some spall material and a large conchoidal fracture which extends through the cover glass to the underlying solar cell. In addition, 4 large cracks radiate out from the feature (ref. 89). However, electrical performance degradation was not discernible in the current/voltage measurement (see Section 11).[96]

A broken silver interconnect of a solar cell was also observed on a solar array panel from the A0171 experiment, located at LDEF Bay A08. The interconnect was blown apart from its connection with the solar cell, possibly by an impact or by an electrical discharge. In either case, it created a large spray pattern which covers approximately one quarter of the underlying solar cell area.

Clearly, a significant factor for impacts into these very brittle materials is the propensity to readily propagate cracks, sometimes causing complete penetration and breakup into separate pieces. Hence, designers should note the cracks, which allow space environments, particularly electrons and protons, to have access to the underlying solar cells.

2.4 THERMAL CYCLING-INDUCED MICROCRACKING EFFECTS

2.4.1 Introduction

Microcracking of a composite causes the following dimensional stability problems:

- Hysteresis effect in the structure
- Significant coefficient of thermal expansion (CTE) changes
- Increases in the moisture response rates

Microcracking is occasionally employed to achieve a desired CTE. The Hubble Telescope Metering Structure was subjected to microcracking in order to "tune" the various struts to achieve a desired CTE.[97]

Thermal cycling induced microcracking is attributed to the difference in the CTE of each individual ply parallel and normal to the fiber direction. The CTE normal to the fibers is about half that of the resin's CTE, whereas the CTE parallel to the reinforcement is virtually zero and sometimes slightly negative. Hence, in any crossplied lay-up this difference in thermal expansion induces internal stresses. During repeated thermal cycling each ply within a crossplied laminate will be subjected to thermal fatigue, which may result in the generation of cracks parallel to the fibers as well as through the thickness of each lamina.

2.4.2 Effect of Fiber/Resin Properties

The degree of thermal cracking due to induced internal stresses has been reviewed by Tenney et al.[98] where the effects of thermal cycling between -156°C and 94°C were studied in Pitch and PAN carbon-fiber reinforced epoxies. In each of the samples examined, the microcracks density did not reach equilibrium after 500 cycles. Approximately 10 microcracks/cm were observed with P75S-reinforced epoxy. However, less than 1 microcrack/cm was developed with the same matrix material containing the less stiff T300 fibers, reflecting lower internal stress levels. Hence, the fiber modulus is very important in determining the degree of microcracking. With a polyacrylonitrile (PAN) based 62 Msi (430-GPa) modulus carbon fiber, extensive microcracking was obtained, while with a PAN-based 40 Msi (280-GPa) modulus fiber no cracking was seen under more severe testing conditions. Composites using the higher modulus fibers such as P75S will microcrack more readily than composites using AS-4/T300 type carbon fiber.

In addition to the fiber, the resin and its cure temperature will influence the extent of the microcracking that occurs. In a study by NASA Langley[99] differences in the crack density induced

in three tubes of different materials were observed with increasing number of thermal cycles between -156°C and 94°C, as shown in Figure 2-35. The P75S/934 is a high modulus brittle epoxy system, the P75S/CE339 is a high modulus toughened epoxy system, and the T300/934 is a low modulus brittle epoxy system. The crack densities for each material asymptotically approach equilibrium values as the number of cycles increases. The effects of the thermal cycling or microcracking on the torsional stiffness of these tubes are also shown in Figure 2-35. The torsional stiffness of tubes of each of the three materials was reduced by about 40% and the change in the stiffness appeared independent of the composite material system. These data illustrate the sensitivity of matrix dominated properties to microcracking.

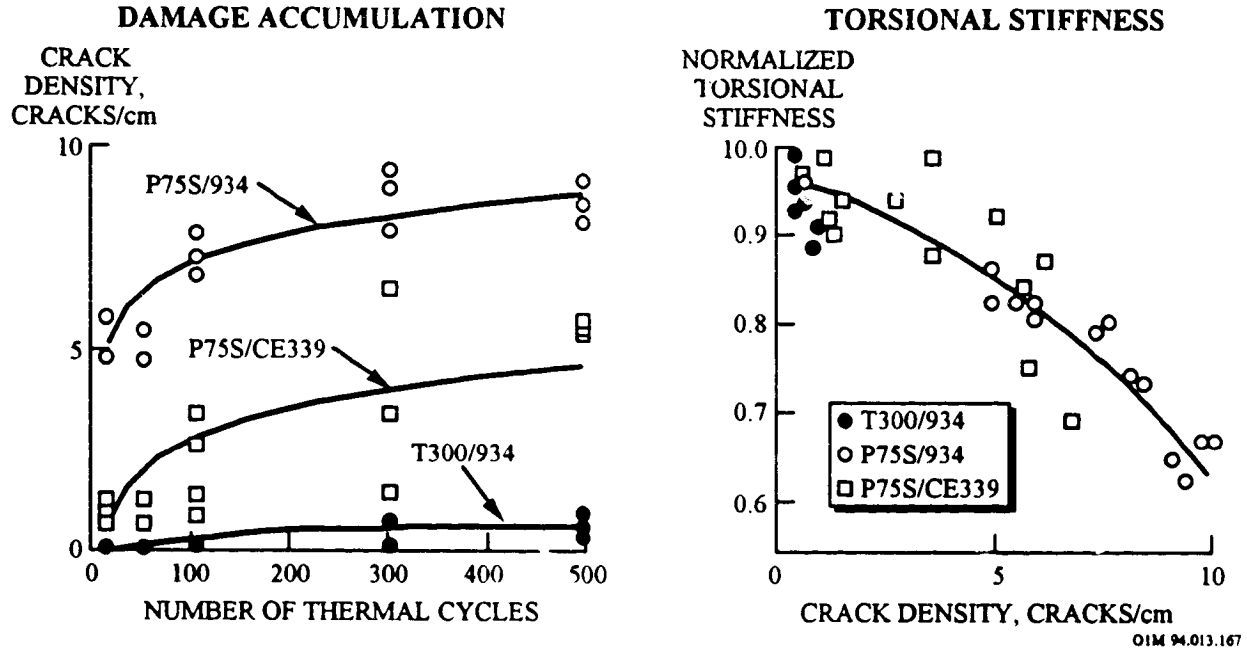

Figure 2- 35. Effects of Thermal Cycling on Composite Tubes

Tough epoxy resins have been developed over the past 10 years, including Hercules 8551-7 and Fiberite 977-2. These resin systems both have excellent residual strength after impact and are very resistant to microcracking. The ERL 1962 toughened epoxy was formulated for space applications by Amoco to minimize microcracks induced by thermal cycling.

The 930 epoxy was formulated by Fiberite ICI for space applications to minimize microdamage by having a low cure temperature to reduce the residual thermal stresses that are induced during the composite fabrication. The 934 resin is a space qualified standard epoxy that has been successfully cured at both 250°F and 350°F. Analytical studies have shown that residual stress is a strong function of the product of the matrix modulus, matrix CTE and the difference between the stress-free temperature (usually near the cure temperature) and the use temperature.[100]

Thermoplastics are inherently tough composite matrix resin systems. The PEEK resin is a thermoplastic polymer which, when reinforced by low modulus, high strength carbon fiber, shows good resistance to thermal cycling after radiation. In a comparative study of material performance between carbon-fiber reinforced PEEK and epoxy composite systems,[101] after 500 thermal cycles between -156°C and 120°C the PEEK-based composite developed 1 microcrack/cm while the baseline epoxy developed 8 microcracks/cm. However, the PEEK thermoplastic exhibited excellent microcracking resistant, but only with high strength carbon fibers (e.g., AS4/PEEK).[102]

Polycyanate matrix composites reinforced with carbon fibers offer lower moisture absorption and enhanced microcracking resistant compared to carbon/epoxy composites. Commercially available 350°F cured polycyanate resins include YLA's RS-3 and Fiberite's 954-3. Amoco's ERL 1939-3 is a relatively new cyanate and epoxy blend designed for space applications. Both the toughness of the polycyanates and their low shrinkage during cure result in a more stable matrix during thermal cycling as shown in Figure 2-36. Using similar P75 laminate constructions and thermal cycling conditions, the data indicated that the number of microcracks/inch converged after 1000 cycles, with the RS-3 polycyanate composite displaying the best performance.[103]

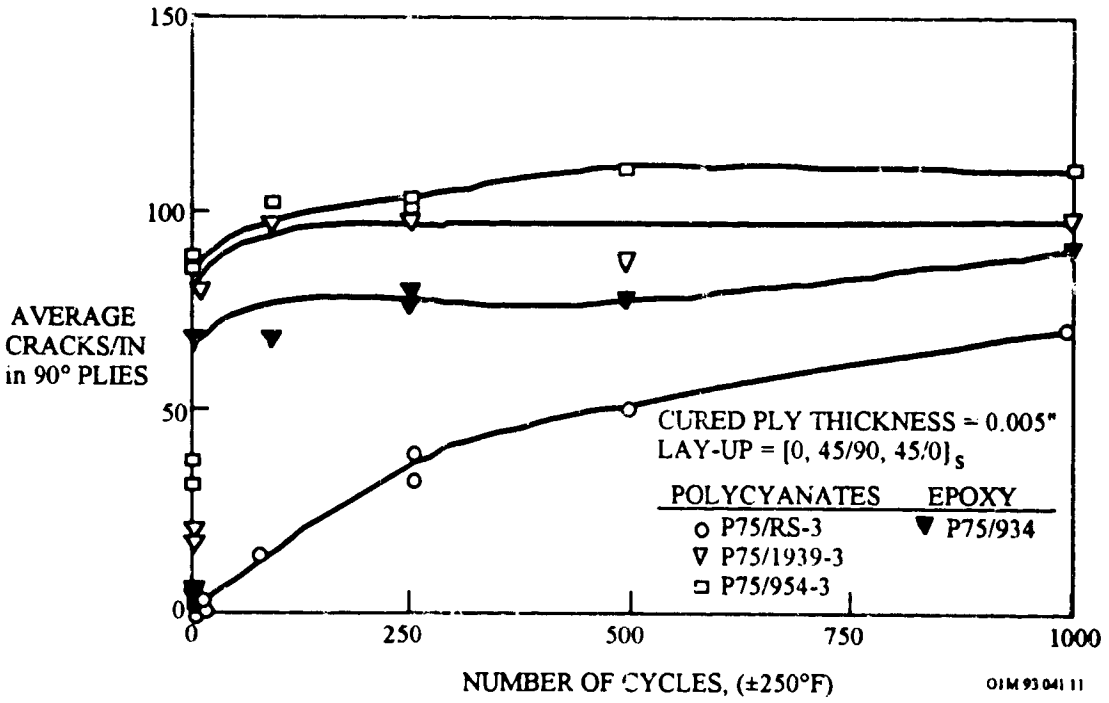

Figure 2- 36. Comparative Microcracking Behavior for Thermoset Composites

2.4.3 Effect of the Space Environment

Exposure of composite structures to the repeated thermal cycling of space can cause microcracking in composites. A complicating feature of the Highly Elliptical Orbit (HEO) and GEO space environment with their higher particle radiation dose is the synergistic effect of combined electron radiation and thermal fatigue, which may cause dramatic changes in the performance of composite systems. Data from NASA Langley[101,102,104] showed that most composite systems exposed to sequential electron radiation and thermal fatigue are highly susceptible to microcracking damage due to embrittlement of the matrix material.

In a study of candidate panel facesheet composite materials for a space reflector, microcrack density data were measured for quasi-isotropic laminates as-fabricated and after exposure to electron and thermal cycling simulating CLEO and HEO.[105] The environmental parameters and the testing results are summarized in Tables 2-16 and 2-17, respectively.

Table 2- 16. Predicted Mission Environmental Parameters

Space Parameters	Circular Low Earth Orbit (CLEO)	Highly Elliptical Orbit (HEO)
Estimated life time electron radiation dose, Mrads	10	1000
Thermal cycle, °F	-100° ±36°	-226° ±36°
Lifetime, years	>10	>10
Orbit, nautical miles	378 28.5°	540 x 37,800 28.5°

Table 2- 17. Durability of Candidate Materials in Simulated CLEO and HEO Environments

Material System	Vf %	Lay-up	Cracks per inch				
			As-Fabricated	±150°F 25 cycles	CLEO 100 cycles		HEO 100 Cycles
					10 Mrads	1000 Mrads	1000 Mrads
C6000/ F155	56.7	A	0	0	E		
UHM/ F584	54.8	B A	0 0	8 14	12	17	C C
T50/ ERL 1962	67.6 62.5	B A	0 0	0	0	0	0
P75/ERL 1939-3	66.9	B	5	64		64	C
P75/ PEEK	63.8	A	50	52		58	C
P75/934 250°F 350°F	 55.9 54.7	 B B	 0 81	 38 85	 41	 58	 C C
P75/930	51.3 57.2	B B	0 0	0 0	0	8	C C
T50/934 250°F	60.1	B	0	0			6

A- lay-up [0,90,45,-45]$_s$
B- lay-up [0,45,90,-45]$_s$
C- Testing stopped due to excessive damage
D - Testing stopped due to poor quality material
E- Testing stopped due to properties outside requirements.

With the exception of P75/ERL 1939-3, P75/PEEK, and the 350°F cured P75/934, the laminates were free of microdamage in the as-fabricated state. The P75/ERL 1939-3, P75/PEEK, and P75/934 contained about 5, 50, and 81 cracks per inch, respectively, in the as-fabricated state. The damage in each of these laminates was attributed to thermal stresses induced during cool down from the fabrication temperatures. Note that when the P75/934 laminate was cured at 250°F, no cracks were seen, indicating that the lower cure temperature sufficiently reduced the stresses to avoid microdamage on cool down during fabrication.

After 25 cycles between -150°F and 150°F, the P75/ERL 1939-3, 350°F cured P75/934, and P75/PEEK continued to microcrack, with the P75/ERL 1939-3 reaching a crack density of about

64 cracks per inch. These cycles also induced microcracks in the UHM/F584 (8-14 cracks per inch) and the 250°F cured P75/934 (38 cracks per inch). The remaining four laminates (C6000/F155, T50/ERL 1962, P75/930, and T50/934) did not microcrack. Two materials, the 350°F cured P75/934 and C6000/F155, were not carried any farther in the test matrix because of excessive microdamage, poor quality (excessive voids).

Five of the remaining six materials were subjected to the simulated CLEO thermal cycling environment with electron radiation doses of both 10 Mrads and 1000 Mrads. (The 250°F cured T50/934 was subjected only to the more severe HEO simulation.) Of these five materials, only the T50/ERL 1962 remained damage free. The other four materials continued to microcrack as a result of continued thermal fatigue and/or matrix embrittlement due to electron radiation.

The only two materials subjected to the simulated HEO environment were the T50/ERL 1962 and the 250°F cured T50/934. No damage was induced in the T50/ERL 1962 laminate during the HEO simulation. The T50/934 did exhibit some slight microdamage with a microcrack density of about 6 cracks per inch. The T50/ERL 1962 composite did not degrade in either environment.

2.4.4 Design Considerations for Reducing Microcracking

The influence of ply lay-up on the extent of microcracking was reported by Wolff[106] for carbon composite tubes. Predicted values for the onset temperature (T_N) of microcracking on the first thermal cycle as a function of the laminate ply angle are shown in Figure 2-37. At low ply angles no microcracking was predicted.

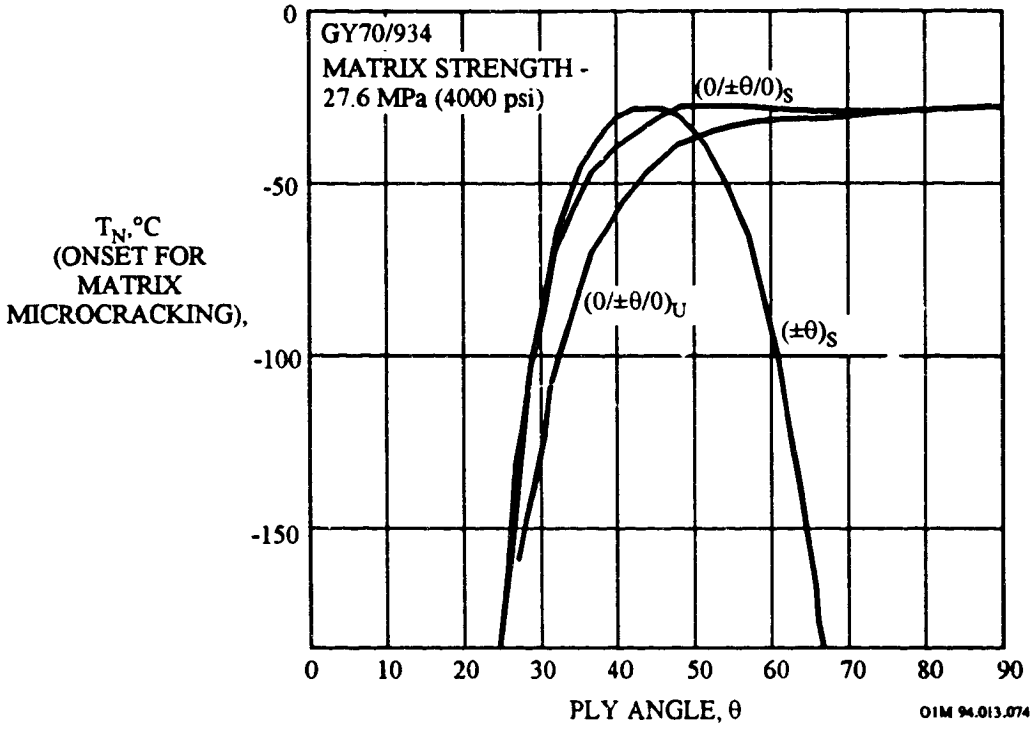

Figure 2- 37. Onset Temperature for Microcracking with Ply Angle

Table 2-18 shows three values of T_N for each of several ply lay-ups. The first corresponds to a flat laminate without edge effects, the second for a circular tube infinite in length, and the third for the stress field near the ends of a circular tube. A flat plate with a 90/0/±45 lay-up would warp on cooldown but a tube is constrained to a circular cross section so that end distortion occurs.

Table 2- 18. Predicted Matrix Cracking on First Cooldown of Carbon Composites

Material	Lay-up	Onset Temperature (°C) for Microcracking		
		Laminate	Tube	Tube Ends
GY70/934	$[\pm 30]_s$	-94	-94	-94
GY70/934	$[\pm 45]_s$	-25	-25	-25
GY70/934	[0/±60/0]	-28	-24	-24
GY70/934	$[0/45/90/135]_{2s}$	-53	-37	-37
HMS/3501-6	[90/±45/0]	-44	-25	-11
HMS/3501-6	[0/±45/90]	-44	-25	-16

2.5 CONTAMINATION

2.5.1 Introduction

Spacecraft in low Earth orbits are exposed to an ambient atmosphere that will affect the contaminant generation, redistribution and deposition. Contaminants that outgas or vent from the spacecraft can be scattered back to the spacecraft as a result of collisions with the atmosphere. This adds to the deposition from direct line of sight transport. Solar ultraviolet irradiation can increase contamination as a result of a photochemical deposition process. Atomic oxygen will remove contaminants, such as hydrocarbons, which produce different volatile species during oxidation removal. In addition, erosion of the surface by atomic oxygen can add other species to the gas cloud. Contaminants, such as silicones that produce solid oxides when exposed to atomic oxygen, will remain on the surface. The net contaminant generation, migration, deposition, or removal will depend upon the rates of each mechanism and on the spacecraft materials. Hence, orbit contamination can be considered an induced environmental effect composed of many dynamic processes.

2.5.2 Spacecraft Sources of Contamination

Space-based optical payloads and components are exposed to a wide variety of particulate and molecular contamination sources. The primary concern is spacecraft system performance degradation as a result of contamination deposition on surfaces or particulates being in the field of view of sensors.

Molecular contamination arises from various sources, including thruster plume exhaust and spacecraft material molecular outgassing from host platform electronics, lubricants, adhesives and composite structural materials (see Section 2.6). The LDEF Materials Special Investigation Group found that the molecular contaminant film on the LDEF satellite consisted primarily of silicones, from sources such as the Z-306 paint used on the interior of the structure, and hydrocarbons.[107] This contaminant film varied in thickness between 0.1 μm to 100 μm and averaged approximately 3 μm (30,000 Å).

Particulate contamination of optical payloads arises from several sources, including fabrication (metal shavings, chips, paint flakes), atmospheric fallout during assembly and integration (dust), and human sources (hair, lint, skin flakes). During launch and subsequent on-orbit operations this particulate matter, along with contaminants from the launch vehicle, may re-distribute due to vibration, shock, and venting.

2.5.3 Contamination Effects on Thermo-Optical Properties

2.5.3.1 Molecular Contamination

Molecular contamination has caused significant changes in solar absorptance on many satellites. Figure 2-38 shows that many satellites have been afflicted by contamination degradation in the solar absorptance.[108] Note that the cleaner SCATHA spacecraft in Figure 2-38 had stringent cleanliness requirements. On the NOAA-7 spacecraft,[109] which was launched in 1981 and orbited at an altitude of 833 km, the deposition of contaminants onto Temperature-Controlled Quartz Crystal Microbalances (TQCMs) was measured for 2 years. It was found that α leveled off after about 1000 Å were deposited on the TQCMs. By then, α had increased by a factor of 2.5 and 3.3 for several TQCMs.

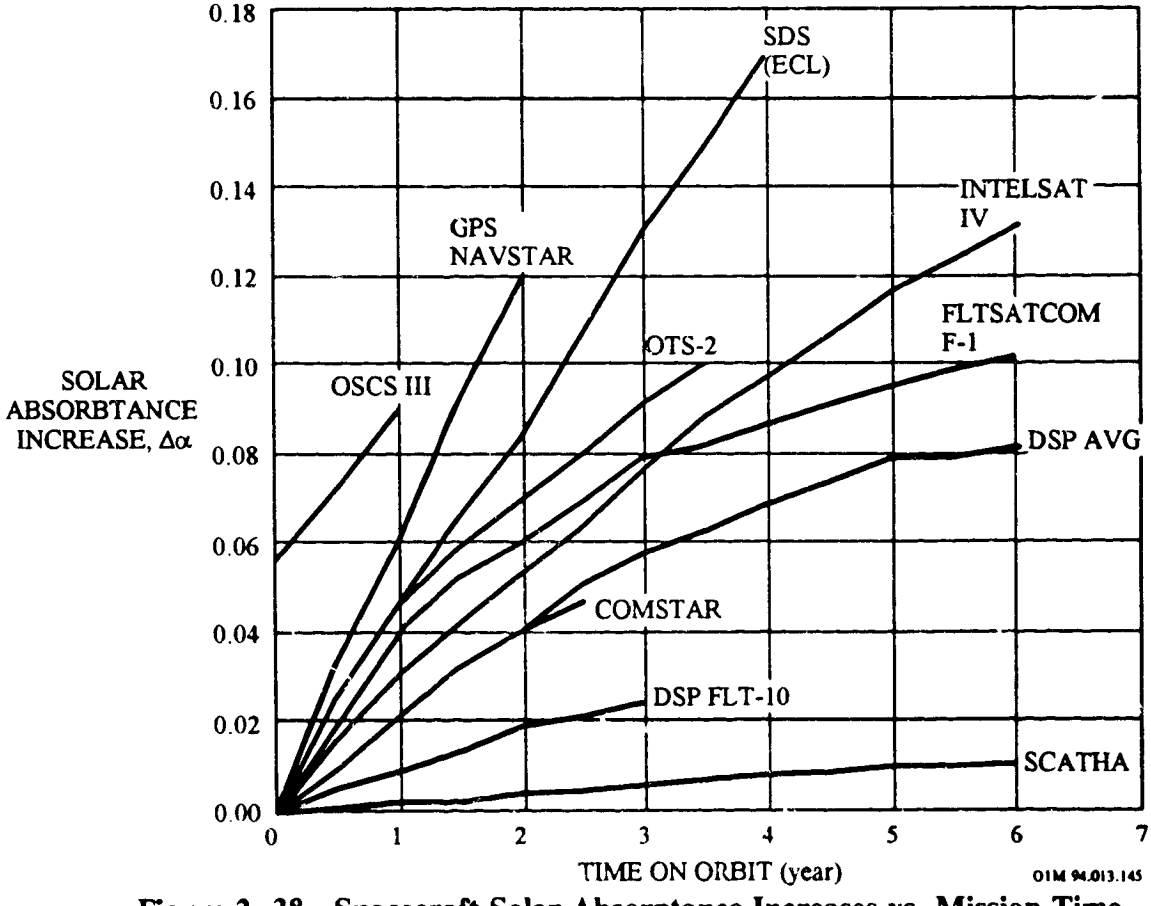

Figure 2- 38. Spacecraft Solar Absorptance Increases vs. Mission Time.

Comparison of the LDEF satellite with other spacecraft indicates that LDEF was one of the cleaner spacecraft to have flown in recent years. Although optical properties of several materials were altered drastically in selected localized areas on LDEF, overall effects on anodized aluminum, which covered 60 percent of the surface, were minimal. Total absorptance changes on the chromic acid anodized aluminum ranged from 0 to about 8 percent.[110]

Molecular contamination can degrade the performance of thermal control surfaces. This can be particularly important if sensors are cooled passively by second surfaces mirrors that are illuminated by the Sun. The effects of relatively thin molecular films on the solar absorptance of second surface mirrors is shown in Figure 2-39.[111] Typically molecular films must not exceed 1000 Å on these sensitive surfaces at the end of the spacecraft's life or the consequences are impaired performance or early mission termination

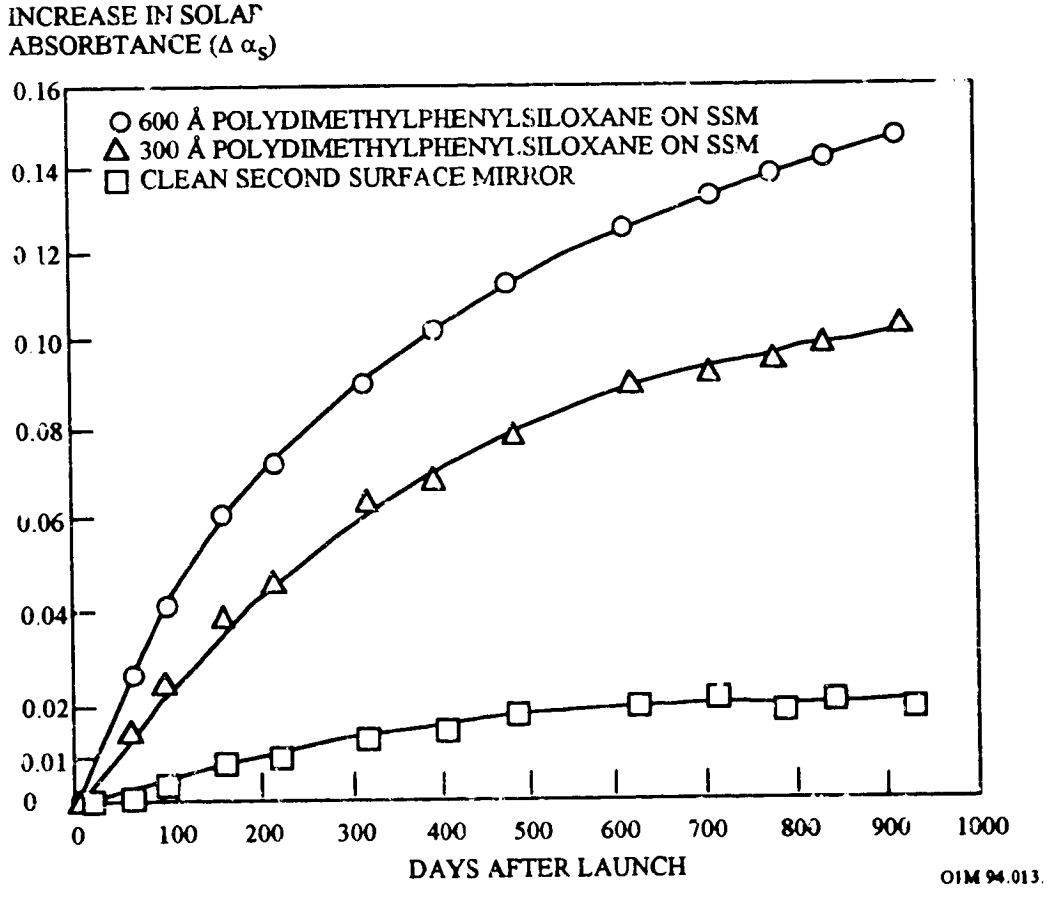

Figure 2- 39. Solar Absorptance Increases on SSM Observed from DSP Calorimeters

Molecular RTV silicone contamination has been observed to degrade both optical and thermal control systems. Figure 2-40 shows that approximately 500 Å of the RTV 560 outgas product (specific gravity ~1.2) can cause a 0.03 increase in the solar absorptance of an aluminized second surface mirror (Note: 10^{-5} surface density for RTV 560 ≅ 10^{3} Å). [112]

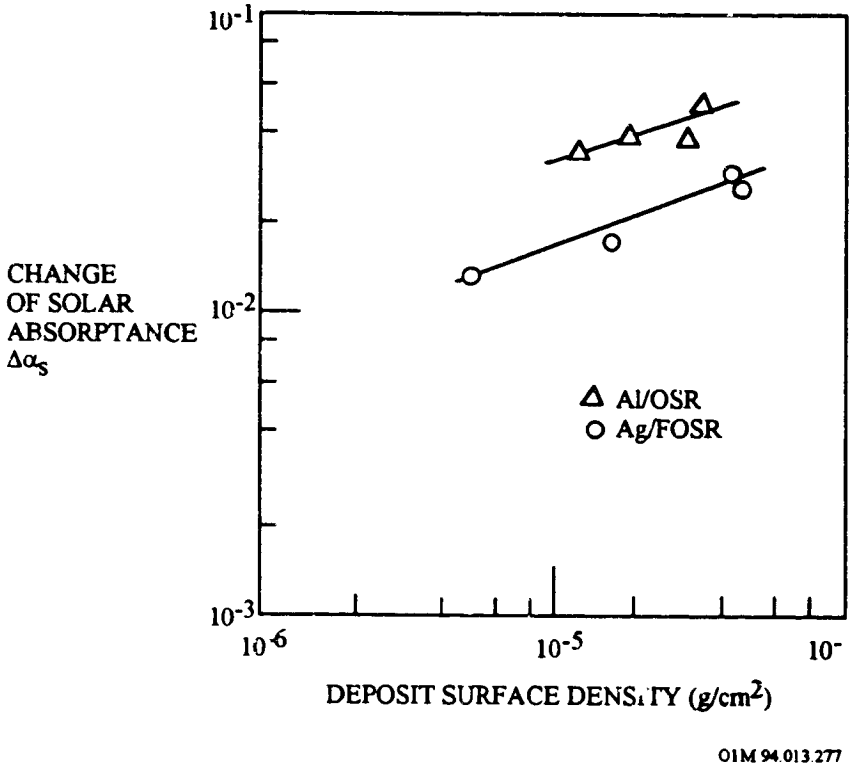

Figure 2- 40. Change of Solar Absorptance by RTV560 Outgas Products

An experiment flown on two CPS vehicles that was designed to measure the change in absorptance of four thermal control coatings indicated a rapid increase in α_s for all samples.[113] The experiment measured the changes in α_s, inferred from temperature measurements, for samples of 5-mil silvered Teflon, fused silica mirror (OSR), 5-mil silvered Teflon coated with indium tin oxide, and S13G/LO white paint. Although the initial values of α_s for the four coatings were all different, the slopes of the $\Delta\alpha_s$ curves for the first three materials were similar, suggesting that the degradation mechanism was acting approximately equally on all three coupons - characteristic of contamination accretion. The last coating, the white paint, indicated a much more rapid change in α_s. However, there is reason to suspect it is the radiation vulnerability of the silicone binder of the S13G/LO white paint that is responsible for the rapid increase of its αs.[114] The silicone is a hydrocarbon organic, and their chemical bonds are known to have lower binding energies than those of the fluorocarbon bonds of Teflon. Thus, it is probably reasonable to ascribe the difference between the $\Delta\alpha_s$ of the S13G/LO white paint and that of the other coupons to radiation damage.

The data on the other three coupons could be explained on the basis of contamination alone, if the contamination accumulated at the rate of about 2.5 Å/day.

The absorptance of silver Teflon may be substantially changed by surface accumulation of a molecular contaminant film (generally hydrocarbons and silicones). The contaminant acts as an absorbing layer, hence the α of contaminated silver Teflon rises as the contaminant thickness increases, eventually approaching an asymptotic value equal to the α of the contaminant.[c]

Most of the silver Teflon samples on the Solar Maximum Mission satellite[115] had a very small change in α (delta $\alpha \leq 0.04$). However, some samples that were visibly contaminated went from an initial α of 0.06 to a final α of 0.28 after 4 years of flight at an altitude of ~500 km. Unfortunately, the contaminant layer thickness was not measured.

On LDEF the effect on the thermal control performance of silver Teflon blankets due to contamination was at most 2 to 3 percent. There was virtually no change in absorptance and very slight changes (<5 percent) in emissivity of silver Teflon for the exposed portions of these blankets (ref. 110). A silicone-containing molecular contamination film was observed on selected silver Teflon second surface mirror specimens on the LDEF UHCRE Experiment, as shown in Figure 2-41.[116] The amber-colored silicon-containing contamination may have resulted from the outgassing of the adhesive which secured the velcro hook and loop tape onto the thermal blankets which, in turn, secured the thermal blanket on the experiment tray. These pads, some as large as 1-in by 4-in, were bonded with DC6-1104 RTV silicon adhesive. A visual inspection of two velcro strips on a section of blanket showed that the adhesive had been liberally applied. Approximately 50 pads were attached to the blanket material. A matching set of pads were bonded to the tray itself. Thus, a significant amount of silicon adhesive was used in this particular application, since at least 16 blankets were held in place using this technique. The silicon from this source, perhaps in the form of an organic silicone, probably contributed to the general molecular contamination observed at various locations on LDEF experiments and structure. IR analysis performed on wipes of the contamination were taken from several positions on the experiment tray corners. The IR spectrum indicates a silicone contaminant. It was concluded that the stains observed are a result of oxidation of outgassed silicones by atomic oxygen. The potential significance of this particular contaminant is the possibility of conversion to an inorganic silicate due to reaction with atomic oxygen Silica/silicates have been shown to be effective barriers to AO erosion. Thus, surfaces which were

---

[c] Note that although the absolute value of α depends on the initial absorptance of the clean Ag/Teflon, the change in α depends only on the contaminant layer thickness and the chemical identity of the contaminant. Therefore contamination data involving substrates other than Ag/Teflon can still be used to predict solar absorptance degradation.

covered with this contaminant may have responded differently to the LDEF environment than surfaces which were not contaminated.

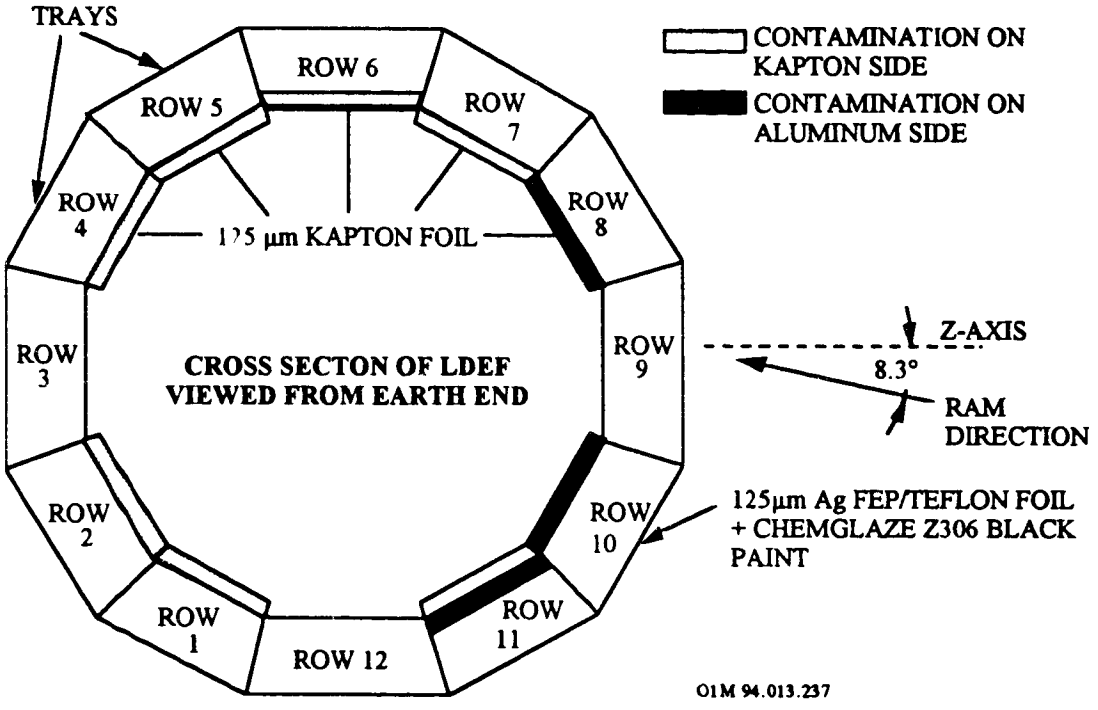

Figure 2- 41. Contamination on LDEF Satellite.

Contamination stains were also mapped on the Kapton foil of the LDEF Satellite. Foils in rows 8, 10, and 11 were contaminated on the aluminized side whereas foils in rows 1, 2, 4, 5, 6, 7, and 11 were contaminated on the Kapton side. The most heavily contaminated surfaces were the Kapton side of foils 2, 4, 5 and the aluminized foils 8, 10, and 11. Chemical analysis of the contaminant layer confirmed the presence of silicone and oxygen. Hence, since the contamination in the majority of cases is facing the ram direction, one can postulate that outgassed silicone products have been oxidized by atomic oxygen to form a silicon oxide layer on the foils. Silicon oxide being resistant to atomic oxygen erosion would not be removed by the cleaning action of atomic oxygen and thus form a protective layer for the Kapton

In addition to organic films, cryodeposits of water ice have been observed to cause significant changes in optical properties (ref. 112). Figure 2-42 shows examples of both theoretical and empirical data as deposited on a gold mirror.

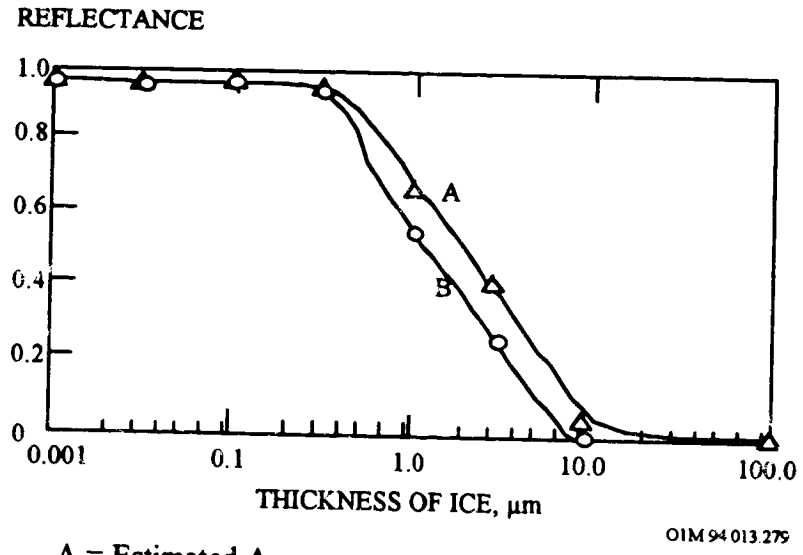

A = Estimated Average
B = Worst Case

Figure 2- 42. Reflectance of a Gold Mirror (mid IR) as a Function of Water Ice Thickness

2.5.3.2 Particulate Contamination

Thermal Control Surfaces. In addition to molecular contamination films, particles can cause changes in the radiative properties of thermal control surfaces. Figure 2-43 shows that carbon particles from solid rocket motors can have a deleterious effects on spacecraft performance (ref. C.R. Maag, 1989).

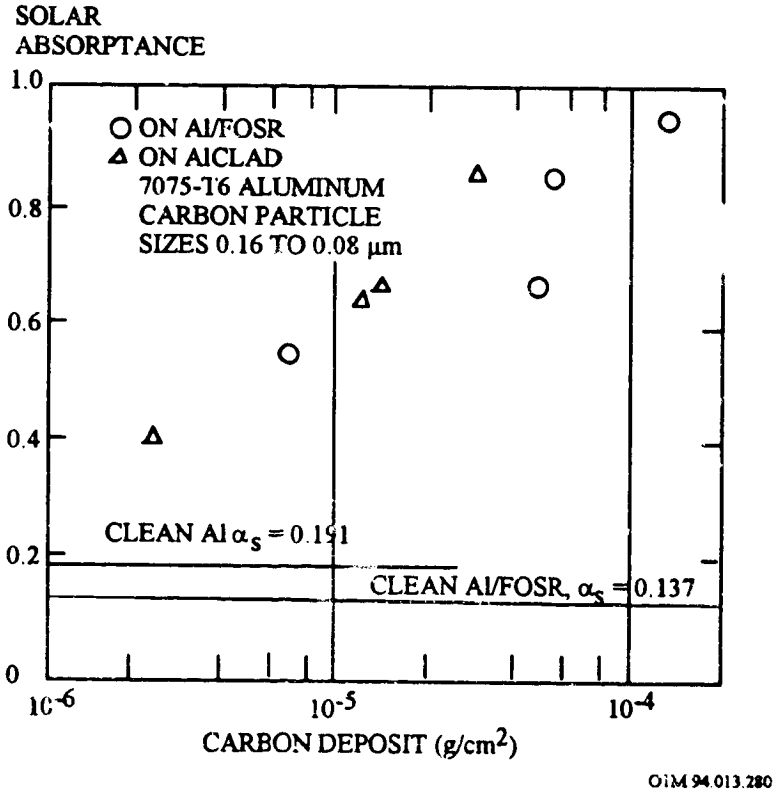

Figure 2- 43. Change of Solar Absorptance by Carbon Particle Deposit

Optical Components. Two specific telescope performance requirements that drive particulate contamination control levels are stray light rejection and optical throughput. The ability of a space based telescope to reject stray radiation from sources that are out of the field of view is a strong function of the particulate contamination level on the optical surfaces. Space sensor stray light rejection requirements are driven by signal to noise, resolution, and/or radiometric calibration, depending on the payload mission. For example, detecting a dim object near a bright source such as the Earth or Sun will be difficult or impossible if stray light from the bright source is scattered from the particulate matter on the mirror surfaces and reaches the focal plane, raising the photon background. For an Earth viewing sensor, such as those to be located on the EOS platforms, stray light from the region of the Earth outside of the sensor field of view can reach the focal plane if the radiation is scattered from particles on the optical surfaces. This effectively blurs the resolution of

the instrument and causes radiometric errors. The effect is most obvious when a sensor views a dark area such as an ocean with bright clouds surrounding the field of view. The signal from the scene in the field of view is effected by the brightness of the scene outside of the field of view.

In some instances, particulate contamination can decrease the optical throughput significantly. On the AXAF telescope with its grazing incidence optics, particles can obscure a significant portion of the collecting area of the optics by the shadows their profiles cast. Since X-ray wavelengths are strongly absorbed by particulates, the contamination can significantly reduce the signal at the focal plane array.

Particulates that become dislodged from the spacecraft can remain near the platform for a significant period of time. If these particles with velocities equivalent to the spacecraft are large enough, they can cause sensors to have flowed or false readings depending on how these particles float through the field of view and how they scatter illumination.

2.5.4 Contamination Effects on Solar Array Power Output

Estimates of photochemically deposited molecular contamination on the Global Position System (GPS) Satellites concluded that a few percent of contamination incident on any solar illuminated surfaces may remain permanently, resulting in a decrease in the power of the solar arrays.[117] Although the GPS satellites were launched into a 55° inclination orbit at 1/2 geosynchronous altitude, i.e., 20,000 km, any investigations on the effects of contamination that results from outgassing by the spacecraft on the solar array output can easily be applied to LEO satellites.

A greater than expected decrease in electrical power output from the solar photovoltaic cells on the GPS solar arrays with on-orbit time pointed to either unexpected radiation damage or contamination accumulation from the spacecraft itself. The Van Allen belts are known to produce solar cell degradation due to their effects on charge carrier lifetime.[d] However, the GPS observation required that either the Van Allen environment is more severe than expected, or that the Van Allen belts produce unexpected effects on some component of the solar cell stack (including antireflective coating, cover slide, or adhesive). The main reason for suspecting the Van Allen belts is the fact that, when solar cell degradations for various spacecraft in different orbits (altitudes) are compared, the observed solar cell degradations are greatest for spacecraft exposed to the largest total radiation dose, and the GPS spacecraft orbits in the most intense portions of the outer van Allen belts.[118,119,120,121]

However, initial estimates by Stewart et al.[122] indicated that there might be enough material outgassed by the GPS vehicles sticking on the solar panels to account for the anomalous degradation in GPS solar array output. Furthermore, in situ observations by the SCATHA spacecraft also indicated that the presence of UV light greatly increased the amount of contaminants that can accumulate on spacecraft surfaces.[123] Laboratory investigations have verified that the presence of ultraviolet light greatly increases the sticking probability of molecules striking the surface in a vacuum environment.[122,124,125,126]

An extensive analysis of the outgassing properties of the materials used on the GPS Block I vehicles, as well as their masses, temperatures, locations, and possible outgassing paths, indicated that if only a small fraction of the matter impinging upon the solar panels underwent a

---

[d] Satellites in MEO orbits are exposed to the radiation belts, which trap and hold high energy charged particles. A satellite passing through these belts is subjected to a high flux of electrons and protons, and trapped protons are capable of causing single event latchups (i.e., digital microcircuits short their power supplies to ground) in certain types of chips.

photochemical reaction initiated by the solar UV and adhered to the panels, the amount of matter that would remain on the panels was sufficient to account for the unexplained degradation. The effect of the contaminant layer on the output of the solar cells was obtained by multiplying the optical attenuation of the contamination as a function of wavelength by the spectral response of each cell and the solar flux. The results, illustrated in Figure 2-44, show the contamination film effects on solar panel output (ref. 117).

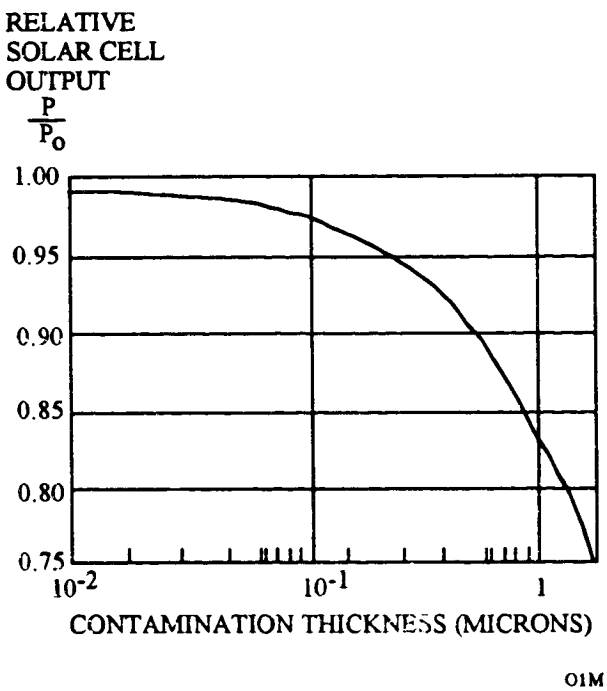

Figure 2- 44. Contamination Film Effect on Solar Panel Output.

The conclusion that contamination is responsible for the anomalous degradation is surprising in that solar arrays, nominally at a temperature of about 60°C, are normally thought to be relatively impervious to molecular contamination. This may have implications for future spacecraft because designers must take into consideration the fact that a few percent of the contamination incident on any solar illuminated surface may remain permanently, resulting in decreased power in the case of solar arrays, or increased values of α_s in the case of thermal control coatings. The effect of this contamination on the GPS vehicle would have been lessened had the solar arrays been farther from the vehicle, decreasing the amount of contaminants reaching the arrays, or had the strings of solar cells been oriented normal to the boom, rather than normal to the spacecraft, thereby decreasing the number of strings affected by the contamination.

2.5.5 Contamination Effects on Optics Performance

Contamination plays an important part in the performance degradation of optical components, which can be measured by decreased optical throughput and increased solar absorptivity. Thin deposits of molecular contaminants that condense on cold optical surfaces and infrared sensors can seriously reduce optical throughput. Molecular films as thin as a few hundred angstroms can reduce the sensor performance, especially when viewing targets close to bright sources of light such as the Sun (see Section 2.7.4). Furthermore, molecular contamination from composite materials can lead to the formation of a "cloud" of outgassed molecular particles, resulting in a significant increase in light scattering that attenuates the signals that the sensors are receiving. Small particles can significantly alter the bi-directional reflectance distribution function (BRDF) of optical surfaces as shown in Figure 2-45 (C.R. Maag, 1989). R.P. Young has performed both experiments and computations (using Mie optical scatter theory) to derive increases in BRDF as functions of contamination levels for small particles on mirror surfaces.[127] Consequently, optical payloads and components are over designed to overcome the expected debilitating effect of contaminants on the mission performance. See Section 2.6.2.2 for an additional discussion on particulate contamination effects on optical surfaces.

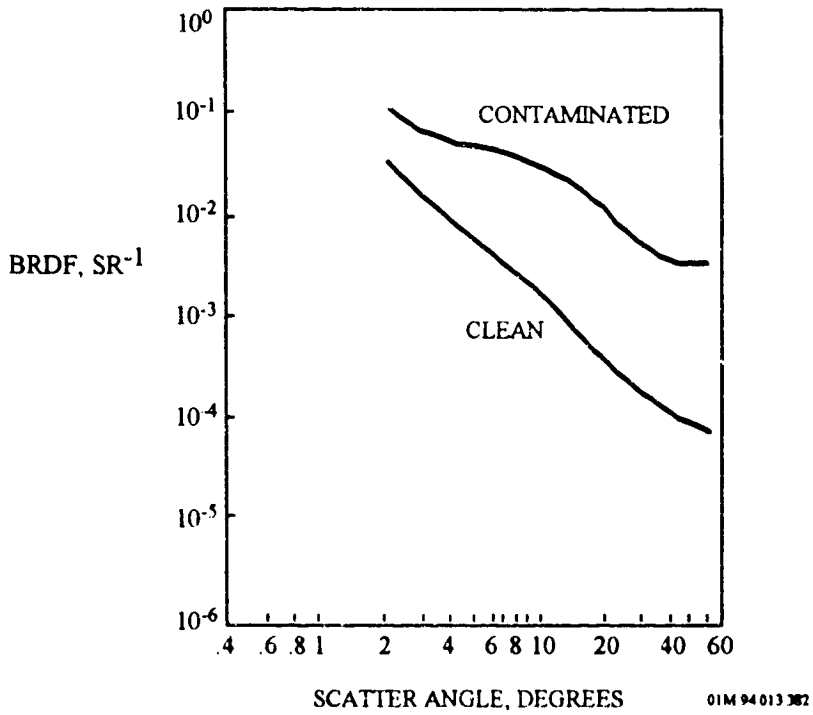

Figure 2- 45. Effects of Contamination on the BRDF of an Aluminum Mirror

2.5.6 Atomic Oxygen Erosion and Secondary Ejecta Impact-Induced Surface Contamination

LDEF provided supporting evidence of the contribution of atomic oxygen erosion and secondary ejecta impact to surface contamination. This type of damage had been known to exist for over fifty years and had been seen on a small scale in the Solar Maximum Mission where the detection of small impact crater and particulate contamination on aluminum louvers were attributed to high velocity secondary ejecta from primary impact into the backside of the nearby solar panel.[128] Chemical analysis of the detectable residue from the impact craters indicated compositions of typical paint pigments used on the solar panels. Figure 2-46 summarized the contamination flux of particulate contamination on the various regions of the aluminum louvers. These particles are mostly titanium dioxide from the paint pigment particles, and consequently, came from the solar panel. The particles are clean-appearing and lacked the binder typical of unflown paints, hence suggesting that the near-surface binder of this paint has been eaten away by atomic oxygen erosion and the included pigment particles have been released by thermal cycling or other mechanisms and have drifted to the louvers and have been deposited on their surface. Hence, self-contamination from released paint pigment presents a potential source of particulate contamination.

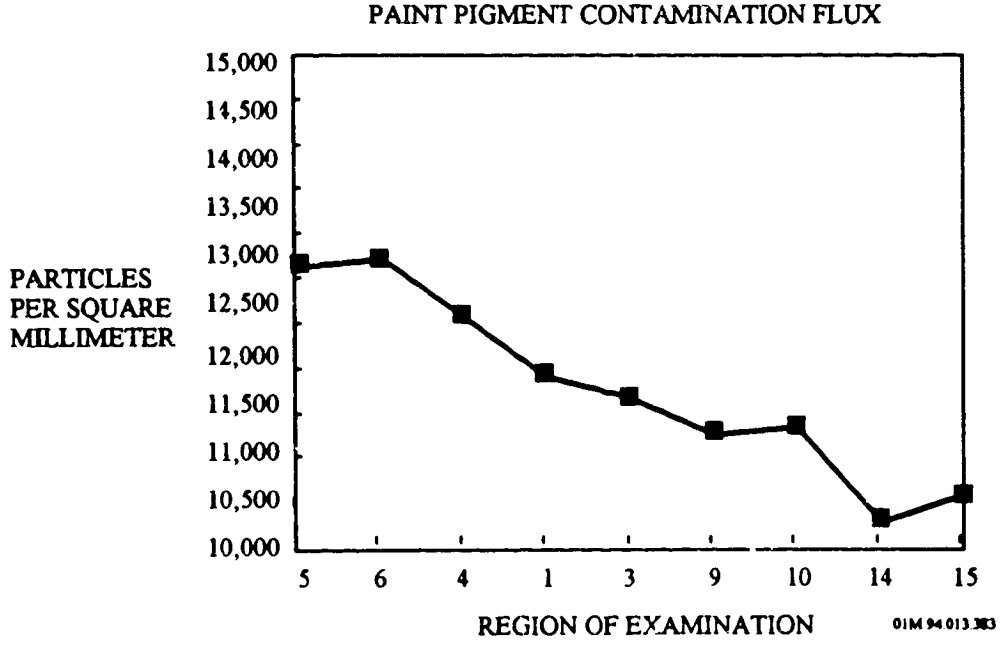

Figure 2- 46. Paint Pigment Contamination Flux on the SSM

LDEF's large surface area and large number of material samples showed the true extent of this type of damage. Surface contamination caused by impacts is most threatening to optics, solar cells and thermal control materials. For optics, this contamination could be caused by impacts into baffles, telescope shrouds, and optical structures, or by penetrations through telescope shrouds. Optical surface contamination causes increased scatter and may reduce reflectivity and transmissivity. For thermal control materials and solar cells, impact-caused contamination originates primarily from impacts into nearby structures.

Another source of surface contamination comes from impacts by urine. The urine originates from Space Shuttle and space station holding tank dumps and remains in orbit as ice crystals. Upon impact these ices melt and form contaminating splashes. This type of contamination was found on every surface of LDEF. They have been seen on all space-returned materials, particularly since the advent of the Space Shuttle.

2.5.7 Design Methods for Minimizing Contamination

2.5.7.1 End-of-Life Spacecraft Subsystem Performance Predictions

Contamination can be considered an induced environmental effect. Contamination, both molecular and particulate, has caused degradation in both optical and thermal control systems. For a designer, the essential question is how much contamination from all sources can be tolerated without causing a given spacecraft system to degrade below a critical performance level, or fail altogether. Table 2-19 provides performance degradation predictions for spacecraft subsystems effected by contamination.

Table 2- 19. Performance Degradation Predictions Due to Contamination

Subsystem	Predictions
Thermal Control Surfaces	Solar Absorptance Increase ($\Delta\alpha_s$) of 0.03 per 100 Å of molecular film
Solar Array	1% Decrease in Power Output per 1000 Å (Degradation Not Well Understood)
Optics	Degradation Dependent on Wavelength (UV Particularly Sensitive to Contamination)

The effect of these contaminant layers on the optical properties of materials depends on the type, location, and amount of contaminants as well as the initial optical properties. Contamination is expected to increase the absorptance of a surface by an amount dependent on the thickness of the contaminant layer, and the optical properties (transmission, absorption and refractive indices) of the layer and the substrate. One study showed that a UV-irradiated RTV silicone contaminant up to 0.02 μm (200 Å) thick caused minimal effects on the absorptance of a gold mirror (α=0.35).[129] However, at 0.1 μm (1000 Å), a significant increase in absorptance of an initially α=0.06 second surface mirror was seen.[130] For chromic acid anodized coatings, it has been suggested that ram-direction AO reacted with the silicone contaminant layer, resulting in a clear contaminant layer which did not significantly affect absorptance.[131] A contaminant layer of up to 30,000 Å had a negligible effect on emittance on the chromic acid anodic coatings with low initial emittances.

The data on silver/Teflon blankets indicate that the change in α due to contamination is anywhere from 0.01 to 0.05 per 100Å of deposited contaminant.[e] The large variation is most likely due to the different absorptivities of different species of contaminants.

Previous and recent contamination analyses for EOS predict worst-case depositions after 5 years of 300 to 500 Å in the vicinity of the instruments. The exact deposition obviously depends on instrument location and the facing direction of contamination-sensitive surfaces, as well as on the amount of outgassing material on the spacecraft.

Combining the observed α degradations with the predicted EOS contamination levels, the minimum, nominal, and maximum changes in α can be calculated:

$$(\text{delta } \alpha)_{min} = 300\text{Å } (0.01/100\text{Å}) = 0.03$$

$$(\text{delta } \alpha)_{nom} = 400\text{Å } (0.03/100\text{Å}) = 0.12$$

$$(\text{delta } \alpha)_{max} = 500\text{Å } (0.05/100\text{Å}) = 0.25$$

Hence, for Ag/Teflon, with an initial α of 0.10, the end-of-life α values would then be 0.13 minimum, 0.22 nominal, and 0.35 maximum. Since one generally designs to a plausible worst case scenario, assuming an end-of-life α of approximately 0.3 for silver Teflon would not be unreasonable

[e] There are very few spacecraft on which both α changes and contaminant layer thickness were measured. Furthermore, the change in α depends on the chemical species of contaminant, and there are no flights for which α, contaminant thickness, and contaminant species are all measured. Even if there were, the actual deposition on any spacecraft surface is a complicated combination of all the condensable species outgassed by the spacecraft. The best that can be done is to give the range of observed delta α vs. thickness values for past spacecraft and assume that future spacecraft are going to outgas similar species and therefore exhibit similar solar absorptance degradation.

2.5.7.2 Passive Contamination Control Techniques

To minimize performance degradation requires the implementation of passive contamination control efforts. For a designer, the choices are either to minimize the quantity of source materials or to physically block the materials from the source so it cannot redeposit on a surface which must remain clean. Three methods of passive contamination control are:

- Selection of low outgassing materials;
- Atomic oxygen cleaning;
- Spacecraft configuration (i.e., contaminant migration and transport paths); and
- Spacecraft temperature.

2.5.7.2.1 Selection of Low-Outgassing Materials

Materials which outgas, such as paints, composites, thin polymeric films, or adhesives which are organic based, will likely outgas over a long period of time. Some materials may outgas at a significant rate for an extremely long time. For these materials, short-term (24 h) outgassing test may not be appropriate for characterizing their performance. For example, sixteen specimens of DC 6-1104 RTV silicone adhesive used to attach the Velcro strips on the LDEF AO178 experiment showed an average total mass loss (TML) of 0.34 wt%, as determined by ASTM E595,[132] compared with original ground control measurements of 0.14 wt%. Specimens taken from the exposed bond line and from under the center portion of the Velcro showed no essential difference in the TML measurements (ref. 110). The conclusion is that, left indefinitely, this material will continue to outgas very slowly until it is gone. Under these conditions, the total amount of material becomes a significant consideration because the material never appears to "bake out." In addition, bearing in mind the effects of oxidation caused to many substances by atomic oxygen (i.e., volatile byproducts), standardized VCM criteria are obviously no longer enough to be representative of the outgassing of materials in LEO and to allow their selection for use in a space environment.

2.5.7.2.2 Atomic Oxygen Cleaning

In LEO, ram and near-ram surfaces will "clean" by exposure to AO. For example, cleaning a hydrocarbon from an optical sensor surface could be achieved by turning the surface to the ram direction. However, other materials which also react with AO could be present. If siloxane-based films are present, these materials can be converted to nonvolatile silica type (SiO_x) species,

potentially trapping other contaminant species and allowing the opportunity for darkening of surfaces by radiation and the subsequent permanent spacecraft performance degradation. In addition, such exposure can damage the substrate, so this "cleaning" is limited in practice.

2.5.7.2.3 Spacecraft Configuration

Physically blocking sensitive locations from the line-of-sight of any potentially significant outgassing source is the most direct method of minimizing contamination. Heavy deposits around selected vent paths from the interior of LDEF demonstrate the need for careful consideration of the location and orientation of vents relative to spacecraft surfaces (ref. 110). Venting should be directed normal to spacecraft surfaces. In addition, vent paths normal to the direction of motion should also minimize return flux. This solution is best considered in the design phase.

2.5.7.2.4 Spacecraft Temperature

The higher the surface temperatures of the spacecraft can be maintained early in the mission, and without damaging essential components, the less opportunity for material redeposition. However, orientation of surfaces toward the Sun to increase volatility by temperature increases would also run the risk of permanent photo-induced deposition.

2.5.7.3 Contamination Control Plan

The process of achieving the required cleanliness levels requires a contamination control program that starts during the preliminary design phase and continues through to the end of mission life. Table 2-20 summarizes the required design activity and the subsequent impact on the contamination control program.

Table 2- 20. Relationships Between Design Activities and Contamination Control Plan

Design Activity	Impact on Contamination Control
Determination of Performance Requirements	Defines system sensitivities
Definition of Configuration	Defines relationship between sensitive elements and sources of contamination
Selection of Materials, Components, Subsystems	Affects outgassing, particle, generation, and other functions
Planning of Operations for Factory, Launch Site, and Flight	Affects the ability to meet requirements and minimize cost
Perform Contamination Analyses	Determines if the configuration, materials, components, and subsystems that are used are likely to result in the cleanliness levels needed to meet system performance requirements
Prepare a Contamination Control Plan	Summarizes the requirements, goals, and procedures Used to provide guidance to all activities including monitoring that impact contamination control
Perform Development Tests	Tests should be performed early enough to affect designs without increasing costs

The determination of system performance requirements leads to a definition of the sensitivity of the system to contaminants and the generation of a contamination budget. This budget is based on the stray light rejection requirements and optical throughput requirements at end of life. If particulates are deemed to be a critical driver in the design, a particulate budget is allocated to the various steps required to fabricate, assemble, and integrate the payload. In order to allocate contamination levels to the various surfaces of the structure, an assumption is made regarding re-distribution of the particulate matter from the structure to the optics during the launch process.

The configuration of the system defines the relationship between the elements that are sensitive to contamination and the sources of contamination. This configuration can be changed to eliminate or, at least, minimize the contamination. The sources of contaminants include materials and components on the surface of the spacecraft as well as materials and components inside the spacecraft that get out through intentional and unintentional vents. The locations of these vents are frequently a critical factor in the contamination of sensitive components. The configuration also has a bearing on how easy or difficult it is to clean sensitive elements during the various phases of ground operations.

The selection of the materials, components, and subsystems so as to minimize outgassing and generation of particles involves tradeoffs with the need to meet the other functional requirements. These other functional requirements include temperature and radiation stability, mechanical and electrical properties, and resistance to atomic oxygen.

As the design develops it is possible to consider preliminary planning for ground and flight operations including those procedures that will monitor and minimize contamination. In this way design changes can be implemented early.

The contamination analyses are used to determine if the materials, components, and subsystems can be expected to meet the performance requirements for the system. When the analyses are performed early in the design process it is possible to make necessary changes with a minimum impact on schedule and cost. As the design develops, the analyses can be fine tuned for critical items.

The contamination control plan is a summary of the requirements and the procedures to be used to meet these requirements. The contamination control plan should start early in the design phase of a project. There may be many unresolved issues and blanks in the plan, but these indicate work that must be accomplished and to allow schedules to be set for implementation. One important purpose of the contamination control plan is to assure that the requirements and procedures are implemented in the working documents. It also allows all parties to review it and reach a consensus on the approaches to be followed starting early in the design activity.

Development tests should be used to get data that are needed in the design of the new space system. Typical development tests include outgassing tests on materials and components where there is a lack of data in the literature or special test conditions are required. Monitoring of the manufacturing and assembly processes ensures that the requirements set forth in the contamination control plan are met.

2.6 VACUUM-INDUCED OUTGASSING EFFECTS

2.6.1 Introduction

When exposed to thermal-vacuum conditions, polymer matrix composites are known to outgas due to moisture desorption or material volatilization or decomposition. Once the outgassed species leave the surfaces, they will be at such a low pressure that they travel in a line-of-sight trajectory until they either hit thespacecraft surface (where they will bounce or adhere) or leave the vicinity of the spacecraft at a relative velocity of several kilometers/second. Approximately 1 in 10,000 to 1 in 100,000 molecules will collide with another molecule (ambient or contaminant) and return to the spacecraft where they might hit a sensitive surface. A portion of the contaminants that contact spacecraft surfaces will stick forming a molecular layer that can darken or be eroded with subsequent exposure to the space environment (e.g., UV, atomic oxygen)

2.6.2 Spacecraft Performance Effects

Molecular contamination can degrade the performance of thermal control surfaces and solar cells. This can be particularly important if sensors are cooled passively by second surfaces mirrors that are illuminated by the Sun. The effects of relatively thin molecular films on the solar absorptance of second surface mirrors has been shown in Figure 2-39. Typically molecular films must not exceed 1000 Å on these sensitive surfaces at the end of the spacecraft's life. In addition, thin deposits of molecular contaminants that condense on the cold optical surfaces and infrared sensors can seriously reduce optical throughput. Furthermore, molecular contamination from composite materials can lead to the formation of a "cloud" of outgassed molecular particles, resulting in a significant increase in light scattering that attenuates the signals that the sensors are receiving. Molecular films as thin as a few hundred angstroms can seriously reduce the sensor performance, especially when viewing targets close to bright sources of light such as the Sun.

2.6.3 Spacecraft Material Outgassing Databases

The outgassing/volatiles characterization of composites is determined by the procedures of the ASTM Test for Total Mass Loss and Collected Volatile Condensable Materials from Outgassing in a Vacuum Environment (E 595). This industry standard material contamination screening procedure is based on measuring the total mass loss (TML), collected volatile condensable material (CVCM), and water vapor regained (WVR). TML is important from a molecular "cloud" effect which can degrade instrument performance, while CVCM is a measure of the potential for outgassed products to deposit on critical optical surfaces. WVR is the mass of the water vapor regained by the specimen after an optional reconditioning step. WVR is calculated from the differences in the specimen mass determined after the test for TML and CVCM and again after exposure to a 50% RH atmosphere at 23°C for 24 hours. Values below 1.0% TML and 0.1% CVCM have been acceptable for current spacecraft performance needs, but the requirements are expected to become more stringent for future surveillance spacecraft systems (see below).

Outgassing data for spacecraft materials can be obtained from the following source documents:

- JSC Report 08962, "Compilation of VCM Data of Nonmetallic Materials,"
- ESTEC, "Outgassing and Thermo-Optical Data For Spacecraft Materials," April 1992
- Goddard Space Flight Center, "Outgassing Data for Selecting Spacecraft Materials, NASA Reference Publication 1124, 1984.
- MSFC Handbook 1674

Figure 2-47 compares typical ASTM E595 outgassing test results for a variety of carbon reinforced polymer matrix composite system.[133] Table 2-21 presents outgassing test results for a variety of spacecraft composite materials. A comparison of the outgassing results points to significantly lower outgassing TML values for carbon polycyanates and carbon thermoplastics composites compared to the conventional carbon epoxy composites.

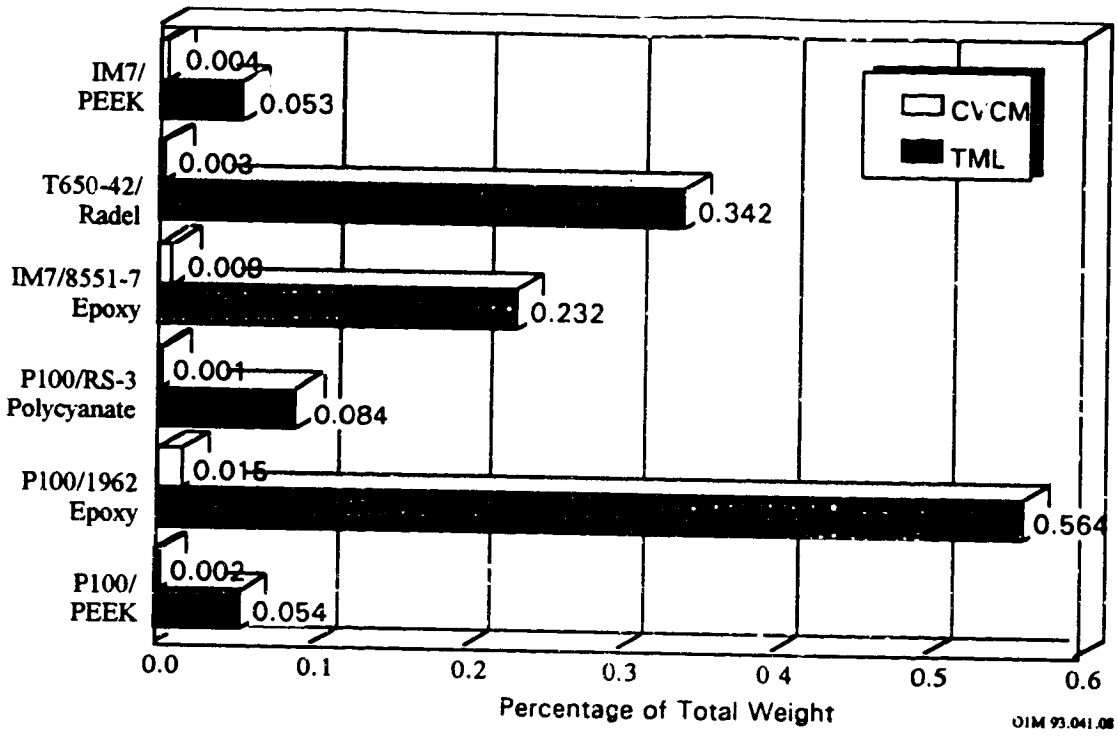

Figure 2- 47. Comparative Outgassing of Polymer Matrix Composites

Table 2- 21. Outgassing Properties of Laminated Composites

Material	Matrix Type	TML %	VCM %	WVR%	Ref.
T300/934	Epoxy	0.58	.00	.00	NASA JSC[134]
PAN50/954-3	Epoxy	0.135	0.00549	0.195	TRW[133]
T50/934	Epoxy	0.4	0.09	.00	NASA JSC
HMS/934	Epoxy	1.09	0.00	0.51	NASA JSC
GY70/954-3	Epoxy	0.104	0.00792	0.0736	TRW
P75/930	Epoxy	0.384	0.007		TRW
XN50/RS-3	Polycyanate	0.0851	0.00379	0.0287	TRW
IM7/PEEK	Thermoplastic	0.053	0.004		TRW

2.6.4 Spacecraft Material Outgassing for Cryogenic Applications

Although typical carbon/epoxy structures meet the current NASA outgassing acceptance levels of 1.0% TML and 0.1% CVCM, certain spacecraft systems and sensors that operate at extremely cold temperatures are sensitive to much lower outgassing acceptance levels. The development of spacecraft systems (e.g., FEWS, Brilliant Pebbles, Brilliant Eyes, CERES, AXAF) with sensors, astronomical telescopes, and spectrographs operating at extremely cold temperatures (i.e.,<100 K) have imposed lower contamination levels requirements for spacecraft structures and hence, the need for spacecraft materials with reduced outgassing at these lower temperatures. In addition, the current industry outgassing measurement test, ASTM E 595, is conducted at test conditions that do not simulate the stringent space environment and hence, does not adequately characterize the contamination potential of composite materials.

Over the past 3 years ASTM Committee E21 has been in the process of approving a new test method that utilizes quartz crystal microbalances to determine the outgassing kinetics of spacecraft materials at 3 different deposition temperatures and 3 different source temperatures. The purpose of this new test method is to provide the data necessary for spacecraft contamination models to accurately predict how much will collect on spacecraft surfaces. Preliminary data on outgassing products collected on QCMs at 150 K were obtained on a prototype test apparatus developed by the Lockheed Missile and Space Company.[135]

The TRW Contamination Effects Facility, which derives a molecular outgassing rate from the mass accumulation on a temperature controlled quartz crystal microbalance below 150 K, have demonstrated marked improvements in reduced outgassing from polycyanates and thermoplastics. Table 2-22 reveals lower outgassing rates for both the IM7/PEEK and the XN50/RS-3 polycyanate composites by an order of magnitude in comparison with the outgassing rate measured for the P75/ERL-1962 epoxy composite.[136] Water represented most of the condensable material from both the carbon PEEK and the polycyanate composites as verified by mass spectrometry analysis (water has a condensation temperature of 150 K under vacuum).

Table 2- 22. Outgassing Rates for Structural Materials

Material	Outgassing Rate, 100 K
P75 Carbon/ERL-1962 Epoxy	1.60 ng/cm^2-s
XN50 Carbon/RS-3 Polycyanate	0.24 ng/cm^2-s
IM7 Carbon/PEEK Thermoplastic	0.17 ng/cm^2-s

A series of in-situ bakeouts were conducted to determine the change in the outgassing rates with time and to determine the total time to eliminate outgassing from the polymer matrix composites. Figure 2-48 shows the linear decay in the outgassing rates for both the PEEK and the polycyanate composites with increasing bakeout times at 323 K (50°C) (ref. 136). The mass accumulation on the TQCM were measured both at 175 K and 100 K with the composite specimens at 298 K (25°C). The outgassing rate at 100 K was higher than that measured at 175 K, which is attributed to the significant desorption of water from both the PEEK and polycyanate composites. Both the PEEK and the polycyanate composites exhibited similar behavior in the changes in the outgassing rates with time. The 175 K outgassing rate decreased to zero (i.e., 1x10-15 g/cm^2-sec) by approximate 300 hours The 100 K outgassing rate decreased to 1x10-12 g/cm^2-sec by 400 hours. Extrapolation to a zero outgassing rate indicated that more than 1000 hours (~42 days) of extended bakeout at 323 K (50°C) would be required for the composites to completely desorb their absorbed water. This predicted outgassing time is similar to that observed from the LDEF UTIAS Experiment No. A0180 where it took about 40 days for the T-300 carbon/934 epoxy and the T-300 carbon/SP-288 epoxy to outgas and 80 days for the T-300 carbon/5208 epoxy to outgas (see page 3-31).

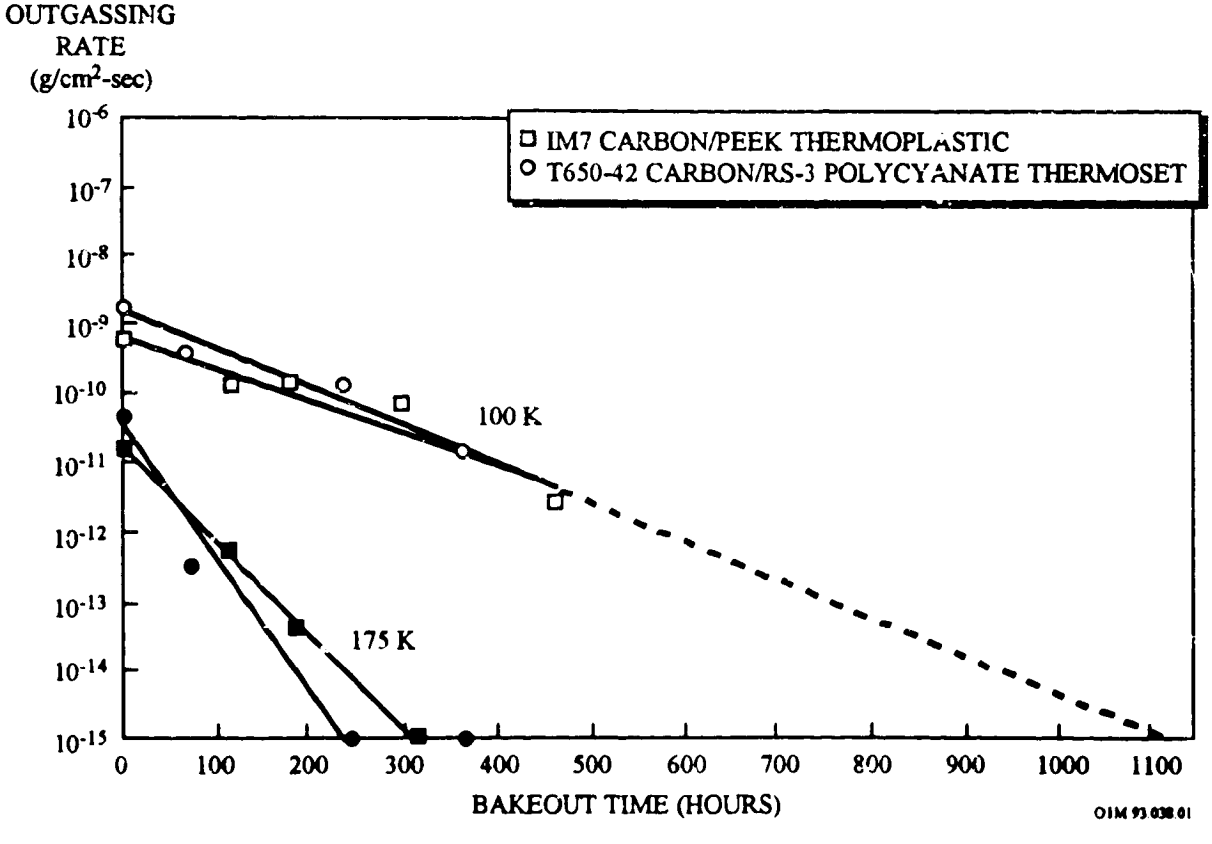

Figure 2- 48. Outgassing Rates as a Function of Bakeout Time and Absorption Temperature

2.7 SPACECRAFT CHARGING EFFECTS

2.7.1 Introduction

Technically, spacecraft charging is a variation in the electrostatic potential of a spacecraft surface with respect to the surrounding plasma. Two types of spacecraft charging are typically encountered. The first, called absolute charging, occurs when the entire spacecraft potential relative to the ambient space plasma is changed uniformly by the encounter with the charging environment. The second type, called differential charging, occurs when parts of the spacecraft are charged to different negative potentials relative to each other. In this type of charging, strong local electric fields may exist.

2.7.2 Spacecraft Charging Concerns

2.7.2.1 Surface Charging

Surface charging of spacecraft materials is caused primarily by electrons with energies in the few keV (kiloelectron volt) to tens of keV range. The potential reached during charging events depend on many additional factors, the most important being secondary-electron emission due to solar ultraviolet radiation and due to primary electrons and ions, and the density of the cold plasma which may supply a neutralizing current to a charged body. Differential potentials between different locations on a spacecraft are controlled by geometric considerations, material properties, and charging time-constants. For example, spacecraft surfaces are not uniform in their material properties, surfaces will be either shaded or sunlit, and the ambient fluxes may be anisotropic. Materials with different properties and adjacent to each other, can charge to different voltages and produce electrostatic discharges if the electric field gradient becomes too large. Insulators shadowed by the vehicle may charge differentially with respect to nearby vehicle frame which is "clamped" to the space plasma potential by secondary emission from an illuminated portion of the vehicle frame. These and other charging effects can produce potential differences between spacecraft surfaces or between spacecraft surfaces and spacecraft ground.

2.7.2.2 Bulk Charging

Bulk charging of spacecraft materials is caused primarily be electrons with energies of a few hundred keV to 1.5 MeV (megaelectron volts). These energetic electrons can penetrate thin shielding (spacecraft skin, cable shielding, etc.) and deposit charge in cables, circuit boards, and conductors. Depending on the fluence of the primary electrons and the conductivity of the dielectric, the material may experience a discharge (see below), which may couple into sensitive electronic circuits. In typical dielectrics, the breakdown may occur with fluences on the order of 10^{11} to 10^{12} e^-/cm^2. Electron fluxes with energies above a few hundred keV maximize at altitudes several Earth radii below geosynchronous orbit following large magnetic storms. However, even at geosynchronous altitude, energetic electrons can alter electrical properties of dielectrics and influence differential charging effects. Certain design approaches can reduce discharges due to bulk charging. Shielding and grounding of cables and circuit are among these methods (see below).

2.7.2.3 Discharging

When the electric field between two objects exceeds a critical value (about 10^6 volts/meter), a discharge can occur. The buildup of large potentials on spacecraft relative to the ambient plasma can present a serious electrostatic discharge (ESD) design concern because structural damage is a real possibility. Even weak discharges have been related to a variety of problems which include:

- Upsets of electronics ranging from logic switching to complete system failure. (such as turning of a recorder or activating a radio)
- Breakdown of vehicle thermal coatings
- Amplifier and solar cell degradation
- Degradation of optical sensors

Electrostatic discharges resulting from satellite orbital charging are characterized in Figure 2-49.[137]

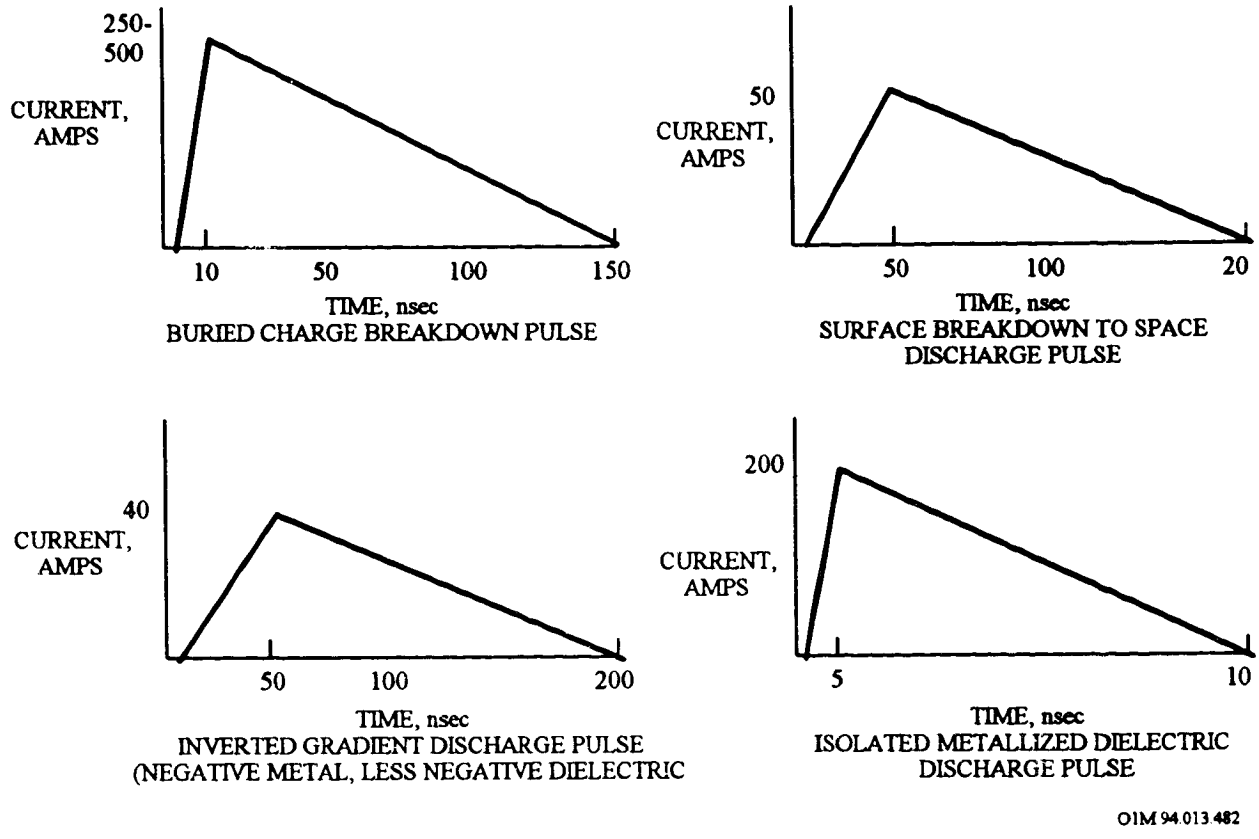

Figure 2- 49. Electrostatic Discharge Characteristics

2.7.2.4 Contamination

Spacecraft charging enhances surface contamination, which degrades thermal properties. Molecules emitted by the spacecraft can be ionized by solar radiation while still within the spacecraft plasma sheath and be reattracted to negatively charged surfaces. The more negative the potential on the surface, the higher the probability of contamination. Trying to control the potential of a spacecraft ground may increase the differential potential to adjacent dielectric surfaces and might even increase contamination buildup on some surfaces. Analysis of data from the P78-2 satellite (part of the joint USAF-NASA Spacecraft Charging at High Altitudes SCATHA program) indicates that contamination rates are increased during periods of spacecraft charging.

The P78-2 satellite experiment included a Temperature Controlled Quartz Crystal Microbalance which was designed to measure the rate of deposition of contaminants on satellite surfaces.[138] The TQCM included a grid upon which a voltage could be imposed to repel ions. Long-term average mass accumulation rates over the four periods studied ranged from 0 to 31% mass accumulation rates over the four periods studied ranged from 0 to 31% greater when 0 to 500 eV ions were allowed to reach the mass detector than when they were reflected.[139]

2.7.3 Design Guidelines for Controlling Spacecraft Charging Effects

On orbit charging can and has resulted in spacecraft anomalies. The design approach for the control of orbital spacecraft charging is to minimize the development of differential potentials sufficient to initiate arc discharges wherever possible. Current spacecraft design utilizes large areas of dielectrics for thermal management (thermal blankets, optical solar reflectors, solar cell cover glass) and antenna covers. These requirements eliminate the possibility of avoiding arc discharges. As a result, the design philosophy is to minimize the differential potentials from developing wherever practically possible. Where discharges are possible, an evaluation is performed to assess the effect of a discharge, and where unacceptable results will occur, a design change is implemented.

The reason for this philosophy is that a thermal failure can be demonstrated as a system failure, whereas an arc discharge may influence system operations. In assessing the impact of orbital charging mitigation on thermal design, thermal design will always take precedence, where the two are not compatible. In these cases of conflict, the alternate is to ensure that any discharges do not cause unacceptable responses by the spacecraft electronics.

2.7.3.1 Grounding

The spacecraft design needs to provide electrostatic grounding connections between all metallic and composite (carbon fiber reinforced composite) elements of the spacecraft and the structural ground reference plane. All structural and mechanical parts, electronics boxes, enclosures, etc., of the spacecraft are to be electrically bonded to each other. According to the NASA charging guidelines,[140] all principal structural elements shall be bonded by methods that assure a direct-current (dc) resistance of less than 2.5 mΩ at each joint. The collection of electrically bonded structural elements is referred to as "structure" or structure ground. The objective is to provide a low-impedance path for any ESD-caused currents that may occur and to provide an excellent ground for all other parts of the spacecraft needing grounding. If structure ground must be carried across an articulating joint or hinge, a ground strap, as short as possible, should carry the ground across the joint.

2.7.3.2 Exterior Surface Materials

For differential charging control, all spacecraft exterior surfaces should be at least partially conductive. The best way to avoid differential charging of spacecraft surfaces is to make all surfaces conductive and grounded to the spacecraft structure. However, typical spacecraft surface materials often include insulating films such as Mylar, Kapton, Teflon, Fiberglas, glass, quartz, or other dielectric materials. Conductive surface coatings are used to minimized the differential charging of spacecraft surfaces. These include conductive conversion coatings on metals, conductive paints, and transparent partially metallic vacuum-deposited films, such as indium tin oxide. The following materials have been used to provide conducting surfaces on the spacecraft:

- Vacuum-metalized dielectric materials in the form of sheets, strips, or tiles. The metal-on-substrate combinations include aluminum, gold, silver, and Inconel on Kapton, Teflon, Mylar, and fused silica.
- Thin, conductive front-surface coatings, especially indium tin oxide on fused silica, Kapton, Teflon, or dielectric stacks
- Conductive paints, carbon-filled Teflon, or carbon-filled polyester on Kapton (e.g., Sheldahl black Kapton)
- Conductive adhesives
- Exposed conductive facesheet materials)carbon/epoxy or metal)
- Etched metal grids or bonded (or heat embedded) metal meshes on nonconductive substrates
- Aluminum foil or metalized plastic film tapes

It should be recognized in the design phase that there may be areas for which use of conductive surfaces is particularly crucial, such as areas adjacent to receivers/antennas operating at less than 1 GHz, sensitive detectors (Sun and Earth detectors) or areas where material contamination or thermal control is critical. For these applications use of indium tin oxide (ITO) coatings is recommended.

2.7.3.3 Thermal Control Materials

All layers in multilayer insulation (MLI) blankets should be electrically grounded to the structure because ungrounded blankets will charge to high negative potentials. This requirement is applicable to multi-layer thermal blankets and other thermal control surfaces employing metallized films which offer more than 25 cm^2 of exposed surface. Figure 2-50 illustrates the charging characteristics for a Kapton thermal blanket in a 1% substorm environment[141] (a 1% substorm environment represents the charged particle flux that will be experienced in a GEO orbit 1% of the time). All layers of the thermal blanket must be grounded because high energy electrons will penetrate into the inner layers and charge those layers. Ungrounded inner layers will result in large internal electric fields which could lead to discharges. Figure 2-51 shows the potential and electric field that can be built up in a thermal blanket as a function of blanket depth (ref. Stillwell et al., 1992). Figure 2-51 is for a 500 second exposure in a 1% substorm, with only the top and bottom VDA layers grounded. The requirement to ground all layers is consistent with the recommended practices of the NASA charging document (ref. 146).

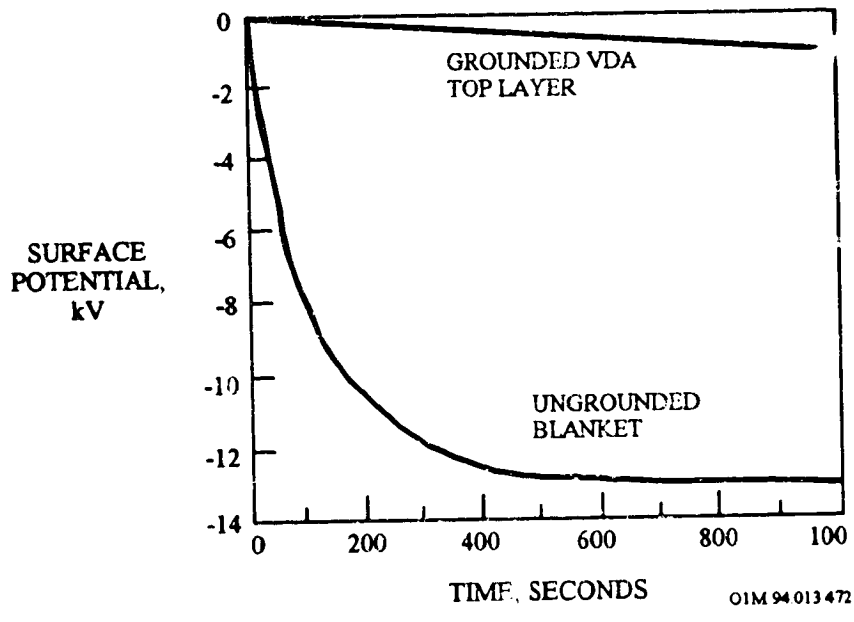

Figure 2- 50. Charging Characteristics of Kapton Thermal Blankets in a 1% Substorm Environment

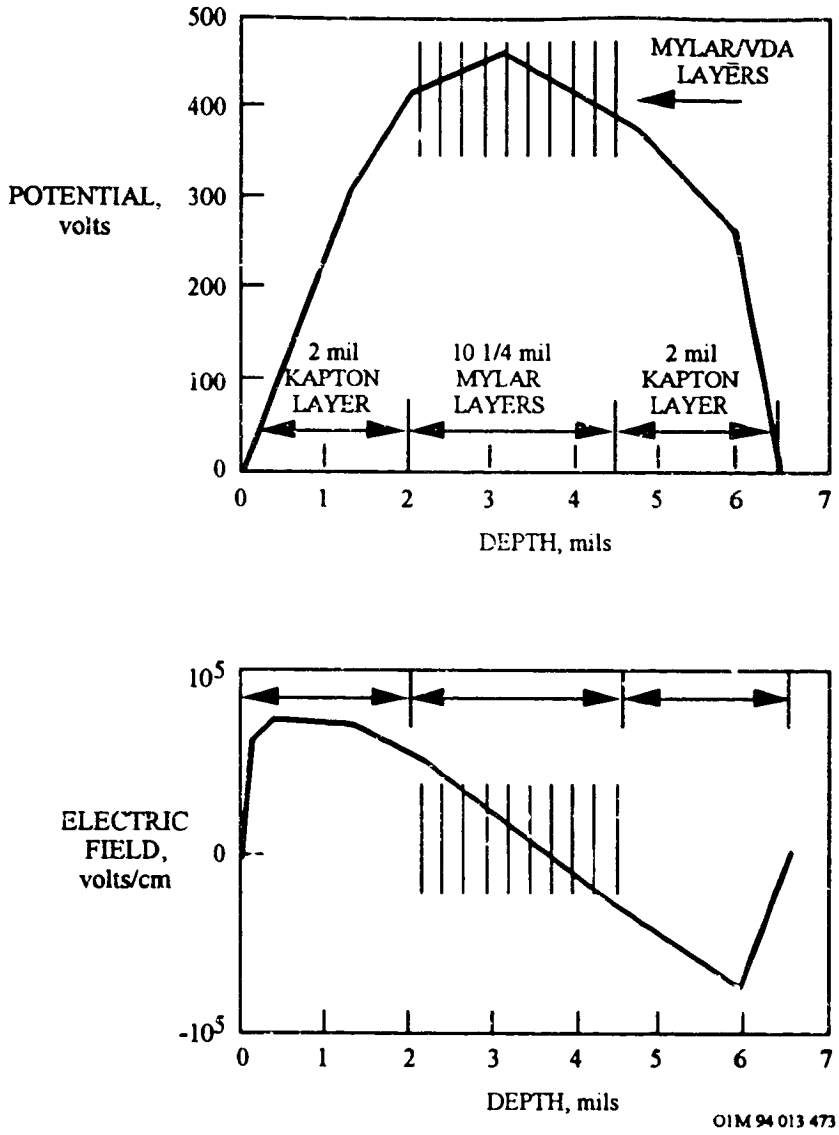

Figure 2- 51. Interior Potential and Electric Field in Thermal Blankets with only Top and Bottom Layers Grounded

Ground straps are typically used to meet a less than 25 Ω dc grounding requirement[142] (measured during manufacturing).[f] The NASA charging guidelines recommend a less than 10 Ω dc resistance between blanket and structure. The number of ground straps required is based on blanket area and is given in Table 2-23. For blankets with thick outer layers (>3 mils) or Teflon (Teflon is a highly dielectric material), signal lines and cabling placed within 3 inches of the blanket periphery should be minimized.

Table 2- 23. Number of Ground Straps Required for Thermal Blankets

Surface Area (A) of Blanket cm^2	Number of Straps
$A \leq 25$	0
$25 < A \leq 100$	2 - If signal cable passes within 3 inches of periphery 0 - elsewhere
$100 < A \leq 900$	2
$900 < A \leq 8000$	3
$8000 < A \leq 16000$	4
Each Additional 8000	1 Additional Strap

Multiple ground straps are required for large area blankets to minimize the surface potential in case of the VDA (vacuum deposited aluminum) breaking up. While grounding the VDA layers will not eliminate the charge buildup on the dielectric surface, it will eliminate metal-to-metal discharges. Metal-to-metal discharges deliver much larger peak currents than dielectric-to-metal discharges, and therefore, pose a greater EMI (electromagnetic interference) hazard.

[f] The thermal blanket resistance requirement is 1000 Ω dc. However, a requirement of 25 Ω dc is imposed at the manufacturing level because handling and insulation is expected to increase the resistance. The 25 Ω dc requirement is to insure that the blanket starts with a good electrical connection.

2.7.3.4 Shielding

The primary spacecraft structure, electronic component enclosures, and electrical cable shields shall provide a physically and electrically continuous shielded surface around all electronics and wiring (Faraday cage).

The primary spacecraft structure should be designed as an electromagnetic-interference-tight shielding enclosure (Faraday cage). The purposes of the shielding are (1) to prevent entry of space plasma into the spacecraft interior and (2) to shield the interior electronics from the radiated noise of an electrical discharge on the exterior of the spacecraft. All shielding should provide at least 40-dB attenuation of radiated electromagnetic fields associated with surface discharges. An approximately 1-mm thickness of aluminum or magnesium will generally provide the desired attenuation. This enclosure should be as free from holes and penetrations as possible. Many penetrations can be made relatively electromagnetic interference tight by use of well-grounded metallic meshes and plates. All openings, apertures, and slits shall be eliminated to maintain the integrity of the Faraday cage.

The metalization on multilayer insulation is insufficient to provide adequate shielding. Layers of aluminum foil mounted to the interior surface and properly grounded can be used to increase the shielding effectiveness of blankets or films. Aluminum honeycomb structures and aluminum facesheets can also provide significant attenuation. Electronic enclosures and electrical cables exterior to the main Faraday cage region should also be shielded to extend the coverage of the shielded region to 100 percent of the electronics.

2.8 PENETRATING CHARGED PARTICLES EFFECTS

2.8.1 Single Event Upsets

Single event upsets (SEUs) are bit flips in digital microelectronic circuits. SEUs can cause:

- Damage to stored data
- Damage to software
- The central processing unit (CPU) to halt
- The CPU to write over critical data tables
- Various unplanned events including loss of mission

Single event latchups (SELs) are when digital microcircuits short their power supplies to ground. These events can cause:

- Inoperability
- Permanent failure of the affected components
- Computer failure

SEUs in spaceborne electronics are caused by the direct ionization of silicon material by a high energy ion passing through it. The near Earth particle environment includes galactic cosmic radiation (GCR), energetic particles from the Sun, and trapped protons. The normal factor in SEU production is the heavy ion cosmic ray, although large solar flares can produce a substantial increase in SEUs. Fortunately, such large flares occur only once every few years (see Chapter 1). For satellites in near Earth orbits (less than four Earth radii), an additional factor is the radiation belts, which trap and hold high energy charged particles. A satellite passing through these belts is subjected to a high flux of electrons and protons, and trapped protons are capable of causing SEUs in certain types of chips (see Chapter 1).

Hence, high energy particles degrade electronics performance by the accumulation of material microstructural damage. Different devices have varying degrees of total dose vulnerability which can range from very soft (700 rads) to very hard (10^6 rads). Figure 2-52 shows the accumulated radiation dosage for a five year mission due to Van Allen particles for a variety of orbits.[143] Also plotted are the typical shielding thicknesses available from the satellite skin and electronic boxes.

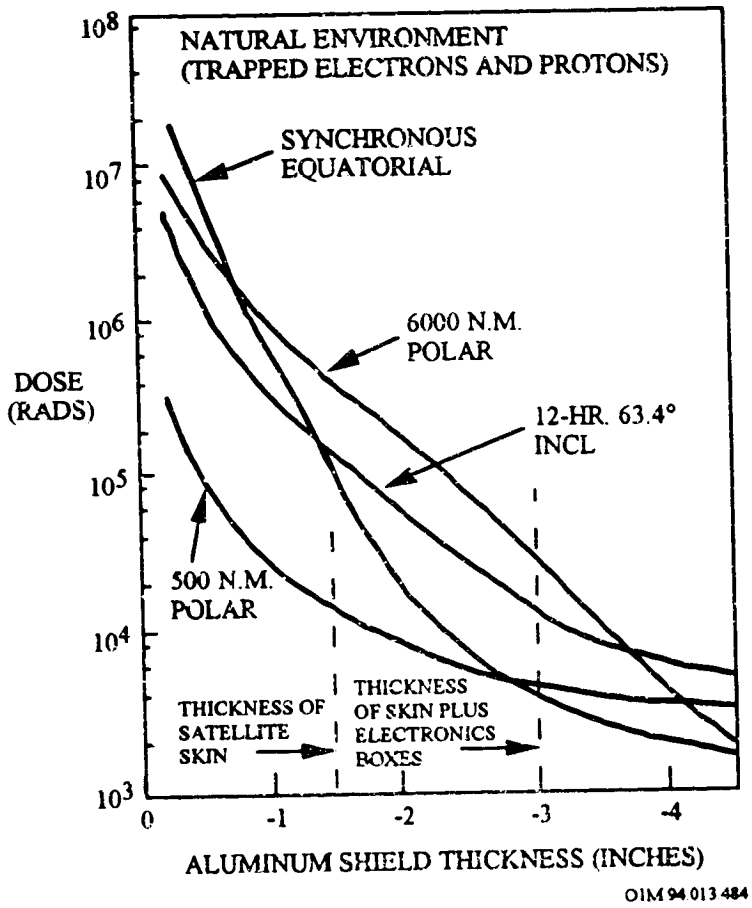

Figure 2- 52. Accumulated Radiation Dosage Over a Five Year Mission due to Van Allen Belt Particles

2.8.2 Design Guidelines

Four methods or techniques are available to protect satellite electronics from the effects of radiation. Satellite designers must evaluate these methods in order to trade off the penalties and develop a protection scheme while still meeting the system performance requirements.

Shielding is an obvious solution. Figure 2-53 depicts the cosmic ray flux as a function of energy deposition in silicon.[144] The deposition curve is plotted for several thicknesses of shielding. Note that shielding of 20g/cm^2 reduces the flux by less than a factor of 10 compared to the standard satellite shielding of 2 g/cm^2 provided by a typical skin plus electronics box. Clearly, from Figure 2-53, a factor of 10 decrease in occurrence is not a great victory since an upset every 15 days is not much better than one every 1.5 days in the life of a 10-year system. Also, the weight and volume of 20 g/cm^2 shielding, 2.0 inches of aluminum, is not a very reasonable solution.

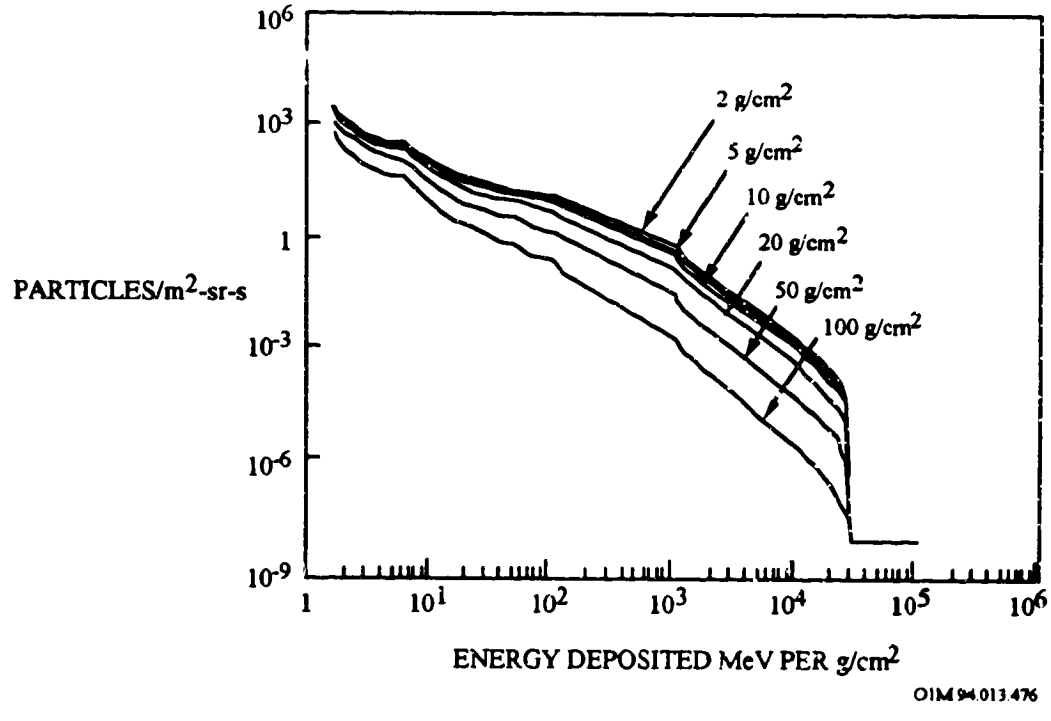

Figure 2- 53. Cosmic Ray Flux as a Function of Shielding

Avoiding the problem through parts selection is the most obvious solution. In fact, many older technologies such as plated wire, or core or solid state memory with large feature size element (>10 microns) can be used to achieve a small, or zero, upset rate. The problem here is usually operating speed and power consumption. The parts may not meet design or system performance goals. Various investigators have designed and built upset-resistant parts while maintaining circuit performance.

Triple memory redundancy can beat the speed problem as well as provide a high degree of fault tolerance from other causes, such as parts failure. Negative factors include the additional weight and power required for the additional memory.

Error detection and correction (EDAC) offers the advantage of a single memory, but with additional bits stored to support the EDAC. Also, the processor and software must perform EDAC on some sort of regular basis to ensure a correct memory. As upset rates increase, the point could quickly be reached where most of the time is spent doing EDAC rather than any productive work.

The final method of dealing with SEUs is to regularly reset the onboard computers. A variation of this is to use a regular sequence when commanding the satellite; any change in the sequence would be easy to detect and correct. Computer systems which can be reprogrammed from the ground might allow other alternatives. This method is usually unsatisfactory, unless an occasional reset is acceptable within the system performance requirements.

2.9 ENVIRONMENTAL SYNERGISTIC EFFECTS

2.9.1 Introduction

In order to determine or predict the performance capability of space systems during their operational lifetimes, assessments must be made of the combined, synergistic space environment effects.

2.9.2 Combined Atomic Oxygen and Ultraviolet Radiation Effects on Polymers

In the early shuttle flights, which had a very short flight duration of approximate 40 hours, fluorocarbon FEP Teflon appeared to be stable. Hence, suggesting a potential use for long-term use in LEO. In fact, due to the short mission of these Effects of Oxygen Interaction with Materials (EOIM) experiments, which limited oxygen atom fluence and also the UV exposure, the erosion of the Teflon was too low on EOIM I and II to make an accurate measurement. A limit for the erosion rate was determined to be $\leq 0.05 \times 10^{-24}$ cm^3/atom.[145] The Teflon surfaces returned from the Solar Max Repair Mission did show evidence of the characteristic texture of an oxygen atom-eroded surface, but measurements of material loss were not reported.[146]

Recent experiments, however, appear to indicate that the FEP Teflon exhibits an induction period, after which degradation takes place. A study performed by Koontz, et al.[147] determined that the reaction rate for FEP Teflon with AO in a flowing afterglow source was significantly increased by the presence of vacuum ultraviolet (VUV) radiation provided by a Krypton resonance lamp. They found the reactivity of Kapton with atomic oxygen in the presence of VUV increased, but not as significantly as that of Teflon. Hence, synergistic effects of atomic oxygen and ultraviolet radiation must be evaluated when determining the overall durability of a material.

FEP Teflon exposed to atomic oxygen for the first 2 months on the Lockheed flight experiment also showed little recession.[148] However, there seemed to be a non-linear degradation response in the thermal surface properties (i.e., α/ε) with increasing AO fluence. For the first 30 days the surface properties were constant, indicating that there was an induction period before Teflon underwent oxidation in LEO. After about 60 days and an atomic oxygen fluence of about 1.0×10^{22} atoms/cm^2, thermal analysis predicted the start of an average sample emittance decrease. (Estimates of polymer thicknesses at progressive times/oxygen fluences were made by using previously determined thickness versus infrared emittance data for FEP Teflon.) In fact, after 2 months and ~100 esh UV, the optical properties of the silver Teflon on the Lockheed flight began to change in a manner suggesting material recession. This indicated either thickness loss or some bulk property change in the FEP Teflon film. After 105 days and a fluence of 1.85×10^{22} atoms/cm^2,

the sample emittance, ε, had decreased from 0.56 to 0.37. The thickness loss inferred, from this reduction in ε was at least 50% of the original 0.025 mm sample. For the last few days of exposure on the Lockheed experiment, the calculated recession rate was only about 0.13×10^{-24} cm^3/atom, barely one-third of the average LDEF rate, but significantly higher than the previously reported recession rate of $\leq 0.05 \times 10^{-24}$ cm^3/atom.

The thickness loss versus oxygen fluence relationship for FEP Teflon is shown in Figure 2-54 (ref. Knopf et al., 1985). Also shown is the relationship for Kapton. For the Kapton sample, the average oxidation rate, concluded from the 0.052 mm removal of material and a known atomic oxygen fluence of 0.121×10^{22} atoms/cm^2, was 4.3×10^{-24} cm^3/atom. When uncertainties were included, this 40% higher Kapton recession rate was in general agreement with the value of 3.0×10^{-24} cm^3/atom reported by Leger, et al.[149]

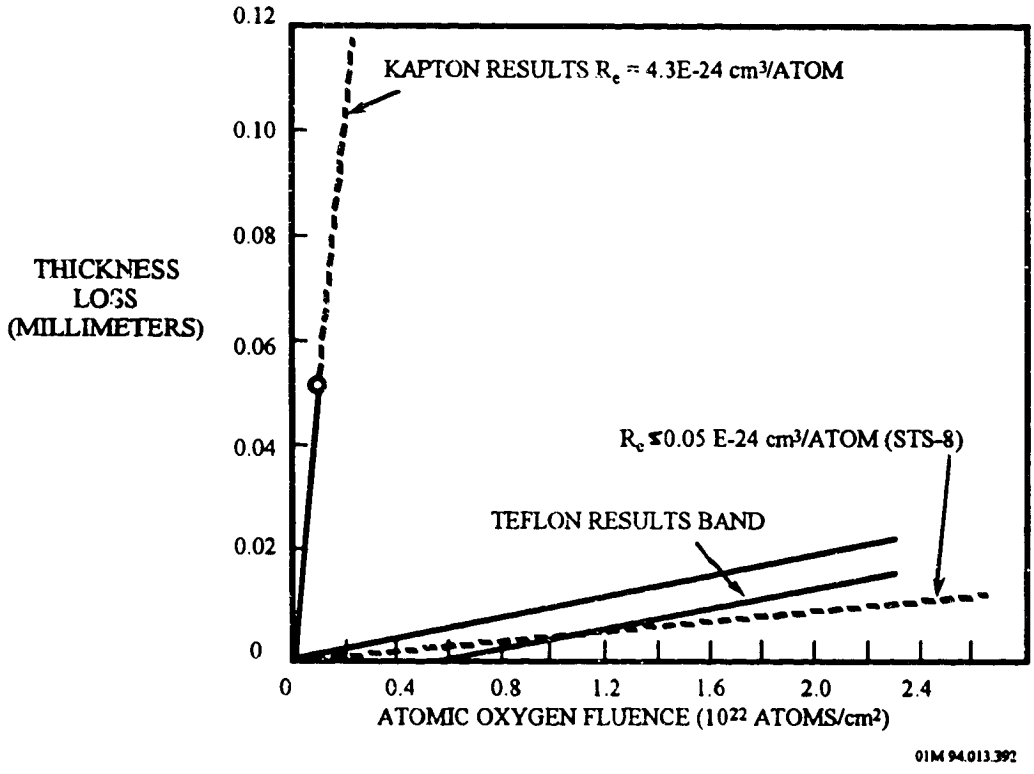

Figure 2- 54. Thickness Loss versus AO Fluence for Kapton and FEP Teflon

The well-documented erosion observed for silver Teflon on the leading edge of LDEF results[150] in a higher reaction efficiency for FEP Teflon than observed previously. Table 2-24 summarizes the various flight measurements of Teflon AO reaction efficiency.[151] The LDEF mission had a high UV exposure followed by an increasing atomic oxygen fluence during the flight, which resulted in nearly an order of magnitude higher reaction efficiency than observed on earlier

flights. The UV degradation, clearly indicated in the studies of the trailing-edge Teflon surface from LDEF, is undoubtedly responsible for the higher erosion observed on LDEF.[152] These data confirmed that atomic oxygen-induced recession of FEP in LEO is also a function of UV exposure level. This indicates that a synergistic effect exists with the atomic oxygen and UV. In contrast, linear relationships were observed for polymers such as Kapton, and there is good agreement on reaction efficiency between these same missions.

Table 2- 24. Flight Measurements of FEP Teflon Reaction Efficiency

Flight	AO Fluence atoms/cm^2	UV (esh)	Reaction Efficiency cm^3/O atom
STS-8 (EOIM-I)	8.58×10^{19}	≤50	Not measured
STS-41G (EOIM-II)	3.5×10^{20}	≤50	$<0.05 \times 10^{-24}$
Solar Max	$\sim 7 \times 10^{20}$	Unknown	Not measured
Lockheed Experiment	1.85×10^{22}	300	0.075 to 0.13×10^{-24}
LDEF	3.3 to 9.0×10^{21}	6,000 to 11,000	0.34×10^{-24}

Studies of this nature can provide insight as to mechanisms of polymer degradation due to LEO synergistic environmental effects as well as providing guidance as to requirements for proper ground based simulation facilities. Comparison of laboratory and flight data has indicated that there are two degradation mechanisms taking place in the LEO environment: (1) a fast surface oxidation; and (2) a slower, diffusion limited bulk oxidation (ref. 148). For most polymers, the oxidation rate controlling step is identified by numerous investigators as hydrogen abstraction and hydroperoxide formation.[153] Therefore, oxidation is dependent on the types of carbon-hydrogen bonds present in the polymer. When elements other than carbon and hydrogen are present in the polymer chain, dissociation energy of the additive bonds becomes a contributing factor in the stability of the polymer in an oxidative environment. For example, Teflon, a fluorocarbon which has all the hydrogens replaced by fluorines, is significantly more resistant to oxidation than its hydrocarbon counterpart. In contrast, the degradation of Kapton films within the LEO environment is attributed to a chain reaction involving hydroperoxide formation and free-radical initiation. This results in rapid surface oxidation accompanied by loss of mass and changes in surface morphology, while the bulk properties remain unchanged. However, silicone or siloxane coated Kapton and FEP Teflon films, as a result of their physical structures, are resistant to surface oxidation. Diffusion-limited oxidation then becomes the predominant reaction and leads to bulk property changes. Since diffusion limits the rate of oxygen buildup and, therefore, the rate of oxidation, these classes of materials will exhibit an induction period prior to degradation. Due to bulk property changes, surface cracking and crazing can take place.

2.9.3 Atomic Oxygen Undercutting of Impact Damage

Of particular importance for evaluating system performance are the interactions and synergisms of the various space environments (e.g., UV and AO) with the impact environments. Space environment exposure alters material properties, thereby changing the defects created by impacts. This is exemplified by the impact effects on LDEF's thermal control paints and composites. The impacts themselves can alter material states and expose underlying materials, allowing the space environments (e.g., AO) to further increase the damage area and to begin damaging previously unexposed areas. This is epitomized by the impact effects on LDEF's thermal control blankets. AO "undercutting" of polymer substrates under protective coatings is a phenomenon that can be a particular concern for space applications of multilayer insulation as demonstrated by DeGroh and Banks.[154] The phenomenon is illustrated in Figure 2-55. The low reaction probability with a polymer such as Kapton at the initial impact of monatomic oxygen causes the atom to scatter with a cosine distribution, so that even for coating defects (i.e., holes or cracks) facing the atomic oxygen ram direction, the underlying Kapton substrate will be undercut.

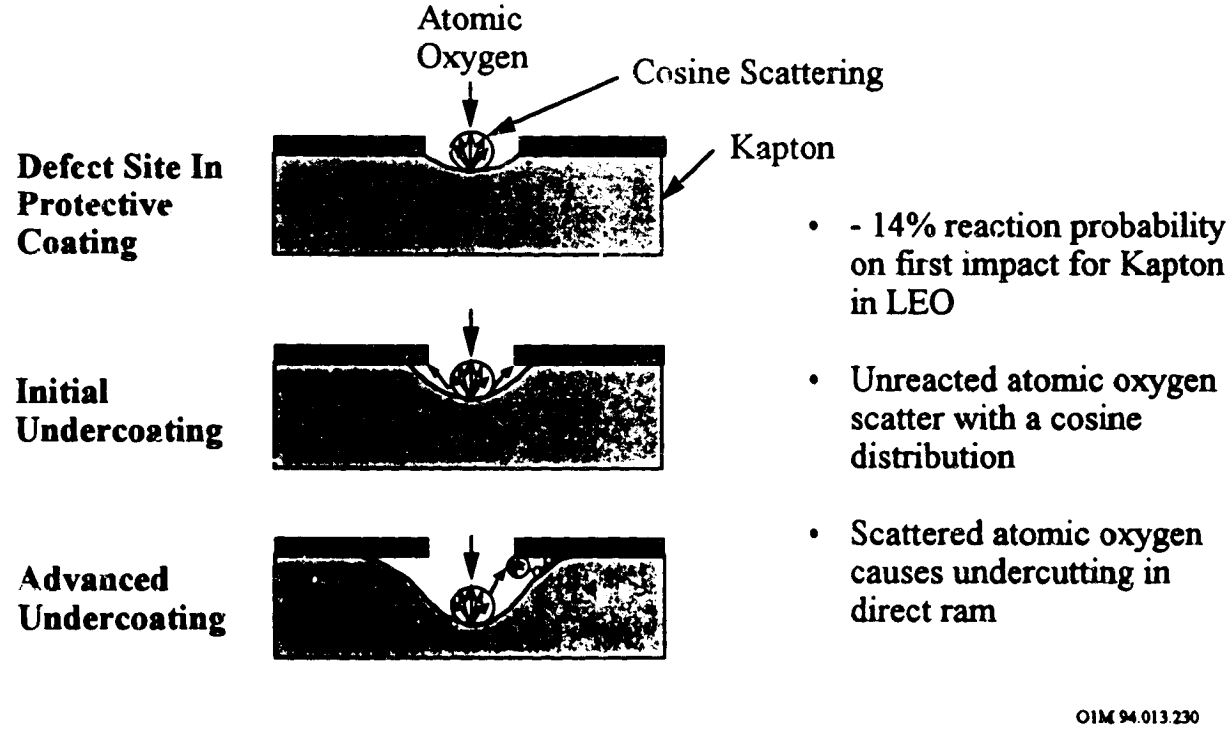

Figure 2- 55. Atomic Oxygen Undercutting of Coated Polymeric Materials on LDEF

Atomic oxygen undercutting of impact damage was measured on LDEF multilayer insulations of aluminized Kapton, and the results are shown in Figure 2-56 (ref. DeGroh and Banks, 1991). Undercut widths range from approximately eight times the defect crack width for small cracks (~0.1mm wide) to approximately three times for larger cracks (~0.6mm wide). Thus the LDEF data gives a good engineering perspective on this phenomenon.

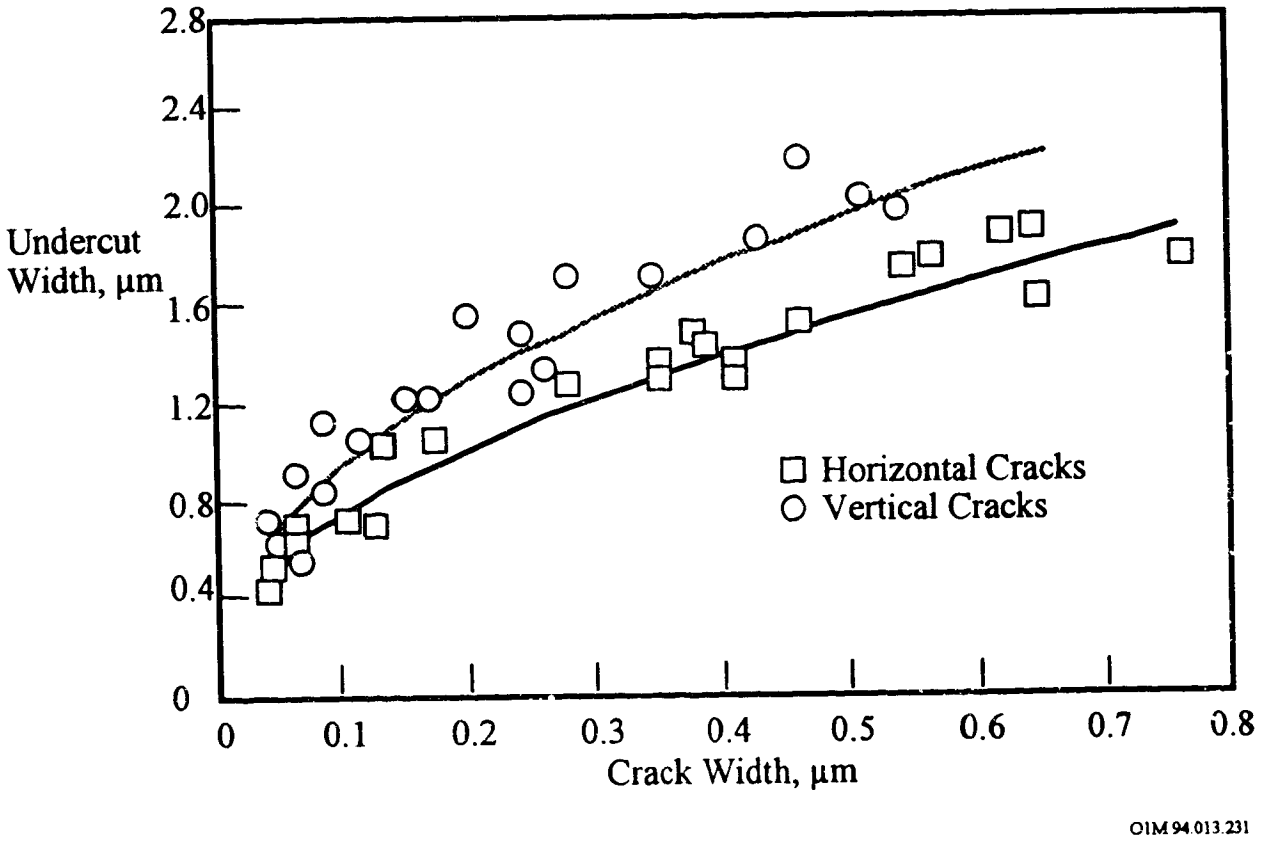

Figure 2- 56. Atomic Oxygen Undercut Widths in Cracked Multilayer Insulations

2.9.4 Impact-Induced Contamination

The space environments (i.e., AO and UV) combine with impact ejecta to cause extensive contamination. This is illustrated by the impact-caused contamination on LDEF's optics, solar cells and thermal control materials.

2.9.5 UV Photochemical-Induced Contamination

Molecular species ou[illegible]ed from spacecraft materials adhere tenaciously to and darken spacecraft surfaces when exposed to solar ultraviolet (UV) radiation. Such deposits severely degrade the performance of optical systems operating at UV and visible wavelengths. It has been commonly observed[155,156,157] that spacecraft surfaces exposed to solar irradiation for extended periods become endarkened in the presence of molecules outgassed from the spacecraft itself, and that ground-based contamination control measures are generally insufficient to prevent the problem. Contaminant observations on LDEF were consistent with the influence of UV radiation in enhancing molecular contaminant deposition (ref. 110).

Surface darkening has been quantified in terms of increased solar spectrum absorptance ($\Delta\alpha_s$) for a number of spacecraft, as shown in Figure 2-38. In the special case of solar observation missions, the useful lifetime of optical systems which view the Sun directly may be measured in days, as illustrated in Figure 2-57 (ref. 108).

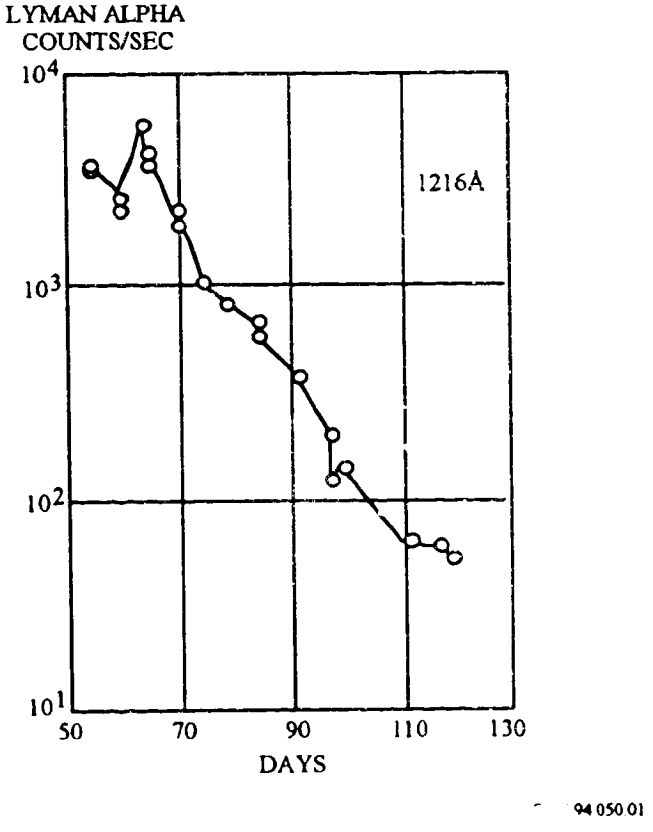

Note: Decrease is due to absorptance of photodeposits on the optical system mirrors.

Figure 2- 57. Signal Strength at 121.6 nm Wavelength During Observations of the Sun by Solar Max

Solar observing optical systems, especially in the UV, are particularly vulnerable to photodeposits because

- the absorptance of the deposits is typically markedly higher in the UV,
- allowable margin for degradation is quite small, typically a few percent,
- all optical surfaces in the system are affected, and
- since the rate of deposition is a function of UV intensity, optical magnification aggravates the problem.

When outgassed molecular species are exposed to solar UV radiation and absorb photons in the wavelength range of <200 nm, the chemical properties of those molecules are altered and molecule-to- surface bonding can occur. The details of this photo-deposition process (surface bonding) are not known, but the result is well known to be a tenacious dark brown film covering the irradiated surface. Laboratory results[157,158] have verified that vacuum UV irradiation (<200 nm) causes the permanent adhesion of a wide variety of molecular species which strike the irradiated surface. As shown in Figure 2-58 (ref. Frink et al., 1992), the spectral absorptance of the resulting film is substantial, and is surprisingly independent of the composition of the deposited species.

A review of the relatively scant available data indicates that the allowable photodeposited contaminant film thickness for an observatory such as the Orbiting Solar Laboratory (OSL) is about 10 nm (1 $\mu g/cm^2$) for operation at 380 nm wavelength, and about 4 nm (400 ng/cm^2) for operation at 200 nm wavelength, cumulative over three years of operation. Contamination control to such levels may not be possible in the absence of an ability to clean the mirrors on orbit.

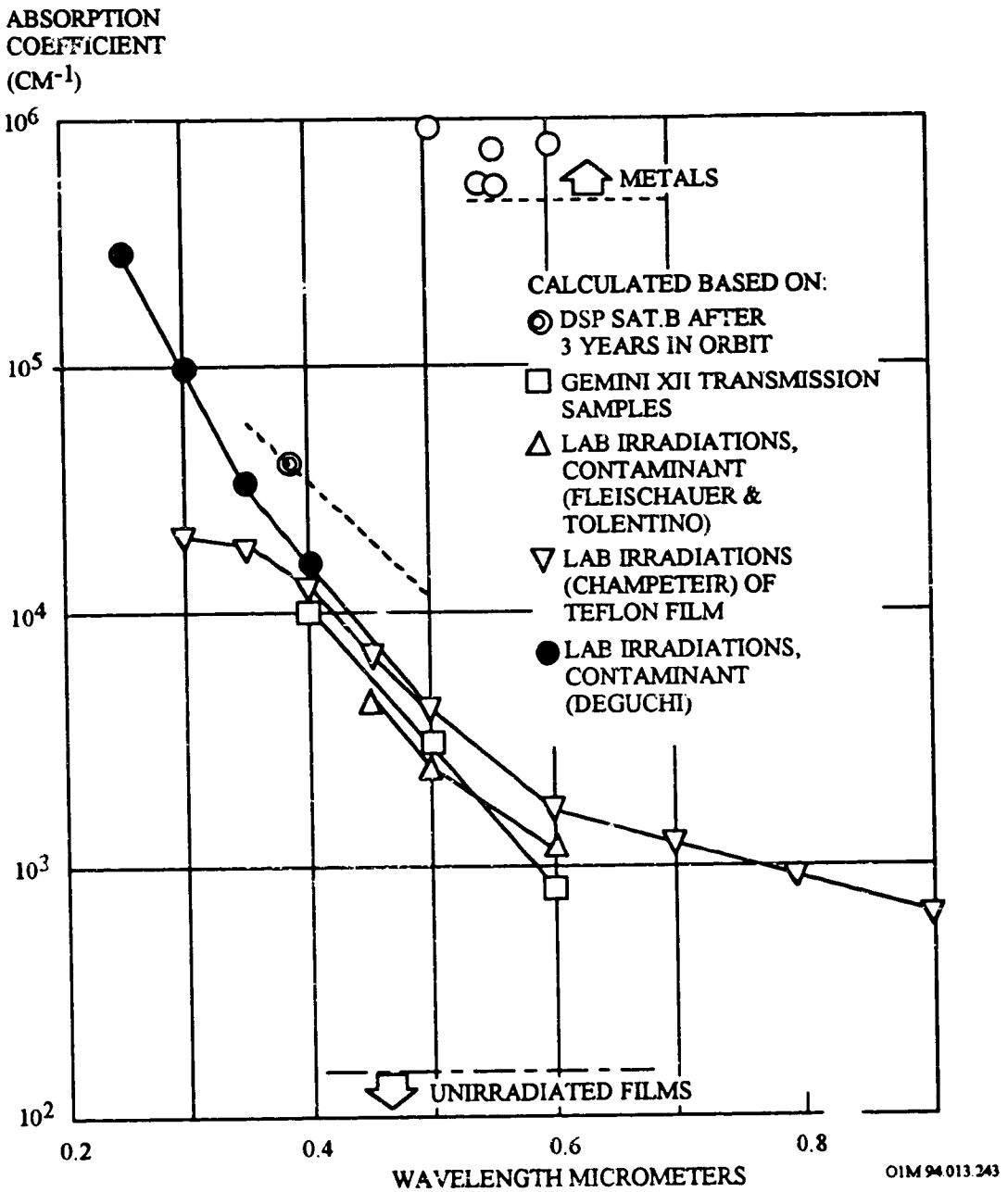

Figure 2- 58. Spectral Absorption Coefficient of Photodeposited Films of Various Contaminants by Various Workers.

RELATIONSHIPS OF SPACE ENVIRONMENT - MATERIAL INTERACTIONS

REFERENCES

[1] J. Visentine, ed., "Atomic Oxygen Effects Measurements for Shuttle Missions STS-8 and 41-G," vols. I-III, NASA TM 100459, September 1988.

[2] J.T. Visentine and L.J. Leger, "Material Interactions with the Low Earth Orbital Environment: Accurate Reaction Rate Measurement," AIAA Paper 85-7019, AIAA Shuttle Environment and Operations II Conference, Houston, Texas, November 1985.

[3] L.J. Leger, "Oxygen Atom Reaction with Shuttle Materials at Orbital Altitudes," NASA TM-58246, May 1982.

[4] T.R. Gull et al., "Effects of Optical Surfaces at Shuttle Altitudes," AIAA Paper 85-0418, AIAA 23rd Aerospace Sciences Meeting, Reno, Nevada, January 14-17, 1985.

[5] J.C. Gregory and P.N. Peters, "Measurement of Reaction Rates and Activation Energies of 5 eV oxygen Atoms with Graphite and Other Solid Surfaces," AIAA Paper 85-0417, AIAA 23rd Aerospace Sciences Meeting, Reno, Nevada, January 14-17, 1985.

[6] K. Smith, "Evaluation of Oxygen Interaction with Materials (EOIM) - STS-8 Atomic Oxygen Effects," AIAA Paper 85-7021, AIAA Shuttle Environment and Operations II Conference, Houston, Texas, November 1985.

[7] A.F. Whitaker et al., "LEO Atomic Oxygen Effects on Spacecraft Materials," AIAA Paper 83-2632, AIAA Shuttle Environment and Operations Meeting, Wash., D.C. October-November 1983.

[8] A.T. Fromhold et al., "Reaction of Metals in Lower Earth Orbit During Space Shuttle Flight 41-G," AIAA Paper 85-7028, AIAA Shuttle Environment and Operations II Conference, Houston, Texas, November 1985.

[9] D.G. Zimcik and C.R. Maag, "Results of Apparent Atomic Oxygen Reactions with Spacecraft Materials During Shuttle Flight STS 41-G," AIAA Paper 85-7020, AIAA Shuttle Environment and Operations II Conference, Houston, Texas, November 1985.

[10] R. Liang and A. Gupta, "Mechanistic Studies of Kapton Degradation in Shuttle Environments," AIAA Paper 83-2656, AIAA Shuttle Environment and Operations Meeting, Wash., D.C., October-November 1983.

[11] P.N. Peters, J.C. Gregory, and J.T. Swann, "Effects on Optical Systems from Interactions with Oxygen Atoms in Low Earth Orbits," Applied Optics, Vol. 25, No. 8, April 15, 1986.

[12] J.T. Visentine et al., "STS-8 Atomic Oxygen Effects Experiment," AIAA Paper 85-0415, AIAA 23rd Aerospace Sciences Meeting, Reno, Nevada, January 14-17, 1985.

[13] B. Banks, "Atomic Oxygen," Proc. LDEF Materials Data Analysis Workshop, NASA KSC, February, 1990, NASA CP 10046, July 1990.

[14] L.J. Leger, J.T. Visentine, and J.F. Kuminecz, "Low Earth Orbit Atomic Oxygen Effects on Surfaces," AIAA Paper 84-0548, Jan. 1984.

[15] J.T. Visentine, L.G. Leger, J.F. Kuminecz, and I.K. Spiker, "STS-8 Atomic Oxygen Effects Experiment," AIAA Paper 85-0415, Jan. 1985.

[16] C.K. Purvis, D.C. Ferguson, D.B. Synder, N.T. Grier, J.V. Staskus, and J.C. Roche, "Environmental Interactions Considerations for Space Station and Solar Array Design," Dec. 1986.

[17] L.J. Leger, B. Santos-Mason, J.T. Visentine, and J.F. Kuminecz, "Review of LEO Flight Experiments," in Proceedings of the NASA Workshop on Atomic Oxygen Effects, D.E. Brinza, ed., NASA CR-181163 (NASA, Washington, D.C., 1987) pp. 1-10.

[18] L.J. Leger, I.K. Spiker, J.F. Kuminecz, T.J. Ballentine, and J.T. Visentine, "STS-5 LEO Effects Experiment - Background Description and Thin Film Results," AIAA Paper 83-2631-CP, AIAA Shuttle Environment and Operations Meeting, Washington, D.C., October - November, 1983.

[19] L.J. Leger, "Oxygen Atom Reaction with Shuttle Materials at Orbital Altitudes - Data and Experiment Status," AIAA Paper 83-0073, Jan. 1983.

[20] D.R. Coulter, R.H. Liang, S.H. Chung, K.O. Smith, and A. Gupta, "O-Atom Degradation Mechanisms of Materials," in Proceedings of the NASA Workshop on Atomic Oxygen Effects, D.E. Brinza, ed., NASA CR-181163 (NASA, Washington, D.C., 1987) pp. 39-46.

[21] Johnson Space Center

[22] Washington University

[23] Langley Research Center

[24] University of Alabama at Huntsville

[25] J.C. Gregory, "Interaction of Hyperthermal Atoms on Surfaces in Orbit: The University of Alabama Experiment," in Proceedings of the NASA Workshop on Atomic Oxygen Effects, D.E. Brinza, ed., NASA CR-181163 (NASA, Washington, D.C., 1986), pp. 29-36.

[26] Jet Propulsion Laboratory

[27] A.F. Whitaker, "LEO Atomic Oxygen Effects on Spacecraft Materials: STS-5 Results," NASA TM-86463, 1984.

[28] B.A. Banks, M.J. Mirtich, S.K. Rutledge, and H.K. Nahra, in Eighteenth IEEE Photovoltaic Specialists Conference, (Institute of Electrical and Electronics Engineers, Piscataway, NJ, 1985), pp 381-386.

[29] K.A. Smith, "Evaluation of Oxygen Interaction with Materials (EOIM) - STS-8 Atomic Oxygen Effects," AIAA Paper-85-7021, Nov. 1985.

[30] A.F. Whitaker, S.A. Little, R.J. Harwell, D.B. Griner, and R.F. DeHaye, "Orbital Atomic Oxygen Effects on Thermal Control and Optical Materials: STS-8 Results," AIAA 23rd Aerospace Sciences Meeting, January,1985.

[31] A.F. Whitaker, "Atomic Oxygen Effects on LDEF Experiment AO171," LDEF Second Post-Retrieval Symposium, NASA CP-3194, 1993, pp. 1125-1135.

[32] Marshall Space Flight Center

[33] P.E. George, H.W. Dursch, and S.G. Hill, "Space Environmental Effects on LDEF Composites: A Leading Edge Coated Graphite Epoxy Panel," LDEF Second Post-Retrieval Symposium, NASA CP-3194, 1993, pp.923-939.

[34] P. George, "Space Environmental Effects on LDEF Low Earth Orbit Exposed Graphite Reinforced Polymer Matrix Composites," LDEF Materials Workshops '91, NASA CP-3162, 1992, pp. 543-570.

[35] R.C. Tennyson et al., "Preliminary Results from the LDEF/UTIAS Composite Materials Experiment," LDEF First Post-Retrieval Symposium, NASA CP-3134, 1991, pp. 1057-1072.

[36] A.F. Whitaker, "Atomic Oxygen Effects on LDEF Experiment AO171," LDEF Second Post-Retrieval Symposium, NASA CP-3194, 1993, pp.1125-1135.

[37] Goddard Space Flight Center

[38] Aerospace Corporation

[39] J.T. Visentine and A.F. Whitaker, "Material Selection Guidelines to Limit Atomic Oxygen Effects on Spacecraft Surfaces," NASA TM-100351, February 1989.

[40] British Aerospace

[41] J.T. Durcanin, D.R. Chalmers, and J.T. Visentine, "The Definition of the Low Earth Orbital Environment and its Effect on Thermal Control Materials," AIAA Paper-87-1599, June, 1987.

[42] Lewis Research Center

[43] L.J. Leger and J.T. Visentine, "A Consideration of Atomic Oxygen Interactions with the Space Station", J. Of Spacecraft and Rockets, Vol. 23, No. 5, Sept/Oct 1986, pp. 505-511.

[44] A.E. Hedin, "A Revised Thermospheric Model Based on Mass Spectrometer and Incoherent Scatter Data: MSIS-83," Journal of Geophysical Research, Vol. 88, No. A12, Dec 1983, pp. 10,170-10,188.

[45] J.T. Visentine and A.F. Whitaker, "Material Selection Guidelines to Limit Atomic Oxygen Effects on Spacecraft Surfaces," NASA TM-100351, February 1989.

[46] W.W. Vaughan, "Natural Environment Design Criteria for the Space Station Definition and Preliminary Design," 1st Rev., NASA TM-86460, September 1984.

[47] TRW unpublished data.

[48] W.S. Slemp, B. Santos, G.F. Sykes, Jr., and W.G. Witte, Jr., "Effects of STS-8 Atomic Oxygen Exposure on Composites, Polymeric Films, and Coatings," AIAA Paper 85-0421, Jan. 1985.

[49] A.F. Whitaker, J.A. Burka, J.E. Coston, Z. Dalins, and S.A. Little, "Protective Coatings for Atomic Oxygen Susceptible Spacecraft Materials - STS-41G Results," AIAA Paper 85-7017, Nov. 1985.

[50] M.J. Meshishnek, W.K. Stuckey, J.S. Evangelides, L.A. Feldman, R.V. Peterson, C.S. Arnold, and D.R. Peplinski, "Effects on Advanced Materials: Results of the STS-8 EOIM (Effects of Oxygen Interaction with Materials) Experiment," Report SD-TR-87-34, Aerospace Corporation, El Segundo, CA, July 20, 1987.

[51] D.G. Zimcik, and C.R. Maag, "Results of Apparent Atomic Oxygen Reactions with Spacecraft Materials During Shuttle Flight STS-41-G," AIAA Paper 85-7020, Nov. 1985.

[52] J.J. Park, T.R. Gull, H. Herzig, A.R. and Toft, "Effects of Atomic Oxygen on Paint and Optical Coatings," AIAA Paper 83-2634, AIAA Shuttle Environment and Operations Meeting, Washington, D.C., October-November 1983.

[53] Martin Marietta

[54] A.F. Whitaker, J.A. Burka, J.E. Coston, Z. Dalins, and S.A. Little, "Protective Coatings for Atomic Oxygen Susceptible Spacecraft Materials - STS-41G Results," AIAA Paper 85-7017, Nov. 1985.

[55] W.S. Slemp, "Ultraviolet Radiation Effects," NASA/SDIO Space Environmental Effects Workshop, NASA CP 3035, 1988, pp. 425-446.

[56] A.C. Somersall and J.E. Guillet, "Modeling of Photodegradation in Solar Cell Modules of Substrate and Superstrate Design Made with Ethylene-Vinyl Acetate as Pottant Material," Annual Report, NASA Contract NAS7-100, 1983.

[57] A.K. St. Clair and W.S. Slemp, "Evaluation of Colorless Polyimide Film for Thermal Control Coating Applications," Proceedings of the 30th SAMPE National Symposium and Exhibition, March 1985, pp. 28-41.

[58] J.C. Guillaumon and A. Paillous, "Spacecraft Materials: Comparison Between Flight Results Obtained on LDEF and Mir," LDEF Materials Results for Spacecraft Applications, NASA CP 3257, 1994, pp. 485-498.

[59] G. Pippin, W. Stuckey, and C. Hemminger, "Performance of Silvered Teflon Thermal Control Blankets on Spacecraft," LDEF Materials Results for Spacecraft Applications, NASA CP-3257, 1994, pp. 21-30.

[60] J.J. Park, "Results of Examination of Materials from the Solar Maximum Recovery Mission," Proceedings of the SMRM Degradation Study Workshop, NASA Publication 408-SMRM-79-0001, pp. 211-225.

[61] J.J. Triolo, J.B. Heaney, and G. Hass, "Coatings in Space Environment," Optics in Adverse Environments, SPIE vol. 121, 1977, pp. 46-66.

[62] D.E. Prince, "ML-101 Thermal Control Coating Spaceflight Experiment," AFML-TR-75-17, August 1975, and R.A. Winn, "ML-101 Thermal Control Coating Spaceflight Experiment," AFML-TR-78-99, July 1978.

[63] J. Visentine, ed., "Atomic Oxygen Effects Measurements for Shuttle Missions STS-8 and 41-G," vols. I-III, NASA Technical Memorandum 100459, September 1988.

[64] W.S. Slemp, "Ultraviolet Radiation Effects," NASA/SDIO Space Environmental Effects Workshop, NASA CP 3035, 1988, pp. 425-446.

[65] F. Levadou and G. Pippin, "Effects of the LDEF Environment on the Ag/FEP Thermal Blankets," LDEF Materials Workshop "91, eds. B.A. Stein and P.R. Young, NASA CP-3162, 1992, pp. 311-344.

[66] M.J. Meshishnek et al., "Long Duration Exposure Facility Experiment M0003 Meteoroid and Debris Survey," LDEF Second Post-Retrieval Symposium, NASA CP 3194, 1993, pp. 357-415.

[67] B.G. Cour-Palais et al., "Meteoroid Environment Model - 1969 (Near Earth to Lunar Surface)." NASA SP-8013, March 1969.

[68] D.J. Kessler et al., "Orbital Debris Environment for Spacecraft Designed to Operate in Low-Earth Orbit," NASA TM-100471, September 1988.

[69] E. Grun et al., "Collision Balance of the Meteoritic Complex," Icarus, Vol. 62, 1985.

[70] C. Coombs, A.J. Watts, J. Wagner, and D. Atkinson, "LDEF Data: Comparisons with Existing Models," Lockheed ESC/NASA Johnson Space Center; Contract No. 960-12-171, SC 02N0165768, September 1992.

[71] M.J. Meshishnek et al., "Long Duration Exposure Facility (LDEF) Experiment M0003 Meteoroid and Debris Survey," LDEF Second Post-Retrieval Symposium, NASA CP 3194, 1993, pp.357-415.

[72] G. Drolshagen, "Predicted and Observed Directional Dependence of Meteoroid/Debris Impacts on LDEF Thermal Blankets," LDEF Second Post-Retrieval Symposium, NASA CP 3194, 1993, pp 325-337.

[73] T. See et al., "Meteoroid and Debris Impact Features Documented on the Long Duration Exposure Facility," NASA JSC Publication #84, JSC #24608, August 1990.

[74] D.H. Humes, "Large Craters on the Meteoroid and Space Debris Impact Experiment," NASA CP-3134, part 1, p. 399, 1992.

[75] J.M. Zwiener and M.M. Finckenor, "Micrometeoroid/Space Debris Effects on Materials," LDEF Materials Results for Spacecraft Applications, NASA CP-3257, 1994, pp. 259-280.

[76] B. Banks and L. Gebauer, "LDEF Yaw and Pitch Angle Estimates," LDEF Materials Workshop '91, NASA CP-3162, 1992, pp. 71-92.

[77] R.C. Tennyson and G. Manuelpillai, "Analysis of LDEF Micrometeoroid/Debris Data and Damage to Composite Materials," LDEF Second Post-Retrieval Symposium, NASA CP 3194, 1993, pp. 493-511.

[78] D.S. McKay, "Microparticle Impacts in Space: Results From Solar Max Satellite and Shuttle Witness Plate Inspection," NASA/SDIO Space Environmental Effects on Materials Workshop, NASA CP 3035, 1989, pp. 301-327.

[79] W.T. Kemp et al., "Long Duration Exposure Facility Space Optics Handbook," Air Force Document PL-TN-93-1067, September 1993, pp. 6-12 to 6-14.

[80] N. Divine, and R.C. Aguero, "New Meteoroid Model Predictions for Directional Impacts on LDEF," LDEF Second Post-Retrieval Symposium Abstracts, NASA CP-10097, June 1992.

[81] M. Zolensky, D. Atkinson, T. See, M. Allbrooks, C. Simon, M. Finckenor, and J. Warren, "Meteoroid and Orbital Debris Record of the Long Duration Exposure Facility's Frame," Journal of Spacecraft, Vol. 28, No. 2, 1991.

[82] H.A. Zook, "Asteroidal Versus Cometary Meteoroid Impacts on the Long Duration Exposure Facility," LDEF Second Post-Retrieval Symposium Abstracts, NASA CP-10097, June 1992.

[83] A. Watts et al., "LDEF Penetration Assessment Final Report," Final Report, Contract F33615-90-C-5903, Task 0008, June 1992.

[84] F. Rose, "Hypervelocity Impact and Scaling Above 10 Km/sec," Contract NAS8-39131, DO #1, November 1992.

[85] B.G. Cour-Palais, "Meteoroid Environment Model - 1969 - Near Earth to Lunar Surface", NASA SP-8013, 1969.

[86] J.W. Haffner et al., "Natural Environmental Effects on SDI Spacecraft Surface Materials," Rockwell International, Report No. AFGL-TR-89-0084, Air Force Geophysical Laboratory, May 20. 1989.

[87] J.A.M. McDonnell and T.J. Stevenson, "Hypervelocity Impact Microfoil Perforations in the LEO Space Environment (LDEF, MAP AO 023 Experiment)," LDEF First Post-Retrieval Symposium, NASA CP 3134, 1991, pp.443-458.

[88] L. E. Young, "Impact of LDEF Photovoltaic Experiments Findings upon Future Spacecraft Solar Cell Assembly Design and Development Requirements," LDEF Materials Results for Spacecraft Applications, NASA CP-3257, pp. 201-216.

[89] M. Allbrooks and D. Atkinson, "The Magnitude of Impact Damage on LDEF Materials," NASA Contractor Report NCR 188258, July 1992.

[90] R.C. Tennyson, G.E. Mabson, W.D. Morison, and J. Kleiman, 'Preliminary Results From the LDEF/UTIAS Composite Materials Experiments," LDEF First Post-Retrieval Symposium, 1991, NASA CP-3134, pp. 1057-1072.

[91] R.C. Tennyson, "Additional Results on Space Environmental Effects on Polymer Matrix Composites - Experiment AO180," ," LDEF First Post-Retrieval Symposium, 1991, NASA CP-3134, pp. 571-592.

[92] J.A. Zukas et al., "Impact Dynamics: Chapter 6 - Hypervelocity Impact Mechanics," A Wiley-Interscience Publication, John Wiley & Sons, 1982.

[93] M.J. Mirtich and W.R. Kerslake, "The Effect of the Near Earth Micrometeoroid Environment on a Mirror Surface after 20 Years in Space," presented at the TMS Meeting, Los Angeles, 19-21 February, 1990.

[94] M.J. Mirtich et al., "Effect of Eleven Years in Earth Orbit on a Mirror Surface," Journal of Spacecraft and Rockets, vol. 27, no. 3, May-June 1990.

[95] L.D. Lamb, "The Scattering of Infrared Light by Small Particles on Substrates," Ph.D. Thesis, Department of Physics, The University of Arizona, October 1991.

[96] P.M. Stella, "LEO Effects on Candidate Solar Cell Cover Materials," LDEF Second Post-Retrieval Symposium, NASA CP-3194, 1993, pp. 1303-1313.

[97] C.T. Golden and E.E. Spear, "Graphite/Epoxy Structure of the Spar Telescope's Optical Telescope Assembly," Proceedings of the 29th SAMPE International Symposium and Exhibition, April 1984, pp. 33-45.

[98] D.R. Tenney, G.F. Sykes, and D.E. Bowles, "Composite Materials for Space Structures," Third European Symposium On Spacecraft Materials in the Space Environment, Oct 1985, Noordwijk.

[99] S.S. Tompkins, "Effects of Thermal Cycling on Composite Materials for Space Structures," NASA/SDIO Space Environmental Effects on Materials Workshop, NASA CP 3035, Part 2, 1989, pp. 447-470.

[100] D.E. Bowles and O.H. Griffin, Jr., "Analysis of Thermal Stresses in Polymer Matrix Composites," Proceedings of 34th International SAMPE Symposium, May 1989, pp. 575-584.

[101] G.F. Sykes, J.G. Funk, and W.S. Slemp, "Assessment of Space Environment Induced Microdamage in Toughened Composite Materials," Proceedings of the 18th SAMPE International Technical Conference, October 1986, pp. 520-534.

[102] J.G. Funk and G.F. Sykes, Jr., "The Effects of Simulated Space Environmental Parameters on Six Commercially Available Composite Materials," NASA Technical Paper 2906, April 1989.

[103] NASA Langley unpublished data.

[104] S.S. Tompkins, G.F. Sykes, and D.E. Bowles, "The Thermal Mechanical Stability of Composite Materials for Space Structures," IEEE/ASM/ASME/SME Space Technical Conference, Anaheim, CA, Sept. 1985.

[105] S.S. Tompkins, J.G. Funk, D.E. Bowles, T.W. Towell, and J.W. Connell, "Composite Materials for Precision Space Reflector Panels," SPIE Vol. 1690 Design of Optical Instruments, 1992, pp. 250-261.

[106] E.G. Wolff, "Dimensional Stability of Carbon Fiber Reinforced Plastic Tubes," SAMPE Quarterly, October 1984, pp. 26-33.

[107] Preliminary Report on LDEF-Related Contaminants, LDEF Materials Special Investigation Group, prepared by Boeing Aerospace, August 1990.

[108] M. Frink, M. Folkman, and L. Darnton, 'Photodeposition of Molecular Contaminants with a Vacuum Ultraviolet Solar Illumination Lamp," SPIE Vol. 1754 Optical System Contamination, 1992, pp. 46-57.

[109] Goddard Space Flight Center internal memo entitled "Summary of Results to Date on QCM Data from the NOAA-7 Spacecraft" from 732/Thermal Engineering Branch to 480/Tiros Instrument Manager, January 1984.

[110] G. Pippin and R. Crutcher, "Spacecraft Contamination Issues From LDEF: Issues for Design," LDEF Materials Results for Spacecraft Applications, NASA CP 3257, 1994, pp. 97-103.

[111] TRW unpublished data.

[112] C.R. Maag, "Effects of the Contamination Environment on Surfaces and Materials," NASA CP 3035, Part 1, 1989, pp.353-366.

[113] W.R. Pence and T.J. Grant, "Measurements of Thermal Control Coatings on Navstar Global Positioning System Spacecraft," Progress in Astronautics and Aeronautics, Vol. 83, 1982, p. 234.

[114] F.L. Bouquet, W.E. Price, and D.M. Newell, "Designer's Guide to Radiation Effects on Materials for Use on Jupiter Fly-bys and Orbiters," IEEE Transactions on Nuclear Science, Vol. NS-26, No. 4, Aug 1979, p. 4660.

[115] Proceedings of the Solar Maximum Repair Mission Degradation Study Workshop, Goddard Space Flight Center, May 1985, Document #408-SMRM-79-0001. See especially the paper by G.D. Rhoads of Lockheed entitled "Solar Maximum Thermal Surface Assessment."

[116] F. Levadou, M. Froggatt, M. Rott, and E. Schneider, "Preliminary Investigation into UHCRE Thermal Control Materials", LDEF First Post-Retrieval Conference, CP-3134, 1992, 875-898.

[117] A.C. Tribble and J.W. Haffner, "Estimates of Photochemically Deposited Contamination on the GPS Satellites," J. Of Spacecraft and Rockets, V.28, No.2, March/April 1991, pp. 222-228.

[118] J.R. Rittenhouse and J.R. Singletary, "Space Materials Handbook," 3rd ed., Air Force Materials Lab., TR-68-205, July 1968.

[119] R.B. Gillette, "Ultraviolet-Proton Radiation Effects on Solar Concentrator Reflective Surfaces," NASA CR-1024, May 1968.

[120] M.J. Teague, K.W. Chan, and J.I. Vette, "AE 6: A Model Environment of Trapped Electrons for Solar Maximum," National Space Science Data Center/World Data Center for Rockets and Satellites, 76-04, May 1976.

[121] D.M. Sawyer and J.I. Vette, "AP-8 Trapped Proton Environment for Solar Maximum and Solar Minimum," National Space Science Data Center/World Data Center A for Rockets and Satellites, 76-06, Dec. 1976.

[122] T.B. Stewart, G.S. Arnold, D.F. Hall, D.C. Marvin, W.C. Hwang, R.D. Chandler, and H.D. Martin, "Photochemical Spacecraft Self-Contamination - Laboratory results and Systems Impacts," J. Of Spacecraft and Rockets, Vol. 26, No. 5, Sept/Oct. 1989, p. 358.

[123] D.F. Hall, "Current Flight Results from the P78-2 (SCATHA) Spacecraft Contamination and Coatings Degradation Experiment," International Symposium on Spacecraft Materials in Space Environment, European Space Agency, Toulouse, France, SD-178, June 1982.

[124] R. Kruger and H. Shapiro, "Experiments on the Effect of Ultraviolet on Contamination in Vacuum Systems," NASA TM 81999, N81-12976, 1989.

[125] D.F. Hall, T.B. Stewart, R.R. Hayes, "Photo-Enhanced Spacecraft Contamination Deposition," AIAA Paper 85-0953, June 1985.

[126] T.B. Stewart, G.S. Arnold, D.F. Hall, and H.D. Marten, "Absolute Rates of Vacuum Ultraviolet Photochemical Deposition of Organic Films," Journal of Physical Chemistry, Vol. 93, March 1989, p. 2393.

[127] R.P. Young, "Low-Scatter Mirror Degradation by Particulate Contamination," Optical Engineering, vol. 15, no. 6, November-December 1976.

[128] D.S. McKay, "Microparticle Impacts in Space: Results From Solar Max Satellite and Shuttle Witness Plate Inspection," NASA/SDIO Space Environmental Effects on Materials Workshop, NASA CP 3035, 1989, pp. 301-327.

[129] T.A. Hughes, T.H. Allen, R.M.F. Linford, and T.E. Bonham, "Investigation of Contamination Effects on Thermal Control Materials," AFML-TR-74-218, January 1975.

[130] T.A. Hughes, T.E. Bonham, and T.H. Allen, "Investigation of Contamination Effects on Thermal Control Materials," AFML-TR-76-5, March 1976.

[131] E.R. Crutcher and K.J. Warner, "Molecular Films Associated with LDEF," LDEF First Post-Retrieval Symposium, NASA CP-3134, 1991, pp. 155-178.

[132] ASTM E 595-83, "Total Mass Loss and Collected Volatile Condensable Materials from Outgassing in a Vacuum Environment," 1983 Annual Book of ASTM Standards, 14.02, ASTM, Philadelphia, PA, 1983.

[133] TRW unpublished data.

[134] MSFC Handbook 1674

[135] A.P.M. Glassford and J.W. Garrett, "Characterization of Contamination Generation Characteristics of Satellite Materials," Report No. WRDC-TR [illegible]-4114, Lockheed Missiles & Space Company, November 1989.

[136] TRW unpublished data.

[137] TRW internal report.

[138] D.F. Hall, "Experiment to Measure Enhancement of Spacecraft Contamination by Spacecraft Charging," NASA SP-379, National Technical Information Service, 1975.

[139] D.F. Hall and J.N. Wakimoto, "Further Flight Evidence of Spacecraft Surface Contamination Rate Enhancement by Spacecraft Charging," AIAA 84-1703, June 1984.

[140] C.K. Purvis, H.B. Garrett, A.C. Whittlesy, and N.J. Stevens, "Design Guidelines for Assessing and Controlling Spacecraft Charging Effects," NASA TP-2361, September 1984.

[141] R.P. Stillwell, N.J. Stevens, and C.S. Underwood, "On Orbit Charging: Current TRW Design Requirements," AIAA 92-1100 paper, 1992 Aerospace Design Conference, February 3-6, 1992.

[142] TRW charging requirement for thermal blankets.

[143] M.C. Stauber, M.L. Rossi and E.G. Stassinopoulos, An Overview of Radiation Hazards in Earth Orbits, AAS Proceedings, Space Safety and Rescue, 1983.

[144] J.H. Adams, Cosmic Ray Effects on Microelectronics Part 1: The Near-Earth Particle Environment, NRL Report No. 4506, 25 August 1981.

[145] J. Visentine, ed., "Atomic Oxygen Effects Measurements for Shuttle Missions STS-8 and 41-G," vols. I-III, NASA Technical Memorandum 100459, September 1988.

[146] J.J. Park, "Results of Examination of Materials from the Solar Maximum Recovery Mission," Proceedings of the SMRM Degradation Study Workshop, NASA Publication 408-SMRM-79-0001, pp. 211-225.

[147] S. Koontz, L. Leger, K. Albyn and J. Cross, "Vacuum Ultraviolet Radiation/Atomic Oxygen Synergism in Materials Reactivity," Journal of Spacecraft and Rockets, Vol. 27, May-June 1990, pp. 346-348.

[148] P.W. Knopf, R.J. Martin, R.E. Damman, and M. McCargo, "Correlation of Laboratory and Flight Data for the Effects of Atomic Oxygen on Polymeric Materials," AIAA 20th Thermophysics Conference, Williamsburg, VA, June 19-21, 1985.

[149] L.J. Leger, J.T. Visentine, J.F. Kumineez, and I.K. Spiker, "STS-8 Atomic Oxygen Effect Experiment," AIAA Paper 85-0415, January 1985.

[150] B.A. Banks, L. Gebaurer, and C.H. Hill, "Atomic Oxygen Interactions with FEP Teflon and Silicones on LDEF," LDEF First Post-Retrieval Symposium, NASA CP 3134, 1992, pp. 801-815.

[151] G. Pippin, W. Stuckey, and C. Hemminger, "Performance of Silvered Teflon Thermal Control Blankets on Spacecraft," LDEF Materials Results for Spacecraft Applications, NASA CP 3257, 1994, pp. 21-30.

[152] C.S. Hemminger, W.K. Stuckey, and J.C. Uht, "Space Environmental Effects on Silvered Teflon Thermal Control Surfaces," LDEF First Post-Retrieval Symposium, NASA CP 3134, 1992, pp. 831-845.

[153] G.S. Arnold and D.R. Peplinski, "Kinetics of Oxygen Interactions with Materials," AIAA Paper 85-0472, January 1985.

[154] K.K. DeGroh and B.A. Banks, "Atomic Oxygen Undercutting of LDEF Aluminized-Kapton Multilayer Insulations," LDEF First Post-Retrieval Symposium, NASA CP 3134, 1991, pp.781-795

[155] D.F. Hall, T.B. Stewart, and R.R. Hayes, "Photo-Enhanced Spacecraft Contamination Deposition," AIAA-85-0953, AIAA Thermophysics Conference, Williamsburg, VA, June 19--21 1985.

[156] T.B. Stewart, G.S. Arnold, D.F. Hall, D.C. Marvin, W.C. Hwang, R.D. Chandler, and H.D. Martin, "Photochemical Spacecraft Self-Contamination - Laboratory results and Systems Impacts," J. Of Spacecraft and Rockets, Vol. 26, No. 5, Sept/Oct. 1989, p. 358.

[157] T.B. Stewart, G.S. Arnold, D.F. Hall, and H.D. Marten, "Absolute Rates of Vacuum Ultraviolet Photochemical Deposition of Organic Films," Journal of Physical Chemistry, Vol. 93. March 1989, p.. 2393.

[158] T.B. Stewart, G.S. Arnold, D.F. Hall, D.C. Marvin, W.C. Hwang, R.D. Chandler, and H.D. Martin, "Photochemical Spacecraft Self-Contamination - Laboratory results and Systems Impacts," J. Of Spacecraft and Rockets, Vol. 26, No. 5, Sept/Oct. 1989, p. 358.

3.0 ADVANCED COMPOSITES

3.1 INTRODUCTION

Advanced composite materials are being considered for stiffness-critical space structures, such as bus structures and solar array structures, and for dimensionally stable space structures, such as optical benches and antenna systems. Thus, properties of major interest to the space designers include modulus, coefficient of thermal expansion (CTE), coefficient of moisture expansion (CME), outgassing, specific heat, and thermal conductivity, as well as fiber volume, void content, and density. Figure 3-1 compares the specific strength and stiffness of polymer matrix composites with common metals and metal matrix composites.

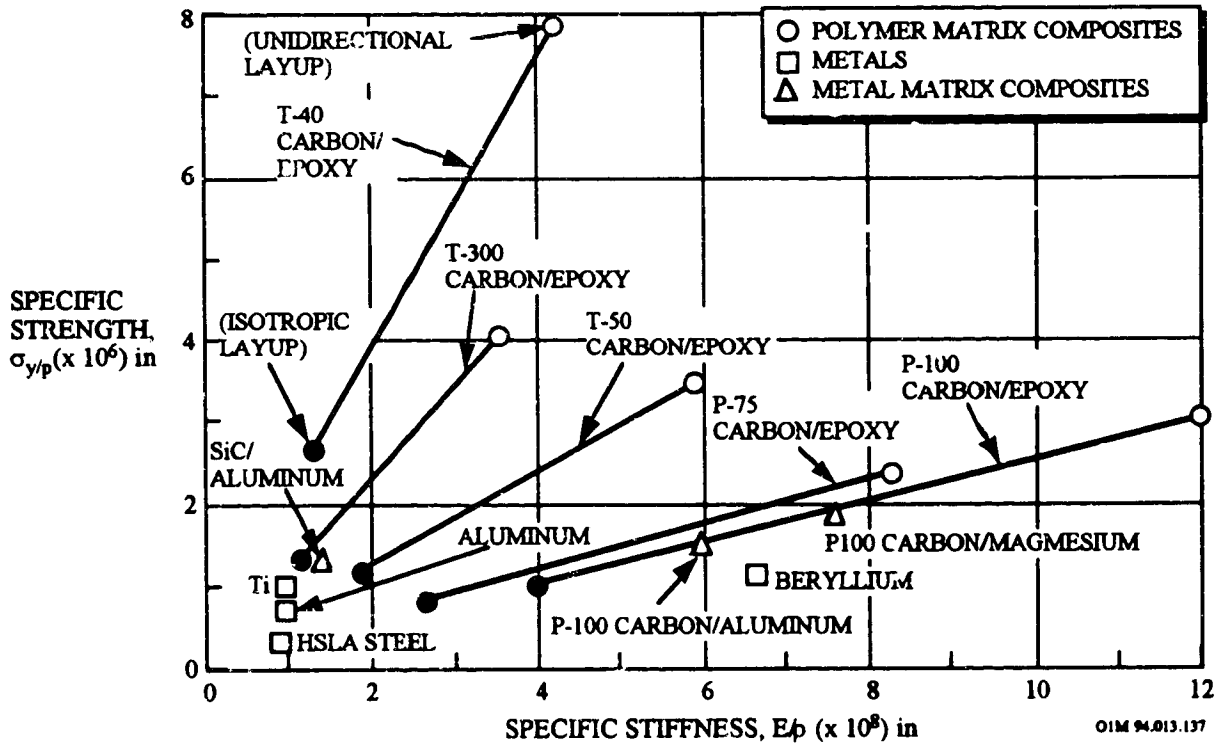

Figure 3-1. Comparison of Specific Stiffness and Strength Properties of Advanced Composites and Metals

Polymer-matrix composites (PMCs), primarily carbon- and glass-fiber reinforced epoxies and carbon-reinforced polysulfone and polyimide, with and without thermal-control or protective coatings, metal-matrix composites (MMCs), primarily carbon-fiber reinforced aluminum and magnesium, and carbon-carbon composites have flown on the LDEF and several Space Shuttle flights. Table 3-1 summarizes the space flight experiments and composite materials exposed to the LEO environment. The primary objectives of these experiments were to evaluate the cumulative and synergistic effects of the orbital space environment (e.g., atomic oxygen, UV radiation, micrometeoroid and debris, thermal cycling, vacuum) on the composites' physical and mechanical properties, and to extrapolate these results to longer exposures for timely materials R&D and/or systems-design modifications.

Table 3-1. Advanced Composites Exposed to the LEO Environment

Experiment	Ref.	PI/Org	Environment	Materials	Property Measurement
LDEF M0003-10 Row D4 (TE) Row D8 (LE)	1 ,2 , 3 ,4	Steckel/ Aerospace	AO, UV M&D Thermal Cycling	Metal Matrix Composites Carbon/Glass Composite Carbon/Epoxy Carbon/Polyimide Carbon/Polysulfone	AO Erosion Surface damage of composites Thermal Expansion
LDEF/UTIAS (AO180) (row D12, 90° to LE)	5 ,6	Tennyson/ U.of Toronto	AO, UV M&D Thermal Cycling	Carbon/Epoxy	Thermal/Strain, CME, CTE Vacuum outgassing time AO Erosion Surface damage of composites
LDEF/M0003-9 - LE row 9 - TE row 3	7 ,3	Petrie/ Lockheed	AO, UV Thermal cycling	Carbon/Composites Glass/Composites Kevlar/Composites	Mass loss Microcracking, CTE Mechanical
LDEF/ M0003-8(Row D9, LE) M0003-10(Row D3,TE)	8 ,9	Pippin/ George/ Boeing	AO, UV M&D Thermal Cycling	T300/934 epoxy T300/P1700 polysulfone C6000/PMR-15 White/Black coatings	AO Erosion, Microcracking Surface damage of composites Mechanical properties Residual stress
LDEF/A0134 Composites for LSS (Row 9B,LE)	10 , 11	Slemp/ Young NASA	AO, UV, M&D Thermal Cycling	T300/934 epoxy T300/5208 epoxy T300/C6000 polysulfone	Chemical Analysis
LDEF/A0138-9	12	Aerospatiale	AO, UV	T300/epoxy, GY70/epoxy	CTE, Mechanical Properties
LDEF/A0175 A7(LE), A1(TE)	13	Vyhnal/ Rockwell	AO, UV Thermal Cycling	Epoxy, Bismaleimide, Polyimide Composites; Honeycomb panel	Weight loss Mechanical Properties Warpage
LDEF/A0171	14	Whitaker/ NASA	AO, UV	Composites, Polymers, Metals, Glassy Ceramics	AO Erosion
STS-8/EOIM	15	NASA	AO, UV	Polymer Composites Metal Matrix Composites	AO Erosion
STS-46/EOIM-3	16 17 18	JPL Aerospace	AO, UV	Polymeric Composites Carbon-Carbon Metal Matrix	AO Erosion
STS-46/LDCE	19	CWRU	AO, UV	AZ91-Mg-SiCp Carbon Polymer Composites	AO Erosion

LE = leading edge
TE = trailing edge

3.2 POLYMER MATRIX COMPOSITES

3.2.1 Carbon/Thermosets

Table 3-2 summarizes the flight experiments that evaluated the effects of the space environment on several classes of carbon fiber reinforced polymer-matrix thermoset composite materials, such as epoxy, polyimide, and bismaleimide matrix composites. The AO fluence, and ultraviolet radiation fluence are tabulated for each exposure location.

Table 3-2. Polymer Composites Exposed to the LEO Environment

Flight Experiment (reference)	Angle off RAM	LDEF Row	AO atoms/cm^2	UV ESH	Epoxy (Ref.)	Polyimide	Bismaleimide
LDEF - M0003-9 (7) - M0003-8 (8) - A0134 (11)	8 (LE)	9	8.99×10^{21}	11,200	T300/934 P75/934, GY70/CE339 T50/F263 T50/934, /X904B Celion 6000/E788 HMF 176/934 T50/E788 HMS/3501-5A GY70/X904B P75/F593 T300/5208	C6000/PMR-15	
LDEF - M0003-10 (1,3,4) - A0171 (14)	38	8	7.15×10^{21}	9,400	T300/934 AS-4/3501-6 P75S/CE339,934 HMS/934 GY70/CE339,934 T300/5208	C6000/PMR-15 Carbon/LARC-16	T300/ V378A
LDEF- A0175 (13)	68	7	3.39×10^{21}	7,100		C6000/PMR-15	T300/F178A
LDEF -A0180 (5,6)	82	12	1.33×10^{21}	6,800	T300/934, T300/5208 T300/SP288 Epoxy Kevlar/SP328 Epoxy Boron/SP290 Epoxy		
LDEF- A0175 (13)	112	1	2.92×10^{17}	7,400	T300/934	C6000/LARC-160	
LDEF -M0003-10 (1)	158	4	2.31×10^{5}	10,500	P75/934 GY70/CE339 T300/5208		
LDEF - M0003-8 (8)	172 (TE)	3	1.32×10^{17}	11,100	T300/934	C6000/PMR	
STS-46/EOIM-3 (16,17,18)	0		0.193×10^{21}	8.3	P75S/934	AS4/PMR-15	
STS-46/LDCE (19)	0		0.193×10^{21}	8.3	AS4/3501-6		
STS-8 (15)	0	-	0.35×10^{21}	41.75	Carbon/Epoxy		

TE: trailing edge; LE: leading edge

3.2.1.1 Mass Loss

The mass loss of several carbon/epoxy composite samples located on LDEF leading edge (Experiment M0003-9) and exposed to an atomic oxygen fluence of 8.99×10^{21} atoms/cm^2 are summarized in Table 3-3 (ref. 7). All leading edge uncoated samples exhibited mass loss. This is in contrast to the trailing edge samples that exhibited no significant mass loss. Hence, the mass loss is sample erosion due to AO and any micrometeoroid impact.

Table 3-3. Typical Mass Loss of Carbon/Epoxy Composite Materials

Material[a]	Fiber/Resin Suppliers	Weight Change %
GY70/CE339 Carbon/Epoxy	BASF/Ferro	-3.67
T50/F263 Carbon/Epoxy	Amoco/Hexcel	-3.10
T50/934 Carbon/Epoxy	Amoco/Fiberite	-3.05
T50/X904B Carbon/Epoxy	Amoco/Fiberite	-5.35
T50/E788 Carbon/Epoxy	Amoco/Hexcel	-4.61
Celion 6000/E788 Carbon/Epoxy	Celanese/Hexcel	-3.21
GY70/X904B Carbon/Epoxy	BASF/Fiberite	-3.92

(a) sample dimensions of 3.50-in. x 0.754-in. x 0.080-in. in thickness.

3.2.1.2 Thickness Erosion from Atomic Oxygen Exposure

Table 3-4 summarizes the average thickness loss due to atomic oxygen exposures and the atomic oxygen reaction efficiency for the carbon fiber composite systems from LDEF Experiments A0134, M0003-8, M0003-9, M0003-10, the Solar Array Materials Passive LDEF Experiment (SAMPLE) A0171, and LDEF Experiment AO180 (UTIAS). Also included for comparison are the Space Shuttle atomic oxygen flight experimental results (STS-8, STS-46).

Table 3-4. Atomic Oxygen Erosion Rates for Carbon Thermosets

Composite Materials	Laminate Orientation	Flight Experiment	Ref	Angle off ram	AO Fluence atoms/cm^2	Avg. Thickness Loss mils (μm)	AO Reaction Efficiency[1] 10^{-24}cm^3/atom
T300/5208 Epoxy	$[\pm 45]_s$	LDEF A0134	11	8	8.99×10^{21}	4.5 mil (114 μm)	
T300/934 Epoxy	$[0_2, \pm 45, 0_2, \pm 45, 90, 0]_s$	LDEF M0003-8	9	8	8.99×10^{21}	3.4 mil (86 μm)	0.99
T300/934 Epoxy	$[0]_{16}$	LDEF M0003-8	8	8		5.2 mil (132μm)	
C6000/PMR-15 Polyimide	$[0/\pm 45/0/\pm 45]_s$	LDEF M0003-8	8	8		7.8 mil (198μm)	
T50/934 Epoxy	$[+45/-45_2/+45]_{4T}$	LDEF M0003-9	7	8	8.99×10^{21}	4 - 6 mil	
GY70/CE339 Epoxy	$[+45/-45_2/+45]_{4T}$					(102-152 μm)	
P75S/934 Epoxy	$[0/45/90/135]_{2s}$	LDEF M0003-10	1	38	7.15×10^{21}	2 - 3.5 mil (50-90 μm)	
P75S/CE-339 Epoxy	$[0/45/90/135]_{2s}$						
GY70/934 Epoxy	$[0/45/90/135]_{2s}$						
GY70/CE-339 Epoxy	$[0/45/90/135]_{2s}$						
GY70/X-30	$[0/45/90/135]_{2s}$						
T300/V378A	$[0/45/90/135]_{2s}$						
AS-4/3501-6 Epoxy	$[0]_{16}$	LDEF M0003-10	4	38	7.15×10^{21}		0.8
T300/934 Epoxy	$[0]_{16}$			158	2.31×10^{5}		1.35
C6000/PMR-15 Polyimide	$[0/\pm 45/0/\pm 45]_s$						0.9
Carbon/LARC-160 Polyimide	$[0]_{16}$						
HMS/934 Epoxy	$[90]_8$	LDEF A0171	14	38	7.15×10^{21}	2.5 mil (63.5μm)	0.920
HMS/934 Epoxy	$[90]_8$	LDEF A0171	14	38	7.15×10^{21}	2.7 mil (69 μm)	1.0
P75S/934 Epoxy	$[90]_8$	LDEF A0171	14	38	7.15×10^{21}	2.7 mil (69 μm)	1.0
P75S/934 Epoxy	$[90]_8$	LDEF A0171	14	38	7.15×10^{21}	2.8 mil (71 μm)	1.0
T300/934 Epoxy	$[\pm 45]_{2S}$	LDEF A0180	5	82	1.33×10^{21}	.6 mil (15 μm)	1.25
T300/934 Epoxy	(tube);$[90]_4$, $[\pm 45]_{2s}$	LDEF A0180	5	82	1.33×10^{21}	2.4-6.3mil (60-160um)	1.9
T300/934 Epoxy	$[\pm 45]_s$, $[\pm 45]$	STS-8	15	0	0.35×10^{21}	.35 mil (9 μm)	2.6
T300/5208 Epoxy	$[\pm 45]$	STS-8	15	0	0.35×10^{21}	.35 mil (9 μm)	2.9
AS4/PMR-15 Polyimide		STS-46 EOIM-3	18	0	0.193×10^{21}	.3-.4mil (8-10μm)	
P75S/934 Epoxy	$[90/\pm 30/90]_S$	STS-46 EOIM-3	17	0	0.193×10^{21}	.2 mil (6 μm)	

1. The reaction efficiency was determined by dividing the specimen mass loss by the atomic oxygen fluence.

AO reactivity values generated from short term Space Shuttle exposures yielded two to three times the LDEF values noted in Table 3-4. A reasonable explanation is that high fluences accumulated through long exposures readily erode the matrix rich composite surface layer so that the fiber rich bulk region receives comparatively higher exposure than composites exposed to lower fluence levels. Reactivity values for high fluence exposed or long term exposed composites are thus more characteristic of the carbon fiber than the more reactive matrix material. Carbon AO reactivity were 0.5-1.3 x 10^{-24} cm^3/atom from the STS-5 mission.[20]

Consequently, long term surface erosion prediction of carbon fiber composites should be based on carbon AO reactivity to give a more realistic measure of material loss. Short term exposures of composites will yield erosion rates higher than predicted for longer-term exposures. Hence, the erosion depth as a function of AO fluence, plotted in Figure 3-2, would show a linear relationship if the short term Space Shuttle results are excluded.

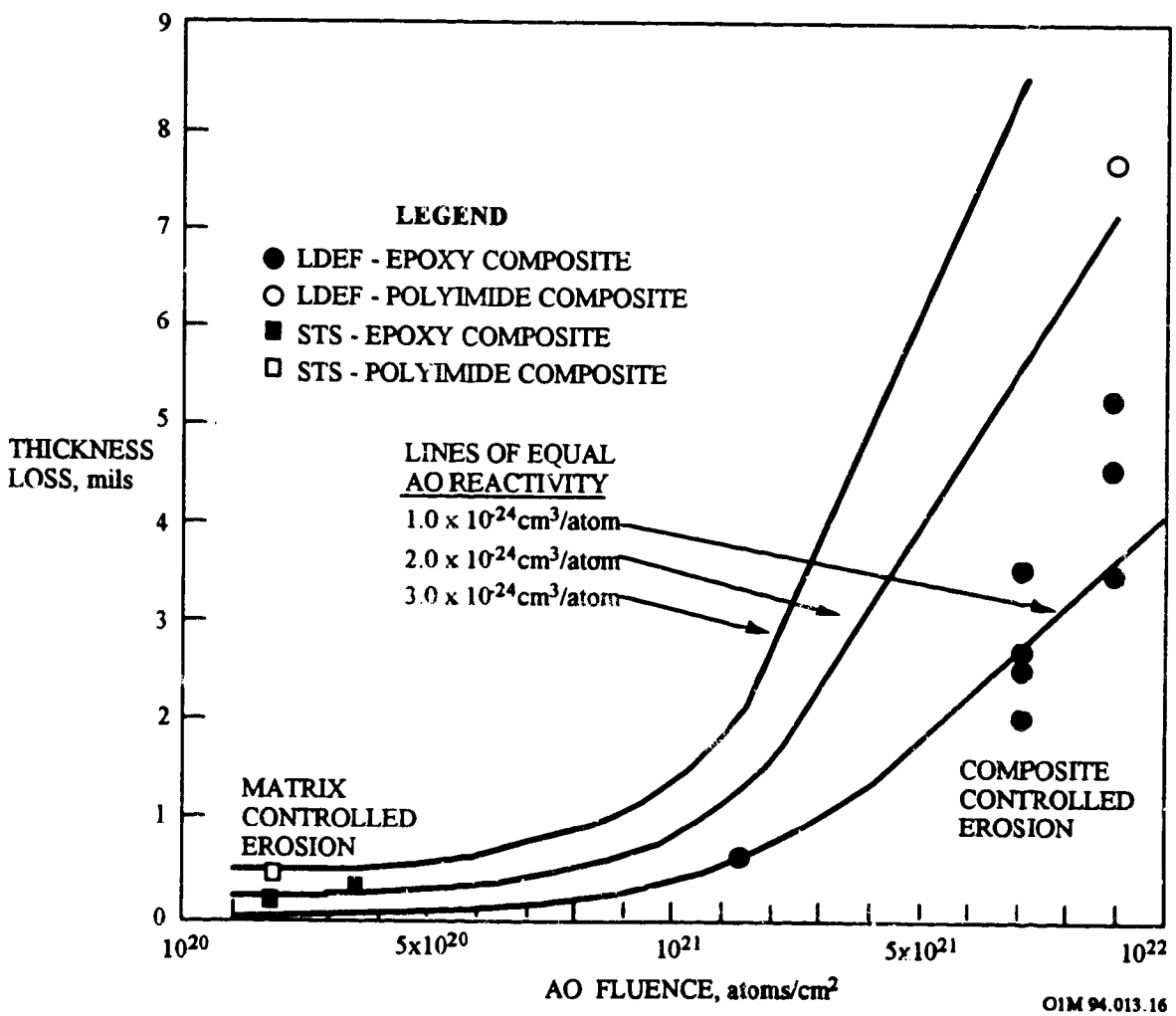

Figure 3-2. Thickness Loss of Carbon Composites as a Function of AO Fluence

A summary of the experimental details of the surface erosion for the polymer composites located on LDEF is provided below.

LDEF Experiment AO134. Surface degradation of an uncoated 4-ply, $[\pm 45]_s$ T300/5208 composite specimen exposed to an atomic fluence of 8.99×10^{21} atoms/cm^2 (tray B9 which was closest to the leading edge) indicated that virtually one ply of composite material (approximately 0.11 mm; 4.5 mil) was eroded during the 5.8-year exposure (ref. 11). The epoxy matrix eroded somewhat more rapidly than the carbon fibers. An ash-like residue remained on the eroded surface after the flight.

LDEF Experiment M0003-8. This experiment revealed dramatic loss of material due to atomic oxygen erosion for the leading edge (row D9) composite specimens (T300/934 epoxy, C6000/PMR-15 polyimide) (ref. 8). An AO reactivity of 0.99×10^{-24} cm^3/atom was calculated for the bare composite T300/934 epoxy panel $[O_2/\pm 45/O_2/\pm 45/90/O]_S$ based on thickness loss (ref. 9).

LDEF Experiment M0003-9. Photographs of several carbon/epoxy composites on the leading edge (atomic fluence of 8.99×10^{21} atoms/cm^2) revealed that the carbon fibers were eroded by the AO and formed no unreactive protective layers as observed with the glass/epoxy samples. (ref. 7). The total amount of thickness loss was approximately 0.10 - 0.15 mm (4 - 6 mils) for the carbon/epoxy samples (thickness loss due to AO and micrometeoroid impact for the carbon/epoxy samples was measured from cross sectional microphotographs). This compares to 0.08-0.13 mm (3 - 5 mils) for Kevlar/epoxy samples, and 0.013-0.03 mm (.5 - 1 mil) for glass/epoxy samples. Of the materials tested, the glass/epoxy was the least affected by the atomic oxygen (see Section 3.2.3.1). The thickness loss for the carbon/epoxy samples was slightly less than the predicted thickness loss of 0.167 mm (6.6 mil) estimated using the reaction efficiency values from previous shuttle flight ($\Delta x = F_T \times R_e$).

LDEF Experiment M0003-10. Erosion depths[a] for several polymer matrix composites on LDEF's leading edge (Row D8) and exposed to an atomic fluence of 7.15×10^{21} atoms/cm^2 were observed to be inversely proportional to their fiber content (refs. 1 and 3). The results, shown in Figure 3-3, are for several carbon/epoxy composites $[0/45/90/135]_{2s}$ having several different fiber-matrix combinations and a wide range of fiber content.

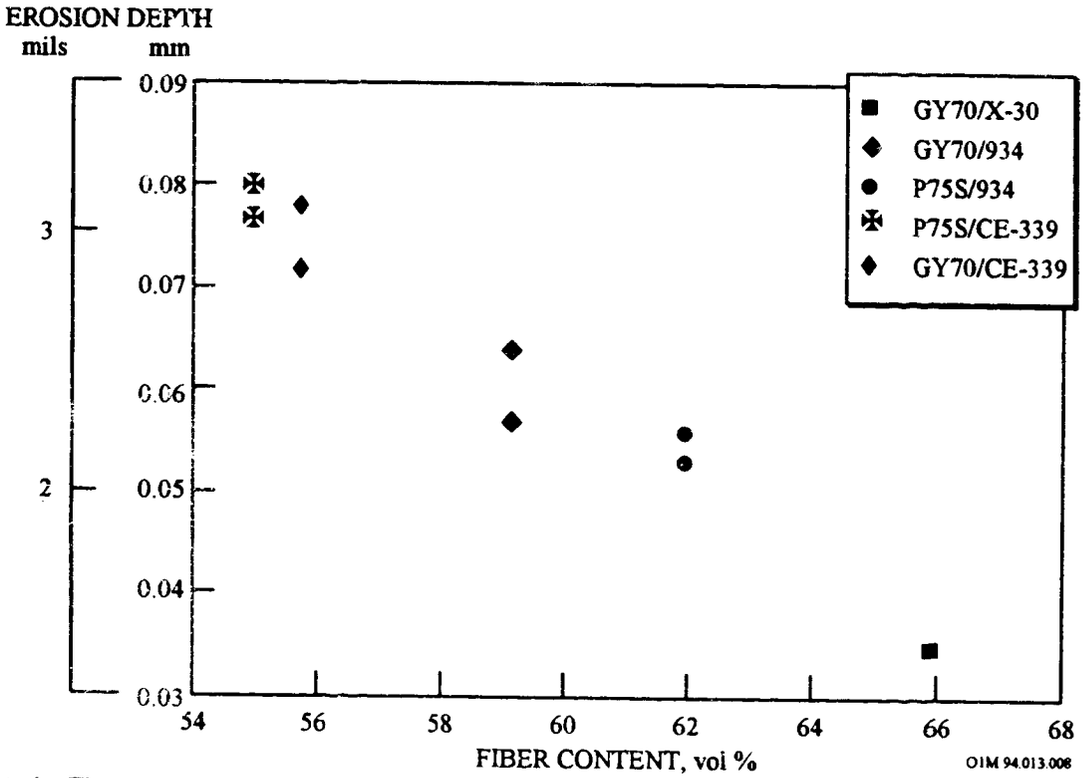

Note 1 The mass measurements were made after the samples had equilibrated in a constant temperature, constant humidity laboratory. Thus, moisture variations were eliminated and the only significant mass changes were those that could be attributed to atomic oxygen erosion on the exposed leading edge.

Note 2 The composites were made by General Dynamics Space Systems Div. and have similar surface conditions and identical fiber orientations. Carbon fiber suppliers are: BASF Structural Materials Inc. (Celion GY70) and Amoco performance Products inc. (Thornel P75S). Epoxy-resin suppliers are: Composites Div., Fiberite Corp. (X-30 and 934) and Composites Div., Ferro Corp. (CE-339)

Note 3 All of the composites were fabricated following similar processing procedures. In particular, the same bleeder cloth was used so that the composites had similar surface conditions. Composites prepared by other experiment participants having significantly different surface conditions (either more matrix rich or less matrix rich) did not fall on the erosion depth versus fiber content curve. This implies that fiber content and surface condition are more important variables than fiber or matrix type in determining susceptibility to atomic-oxygen erosion.

Figure 3-3. Atomic Oxygen Erosion Depth Versus Fiber Content for LDEF Carbon/Epoxy Composites

[a] The extent of the average atomic-oxygen erosion depth for these uncoated polymer matrix composites was calculated using weight-loss data, the known composite density, exposure area, and the measured mass loss. Since the fibers and matrix have different erosion rates and densities, this technique of determining the erosion depth is an approximation. The actual erosion depths are probably somewhat higher because the samples had resin-rich surfaces and the epoxy erodes at a higher rate than the higher density carbon fibers.

Experiment AO171. This experiment, located on Row 8 position A, allowed all materials to be exposed to an atomic oxygen fluence of 7.15×10^{21} atoms/cm^2 as a result of being positioned 38° off the ram direction. The erosion depths for the uncoated polymer matrix composites were significantly less than that for monolithic polymers. For example, the estimated erosion depth for most of the epoxy composites was less than 0.07 mm (2.8 mil), which is much less than the predicted erosion of 0.12 mm for monolithic epoxies[21] at the LDEF atomic oxygen fluence of approximately 7.15×10^{21} atoms/cm^2 for Row 8. This is attributed to the lower erosion for the carbon fibers in comparison to the composite epoxy matrix erosion. Atomic oxygen reactivity values for the carbon/epoxy composites on averaged 1×10^{-24} cm^3/atom (see Table 3-4). All thickness losses measured on the flight specimens were consistent with their measured mass loss.

Experiment AO180. This experiment was located at D12 on LDEF, 90° to the leading edge. LDEF was yawed 8° relative to the orbital velocity vector, with a corresponding atomic oxygen fluence at D12 of about 1.33×10^{21} atoms/cm^2.[22] All of the LDEF AO180 experiment composite tube and flat coupon samples were mounted on the trays with aluminum end fixtures. Low-incident-angle atomic oxygen eroded the composite-material samples, which were located approximately 82° of the ram direction. Scanning electron microscopy photographs of the exposed area showed that essentially only the surface resin layer was eroded. Thickness loss measurements for the carbon/epoxy T300/934 flat laminate (4-ply; $(\pm 45)_{2s}$) was measured at 15 μm (~.6 mil). Neglecting any fiber loss, the erosion yield for this epoxy is estimated at $\sim 1.25 \times 10^{-24}$ cm^3/atom. This compared favorably with data from Space Shuttle Flight experiments that quote a value of $\sim 1.7 \times 10^{-24}$ cm^3/atom.[23,24]

Atomic oxygen erosion of circular tubes was also studied (ref. 5). Because of the curvature, it is possible to investigate erosion loss and surface morphology changes as a function of angular position around the tube. The maximum loss was estimated at ~160μm (~6.3 mil) during the 69 months in low Earth orbit; about one ply of material for near ram conditions. The erosion yield for this material is estimated at $\sim 1.9 \times 10^{-24}$ cm^3/atom, which is again slightly less than the range of values reported for different carbon/epoxy materials of $2.1\text{-}2.6 \times 10^{-24}$cm^3/atom from the previous shuttle flights.[25]

3.2.1.3 Impact Damage from Micrometeoroid and Debris

Micrometeoroid and debris impact on the polymer composites does not produce the typical hemispherical craters found on metallic structures. Instead, due to the brittle nature of the resin matrix, the damage consist of penetration holes with adjacent surface damage (e.g., jagged edges), and some internal ply delamination and local fiber fractures. A schematic diagram of the damage morphology and diameter measurements for impacts into composites is shown in Figure 3-4.[26]

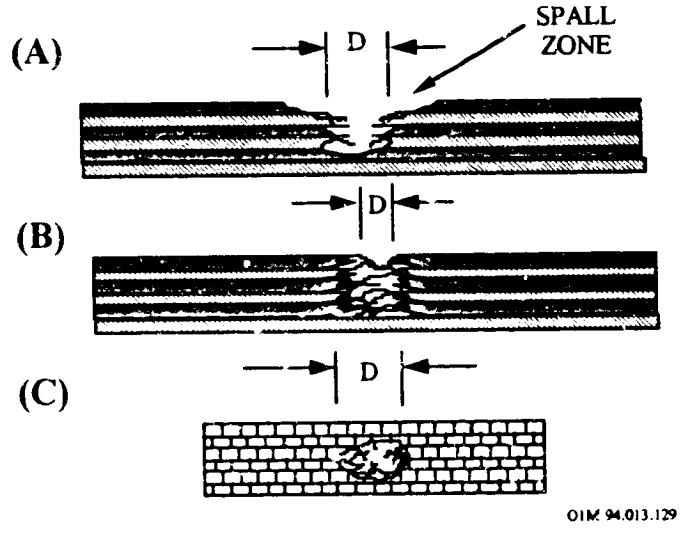

(A) Cross-sectional view of feature with surrounding spall zone
(B) Feature with a larger damage zone, beneath the composite surface, than is visually seen at the original material surface
(C) Top view of a feature in a composite surface.

Figure 3-4. Schematic of Damage Morphology For Impacts Into Composites

For the more brittle composite structural materials, the damage is rarely a simple crater. Instead, significant in-depth damage can occur and may be anisotropic, following the structure of fibers. For complete penetrations the rear surface damage area is frequently larger than the entry hole area. This usually occurs with brittle fibers, such as carbon, in which case the impact and exit holes exhibit brittle fiber fractures as well as rear exit hole surface spallation (T300/5208 epoxy, $[\pm 45]_S$). The spallation damage-to-hole size ratio is about 5:1. On the other hand, tough non-brittle fibers such as aramid fibers fail in a "brush or broom" mode surrounding the impact damage region (Kevlar/epoxy tube SP-328, $[\pm 45]_{4S}$).

Although no catastrophic failure occurred from the impacts experienced on LDEF, this type of impact damage can still lead to failure in highly stressed components due to the breaking of the fibers, cracking of the matrix, and removal of part of the matrix via the spallation process. This could also lead to further erosion of the composite material during subsequent exposure to other

space environments such as atomic oxygen or ultraviolet light, creating additional delaminations and interply cracking.

Impact damage from micrometeoroid and debris for various carbon fiber-reinforced epoxy materials occurred on the LDEF UTIAS Experiment AO180.[27] The samples were mounted at D12, about 82° from the ram direction. The exposed surface area was ~0.6m^2. The UTIAS experiment suffered 84 randomly distributed impacts by micrometeoroids or space debris; 74 of them produced craters having diameters less than 0.5 mm (0.02 in.). The predicted number of impacts for this area after 5.75 years is ~80, which is based on the nomogram of Figure 2-9 (assuming $\theta = 90°$).

From a detailed inspection of the composite samples (both tubes and flat plates), only 10 of the 84 hits were found on these materials, the balance located on end-fixtures and on the aluminum base plates. A summary of the 10 impact sites (out of 84) found on the composite samples is given in Table 3-5 with estimates of surface damage area, hole size and penetration depth. Also included are the impact damage on Kevlar fiber-reinforced epoxy samples. Such data are useful for estimating total damage on composite structures that arises from micrometeoroids/debris.

Table 3-5. Summary of Impact Features on Carbon Epoxy Composite Specimens

Material Type	Sample Type	# of Plies	Surface Damage Area (mm^2)	Hole Area (mm^2)	Nominal Hole Diameter (mm)	Particle Penetration Depth (# of Plies)
Carbon/Epoxy (T300/5208)	Plate	4	0.222	0.222		>4
Carbon/Epoxy (T300/SP 288)	Tube	4	1.064	0.083	0.325	>4
Kevlar/Epoxy (SP 328)	Tube	4	1.162	0.036	0.215	1~2
	Tube	4	0.498	0.015	0.139	~1
	Tube	4	0.423	0.018	0.152	~1
	Tube	4	1.253	0.076	0.312	2~3
	Tube	4	0.223			1~2
			1.445	0.033	0.204	2~3
			0.370			~1
			0.881	0.020	0.159	2~3

Note: Micrometeoroid/debris impacts can penetrate four-ply laminates with substantial rear-face spallation damage.

3.2.1.4 Mechanical Property Degradation from Atomic Oxygen

The effect of LEO exposure on the mechanical properties of polymeric composites that flew on LDEF are discussed below.[b] Emphasis is on the effects of specimen location on the spacecraft as well as on how the laminate design of the composite specimens plays a significant role in determining the residual properties of the composites.

3.2.1.4.1 Tensile

Figures 3-5 and 3-6 show the ultimate tensile strength and tensile modulus for T300 carbon/epoxy (934 and 5208) composites[c] that received over 5 years and 9 months of on LDEF Experiment A0134 (ref. 11). These composites were fabricated from unidirectional prepregs oriented into a 4-ply $[\pm 45]_s$ lay-up so as to be matrix sensitive during tensile testing.[d] The tensile specimens were 0.500-inch and 0.375-inch wide by 8-inches long with laminate thickness varying from 0.016-inch to 0.024-inch. The location of this experiment (in Tray B on Row 9) was the leading edge of LDEF and hence, received an atomic fluence of 8.99×10^{21} atoms/cm^2.

These off-axis composite specimens exhibited a significant deterioration in both tensile strength and modulus. Tensile strengths were between 45 to 65% lower than the baseline composite specimens (e.g., tensile strength of the T300/5208 composite decreased to 7.3 ksi (50 MPa) from 21.0 ksi (145 MPa)). Tensile modulus were between 20 to 33% lower than the baseline composite specimens (e.g., tensile modulus of the T300/5208 composite decreased to 1.9 Msi (13 GPa) from 2.5 Msi (17 GPa)). However, no major differences were noted in the baseline values for the composites tested in 1982, the ground control composites that remained at Langley, and the composites that flew protected (the T300/934 epoxy composites were coated with sputter-deposited metals to evaluate the metal's effectiveness for atomic oxygen protection of composites; see Section 3.3.2). More than a loss in matrix resin contributed to this phenomena since the thickness loss is not proportional to the loss in tensile properties by rule of mixtures (thickness losses varied from 0.003 to 0.0045 inch of the 0.0055-inch thick outer ply).

---

[b] A significant number of composite specimens were part of several sub-experiments of LDEF Experiment M0003, "Space Environmental Effects on Spacecraft Materials." M0003-8 was a Boeing Defense and Space Group experiment, M0003-9 was a Lockheed Missiles & Space Company experiment, and M0003-10, the Advanced Composites Experiment, was a joint government and industry effort. General Dynamics Space Systems Company (GDSSD), Lockheed Missiles & Space Company (LMSC), Boeing Defense and Space Group, McDonnell Douglas Space Systems Company (MDSSC), and United Technologies Research center (UTRC) participated in this subexperiment. The Aerospace Corporation was the principal investigator for the M0003-16 experiment. LDEF Experiment A0134 also evaluated polymeric composites.

[c] Fiberite 934 resin; Narmco 5208 resin; Union Carbide T300 fiber.

[d] In-plane shear strength and modulus are obtained from tension tests on $[\pm 45]$ laminates conducted according to the ASTM Practice for In-plane Shear Stress-Strain Response of Unidirectional Reinforced Plastics (D 3518).

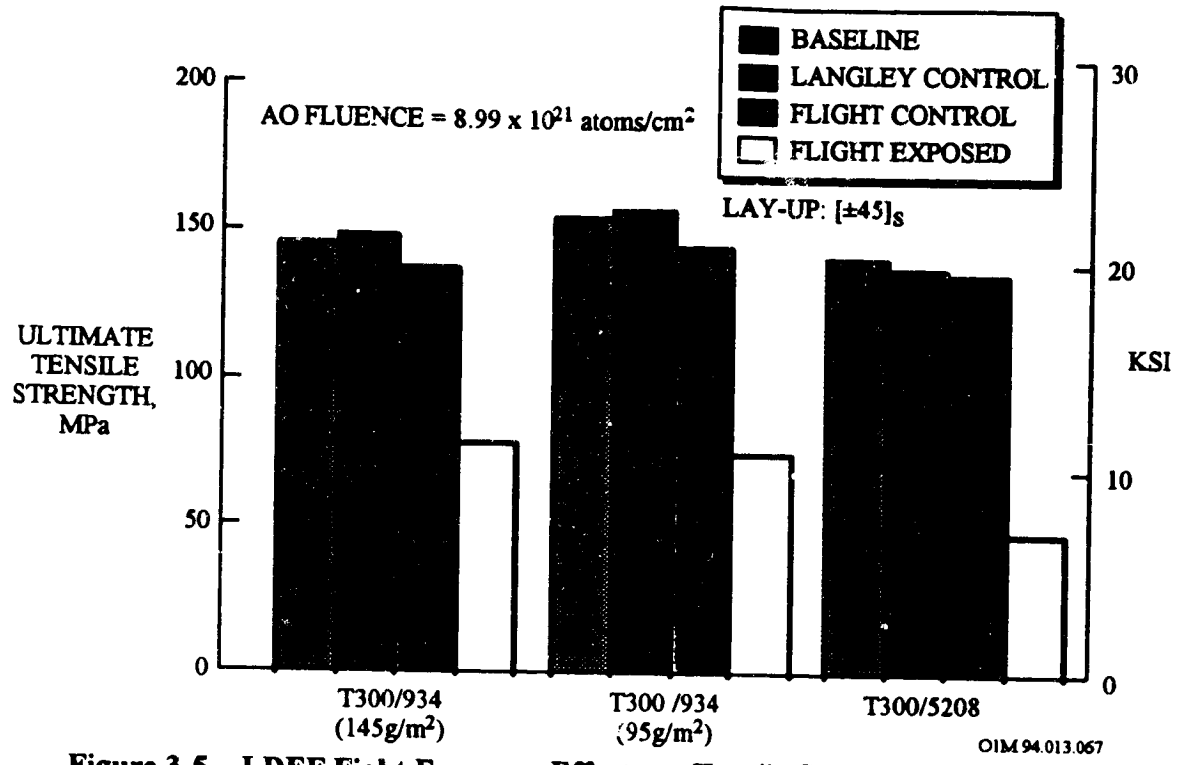

Figure 3-5. LDEF Fight Exposure Effects on Tensile Strength of Epoxy Composites

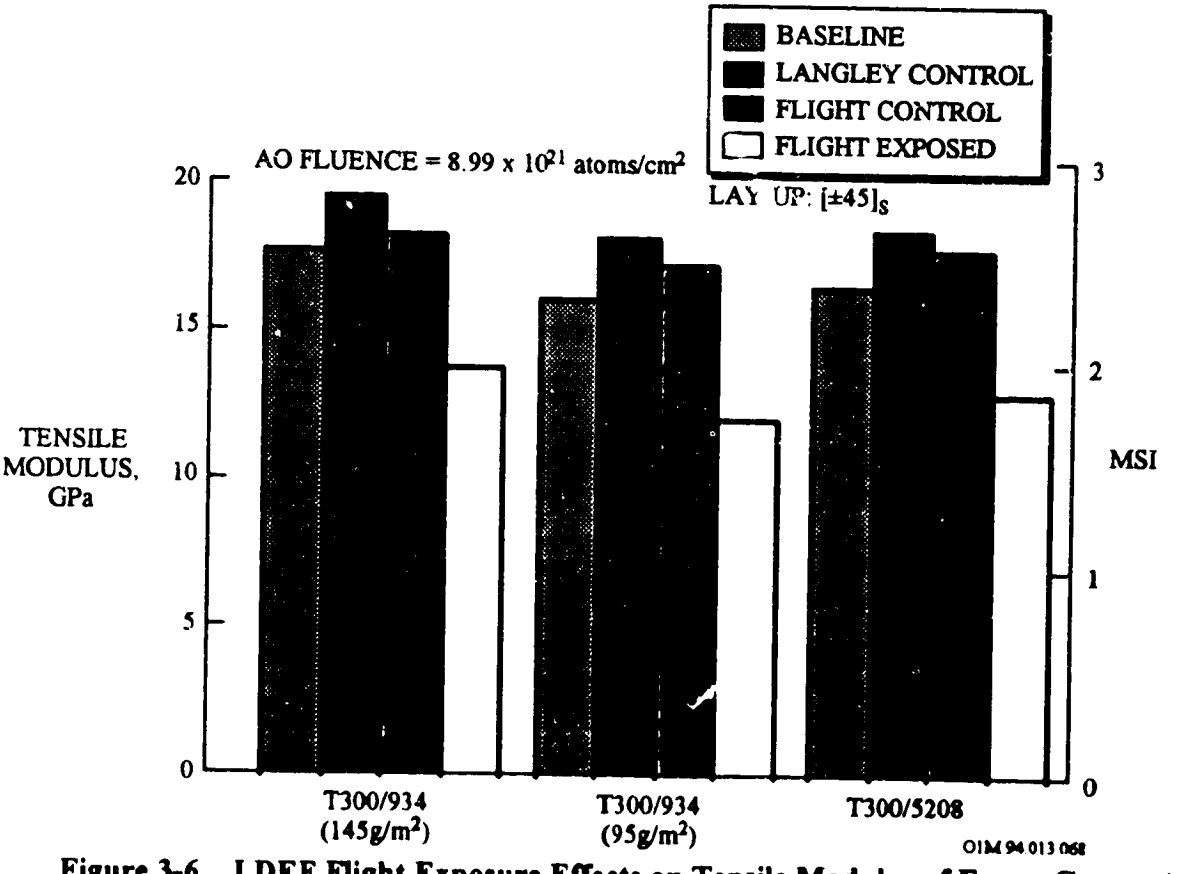

Figure 3-6. LDEF Flight Exposure Effects on Tensile Modulus of Epoxy Composite

LEO exposure does not appear to significantly reduce the tensile strength of a unidirectional T300/934 epoxy composite $[0]_{16}$. These composite specimens, part of LDEF Experiment M0003-8 (Boeing), were located at the trailing edge position D3 (atomic oxygen fluence of 1.32×10^{17} atoms/cm^2), and were held in stress during the flight using preload fixtures adjusted to maintain a predetermined level of strain (ref. 8). Table 3-6 summarizes the tensile test results. In addition tensile moduli values compared favorably with pre-flight values.

Table 3-6. Tensile Properties of T300 Carbon/934 Epoxy $[0]_{16}$

Conditions	Pre-flight			Post-flight		
	Strength, ksi (MPa)	Modulus, Msi (GPa)	# Tested	Strength, ksi (MPa)	Modulus, Msi (GPa)	# Tested
Baseline	152.7 (1052.8)	est 18-20 (124-138)	3			
Prestressed trailing edge				148.1 (1021.1)	21.0 (144.8)	2

Note:The tensile test results are inconclusive due to the spread of the data and the limited sample population. Pre and post flight strength values are very similar but all are well below anticipated levels for this material system. Most of the post flight test failures occurred outside of the gauge area or at locations with rough edges. The same problems may have existed for pre-flight testing, thus lowering the strength values.

LEO exposure appeared to have degraded the tensile properties for a C6000 carbon/PMR-15 polyimide $[0/\pm45/0/\pm45]_s$. These composite specimens, part of LDEF Experiment M0003-8 (Boeing), were located at the trailing edge position D3 (atomic oxygen fluence of 1.32×10^{17} atoms/cm^2), and were held in stress during the flight using preload fixtures adjusted to maintain a predetermined level of strain (ref. 8). Table 3-7 summarizes the tensile test results. This reduction in mechanical property was unexpected since these were trailing edge exposed composites and hence, shielded from any atomic oxygen erosion that typically occurs on leading edge exposed composites.

Table 3-7. Tensile Properties of C6000 Carbon/PMR-15 Polyimide $[0/\pm45/0/\pm45]_s$

Conditions	Pre-flight			Post-flight		
	Strength, ksi (MPa)	Modulus, Msi (GPa)	# Tested	Strength, ksi (MPa)	Modulus, Msi (GPa)	# Tested
Baseline	69.6 (479.9)		3			
Prestressed trailing edge				45.4 (313.0)	8.0 (55.2)	2

Note: Tensile test results are inconclusive due to the spread of the data and the limited sample population.

3.2.1.4.2 Compression

LEO exposure does not appear to significantly reduce the compression strength of a T300/934 epoxy composite $[0^{\circ}]_{16}$ and for a C6000 carbon/PMR-15 polyimide $[0/\pm45/0/\pm45]s$. These composite specimens, part of LDEF Experiment M0003-8 (Boeing), were located at the trailing edge position D3 (atomic oxygen fluence of $1.32x10^{17}$ atoms/cm^2), and were held in stress during the flight using preload fixtures adjusted to maintain a predetermined level of strain (ref. 8). Table 3-8 and 3-9 summarizes the compressive test results for the M0003-8 composites. Compression moduli data for the epoxy system is questionable due to the severe end brooming which occurred during testing and may have been caused by damage to the specimen ends from the preload fixture.

Table 3-8. Compression Properties of T300 Carbon/934 Epoxy $[0]_{16}$

Conditions	Pre-flight			Post-flight		
	Strength, ksi (MPa)	Modulus, Msi (GPa)	# Tested	Strength, ksi (MPa)	Modulus, Msi (GPa)	# Tested
Baseline	118.1	est 18-20	3			
Prestressed trailing edge				106.8	8.3	2

Note:The compression test results are inconclusive due to the spread of the data and the limited sample population. Pre and post flight strength values are very similar but all are well below anticipated levels for this material system. Most of the post flight test failures occurred outside of the gauge area or at locations with rough edges. The same problems may have existed for pre-flight testing, thus lowering the strength values.

Table 3-9. Compression Properties of C6000 Carbon/PMR-15 Polyimide $[0/\pm45/0/\pm45]_s$

Conditions	Pre-flight			Post-flight		
	Strength, ksi (MPa)	Modulus, Msi (GPa)	# Tested	Strength, ksi (MPa)	Modulus, Msi (GPa)	# Tested
Baseline	64.5 (444.7)	-	3			
Prestressed trailing edge				61.0 (420.6)	6.9 (47.6)	2

Note:The compression test results are inconclusive due to the spread of the data and the limited sample population. Pre and post flight strength values are very similar but all are well below anticipated levels for this material system. Most of the post flight test failures occurred outside of the gauge area or at locations with rough edges. The same problems may have existed for pre-flight testing, thus lowering the strength values.

3.2.1.4.3 Short Beam Shear

Short beam shear strengths of carbon/epoxy composites exposed to the LEO environment are summarized in Table 3-10.[e] These composites were part of LDEF Experiment M0003-9 (LMSC) (ref. 7), which were located on Bay D, Row 9 on the leading edge (AO fluence = 8.99×10^{21} atoms/cm^2) and on Bay D, Row 3 on the trailing edge of LDEF (AO fluence = 1.32×10^{17} atoms/cm^2). Specimens were 16 ply unidirectional [0] laminates and $[\pm 45]_{4s}$ fabric laminates.

The results show that the strengths of the exposed composite specimens degraded only to the extent of the mass loss percentage (strength calculations were based upon the final area of the specimen). Hence, the LDEF exposure had no apparent effect on the short beam shear strength for any of the epoxy matrix composites. This indicates that except for the physical eroding of the material there was no mechanically detrimental effects caused by the low Earth orbit environment.

Table 3-10. Short Beam Shear Strength for Flight Exposed Carbon Epoxies on LDEF

Material	Laminate Orientation	Fiber/Resin Supplier	Sample Location	Short Beam Shear, ksi (MPa)
GY70/CE-339	$(0)_{16}$	BASF/Ferro	Leading Edge	8.6 (59.3)
GY70/CE-339	$(0)_{16}$	BASF/Ferro	Trailing Edge	8.1 (55.8)
GY70/CE-339	$(0)_{16}$	BASF/Ferro	Control	7.6 (52.4)
T50/F263	$(0)_{16}$	Amoco/Hexcel	Leading Edge	12.7 (87.6)
T50/F263	$(0)_{16}$	Amoco/Hexcel	Trailing Edge	12.6 (86.8)
T50/F263	$(0)_{16}$	Amoco/Hexcel	Control	12.6 (86.8)
T50/934	$(0)_{16}$	Amoco/Fiberite	Leading Edge	11.8 (81.3)
T50/934	$(0)_{16}$	Amoco/Fiberite	Trailing Edge	12.1 (83.4)
T50/934	$(0)_{16}$	Amoco/Fiberite	Control	10.0 (68.9)
T50/X904B	$(0)_{16}$	Amoco/Fiberite	Leading Edge	10.6 (73.1)
T50/X904B	$(0)_{16}$	Amoco/Fiberite	Trailing Edge	10.8 (74.4)
T50/X904B	$(0)_{16}$	Amoco/Fiberite	Control	7.7 (53.1)
HMF 176/934	$(\pm 45)_{4s}$	Amoco/Fiberite	Leading Edge	10.9 (75.1)
HMF 176/934	$(\pm 45)_{4s}$	Amoco/Fiberite	Trailing Edge	12.1 (83.4)
HMF 176/934	$(\pm 45)_{4s}$	Amoco/Fiberite	Control	10.7 (73.7)

Note: . The shear test was run per ASTM D 2344.

[e] The short beam shear test, a resin dominated property, is typically chosen because of the sample size limitations and since shear changes would be expected to appear more distinctly than other mechanical property changes.

Effects of the LEO environment on the short beam shear strength of thermoset composites on LDEF Experiment M0003-10 (GDSSD) are shown in Figure 3-7 (ref. 3). These composites, located on both the leading (Bay D, Row 8; AO Fluence = 7.51×10^{21} atoms/cm^2) and on the trailing edges (Bay D, Row 4; AO fluence = 2.31×10^5 atoms/cm^2), consisted of GY70/X-30, GY70/CE-339, P75S/CE-339, P75S/934 and GY70/934 carbon/epoxy composites and T300/V378A carbon/bismaleimide composites with a $[0/45/90/135]_{2s}$ laminate configuration.

There was no reduction in the short beam shear strength except that due to atomic oxygen erosion on the leading edge. In order to quantify the property loss on the leading edge, the average property value for the leading edge samples was divided by the average value for all of the remaining samples (e.g., laboratory controls, trailing edge samples). The composites located on the leading edge suffered only 10% reduction in the short beam shear strength (see Figure 3-7) whercas the composites located on the trailing edge did not suffer any strength degradation. The composites suffered larger reduction in their flexural properties compared to the short beam shear strength (see next section). This is not surprising since short beam shear strength is not as sensitive to surface degradation as is the flexural strength.

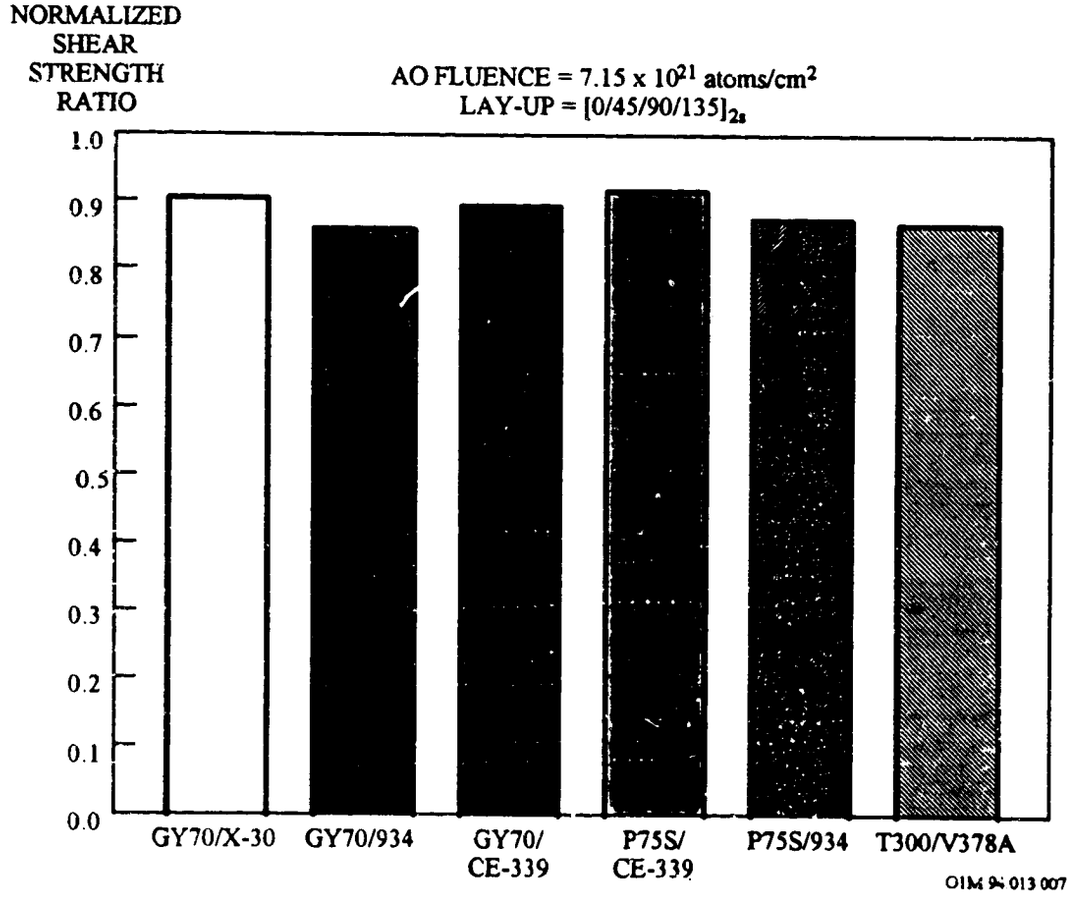

Figure 3-7. Reduction in Short Beam Shear Strength for LDEF Leading Edge Carbon Composites

3.2.1.4.4 Flexural

Flexural properties of carbon/epoxies exposed to the LEO environment are summarized in Table 3-11 (ref. 7). These composite specimens, part of LDEF Experiment M0003-9 (LMSC), were located on Bay D, Row 9 on the leading edge and Bay D, Row 3 on the trailing edge of LDEF. Specimen configuration were either 16 ply $(45/-45_2/45)_{4T}$ or $(+45)_{4s}$ fabric laminates.[f]

The results showed that the strength and modulus of the exposed specimens were degraded only to the extent of the mass loss percentage (see Table 3-3). Hence, except for the physical eroding of the material the LEO environment did not caused any detrimental effects.

Table 3-11. Flexural Test Data for Carbon Thermosets on LDEF M0003-9

Material	Laminate Orientation	Fiber/Resin Supplier	Sample Location	Strength ksi (MPa)	Modulus Msi (GPa)
GY70/CE-339	$(45/-45_2/45)_{4T}$	BASF/Ferro	Leading Edge	35.2 (242)	2.14 (14.7)
GY70/CE-339	$(45/-45_2/45)_{4T}$	BASF/Ferro	Trailing Edge	37.9 (261)	2.55 (17.6)
GY70/CE-339	$(45/-45_2/45)_{4T}$	BASF/Ferro	Control	38.2 (263)	2.48 (17.1)
T50/F263	$(45/-45_2/45)_{4T}$	Amoco/Hexcel	Leading Edge	49.4 (340)	3.49 (24.1)
T50/F263	$(45/-45_2/45)_{4T}$	Amoco/Hexcel	Trailing Edge	47.0 (324)	3.14 (21.6)
T50/F263	$(45/-45_2/45)_{4T}$	Amoco/Hexcel	Control	47.7 (328)	3.26 (22.4)
T50/934	$(45/-45_2/45)_{4T}$	Amoco/Fiberite	Leading Edge	48.7 (335)	2.71 (18.7)
T50/934	$(45/-45_2/45)_{4T}$	Amoco/Fiberite	Trailing Edge	52.1 (359)	3.01 (20.7)
T50/934	$(45/-45_2/45)_{4T}$	Amoco/Fiberite	Control	48.3 (333)	2.90 (19.9)
T50/X904B	$(45/-45_2/45)_{4T}$	Amoco/Fiberite	Leading Edge	46.3 (319)	2.29 (15.8)
T50/X904B	$(45/-45_2/45)_{4T}$	Amoco/Fiberite	Trailing Edge	40.0 (275)	1.97 (13.6)
T50/X904B	$(45/-45_2/45)_{4T}$	Amoco/Fiberite	Control	47.1 (324)	2.31 (15.9)
HMF176/934	Fabric $(\pm45)_{4s}$	Amoco/Fiberite	Leading Edge	66.8 (460)	3.16 (21.8)
HMF176/934	Fabric $(\pm45)_{4s}$	Amoco/Fiberite	Trailing Edge	67.6 (466)	3.14 (21.6)
HMF176/934	Fabric $(\pm45)_{4s}$	Amoco/Fiberite	Control	67.0 (461)	3.23 (22.2)

Note: For the leading edge samples which experienced a loss of material from atomic oxygen, strength and modulus calculations were based on the final thickness of the composites in order to show the true loss in load carrying ability. Thus, results show that the strength and modulus of the composites were unaffected by the mass loss. However, for a real structure, one would need to determine the effect of the mass loss on the load carrying capability and stiffness.

Note: The flexure test was run per ASTM D 790; composite specimens were 3.5-in. long by 0.75-in. wide.

[f] The flexure test is typically chosen where there are sample size limitations and to show more distinct mechanical property changes since flexure is a fiber dominated property.

Effects of the LEO environment on the flexural properties for the carbon thermoset composites of the LDEF Aerospace Experiment M0003-10 (GDSSD) are summarized in Figures 3-8 and 3-9 (ref. 3). These composites, located on both the leading (Bay D, Row 8) and trailing edges (Bay D, Row 4), consisted of GY70/X-30, GY70/CE-339, P75S/CE-339, P75S/934 and GY70/934 carbon/epoxy and T300/V378A carbon/bismaleimide composites, all with a $[0/45/90/135]_{2s}$ laminate configuration.

The five carbon/epoxy composites all had normalized leading edge strength values that were at least 70% of the original value, about as expected considering that the outer 0° ply was mostly or completely eroded away. This explains the minimum reduction in flexural properties for the composites which had a 45° ply at the outer surface (Experiment M0003-9; Table 3-1). In a flexural test, the loss of a 0° ply from the surface will have a much more pronounced effect on the strength than the loss of a 45° ply. In assessing the effect of atomic oxygen erosion on the strength and modulus of composites, the composite lay-up is an important consideration.

In contrast to the epoxy composites, the flexural strength of the exposed T300/V378A carbon/bismaleimide composite specimen located on the leading edge was only 40% of the original strength (see Figure 3-8). The mass loss for this material was somewhat greater than for the other composites, but not to the extent that one would expect such a large loss of strength

Figure 3-9 show the reduction in the flexural modulus for these LDEF leading edge composites. The T300/V378A composite along with the P75S/934 composite showed the largest modulus reduction, at approximately 70% of the original modulus. But the reduction in the modulus was not nearly as great as observed for the strength.

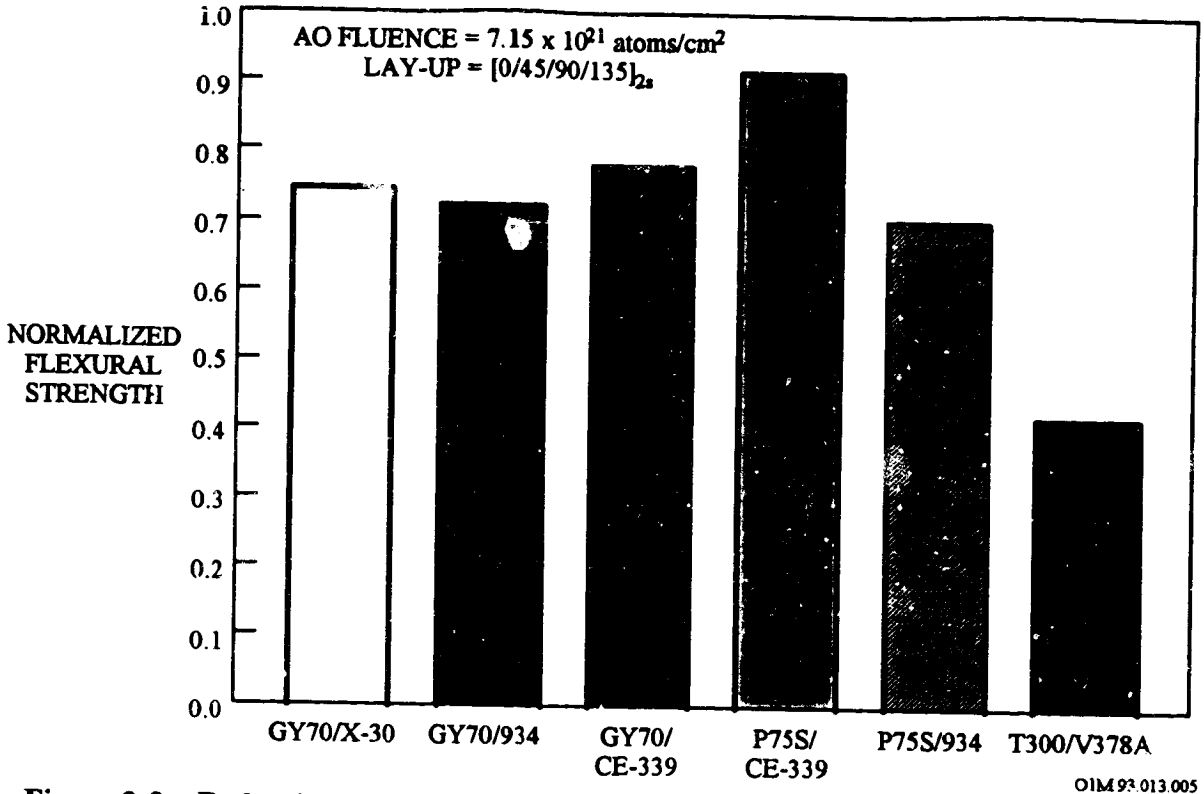

Figure 3-8. Reduction in Flexural Strength for LDEF Leading Edge Carbon Composites

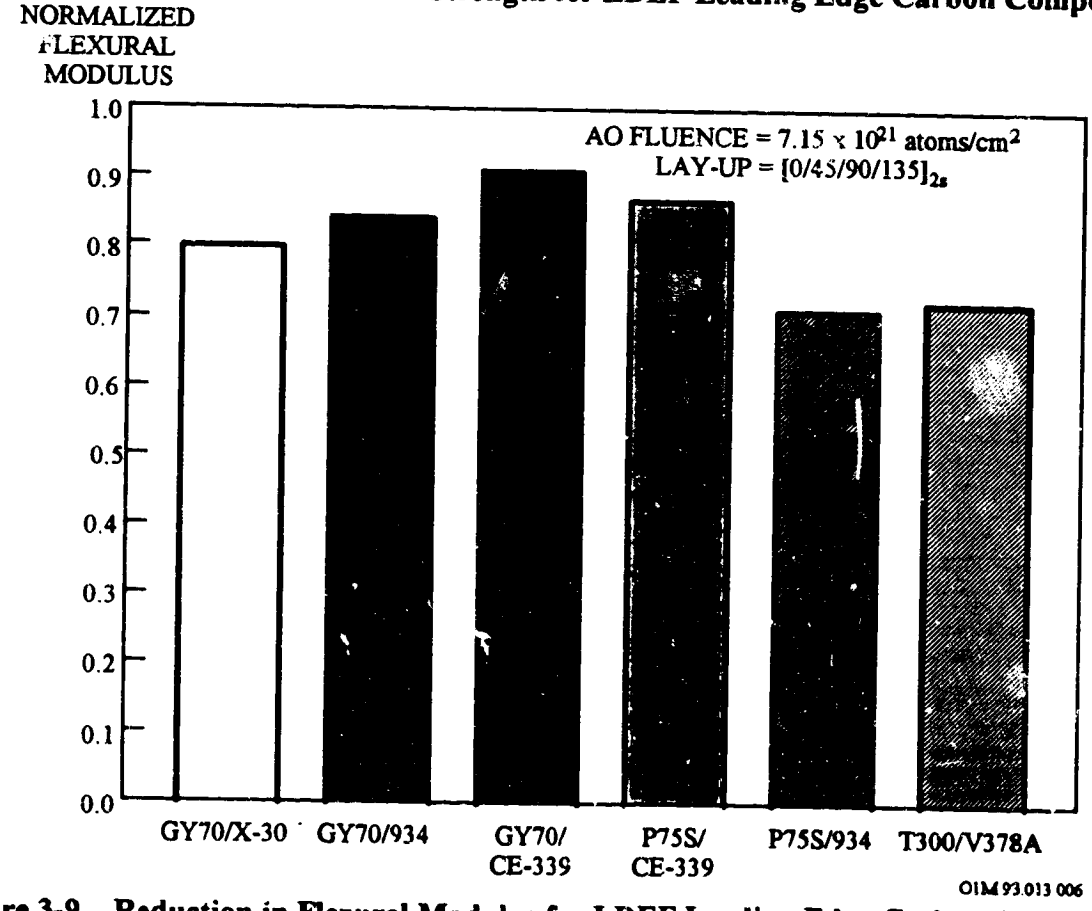

Figure 3-9. Reduction in Flexural Modulus for LDEF Leading Edge Carbon Composites

Effects of the LEO environment on the flexural properties of several carbon composites on the LDEF Boeing "Advanced Composites Experiment M0003-10, are summarized in Figures 3-10 to 3-13 (ref. 4). These composites consisted of T300 carbon/934 epoxy $[0]_{16}$, AS-4 carbon/3501-6 epoxy $[0]_{16}$, C6000 carbon/PMR-15 polyimide $[0,\pm45,0,\pm45]_s$, and carbon/LARC-160 polyimide $[0]_{16}$.

The experiment occupied approximately one-sixth of a 6 in.-deep peripheral tray on both the leading and trailing edges of LDEF. The trays were located on LDEF Bay D, Row 4 on the trailing edge and Bay D, Row 8 on the leading edge. The samples were mounted on both sides of cassettes with one side (Deck A) exposed to the space environment (leading Row 8: AO fluence of 7.15×10^{21} atoms/cm^2, 9,400 esh, 32,422 thermal cycles between -47°C (-53°F) and 84°C (183°F); trailing edge Row 4: AO fluence of 2.31×10^{5} atoms/cm^2, 10,500 esh, 32,422 thermal cycles between -3°C (-27°F) and 77°C(170°F). The other side, Deck B, faced inward and hence, the specimens did not receive any AO or UV exposure. Although the samples on the B decks were not exposed to the radiation environment, the experiment design was such that they experienced thermal excursions similar to those of the exposure samples located on Deck A.

The T300/934 epoxy specimens $[0]_{16}$ did not show any significant loss in flexure properties between the different positions on LDEF and the ground control. Figure 3-10 show the flexure test results for the space exposed, shielded and ground control specimens. These results are based on the post flight cross-sectional areas. The loss of material for the leading edge exposed specimens results in a performance reduction for a given specimen. As these specimens were unidirectional [0] reinforced, the load that would have been carried by the eroded material on the leading edge exposed specimens was carried by the remaining 0° ply. For these specimens the only mechanical performance loss was due to material loss on the leading edge exposed specimens. Ply orientation plays a significant role in flexure properties behavior when AO erosion is involved.

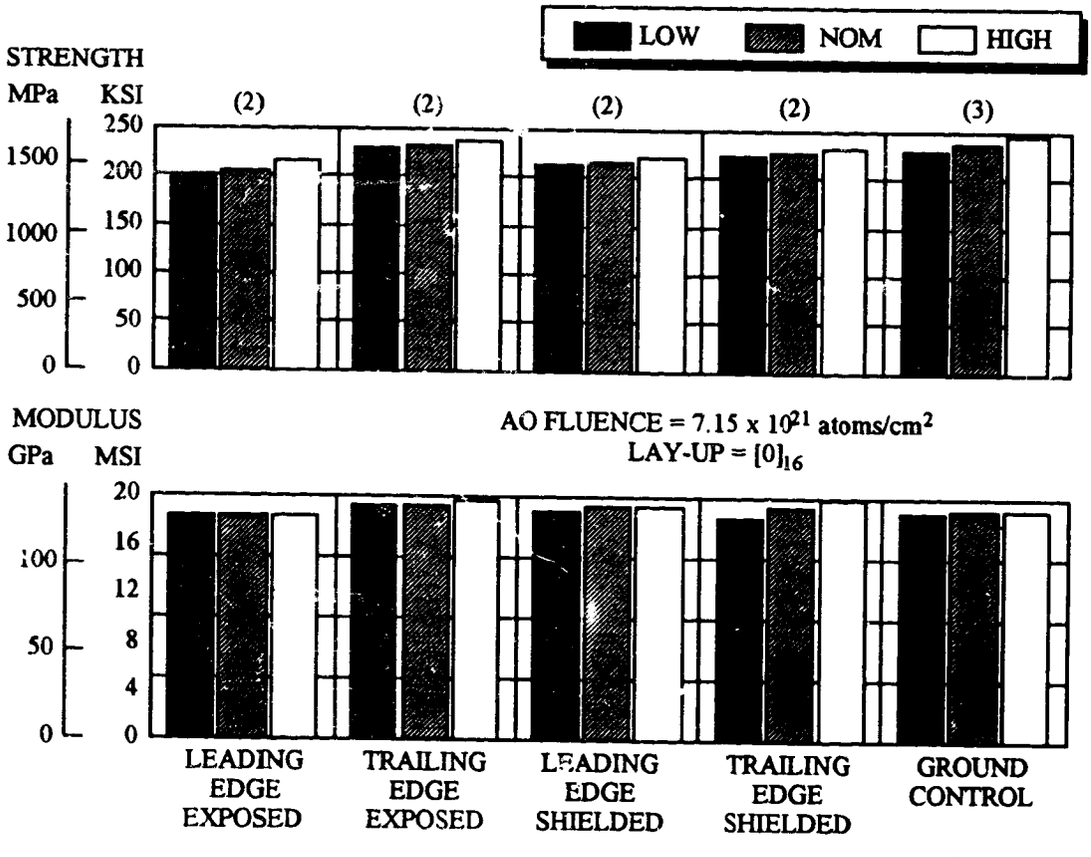

Complete sets of this material were flown in both direct space exposure positions on the "A-deck" as well as in shielded positions on the "B-deck" at the leading and trailing edges. Also, a complete set of specimens were kept at controlled temperature and humidity conditions at the Aerospace Corporation. These specimens were shielded from exposure to ambient light and were used as ground controls.

Figure 3-10. LDEF Exposure Effects on Flexural Properties of T300/934 Epoxy

The AS-4/3501-6 epoxy flexure test results show very little change in modulus values among the different exposure conditions and the ground control (see Figure 3-11). The strength values show some variation from position to position, most likely due to the inherent scatter with polymer matrix composite strength measurements and the small sample size. The 0° orientation of the reinforcement allows the underlying plies to pick up the load from the eroded surface ply on the leading edge exposed specimens. As with the T300/934 results, mechanical performance reductions are due to erosion of material on the leading edge specimens.

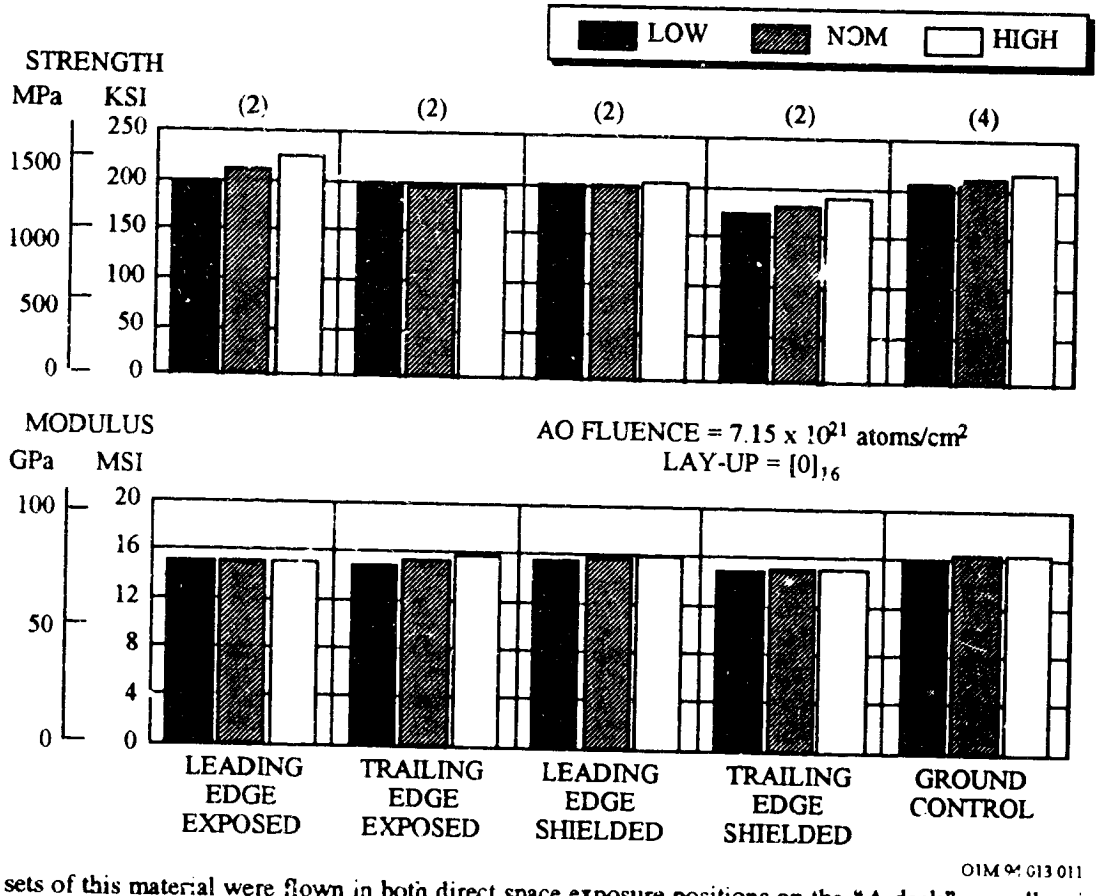

Complete sets of this material were flown in both direct space exposure positions on the "A-deck" as well as in shielded positions on the "B-deck" at the leading and trailing edges. Also, a complete set of specimens were kept at controlled temperature and humidity conditions at the Aerospace Corporation. These specimens were shielded from exposure to ambient light and were used as ground controls.

Figure 3-11. LDEF Exposure Effects on Flexural Properties of AS-4/3501-6 Epoxy

The C6000/PMR-15 polyimide specimens were reinforced with an angle ply stacking sequence of $[0,+45,0,+45]_s$. As can be seen from the data in Figure 3-12 the strength and modulus values drop off significantly for the leading edge exposed specimens. This is due to the almost complete loss of the 0° ply on the exposed surface of the specimen due to AO erosion. Unlike the unidirectional reinforced specimens, the ply underneath is at +45° and has a lower stiffness and strength in the load direction. This behavior has been seen in other leading edge LDEF specimens with multidirectional reinforcement (ref. 8). The non-AO exposed specimen data show no significant change in flexure properties compared with the ground control data.

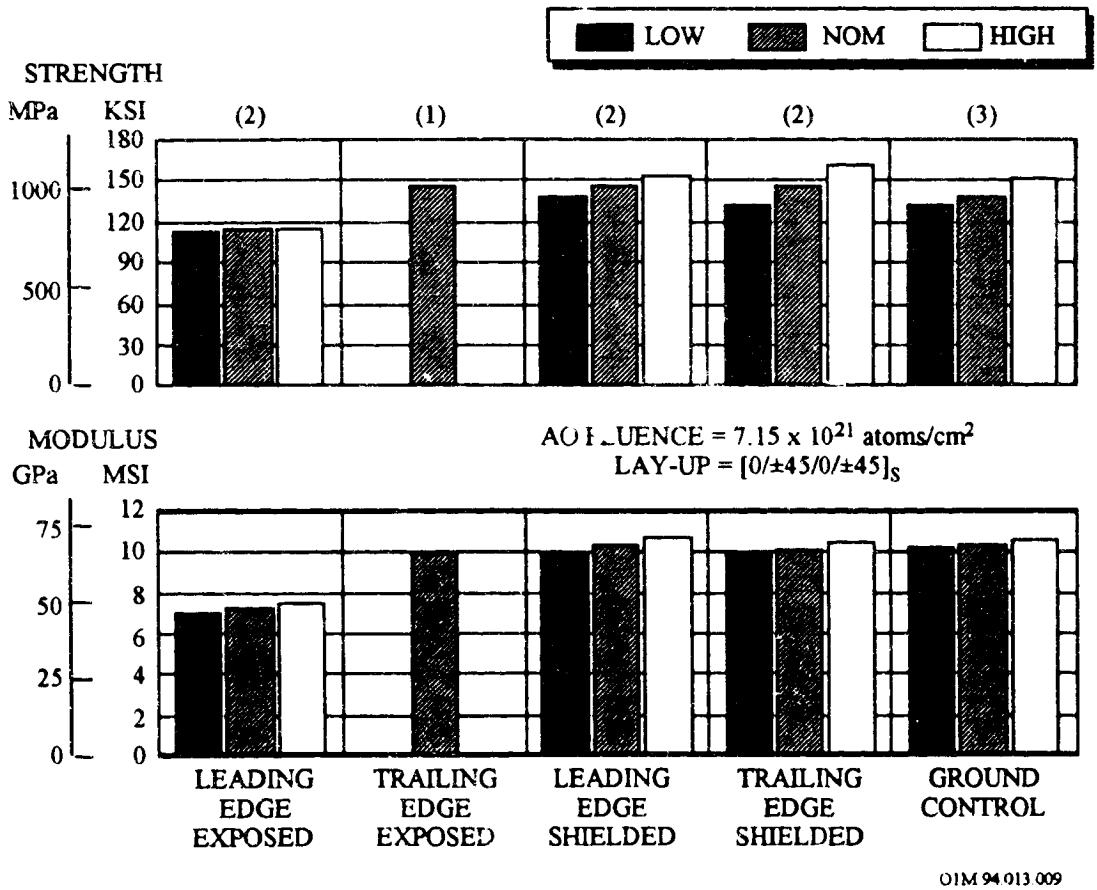

Complete sets of this material were flown in both direct space exposure positions on the "A-deck" as well as in shielded positions on the "B-deck" at the leading and trailing edges. Also, a complete set of specimens were kept at controlled temperature and humidity conditions at the Aerospace Corporation. These specimens were shielded from exposure to ambient light and were used as ground controls.

Figure 3-12. LDEF Exposure Effects on Flexural Properties for C6000/PMR-15

The carbon/LARC 160 polyimide $[0]_{16}$ flexure test results show very little change in modulus values among the different exposure conditions and the ground control (see Figure 3-13). The strength values show some variation from position to position, most likely due to the inherent scatter of strength measurements associated with polymer composites and the small sample size of this experiment (1 to 4). Once again the 0° orientation of the reinforcement allows the underlying plies to pick up the load from the eroded surface ply on the leading edge exposed specimens. This is a similar situation to the other unidirectional reinforced material results where mechanical performance reductions are due to erosion of material on the leading edge specimens.

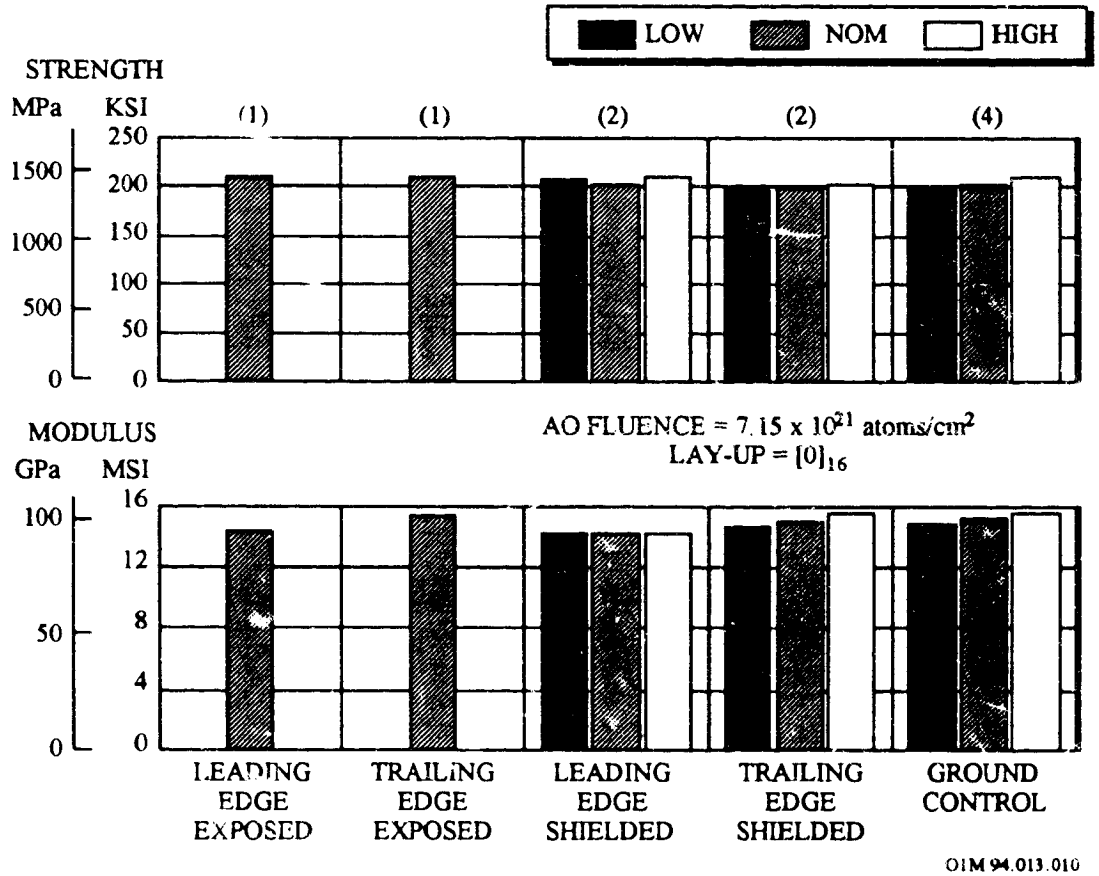

Complete sets of this material were flown in both direct space exposure positions on the "A-deck" as well as in shielded positions on the "B-deck" at the leading and trailing edges. Also, a complete set of specimens were kept at controlled temperature and humidity conditions at the Aerospace Corporation. These specimens were shielded from exposure to ambient light and were used as ground controls.

Figure 3-13. LDEF Exposure Effects on Flexural Properties for Carbon/LARC 160

LEO exposure did not significantly reduce the flexural strength for $[0]_{16}$ T300/934 epoxy. These composites, part of LDEF Experiment M0003-8 (Boeing), were located at positions D9 (leading edge) and D3 (trailing edge) and were held in stress during the flight using preload fixtures adjusted to maintain a predetermined level of strain (ref. 8). Table 3-12 summarizes the flexural test results. Strength values varied greatly but the lowest values are associated with leading edge specimens. The leading edge unstressed specimens suffered a decrease in the flexural modulus.

Table 3-12. Flexural Properties of T300 Carbon/934 Epoxy $[0]_{16}$

Conditions	Strength ksi (MPa)	Modulus Msi (GPa)	# Tested
Baseline - Pre-flight	220.5 (1520.3)	16.2 (111.7)	3
Leading edge unstressed	207.0 (1427.2)	13.6 (93.8)	4
Leading edge unstressed, thermal cycled	229.0 (1578.9)	16.2 (111.7)	4
Trailing edge unstressed	238.0 (1640.9)	17.7 (122.0)	4
Trailing edge unstressed, thermal cycled	224.9 (1550.6)	16.1 (111.0)	4
Trailing edge prestressed	241.8 (1667.1)	16.3 (112.4)	5
Trailing edge prestressed, 350°F	119.7 (835.3)	est. 18-2 (124-138)0	3

LEO exposure appeared to have degraded the flexural properties for a C6000/PMR-15 polyimide $[0/\pm45/0/\pm45]_s$. The flexure specimens showed a decrease in moduli compared to pre-flight values. The most severe decrease was observed for the leading edge specimens which also displayed the lowest strength values The AO erosion of material from the leading edge exposed composites was responsible for the mechanical property reductions. It is recommended that leading edge exposed composites have AO protection for long term LEO exposure applications.

Table 3-13. Flexural Properties of C6000 Carbon/PMR-15 Polyimide $[0/\pm45/0/\pm45]_s$

Conditions	Strength ksi (MPa)	Modulus Msi (GPa)	# Tested
Baseline -Pre-flight	118.9 (819.8)	17.8 (122.7)	3
Leading edge unstressed	104.6 (721.2)	6.3 (43.4)	4
Trailing edge unstressed	137.0 (944.6)	10.5 (72.4)	4
Trailing edge prestressed	155.1 (1069.4)	11.4 (78.6)	5
Trailing edge prestressed, 350°F	81.1 (559.2)	6.6 (45.5)	3

3.2.1.5 Dimensional Changes

One of the issues relating to the use of polymer matrix composites in space involves the long term effects of vacuum outgassing and thermal cycling. In addition to contamination of adjacent satellite surfaces and components resulting from outgassing, changes in structural dimensions (e.g., coefficient of thermal expansion) and the development of laminate microcracks can have serious consequences on the behavior of truss joints, optical systems and communication platforms.

3.2.1.5.1 Outgassing

Outgassing produces dimensional changes of polymer matrix composites, which asymptotically approach a constant value once the outgassing process has essentially ceased.[6,28] One of the composite experiments on board LDEF, the UTIAS (University of Toronto Institute for Aerospace Studies) Experiment No. A0180,[8] demonstrated the effects of outgassing on the dimensional changes of a variety of carbon fiber reinforced epoxy matrix composites.

Outgassing time, t_o, and associated dimensional change, $\Delta\varepsilon$, obtained from strain vs. temperature plots, are summarized in Table 3-14 for the carbon/epoxy laminates of 90° construction. It took about 40 days for the T-300 carbon/934 epoxy and the T-300 carbon/SP-288 epoxy to outgas and 80 days for the T-300 carbon/5208 epoxy to outgas. (For comparison, a Kevlar/SP-288 epoxy 4-ply/90° laminate took about 120 days to outgas; see Section 3.2.3.3). Interestingly, a post-flight measurement of the 90° strain at ambient temperature showed a recovery in the dimensional change. This reflects re-absorption of moisture after retrieval of LDEF. In general, the outgassing time required to reach an equilibrium state in space depends on such factors as the initial moisture concentrations, the volatile content, laminate thickness, ambient temperature and constituent material diffusion properties.

---

[8] The experiment, located at D12 on LDEF, 90° to the leading edge, was custom-designed and constructed to record 16 thermal/strain gauges every 16 hours for a period of 371 days. LDEF was yawed ~8° relative to the orbital velocity vector (i.e., ~82° relative to velocity vector), with a corresponding atomic oxygen fluence at station D-12 of about 1.2×10^{21} atoms/cm^2. The experiment No. A0180 sample trays contained a stainless-steel calibration tube, 62 composite tubes, and 45 composite coupons. Details on this aspect of the experiment can be obtained from R.C. Tennyson, "Composite Materials in Space - Results From the LDEF Satellite," J. Canadian Aeronautics and Space Institute, Vol. 37, no. 3, Sept. 1991.

Table 3-14. Outgassing Time and Dimensional Change for Carbon/Epoxy Composites

Material[1,2]	Outgassing Time t_o, days	Dimensional change, Δε strain, 10^{-6}				
		Initial			Final Asymptote	
		Laboratory Calibration	First Deployed	Δε	Strain	Δε
Carbon/epoxy T300/934, 4-ply/90°	40	-1360 at -34°C (-30°F)	-1350	10	-2550	-1200
Carbon /epoxy T300/SP-288, 4-ply/90°	40	-1200 at -26°C (-15°F)	-1200	0	-2100	-900
Carbon /epoxy T300/5208, 4-ply/90°	80	-1070 at -23°C (-10°F)	-550	520	-2100	-1550

[1] Thornel T-300 (Amoco Performance Products Inc., Greenville, S.C.); 934 (Composites Div., Fiberite Corp., Winona, Wis.); Scotchply SP-328, SP-288, and SP-290 (Structural Products Department, 3M Co., St. Paul, Minn.); and 5208 (Narmco Materials, BASF Structural Materials Inc., Anaheim, CA).

[2] It should be noted that an elapsed time of almost two years occurred after manufacturing the samples, prior to their launch. During this time the samples were exposed to ambient conditions and thus had achieved an equilibrium state in terms of moisture absorption. However, they were not in a saturated state and are probably representative of typical composite space structures. A post-flight measurement of the 90° strain at ambient temperature showed a recovery in the dimensional change. This reflects re-absorption of moisture after retrieval of LDEF over a period of ~184 days in storage at ambient conditions.

A total dimensional strain change of 1550×10^{-6} occurred after about 80 days in orbit for the 4-ply [90] T-300 carbon/5208 epoxy laminate. In contrast, in the fiber direction (i.e., a [0] laminate), very small Δε changes were observed for the T-300 carbon/934 epoxy and T-300/SP288 epoxy $[0]_4$ laminates (not reported). In general, it is possible that preconditioning of composites to remove moisture prior to flight could substantially reduce, if not eliminate, dimensional instability of polymer matrix composites due to outgassing in orbit.

From a design viewpoint, the dimensional changes for the [0] and [90] laminates can be used to predict the Δε for an arbitrary laminate configuration. Clearly, the matrix-dominated properties are most affected by outgassing (i.e., see the [90] results) but it is also evident that the angle ply laminate of boron/epoxy (see Section 3.2.4.3) underwent a significant Δε change. Outgassing can lead to dimensional changes in orbit that must be taken into account in the design of composite structures and joints where dimensional tolerances are critical.

3.2.1.5.2 Coefficient of Thermal Expansion

No substantial degradation in the thermal response of several polymer matrix composites was observed, other than that associated with outgassing. Coefficient of thermal expansion (CTE) values for the UTIAS (University of Toronto Institute for Aerospace Studies) LDEF Experiment No. A0180 are summarized in Table 3-15 (ref. 6). A comparison of the CTE values measured in space (after 371 days in orbit) with those measured in simulator tests (after 2114 days in orbit and 184 days at ambient conditions) showed reasonable agreement.

Table 3-15. CTE values for UTIAS/LDEF Thermoset Composites Samples

Material[2]	Gage No.		Coefficient of Thermal Expansion, CTE, 10^{-6}/°C[1] (10^{-6}/°F)		
	Strain	Thermal	Ambient[3]	Space[4]	Thermal-vacuum facility[5]
Stainless steel calibration-tube	1	1	17.7 (9.84)	18.0 (10.0)	18.0 (10.0)
Graphite/epoxy T-300/934,flat,4-ply/0°	2 (0°) 3 (90°)	2	2.38 (1.32) 26.5 (14.7)	6.0 (3.33) 25.0-27.0 (13.9-15)	4.5 (2.50) 29.0 (16.1)
Graphite/epoxy T-300/SP-288, tube, 4-ply/0°	6 (90°) 7 (0°)	4	26.3 (14.6) 1.75-2.83 (0.97-1.57)	24.5-25.7 (13.6-14.3) -2.05-6.0 (-1.14-3.33)	27.7 (15.4) 6.75 (3.75)
Graphite/epoxy T-300/5208,tube, 4-ply/90°	8 (90°)	5	28.1 (15.6)	22.5-27.5 (12.5-15.3)	29.0 (16.1)

[1]Multiply by 1.8 to obtain CTE value in 10-6/°C
[2]Thornel T-300 (Amoco Performance Products Inc., Greenville, S.C.) 934 (Composites Div., Fiberite Corp., Winona, Wis.); Scotchply SP-328, SP-288, and SP-290 (Structural Products Department, 3M Co., St. Paul, Minn.); and 5208 (Narmco Materials, BASF Structural Materials Inc., Anaheim, CA)
[3]Measured at atmospheric pressure prior to launch
[4]Measured in space environment on LDEF during first 371 days in orbit
[5]Measured in laboratory thermal-vacuum test facility after 2 days in orbit and 184 days at ambient conditions

Table 3-16 summarized the post-flight coefficient of thermal expansion (CTE) measured on several carbon composites located on the LDEF satellite. These composites of LDEF Experiment M0003-9 (LMSC) were located on Bay D, Row 9 on the leading edge and Bay D, Row 3 on the trailing edge of LDEF (ref. 7). Specimen were 16 ply unidirectional [0°] laminates and fabric laminates. The CTE measurements for most of the samples appears to be unchanged; the CTE of the flight samples and the control samples are within the measurement error of the dilatometer.

Table 3-16. Coefficient of Thermal Expansion of Carbon Epoxy Composites on LDEF

Material	Fiber/Resin Supplier	Sample Location	CTE (10^{-6}/°C)
GY70/CE-339	BASF/Ferro	Leading Edge	-0.9257
GY70/CE-339	BASF/Ferro	Trailing Edge	-0.9791
GY70/CE-339	BASF/Ferro	Control	-0.9332
T50/F263	Amoco/Hexcel	Leading Edge	-0.2967
T50/F263	Amoco/Hexcel	Trailing Edge	-0.5122
T50/F263	Amoco/Hexcel	Control	-0.5039
T50/934	Amoco/Fiberite	Leading Edge	-0.5946
T50/934	Amoco/Fiberite	Trailing Edge	-0.6288
T50/934	Amoco/Fiberite	Control	-0.2309
T50/X904B	Amoco/Fiberite	Leading Edge	-0.4714
T50/X904B	Amoco/Fiberite	Trailing Edge	0.1032
T50/X904B	Amoco/Fiberite	Control	-0.2723

Several conclusions can be drawn based on the results of the analyses of the UTIAS/LDEF composite-material samples:

- Carbon polymer composites outgassed for 40 to 80 days, depending on the material system.
- Outgassing caused significant permanent dimensional changes, which must be factored into the design of low-distortion laminates.
- Outgassing also produced modest changes in the coefficient of thermal expansion (CTE), leading to asymptotic values that should be used in the design of "zero-CTE" laminates for space service.

3.2.1.5.3 Microcracking

Quantitative microcracking analysis was conducted on the polymer matrix composites of the LDEF Boeing Experiment M0003-10 (ref. 3), which experienced 32,422 thermal cycles. These composites, consisting of T300 carbon/934 epoxy $[0]_{16}$, AS-4 carbon/3501-6 epoxy $[0]_{16}$, C6000 carbon/PMR-15 polyimide $[0,\pm45,0,\pm45]_s$, and carbon/LARC-160 polyimide [0] were flown in the direct space exposure positions on the "A-deck" as well as in shielded positions on the "B-deck," both at the leading (Bay D, Row 8) and trailing edges (Bay D, Row 4). Also, a complete set of ground control specimens were kept at controlled temperature and humidity conditions and shielded from exposure to ambient light at the Aerospace Corporation. Table 3-17 summarize the LDEF thermal cycling environment and the microcracks/inch values for these composites.

Microcracking was only detected in the C6000 carbon/PMR-15 polyimide laminates with a nonunidirectional lay-up (i.e.,$[0,\pm45,0,\pm45]_s$). Most of the microcracks observed were intraply (within an individual ply). However some cracks extended through two plies. Greater thermally induced stresses under thermal cycling are generally produced in nonunidirectional lay-up. The exposed (A-deck) PMR-15 specimens, located in the leading and trailing edge positions, displayed the most microcracking. A smaller but significant level of cracking was found for the leading edge shielded (B-deck) PMR-15 specimens. The leading edge exposed specimens had a significantly higher emissivity due to the rough texture produced by atomic oxygen erosion (ref. 5), which may account for the colder cycling extremes (ref. 8). The trailing edge shielded (B-deck) PMR-15 displayed little or no microcracking. The shielded specimens may have experienced milder thermal cycling extremes as their microcrack densities were significantly lower than the exposed specimens.

Table 3-17. Microcracks/Inch of Space Exposed Carbon Thermoset Composites

Location	LDEF Thermal Cycling Environment	T300/934 Epoxy [0]	AS-4/3501-6 Epoxy [0]	C6000/PMR15 Polyimide $(0/\pm45/0/\pm45)_s$	Carbon/ LARC160 Polyimide [0]
Leading Edge Exposed A-Deck	-47°C to 84°C (-53°F - 183°F)	0[a]	0	33(45[b])	0
Trailing Edge Exposed A-Deck	-33°C to 77°C (-27°F - 170°F)	0	0	47	0
Leading Edge Shielded B-Deck	Less Than Above	0	0	7	0
Trailing Edge Shielded B-Deck	Less Than Above	0	0	0	0
Ground Control	None	0	0	0	0

(a) Microcracking analysis was performed using optical microscopy on polished cross sections perpendicular to the 0° direction. A total of 0.55 inches of cross section was examined and the count of cracks was normalized to cracks per inch.

(b) Most of the surface ply of the leading edge exposed C6000/PMR-15 specimen was eroded away. The number of cracks per inch for the PMR-15 specimen was extrapolated this estimated value.

A study of the effects of thermal control coatings on the thermal-cycled induced microcracking behavior in carbon/epoxy composites indicated adequate coating capability by A276 white polyurethane in effectively reducing thermal cycling extremes and shocks (ref. 9). A T300/934 epoxy panel in a $[0_2/\pm45/0_2/\pm45/90/0]_s$, 20-ply lay-up was covered with thermal control coatings in three of its four quadrants (A276 and BMS 10-60 white urethane and Z306 black urethane) with the fourth quadrant uncoated. The composite panel, which underwent ~34,000 thermal cycles, experienced different thermal cycling temperature extremes in each quadrant due to the different optical properties of the coatings and bare composite. The thermal histories of these areas are shown in Figure 3-14.

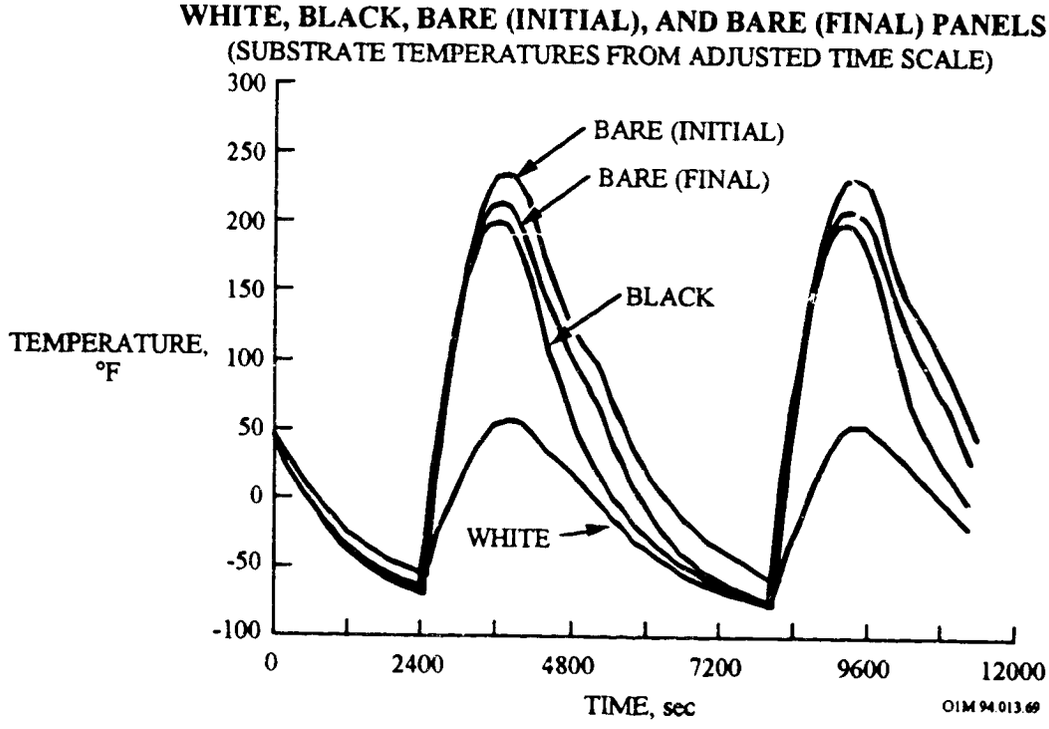

Figure 3-14. Thermal History for Coated and Uncoated Composites on LDEF

The panel, located on the leading edge (Row D9) experiment M0003-8, was exposed to an atomic oxygen fluence of 8.99×10^{21} atoms/cm^2. An AO reactivity of 0.99×10^{-24} cm^3/atom was calculated for the bare composite based on a thickness loss of 3.4 mils, which compares favorably with other reported reactivities for T300/934 epoxy specimens flown on LDEF (see Table 3-4). The white urethane thermal control coatings (A276 and BMS 10-60) prevented AO attack of the composite substrate while the black urethane thermal control coating (Z306) was severely eroded by atomic oxygen, allowing some AO attack of the composite substrate. Microcrack densities, shown in Figure 3-15, indicated that the white coated composite substrate displayed almost no microcracking while the black coated and bare composite showed extensive microcracking. Significant AO erosion was seen in many of the cracks in the bare composite. White coatings, which significantly reduced the thermal cycling temperature range, thus prevented significant microcracking. The bare and black coated portions of the panel had significant microcracks in the 3 outer plies on both outer (exposed to LEO environment) and inner surfaces. AO exposure eroded microcracked areas, even areas under coatings. Other LDEF experimenters[13,29] reported composite microcracking or showed data indicating that it may have been present.

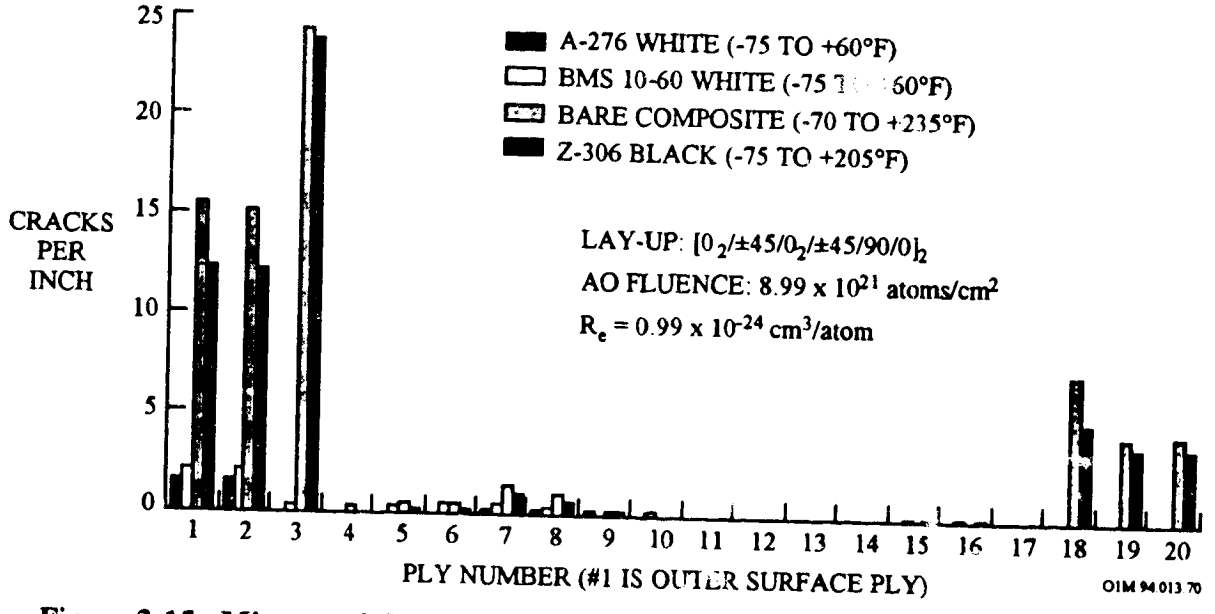

Figure 3-15. Microcrack Density vs. Location for Coated and Uncoated Composites on LDEF

3.2.1.5.4 Warpage

It is commonly observed in composites that even balanced, symmetric laminates cured on a flat surface exhibit some small degree of nonflatness, which is a manifestation of the state of residual stress within the laminate. Hence, changes in this physical characteristic might be related to the space environment exposure conditions, such as thermal cycling, or to other potential changes in the laminates due to exposure such as microcracking or one-sided surface attrition.

LDEF Experiment A0175 measured the flatness of several carbon-fiber-reinforced resin-matrix advanced composite panels contained in two trays, A7 and A1, before and after exposure (ref. 13). These two trays were located, respectively, on the leading and trailing faces of LDEF, obliquely oriented to the ram (Row 9) and wake (Row 3) directions, with atomic oxygen fluences of 8.99×10^{21} atoms/cm^2 and 1.32×10^{17} atoms/cm^2, respectively. The advanced composites included T300/934 epoxy, T300/F178 bismaleimide, C6000/LARC-160 polyimide, and C6000/PMR-15 polyimide. Laminate orientation was $[0_2/\pm45/90_2/\pm45/0_2/\pm45/90_2/\pm45/0_2]$ for all of the composite panels. Comparison of the pre-flight and post-flight warpage is summarized in Table 3-18.

Table 3-18. Comparison of Pre-flight and Post-flight Warpage of Polymer Composites

Material	Deflection (inches)*	
	Pre-flight	Post-flight
T300/F178 precured at 85 psi	0.277	0.004
T300/F178 cocured at 45 psi	0.166	0.190
C6000/PMR-15	0.232	0.107
C6000/LARC 160	0.370	0.177
C6000/LARC 160	0.615	0.018

*Values represent average of three values taken from corner-midpoint-corner of free standing edge of laminate with opposite edge held down against surface table. The panels were placed on a surface table, weighted down along one edge with the exposed surfaces up, and the deflection measured along the opposite edge at the midpoint and both corners.

In the pre-flight measurements, all of the bismaleimide and polyimide panels were concave upward; in the post-flight measurements, they were still concave upward, although generally to a much lesser degree. The carbon/epoxy laminate was both flat, both before and after exposure. As shown in the above table, the remaining laminates exhibited a marked reduction in warpage following exposure, with the single exception of the cocured bismaleimide laminate, which exhibited, on average, a slight increase in warpage.

3.2.2 Carbon/Thermoplastics

Carbon fiber-reinforced thermoplastic matrix composite materials, such as carbon/polyetheretherketone (PEEK), have been considered for satellite applications due to their promise for reducing the acquisition and life cycle costs for spacecraft structures over current carbon/epoxy composites. The cost reduction is obtained through innovative and rapid forming processes, in contrast to the long processing cycles typical of thermoset materials. Also, the reprocessibility of thermoplastics enables the co-consolidation of subassemblies and the reworkability of fabricated components. The meltability of thermoplastic composites allows rapid joining of thermoplastic components using a variety of techniques such as induction bonding, ultrasonic welding, focus infrared heating, and amorphous bonding with thermoplastic film resin. In addition, thermoplastic composites have been shown to offer performance improvements over thermoset materials in the areas of lower moisture absorption, greater damage tolerance, reduce thermally-induced microcracking, and minimum outgassing.

Table 3-19 lists the space experiments and thermoplastic composite materials exposed to the LEO environment.

Table 3-19. Carbon/Thermoplastics Exposed to the LEO Environment

Flight Experiment	Angle off RAM	AO fluence atoms/cm^2	UV ESH	Ref.	Thermoplastics
LDEF - A0134 - M0003-8	8 (LE) Row 9	8.99×10^{21}	11,200	8, 9	C3000/P1700 C6000/P1700 T300(fabric)/P1700
LDEF - A0171 - M0003-10	38 Row 8	7.15×10^{21}	9,400	1, 14	HMF-322/P1700/$\pm$45° T300(fabric)/P1700 T300/PES
LDEF M0003-10	158 Row 4	2.31×10^{5}	10,500	4	T300(fabric)/P1700 T300/PES
LDEF - M0003-8	172 (TE) Row 3	1.32×10^{17}	11,100	13, [30]	T300(fabric)/P1700
STS-46 EOIM-3	0	0.193×10^{21}	8.3	17	AS4/PEEK
STS-46 LCDE	0	0.193×10^{21}	8.3	18,31	IM7/PEEK

3.2.2.1 Thickness Erosion from Atomic Oxygen Exposures

The average thickness loss due to atomic oxygen exposures and the atomic oxygen reactivity of several advanced thermoplastic composites are summarized in Table 3-20.

Table 3-20. Atomic Oxygen Erosion Rates for Carbon Thermoplastic Composite Materials

Composite Materials	Flight Experiment	Ref.	Angle off Ram	AO Fluence $x10^{21}$ atoms/cm^2	Avg. Thickness Loss mils (μm)	AO Reactivity $x10^{-24}$ cm^3/atom
HMF 322/P1700 Polysulfone [±45]	LDEF AO171	14	38(1)	7.15	2.5 to 6.2 mil[1] (64-157μm)	0.92 to 2.3
T300/P1700 Polysulfone $[0,90]_8$ Fabric	LDEF M0003-10	4	38	7.15	-	1.1
T300/P1700 Polysulfone $[0,90]_8$ Fabric	LDEF M0003-8	8	8	8.99	5.3 mils (135 μm)	
IM7/PEEK	STS-46 LDCF	32	0	0.193	mils (5-7 μm)	
IM7/PEEK	STS-46 LDCE	33	0	0.193	mils (5.36 μm)	2.69
AS4/PEEK	STS-46 EOIM-3	17	0	0.193	mils (6 μm)	

(1)Matrix erosion much greater than fiber

Composite matrix erosion was greater than that of the carbon fibers. The erosion of the polysulfone P1700 system was more pronounced than for the epoxy matrix erosion (see Table 3-4. Atomic oxygen reactivity values generally averaged $1x10^{-24}$ cm^3/atom with the exception of the S-glass epoxy composites which tend to become self protecting.

3.2.2.2 Impact Damage from Micrometeoroid and Debris

None reported

3.2.2.3 Mechanical Property Degradation from Atomic Oxygen

3.2.2.3.1 Tensile

Figures 3-16 and 3-17 show the ultimate tensile strength and tensile moduli for several carbon reinforced polysulfone (P1700) matrix resin composites that received over 5 years and 9 months of exposure to the LEO environment on the LDEF Experiment A0134 (ref. 11). The location of this experiment (in Tray B on Row 9) was the leading edge of LDEF which received an atomic fluence of 8.99×10^{21} atoms/cm^2. These composites were fabricated from unidirectional prepreg into 4-ply $[\pm 45]_s$ lay-up so as to be matrix sensitive during tensile testing. The tensile specimens were 0.500-inch and 0.375-inch wide by 8-inches long with laminate thickness varying from 0.016-inch to 0.024-inch.

Both the C3000/P1700 and the C6000/P1700 exposed composite specimens experienced a deterioration in tensile strength and modulus.[h] Tensile strengths of the exposed composite specimens were between 15 to 30% lower than the baseline composite specimens (e.g., tensile strength of the C6000/P1700 composite decreased to 9.5 ksi (65 MPa) from 11.0 ksi (MPa)). Tensile moduli of the exposed composite specimens were between 15 to 30% lower than the baseline composite specimens (e.g., tensile modulus of the C6000/P1700 composite decreased to 1.1 Msi (7.5 GPa) from 1.3 Msi (9 GPa)). However, no major differences are noted between baseline values obtained when the composites were tested in 1983 and the ground control composites which remained at Langley. More than a loss in matrix resin contributed to this phenomena since the thickness loss is not proportional to the loss in tensile properties by rule of mixtures (thickness losses varied from 0.003 to 0.0045 inch of the 0.0055-inch thick outer ply).

[h] P1700 resin produced by Union Carbide Corp; C3000 and C6000 fibers produced by Celanese

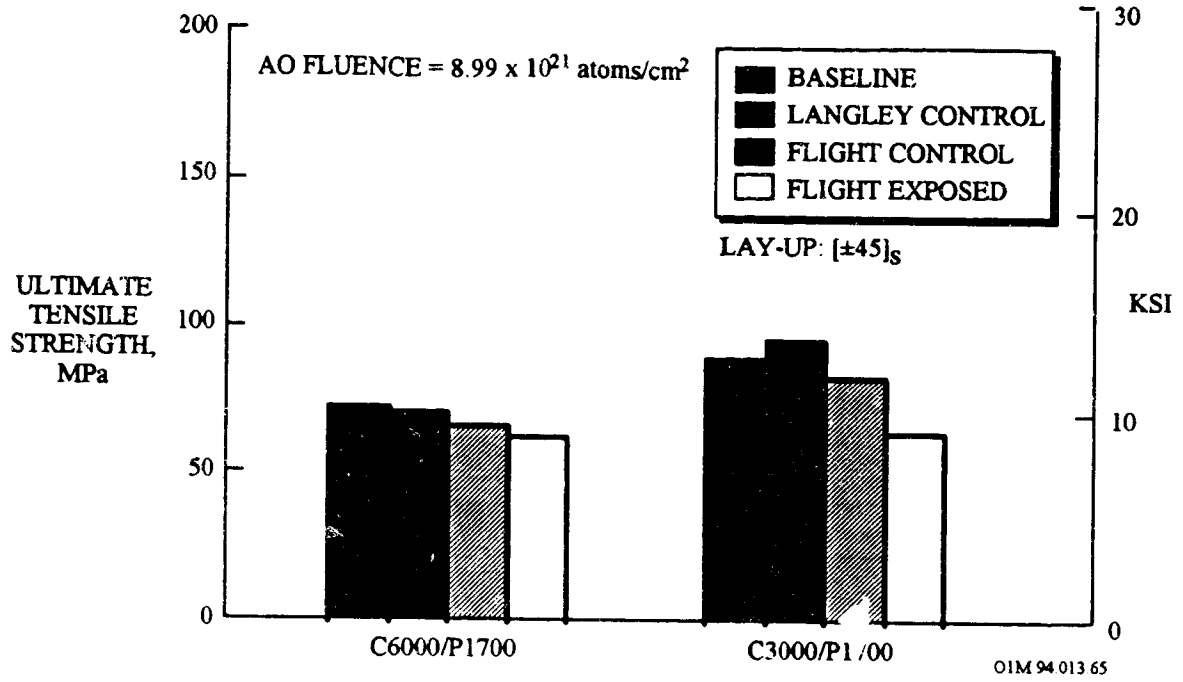

Figure 3-16. LDEF Flight Exposure Effects on Tensile Strength of Carbon/Polysulfone

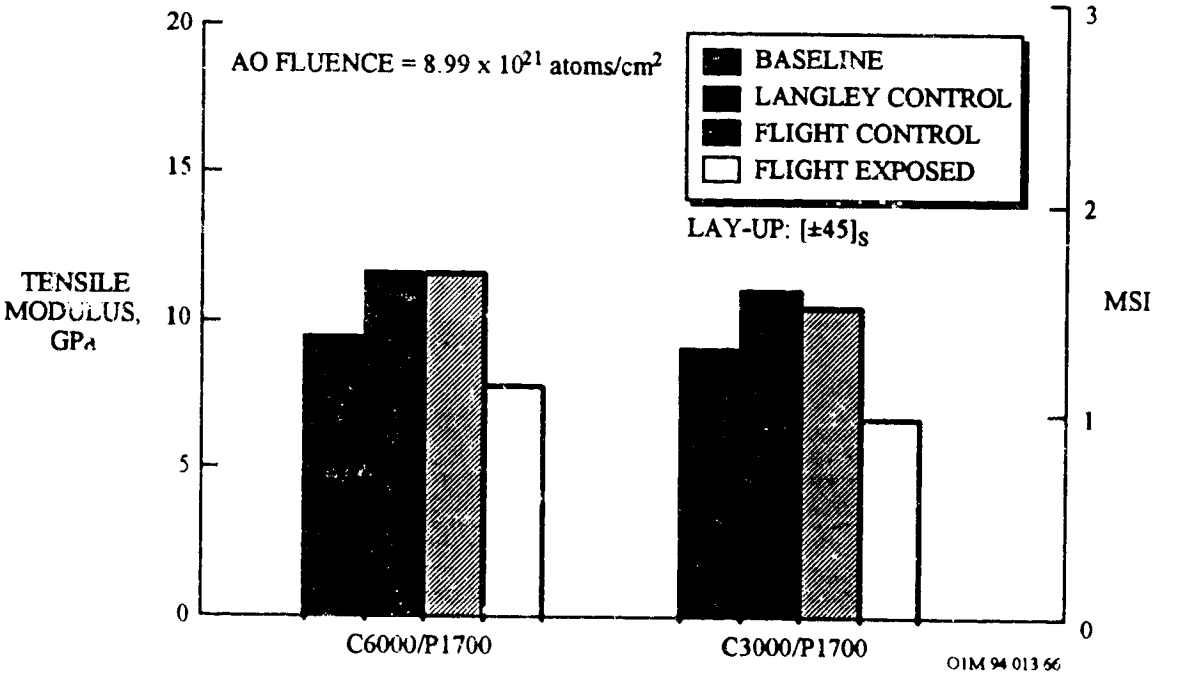

Figure 3-17. LDEF Flight Exposure Effects on Tensile Modulus of Carbon/Polysulfone

LEO exposure does not appear to significantly reduce the tensile properties of a T300/P1700 polysulfone composite reinforced with 8 plies of a 0,90 fabric. This composite specimen, part of LDEF Experiment M0003-8 (Boeing) (ref. 8), was located at the trailing edge position D3 (AO fluence of $1.32x10^{17}$ atoms/cm^2), and were held in stress during the flight using preload fixtures adjusted to maintain a predetermined level of strain. Table 3-21 summarizes the tensile test results. Tensile strength and modulus values compare favorably with pre-flight values.

Table 3-21. Tensile Properties of T300 Carbon/P1700 Polysulfone Fabric [0,90]

Tests	Pre-flight			Post-flight		
	Strength, ksi (MPa)	Modulus, Msi (GPa)	# Tested	Strength, ksi (MPa)	Modulus, Msi (GPa)	# Tested
Baseline	68.1 (469.5)	est 7-9 (48-62)	3			
Prestressed trailing edge				66.2 (456.4)	7.9 (54.5)	2

Note:The tensile test results are inconclusive due to the spread of the data and the limited sample population. Pre and post flight strength values are very similar but all are well below anticipated levels for this material system. Most of the post flight test failures occurred outside of the gauge area. The same problems may have existed for pre-flight testing, thus lowering the strength values

3.2.2.3.2 Compression

LEO exposure does not appear to significantly reduce the compression property of a T300/P1700 polysulfone composite reinforced with 8 plies of a 0,90 fabric. This composite specimen, part of LDEF Experiment M0003-8 (Boeing), (ref. 8) was located at the trailing edge position D3 (atomic oxygen fluence of $1.32x10^{17}$ atoms/cm^2), and were held in stress during the flight using preload fixtures adjusted to maintain a predetermined level of strain. Table 3-22 summarizes the compression test results. Compression moduli data for the polysulfone system is questionable due to the severe end brooming which occurred during testing and may have been caused by damage to the specimen ends from the preload fixture.

Table 3-22. Mechanical Properties of T300 Carbon/P1700 Polysulfone Fabric [0,90]

Tests	Pre-flight			Post-flight		
	Strength, ksi (MPa)	Modulus, Msi (GPa)	# Tested	Strength, ksi (MPa)	Modulus, Msi (GPa)	# Tested
Baseline	54.5 (375.8)	est 7-9 (48-62)	3			
Prestressed trailing edge				50.8 (350.3)	7.2 (49.6)	2

Note:The compression test results are inconclusive due to the spread of the data and the limited sample population. Pre and post flight strength values are very similar but all are well below anticipated levels for this material system. Most of the post flight test failures occurred outside of the gauge area. The same problems may have existed for pre-flight testing, thus lowering the strength values

3.2.2.3.3 Flexural

Exposure to the LEO environment did not caused any significant changes in the flexural properties for a T300/P1700 polysulfone composite reinforced with 8 plies of a [0,90] woven fabric. Figure 3-18 shows no significant loss in the flexure properties between the different positions on LDEF (both space exposed and shielded) and the ground control T300/P1700 polysulfone specimens of the LDEF Boeing M0003-10 experiment (refs. 3 and 4). These composites were located on both the leading (Bay D, Row 8; AO = 7.15×10^{21} atoms/cm^2, 9,400 ESH, 32,422 thermal cycles between -47°C to 84°C [-53°F and 183°F]) and the trailing edges (Bay D, Row 4; AO = 2.31×10^5 atoms/cm^2, 10,500 ESH, 32,422 thermal cycles between -33°C to 77°C [-27°F and 170°F]). These results are based on the post flight cross-sectional areas.

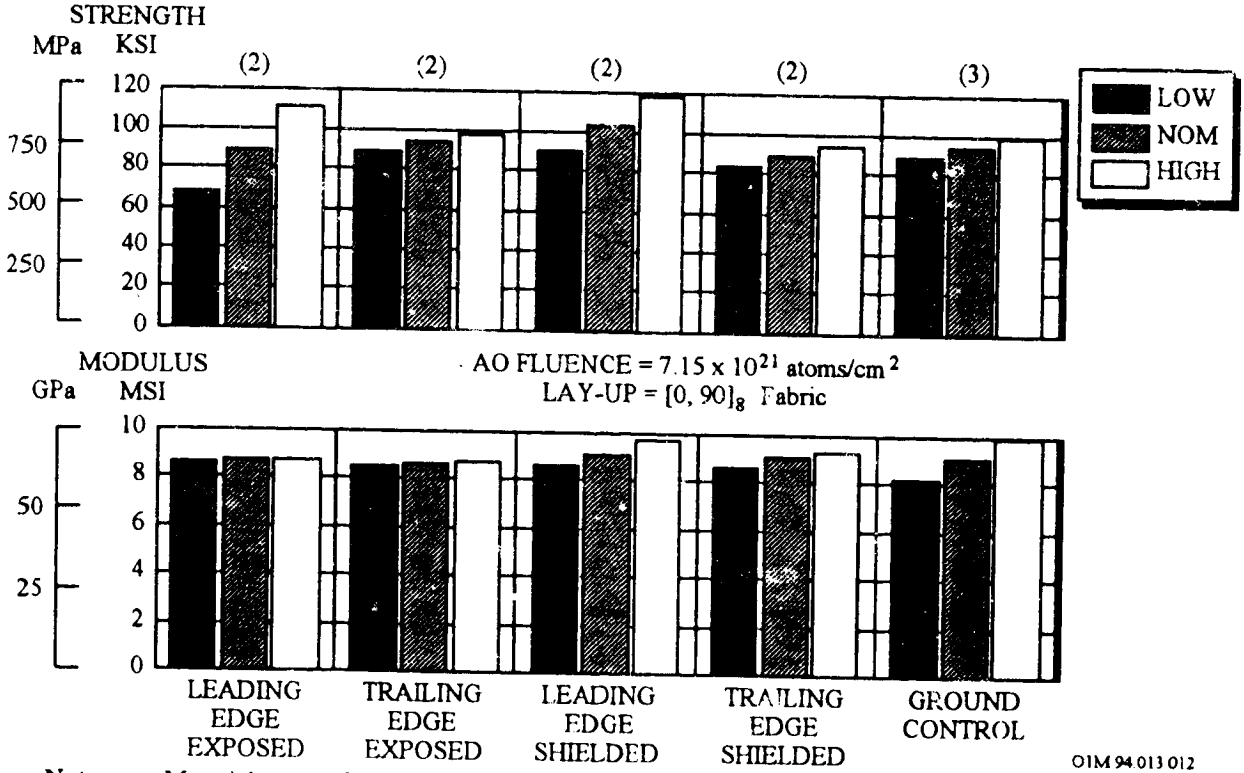

Note: Materials were flown in both direct space exposure positions on the "A-deck" as well as in shielded positions on the "B-deck" at the leading and trailing edges. The environments for the samples mounted on the leading and trailing A decks were similar except those on the leading edge were also exposed to relatively high fluxes of atmospheric constituents (primarily atomic oxygen). Although the samples on the B decks were not exposed to the radiation environment, the experiment design was such that they experienced thermal excursions similar to those of the exposure samples. Also, a complete set of specimens were kept at controlled temperature and humidity conditions at the Aerospace Corporation. These specimens were shielded from exposure to ambient light and were used as ground controls.

Figure 3-18. LDEF Flight Exposure Effects on Flexural Strength and Modulus for T300/P1700

Reductions in strength and modulus of 10 to 25% resulted from AO erosion on uncoated, leading edge T300/P1700 polysulfone composite reinforced with 8 plies of a [0,90] f[illegible]. This composite specimen, part of LDEF Experiment M0003-8 (Boeing) (ref. 8), was located at the leading edge position D9 (atomic oxygen fluence of 8.99×10^{21} atoms/cm^2), and were held in stress during the flight using preload fixtures adjusted to maintain a predetermined level of strain. Table 3-23 summarizes the flexural test results. No significant changes in flexural strength or modulus were observed for any uncoated composites in this experiment on the trailing edge of LDEF. The T300/P1700 polysulfone fabric moduli values decrease in the order: pre-flight, trailing edge, stressed trailing edge, leading edge. Strength values varied with the leading edge specimens being the lowest.

Table 3-23. Mechanical Properties of T300 Carbon/P1700 Polysulf[illegible] Fabric [0,90]

Tests	Pre-flight			Post-flight		
	Strength, ksi (MPa)	Modulus, Msi (GPa)	# Tested	Strength, ksi (MPa)	Modulus, Msi (GPa)	# Tested
Flexure						
Baseline	106.5 (734.3)	12.7 (87.6)	3			
Leading edge unstressed				97.3 (670.9)	7.8 (53.8)	4
Trailing edge unstressed				116.0 (799.8)	10.4 (71.7)	4
Trailing edge prestressed				118.8 (819.1)	8.0 (55.2)	5
Trailing edge prestressed, 350°F				16.7 (115.1)	4.5 (31.0)	3

Note: The flexural test results are inconclusive due to the spread of the data and the limited sample population. Pre and post flight strength values are very similar but all are well below anticipated levels for this material system. Most of the post flight test failures occurred outside of the gauge area or at locations with rough edges. The same problems may have existed for preflight testing, thus lowering the strength values

As with specimens of unidirectional [0] reinforced, there is continuous reinforcement in the load direction in each ply, i.e., the load that would have been carried by the eroded material on the leading edge exposed specimens was carried by the remaining [0] material. For these specimens the only mechanical performance loss was due to material loss on the leading edge exposed specimens. Ply orientation plays a significant role in flexure properties behavior when AO erosion is involved.

3.2.2.4 Dimensional Changes

3.2.2.4.1 Outgassing

No information reported from the flight experiments. However, carbon/thermoplastics have significantly lower outgassing properties compared to carbon/thermosets as measured from the laboratory ASTM E595 outgassing.[32] A comparison of the outgassing results points to significantly lower outgassing TML and CVCM values for IM7/PEEK thermoplastic composites compared to the conventional IM7/8551-7 epoxy composite, 0.053% and 0.004% vs. 0.232% and 0.009%, respectively.

3.2.2.4.2 Coefficient of Thermal Expansion

No information available from flight experiments.

3.2.2.4.3 Microcracking

Quantitative microcracking analysis was conducted for a T300 carbon/P1700 polysulfone composite reinforced with 8 plies of [0,90] fabric located on the LDEF Boeing M0003-10 experiment (ref. 3), which experienced 32,422 thermal cycles. This specimen, located on both the leading (Bay D, Row 8) and trailing edges (Bay D, Row 4) was flown in both direct space exposure positions on the "A-deck" as well as in shielded positions on the "B-deck" at the leading and trailing edges. Also, a complete set of control specimens were kept at controlled temperature and humidity conditions and shielded from exposure to ambient light at the Aerospace Corporation. Table 3-24 summarize the LDEF thermal cycling environment and the microcracks/inch values.

Table 3-24. Microcracks/Inch of Carbon/Polysulfone Composites

Location	LDEF Thermal Cycling	T300 Carbon/P1700 Polysulfone $[0,90]_s$
Leading Edge Exposed	-47°C to 84°C (-53°F to 183°F)	35[(a)]
Trailing Edge Exposed	-33°C to 77°C (-27° to 170°F)	35
Leading Edge Shielded	Less Than Above	6
Trailing Edge Shielded	Less Than Above	2
Ground Control	None	0

(a)Microcracking analysis was performed using optical microscopy on polished cross sections. These cross sections were taken perpendicular to the 0 degree direction and were examined at 100x magnification with the aid of a dye penetrant to enhance the contrast of the cracks. A total of 0.55 inches of lineal cross section was examined and the count of cracks was normalized to cracks per inch.

The T?00/P1700 polysulfone specimens of a [0,90] lay-up orientation exhibited extensive microcracking. Most of the microcracks observed were intraply (within an individual ply). Greater thermally induced stresses under thermal cycling are generally produced in nonunidirectional lay-up. The exposed (A-deck) laminates specimens displayed the most microcracking. The leading edge exposed specimens had a significantly higher emissivity due to the rough texture produced by atomic oxygen erosion (ref. 5), which may account for the colder thermal extremes (ref. 8). A smaller but significant level of cracking was found for the leading edge shielded (B-deck) specimens. The trailing edge shielded (B-deck) displayed little or no microcracking. The shielded specimens may have experienced milder thermal cycling extremes as their microcrack densities were significantly lower than the exposed specimens.

3.2.3 Glass/Thermosets

3.2.3.1 Mass Loss

The mass loss of a glass composite located on the leading edge of the LDEF satellite is summarized in Table 3-25 (ref. 7). The mass loss given is for a sample approximately 0.080 inch in thickness. The trailing edge samples, flight control samples and the ground control samples had no significant mass loss. Because the leading edge samples were the only samples to exhibit mass loss, the mass loss is sample erosion due to AO and micrometeoroid impact.

Table 3-25. Typical Mass Loss of Glass Epoxy Composite Materials

Material	Fiber/Resin Suppliers	Weight Change %
E Glass/X904B Fabric	Owens Corning/Fiberite	-1.50

The total amount of thickness loss was 0.013-0.030 mm for glass/epoxy sample. This is significantly less than the thickness loss of approximately 0.100 - 0.150 mm for carbon/epoxy samples and 0.080-0.130 mm thickness loss for Kevlar/epoxy samples.

3.2.3.2 Thickness Erosion from Atomic Oxygen Exposures

Table 3-26 summarizes the average thickness loss due to atomic oxygen exposures and the AO reaction efficiency for glass fiber composite systems contained within the Solar Array Materials Passive LDEF Experiment (SAMPLE) A0171 (ref. 14). Experiment AO171 was located on Row 8 position A, which allowed all experiment materials to be exposed to an atomic oxygen fluence of 7.15×10^{21} atoms/cm^2 as a result of being positioned 38 degrees of the RAM direction. Thickness losses measured on the flight specimens were consistent with their measured mass loss.

Table 3-26. AO Erosion Rates for Glass/Epoxy Composites on LDEF Experiment A0171

Composite Materials (No. of Specimens)	Angle off ram	AO Fluence 10^{21} atoms/cm^2	Avg. Thickness Loss (mils)	Weight Loss mg/cm^2	AO Reaction Efficiency, 10^{-24} cm^3/atom
S Glass-Epoxy (3)	38	6.93	0.36	2.40	0.14
Thermal Control S-Glass Epoxy with/Aluminized Taped (3)	38	6.93	Indeterminate	0.59	——

Fibers uneroded and become protective after initial matrix mass loss.
S-glass epoxy much darker probably from UV effects. Fibers evident in materials.

Compared with carbon/epoxy, glass/epoxy was the least affected by exposure to atomic oxygen. Photographs of the glass/epoxy show that the epoxy is eroded by the AO but the fibers appear to be unaffected. The AO eroded only the outside resin layer and the resin between fibers

before a protected glass fiber outer layer was formed, which was inert to AO. ***The E-glass/epoxy does not have a linear relationship between the AO fluence and the mass loss.***

The non-linear relationship is caused by the difference in reactivity of the fibers and the matrix in the presence of AO. The epoxy reacts aggressively with the AO, whereas the glass fibers are relatively inert to AO. As more of the epoxy is eroded from the surface of the laminate, the higher the concentration of glass fibers on the surface. This causes the erosion of the laminate to slow down, and when the surface of the laminate is all glass fibers, the reaction is essentially stopped.

3.2.3.3 Impact Damage from Micrometeoroid and Debris

None reported.

3.2.3.4 Mechanical Property Degradation from Atomic Oxygen

Short beam shear property testing was conducted on several glass composites located on the LDEF satellite (ref. 7). The shear test, a resin dominated property, was chosen because of the sample size limitations and shear changes would be expected to appear more distinctly than other mechanical property changes. The shear test was run per ASTM D 2344. The laminate ply orientations for short beam shear were $(0_{16})_T$.

The results of the mechanical property testing are summarized in Table 3-27. The samples that were tested for short beam shear were all 16 ply unidirectional laminates. The results show that the flight samples strength was degraded only to the extent of the mass loss percentage. This indicates that except for the physical eroding of the material there was no mechanically detrimental effects caused by the low Earth orbit environment.

Table 3-27. Short Beam Shear Strength of Glass Epoxy Composites on LDEF

Material	Fiber/Resin Supplier	Sample Location	Short Beam Shear, ksi (MPa)
Glass/CE399 Fabric	Owens Corning/Ferro	Leading Edge	7.4 (51.0)
Glass/CE339 Fabric	Owens Corning/Ferro	Trailing Edge	7.4 (51.0)
Glass/CE339 Fabric	Owens Corning/Ferro	Control	7.1 (48.9)

3.2.3.5 Dimensional Changes

No information available from the flight experiments.

3.2.4 Kevlar/Thermosets

3.2.4.1 Mass Loss

The mass loss of a Kevlar/epoxy composite located on the leading edge of the LDEF satellite is summarized in Table 3-28 (ref. 7). The mass loss given is for samples approximately 0.080 inch in thickness. The trailing edge samples, flight control samples and the ground control samples had no significant mass loss. Because the leading edge samples were the only samples to exhibit mass loss, the mass loss is sample erosion due to AO and micrometeoroid impact.

Table 3-28. Typical Mass Loss of Kevlar Epoxy Composite Materials

Material	Fiber/Resin Suppliers	Weight Change %
Kevlar 49/X904B Fabric	DuPont/Fiberite	-2.91

The Kevlar/epoxy performed similar to the carbon/epoxy samples, both the fibers and matrix appeared eroded. The total amount of thickness loss was approximately 0.08-0.13mm for Kevlar/epoxy samples. This compares to 0.10 - 0.15 mm for carbon/epoxy samples and 0.013-0.03 mm for glass/epoxy samples.

3.2.4.2 Thickness Erosion from Atomic Oxygen Exposures

None reported.

3.2.4.3 Impact Damage from Micrometeoroid and Debris

Impact damage from micrometeoroid and debris for various Kevlar fiber-reinforced epoxy materials was observed on the LDEF UTIAS Experiment AO180 (ref. 27). These samples were mounted at station D-12, about 82° from the LDEF velocity vector. The exposed surface area was ~0.6m^2. The UTIAS experiment suffered 84 randomly distributed impacts by micrometeoroids or space debris; 74 of them produced craters having diameters less than 0.5 mm (0.02 in.). The predicted number of impacts for this area after 5.75 years is ~80.

From a detailed inspection of the composite samples (both tubes and flat plates), only 10 of the 84 hits were found on these materials, the balance located on end fixtures and the aluminum base plates. A summary of the 10 impact sites (out of 84) found on the composite samples is given in Table 3-29 with estimates of surface damage area, hole size and penetration depth. Also included are the impact damage on carbon fiber-reinforced epoxy samples. Such data are useful for estimating total damage on composite structures that arises from micrometeoroids/debris.

The impacts on the polymer matrix composites do not produce the typical hemispherical craters found on metallic structures. Rather, because of the brittle nature of the resin matrix, one generally finds penetration holes with adjacent surface damage, some internal ply delamination and local fiber fractures. For tough non-brittle fibers, such as aramid, these fibers fail in a "brush or broom" mode surrounding the impact damage region (Kevlar/epoxy tube SP-328, $(\pm 45°)_{4S}$). On the other hand, for brittle fibers such as carbon, the impact and exit holes exhibit brittle fiber fractures as well as rear exit hole surface spallation (T300/5208 epoxy; $(\pm 45°)_S$). Note that the spallation damage-to-hole size ratio is about 5:1.

Table 3-29. Summary of Impact Feature on Kevlar Epoxy Composite Specimens (LDEF Experiment AO180)

Material Type	Sample Type	# of Plies	Surface Damage Area (mm^2)	Hole Area (mm^2)	Nominal Hole Diameter (mm)	Particle Penetration Depth (# of Plies)
Kevlar/Epoxy (SP 328)	Tube	4	1.162	0.036	0.215	1~2
	Tube	4	0.498	0.015	0.139	~1
	Tube	4	0.423	0.018	0.152	~1
	Tube	4	1.253	0.076	0.312	2~3
	Tube	4	0.223			1~2
			1.445	0.033	0.204	2~3
			0.370			~1
			0.881	0.020	0.159	2~3
Carbon/Epoxy (T300/5208)	Plate	4	0.222	0.222		>4
Carbon/Epoxy (T300/SP 288)	Tube	4	1.064	0.083	0.325	>4

Note: Micrometeoroid/debris impacts can penetrate four-ply laminates with substantial rear-face spallation damage.

3.2.4.4 Mechanical Property Degradation from Atomic Oxygen

Two mechanical property tests, shear and flexure, were conducted on several Kevlar composites located on the LDEF satellite (ref. 7). The shear test is a resin dominated property where the flexure test is a fiber dominated property. These tests were chosen because of the sample size limitations and shear and flexure changes would be expected to appear more distinctly than other mechanical property changes. The shear test was run per ASTM D 2344, and flexure test was run per ASTM D 790. The laminate ply orientations for short beam shear and flexure were $(0_{16})_T$ and $(+45/-45_2/+45)_{4T}$, respectively.

The results of the mechanical property testing are summarized in Tables 3-29 and 3-30. Table 3-30 shows the short beam shear test results. The samples that were tested for short beam shear were all 16 ply unidirectional laminates. Table 3-31 gives the results of the flexure testing. All of the samples that were tested for flexure were 16 ply $[+45/-45_2/+45]_{4T}$ laminates. The results show that the flight samples strength was degraded only to the extent of the mass loss percentage. This indicates that except for the physical eroding of the material there was no mechanically detrimental effects caused by the low Earth orbit environment.

Table 3-30. Short Beam Shear Strength of Kevlar/X904B Epoxy Fabric(a)

Sample Location	Short Beam Shear, ksi (MPa)
Leading Edge	3.6 (24.8)
Trailing Edge	3.8 (26.2)
Control	3.7 (25.5)

(a) Fiber/Resin Supplier: Fiber/Resin Supplier

Table 3-31. Flexural Properties of of Kevlar/X904B Epoxy Fabric(a)

Sample Location	Flexural Strength ksi (MPa)	Flexural Modulus Msi (GPa)
Leading Edge	1344.5 (195)	1.1 (7.5)
Trailing Edge	1158.3 (168)	0.9 (6.4)
Control	1344.5 (185)	1.2 (7.9)

(a) Fiber/Resin Supplier: Fiber/Resin Supplier

3.2.4.5 Dimensional Changes

3.2.4.5.1 Outgassing

Outgassing produces dimensional changes of polymer matrix composites which asymptotically approach a constant value once the outgassing process has essentially ceased. One of the composite experiments on board LDEF, the UTIAS Experiment No. A0180, showed clearly the effect of outgassing on the dimensional changes of a Kevlar fiber reinforced epoxy matrix composites and the corresponding coefficients of thermal expansion. The experiment, located at station D-12 on LDEF, 90° to the leading edge, was custom-designed and constructed to record 16 thermal/strain gauges every 16 hours for a period of 371 days (ref. 6 and 28). Details on this aspect of the experiment can be obtained from Tennyson.[33] LDEF was yawed ~8° relative to the orbital velocity vector (i.e., ~82° relative to velocity vector), with a corresponding atomic oxygen fluence at station D-12 of about 1.2×10^{21} atoms/cm^2. Experiment No. A0180's sample trays contained a stainless-steel calibration tube, 62 composite tubes, and 45 composite coupons.

Outgassing time, t_o, and associated dimensional change, $\Delta\varepsilon$, obtained from strain vs. temperature plots, are summarized in Table 3-32 for the Kevlar/epoxy. It took about 120 days for the Kevlar/SP-288 epoxy 4-ply/90° to outgas. In comparison, the T-300 carbon/934 epoxy and the T-300 carbon/SP-288 epoxy took 40 days to outgas and 80 days for the T-300 carbon/5208 epoxy to outgas.

Table 3-32. Outgassing Time and Dimensional Change for Kevlar Epoxy Composite

Material	Outgassing Time t_o, days	Dimensional change, $\Delta\varepsilon$, strain, 10^{-6}				
		Initial			Final Asymptote	
		Laboratory Calibration	First Deployed	$\Delta\varepsilon$	Strain	$\Delta\varepsilon$
Aramid/epoxy SP-328, 4-ply/90°	120	-2370 at -18°C (0°F)	-1200	1170	-4000	-2800

3.2.4.5.2 Coefficient of Thermal Expansion

CTE values for the LDEF Experiment No. A0180 are summarized in Table 3-33.

Table 3-33. CTE values for UTIAS/LDEF Kevlar Epoxy Composite

Material	Gage No.		Coefficient of Thermal Expansion, CTE, 10^{-6}/°C (10^{-6}/°F)[1]		
	Strain	Thermal	Ambient[3]	Space[4]	Thermal-vacuum facility[5]
Stainless steel calibration-tube	1	1	17.7 (9.84)	18.0 (10.0)	18.0 (10.0)
Aramid/epoxy SP-328,[2] tube, 4-ply/90°	4 (90°) 5 (0°)	3	61.0 (33.9) 0.18 (0.10)	54-99 (30-55) 1.28 (0.71)	63.5 (35.3) 1.13 (0.63)

[1]Multiply by 1.8 to obtain CTE value in 10^{-6}/°C
[2]Scotchply SP-328 (Structural Products Department, 3M Co., St. Paul, Minn
[3]Measured at atmospheric pressure prior to launch
[4]Measured in space environment on LDEF during first 371 days in orbit
[5]Measured in laboratory thermal-vacuum test facility after 2,1.4 days in orbit and 184 days at ambient laboratory conditions

3.2.4.5.3 Microcracking

No information reported from flight experiments.

3.2.5 Boron/Thermosets

3.2.5.1 Thickness Erosion from Atomic Oxygen Erosion

None reported.

3.2.5.2 Impact Damage from Micrometeoroid and Debris

None reported.

3.2.5.3 Mechanical Property Degradation from Atomic Oxygen

None reported.

3.2.5.4 Dimensional Changes

3.2.5.4.1 Outgassing

Outgassing produces dimensional changes of polymer matrix composites which asymptotically approach a constant value once the outgassing process has essentially ceased. One of the composite experiments on board LDEF, the UTIAS Experiment No. A0180, showed clearly the effect of outgassing on the dimensional changes of a Boron fiber reinforced epoxy matrix composites and the corresponding coefficients of thermal expansion. The experiment, located at station D-12 on LDEF, 90° to the leading edge, was custom-designed and constructed to record 16 thermal/strain gauges every 16 hours for a period of 371 days (refs. 6 and 28). Details on this aspect of the experiment can be obtained from Tennyson (ref. 36). LDEF was yawed ~8° relative to the orbital velocity vector (i.e., ~82° relative to velocity vector), with a corresponding atomic oxygen fluence at station D-12 of about 1.2×10^{21} atoms/cm^2. Experiment No. A0180's sample trays contained a stainless-steel calibration tube, 62 composite tubes, and 45 composite coupons.

Outgassing time, t_o, and associated dimensional change, $\Delta\varepsilon$, obtained from strain vs. temperature plots, are summarized in Table 3-34 for the boron/epoxy. It took about 85 days for the boron/SP-290 epoxy 4-ply/30° to outgas. In comparison, the T-300 carbon/934 epoxy and the T-300 carbon/SP-288 epoxy took 40 days to outgas, and 80 days for the T-300 carbon/5208 epoxy to outgas.

Table 3-34. Outgassing Time and Dimensional Change for Boron Epoxy

Material	Outgassing Time t_o, days	Dimensional change, $\Delta\varepsilon$, strain, 10^{-6}				
		Initial			Final Asymptote	
		Laboratory Calibration	First Deployed	$\Delta\varepsilon$	Strain	$\Delta\varepsilon$
Boron/epoxy SP290, 4-ply/±30°	85	-800 at -23°C (-10°F)	-75	725	75	150

3.2.5.4.2 Coefficient of Thermal Expansion

CTE values for the UTIAS LDEF Experiment No. A0180 are summarized in Table 3-35.

Table 3-35. CTE values for UTIAS/LDEF Boron Epoxy

Material	Gage No.		Coefficient of Thermal Expansion, CTE, 10^{-6}/°C (10^{-6}/°F)[1]		
	Strain	Thermal	Ambient[3]	Space[4]	Thermal-vacuum facility[5]
Stainless steel calibration-tube	1	1	17.7 (9.84)	18.0 (10.0)	18.0 (10.0)
Boron/epoxy SP-290,[2] tube,4-ply/±30°	9 (±30°)	6	2.83 (1.57)	3.0-4.0 (1.67-2.22)	0.79-3.6 (0.44-2.0)
	10 (±60°)		21.1 (11.7)	13.5-20.0 (7.5-11.1)	22.9 (12.7)

[1]Multiply by 1.8 to obtain CTE value in 10^{-6}/°C
[2]SP-290 (Structural Products Department, 3M Co., St. Paul, Minn
[3]Measured at atmospheric pressure prior to launch
[4]Measured in space environment on LDEF during first 371 days in orbit
[5]Measured in laboratory thermal-vacuum test facility after 2,114 days in orbit and 184 days at ambient laboratory conditions

3.2.5.4.3 Microcracking

No information reported from flight experiments.

3.3 PROTECTIVE COATED POLYMER MATRIX COMPOSITES

Spacecraft designers who selects polymeric-matrix composites for critical low-Earth orbit applications requiring very low coefficient of thermal expansion, reduced weight and high specific moduli compared to other candidate isotropic spacecraft materials need to be concerned with the long-term effects of the space environment on the performance of these materials. Factors involved in determining whether composites exposed to the space environment will provide the long life desired for long-term space missions, e.g., International Space Station Alpha, include the selection of the resin and fiber systems as well as an effective atomic oxygen protective coating.

AO barrier coatings should have the following properties:

- The barrier must be resistant to atomic oxygen bombardment;
- It should be flexible, abrasion-resistant, and allow adhesive bonding;
- It should have desirable optical properties;
- It should be UV tolerant; and
- Finally, surface conductivity should be high in order to prevent the build-up of harmful potential gradients that might result from charging.

3.3.1 Anodized Al Foil

Anodized aluminum foil is an excellent coating for use on tubular and flat shapes.[34,35,36] The aluminum provides stable optical properties, provides a barrier to atomic oxygen erosion and to moisture/outgassing and provides the best mircrometeoroid impact resistance, i.e., impact hole diameter doesn't change with time. Anodized aluminum foil adhesively co-cured to composites has excellent bond strength to the composite substrates.

The life of the protected composites is strongly dependent on the number and severity of high velocity impact (HVI) hits penetrating the foil cover and subsequently exposing the resin and fibers to AO. For example, HVI statistical analysis showed that for a 0.13 mm foil on a 2.5 mm thick, 50 mm diameter tube, there will be approximately 13 tubes penetrated in 30 years (a bonded foil cover or extruded and thinned aluminum tube was initially chosen to provide AO protection for the truss tubes and mobile transporter base for International Space Station Alpha), as well as hundreds or thousands of penetrations through the aluminum foil on each tube. One model in a study using two different orbital debris models showed 141 penetrations of a 0.13 mm aluminum foil in 30 years, while the other model predicted 1633 penetrations. Increasing the foil thickness to

0.20 mm will reduce the number of foil penetrations by about 60%. The erosion of the unprotected composite in the worst orientation is around 0.1 mm per year, indicting that there may be some through holes created by AO in the lifetime of the truss tubes.[37]

3.3.2 Sputtered Coatings

Sputtered coatings on composite materials are attractive due to the ability to apply very thin coatings and their tailorability of optical properties. However, there is limited application for use due to the complexity of the coating deposition (i.e., partial vacuum requirements limit substrate sizes).

Table 3-36 summarizes the thermo-optical performance of several sputter-deposited coatings applied to carbon-epoxy composite substrates flown on the various flight experiments.[38,39] The coatings evaluated on the STS-8 were generally unaffected by the atomic oxygen environment. The opaque nickel coating appeared slightly rougher after exposure than the preflight coating. The atomic oxygen stability demonstrated by these sputter deposited coatings suggest that this technique could be used to protect polymer matrix composites from erosion in long-term LEO applications.

Table 3-36. Sputter Coatings on Carbon/Epoxy Composites.

Designation	Sputter Coatings	Substrate	Exp't	AO Fluence 10^{21} atoms/cm^2	α/ε ratio	
					BOL	EOL
Opaque Nickel	1600 Å of C.999 Nickel	0.025 cm thick T300/5208	STS-8	0.35	0.52/0.45	0.52/0.45
Ni/SiO2	600 Å SiO_2 over 1600 Å Nickel	0.025 cm thick T300/5208	STS-8	0.35	0.50/0.27	0.49/0.27
Al_2O_3/Al	800 Å Al_2O_3 over 1800 Å of 0.9995 pure Aluminum	0.025 cm thick T300/5208	STS-8	0.35	0.29/0.78	0.29/0.78
Al	Aluminum (420-2520 Å thick)	Carbon/Epoxy	LDEF	8.99	0.16/0.24	0.05-0.09/ 0.19-0.30

Sputter-deposited metallic coatings on T300/934 composites were observed to be effective in preventing mass loss from exposure to the LEO atomic oxygen environment in experiment A0134 on the LDEF (ref. 11). The T300/934 composite, a 4-ply [±45]$_s$ lay-up with a coating of 1000 Å of nickel with a 600 Å overcoat of silicon dioxide, exhibited no mass loss after 5 years and 9 months of LEO exposure. A vapor deposited, 1200 Å-thick aluminum coating also protected the T300/934 from atomic oxygen with negligible weight penalty. No coating delamination from the composite surface was noted after approximately 34000 thermal cycles in. In contrast, the

unprotected composite on the same experiments experienced a thickness loss of 0.0045 inch of the 0.0055-inch thick outer ply.

A 0.41 mm (16 mils) thick T300 carbon fiber 934 epoxy composite sample with a protective coating consisting of < 1000 Å of Al_2O_3 was exposed to an atomic oxygen fluence of 8.99 x 10^{21} atoms/cm^2 on row 9 of LDEF.[40] This atomic oxygen protective coating was extremely thin, poorly attached to the substrate, and proliferated with defects as observed by scanning electron photomicroscopy.

A 0.64 mm (25 mils) thick T300 carbon fiber 934 epoxy composite sample with a protective coating of 400 Å of aluminum on top of 800 Å of chromium was exposed to an atomic oxygen fluence of 8.99 x 10^{21} atoms/cm^2 on row 9 of LDEF (ref. 43). The highly irregular quilted surface texture of the composite sample due to the carbon fiber fabric greatly contributed to the occurrence of defects in the protective coating.[41] Scanning electron microscopy revealed a significantly larger undercut cavity diameter compared to the respective protective coating defect. Measurement of the area of the undercut cavity given the row 9 LDEF atomic oxygen fluence of 8.99 x 10^{21} atoms/cm^2 resulted in an effective erosion yield under the defect site of 2.46 x 10^{-24} cm^3/atom. This erosion yield is approximately twice that of unprotected carbon epoxy based on previous LEO evaluation of carbon fiber epoxy composites.[42] The higher effective erosion yield for atomic oxygen entering defects, compared to atomic oxygen impinging upon unprotected material, is thought to be due to the opportunities for it to react with the underlying organic material.

An indium-tin eutectic coating was exposed to an atomic oxygen fluence of 7.15x10^{21} atoms/cm^2 (leading edge) and 2.31x10^5 atoms/cm^2 (trailing edge) as part of the M0003-10 experiment (ref. 38). This moisture barrier coating prevented composite mass loss even though the exposed surfaces became dull and discolored. There was minor visual difference between leading and trailing edge specimens.

3.3.3 Thermal Control Paints

Most standard space qualified paints are good for short-term missions. Spray application makes these coatings easy to apply. A study of the effects of thermal control coatings on the thermal-cycled induced mircrocracking behavior in carbon/epoxy composites indicated adequate coating capability by A276 white polyurethane in effectively reducing thermal cycling extremes and shocks (see page 3-36 and ref. 9).

Z-93 and YB-71 are best for long-term missions (see Chapter 10, Sections 10.3). These coatings are the leading candidate for the space station radiator coatings, providing excellent α/ε ratios. However, the adhesion to bare composite needs to be verified.

3.3.4 Aluminum Thermal Control Tape

S glass epoxy composite samples (0.5-in. x 6-in.) covered with an aluminum thermal control tape were flown as part of the LDEF flight experiment A0171, the Solar Array Materials Passive LDEF Experiment (SAMPLE).43 The thermal control tape was a 2 mil aluminum with 2 mil pressure sensitive silicone adhesive SR574. The LDEF A0171 tray was located on the leading edge row A8 of the LDEF satellite, and was in orbit at an angle of ~38o from the ram vector. The environmental exposure conditions included UV radiation of 9,400 esh, atomic oxygen exposure of 7.15 x 1021 atoms/cm2, ~32,000 thermal cycles, and 2 to 7 impacts of < 1mm per composite. Comparative mechanical and optical properties of bare and tape covered composites are summarized in Table 3-37.

The thermal control tape proved successful in protecting the underlying composite from the atomic oxygen/UV radiation resin erosion as evident in the comparative mass loss data of Table 3-37. The mass loss for the bare composite was four times greater than for the tape covered composite. The small degree of mass loss on the tape covered specimens was due to erosion along the specimen edges where the composite was exposed. The tape silicone adhesive also proved to withstand the rigors of the environment, with the flight specimens showing an increase in peel strength over the control by a factor greater than 2 to 1. This increase in peel strength is again probably due to thermal cycling effects. Difficulties in conducting the peel tests on the flight tape specimens also suggested that the flight tape had become embrittled by the space exposure. The solar absorptance and IR emittance on the tape covered specimens showed little change between the flight and control specimens, with the differences in recorded values considered to be in the noise range of the portable instruments used to measure the properties. The tape did not however provide complete protection from micrometeoroid/debris. One debris hit did penetrate the protective tape, causing damage to the composite substrate, while a second impact, originating most probably from a shuttle fluid dump, was unable to penetrate the tape.

Table 3-37. Mechanical and Optical Properties of Bare and Tape Covered Composite

Properties	Bare Composite		Tape Covered Composite	
	Control	Flight	Control	Flight
Peel Strength (lb./in)	-	-	1.9	4.6
Mass Loss (mg/cm^2)	-	2.40	-	0.59
Solar α (avg.)	0.723	0.787	0.140	0.103
IR ε (avg.)	0.894	0.895	0.025	0.020

3.3.5 RTV Silicone Atomic Oxygen Protective Overcoat

McGhan NuSil CV-1144-0 is a one-part, silicone dispersion specially designed and processed for applications requiring extreme low temperature, low outgassing and minimal volatile condensables under extreme operating conditions. CV-1144-0 is based on a dimethyl diphenyl silicone copolymer with a service temperature range of -115°C to 232°C.

This silicone coating was applied to the original Hubble Space Telescope Solar Arrays. It was applied to carbon/epoxy composites, Kapton, Dacron and Chemglaze paint. This coating was recently flight tested on the STS-46 LDCE-3 experiment.[44] No correlation was observed between the flight weight loss of 0.491 percent and the ASTM E-595 CVCM and TML values of 0.00 and 0.31 percent, respectively. Possible mechanisms for the reaction of the silicone elastomer with oxygen atoms that caused the weight loss. are:

- $SiCH_3 + 4\ O$----------$SiOSi + 3H_2O + 2C$
- $SiCH_3 + 4\ O$----------$SiC + SiOH + H_2O + CO_2$

This silicone coating was also applied to a carbon/PEEK thermoplastic composite. No measurable erosion was observed in the protected layer.[45]

3.4 METAL MATRIX COMPOSITES

Aluminum and magnesium reinforced with P75 or P100 pitch base carbon fibers are leading candidate composites for precision space structures. Graphite/aluminum and graphite/magnesium composites offer better thermal conductivity than polymer matrix composites, and hence, offer advantages for space structures particularly where very tight thermal stability requirements are needed. Other desirable attributes of metal-matrix composites are no outgassing, zero moisture absorption, high material damping, and lower susceptibility to space environmental effects (e.g., atomic oxygen, electron, proton, ultraviolet radiation stability) as compared to polymer matrix composites (refs. 3, 8, and 11). The main disadvantages of metal matrix composites are that they are difficult to process and are expensive.

3.4.1 Graphite/Aluminum

3.4.1.1 Thickness Erosion from Atomic Oxygen Exposure

No information available from flight experiments. However, metal matrix composites are not expected to suffer any significant surface erosion due to its resistance to atomic oxygen erosion.

3.4.1.2 Impact Damage from Micrometeoroid and Debris

Numerous micrometeoroid or debris impact craters were observed on exposed samples of metal matrix composites on the LDEF flight experiment. Graphite/aluminum metal matrix specimens were part of the "Advanced Composites Experiment," which was a sub-experiment of LDEF Experiment M0003-10, "Space Environmental Effects on Spacecraft Materials" (ref. 1). The metal matrix composites included in the experiment are listed in Table 3-38. The graphite/aluminum strip samples included three different graphite fibers and two different alloy matrices with four different lay-ups.

The diameter of most of the crater was less than 100 μm. Since the graphite/aluminum had an aluminum alloy surface foil, the crater had the same appearance as for monolithic aluminum. A cross section of this crater showed that it extended completely through the 0.004 in. (0.010 cm) 2024 aluminum surface foil, but did not extend into the underlying graphite fiber-reinforced interior. This may imply that penetration through the foil is much easier than through the fiber-reinforced region of the composite, but may also be the characteristic depth of penetration into aluminum for this particular size of impact particle.

Table 3-38. Graphite Aluminum Metal Matrix Composites Exposed to the LEO Environment

Material	Lay-up	Number of Samples				
		Leading Edge		Trailing Edge		Control
		A-Deck Space Exposed	B-Deck Shielded	A-Deck Space Exposed	B-Deck Shielded	
GY70/201/2024 Strips	0,90, $(0/\pm60)_s$	15	14	13	118	20
P55/6061/6061 Strips	0 or 90	8	10	8	8	12
P100/201/2024 Strips	$(\pm20)_s$	2	2	2	2	2
P100/6061 Wires	0	4	1	4	1	2
P55/6061 Wires	0 or $(0)_5$	8	3	8	3	6
GY70/201 Wires	$(0)_8$	2	1	2	1	2
T300/6061 Wires	0	1	2	1	2	

Note: Materials were flown in the direct space exposure positions on the "A-deck" as well as in shielded positions on the "B-deck," both at the leading and trailing edges. The environments for the samples mounted on the leading and trailing A decks were similar except those on the leading edge were also exposed to relatively high fluxes of atmospheric constituents (primarily atomic oxygen). Although the samples on the B decks were not exposed to the radiation environment, the experiment design was such that they experienced thermal excursions similar to those of the exposure samples. Also, a complete set of specimens were kept at controlled temperature and humidity conditions at the Aerospace Corporation. These specimens were shielded from exposure to ambient light and were used as ground controls.

Perhaps the most significant observation is the presence of a delamination of the surface foil over an area approximately three times the crater diameter. It is not known whether the delamination occurred due to the impact energy or formed later due to thermal fatigue. Surface foil delaminations would affect important through-thickness properties, such as the thermal conductivity. In addition, the transverse strength of graphite/aluminum and graphite/magnesium is primarily provided by the surface foil. Large foil delaminations could therefore have serious consequences on the performance of these composites. Thus, if the delaminations propagate due to thermal fatigue, they could reach much larger sizes during extended missions and have substantial adverse effects.

3.4.1.3 Dimensional Changes

3.4.1.3.1 Outgassing

No information available from flight experiments. However, metal matrix composites do not outgass due to the characteristics of its metal matrix.

3.4.1.3.2 Coefficient of Thermal Expansion

Graphite/aluminum composites showed a stable, linear thermal expansion behavior with near-zero thermal hysteresis over the LDEF temperature range.[i] Graphite/aluminum metal matrix specimens with continuous graphite fiber reinforcements were part of the "Advanced Composites Experiment," which was a sub-experiment of LDEF Experiment M0003-10, "Space Environmental Effects on Spacecraft Materials" (ref. 2). The locations of the flight samples on LDEF were Bay D, Row 4 on the trailing edge and Bay D, Row 7 on the leading edge. The samples were 3.5 in. long x 0.5 in. wide x 0.032 in. thick strips.

The thermal expansion behavior of P55/6061/6061 composites was fairly linear with only a small hysteresis. Typical plots of dimensional change vs. time for graphite/aluminum revealed normal behavior of expansion and contraction with heating and cooling throughout the cycle. Post-flight thermal expansion behavior of the flight samples and lab-control samples using laser interferometer data analysis indicated that after a certain number of thermal cycles in space, strain hardening in the matrix stabilized the composites, reducing thermal hysteresis for subsequent thermal cycles. A similar behavior was observed for the GY70/201/2024 composites, except that this material showed more thermal hysteresis, particularly in the trailing edge sample. However, in all cases, the total changes in dimension and the slopes remained constant during the entire time of recording.

---

[i] The flight data revealed that in the space environment, the temperature distribution in a structure is non-uniform due to radiant heating. For a satellite like LDEF in a low Earth orbit with alternating eclipse and sun exposure, the data showed that the materials experienced thermal cycling over different temperature extremes (-29°C (-20°F) to 71°C (160°F) ±12°C (±20°F)), with different heating/cooling rates depending on the location of samples on the satellite. In a thermal cycle, the heating/cooling rates could vary from 0°C/min. to 12°C/min. when LDEF was going in or out of the Earth's shadow. On the LE, the rates were almost double those on the TE. Hence, the differential heating/cooling rates caused a difference in the total changes in dimension between LE and TE samples over the same temperature range as observed in graphite/aluminum composites.

The average CTEs for the graphite/aluminum composite samples determined over the entire temperature range are listed in Table 3-39. Apparently, the CTEs of both composite materials were unaffected by the extended space exposure. These results indicated that the LDEF space environment has little effect on the thermal behavior of graphite/aluminum. Thermal cycling in orbit stabilized the graphite/aluminum composites, eliminating thermal hysteresis effects.

Table 3-39. CTE of Graphite/Aluminum Composites on LDEF

Materials	Coefficient of Thermal Expansion 10^{-6}/°C (10^{-6}/°F)		
	Lab-Control	Leading Edge	Trailing Edge
GY-70/201/2024 (1 ply)	6.3 (3.5)	5.8 (3.2)	6.8 (3.8)
P55/6061/6061 (1 ply)	5.4 (3.0)	5.9 (3.3)	6.3 (3.5)

3.4.1.3.3 Microcracking

Graphite/aluminum revealed no evidence of matrix microcracking during the LDEF flight experiment.[j] Since these samples were exposed to over 34,000 thermal cycles, this indicated that these composites have excellent resistance to thermal fatigue for the LDEF thermal environment. However, extensive thermal fatigue cracking was observed on the surface foils of selected GY70/201/2024 graphite/aluminum strip samples. This was surprising since the thermal stresses should be lower within the surface foils than within the fiber-reinforced regions of the composites. However, further inspection revealed that the cracks were always associated with a surface contaminant that was clearly visible on several trailing edge samples that had been mounted adjacent to one another. X-ray Photoelectron Spectroscopy showed the presence of silicon and oxygen, probably from on-orbit silicone contamination. The cracks probably initiated in a brittle oxide or aluminum silicate layer on the sample surface. Once the cracks were initiated, they propagated into the bulk of the foil. In some cases, the cracks propagated completely through the surface foil. However, there was no evidence of the cracks extending into the underlying Gr/Al region or along the interface between this region and the foil.

Less severe, isolated fatigue cracks also were observed on several graphite/aluminum specimens. These cracks are associated with surface defects such as surface-foil blemishes, micrometeoroid craters, and engraved identification numbers, which presumably acted as stress concentrators and crack-initiation sites.

---

[j] Etching of graphite/aluminum cross sections produced matrix darkening in the fiber-reinforced regions, which is an indication of plastic deformation. This is not surprising since the coefficient of thermal expansion mismatch between the graphite fibers and matrix induces high stresses in the matrix during thermal cycling.

3.4.2 Graphite/Magnesium

3.4.2.1 Thickness Erosion from Atomic Oxygen Exposure

No information available from flight experiments. However, metal matrix composites are not expected to suffer any significant surface erosion due to their resistance to atomic oxygen erosion.

3.4.2.2 Impact Damage from Micrometeoroid and Debris

No information available from flight experiments.

3.4.2.3 Dimensional Changes

3.4.2.3.1 Outgassing

No information available from flight experiments. However, metal matrix composites do not outgass due to the characteristics of its metal matrix.

3.4.2.3.2 Coefficient of Thermal Expansion

Graphite/magnesium composites showed non-linear, unstable thermal expansion behavior, even after extensive cycling during orbiting, with significant thermal hysteresis over the LDEF temperature range.[k] Graphite/magnesium metal matrix specimens with continuous graphite fiber reinforcements were part of the "Advanced Composites Experiment," which was a sub-experiment of LDEF Experiment M0003-10, "Space Environmental Effects on Spacecraft Materials" (ref. 2). The locations of the flight samples on LDEF were Bay D, Row 4 on the trailing edge and Bay D, Row 7 on the leading edge. The samples were 3.5 in. long x 0.5 in. wide x 0.032 in. thick strips.

Post-flight samples of the P100/EZ33A/AZ31B composite system exhibited non-linear thermal behavior with a large residual thermal strain at room temperature of ~280 μ-strain. The large residual strain of the material is typical of metal matrix composites, and is caused by yielding of the matrix. For example, the composite behavior near the cold end of the thermal cycle is

---

[k] The flight data revealed that in the space environment, the temperature distribution in a structure is often time varying or non-uniform due to radiant heating. For a satellite like LDEF in a low Earth orbit with alternating eclipse and sun exposure, the data showed that the materials experienced thermal cycling over different temperature extremes with different heating/cooling rates depending on the location of samples on the satellite. In a thermal cycle, the heating/cooling rates could vary from 0°C/min. to 11°C/min. when LDEF was going in or out of the Earth's shadow. On the LE,, the rates were almost double those on the TE. Hence, the differential heating/cooling rates caused a difference in the total changes in dimension between LE and TE samples over the same temperature range as observed in graphite/aluminum composites.

dominated by the expansion of the fibers causing yielding in the matrix. This leads to an increase in dimension and consequently an open loop with large permanent offset at room temperature. The thermal expansion behavior of post-flight samples showed that the amount of permanent offset and the magnitude of thermal hysteresis over the temperature range decreased remarkably after thermal cycling. The implication of the results is that extensive thermal cycling had a large effect on stabilizing the behavior of these materials. However, the thermal expansion behavior remained non-linear and the thermal hysteresis could not be cycled out as in the case of graphite aluminum composites. These data indicate that the EZ33A Mg alloy, unlike the high strength 6061 and 201 Al alloys, was not effectively strain-hardened by thermal cycling, which would have increased the yield strength and minimized strain hysteresis over the LDEF temperature range. It should be noted however that the total dimensional change and average CTE of the graphite/magnesium composites are smaller than those of the graphite/aluminum composites. This is due to the low elastic modulus of the magnesium alloys (6.5 Msi) and the high modulus, low CTE P100 fiber. The CTEs are near-zero and similar for both LE and TE samples within the error range of the experiment.

Typical plots of dimensional change versus time indicates anomalous behavior for a typical LDEF thermal cycle. As the cycle started, temperature increased slowly and the sample expanded as expected. However, as the heating rate rapidly increased, the sample contracted instead of expanding. This can be attributed to the low matrix conductivity of the Mg alloy (54 W/m-K [31 Btu-in/hr-ft-°F]).[1] When the exposed surface of the graphite/magnesium samples was heated or cooled slowly (e.g., 1.0°C/min. [1.5°F/min] or less), thermal equilibrium was maintained throughout the sample leading to normal behavior. However, when just leaving or entering the shadow, the samples were heated or cooled at a much faster rate (5.5°C/min [10°F/min]). Due to the low thermal conductivity of the graphite/magnesium, a steep thermal gradient existed through the thickness. A larger temperature gradient existed between exposed front-surface and back-side surface in the graphite/magnesium composite materials than for graphite/aluminum. Upon heating,, the exposed surface was therefore much hotter and consequently expanded faster than the back surface, causing sample bending and inducing compression in the back surface These bending deformations give the erroneous indication of a negative CTE. Similar arguments apply for the fast cooling condition, the exposed surface cooled faster making the sample bend the other way.

From the results of flight data analysis, it is clearly shown that in a space environment, the temperature distribution in a structure is not uniform. Nonuniform temperatures arise from radiant heating on one side of a structure as typically occurs in a geostationary satellite or by transient heating/cooling as in the LDEF structure placed in a day-night low Earth orbit with alternating

[1] Matrix conductivity of aluminum alloy is 1104 Btu-in/hr-ft°F

eclipse and sun exposure. Depending on the location, as in this case LE or TE, materials are subjected to widely different temperature ranges and heating/cooling rates. The disparity of the temperature range and rates of heating/cooling lead to a differential total change in dimensions that could eventually lead to thermal distortion. In low thermal conductivity materials, such as graphite/magnesium or graphite/epoxy composites, the thermal gradient effects on distortion are more severe. Therefore, besides the thermal expansion behavior (CTE and thermal hysteresis), thermal conductivity must be considered in predicting the structural stability of a material in the space environment.

3.4.2.3.3 Microcracking

Graphite/magnesium exhibited no evidence of matrix microcracking after more than 34,000 thermal cycles on the LDEF satellite, indicating excellent resistance to thermal fatigue for the LDEF thermal environment. Graphite/magnesium metal matrix specimens were part of the Advanced Composites Experiment, which was a sub-experiment of LDEF Experiment M0003, "Space Environmental Effects on Spacecraft Materials" (ref. 1). The metal matrix composites included in the experiment are listed in Table 3-40. The samples were located on LDEF Bay D, Row 4 on the trailing edge and Bay D, Row 8 on the leading edge. The samples were mounted on both sides of cassettes with one side (Deck A) exposed to the space environment and the other side (Deck B) facing inward. The graphite/magnesium strips included P100/EZ33A/AZ31B and P100/AZ91C/AZ61A composites. Poor strength properties for P100/EZ33A/AZ31B led to the consideration of the P100/AZ91C/AZ61A composite system.

No evidence of matrix microcracking was observed for the graphite magnesium composites. In contrast, extensive thermal-fatigue cracking was visible on the surface foils of selected graphite/magnesium specimens. This was unexpected because thermal stresses should be lower in the foils than in the fiber-reinforced interior regions. Further analysis, however, revealed that the cracking was due to anomalous surface conditions. The cracks in graphite/magnesium may have initiated within a brittle, surface oxide layer that apparently formed prior to launch.

Table 3-40. Graphite Magnesium Composites Exposed to the LEO Environment

Material	Lay-up	Number of Samples				
		Leading Edge		Trailing Edge		Control
		A-Deck Space Exposed	B-Deck Shielded	A-Deck Space Exposed	B-Deck Shielded	
P100/EZ33A/AZ31B Strips	0,90, or $(0/\pm60)_s$	15	14	13	18	20
P100/AZ91C/AZ61A Strips	0,90 or $(\pm10)_s$	6	4	6	6	3
P100/AZ31B Wires	0	3	1	3	1	
P100/AZ61A Wires	0	4	1	4	11	2
P55/AZ91C Wires	$(0)_5$	3	1	3	1	4

Note: Materials were flown in both direct space exposure positions on the "A-deck" as well as in shielded positions on the "B-deck" at the leading and trailing edges. The environments for the samples mounted on the leading and trailing A decks were similar except those on the leading edge were also exposed to relatively high fluxes of atmospheric constituents (primarily atomic oxygen). Although the samples on the B decks were not exposed to the radiation environment, the experiment design was such that they experienced thermal excursions similar to those of the exposure samples. Also, a complete set of specimens were kept at controlled temperature and humidity conditions at the Aerospace Corporation. These specimens were shielded from exposure to ambient light and were used as ground controls.

3.4.3 Silicon Carbide/Aluminum

Silicon carbide/aluminum metal matrix specimens were part of the Advanced Composites Experiment, which was a sub-experiment of LDEF Experiment M0003, "Space Environmental Effects on Spacecraft Materials" (ref. 1). The metal matrix composites included in the experiment are listed in Table 3-41

Table 3-41. Silicon Carbide/Aluminum Metal Matrix Composites Exposed to the LEO Environment

Material	Lay-up	Number of Samples				
		Leading Edge		Trailing Edge		Control
		A-Deck Space Exposed	B-Deck Shielded	A-Deck Space Exposed	B-Deck Shielded	
SiC_w/2124 Strips	Discontinuous	1	1	1	1	5
SiC_w/6061 Strips	Discontinuous	1	1	1	1	5
$SCS2_f$/Al Strips	$(0)_8$	2	2	2	2	6
NICALON SiC_f/6061 Wires	0	18	5	18	5	5

Note:Materials were flown in both direct space exposure positions on the "A-deck" as well as in shielded positions on the "B-deck" at the leading and trailing edges. The environments for the samples mounted on the leading and trailing A decks were similar except those on the leading edge were also exposed to relatively high fluxes of atmospheric constituents (primarily atomic oxygen). Although the samples on the B decks were not exposed to the radiation environment, the experiment design was such that they experienced thermal excursions similar to those of the exposure samples. Also, a complete set of specimens were kept at controlled temperature and humidity conditions at the Aerospace Corporation. These specimens were shielded from exposure to ambient light and were used as ground controls.

3.4.3.1 Thickness Erosion from Atomic Oxygen Exposure

No information available from flight experiments. However, metal matrix composites are not expected to suffer any significant surface erosion due to atomic oxygen erosion.

3.4.3.2 Impact Damage from Micrometeoroid and Debris

No information available from flight experiments.

3.4.3.3 Dimensional Changes

3.4.3.3.1 Outgassing

No information available from flight experiments. However, metal matrix composites do not outgass due to the characteristics of its metal matrix.

3.5 CARBON-CARBON COMPOSITES

The development of high thermal conductivity reinforcing materials has stimulated interest in developing carbon matrix composites tailored for thermal management applications, such as radiators and electronic packaging, for solar probe spacecrafts. This class of composites, designed to provide thermal expansion control as well as improved thermal conductivity, have the potential to provide benefits in the removal of excess heat from electronic devices and to their associated thermal rejection components.

The P130X carbon fiber with a thermal conductivity three times that of copper and a density one-fourth that of copper is available commercially. This fiber has been successfully incorporated into polymer or metal matrices to make prototype substrates/heatsinks for electrical components on printed wiring assemblies and radiator panels. Recent development has focused on using carbon-carbon's low thermal expansion coefficient and high stiffness-to-weight ratio to produce lightweight structures with a high degree of dimensional stability.

3.5.1 Mass Loss

Uncoated and coated carbon-carbon specimens were part of the BMDO STS-46 EOIM-3 experiments, which flew in August 1992. The experiments were exposed to an atomic oxygen fluence of 2.2 - 2.5 $x10^{20}$ atoms/cm^2. The carbon-carbon specimens were supplied by the Survivable Space Power Subsystem (SUPER) program at Martin Marietta. Fiber architecture was 6:1 warp-to-fill ratio using Amoco P95WG 2K carbon fiber for the warp and Amoco T300 1K carbon fiber for the fill. These unidirectional panels were designed for a high thermal conductivity and elastic modulus in the direction parallel to the P95WG fibers.

Significant erosion occurred in the unprote ed carbon/carbon composite (5L5) as compared to the tungsten (1P2) or titanium carbide (5P3, 1L1) overcoated carbon/carbon materials. Results are summarized in Table 3-42.[46] The TiC coated carbon/carbon materials were slightly oxidized with some loss of carbon.

Table 3-42. Mass Change for Unprotected and Coated Carbon/Carbon Composites

Material Specimen	Sample Code	Visual Change	Mass Change mg
Tungsten/graphite cloth/carbon foam	1P2A	Delaminated	No
	1P2C	Cracked	-0.7
CVD TiC/graphite cloth/carbon foam	5P3A	No	-0.6
	5P3C	No	-0.2
TiC-coated carbon/carbon	1L1A	No	No
	1L1C	No	No
Carbon/Carbon composite	5L5A	Blackened	+2.6
	5L5C	Blackened	-0.7

Carbon-carbon specimens were also integrated into the heated and passive trays of the JPL STS-46 EOIM-3 experiments. The experiments were exposed to an atomic oxygen fluence of 2.2 - 2.5 $x10^{20}$ atoms/cm^2. Erosion yield data are presented in Table 3-43.[47]

Table 3-43. Erosion Yield Data for Carbon-Carbon Composites

Specimen I.D.	Location	Erosion mils (μm)
SP18C	Control	---
SP18D	Passive (10^0 - 40^oC)	<0.04 (<1.0)
SP18A	200^oC Tray	~0.08 (~2.0)

The durability of carbon-carbon composites in the LEO environment and the effect atomic oxygen has on the thermal emittance of the surface was determined in a 1989 study[48] using an AO ground test facility.[m] The equivalent atomic oxygen fluence was calculated based on the loss rate of the pyrolytic graphite that was used as a control in all exposures and the erosion yield of carbon in space, i.e., 1.2 x 10^{-24} cm^3/atom.[49] Carbon-carbon composites from five different manufacturers were used for evaluation.[n]

[m] Directed atomic oxygen exposure was performed with an oxygen ion source from Commonwealth Scientific.

[n] These composites were comprised of Pan or Pitch based carbon fibers woven into a cloth, then impregnated with phenolic resin, formed under heat and pressure, carbonized, densified with pitch and graphitized. Two-dimensional weave carbon-carbon composites were supplied by Rohr Industries, Kaiser Aerotech, and Rocketdyne. In addition to the two-dimensional C-C composite, Rocketdyne supplied a harness weave C-C composite with carbon chemically vapor deposited on the surface: two-dimensional weave C-C composite with an Si/B,Zr oxidation inhibitor; and a two-dimensional weave C-C composite with 2.9 at % tantalum as an oxidation inhibitor. Fiber Materials Inc. supplied a four-dimensional weave C-C composite and a composite made with isostatically pressed chopped fibers. General Electric supplied a three-dimensional C-C composite with silicon carbide on the surface formed by deposited silicon that was flame melted into the composite. Pyrolytic graphite manufactured by Union Carbide was included for comparison and as a flux calibration for the atomic oxygen beam.

Results indicated that the thermal emittance of carbon-carbon composite (as low as 0.42) can be enhanced by exposure to a directed beam of atomic oxygen to levels above 0.85 at 800 K. This emittance enhancement is due to a change in the surface morphology as a result of oxidation. High aspect ratio cones are formed on the surface which allow more efficient trapping of incident thermal radiation.

Erosion of the surface due to oxidation is similar to that for carbon, so that at altitudes less than approximately 600 km, thickness loss of the radiator could be significant (as much as 0.1 cm/year). All of the composites exhibited approximately the same mass loss rate. Figure 3-19 illustrates the thickness loss of carbon/carbon that can be expected in 1-year at various altitudes. If operation is above ~700 km in altitude, a 15-year exposure should result in the removal of <11 μm from the surface. For most radiators, this would be an insignificant loss. At lower altitudes, the loss can become significant. A protective coating or oxidation barrier forming additive may be needed to prevent atomic oxygen attack after the initial high emittance surface is formed.

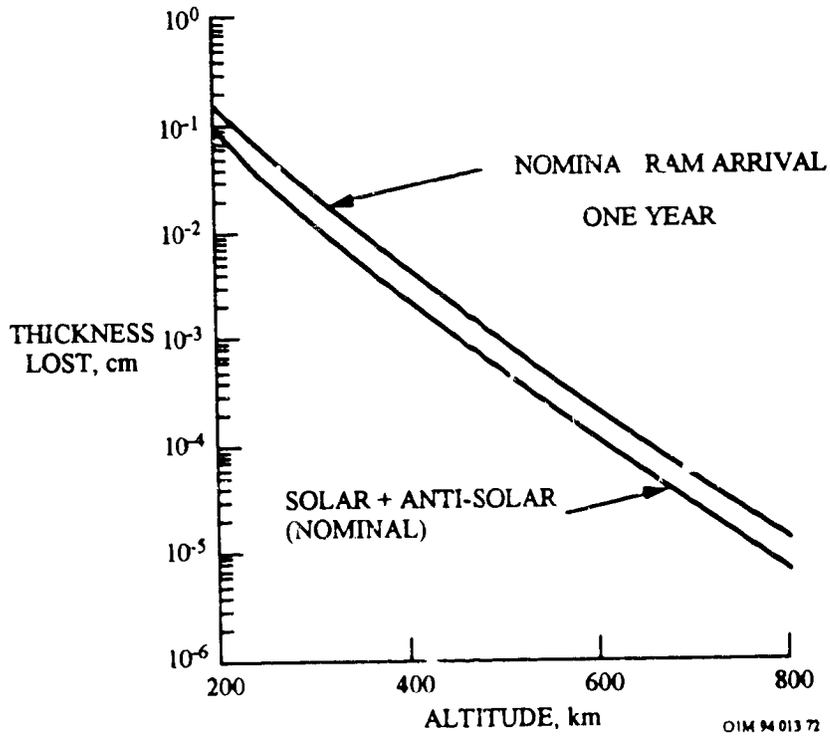

Figure 3-19. Thickness Loss for an Exposed Carbon-Carbon Composite as a Function of Altitude

3.5.2 Optical Properties

Uncoated and coated carbon-carbon specimens were part of the BMDO STS-46 EOIM-3 experiments (samples provided by Martin-Marietta; ref. 46). The STS-46 flew in August 1992, and the experiments were exposed to an atomic oxygen fluence of 2.2 - 2.5 x10^{20} atoms/cm^2. Thermo-optical properties are summarized in Table 3-44.

Table 3-44. Thermo-Optical Properties of Unprotected and Coated Carbon/Carbon Composites

Material Specimen	Sample Code	Visual	α		ε	
			Pre	Post	Pre	Post
Tungsten/graphite cloth/carbon foam	1P2A	Delaminated	0.696	0.729	0.093	0.113
	1P2C	Cracked	0.696	0.707	0.093	0.084
CVD TiC/graphite cloth/carbon foam	5P3A	No	0.661	0.671	0.274	0.270
	5P3C	No	TBD	TBD	TBD	TBD
TiC-coated carbon/carbon	1L1A	No	0.55	0.56	0.14	0.15
	1L1C	No	0.55	0.56	0.15	0.15
Carbon/Carbon composite	5L5A	Blackened	0.82	0.97	0.57	0.75
	5L5C	Blackened	0.82	0.99	0.57	0.69

Carbon carbon specimens were integrated into heated and passive trays of the JPL Shuttle 46 EOIM-3 experiments. Optical property data are presented in Table 3-45 (ref. 47).

Table 3-45. Optical Properties for Carbon-Carbon Composites

Specimen I.D.	Location	α	ε
SP18C	Control	0.76	0.41
SP18D	Passive (10° - 40°C)	0.78	0.44
SP18A	200°C Tray	0.85	0.47

3.6 DESIGN CONSIDERATIONS FOR THE SPACE ENVIRONMENT

3.6.1 Prediction of Surface Recession Rates Due to Atomic Oxygen Exposure.

A design chart, shown in Figure 3-20, permits a user to estimate material thickness loss as a function of satellite orbital altitude, time in orbit and AO angle of incidence relative to the surface normal.[50] Generally, the designer knows the altitude (e.g., 350 km) and time in orbit (500 days) required for a specific satellite application and mission. The intersection of these two lines defines a fluence level as shown in Figure 3-20. One then follows the constant fluence curve until it intersects the specific material reaction efficiency (R_e) curve (e.g., 0.1×10^{-24} cm^3/atom). Moving horizontally from this point of intersection gives the thickness loss in microns (e.g., 10 μm°). This value corresponds to the worst case, i.e., the "ram" direction (8 km/s), assuming a standard atmosphere. Finally, angle of incidence correction of the ram direction can be applied to the "thickness loss" using the nomogram table.

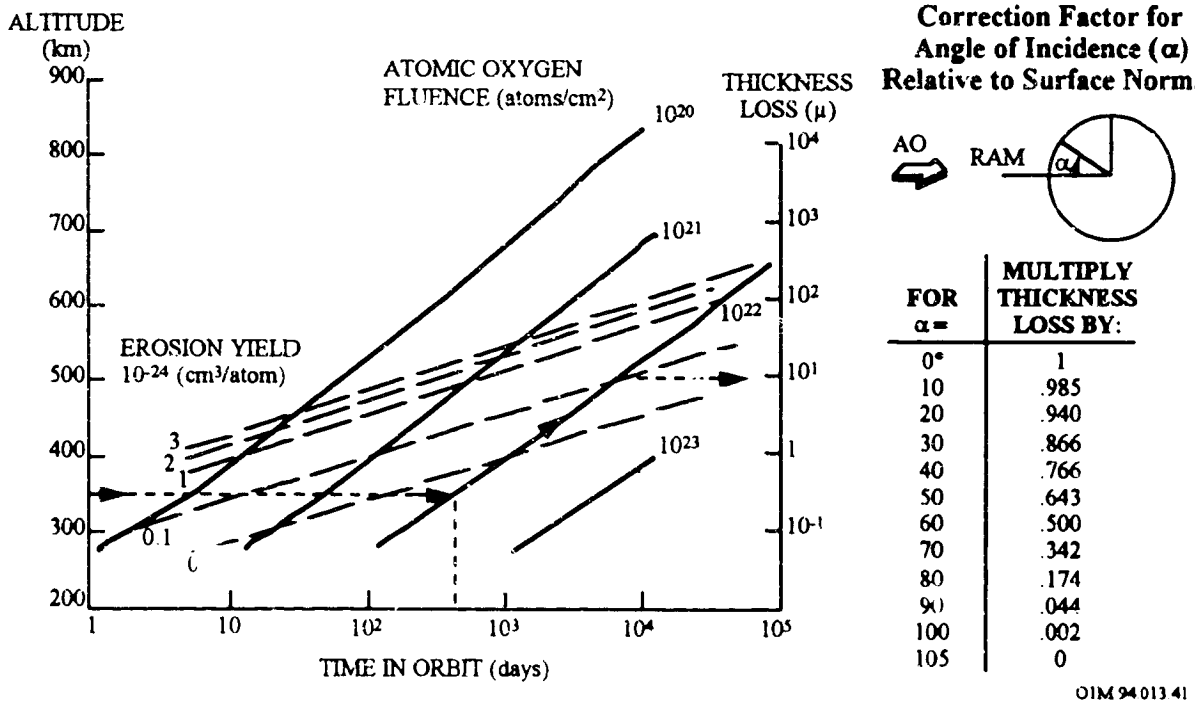

Figure 3-20. Nomogram for Calculating AO Fluence and Material Thickness Loss

° μm = 10^{-6} m = 10^{-4} cm

Fluence, as a function of altitude for various solar activities (10.7 cm solar flux index, $F_{10.7}$; geomagnetic index, A_p) is shown in Figure 3-21.[51] This figure also serves as a nomograph for calculating the amount of surface erosion in microns for a material with $R_e = 3.0 \times 10^{-24}$ cm^3/atom (e.g., Kapton) or for a less reactive material with $R_e = 1.0 \times 10^{-24}$ cm^3/atom (e.g., carbon/epoxy composite). Fluence increases with solar activity. For example, at a nominal altitude of 500 km, the yearly fluence on a ram-exposed surface increases from 4.6×10^{19} to 2.0×10^{21} atoms/cm^2 as solar activity increases from minimal ($F_{10.7}$=70; A_p=0) to maximum ($F_{10.7}$=230; A_p=35).

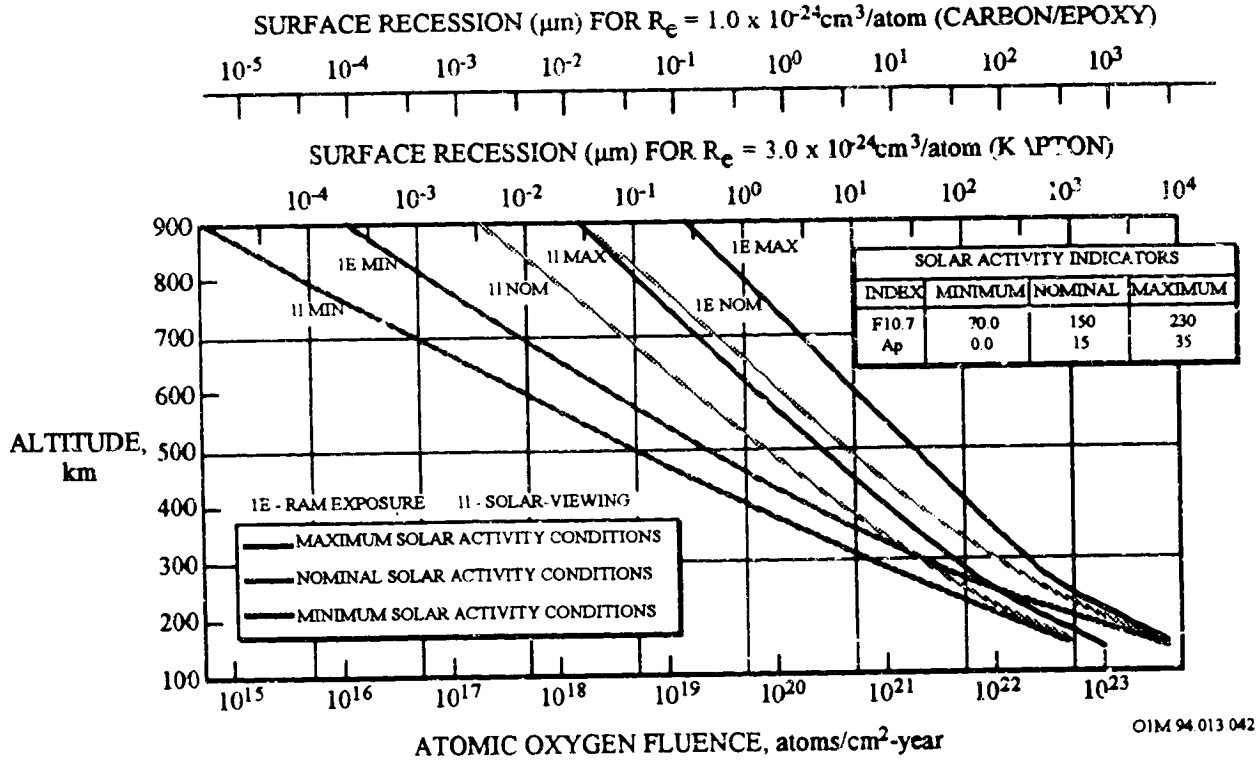

Figure 3-21. AO Fluence Nomograph for Predicting Surface Recession

Example for Determining the Thickness Loss for Carbon/Epoxy. Assume a spacecraft is designed to operate at an altitude of 500 km and is launched into an orbit with an inclination of 28.5°. Also assume the spacecraft is gravity-gradient stabilized, is delivered to orbit during 1990, and has an intended operational lifetime of one year. The amount of surface recession or thickness loss on a ram-oriented carbon/epoxy surface is calculated from the nomograph by first determining the solar activity. From Figure 3-22 (ref. Visentine and Whitaker, 1989), a launch date of 1990 represents maximum solar activity conditions ($F_{10.7}$ = 230).

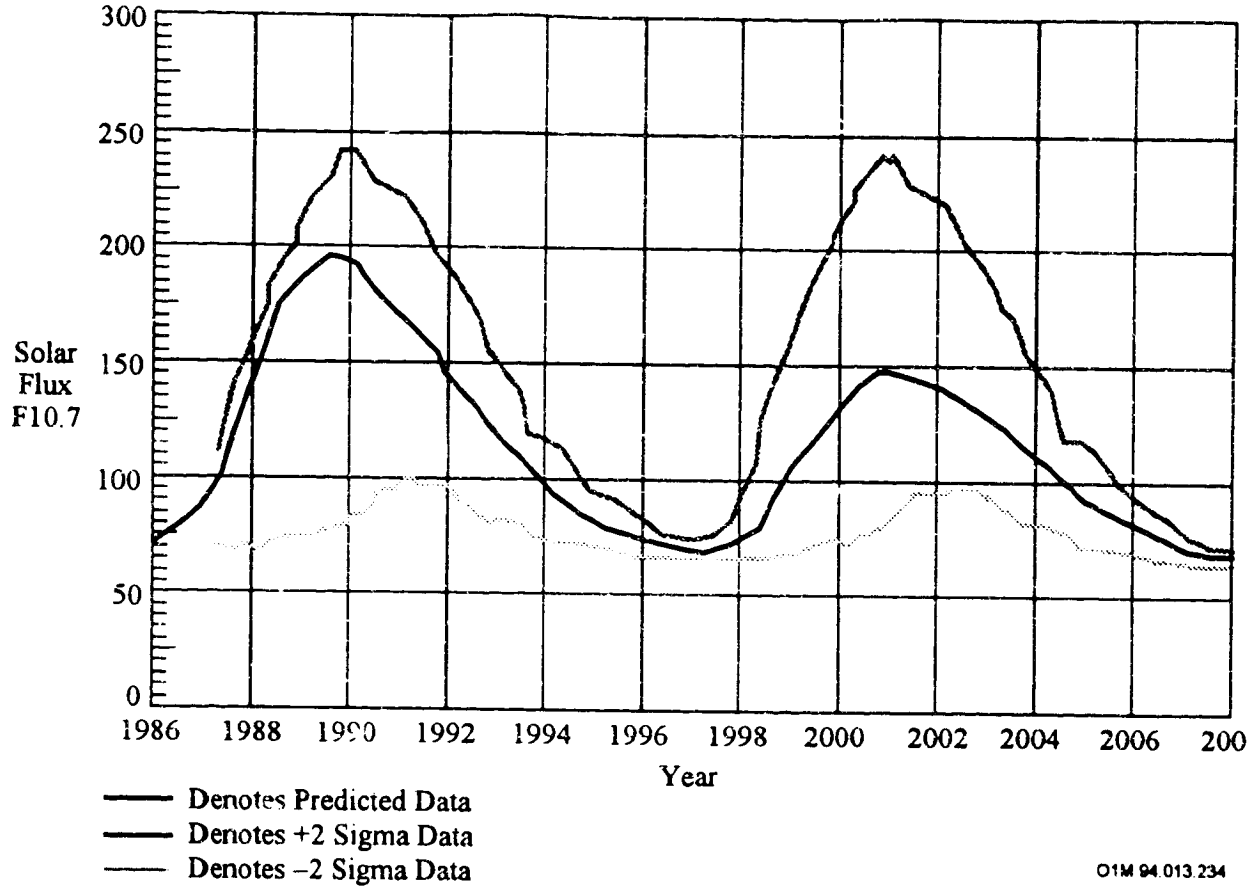

Figure 3-22. Long Range Estimate of 10.7 cm solar flux cycles 22 and 23.

From the nomograph of Figure 3-21, curve "1EMAX" represents ram exposure for these altitude conditions. Reading across the altitude scale of 500 km, the fluence and surface recession are 2×10^{21} atoms/cm^2 year and 20 mm/year, respectively. Alternatively, $\mathbf{F_T \times R_e = \Delta x}$, or 2×10^{21} atoms/cm^2 x 1.0×10^{-24} cm^3/atom = 2.0×10^{-3} cm. Thus, a ram-oriented composite surface with a thickness of .0254 cm (10.0 mil) will lose 20 μm or .79 mil,[P] which is ~8 percent of its thickness during the time the spacecraft is in operation. If the surface in question is solar inertial, such as solar array panel, curve "1IMAX" on the nomograph represents one side exposure for solar inertial surfaces during the time this spacecraft is intended to operate. Under these conditions, the fluence and surface erosion would be 3×10^{20} atoms/cm^2 year and 3 μm/year, respectively. For two-sided exposure, this would represent a thickness loss of 6 μm.

[P] Multiply by 0.03937 to convert to mils: 20 μm = 0.79 mil.

3.6.2 Design of Composite Laminates to Reduce Mechanical Property Loss Due to Atomic Oxygen Exposure

Polymeric composites exposed to atomic oxygen can experienced significant surface recession as observed on the LDEF mission. Composites of carbon fibers with epoxy, polyimide, and polysulfone matrices located on the leading edge of the LDEF satellite (panels that face the direction of atomic oxygen motion) lost up to 0.005 inch (or about one ply of laminate). However, on glass reinforced specimens only the surface resin layer was eroded. More important, material loss due to atomic oxygen erosion can have a deleterious effect on the mechanical properties of composites.

For example, uncoated, leading edge carbon fiber/epoxy samples (e.g., T300/934, T300/5208) suffered a 20 to 65 percent reduction in tensile strength and modulus (see Table 3-46). In contrast, no significant changes in tensile strength or modulus were observed for uncoated composites located on the trailing edge of LDEF; the T300/934 epoxy specimens $[0]_{16}$ did not show any significant loss in tensile properties. Although located on the trailing edge, the C6000 carbon fiber/PMR15 composite suffered a 20 - 30 % drop in the tensile strength (see Table 3-46).

Table 3-46. Loss in the Tensile and Compression Properties of Composites Due to LEO Exposure

Composite	Laminate Design	Ref.	AO Fluence, atoms/cm^2	Tensile		Compressive	
				Strength	Modulus	Strength	Modulus
Epoxy							
- T300/934	$[0]_{16}$	8	1.32×10^{17}	No Effect	No Effect	No Effect	N.A.
- T300/934	$[\pm 45]_{2}$	11	8.99×10^{21}	45%	20%		
- T300/5208	$[\pm 45]_{2}$	8	8.99×10^{21}	65%	33%		
Polyimide							
- C6000/PMR15	$[0/\pm 45/0/\pm 45]_{s}$	8	1.32×10^{17}	20 - 30%	N.A.	No Effect	N.A.
Thermoplastic							
- C3000/P1700 - C6000/P1700	$[\pm 45]_{s}$	8	8.99×10^{21}	15-30%	15-30%		
- T300/P1700	$[0°/90°]_{s}$ Fabric	8	1.32×10^{17}	No Effect	No Effect	No Effect	N.A.

Analysis of the flexural property reduction for composites exposed to the atomic oxygen environment on LDEF provides insights into the importance of the laminate orientation on the extent of the mechanical property degradation. The results for five epoxy composites $[0/45/90/135]_{2s}$ of the LDEF Aerospace Experiment M00003-10 located near the leading edge (atomic oxygen fluence = 7.51×10^{21} atoms/cm^2) indicated a reduction in their mechanical properties (see Table 3-47 and Figures 3-8 and 3-9). The five carbon/epoxy composites all had normalized leading edge strength values that were at least 70% of the original value, which is expected considering that the outer 0° ply was mostly or completely eroded away. In contrast, the trailing edge samples all had strength values similar to their pre-flight values.

A minimum reduction in flexural properties was observed for the composites that had a 45° ply at the outer surface (see Table 3-47). In a flexural test, the loss of a 0° ply from the surface will have a much more pronounced effect on the strength than the loss of a 45° ply. In assessing the effect of atomic oxygen erosion on the strength and modulus of composites, the composite lay-up is an important consideration.

The T300/934 epoxy specimens $[0]_{16}$ did not show any significant loss in flexure properties between the different positions on LDEF and the ground control. As these specimens were unidirectional [0] reinforced, the load that would have been carried by the eroded material on the leading edge exposed specimens was carried by the remaining 0° ply. For these specimens the only mechanical performance loss was due to material loss on the leading edge exposed specimens. Ply orientation plays a significant role in flexure properties behavior when AO erosion is involved.

No significant loss in the flexure properties between the different positions on LDEF (i.e., space exposed and shielded) and the ground control T300 carbon/P1700 polysulfone [0,90] fabric specimens was reported. As with unidirectional, there is continuous reinforcement in the load direction in each ply, i.e., the load that would have been carried by the eroded material on the leading edge exposed specimens was carried by the remaining 0° material. For these specimens the only mechanical performance loss was due to material loss on the leading edge exposed specimens.

Table 3-47. Loss in the Flexural and Shear Strengths of Composites due to LEO Exposure

Composite	Laminate Design	Ref	AO Fluence atoms/cm^2	Flexural		Short Beam Shear Str.
				Strength	Modulus	
Epoxy						
Carbon/Epoxies[1]	$[0/45/90/135]_{2s}$	3	$7.51x10^{21}$	10-30%	10-30%	5 - 10%
Carbon/Epoxies[1]	$[0/45/90/135]_{2s}$	11	$2.31x10^{5}$	No Effect	No Effect	No Effect
- HMF 176/934	$[\pm45]_{4s}$	3	$8.99x10^{21}$	5 - 10%	5 - 10%	5 - 10%
- HMF 176/934	$[\pm45]_{4s}$	3	$1.32x10^{17}$	5 - 10%	5 - 10%	5 - 10%
Carbon/Epoxies[2]	$[45/-45_2/45]_{4T}$	3	$8.99x10^{21}$	5 - 10%	5 - 10%	
Carbon/Epoxies[2]	$[45/-45_2/45]_{4T}$	3	$1.32x10^{17}$	5 - 10%	5 - 10%	
Carbon/Epoxies[2]	$[0]_{16}$	7	$8.99x10^{21}$			5 - 10%
Carbon/Epoxies[2]	$[0]_{16}$	3	$1.32x10^{17}$			5 - 10%
- T300/934	$[0]_{16}$	8	$8.99x10^{21}$	10%	20%	
- T300/934	$[0]_{16}$	7	$1.32x10^{17}$	No Effect	No Effect	
- T300/934	$[0]_{16}$	4	$7.51x10^{21}$	5 - 10%	5 - 10%	
- T300/934	$[0]_{16}$	8	$2.31x10^{5}$	5 - 10%	5 - 10%	
- AS-4/3501-6	$[0]_{16}$	8	$7.51x10^{21}$	5 - 10%	5 - 10%	
- AS-4/3501-6	$[0]_{16}$	8	$2.31x10^{5}$	5 - 10%	5 - 10%	
Bismaleimide						
- V378A	$[0/45/90/135]_{2s}$	11	$7.51x10^{21}$	60%	30%	5-10%
	$[0/45/90/135]_{2s}$	11	$2.31x10^{5}$	No Effect	No Effect	0%
Polyimides						
- PMR-15	$[0/\pm45/0/\pm45]_s$	7	$8.99x10^{21}$	10%	60%	
	$[0/\pm45/0/\pm45]_s$	7	$1.32x10^{17}$	No Effect	40%	
	$[0/\pm45/0/\pm45]_s$	8	$7.51x10^{21}$	25%	25%	
	$[0/\pm45/0/\pm45]_s$	8	$2.31x10^{5}$	No Effect	No Effect	
- LARC-160	$[0]_{16}$	8	$7.51x10^{21}$	5 - 10%	5 - 10%	
	$[0]_{16}$	8	$2.31x10^{5}$	5 - 10%	5 - 10%	
Thermoplastic						
- T300/P1700	[0,90] Fabric	8	$7.51x10^{21}$	5 - 10%	5 - 10%	
	[0,90] Fabric	8	$2.31x10^{5}$	5 - 10%	5 - 10%	
	[0,90] Fabric	7	$8.99x10^{21}$	10%	25%	
	[0,90] Fabric	7	$1.32x10^{17}$	No Effect	5-10%	

[1] GY70/X30, GY70/934, GY70/CE339, P75S/CE339, P75S/934

[2] GY70/CE339, T50/F263, T50/934, T50/X904B

3.6.3 Dimensional Changes Due to Moisture Desorption

3.6.3.1 Laboratory Data on Composites Moisture Desorption

In the space vacuum composites, such as carbon/epoxy, desorbs its absorbed moisture, which can cause large dimensional changes in the composite structures. The loss of this moisture in space is accompanied by a dimensional change as reflected by the coefficient of moisture expansion (CME).[9]

The effects of moisture absorption are well known and have been characterized for some dimensionally stable composite structures.[52,53] Table 3-48 summarizes the percent moisture absorption after exposure, the measured strain, and the calculated CME (β) at saturation for several composite laminates.

Table 3-48. Laboratory Coefficient of Moisture Expansion Results for Composite Laminates

Material	Fiber Direction	Specimen Number	Moisture Content %M	Strain $x10^{-6}$ in./in. ΔL/L	CME $x10^{-6}$ in./in./%M $\beta = \frac{\Delta L/L}{\%M}$	Ref.
T300/934 Epoxy	Isotropic	1	1.13[a]	452	400	54
T300/934 Epoxy	Axial	1	1.22[b]	25	21	55
	Transverse	1	1.28	2435	1902	
P75S/ERL 1962 Epoxy	Isotropic	1	1.03[a]	167	162	51
P75S/RS-3 Polycyanate	Isotropic	1	0.32[a]	34	105	51
IM7/PEEK Thermoplastic	Axial	1	0.11[b]	8	76	55
		2	0.11	8	76	
	Transverse	1	0.12	312	2602	
		2	0.11	320	2913	
		3	0.11	338	3071	

Note: (a) specimens exposed to 100% relative humidity
(b) specimens exposed to 90% relative humidity

[9] CME is defined as a change in length per unit length per weight percent of water absorbed at constant temperature and pressure. Dimensional changes caused by the loss of water in space can be either negative or positive in a multidirectional angle-ply laminate. Prediction of CME in various in-plane and thickness directions requires a knowledge of axial (fiber-direction) and transverse coefficients of moisture expansion for unidirectional laminates. CME values are readily incorporated into finite element and other computer codes of laminate design.

The dimemsional change caused by moisture desorption is strongly influenced by the laminate design. For example, the CMEs of T300/epoxy for an axial, isotropic, and transverse laminate designs are 21, 400, and 1902, respectively. The data are very consistent in terms of both moisture content and strain measurements as shown for the three IM7/PEEK specimens. For example, the final moisture contents of the three transverse specimens at saturation were 0.12, 0.11, and 0.11%, respectively. Similarly, the final strain readings for the three samples were +312, +320, and +338 μ in./in., respectively. Compared to the carbon epoxy data, both the carbon polycyanate and carbon thermoplastic displayed lower equilibrium saturation moisture uptake and lower strain measurements for the different fiber directions. However, the calculated CME values for the carbon/PEEK were higher than for carbon/epoxy, which is attributed to the division of the strain value by a fractional moisture content value.

Hence, the dimensional change caused by moisture desorption is strongly influenced by the matrix selection. Figure 3-21 shows the comparative effect of different laminate matrix resins on strain (ref. Composite Optics, Inc.). The isotropic P75S/954-3 epoxy matrix resin has a significant effect in reducing the composite compared to the isotropic P75S/ERL 1962 epoxy matrix resin.

Recent work on various new hydrophobic resin systems has offered designers an alternative solution to the hygrostrain problem. Modified epoxy resins and cyanate ester resins can reduce the hygrostrain to acceptable levels for dimensionally stable structures. Research work at Lockheed Missiles and Space Company (LMSC)[56] evaluated several modified epoxy resin systems. The results indicated that 3M's PR-500 exhibited a hygrostrain of approximately 45 ppm after one year at 100% RH exposure, while typical epoxies yielded 150 ppm hygrostrain after the same period.

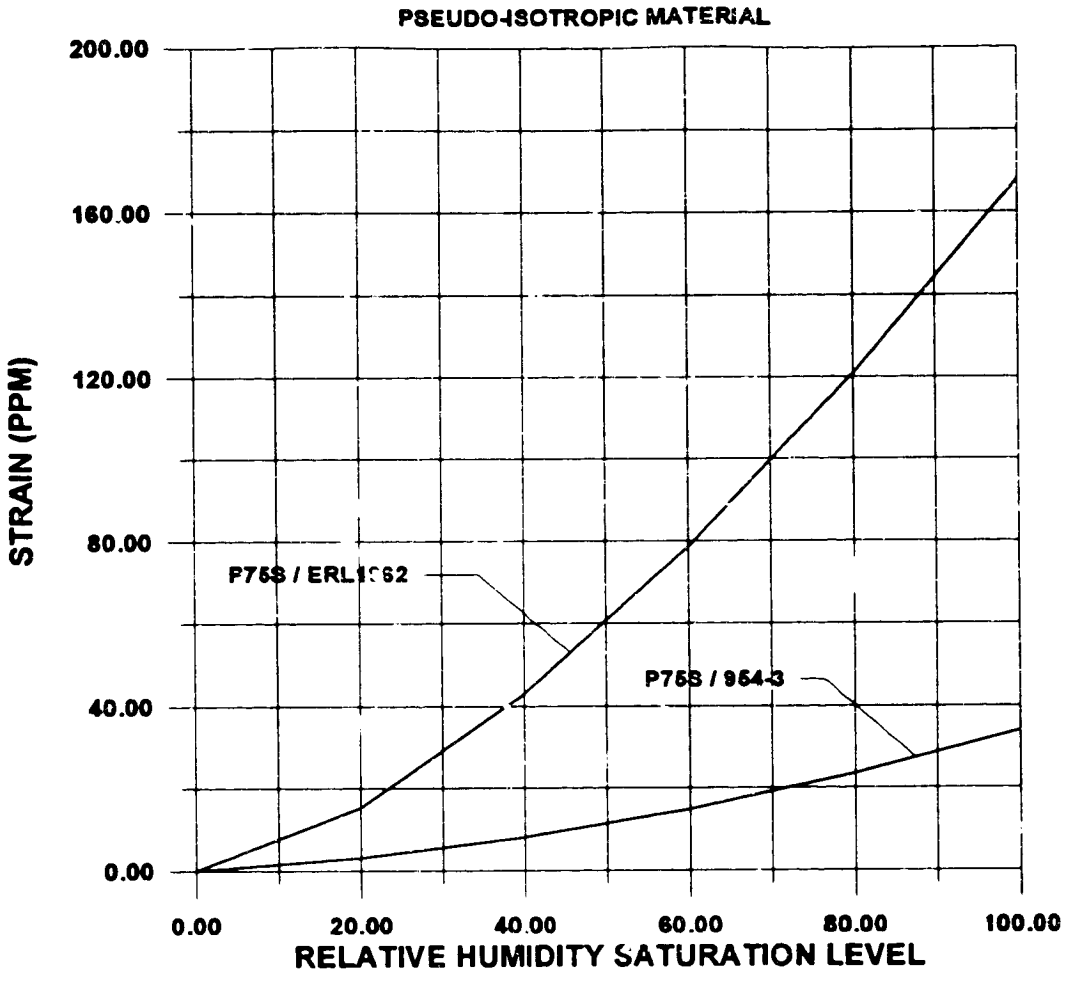

Figure 3-21. Hygrothermal Strain Changes in Pseudo-Isotropic P75S/954-3 and P75S/ERL1962 Composites

3.6.2.2 Flight Experiment Data on Composites Moisture Desorption

The space environment-induced outgassing causes dimensional changes in polymer matrix composites. For example, a 90° carbon/epoxy laminate (T300/5208 epoxy) on the UTIAS/LDEF experiment experienced a total dimensional strain change of 1550×10^{-6} after about 80 days in orbit (ref. 6). Similar behavior was exhibited by other composite materials (ref. 33) as shown in Table 3-49 where outgassing time, t_o, and associated dimensional change, $\Delta\varepsilon$, obtained from strain vs. temperature plots, are tabulated. It took about 40 days for the T300 carbon/934 epoxy and the T300 carbon/SP-288 epoxy to outgas. (Note: The T300/934 dimensional strains in the [90]-direction for the laboratory-derived and flight experiment data are 1200×10^{-6} and 1902×10^{-6}, respectively.) For comparison, a Kevlar/SP-288 epoxy 4-ply/90° laminate took 120 days to outgas.

As expected, very small $\Delta\varepsilon$ changes were observed in the axial fiber direction for the T300 carbon/934 epoxy and T300/SP288 epoxy $[0]_4$ laminates (not reported). Interestingly, a post-flight measurement of the 90° strain at ambient temperature showed a recovery in the dimensional change. This reflects re-absorption of moisture after retrieval of LDEF.

Table 3-49. Outgassing Time and Dimensional Change for Thermoset Composites

Material[1, 2]	Outgassing Time t_o, days	Dimensional change, strain, 10^{-6}				
		Initial			Final Asymptote	
		Laboratory Calibration	First Deployed	$\Delta\varepsilon$	Strain	$\Delta\varepsilon$
Carbon/epoxy T300/934, 4-ply/90°	40	-1360 at -34°C (-30°F)	-1350	10	-2550	-1200
Carbon /epoxy T300/SP-288, 4-ply/90°	40	-1200 at -26°C (-15°F)	-1200	0	-2100	-900
Carbon /epoxy T300/5208, 4-ply/90°	80	-1070 at -23°C (-10°F)	-550	520	-2100	-1550
Aramid/epoxy SP-328, 4-ply/90°	120	-2370 at -18°C (0°F)	-1200	1170	-4000	-2800
Boron/epoxy SP290, 4-ply/±30°	85	-800 at -23°C (-10°F)	-75	725	75	150

[1] Thornel T-300 (Amoco Performance Products Inc., Greenville, S.C.); 934 (Composites Div., Fiberite Corp., Winona, Wis.); Scotchply SP-328, SP-288, and SP-290 (Structural Products Department, 3M Co., St. Paul, Minn.); and 5208 (Narmco Materials, BASF Structural Materials Inc., Anaheim, CA).

[2] It should be noted that an elapsed time of almost two years occurred after manufacturing the samples, prior to their launch. During this time the samples were exposed to ambient conditions and thus had achieved an equilibrium state in terms of moisture absorption. However, they were not in a saturated state and are probably representative of typical composite space structures. A post-flight measurement of the 90° strain at ambient temperature showed a recovery in the dimensional change. This reflects re-absorption of moisture after retrieval of LDEF over a period of ~184 days in storage at ambient conditions.

Thus, it is possible that preconditioning of composites to remove moisture prior to flight could substantially reduce, if not eliminate, dimensional instability of polymer matrix composites in orbit. In general, the outgassing time required to reach an equilibrium state in space depends on such factors as the initial moisture concentrations, the volatile content, laminate thickness, ambient temperature and constituent material diffusion properties.

From a design viewpoint, the dimensional changes for the 0° and 90° laminates can be used to predict the $\Delta\varepsilon$ for an arbitrary laminate configuration. Clearly, the matrix-dominated properties are most affected by outgassing (i.e., see the 90° results) but it is also evident that the angle ply laminate of boron/epoxy (see Table 3-50) underwent a significant $\Delta\varepsilon$ change. Outgassing can lead to dimensional changes of composite laminates in orbit which must be taken into account in the design of composite structures and joints where dimensional tolerances are critical.

Several conclusions can be drawn based on the results of the analyses of the UTIAS/LDEF composite-material samples:

- The carbon epoxy matrix composites outgassed for 40 to 80 days, depending on the material system.
- Outgassing caused significant permanent dimensional changes, which must be factored into the design of low-distortion laminates.

3.6.3.3 Prediction of Dimensional Changes due to Moisture Desorption (Outgassing).

A theoretical model is available that can predict the dimensional changes due to moisture desorption (outgassing) at any temperature once the appropriate diffusion coefficients are known. Using Fick's law, the strain $\varepsilon(t)_{T=constant}$ associated with outgassing can be calculated from the following equation:

$$\varepsilon(t)_{T=const} = \varepsilon_o \exp\left[-7.3\left(\frac{Dt}{h^2}\right)^{0.75}\right] \quad (1)$$

where ε_o = strain at an equilibrium state in space (determined from outgassing tests),
D= diffusion coefficient, and
h = thickness of the composite.

However, to develop a model for predicting the outgassing time of materials over the complete thermal cycling space environment, it is necessary to take temperature into account. It is possible to determine a diffusion coefficient as a function of temperature by performing outgassing tests in a vacuum at different temperatures (T_a and T_b) assuming an Arrhenius relation between D and T. For a given temperature (T) and % relative humidity the strain (ε) for a given material from its dry state as a function of time (t) to saturation is measured. The experiment is repeated at another temperature (T_b). Both experiments employ samples having the same equilibrium moisture saturation (M_o). Using the generated $\varepsilon(T,t)$ curves as shown in Figure 3-22 (ref. 6), the initial slopes determines $D_a(T_a)$ and $D_b(T_b)$ according to equation (2).

$$D(t)_{T=const} = \frac{\pi h^2}{16\varepsilon_o^2}\left[\frac{\varepsilon_2 - \varepsilon_1}{\sqrt{t_2} - \sqrt{t_1}}\right]^2 \quad (2)$$

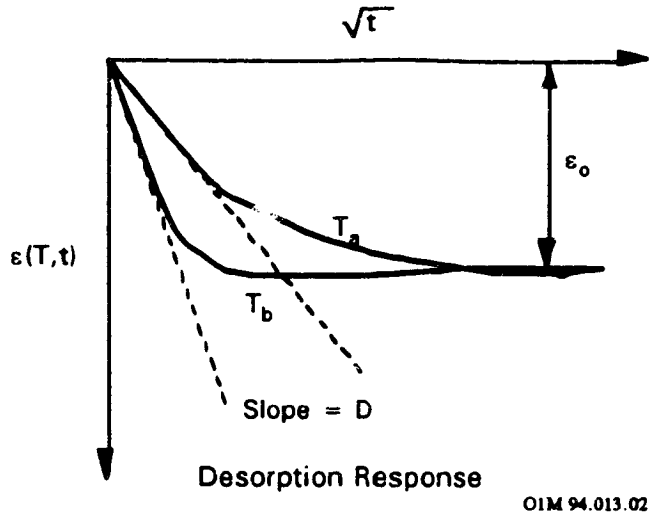

Figure 3-22. Typical Strain Behavior of Materials as a Function of Time and Temperatures

Using the Arrhenius relation where

D = diffusion coefficient = $D_o \exp(-E_d/RT)$
R = gas constant
T = absolute temperature
E_d = activation (diffusion) energy

the following equation is obtained:

$$D(T) = \exp\left[\frac{\ln(D_b) - \ln(D_a)}{1 - \frac{T_a}{T_b}} + \ln(D_a)\right] \cdot \exp\left[\frac{\{\ln(D_b) - \ln(D_a)\}}{\left(\frac{1}{T_a} - \frac{1}{T_b}\right) \cdot T}\right] \quad (3)$$

This equation can be used to calculate the diffusion coefficient at any temperature, T, as long as the diffusion coefficients D_a and D_b at temperatures T_a and T_b are known. (A detailed derivation of the above equations can be found in R.C. Tennyson and R. Matthews, "Thermal-Vacuum Response of Polymer Matrix Composites in Space.")

Hence the strain ε(T,t) associated with outgassing can be calculated for given time intervals (Δt), using D(T) from the above equation evaluated at the appropriate temperature using the temperature/time profile obtained in-orbit. From equation (1), the ε(t) function is given by:

$$\varepsilon(T, t) = \varepsilon_{t-1} - \varepsilon_{t-1}\left(1 - \exp\left[-7.3\left(\frac{D(T_t)\cdot\Delta t}{h^2}\right)^{.75}\right]\right) \quad (4)$$

where T_t = average temperature over Δt, assuming ε_c is known at $t = 0$ from the outgassing test. By using the equation at every time step over the temperature history, it is possible to calculate the strain change of the sample due to outgassing, taking into account temperature effects.

Dividing the total strain by the saturated moisture content yields the coefficient of moisture expansion according to the following equation:

$$\varepsilon = M\beta \quad (5)$$

Example - Prediction of Outgassing Behavior Using Equations (3) and (4)

Using experimental-derived diffusion coefficients together with the LDEF temperature/time profile the predicted dimensional change for a carbon/epoxy 90° laminate (T300/5208) can be compared with the measured LDEF response as a function of time in orbit. A comparison of the β and D results from ground-based simulator tests conducted on two tubes: a control sample (5T5) that had remained under ambient laboratory conditions since the manufacture of the LDEF flight specimens and a LDEF flight sample (2T13) is presented in Table 3-50. The strain response was measured in situ using laser interferometry. Based on the data in Table 3-50, values of D_a = 0.00013 (mm^2/hr) and D_b = 0.00078 (mm^2/hr) were selected, corresponding to temperatures of 22°C and 50°C, respectively. Using these results in equations (3) and (4) together with the temperature/time profile shown in Figure 3-23, the predicted dimensional change for the carbon/epoxy laminate is plotted in Figure 3-24 together with the measured LDEF response as a function of time in orbit (ref. 6).

It is obvious that the predicted values do not fit the actual results very closely. However, if the predicted diffusion coefficient is reduced to 13.4% of its measured value, the predicted response is extremely close to the actual data. This indicates that the model itself is correct. Why is there such a difference in the diffusion coefficients measured in 'space' and in the vacuum chamber? The tests reported show good correlation between 'control' and 'flight' samples. The discrepancies may be due to differences between the test conditions and the space environment, such as a higher pressure or the presence of surface contaminants in the early stages of deployment.

Over time, this contamination was removed from the samples due to atomic oxygen. Hence, when the flight samples were tested in the vacuum chamber, no contamination effects were observed. Thus one can account for the apparent increase in outgassing time observed in orbit. It is also important to note that there is a large variability in the thickness and uniformity of the samples. Manufacturing variations may have caused the different diffusion coefficients of the samples. Ideally, it would be best to measure D(T) from sample 3T6, and see how well this prediction fits the flight data.

Table 3-50. Simulator Moisture Absorption Results for LDEF Flight and Control $[90]_4$ Carbon/Epoxy (T300/5208) Laminates

Sample No.	Type	Temperature °C	M_i %	$\Delta\varepsilon$ $\mu\varepsilon$	CME (β) $\mu\varepsilon/\%$	D mm^2/h
5T5	Control	22	.49	-1200	2449	.0001
5T5	Control	50	.55	-1939	3525	.00047
2T13	Flight	22	.505	-1212	2400	.00013
2T13	Flight	22	.510	-1224	2400	.00008
2T13	Flight	50	.632	-1517	2400	.00078
3T6	Flight	22	.500	-1200	2400	.00014
3T6	Flight	22	.510	-1219	2400	.00009

Note: Before starting the outgassing tests, the samples were completely dried out under vacuum at elevated temperature. The dry weight and length of each sample was measured and recorded. The samples were then placed in a hygroscopic chamber to absorb moisture. Each sample was left until it absorbed the same amount of moisture as was outgassed from the equivalent LDEF sample. This value was determined by measuring the CME (β) of each material and then dividing the strain change measured on-orbit by β to give the total change in moisture content. From CME calculations, it was determined that the flight data from sample 3T6 indicated a total moisture content change of .50%. Therefore, for all the tests on the T300/5208 $[90]_4$ samples, a moisture content as close as possible to this value was used, as summarized in Table 3-50. On average, the 22°C and 50°C tests took about 13 days and 6 days to complete, respectively. Note that the laboratory-derived diffusion coefficients of the control and flight samples agree quite well, indicating no significant changes occurred after 69 months of space exposure.

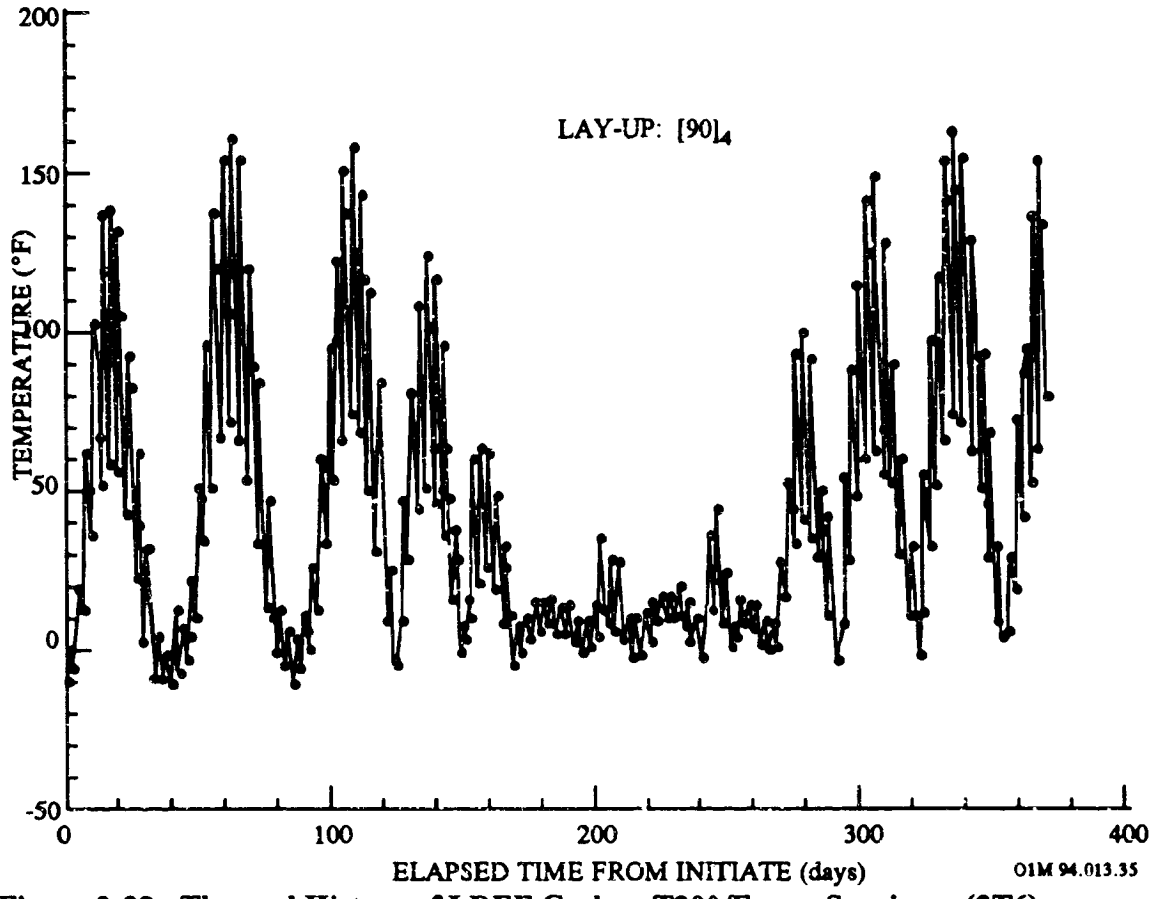

Figure 3-23. Thermal History of LDEF Carbon T300/Epoxy Specimen (3T6)

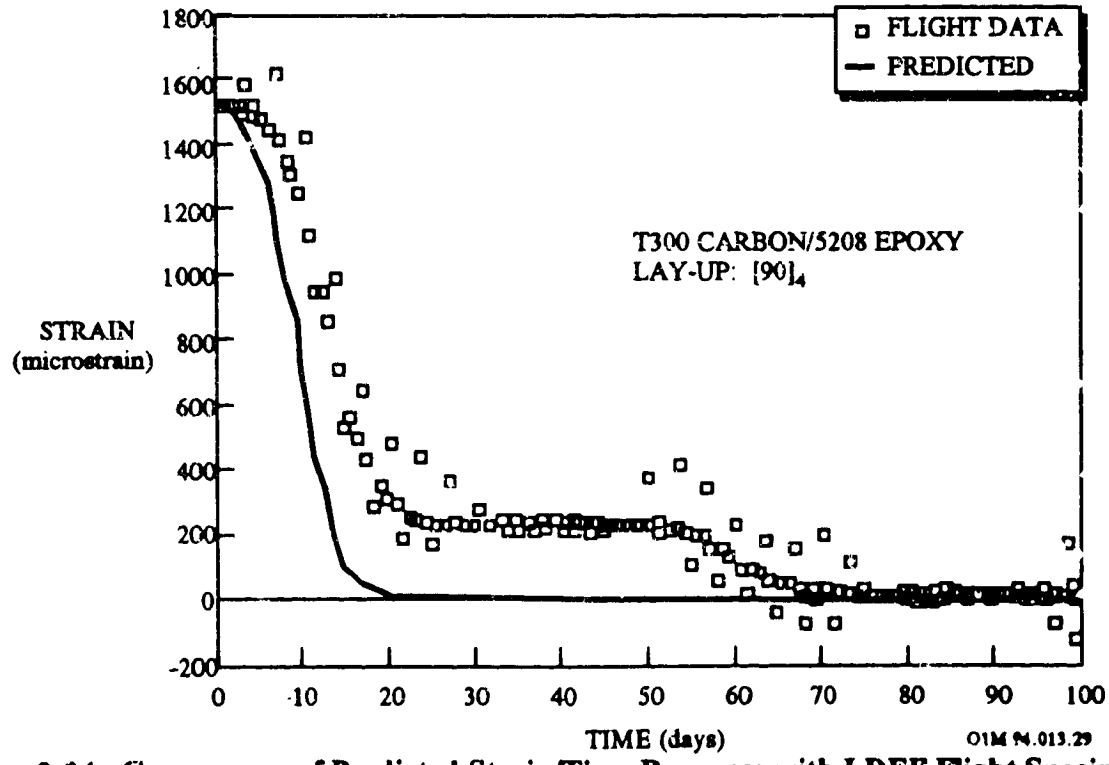

Figure 3-24. Comparison of Predicted Strain/Time Response with LDEF Flight Specimen

3.6.4 Dimensional Changes Due to Temperature Extremes

The coefficient of thermal expansion (CTE) within a laminate can also vary due to exposure to the temperature extremes and hence, be a source of dimensional instability. Since the through-the-thickness expansion of a laminate approaches the magnitude of the matrix resin (25 to 40 $x10^{-6}$ in./in.-°C which is up to 1000 times the expansion effect of the in-plane expansion of the laminate (i.e., 0.04 x 10^{-6} in./in.-°C), severe distortions can result if the design does not compesate for this effect.

Exposures to the space environment were observed not to have a substantial degradation to the pre-launch CTE values. Table 3-51 compares the CTE data from composite specimens on LDEF Experiment AO180. A comparison of the CTE values measured in space (after 371 days) with those measured at atmospheric pressure prior to launch showed reasonable agreement (ref. 6).

Table 3-51. Comparison of CTE Data From LDEF Experiment AO180

Material	Laminate Type	Ambient CTE 10^{-6}/°C	Space CTE 10^{-6}/°C
T300/5208 Epoxy	$[90]_4$	28.1	28.9
T300/934 Epoxy	$[90]_4$	26.5	27.3
T300/SP-28 Epoxy	$[90]_4$	26.3	26.8
Boron/SP-290 Epoxy	$[\pm 30]_s$	2.8	2.21
Boron/SP-290 Epoxy	$[\pm 60]_s$	21.1	20.9
Kevlar/SP-328 Epoxy	$[90]_4$	61.0	59.2
Kevlar/SP-328 Epoxy	$[0]_4$	0.18	0.83

3.6.5 Design of Low Distortion Composite Laminates

The effects of moisture desorption on the dimensional stability of composite structures can be many times greater than the effect of a wide temperature change. For example, a thermally stable structure 100 inches long with a CTE of 0.04×10^{-6} in./in.-°C (0.02×10^{-6} in./in.-°F) will distort 0.0002 inch when exposed to a temperature change of 56°C (100°F). This same structure with a measured strain of 80×10^{-6} in/in. will distort 0.008 inch after 40 days. Hence the distortion due to moisture desorption is 40 times higher than the distortion associated with the maximum temperature change. This situation is representative of the Mars Observer Camera (ref. 53). The camera's sensitivity to moisture is such that in less than an hour it can exceed focus requirements at 50% RH, whereas temperature variation of over a 56°C (100°F) presents no dimensional or focus problem.

The design of low distortion laminates can be achieved by combining laminate analysis of composite materials with diffusion data. For the case of a $(\pm\theta)_s$ structure, the question being addressed is how much axial distortion can occur in a zero CTE laminate. Figure 3-25 presents the variation in the α_x and α_y CTE values for a $(\pm\theta)_s$ laminate fabricated from T300/5208 material. The curves shown were determined from classical laminate theory. The case of $\alpha_x = 0$ occurs when $\theta = 46°$. Using diffusion data to calculate the CME values of β_x and β_y from classical laminate theory, one can obtain from Figure 3-26 a $\beta_x \sim 200 \times 10^{-6}$/%M at $\theta = 46°$. Assuming a 1% moisture uptake prior to launch yields an axial displacement of $\Delta L = 200 \times 10^{-6}$ L where L = length of structure. Thus for a 10 m long structure, the axial contraction would be 2.0 mm for a zero CTE laminate.[57]

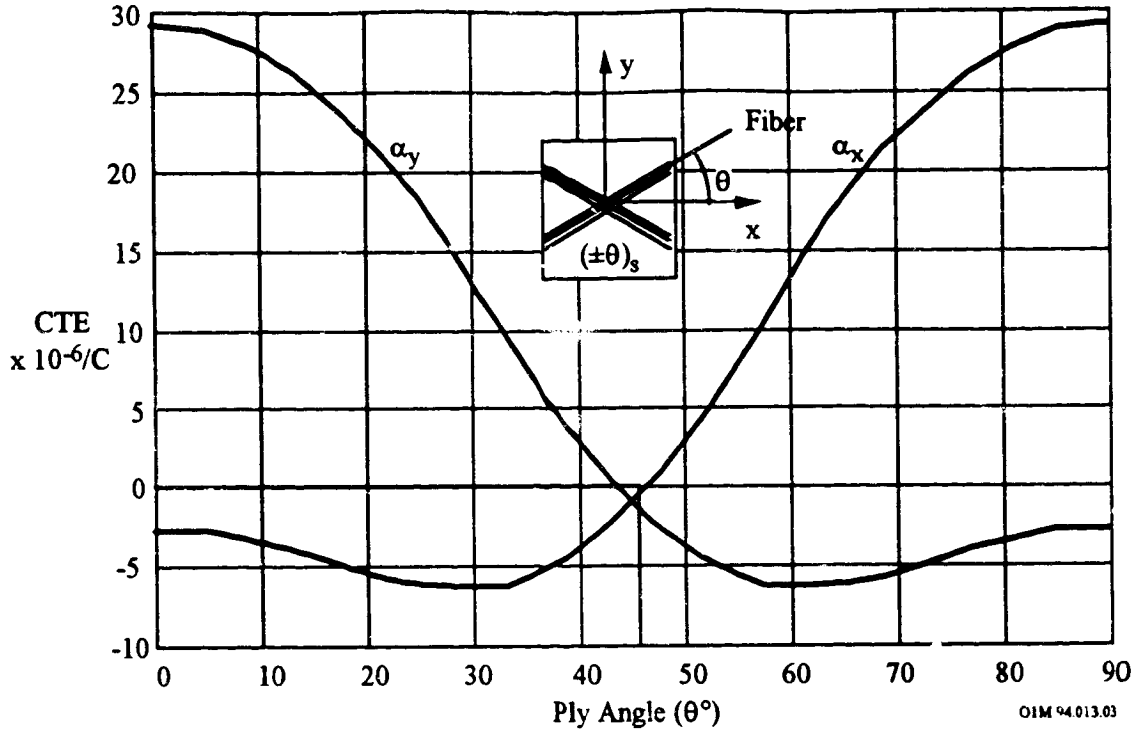

Figure 3-25. CTE for Angle-Ply Laminates (T300/5208 Carbon/Epoxy)

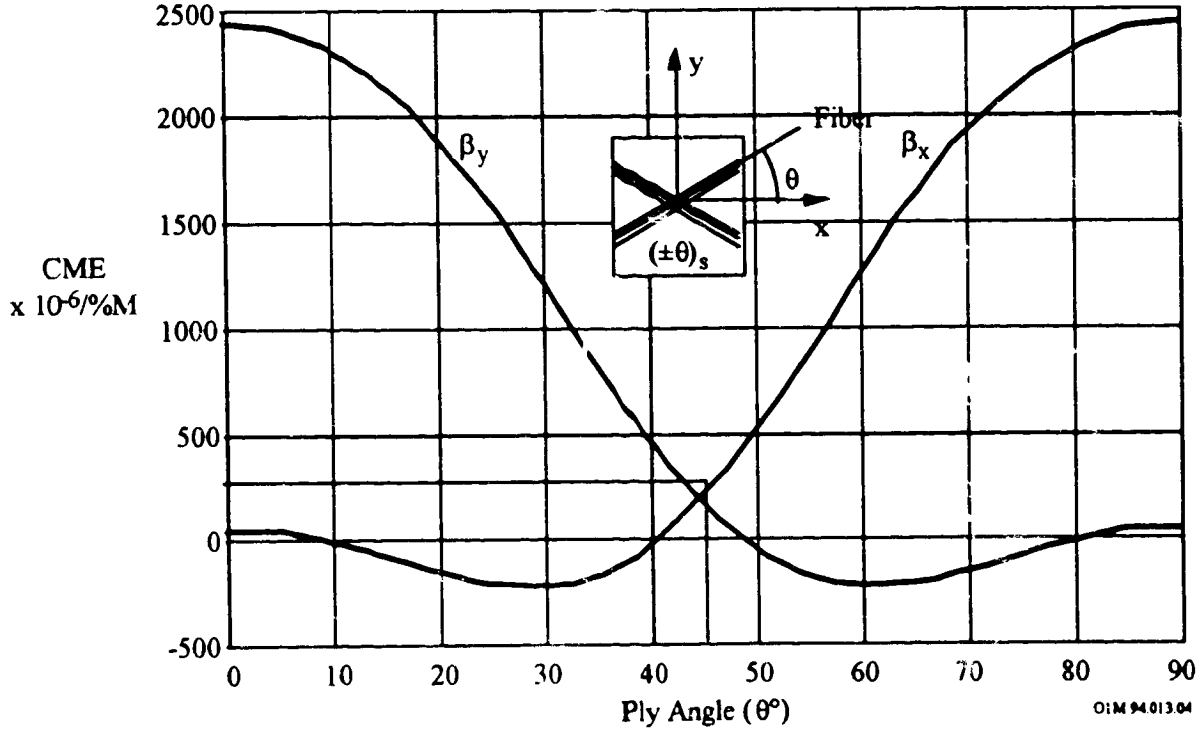

Figure 3-26. CME for Angle-Ply Laminates (T300/5208 Carbon/Epoxy)

The tailoring of the composite laminate to reduce CME effects has some limitation because of the overall requirements of a component, e.g., axial stiffness or CTE may not meet requirements when designing for a low CME. For example, the effects of compressive strength and modulus, CTE and CME with varying ply angle theta (θ) are shown in Figures 3-27 and 3-28 for the [0,$\pm$ θ,0] composite lay-up being considered for a satellite optical bench application. An optical bench requires maximum stiffness with minimum CTE and CME. Using high-modulus carbon fibers, such as P75, will meet the 20 Msi stiffness requirement. The relatively large negative CTE of carbon fibers requires the addition of off-angle plies greater than 70° to raise the CTE towards the $\pm 0.2 \times 10^{-6}$ in/in-°F requirement. However, these large ply angles tend to increase the CME. A successful approach is to use a lower modulus, higher CTE carbon fiber, such as PAN50, for the angle plies and P75 for the unidirectional plies. Following this approach, a lay-up consisting of $[0_{[1]}, \pm 60_{[1]}, 0_{[2]}]$ where [1] is 2 mil PAN50 and [2] is 2.5 mil P75, results in a CTE of 0.17×10^{-6} in/in-°F and a CME 90 of 84×10^{-6} in/in-%moisture (see Figure 3-28). The disadvantage is that the use of the lower modulus PAN50 carbon fiber reduces axial stiffness and strength by 16% and 10%, respectively.[53]

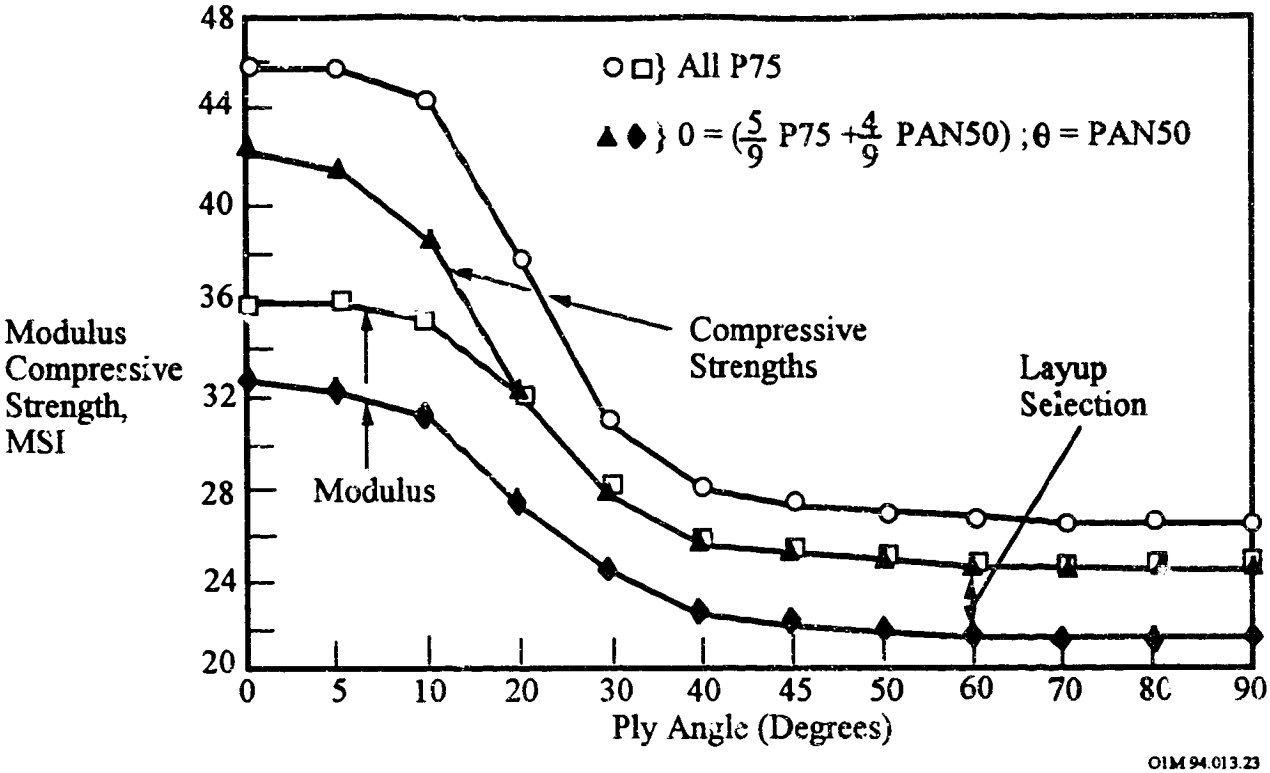

Figure 3-27. Variation of Compressive Properties with Ply Angle θ for a [0,±θ,0] Lay-up.

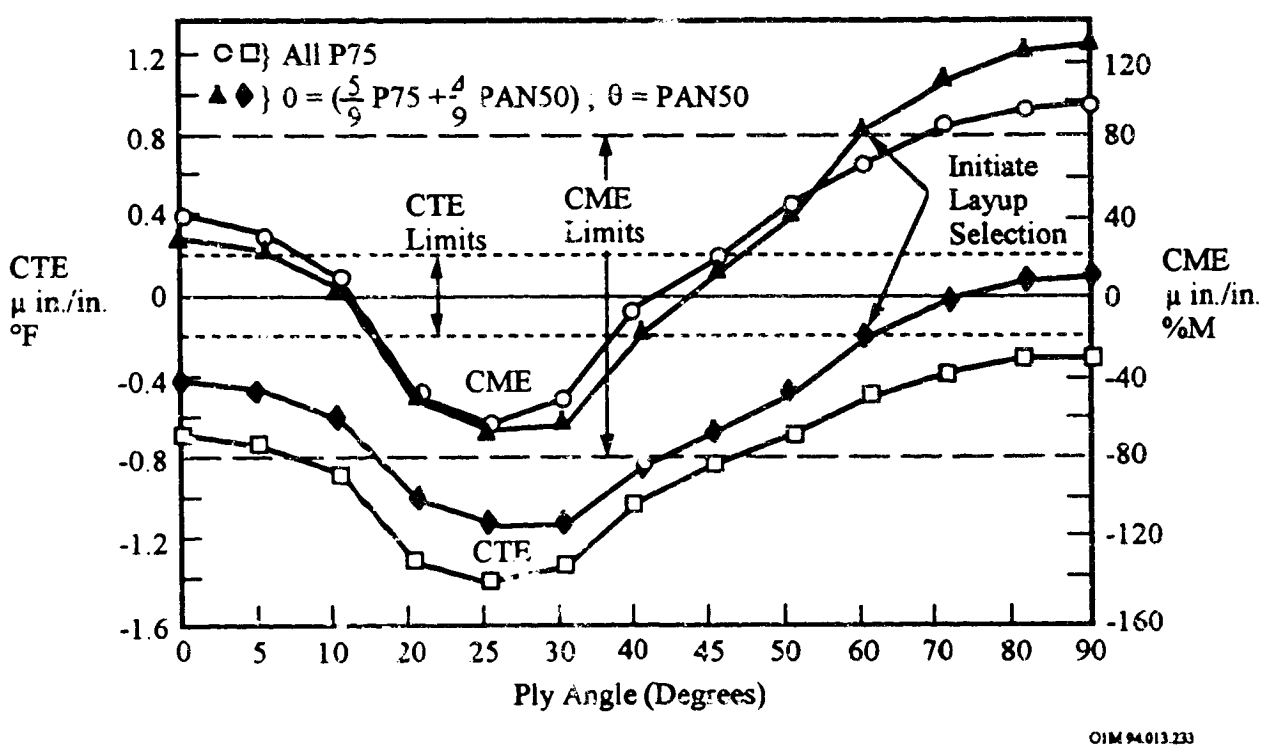

Figure 3-28. Lower Modulus Angle Ply Carbon Fibers (PAN50) for CME and CTE Requirements

3.6.6 Design of Composite Laminates to Reduce Microcracking

Exposure of composite structures to the repeated thermal cycling space can cause microcracking in composites. A complicating feature of the HEO and GEO space environment with their higher particle radiation dose is the synergistic effect of combined electron radiation and thermal fatigue, which may cause dramatic changes in the performance of composite systems. Data from NASA Langley[59,60,61] showed that most composite systems exposed to sequential electron radiation and thermal fatigue are highly susceptible to microcracking damage due to embrittlement of the matrix material.

Microcracking of a composite causes the following dimensional stability problems:

- Hysteresis effect in the structure
- CTE changes, e.g., CTE becomes more negative with increasing thermal cycling
- Increases in the moisture response rates

Microcracking is occasionally employed to achieve a desired CTE. The Hubble Telescope Metering Structure was subjected to microcracking in order to "tune" the various struts to achieve a desired CTE.[62]

Thermal cycling induced microcracking is attributed to the difference in the coefficient of thermal expansion (CTE) of each individual ply parallel and normal to the fiber direction. The CTE normal to the fibers is about half that of the resin's CTE whereas the CTE parallel to the reinforcement is virtually zero and sometimes slightly negative. Hence, in any crossplied lay-up this difference in thermal expansion induces internal stresses. During repeated thermal cycling each ply within a crossplied laminate will be subjected to thermal fatigue, which may result in the generation of cracks parallel to the fibers as well as through the thickness of each lamina.

The degree of thermal cracking due to this mechanism has been reviewed by Tenney et al.[63] where the effects of thermal cycling between -156°C and 94°C were studied in Pitch and PAN carbon-fiber reinforced epoxies. In each of the samples examined the microcracks density did not reach equilibrium after 500 cycles. Approximately 10 microcracks/cm were observed with P75S-reinforced epoxy. However, less than 1 microcrack/cm was developed with the same matrix material containing the less stiff T300 fibers, reflecting lower internal stress levels. Hence, the fiber modulus is very important in determining the degree of microcracking. With a polyacrylonitrile (PAN) based 62 Msi (430-GPa) modulus carbon fiber, extensive microcracking was obtained, while with a PAN-based 40 Msi (280-GPa) modulus fiber no cracking was seen under more severe testing conditions. Composites using the higher modulus fibers such as P75S will microcrack more readily than composites using AS-4/T300 type carbon fiber (ref. 63).

In addition to the fiber, the resin and its cure temperature will influence the extent of the microcracking that occurs. In a study by NASA Langley[64] differences in the crack density induced in three tubes of different materials were observed with increasing number of thermal cycles between -156°C and 94°C, as shown in Figure 3-29. The P75S/934 is a high modulus brittle epoxy system, the P75S/CE339 is a high modulus toughened epoxy system, and the T300/934 is a low modulus brittle epoxy system. The crack densities for each material asymptotically approach equilibrium values as the number of cycles increases. The effects of the thermal cycling or microcracking on the torsional stiffness of these tubes are also shown in Figure 3-29. The torsional stiffness of tubes of each of the three materials was reduced by about 40% and the change in the stiffness appeared independent of the composite material system. These data illustrate the sensitivity of matrix dominated properties to microcracking.

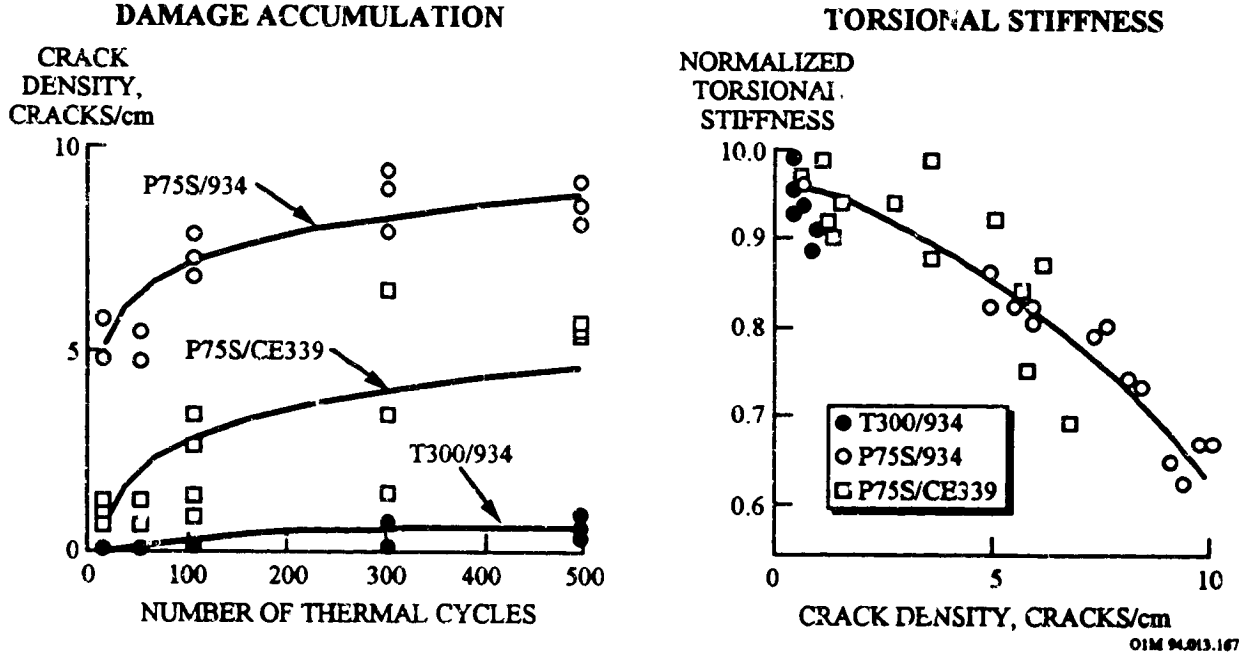

Figure 3-29. Effects of Thermal Cycling on Composite Tubes

Tough epoxy resins have been developed over the past 10 years, including Hercules 8551-7 and Fiberite 977-2. These resin systems both have excellent residual strength after impact and are very resistant to microcracking. The ERL 1962 toughened epoxy was formulated for space applications by Amoco to minimize microcracks induced by thermal cycling.

The 930 epoxy was formulated by Fiberite ICI for space applications to minimize microdamage by having a low cure temperature to reduce the residual thermal stresses that are induced during the composite fabrication. The 934 resin is a space qualified standard epoxy that has been successfully cured at both 121°C (250°F) and 177°C (350°F). Analytical studies have shown that residual stress is a strong function of the product of the matrix modulus, matrix CTE and the difference between the stress-free temperature (usually near the cure temperature) and the use temperature.[65]

Thermoplastics are inherently tough composite matrix resin systems. The PEEK resin is a thermoplastic polymer which, when reinforced by low modulus, high strength carbon fiber, shows good resistance to thermal cycling after radiation. In a comparative study of material performance between carbon-fiber reinforced PEEK and epoxy composite systems (ref. 60), after 500 thermal cycles between -156°C and 120°C the PEEK-based composite developed 1 microcrack/cm while the baseline epoxy developed 8 microcracks/cm. However, the PEEK thermoplastic exhibit excellent microcracking resistant, but only with high strength carbon fibers (e.g., AS4/PEEK) (ref. 61).

In a study of candidate panel facesheet composite materials for a space reflector, microcrack density data were measured for quasi-isotropic laminates as-fabricated and after exposure to electron and thermal cycling simulating CLEO and HEO.[66] The environmental parameters and the testing results are summarized in Tables 3-52 and 3-53, respectively.

Table 3-52. Predicted Mission Environmental Parameters

Space Parameters	Circular Low Earth Orbit (CLEO)	Highly Elliptical Orbit (HEO)
Estimated life time electron radiation dose, Mrads	10	1000
Thermal cycle, °F	-100° ±36°	-226° ±36°
Lifetime, years	>10	>10
Orbit, nautical miles	378 28.5°	540 x 37,800 28.5°

Table 3-53. Durability of Candidate Materials in Simulated CLEO and HEO Environments

Material System	Vf %	Lay-up	Cracks per inch				
			As-Fabricated	±150°F 25 cycles	CLEO 100 cycles		HEO 100 Cycles
					10 Mrads	1000 Mrads	1000 Mrads
C6000/ F155	56.7	A	0	0	E		
UHM/ F584	54.8	B	0 0	8 14	12	17	C C
T50/ ERL 1962	67.6 62.5	B A	0 0	0	0	0	0
P75/ERL 1939-3	66.9	B	5	64		64	C
P75/ PEEK	63.8	A	50	52		58	C
P75/934 250°F 350°F	 55.9 54.7	 B B	 0 81	 38 85	41	58	 C C
P75/930	51.3 57.2	B B	0 0	0 0	0	8	C C
T50/934 250°F	60.1	B	0	0			6

A- lay-up [0,90,45,-45]$_s$
B- lay-up [0,45,90,-45]$_s$
C- Testing stopped due to excessive damage
D - Testing stopped due to poor quality material
E- Testing stopped due to properties outside requirements.

With the exception of P75/ERL 1939-3, P75/PEEK, and the 350°F cured P75/934, the laminates were free of microdamage in the as-fabricated state. The P75/ERL 1939-3, P75/PEEK, and P75/934 contained about 5, 50, and 81 cracks per inch, respectively, in the as-fabricated state. The damage in each of these laminates was attributed to thermal stresses induced during cool down from the fabrication temperatures. Note that when the P75/934 laminate was cured at 250°F, no cracks were seen, indicating that the lower cure temperature sufficiently reduced the stresses to avoid microdamage on cool down during fabrication.

After 25 cycles between -150°F and 150°F, the P75/ERL 1939-3, 350°F cured P75/934, and P75/PEEK continued to microcrack, with the P75/ERL 1939-3 reaching a crack density of about 64 per inch. These cycles also induced microcracks in the UHM/F584 (8-14 per inch) and the 250°F cured P75/934 (38 per inch). The remaining four laminates (C6000/F155, T50/ERL

1962, P75/930, and T50/934) did not microcrack. Two materials, the 350°F cured P75/934 and C6000/F155, were not carried any farther in the test matrix because of excessive microdamage, poor quality (excessive voids).

Five of the remaining six materials were subjected to the simulated CLEO thermal cycling environment with electron radiation does of both 10 Mrads and 1000 Mrads. (The 250°F cured T50/934 was subjected only to the more severe HEO simulation.) Of these five materials, only the T50/ERL 1962 remained damage free. The other four materials continued to microcrack as a result of continued thermal fatigue and/or matrix embrittlement due to electron radiation.

The only two materials subjected to the simulated HEO environment were the T50/ERL 1962 and the 250°F cured T50/934. No damage was induced in the T50/ERL 1962 laminate during the HEO simulation. The T50/934 did exhibit some slight microdamage with a microcrack density of about 6 per inch. The T50/ERL 1962 composite did not degrade in either environment.

Polycyanate matrix composites reinforced with carbon fibers offer lower moisture absorption and enhanced microcracking resistant compared to carbon/epoxy composites. Commercially available 350°F cured polycyanate resins include YLA's RS-3 and Fiberite's 954-3. Amoco's ERL 1939-3 is a relatively new cyanate and epoxy blend designed for space applications. Both the toughness of the polycyanates and their low shrinkage during cure result in a more stable matrix during thermal cycling as shown in Figure 3-30. Using similar P75 laminate constructions and thermal cycling conditions, the data indicated that the number of microcracks/inch converged after 1000 cycles, with the RS-3 polycyanate composite displaying the best performance.[67]

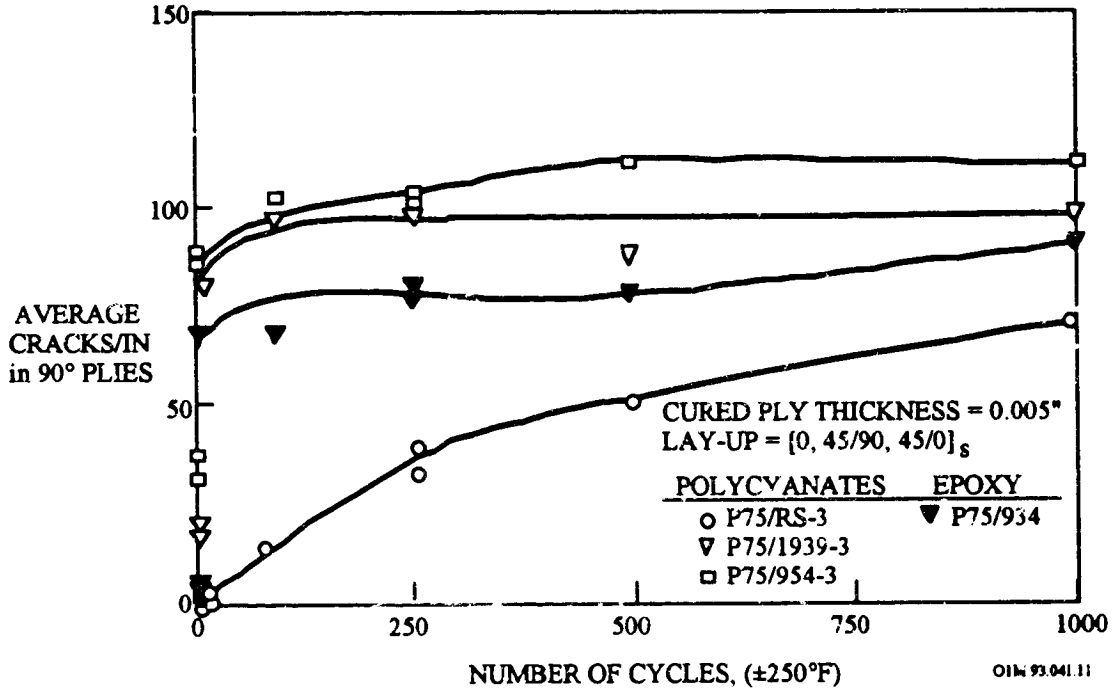

Figure 3-30. Comparative Microcracking Behavior for Thermoset Composites

The influence of ply lay-up on the extent of microcracking was reported by Wolff[68] for carbon composite tubes. Predicted values for the onset temperature (T_N) of microcracking on the first thermal cycle as a function of the laminate ply angle are shown in Figure 3-31. At low ply angles no microcracking was predicted.

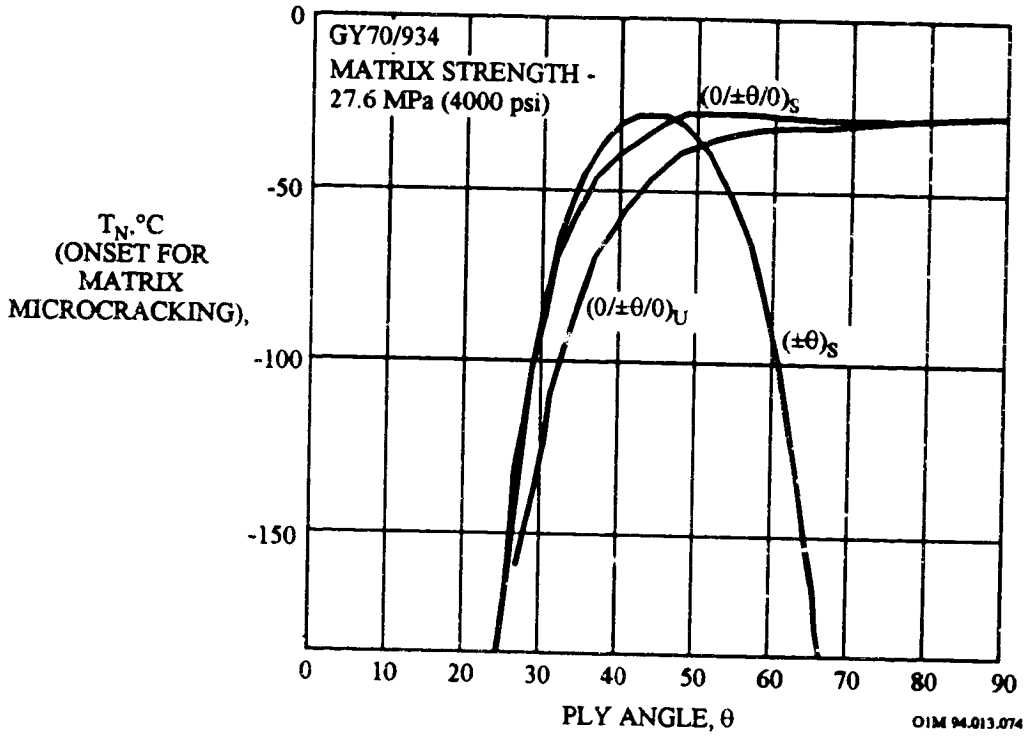

Figure 3-31. Variation of the Temperature for the Onset of Microcracking with Ply Angle

Table 3-54 shows three values of T_N for each of several ply lay-ups. The first corresponds to a flat laminate without edge effects, the second or a circular tube infinite in length, and the third for the stress field near the ends of a circular tube. A flat plate with a 90/0/±45 layup would warp on cooldown but a tube is constrained to a circular cross section so that end distortion occurs.

Table 3-54. Predicted Matrix Cracking on First Cooldown of Carbon Composites

Material	Lay-up	Onset Temperature (°C) for Microcracking		
		Laminate	Tube	Tube Ends
GY70/934	$[\pm 30]_s$	-94	-94	-94
GY70/934	$[\pm 45]_s$	-25	-25	-25
GY70/934	[0/±60/0]	-28	-24	-24
GY70/934	$[0/45/90/135]_{2s}$	-53	-37	-37
HMS/3501-6	[90/±45/0]	-44	-25	-11
HMS/3501-6	[0/±45/90]	-44	-25	-16

3.6.7 Contamination from Composites Outgassing

When exposed to thermal-vacuum conditions, polymer matrix composites are known to outgas due to moisture desorption or material volatilization or decomposition. Once the outgassed species leave the surfaces, they will be at such a low pressure that they travel in a line-of-sight trajectory until they either hit spacecraft surface (where they will bounce or adhere) or leave the vicinity of the spacecraft at a velocity of several kilometers/second. Approximately 1 in 10,000 to 1 in 100,000 molecules will collide with another molecule (ambient or contaminant) and return to the spacecraft where they might hit a sensitive surface. A portion of the contaminants that contact spacecraft surfaces will stick forming a molecular layer that can darken or be eroded with subsequent exposure to the space environment.

Molecular contamination can degrade the performance of thermal control surfaces and solar cells. This can be particularly important if sensors are cooled passively by second surfaces mirrors that are illuminated by the Sun. The effects of relatively thin molecular films on the solar absorptance of second surface mirrors has been shown in Figure 2-17. Typically molecular films must not exceed 1000 Å on these sensitive surfaces at the end of the spacecraft's life. In addition, thin deposits of molecular contaminants that condense on the cold optical surfaces and infrared sensors can seriously reduce optical throughput. Furthermore, molecular contamination from composite materials can lead to the formation of a "cloud" of outgassed molecular particles, resulting in a significant increase in light scattering that attenuates the signals that the sensors are receiving. Molecular films as thin as a few hundred angstroms can seriously reduce the sensor performance, especially when viewing targets close to bright sources of light such as the Sun.

The outgassing/volatiles characterization of composites is determined by the procedures of the ASTM Test for Total Mass Loss and Collected Volatile Condensable Materials from Outgassing in a Vacuum Environment (E 595). This industry standard material contamination screening procedure is based on measuring the total mass loss (TML), collected volatile condensable material (CVCM), and water vapor regained (WVR). TML is important from a molecular "cloud" effect which can degrade instrument performance, while CVCM is a measure of the potential for outgassed products to deposit on critical optical surfaces. WVR is the mass of the water vapor regained by the specimen after an optional reconditioning step. WVR is calculated from the differences in the specimen mass determined after the test for TML and CVCM and again after exposure to a 50% RH atmosphere at 23°C for 24 hours. Values below 1.0% TML and 0.1% CVCM have been acceptable for current spacecraft performance needs, but the requirements are expected to become more stringent for future surveillance spacecraft systems (see below).

Figure 3-32 shows typical ASTM E595 outgassing test results for a variety of carbon reinforced polymer matrix composite system.[69] Table 3-55 presents outgassing test results for a variety of spacecraft composite materials. A comparison of the outgassing results points to significantly lower outgassing TML values for polycyanates and thermoplastics composites compared to the conventional epoxy composites.

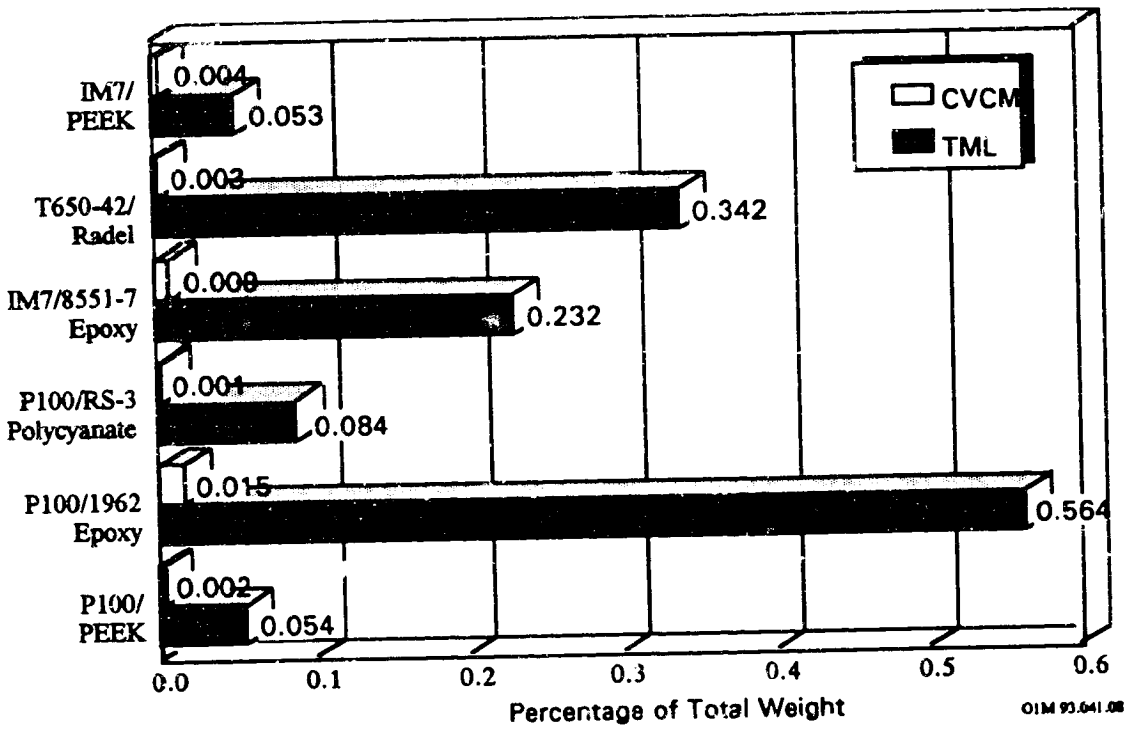

Figure 3-32. Comparative Outgassing of Polymer Matrix Composites

Table 3-55. Outgassing Properties of Laminated Composites

Material	Matrix Type	TML %	VCM %	WVR%	Ref.
T300/934	Epoxy	0.58	.00	.00	NASA JSC[70]
PAN50/954-3	Epoxy	0.135	0.00549	0.195	TRW[69]
T50/934	Epoxy	0.4	0.09	.00	NASA JSC
HMS/934	Epoxy	1.09	0.00	0.51	NASA JSC
GY70/954-3	Epoxy	0.104	0.00792	0.0756	TRW
P75/930	Epoxy	0.384	0.007		TRW
XN50/RS-3	Polycyanate	0.0851	0.00379	0.0287	TRW
IM7/PEEK	Thermoplastic	0.053	0.004		TRW

Although typical carbon/epoxy structures meet the current NASA outgassing acceptance levels of 1.0% TML and 0.1% CVCM, certain spacecraft systems and sensors that operate at extremely cold temperatures are sensitive to much lower outgassing acceptance levels. The development of spacecraft systems (e.g., FEWS, Brilliant Pebbles, Brilliant Eyes, CERES, AXAF) with sensors, astronomical telescopes, and spectrographs operating at extremely cold temperatures (i.e.,<100 K) have imposed lower contamination levels requirements for spacecraft structures and hence, the need for spacecraft materials with reduced outgassing at these lower temperatures. In addition, the current industry outgassing measurement test, ASTM E 595, is conducted at test conditions that do not simulate the stringent space environment and hence, does not adequately characterize the contamination potential of composite materials.

The TRW Contamination Effects Facility, which derives a molecular outgassing rate from the mass accumulation on a temperature controlled quartz crystal microbalance below 150 K, have demonstrated marked improvements in reduced outgassing from polycyanates and thermoplastics. Table 3-56 reveals lower outgassing rates for both the IM7/PEEK and the XN50/RS-3 polycyanate composites by an order of magnitude in comparison with the outgassing rate measured for the P75/ERL-1962 epoxy composite (ref. 69). Water represented most of the condensable material from both the carbon PEEK and the polycyanate composites as verified by mass spectrometry analysis (water has a condensation temperature of 150 K under vacuum).

Table 3-56. Outgassing Rates for Structural Materials

Material	Outgassing Rate, 100 K
P75 Carbon/ERL-1962 Epoxy	1.60 ng/cm^2-s
XN50 Carbon/RS-3 Polycyanate	0.24 ng/cm^2-s
IM7 Carbon/PEEK Thermoplastic	0.17 ng/cm^2-s

A series of in-situ bakeouts were conducted to determine the change in the outgassing rates with time and to determine the total time to eliminate outgassing from the polymer matrix composites. Figure 3-33 shows the linear decay in the outgassing rates for both the PEEK and the polycyanate composites with increasing bakeout times at 323 K (50°C) (ref. 69). The mass accumulation on the TQCM were measured both at 175 K and 100 K with the composite specimens at 298 K (25°C). The outgassing rate at 100 K was higher than that measured at 175 K, which is attributed to the significant desorption of water from both the PEEK and polycyanate composites. Both the PEEK and the polycyanate composites exhibited similar behavior in the changes in the outgassing rates with time. The 175 K outgassing rate decreased to zero (i.e., 1x10-15 g/cm^2-sec) by approximate 300 hours. The 100 K outgassing rate decreased to 1x10-12 g/cm^2-

sec by 400 hours. Extrapolation to a zero outgassing rate indicated that more than 1000 hours (~42 days) of extended bakeout at 323 K (50°C) would be required for the composites to completely desorb their absorbed water. This predicted outgassing time is similar to that observed from the LDEF UTIAS Experiment No. A0180 where it took about 40 days for the T-300 carbon/934 epoxy and the T-300 carbon/SP-288 epoxy to outgas and 80 days for the T-300 carbon/5208 epoxy to outgas (see page 3-31).

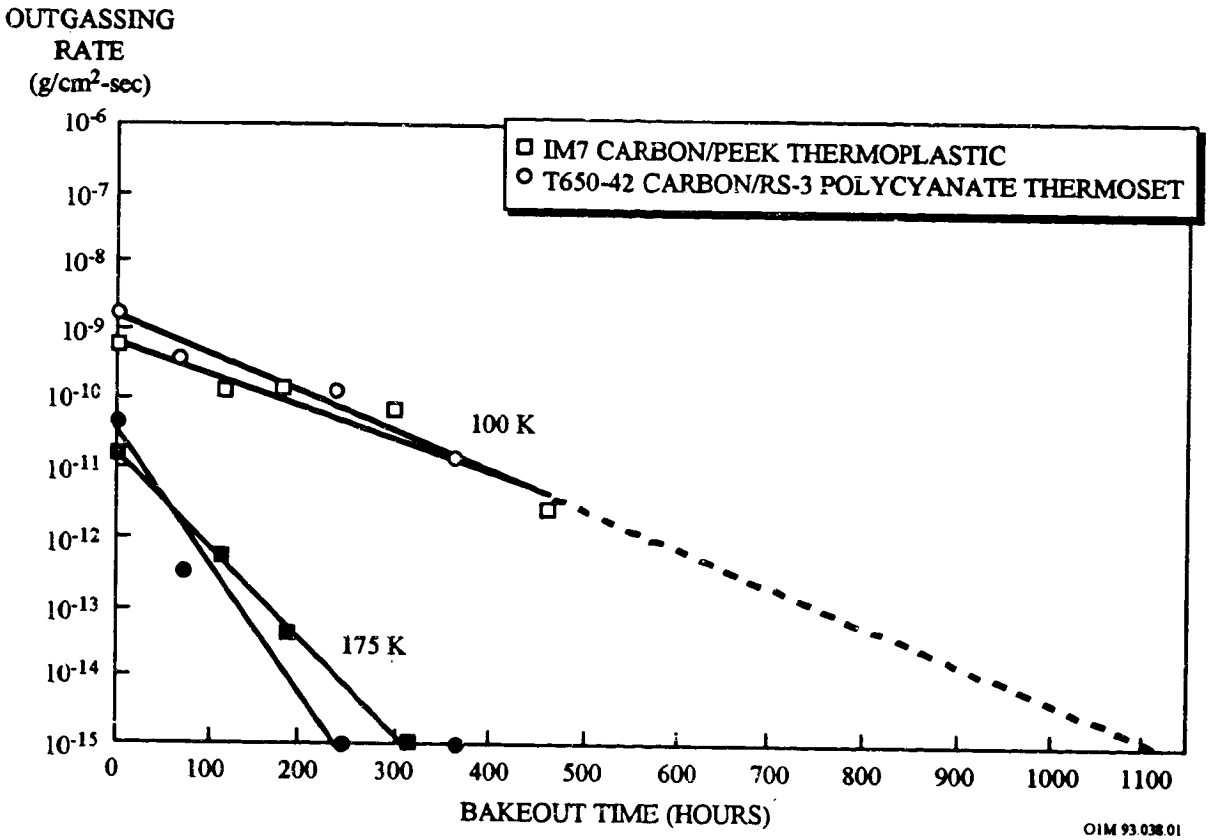

Figure 3-33. Outgassing Rates as a Function of Bakeout Time and Absorption Temperature

RELATIONSHIPS OF SPACE ENVIRONMENT - MATERIAL INTERACTIONS

REFERENCES

1 G.L. Steckel and T.D. Le, "M0003-10: LDEF Advanced Composites Experiment," LDEF First Post-Retrieval Symposium, NASA CP-3134, 1991, pp. 1041-1053.

2 T.D. Le and G.L. Steckel, "Thermal Expansion Behavior of LDEF Metal Matrix Composites," LDEF Second Post-Retrieval Symposium, NASA CP-3194, 1993, pp. 977-1000.

3 G.L. Steckel, T. Cookson, and C. Blair, "Polymer Matrix Composites on LDEF Experiments M0003-9 & 10," LDEF Materials Workshops '91, NASA CP-3162, 1992, pp. 515-542.

4 P. George, "Space Environmental Effects on LDEF Low Earth Orbit Exposed Graphite Reinforced Polymer Matrix Composites," LDEF Materials Workshops '91, NASA CP-3162, 1992, pp. 543-570.

5 R.C. Tennyson et al., "Preliminary Results from the LDEF/UTIAS Composite Materials Experiment," LDEF First Post-Retrieval Symposium, NASA CP-3134, 1991, pp. 1057-1072.

6 R.C. Tennyson and R. Matthews, "Outgassing and Dimensional Changes of Polymer Matrix Composites in Space," LDEF Second Post-Retrieval Symposium, NASA CP-3194, 1993, pp. 877-888.

7 C. Blair and B.C. Petrie, "Low Earth Orbit Environmental Effects on Composite Materials," Proceedings of the 24th International SAMPE Technical Conference, October 1992, pp. T186-T200.

8 P.E. George and S.G. Hill, "Results from Analysis of Boeing Composite Specimens Flown on LDEF Experiment M0003-8," LDEF First Post-Retrieval Symposium, NASA CP-3134, 1991, pp. 1115-1141.

9 P.E. George, H.W. Dursch, and S.G. Hill, "Space Environmental Effects on LDEF Composites: A Leading Edge Coated Graphite Epoxy Panel," LDEF Second Post-Retrieval Symposium, NASA CP-3194, 1993, pp. 923-939.

10 P.R. Young et al., "LDEF Polymeric Materials: 10 Months vs. 5.8 Years of Exposure," LDEF Second Post-Retrieval Symposium, NASA CP-3194, 1993, pp. 827-847.

11 W.S. Slemp, P.R. Young, W.G. Witte, Jr., and J.Y. Shen, "Effects of LDEF Flight Exposure on Selected Polymer Matrix Resin Composite Materials," LDEF First Post-Retrieval Symposium, NASA CP-3134, 1991, pp. 1149-1162.

12 M. Parcelier and J.P. Assie, "Effect of Space Environment on Composite Materials and Thermal Coatings (AO 138-9)," LDEF First Post-Retrieval Symposium, NASA CP-3134, 1991, pp. 1163-1173.

13 R.F. Vyhnal et al., "The Effects of Long-Duration Space Exposure on the Mechanical Properties of some Carbon-Reinforced Resin Matrix Composites," LDEF Second Post-Retrieval Symposium, NASA CP-3194, 1993, pp. 941-955.

[14] A.F. Whitaker, "Atomic Oxygen Effects on LDEF Experiment AO171," LDEF Second Post-Retrieval Symposium, NASA CP-3194, 1993, pp. 1125-1135.

[15] J. Visentine, ed., "Atomic Oxygen Effects Measurements for Shuttle Missions STS-8 and 41-G," NASA Technical Memorandum 100459, vols. I-III, September 1988.

[16] JPL, "Proceedings of the EOIM-3 BMDO Experiment Workshop", June 22-23, 1993.

[17] W. Stuckey, "Spacecraft Materials Studies on the Aerospace Corporation Tray on EOIM-III," LDEF Third Post-Retrieval Symposium, Williamsburg, VA, November 11, 1993.

[18] T. Gillespie and R. Wendt, "Martin Marietta Advanced Interceptor Technologies (AIT) Program," presented at the BMDO/JPL EOIM-3 Working Group, June 18, 1993.

[19] CWRU, "Center on Materials for Space Structures - 1993 Materials in Space Meeting," May 25, 1993.

[20] L.J. Leger, B. Santos-Mason, J.T. Visentine, and J.F. Kuminecz, "Review of LEO Flight Experiments," in Proceedings of the NASA Workshop on Atomic Oxygen Effects, D.E. Brinza, ed., NASA CR-181163 (NASA, Washington, D.C., 1987) pp. 1-10.

[21] B.A. Banks, "Atomic Oxygen Interaction with Materials on LDEF," LDEF Materials Data Analysis Workshop, NASA CP 10046, July 1990, pp. 191-216.

[22] R.J. Bourassa and J.R. Gillis, "LDEF Atomic Oxygen Flux and Fluence Calculation," NASA LDEF MSIG Report NAS1-18224 Task 12, January 1991.

[23] B.A. Banks, "Atomic Oxygen Interaction with Materials on LDEF, Proceedings of the LDEF Materials Data Analysis Workshop, NASA CP 10046, July 1990, pp. 191-216.

[24] L.J. Leger, B. Santos-Mason, J.T. Visentine, and J.F. Kuminecz, "Review of LEO Flight Experiments," Proceedings on the NASA Workshop on Atomic Oxygen Effects, November, 1986, p.6.

[25] B.A. Banks, S.K. Rutledge, J.A. Brady, and J.E. Merrow, "Atomic Oxygen Effects on Materials," NASA/SDIO Space Environmental Effects on Materials Workshop, NASA CP 3035 , Part 1, 1988, pp. 197-239.

[26] M. Allbrooks and D. Atkinson, "The Magnitude of Impact Damage on LDEF Materials," NASA Contractor Report NCR 188258, July 1992.

[27] R.C. Tennyson and G. Manuelpillai, "Analysis of LDEF Micrometeoroid/Debris Data and Damage to Composite Materials," LDEF Second Post-Retrieval Symposium, NASA CP 3194, 1993, pp. 493-511.

[28] R.C. Tennyson et al., "LDEF Mission Update: Composites in Space," Advanced Materials & Processes, May 1991, pp. 33-36.

[29] J.J. Mallon et al., "Surface Analysis of Composites Exposed to the Space Environment on LDEF," Second LDEF Post-Retrieval Symposium, NASA CP-3194, 1993, pp. 963-976.

[30] R.F. Vyhnal, 'The Effects of Long durtion Space Exposure on the Mechanical Properties of Some Carbon-Reinforced Resin Matrix Composites," LDEF First Post-Flight Retrieval Symposium, MASA CP 3194, 1993, pp. 941-947.

[31] Case Western Reserve University, "NASA CCDS on Materials for Space Structures - Limited Duration Candidate Exposure Report", December 1992.

[32] TRW unpublished data.

[33] R.C. Tennyson, "Composite Materials in Space - Results from the LDEF Satellite," J. Canadian Aeronautics and Space Institute, vol. 37, no. 3, September 1991.

[34] H. Dursch et al., "Development of Composite Tube Protective Coatings," NASA CR-178116, 1986.

[35] H. Dursch, "Chromic Acid Anodizing of Aluminum Foil," NASA CR-178417, 1988.

[36] L. Teichman et al., "Evaluation of Selected Thermal Control Coatings for Long-Life Space Structures," NASA TM 4319, January 1992.

[37] H.W. Babel, K.E. Simpson, and C.A. Jones, "Material Considerations for Space Station Freedom," 41st Congress of the International Astronautical Federation, Dresden, GDR, October, 1990.

[38] H. Dursch and P. George, "Composite Protective Coatings for Space Applications," LDEF Third Post-Retrieval Symposium, Williamsburg, VA, November 10, 1993.

[39] W.S. Slemp, B. Santos-Mason, G.F. Sykes, Jr., and W.G. Witte, Jr., "Effects of STS-8 Atomic Oxygen Exposure on Composites, Polymeric Films, and Coatings" NASA TM 100459, Volume I.

[40] B.A. Banks, K.K. de Groh, B.M. Auer, and L. Gebauer, "Monte Carlo Modeling of Atomic Oxygen Attack of Polymers With Protective Coatings on LDEF," LDEF Second-Post Retrieval Symposium, NASA CP-3194, 1993, pp. 1137-1150.

[41] K.K. de Groh, T. Dever, and W. Quinn, "The Effect of Leveling Coatings on the Atomic Oxygen Durability of Solar Concentrator Surfaces," proceedings of the 8th International Conference on Thin Films (ICTF-8) and the 17th International Conference on Metallurgical Coatings (ICMC-17), San Diego, CA, April 1990.

[42] B.A. Banks and S.K. Rutledge, "Low Earth Orbital Atomic Oxygen Simulation for Materials Durability Evaluation," Proceedings of the 4th European Symposium on Spacecraft Materials in a Space Environment, CERT, Toulouse, France, Sept. 1988.

[43] R.R. Kamenetzky and A.F. Whitaker, "Performance of Thermal Control Tape in the Protection of Composite Materials," LDEF Materials Workshop '91, NASA CP 3162, 1992, pp. 223-232.

[44] D. Petraitis, "The Effects of Atomic Oxygen on NuSil Silicone Elastomers and Coatings," presented at the CSRU/NASA 1993 Materials in Space Meeting, Cleveland Ohio, May 25, 1993.

[45] E. Silverman, NASA/CWRU Report on LDCE 1,2 & 3 to TRW, December 1992.

[46] S.Y. Chung et al., "Flight- and Ground-Test Correlation Study of BMDO SDS Materials: Phase I Report," JPL Publication 93-31, December 1993, pp.39-54.

[47] D.E. Brinza, "Early Results from the JPL Experiments on the Evaluation of Oxygen Interactions with Materials (EOIM-3) Experiment Aboard STS-46", Presented at the EOIM-3 BMDO Flight Experiment Workshop, June 22, 1993.

[48] S.K. Rutledge et al., "The Effects of Atomic Oxygen on the Thermal Emittance of High Temperature Radiator Surfaces," NASA TM 103224, April 1989.

[49] B.A. Banks et al., "Simulation of the Low Earth Orbital Atomic Oxygen Interaction With Materials by Means of an Oxygen Ion Beam," NASA TM-10197, 1989.

[50] R.C. Tennyson, "Atomic Oxygen and Its Effect on Materials," The Behavior of Systems in the Space Environment, R.N. DeWitt et al. (eds.), pp. 233-257.

[51] J.T. Visentine and A.F. Whitaker, "Material Selection Guidelines to Limit Atomic Oxygen Effects on Spacecraft Surfaces," NASA TM 100351, February 1989.

[52] D.E. Walrath and D.F. Adams, "Moisture Absorption Analysis of the Thematic Mapper Graphite/Epoxy Composite Structure," Modern Developments in Composite Structure, ASME Winter Meetings, December 1979.

[53] A.R. Telcamp and E.A. Derby, "Design Considerations for Composite Materials Used in the MARS Observer Camera," S.P.I.E. Proceedings Advances in Optical Structural Systems, Vol. 1330, April 1990.

[54] Composite Optics, Inc. Unpublished Data.

[55] E.M. Silverman, C.R. Wiacek, R.A. Griese, "Characterization of IM7 Graphite/Thermoplastic Polyetheretherketone (PEEK) for Spacecraft Structural Applications " Composite Materials: Testing and Design (Tenth Volume), ASTM STP 1120, Glenn C. Grimes, Ed., American Society for Testing and Materials, Philadelphia, 1992, pp. 118-130.

[56] C. Blair and J. Zakreewski, "Coefficient of Thermal and Moisture Expansions and Moisture Absorption for Dimensionally Stable Quasi-Isotropic High Modulus

Graphite/Epoxy Composites," S.P.I.E. Proceedings, Advances in Optical Structure Systems, Vol. 1303, April 1990.

57 LDEF Spaceflight Environmental Effects Newsletter, Vol. III, no. 6, November 1992.

58 TRW unpublished data.

59 S.S. Tompkins, G.F. Sykes, and D.E. Bowles, "The Thermal Mechanical Stability of Composite Materials for Space Structures," IEEE/ASM/ASME/SME Space Technical Conference, Anaheim, CA, Sept. 1985.

60 G.F. Sykes, J.G. Funk, and W.S. Slemp, "Assessment of Space Environment Induced Microdamage in Toughened Composite Materials," Proceedings of the 18th International SAMPE Technical Conference, October 1986, pp. 520-534.

61 J.G. Funk and G.F. Sykes, Jr., "The Effects of Simulated Space Environmental Parameters on Six Commercially Available Composite Materials," NASA Technical Paper 2906, April 1989.

62 C.T. Golden and E.E. Spear, "Graphite/Epoxy Structure of the Spar Telescope's Optical Telescope Assembly," Proceedings of the 29th SAMPE Symposium and Exhibition, 1984, Reno, NV, pp. 33-45.

63 D.R. Tenney, G.F. Sykes, and D.E. Bowles, "Composite Materials for Space Structures," Third European Symposium On Spacecraft Materials in the Space Environment, Oct 1985, Noordwijk.

64 S.S. Tompkins, "Effects of Thermal Cycling on Composite Materials for Space Structures," NASA/SDIO Space Environmental Effects on Materials Workshop, NASA CP 3035, Part 2, 1989, pp. 447-470.

65 D.E. Bowles and O.H. Griffin, Jr., "Analysis of Thermal Stresses in Polymer Matrix Composites," Proceedings of 34th International SAMPE Symposium, May 1989, pp. 575-584.

66 S.S. Tompkins, J.G. Funk, D.E. Bowles, T.W. Towell, and J.W. Connell, "Composite Materials for Precision Space Reflector Panels," SPIE Vol. 1690 Design of Optical Instruments, 1992, pp. 250-261.

67 NASA Langley unpublisehd data.

68 E.G. Wolff, "Dimensional Stability of Carbon Fiber Reinforced Plastic Tubes," SAMPE Quarterly, October 1984, pp. 26-33.

69 TRW unpublished data.

70 MSFC Handbook 1674

4.0 POLYMERS

4.0 POLYMERS

4.1 INTRODUCTION

Polymeric materials exposed to the LEO space environment were included in several LDEF and STS experiments listed in Table 4-1.

Table 4-1. LEO Flight Experiments on Polymers

Materials	Flight Experiment	Environment	Ref.	PI
Polyethylene Terephthalate Polyurethane Silicones Kevlar Teflon Kapton	A0171 (A8)[a]	AO = 7.15×10^{21} atom/cm^2 UV = 9400 esh	1	A. Whitaker
Polystyrene Nylon Polymethylmethylacrylate Polyethylene Terephthalate Kapton Carbon Film	A0114 (C9/C3)	Row C9 Specimens AO = 8.99×10^{21} atom/cm^2 UV = 11,200 esh Row C3 Specimens AO = 1.32×10^{5} atom/cm^2 UV - 11,100 esh	2 3	J. Gregory
Kapton Polyimide P1700 Polysulfone Kynar (PVDF) PIPSX Polyimide-Polysiloxane FEP Teflon Film	A0134 (B9)	10-Month Specimens AO=2.6×10^{20} atoms/cm^2 UV=1,600 esh 5.8-Year Specimens AO=8.99×10^{21} atoms/cm^2 UV=11,200 esh	4 5 6 7	W. Slemp
Kapton Teflon Polysulfone Tefzel Polycarbonate Nylon PPQ	M0003-5 (D9)	AO=8.99×10^{21} atoms/cm^2 UV=11,200 esh	7	C. Hurley
PEN-2,6 Polyester PMDA-DAF Polyimide Kapton	STS-8	AO=3.5×10^{20} atoms/cm^2 UV=41.75 esh	8 9	V. Bell

(a) Denotes LDEF row number and the letter denotes the LDEF tray (see Figure 1-15)

Significant findings from the LDEF flight experiments are:

- FEP Teflon, polyethylene mechanical properties affected by UV.
- Siloxane-modified materials resist AO.
- Non-silicone polymers attacked by AO.
- AO erosion of Kapton linearly predictable.
- Greater erosion than predicted for FEP, polystyrene, PMMA.
- AO attacks carbon films.

4.2 KAPTON

4.2.1 Composition

Polyimide

4.2.2 Manufacturing Source

DuPont

4.2.3 Effects of the Space Environment

4.2.3.1 AO Reactivity and Surface Recession

LDEF and Space Shuttle Flight Experiments. Atomic oxygen erosion of Kapton is linearly predictable with AO fluence, based on comparison of LDEF data with Space Shuttle flight data. Surface recession and AO reactivity (R_e) data are tabulated in Table 4-2. AO reactivity or erosion yield is determined by dividing the eroded depth by the atomic oxygen fluence. The 2.9 x 10^{-24} cm^3/atom value determined for Kapton from LDEF Experiments AO134[6,10] and A0114 (ref. 3) is very close to the 3.0 x 10^{-24} cm^3/atom value measured from the STS-8 flight experiment.[11,12,13,14,15,16]

Table 4-2. LDEF and STS-8 AO Reactivity of Kapton

Experiment	Sample Description	Space Environment		Surface Recession	AO Reactivity 10^{-24} cm^3/atom
		AO atoms/cm^2	UV esh	μm	
LDEF A0114		9.0 x 10^{21}	11,200	260±5	2.89±0.06
LDEF-EECC[(a)]	1.2 mil thick 0.81 in diam.	2.6 x 10^{20}	1,600		2.9
STS-8	0.5, 1.0, 2.0 mils	3.5 x 10^{20}	41.75	10.5	3.0
STS-5	2.0 mils	0.99 x 10^{20}	43.5	2.79	2.8

(a) Kapton film was located on Row 9 in the Experiment Exposure Control Canister (EECC) as part of LDEF Experiment AO134. This canister was closed when LDEF was deployed on April 7, 1984. It opened one month later for 10 months and then closed, providing 10 months of LEO exposure early in the LDEF mission.

The LDEF A0114 value of 2.89±0.06x10^{-24} cm^3/atom is within 3 percent of the normally quoted value of 3.0x10^{-24} cm^3/atom. It is interesting to note that the silicone contamination known to be present on LDEF (and on all shuttle-borne vehicles) does not seem to affect the linearity of the erosion. Perhaps the silicones aggregate upon adsorption or oxidation, or perhaps adsorption is

low on these materials. It is, however, well known that if a continuous film of SiO_2 is actually formed, such a film is very effective in preventing oxidation by fast AO.

STS-5 and STS-8 Space Shuttle Flight Experiments. Kapton films of different thicknesses were flown on both the STS-5 and the STS-8 Space Shuttle missions to measure surface reactivity with atomic oxygen in the low Earth orbital environment. Samples on STS-5 were exposed to an atomic oxygen sweeping impingement across the surfaces with a total exposure fluence of $0.99x19^{20}$ atoms/cm^2 for 43.5 hrs. Samples on STS-8 were exposed to ram (normal to surface) conditions for 41.75 hrs leading to a total atomic oxygen fluence of 3.5×10^{20} atoms/cm^2. The high fluence on STS-8 was achieved by lowering the vehicle altitude to 225 km and by maintaining the payload bay pointing into the velocity vector, nose to the Earth.

Average film thickness loss for Kapton on STS-5 is summarized in Table 4-3.[17] The film samples (2.54 x 25.4 cm) were held in place on heater plates set to three temperatures (24°C, 65°C, and 121°C). Mass loss determinations were made by comparing mass measurements obtained for the control and exposed specimens. Since mass loss is film thickness dependent, these measurements were converted to thickness loss by using bulk film density. Preliminary examination of the data did not show any variations in mass loss for the three temperatures involved within the accuracy ($1\sigma = \pm 20\%$) of the measurements. This relatively large error was attributed to cutting techniques and film thickness variations. Since no temperature dependency was evident (only minor temperature dependency was expected due to the high kinetic energy of the impinging atomic oxygen, all of the data (10 samples per thickness) shown in Table 4-3 were grouped together.

Table 4-3. STS-5 Kapton Surface Recession and AO Reactivity

Thickness μm[a]	AO Fluence 10^{20} atoms/cm^2	Surface Recession μm	AO Reactivity 10^{-24} cm^3/atom[b]
12.7	0.99	1.50	1.5
25.4	0.99	2.18	2.2
50.8	0.99	2.79	2.8

(a) Film thickness of 12.7, 25.4 and 50.8 μm correspond to 0.5, 1.0 and 2.0 mils, respectively

(b) Most probable error is ±30 to 40%

The results show a reaction dependency on film thickness with Kapton showing increasing thickness loss as thickness increases (the opposite is true for Mylar; see Section 4.7). Mass loss measurements obtained on normal and oblique specimens indicate that reactivity of thin film materials to atomic oxygen bombardment is a function of impingement angle, as expected from flux reductions due to cosine angle effects. Specimens inclined at an angle of 45° to the flat surface of

the heater plate experienced approximately 70% of the mass loss of film material attached to the flat surfaces.

The STS-8 mission average thickness loss for strip and disc samples are shown in Table 4-4.[18] The notations "air" and "roll" under the "exposed side" column refer to the manufacturing process for the Kapton film. "Roll" is the film side in contact with the manufacturing rolls, and "air" refers to the opposite side. The roll side of Kapton is inherently rougher than the air side of Kapton. Both sides of the film were exposed to determine reaction rate dependency on manufacturing details. Each strip data point represents three individual specimens (5 cm^2 in size) with a standard deviation of 0.6 μm. In general, the data for Kapton are in good agreement considering all the variables involved in the measurements (i.e., Kapton recession varies by only ±5 to 10 percent).

Table 4-4. STS-8 Kapton Surface Recession and AO Reactivity

Thickness μm (mils)	Exposed side[a]	Surface Recession,[b] μm				AO Reactivity 10^{-24} cm^3/atom
		Strip Samples		Disc Samples	Average[c]	
		121°C	65°C			
12.7 (0.5)	air	9.5	10.5	11.1		
	roll	11.8	10.3			
25.4 (1.0)	air	9.8	10.7		10.5	3.0
	roll	9.9	9.0			
50.8 (2.0)	air	11.1	10.6			
	roll	11.1	11.1			

(a) Refers to manufacturing process
(b) Corrected for flux reduction due to nonnormal impingement (cos ø)
(c) Strip samples and disc samples

No recession rate temperature dependency was evident for any of the Kapton films. Temperature effects on recession rates were assessed by comparing the 121°C and 65°C strip samples with the disc samples, which had an estimated equilibrium temperature of -15°C. This finding is in agreement with the organic film data obtained on the STS-5 (ref. 15) mission and ground simulation results[19] and is not unexpected since the incoming atoms have >5.0 eV of kinetic energy, which appear, based on scattering measurements made by Gregory,[20] to be totally transferred to the surface.

No differences in recession rates for roll and air sides were evident for Kapton. Since the thickness dependence might arise from minor surface density variations introduced in the manufacturing process, reactivity of both sides (roll and air) of the films was examined and the data are included in Table 4-4.

There is no apparent recession rate dependence on sample thickness for Kapton. As the recession rates are not affected by either temperature or the specific side exposed, these data points were combined (average recession for temperature, air and roll) and examined for thickness dependency. This finding is in disagreement with the STS-5 results which show an increased recession rate with increasing film thickness. Hence, thickness dependency for Kapton may be surface-property controlled.

The AO reactivity for the Kapton films shown in Table 4-4 is 3.0×10^{-24} cm^3/atom. This value is based on a total AO fluence of 3.5×10^{20} atoms/cm^2. (AO reactivity is computed by normalizing the total surface recession by the mission atomic oxygen fluence.) This AO reactivity is higher than the values measured for the same materials on STS-5 by approximately a factor of 2. There are three significant differences, all related to exposure conditions, which could affect reaction rates. These are, for STS-8 and STS-5 respectively, incident flux, 2.3×10^{15} atoms/cm^2-sec vs 3.8×10^{14} atoms/cm^2-sec; total fluence, 3.5×10^{20} atoms/cm^2 vs 9.9×10^{19} atoms/cm^2; and sample orientation relative to ram, or normal versus sweeping impingement.

Flux differences do not appear to be a significant factor in influencing reaction rates. In fact, one would expect lower flux to result in higher reaction efficiencies since atom to atom recombination's or other competing reactions should be less favored at lower flux as a result of lower atomic oxygen surface densities. Reaction rates may have been affected by total fluence differences in that low fluence results in small surface recession which could be dominated by surface effects or minor amounts of contamination. High fluence results in rates representative of bulk properties. Aside from fluence considerations, if contaminants were present on the sample surfaces, the STS-5 recession rates should have been lower than the STS-8 rates. It should be noted that the STS-5 strip samples were attached with silicone-based adhesive tape, and although the samples were outgassed prior to flight, some silicone contaminant may have been transferred by migration to the sample surfaces. It has been shown previously[21] that silicones are considerably less reactive than non-silicon-containing organics. To preclude similar problems, tape with acrylic-based adhesive was used exclusively on the STS-8 samples.

Finally, the capture probability for the impinging atoms by the surface may be dependent on impingement angle. The Kapton samples (12.7 and 50.8 μm) on the STS-8 mission were mounted on the inclined portion of both heater plates, positioned 42° of the main beam axis, and were exposed to only 74 percent of the normal impingement flux. When the recession data gathered from the samples inclined at 42° were combined and divided by the respective normal impingement recession, the result is a ratio of 0.64 ± 0.03 rather than 0.74. This indicates that recession at low impingement angles is less than would be expected, as it would be if it were simply due to flux

reduction. This finding is in qualitative agreement with the STS-5 results. The data fit a $(\cos\theta)^{1.5}$ function better than $\cos\theta$. If such dependence exists, it might be expected that low impingement angles, as result from the sweeping-beam case of STS-5, may lead to lower capture probability and lower reaction efficiency. Hence, if impinging angle increases, reaction probability decreases. Although data from the inclined samples support this hypothesis, additional data on impingement angle effects are needed to completely define reaction rate dependency. Thus, differences in the reaction rates determined on the two experiments were most likely due to either minor contaminants or atom impingement angle

COMES/MIR Flight Experiment. On MIR, erosion differences vary according to the position, and hence, the atomic oxygen fluence levels.[22] The 1.1 year COMES/MIR flight experiment consisted of four panels that were deployed by an cosmonaut in space outside of MIR with the possibility of exposing samples on both sides, conventionally identified as "V" and "R". The results, shown in Table 4-5, clearly indicate that the two sides did not undergo the same fluence and also that some samples were more or less protected by contaminants (mainly on the V side). The high level of contamination on MIR prevents one from drawing a definitive conclusion about these anomalies but they seem to indicate that precise, local ambient conditions greatly influence degradation. The films located on the V side were attacked much less (erosion from 0.11 to 2.2 μm) than those on the R side (erosion from 11 to 17 μm). Finally, the Kapton with a protective coating (ITO, aluminum, silicone) did not suffer any erosion (see Section 4.3).

Table 4-5. Kapton Film Erosion After Exposure to LEO on MIR

MIR Position	Environment		# of Samples	Minimum erosion (μm)	Maximum erosion (μm)	Average erosion (μm)
	AO atoms/cm^2	esh				
Side R	3.5×10^{20} to 5.8×10^{20}	1900	3	10.7	16.7	14.6
Side V	1.2×10^{18} to 7.5×10^{19}	2850	9	0.11	2.2	0.5

Environmental Variations on MIR-COMES Space Experiment:

Space Environment	FACE V	FACE R
Oxygen atoms cm^{-2}	1.2×10^{18} to 7.5×10^{19} (a)	3.5×10^{20} to 5.8×10^{20}
Solar UV (esh)	2850 (b)	1900
Temp. Cold case (°C)	-60 to -70	-60 to -70
Temp. Hot case (°C)	+10 to +30	+50 to +60

(a) Estimated from AO reactivity of Kapton (3.0×10^{-24} cm^{3}atom^{-1}) and Terphane (PET) (3.0×10^{-24} cm^{3}atom^{-1})
(b) Estimated from data of experiment calorimeter

4.2.3.2 Thermal-Optical Properties

Generally, in LEO there is much synergy between the different parameters of the natural and induced environments (UV, atomic oxygen, thermal cycles, micrometeorites and debris, contamination). On MIR, tests on the V side of the COMES experiment were conducted to separate the effects of different environmental components. Table 4-6 presents the variations of solar transmittance for Kapton film samples exposed to different environments (AO = $1.2x10^{18}$ to $7.5x10^{19}$ atoms/cm^2; 2850 esh) after their flight on the COMES/MIR. The Kapton HN film suffered deterioration under the combined effect of atomic oxygen and UV radiation.

Table 4-6. AO/UV Effects on the Solar Transmittance of Kapton on the COMES/MIR

Material	Chemical Nature	UV + AO + vacuum[(a)] ΔT_s*	UV (λ>190 nm)[(b)] ΔT_s	UV (λ>360 nm)[(c)] ΔT_s	Vacuum[(d)] ΔT_s
Kapton HN 50 μm	Polyimide Kapton	-0.03	0.00	0.00	0.00

(a) an exposure to all of the parameters: ultra-violet solar radiation (including far UV), atomic oxygen, vacuum and the temperature.

(b) an exposure to ultra-violet radiation with a wavelength greater than 190 nm, to the vacuum and to the temperature

(c) an exposure to radiations with a wavelength greater than 360 nm, to the vacuum and to the temperature

(d) an exposure to the vacuum and to the temperature.

* ΔT_S=final T_S-initial T_S

Space Environment on the V side of the COMES experiment:

Atomic Oxygen, atoms cm^{-2}	$1.2x10^{18}$ to $7.5x10^{19}$ (1)
Solar UV (esh)	2850(2)
Temp. Cold case (°C)	-60 to -70
Temp. Hot case (°C)	+10 to +30

(1) Estimated from AO reactivity erosion of Kapton (3.0×10^{-24} cm^{3}atom^{-1})and Terphane (PET) (3.0×10^{-24} cm^{3}atom^{-1}) samples

(2) Estimated from data of experiment calorimeter

Table 4-7 presents the variations of the solar reflectance and the emissivity of Kapton film samples after their flight on FRECOPA/LDEF.[23] Experiment AO 138-6 was part of the FRECOPA experiment located on the trailing edge of LDEF. The experiment was designed to allow exposure of a part of the samples to the whole spacecraft environment by being laid directly on the FRECOPA tray surface.

Table 4-7. Solar Reflectance and Emissivity Variations of Kapton Film on LDEF

Material	$R_{s\ initial}$	$\varepsilon_{initial}$	ΔR_s	$\Delta\varepsilon$
Polyimide Kapton H (12 microns)	0.21	0.694	0	-0.015
Polyimide Kapton H (50 microns)	0.13	0.778	0.02	-0.004
Polyimide Kapton (50 microns)	0.13	0.778	0.01	-0.004

Environmental Variations of FRECOPA/LDEF Space Experiments: Because of its position on trailing edge row 3 of the LDEF, the AO 138-6 experiment did not receive any oxygen atoms during the mission, with the exception of a short period during the capture when it received a fluence evaluated at 1.32×10^{17} atoms cm^{-2}. The solar illumination was 11100 equivalent sun hours (esh) for the samples located on the tray. The particle irradiation dose (mainly due to the electron flux) was weak: 3×10^5 rads. The number of temperature cycles was 34000 for the following temperature ranges: Cold case (°C) -43 to -52; Temp.; (°C) +45 to +63.

4.2.4 Design Consideration for the Space Environment

The atomic oxygen reactivity ($R_e = 3.0 \times 10^{-24}$ cm^3/atom) or erosion yield for Kapton combined with the specific space vehicle atomic oxygen fluence can be used to determine the expected surface recession for a specific space mission. The product of atomic oxygen fluence and the material AO reactivity is the expected thickness loss for the specific spacecraft mission according to the following equation:

$$\Delta x = F_T \times R_e$$

Hence, as discussed in Chapter 2, the amount of surface recession for a material of known reactivity is directly proportional to atomic oxygen fluence, or the total number of atoms impinging on each square centimeter or surface area during the duration of the intended mission. Fluence, in turn, is dependent on such parameters as spacecraft altitude, surface attitude relative to the spacecraft velocity vector, orbit inclination, duration of exposure, and solar activity conditions during the lifetime of the spacecraft (as atomic oxygen is produced by the photodissociation of molecular oxygen initiated by the absorption of solar near-ultraviolet radiation, its concentration is known to change as sun spot activity varies during the 11-year solar cycle).

Surface recession predictions as a function of atomic oxygen fluence can be determined from the nomograph of Figure 4-1 for a circular orbit with front and back surfaces exposed and inertially fixed and normal to the orbit plane.

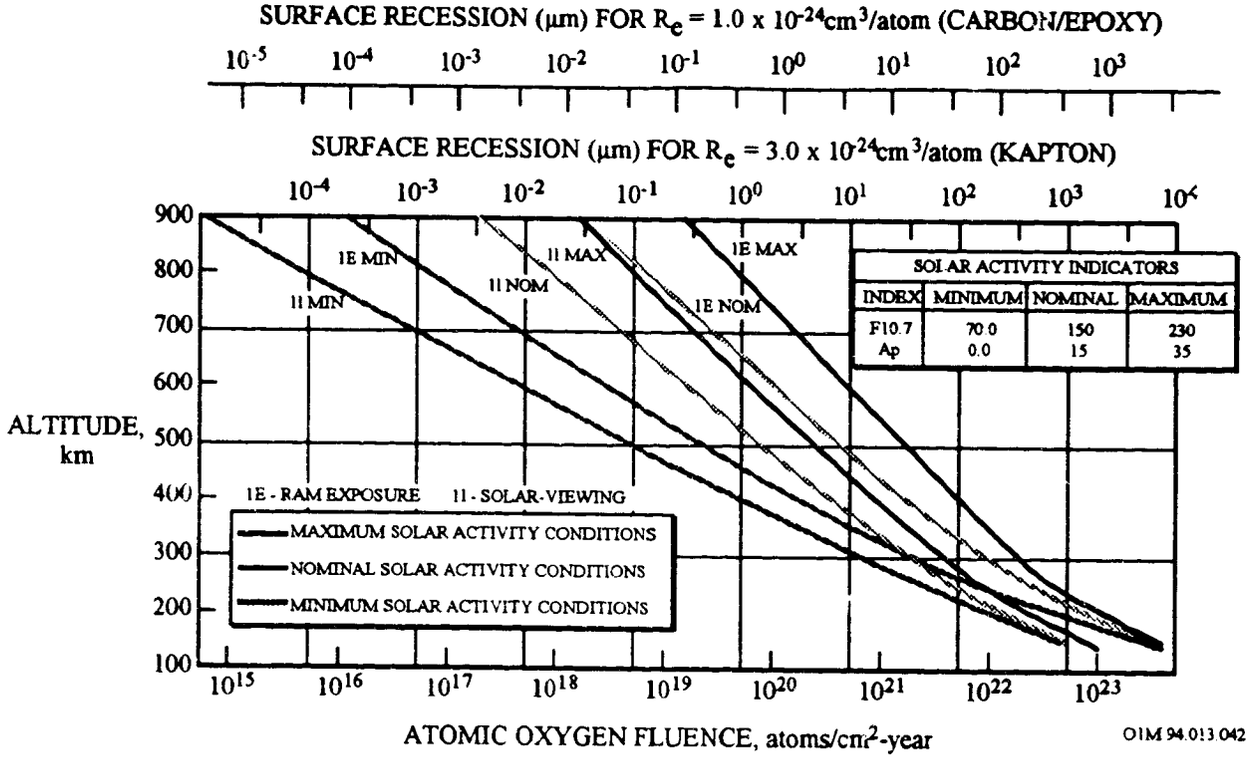

Figure 4-1. Nomograph of Kapton Surface Recession with AO Fluence Levels

4.3 PROTECTED-COATED KAPTON FLEXIBLE SOLAR ARRAY BLANKETS

4.3.1 Introduction

Polyimide (Kapton), the baseline material for the flexible solar array panel the Hubble Space Telescope, is known to be susceptible to attack by atomic oxygen in LEO. The erosion yield, or the volume of organic material oxidized per incident atomic oxygen, for polyimide Kapton was found to be 3.0×10^{-24} cm^3/atom (ref. 18). Considerable research has been performed to identify durable, protective coatings for Kapton against atomic oxygen attack.[24,25]

Polycrystalline ceramic films, such as SiO_X (where $1.9 < X < 2.0$), SiO_2, fluoropolymer-filled SiO_2, and Al_2O_3, have been demonstrated in both ground and space tests (i.e., LDEF, Lockheed flight experiment) to be effective in protecting polyimide Kapton from oxidation by LEO atomic oxygen.[26,27,28] SiO_X coated Kapton was chosen as the baseline design material by Lockheed Missiles and Space Company (LMSC) for use on the Space Station Freedom (now the International Space Station Alpha) solar array panels.

4.3.2 SiO_X-Coated Kapton

4.3.2.1 Composition

Sputtered deposited SiO_X coating of 1300 Å thickness over Kapton.

Coatings of SiO_X are clear and provide protection with minimal impact on solar absorptance and thermal emittance properties of underlying materials.

4.3.2.2 Source

Manufacturer: Sheldahl Inc.
Northfield, MN 55057
Tel: 507/663-8000

4.3.2.3 Effects of The Space Environment

4.3.2.3.1 LDEF Flight Experiment

Uncoated Kapton and several candidate protective coatings on Kapton were exposed to the LEO environment on the LDEF to determine if the coatings could be used to protect polymeric substrates from degradation in the LEO environment (ref. 28). Coatings evaluated included 650 Å of silicon dioxide and 650 Å of a 4% polytetrafluoroethylene - 96% silicon dioxide mixed coating. All of the coatings evaluated were ion beam sputter deposited.

These materials were exposed to a very low atomic oxygen fluence (4.8×10^{19} atoms/cm^2) as a result of the LDEF experiment S1003 tray being located 98 degrees from the ram direction. Comparison of the optical properties of coated and uncoated Kapton exposed to the low-Earth space environment to a control uncoated Kapton sample is presented in Table 4-8.

Table 4-8. Comparative Optical Properties of Coated and Uncoated Kapton on LDEF

Material (LDEF Sample Designation)	Total Reflectance	Total Transmittance	Solar Absorptance	Thermal Emittance
Uncoated Kapton (not flown)	0.135	0.576	0.289	0.70
Uncoated Kapton (LDEF no.6)	0.136	0.580	0.285	0.72
Uncoated Kapton (LDEF no.34)	0.130	0.583	0.286	0.71
SiO_2 on Kapton(not flown)	0.116	0.573	0.311	0.72
SiO_2 on Kapton (LDEF no.9)	0.105	0.561	0.334	0.72
4% PTFE-96 SiO_2 on Kapton (not flown)	0.109	0.584	0.307	0.72
4% PTFE-96 SiO_2 on Kapton (LDEF no.7)	0.103	0.578	0.319	0.72
4% PTFE-96 SiO_2 on Kapton (LDEF no.14)	0.103	0.576	0.321	0.71

Solar absorptance increased between 7 to 8 % for the SiO_X coated Kapton and only 4 % for the mixed coating. Apparently, the addition of a small amount of fluoropolymer reduced the magnitude of absorptance increase due to environmental exposure. Thermal emittance did not change significantly for any of the exposed samples. Scanning electron microscopy revealed few micrometeoroid or debris impacts, where the extent of damage or cracking of the coating around the defect site did not extend beyond a factor of 3 of the impact crater diameter. This limiting of impact damage is of great significance for the durability of thin film coatings used for protection against the LEO environment. Determination of a mass change was not possible for any of the samples including the uncoated Kapton due to the low AO fluence. There was no evidence of spalling of any of the coatings after the approximately 34,000 thermal cycles recorded for LDEF. The surface of the uncoated Kapton, however, did show evidence of grazing incidence texturing.

4.3.2.3.2 Ground Simulation Experiment

NASA Lewis Research Center conducted AO plasma asher testing for a SiO_X coated Kapton.[29] The SiO_X coated Kapton samples used for the ground simulation experiment were 0.00254 cm (1 mil) thick Kapton H samples, which were coated with 1300 Å SiO_X (where $1.9 < X < 2.0$) films on both sides of Kapton by means of RF magnetron sputter deposition. The coatings were deposited by Sheldahl Corporation. The atomic oxygen durability for the SiO_X protected Kapton samples and unprotected Kapton samples was evaluated with an RF plasma asher (SPI Plasma Prep II). The plasma asher discharge creates a mix of atomic, molecular, ionic, excited-state species, as well as vacuum ultraviolet (VUV) and ultraviolet (UV) radiation.

The effectiveness of electrically conductive coatings, including germanium and indium tin oxide, to prevent oxidation on Kapton resulting from reaction with environmental atomic oxygen was also investigated.[30] These coatings have adequate surface electrical conductivity for use in LEO polar applications where draining of electrically charged surfaces is desirable to prevent the occurrence of electrical breakdowns and arcs. Draining of surface charging for geosynchronous spacecraft can be achieved with surface resistivities less than 10^9 ohms per square. Draining of surface charge for LEO polar spacecraft applications requires lower surface resistivity, 10^8 ohms per square because of higher auroral charging current densities.[31] Table 4-9 lists the atomic oxygen protective coatings, their thicknesses, as well as the thickness of the Kapton polyimide substrates and the suppliers of the protective coatings.

Table 4-9. Protective AO Coatings and Kapton Substrates

Protective Coating		Kapton Polyimide Substrate Thickness, mm	Coating Supplier
Materials	Thickness Å		
SiO_x ($1.9<x<2.0$)	1300	0.0254	Sheldahl
Germanium	1500	0.0508	TRW
Indium Tin Oxide	2000	0.0508	TRW
SiO_2	1500	0.0508	TRW
None		0.1270	-

Mass Loss Degradation. Figure 4-2 compares the mass loss per unit area as a function of effective atomic oxygen fluence for the atomic oxygen protective coatings listed in Table 4-9. Based on the plasma exposure to both sides of the protected Kapton specimens, the mass loss per unit area of the protected Kapton relative to the unprotected Kapton ranges between 0.03% for SiOx Sheldahl coated Kapton to 0.5% for ITO protected Kapton (ref. 30).

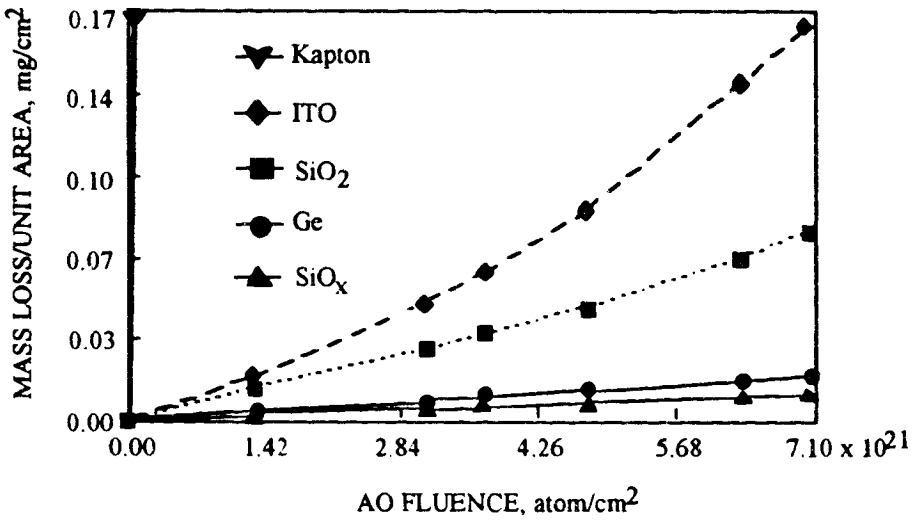

Figure 4-2. Mass Loss Dependence on AO Fluence for Various Protected Kapton Samples and Unprotected Kapton

From Figure 4-2, the worst performing protection coating was indium tin oxide, which exhibited an increase in the slope of mass loss per unit area with fluence. This increase is typically due to atomic oxygen defects which grow in size with atomic oxygen fluence. If the indium tin oxide film is sufficiently stressed, or if the stress increases with atomic oxygen fluence, tearing of the coating at defect sites can allow a gradual increase in exposure of the underlying unprotected Kapton, thus giving rise to an increasing rate of mass loss per unit area with fluence. The most protective coating (SiO_x coated by Sheldahl), has very little intrinsic stress and does not tear with atomic oxygen fluence when undercut cavities become large. This is probably why the plot of mass loss per unit area for the SiO_x Sheldahl coated Kapton has a rather constant slope.

Since silicon dioxide, germanium, and indium tin oxide are all inherently atomic oxygen durable, or develop durable oxides, the range of protection afforded by the various coatings is a measure of the defect area for each type of coating. Hence, the amount of erosion of SiO_x coated Kapton which occurs upon exposure to AO is due to pinhole defects in the SiO_x coating which allow a small amount of AO to reach the Kapton (i.e., AO undercutting via inherent manufacturing

pinhole defects). Tests were also conducted on samples of SiO_x coated Kapton which had undergone a lamination process to determine the effects of handling the material on AO resistance. These tests indicate that scratches introduced during the handling of the SiO_x coated Kapton decreased the effectiveness of the SiO_x to protect the Kapton. However, the erosion rate of the SiO_x coated Kapton after handling is still very low - the erosion rate for the handled sample was measured to be 10% of the erosion rate for unprotected Kapton.[32] Furthermore, Monte Carlo modeling of the processes that occur in plasma ashers as well as in space predicted that the mass loss of SiO_x overcoated Kapton upon exposure to actual space conditions is approximately 1/3 of the mass loss observed in plasma ashers.[33,34] Hence, asher data may provide a much more pessimistic prediction of mass loss than would really occur in LEO.

Based on the mass loss rate shown above, 7.24×10^{-4} gm/cm^2 of SiO_x-protected Kapton would be oxidized as a result of a 15-year anti-solar facing fluence of 5.40×10^{22} atoms/cm^2. This type of protection would be used on the anti-solar side of the Space Station Freedom (now International Space Station Alpha).[39,35] The desired lifetime of the array is 15 years at altitudes ranging from 400-500 km. This represents an atomic oxygen fluence exposure of 5.4×10^{22} atoms/cm^2 on the anti-solar side of the solar array blanket. These flexible arrays are composed of the following two bonded layers: the flexible circuit on the solar facing side which supports the copper foil current carriers, and the coverlay (laminate) on the anti-solar facing side which provides the primary structural support. The coverlay is composed of 1 mil thick Kapton, fiberglass scrim cloth, and silicone adhesive. Hence, typical asher mass loss data for SiO_x-protected 1-mill thick Kapton indicates that ~80 % of the anti-solar facing Kapton blanket would remain after 15 years in LEO.

Thermo-Optical Properties. Table 4-10 shows α and ε values of several samples of SiO_X coated Kapton. Nominal film thickness is 1300 Å on each side of the Kapton. In all cases there were no significant differences in the optical properties before and after a 24 hour oxygen plasma etch (AO testing at Sheldahl was done with an SPI Plasma Prep II plasma asher with a maximum R.F. power of 100 watts). This was expected due to the fully oxidized nature of the SiO_X coating, and the fact that uncoated Kapton exhibited little change in optical properties after AO exposure.[36]

Table 4-10. Solar Absorptance, Infrared Emittance, and Relative AO Reactivity for Unexposed and Oxygen Plasma Exposed SiO_X Coated 1 Mil Kapton H

Sample Number	Solar Absorptance α		Infrared Emittance ε		Relative AO Reactivity[(a)]
	Pre-Exposure	Post-Exposure	Pre-Exposure	Post-Exposure	
1	0.195	0.190	0.849	0.860	.010
2	0.195	0.190	0.850	0.861	.022
3	0.200	0.00	0.850	0.848	.018
4	0.197	0.190	0.850	0.847	.016
5	0.199	0.200	0.850	0.847	.017
6	0.195	0.190	0.850	0.848	.013
Control[(b)]	0.200	0.210	0.850	0.850	0

(a) Mass loss rate of SiO_X coated 1 mil Kapton H relative to mass loss rate of Uncoated 1 Kapton H. Specimen exposure was for 24 hours.

(b) Bare 1 mil Kapton specimen exposed under the same conditions would lose 5.5 mg/cm^2.

4.3.3 Al_2O_3-Coated Kapton

4.3.3.1 Composition

Ion beam sputtered deposited Al_2O_3 coating of 700 Å thickness over Kapton.

4.3.3.2 Manufacturing Source

Sheldahl Inc., Northfield, MN 55057, Tel: 507/663-8000

4.3.3.3 Effects of the Space Environment

4.3.3.3.1 LDEF Flight Experiment

Samples of 700 Å of aluminum oxide protective coated Kapton and uncoated Kapton were exposed to the LEO environment on LDEF Tray S1003 to determine if the coatings could be used to protect polymeric substrates from degradation in the LEO environment (ref. 35). These materials were exposed to a very low AO fluence (4.8×10^{19} atoms/cm^2) as a result of the experiment tray being located 98° from the ram direction. Determination of a mass change was not possible for any of the samples, including the uncoated Kapton, due to the low AO fluence. There was no evidence of spalling of any of the coatings after the approximately 34,000 thermal cycles recorded for LDEF. The surface of the uncoated Kapton, however, did show evidence of grazing incidence texturing. There was a 7 to 8 percent increase in solar absorptance for the aluminum oxide coated Kapton (see Table 4-11). Thermal emittance did not change significantly for any of the exposed samples. Scanning electron microscopy revealed few micrometeoroid or debris impacts, but the impact sites found indicated that the extent of damage or cracking of the coating around the defect site did not extend beyond a factor of 3 of the impact crater diameter. This limiting of impact damage is of great significance for the durability of thin film coatings used for protection against the LEO environment.

Table 4-11. Optical Properties of Exposed Al_2O_3 Coated and Uncoated Kapton on LDEF

Material and Sample Designation	Total Reflectance	Total Transmittance	Solar Absorptance	Thermal Emittance
Uncoated Kapton (not flown)	0.135	0.576	0.289	0.70
Uncoated Kapton (LDEF no.6)	0.136	0.580	0.285	0.72
Uncoated Kapton (LDEF no.34)	0.130	0.583	0.286	0.71
Al_2O_3 on Kapton (not flown)	0.120	0.571	0.309	0.72
Al_2O_3 on Kapton (LDEF no. 12)	0.118	0.545	0.337	0.71
Al_2O_3 on Kapton (LDEF no. 26)	0.119	0.551	0.330	0.72

4.4 TEFLON FEP

4.4.1 Composition and Formulation

Copolymer of fluorinated ethylene propylene

4.4.2 Manufacturing Source

DuPont

4.4.3 Effects of the Space Environment

4.4.3.1 Atomic Oxygen Effects

4.4.3.1.1 AO Reactivity

AO reactivity value of TFE Teflon polymeric washer from the Solar Array Materials Passive LDEF Experiment (SAMPLE), Experiment A0171 (ref. 1), calculated from thickness decreases or mass loss, are contained in Table 4-12 along with similar data generated from short term Space Shuttle exposures. This data is compared to FEP Teflon data from LDEF Experiments S0069 and A0178. This comparative analysis shows a definitive atomic oxygen erosion difference between TFE and FEP Teflon which short term exposure data could not previously resolve.[i]

Table 4-12. Comparative AO Reactivities for Teflon on LDEF and Space Shuttle Flights

Space Experiment	AO Reactivity, 10^{-24} cm^3/atom		Space Environment	
	TFE Teflon	FEP Teflon	AO atoms/cm^2	UV esh
LDEF A0171 Row 8	0.20	(1)	$7.15x10^{21}$	9,400
LDEF A0178 Row 9		0.364±0.5	$8.99x10^{21}$	11,200
LDEF S0069 Row 9		0.35	$8.99x10^{21}$	11,200
STS-5	< 0.05 (estimated)	< 0.05 (estimated)	$0.99x10^{20}$	43.5
STS-8	< 0.03	Not Tested	$3.5x10^{20}$	41.75

(1) The 0.5 mil FEP Teflon on Experiment A0171 was eroded away as a result of the 5.8 years of exposure.

The predicted average AO erosion yield of silver Teflon thermal control blankets exposed on LDEF Experiment A0178 to an AO fluence of $8.99x10^{21}$ atoms/cm.^{2} and to 11,200 equivalent sun hours (esh) is 3.64 $\pm 0.05x10^{-25}$ cm^3/atom for normal incidence atomic oxygen at ram.[37]

---

[i] TFE (i.e., polytetrafluoroethylene) is a completely fluorinated polymer with a 260°C service temperature. FEP copolymer is a product of the copolymerization of tetrafluoroethylene and hexafluoropropylene with a lower service temperature of 200°C.

4.4.3.1.2 Surface Recession

Teflon FEP from silver Teflon thermal control blankets located near the leading edge (Row 10) of the LDEF High Resolution Study of Ultra-Heavy Cosmic Ray Nuclei Experiment A0178 (AO fluence = 8.43×10^{21} atoms/cm^2; UV = 10,700 esh) lost about 31 microns (1.22 mils) from an original thickness of 127 microns (5 mils).[38] The decrease in the thickness of the Teflon film as a function of AO fluence is shown in Figure 4-3. The measured thickness of the leading edge exposed specimens was determined from the mass measurements and the assumption of 2.15 g/cm^3 FEP density. The silver Teflon materials located on LDEF Row 9 of the Thermal Control Surfaces Experiment (TCSE) were observed to lose approximately 25 microns to 33 microns of Teflon due to AO exposure.[39] Eddy current thickness measurements confirmed these values.

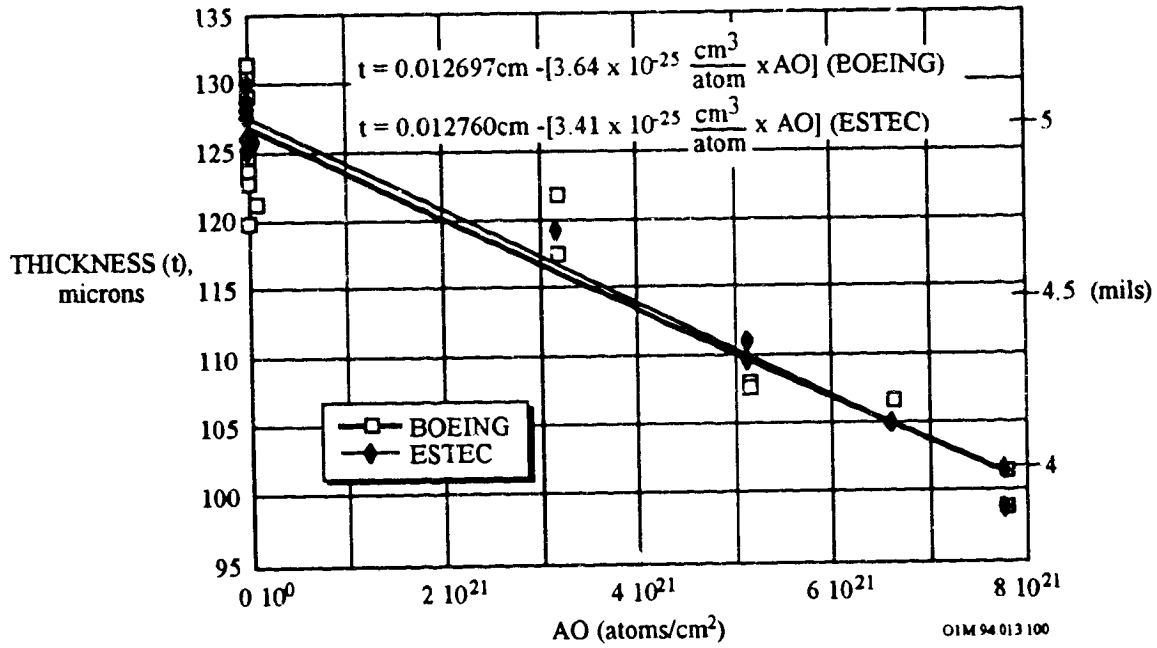

Figure 4-3. Teflon Thickness Variations from LDEF Leading Edge Exposed Specimens

This surface recession is considerably higher than previous data generated for silver Teflon material samples exposed for several days at high AO flux in the Space Shuttle Orbiter payload bay during Space Shuttle missions STS-5 and STS-8 or during other longer space duration missions (e.g., LDEF Experiment A0134 and COMES/MIR).

For example, the FEP film located in the Experiment Exposure Control Canister of Row 9 of the A0134 experiment, showed no visibly effects of UV exposure as shown in Table 4-13. This canister was closed when LDEF was deployed on April 7, 1984. It opened one month later for 10 months and then closed, providing 10 months of LEO exposure early in the LDEF mission. The FEP Teflon film showed no visible effects of exposure. X-ray photoelectron spectroscopic (XPS) analyses of two 10-month specimens and one 5.8 year specimen located at B9 showed no differences in the XPS scans. Multiple carbon 1s peaks associated with a crosslinked FEP surface were absent. Thus, VUV exposure of these films was either insufficient to crosslink the surface, or that AO had eroded the crosslinked surface away.

Table 4-13. Erosion of Teflon Films after exposure to LEO on LDEF[6,37,38,40,40] Space Shuttle Flights[17,18] and MIR[22]

Teflon Polymer	Space Experiment	Environment		Exposed Thickness μm (mil)	Average erosion (μm)
		AO atom/cm^2	esh		
FEP/Teflon	LDEF A0178[(a)]	8.43×10^{21}	10,700	127 (5)	31
FEP/Teflon	LDEF S0069 TCSE[(b)]	8.99×10^{21}	11,200	127 (5)	25-33
FEP	LDEF A0134 EECC[(c)]	2.60×10^{20}	1,600	127 (5)	None
FEP & TFE	STS-5	0.99×10^{20}	43.5	12.7 (0.5)	< 0.50
TFE	STS-8	3.5×10^{20}	41.75	12.7 (0.5)	< 0.10
FEP	COMES/MIR: Side R	3.5×10^{20} to 5.8×10^{20}	1900	127 (5)	1.5[(d)]
FEP	COMES/MIR: Side V	1.2×10^{18} to 7.5×10^{19}	2850	127 (5)	1.0[(e)]

(a) Row 10; 69 months exposure
(b) Row 9; 69 months exposure
(c) 10 months exposure
(d) FEP minimum and maximum erosion between 1.1 and 1.8 μm (3 samples)
(e) FEP minimum and maximum erosion between 0.8 and 1.1 μm (4 samples)

4.4.3.2 Ultraviolet Radiation

4.4.3.2.1 Thermo-Optical Properties

Table 4-14 presents the variations of the solar reflectance and the emissivity of Teflon film samples after their flight on FRECOPA/LDEF (ref. 23). Experiment AO 138-6, which was located on the trailing edge of LDEF. The experiment was designed to allow some of the samples to be protected from the external environment of LDEF for all mission phases, except free flight, by the means of a vacuum-tight FRECOPA canister in which they were stored.

Table 4-14. Solar Reflectance and Emissivity Variations of Teflon Film on LDEF

Type	Material	$R_{s\ initial}$	$\varepsilon_{initial}$	Canister ΔR_s	Canister $\Delta\varepsilon$
Film	FEP Teflon (125 microns)	0.060	0.802	-0.01	-0.003

Environmental Variations of LDEF AO 138-6 Experiment. The AO 138-6 canister experiment did not receive any oxygen atoms during the mission. The solar illumination was only 1448 esh for the samples inside the canister. The number of temperature cycles was 34000 with the following temperature ranges: Cold case (°C) -20 to -26; Hot case (°C) +67 to +85.

4.4.3.3 AO/UV Synergism

The findings of higher erosion rates for some Teflon samples than predicted on the basis of previous short-term flight exposure data appear to be an example of AO/UV synergism wherein a threshold of UV exposure is reached, after an extended time in orbit, which affects the polymer surface and makes it more susceptible to reactions with atomic oxygen.[41] After that time, the erosion is accelerated, as postulated by Koontz et al.[42] Hence, comparison of the LDEF and the Space Shuttle flights results show that the degradation of Teflon FEP depends on the relative quantities of atomic oxygen and UV-radiation received. Detailed chemistry studies of the FEP surfaces of LDEF silver Teflon blankets[43] revealed that atomic oxygen dominated the environmental interactions on LDEF leading edge surfaces (AO Fluence = 8.99×10^{21} atoms/cm^2; UV = 11,200 esh), leaving virgin FEP on the surfaces. Beginning at LDEF row 6 (AO Fluence = 4.94×10^{19} atoms/cm^2; UV = 6,400 esh) the interactions transitioned to solar UV dominated interactions on LDEF trailing edge surfaces.

Teflon film suffered deterioration under the combined effect of atomic oxygen and UV radiation during the COMES/MIR flight experiment. Table 4-15 presents the solar reflectance degradation of Teflon film samples after their flight on COMES/MIR, exposed to different environments. The COMES experiment consisted of four panels which were deployed by a cosmonaut in space outside of MIR with the possibility of exposing samples on both sides, conventionally identified as "V" and "R". The more significant deterioration was surely due on the one hand to the effect of the atomic oxygen which causes a greater diffusion of Teflon by attacking the surface, but was also probably caused partly by contamination of the sample. The high level of contamination on MIR prevents one from drawing a definitive conclusion about these anomalies but they seem to indicate that precise, local ambient conditions greatly influence degradation.

Table 4-15. AO/UV Effects on the Solar Transmittance of Teflon on the COMES/MIR

Material	Chemical Nature	UV + AO + vacuum[a] ΔT_s	UV (λ>190 nm)[b] ΔT_s	UV (λ>360 nm)[c] ΔT_s	Vacuum[d] ΔT_s
Teflon 25μm	FEP	-0.05	0.00	0.00	0.00

(a) an exposure to all of the parameters: UV solar radiation (including far UV), AO, vacuum and the temperature. ΔT_s=final T_s-initial T_s
(b) an exposure to UV radiation with a wavelength greater than 190 nm, to the vacuum and to the temperature
(c) an exposure to radiations with a wavelength greater than 360 nm, to the vacuum and to the temperature
(d) an exposure to the vacuum and to the temperature.

Space Environment on the V side of the COMES experiment:

Atomic Oxygen, atoms cm^{-2}	$1.2x10^{18}$ to $7.5x10^{19}$ (1)
Solar UV (esh)	2850(2)
Temp. Cold case (°C)	-60 to -70
Temp. Hot case (°C)	+10 to +30

(1) Estimated from AO reactivity erosion of Kapton (3.0×10^{-24} $cm^3 atom^{-1}$)and Terphane (PET) (3.0×10^{-24} $cm^3 atom^{-1}$) samples
(2) Estimated from data of experiment calorimeter

The exact synergy of the observed effects is difficult to understand. It may depend on the relative intensity of the elements involved (UV radiation, oxygen atoms and contamination) and also on whether they are or are not simultaneous. We do not know how important is the fact that LDEF received the majority of its atomic oxygen exposure during the last portion of the flight. Damage kinetics during the flights is unknown for most of the LDEF and COMES experiments. We must, therefore, bear in mind that variations in solar activity, altitude, and orientation may influence the importance and nature of damage.

4.5 POLYSULFONE

4.5.1 Composition

An amorphous polymer whose molecular structure features the diaryl sulfone group. Polysulfone has good thermal stability and rigidity at high temperatures with a 300°F continuous use temperature.

4.5.2 Manufacturing Source

Union Carbide

4.5.3 Effects of the Space Environment

4.5.3.1 Atomic Oxygen Reactivity

Polysulfone represents a pure polymer (i.e., polymers containing no components that erode at different rates) which appear to erode linearly with atomic oxygen fluence. Comparable atomic oxygen reactivity values generated from both short term space exposures (STS-5) and long term space exposures (LDEF) are summarized in Table 4-16. Samples on the STS-5 (ref. 15) were exposed to an atomic oxygen sweeping impingement across the surfaces with a total exposure fluence of $9.9x19^{19}$ atoms/cm^2 for 43.5 hrs. Polysulfone located on LDEF Experiment A0171 (ref. 1) was exposed to an atomic oxygen fluence of $8.99x10^{21}$ atoms/cm^2 and to 11,200 equivalent sun hours (esh). The similar reactivity values indicate that long-term thickness changes due to atomic oxygen attack in these materials can be predicted from short exposure data for this pure polymer.

Table 4-16. AO Reactivity of Polysulfone on LDEF and STS-5

Polymer	AO Reactivity 10^{-24} cm^3/atom		Comments
	LDEF AO171	STS-5	
Polysulfone	2.3	2.4	Erodes linearly with atomic oxygen fluence

4.6 MYLAR

4.6.1 Composition and Formulation

Polyethylene Terephthalate Polyester

4.6.2 Manufacturing Source

DuPont Telephone: 800-237-4357

4.6.3 Effects of the Space Environment

4.6.3.1 Atomic Oxygen Reactivity

Mylar films of different thicknesses were flown on both the fifth and the eighth Space Shuttle missions to measure reaction of surfaces with atomic oxygen in the low Earth orbital environment. Samples on STS-5 were exposed to an atomic oxygen sweeping impingement across the surfaces with a total exposure fluence of $9.9x19^{19}$ atoms/cm^2 for 43.5 hrs. Samples on STS-8 were exposed to ram (normal to surface) conditions for 41.75 hrs leading to a total atomic oxygen fluence of 3.5×10^{20} atoms/cm^2. The high fluence on STS-8 was achieved by lowering the vehicle altitude to 225 km and by maintaining the payload bay pointing into the velocity vector, nose to the Earth

Surface Recession. Average film thickness loss for Mylar on STS-5 is summarized in Table 4-17 (ref. 17). The film samples (2.54 x 25.4 cm) were held in place on heater plates set to three temperatures (24°C, 65°C, and 121°C). Mass loss determinations were made by comparing mass measurements obtained for the control and exposed specimens. Since mass loss is film thickness dependent, these measurements were converted to thickness loss by using bulk film density. Preliminary examination of the data did not show any variations in mass loss for the three temperatures involved within the accuracy ($1\sigma = \pm 20\%$) of the measurements. This relatively large error was attributed to cutting techniques and film thickness variations. Since no temperature dependency was evident (only minor temperature dependency was expected due to the high kinetic energy of the impinging atomic oxygen., all of the data (10 samples per thickness) shown in Table 4-17 were grouped together.

The results show the dependency of the atomic oxygen reactivity with material film thickness, i.e., the Mylar recession rate decreases slightly with increase in film thickness. Mass loss measurements obtained on normal and oblique specimens indicate that reactivity of thin film materials to atomic oxygen bombardment is a function of impingement angle, as expected from flux

reductions due to cosine angle effects. Specimens inclined at an angle of 45° to the flat surface of the heater plate experienced approximately 70% of the mass loss of film material attached to the flat surfaces.

Table 4-17. STS-5 Mylar Surface Recession and AO Reactivity

Thickness μm[a]	Fluence 10^{20} atoms/cm^2	Thickness Loss μm	Reaction Efficiency 10^{-24} cm^3/atom[b]
12.7	0.99	2.16	2.2
25.4	0.99	1.83	1.5
50.8	0.99	1.5	1.3

(a) Note: Film thickness of 12.7, 25.4 and 50.8 μm correspond to 0.5, 1.0 and 2.0 mils, respectively

(b) Most probable error is ±30 to 40%

STS-8 average thickness loss or surface recession for strip and disc samples are shown in Table 4-18 (ref. 18). The notations "air" and "roll" under the "exposed side" column refer to the manufacturing process for the Mylar film. "Roll" is the film side in contact with the manufacturing rolls, and "air" refers to the opposite side. Both sides of the film were exposed to determine reaction rate dependency on manufacturing details. Each strip data point represents three individual specimens (5 cm^2 in size) with a standard deviation of 0.6 μm. In general, the data for Mylar are in good agreement considering all the variables involved in the measurements (i.e., Mylar recession varies by only ±5 to 10 percent).

Table 4-18. STS-8 Mylar Surface Recession and AO Reactivity

Material	Thickness μm (mils)	Exposed side[a]	Surface Recession,[b] μm				Reactivity 10^{-24} cm^3/atom
			Strip Samples		Disc Samples	Average[c]	
			121°C	65°C			
Mylar A	12.7 (0.5)	air	12.7	12.3	12.7	12.6	3.6
Mylar A	40.6 (1.6)	air	12.1	11.9		12.0	3.4
Mylar D	50.8 (2.0)	air roll	9.9 11.0	10.2 10.4		10.4	3.0

(a) Refers to manufacturing process

(b) Corrected for flux reduction due to nonnormal impingement (cos θ)

(c) Strip samples and disc samples

No recession rate temperature dependency was evident for any of the Mylar films over the temperature range involved as shown in Table 4-18. Temperature effects on recession rates were assessed by comparing the 121°C and 65°C strip samples with the disc samples, which had an

estimated equilibrium temperature of -15°C. This finding is in agreement with the film data obtained on the STS-5 mission, and is not unexpected since the incoming atoms have >5.0 eV of kinetic energy, which appear, based on scattering measurements made by Gregory (ref. 20) to be totally transferred to the surface.

No differences in recession rates for roll and air sides were evident for Mylar D. Since the thickness dependence might arise from minor surface density variations introduced in the manufacturing process, reactivity of both sides (roll and air) of the films was examined and the data are included in Table 4-18.

The Mylar recession rate decreases slightly with increasing film thickness. As the recession rates are not affected by either temperature or the specific side exposed, these data points were combined (average recession for temperature, air and roll) and examined for thickness dependency. The Mylar thickness dependency is in general agreement with he STS-5 results. Because Mylar has similar recession dependency on thickness for considerably different total recession levels (STS-5 and STS-8), thickness effects seem to be a characteristic of bulk properties.

AO Reactivity. The atomic oxygen reactivity for the Mylar films on STS-5 and STS-8 are shown in Tables 4-17 and 4-18, respectively. The atomic oxygen reactivity was computed by normalizing the total surface recession by the mission atomic oxygen fluence. A fluence of 0.99×10^{20} atoms/cm^2 for STS-5 and a total fluence of 3.5×10^{20} atoms/cm^2 for STS-8.

The STS-8 AO reactivities are higher than the AO reactivities measured for the same materials on STS-5 by approximately a factor of 2. There are three significant differences, all related to exposure conditions, which could affect reaction rates. These are, for STS-8 and STS-5 respectively, incident flux, 2.3×10^{15} atoms/cm^2-sec vs. 3.8×10^{14} atoms/cm^2-sec; total fluence, 3.5×10^{20} atoms/cm^2 vs. 9.9×10^{19} atoms/cm^2; and sample orientation relative to ram, or normal vs. sweeping impingement.

Flux differences do not appear to be a significant factor in influencing reaction rates. In fact, one would expect lower flux to result in higher reaction efficiencies since atom to atom recombination or other competing reactions should be less favored at lower flux as a result of lower atomic oxygen surface densities.

AO reaction rates may have been affected by total fluence differences in that low fluence results in small surface recession which could be dominated by surface effects or minor amounts of contamination. High fluence results in rates representative of bulk properties. Aside from fluence considerations, if contaminants were present on the sample surfaces, the STS-5 recession rates

should have been lower than the STS-8 rates. It should be noted that the STS-5 strip samples were attached with silicone-based adhesive tape, and although the samples were outgassed prior to flight, some silicone contaminant may have been transferred by migration to the sample surfaces. It has been shown previously (ref. 21) that silicones are considerably less reactive than non-silicon-containing organics. To preclude similar problems, tape with acrylic-based adhesive was used exclusively on the STS-8 samples.

Finally, the capture probability for the impinging atoms by the surface may be dependent on impingement angle. The Mylar samples (12.7 and 40.6 μm) on the STS-8 mission were mounted on the inclined portion of both heater plates, positioned 42° of the main beam axis, and were exposed to only 74 percent of the normal impingement flux. When the recession data gathered from the samples inclined at 42° were combined and divided by the respective normal impingement recession, the result is a ratio of 0.64 $\pm$0.03 rather than 0.74, which indicates that recession at low impingement angles is less than would be expected, as it would be if it were simply due to flux reduction. This finding is in qualitative agreement with the STS-5 results. The data fit a $(\cos\theta)^{1.5}$ function better than $\cos\theta$. If such dependence exists, it might be expected that low impingement angles, as result from the sweeping-beam case of STS-5, may lead to lower capture probability and lower reaction efficiency, as can be seen by comparing the curves in Figure 4-4. Hence, if impinging angle increases, reaction probability decreases. Although data from the inclined samples support this hypothesis, additional data on impingement angle effects are needed to completely define reaction rate dependency. Thus, differences in the reaction rates determined on the two experiments were most likely due to either minor contaminants or atom impingement angle.

4.6.3.2. Tensile Strength

Exposure to UV radiation reduces the tensile strength of Mylar. Figure 4-5 illustrates the effect of ground-simulated UV radiation on the performance of protected and unprotected Mylar. Solar ultraviolet irradiation can lead to crosslinking of polymer surfaces which may lead to embrittlement and possibly to surface cracking.[44]

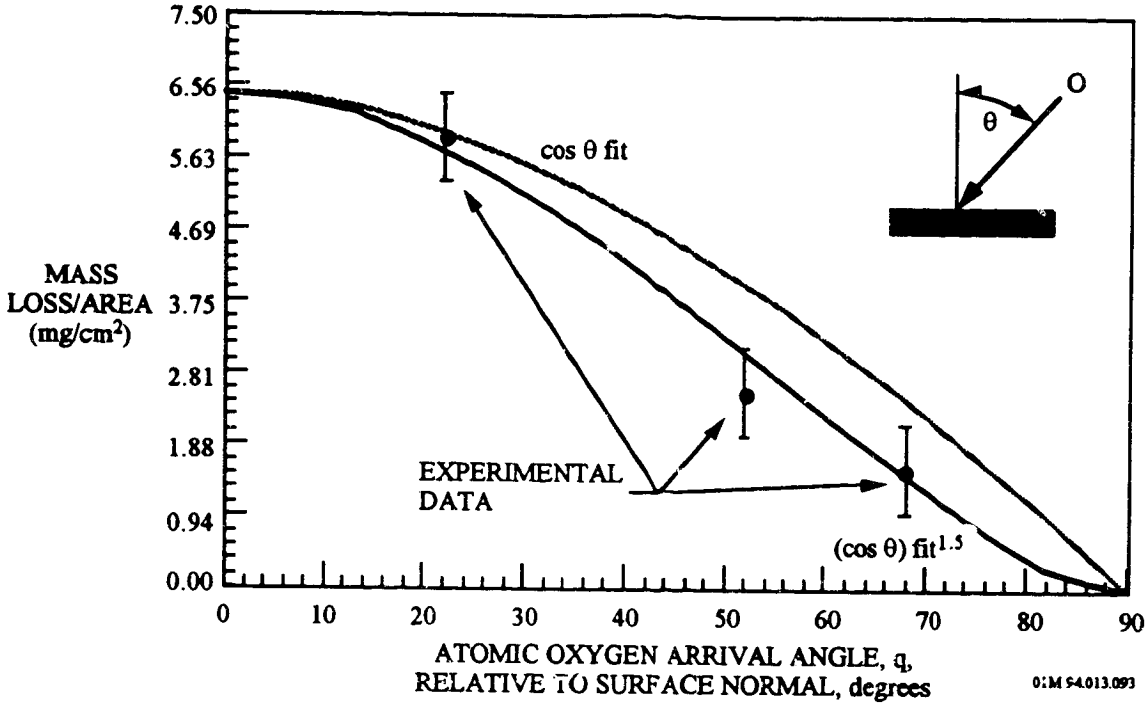

Figure 4-4. Mylar Mass Loss Per Unit Area As A Function of Atomic Oxygen Arrival Directions

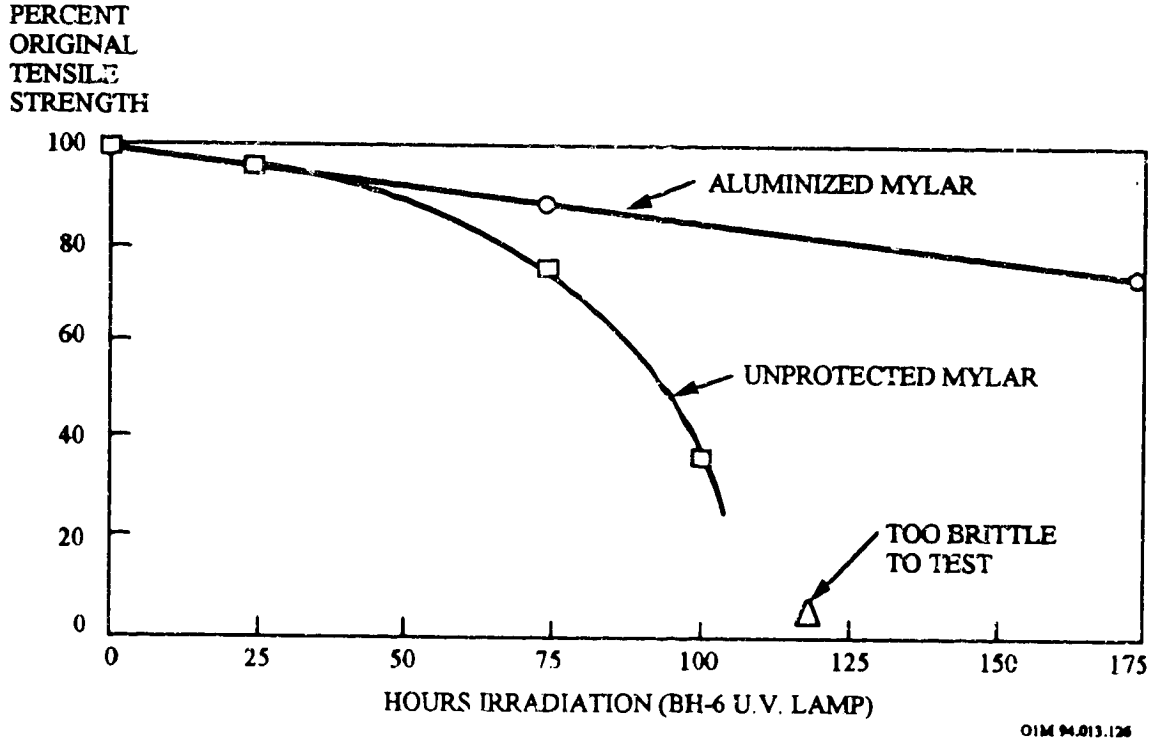

Figure 4-5. Effect of Simulated UV Radiation on the Tensile Strength of Mylar

4.7 TEDLAR

4.7.1 Composition

A highly crystalline polyvinylflouride (PVF) film with thermal properties: $\alpha = 0.301$; $\varepsilon = 0.890$. PVF film is used as glazing in solar energy collectors

4.7.2 Manufacturing Source

DuPont

4.7.3 Effects of the Space Environment

4.7.3.1 Atomic Oxygen Reactivity

Clear and white Tedlar films were flown on the Space Shuttle STS-5 (ref. 17) and STS-8 (ref. 18) missions and on LDEF (ref. 1) to measure reaction of surfaces with atomic oxygen in the low Earth orbital environment. Table 4-19 summarizes the atomic oxygen fluence, thickness loss, and reaction efficiency. Samples on STS-5 were exposed to an atomic oxygen sweeping impingement across the surfaces with a total exposure fluence of $9.9x19^{19}$ atoms/cm^2 for 43.5 hrs. Samples on STS-8 were exposed to ram (normal to surface) conditions for 41.75 hrs leading to a total atomic oxygen fluence of 3.5×10^{20} atoms/cm^2. The high fluence on STS-8 was achieved by lowering the vehicle altitude to 225 km and by maintaining the payload bay pointing into the velocity vector, nose to the Earth. The atomic oxygen reactivity for white Tedlar, flown on the LDEF Experiment A0171, is $0.29x10^{-24}$ cm^3/atom. This was calculated from thickness decreases or mass loss. This data is in general agreement with the reaction efficiency calculated for the White Tedlar sample on the STS-5 mission.

Table 4-19. LDEF and Space Shuttle Tedlar Surface Recession and AO Reactivity

Space Shuttle Mission	Material	Thickness μm[(a)]	Thickness Loss μm	Fluence 10^{21} atoms/cm^2	AO Reactivity 10^{-24} cm^3/atom[(b)]
STS-5	Tedlar, Clear	12.7	1.30	0.099	1.3
STS-8	Tedlar, Clear	12.7	11.2	0.350	3.8
STS-5	Tedlar, White	25.4	< 0.50	0.099	< 0.5
LDEF	Tedlar, White			7.150	0.29

(a) Film thickness of 12.7 and 25.4 μm correspond to 0.5 and 1 0 mils, respectively

(b) Most probable error is ±30 to 40%

4.7.3.2 Solar Absorptance

The LEO environment had minimum effects on the solar absorptance of Tedlar film. The changes in the solar absorptance of a white Tedlar film as a function of mission duration on the LDEF satellite are summarized in Table 4-20.[45] The TCSE experiment combined in-space measurements with extensive post-flight analyses of thermal control surfaces to determine the effects of exposure to the low earth orbit space environment. The primary TCSE in-space measurement was hemispherical reflectance as a function of wavelength (100 wavelength steps from 250 to 2500 nm) using a scanning integrating sphere reflectometer. The measurements were repeated at preprogrammed intervals over the mission duration. The secondary measurement used calorimetric methods to calculate solar absorptance and thermal emittance from temperature-versus-time measurements.

Table 4-20. Variations in the Optical Properties of White Tedlar Film Control Coating on LDEF TCSE Experiment

Material	Solar Absorptance (α_s) (a),(b)			
	Pre-flt	In-flt (15 Months)	Post-flt (69 Months)	$\Delta\alpha_s$
White Tedlar Film	.25	.26	.22	-0.03

(a) Mission Duration: The TCSE operated for 582 days before battery depletion. The battery power was finally expended while the sample carousel was being rotated. This left the carousel in a partially closed position. This carousel position caused 35 of the samples to be exposed for the complete LDEF mission (69.2 months), and 14 exposed for only 582 days (19.5 months) and therefore protected from the space environment for the subsequent four years

(b) Space Environmental Exposure: The LDEF was deployed with the TCSE located on the leading edge (row 9) and at the earth end of this row (position A9). In this configuration, the TCSE was facing the ram direction. The LDEF was rotated about the long axis where row 9 was offset from the ram direction by about 8°. The exposure environment for the TCSE was:

Atomic oxygen fluence	8.99×10^{21} atoms/cm^2
Solar UV exposure	11,200 esh
Thermal cycles	3.3×10^4 cycles
Radiation (at surface)	3.0×10^5 rads

4.8 PEEK

4.8.1 Composition

Polyetheretherketone. PEEK is a semi-crystalline thermoplastic with a glass transition of 144°C (291°F) and a melting point of 366°C (690°F). It has a low water absorption of 0.15%.

4.8.2 Manufacturing Source

ICI

4.8.3 Effects of the Space Environment

4.8.3.1 Atomic Oxygen Reactivity

Different atomic oxygen reactivity values, shown in Table 4-21, were generated from both short-term STS-5 (~40 hrs) and LDEF (69 months) exposures. Samples on STS-5 were exposed to an atomic oxygen sweeping impingement across the surfaces with a total exposure fluence of $9.9x19^{19}$ atoms/cm^2 for 43.5 hrs. Samples on the LDEF flight experiment were located 38° of the ram direction and exposed to 7.15×10^{21} atoms/cm^2. The reactivity value of PEEK from Experiment A0171 (ref. 1) was calculated from thickness decreases or mass loss. This difference in atomic oxygen reactivities between STS-5 and LDEF indicates that for PEEK, long-term thickness changes due to atomic oxygen attack in these materials cannot be reliably predicted from short exposure data.

Table 4-21. AO Reactivity for PEEK on LDEF and Space Shuttle

Polymer	AO Reactivity 10^{-24} cm^3/atom		Comments
	LDEF AO171	STS-5	
PEEK	2.3	3.7 ± 1.0	Space Shuttle tested material was thin film with low emittance

4.9 HALAR

4.9.1 Composition

Ethylene-chlorotrifluoroethylene resin is a predominantly 1:1 alternating copolymer, the product of copolymerization of ethylene and chlorotrifluoroethylene.

4.9.2 Manufacturing Source

DuPont

4.9.3 Effects of the Space Environment

4.9.3.1 Atomic Oxygen Reactivity

Halar represents a pure polymer (i.e., polymers containing no components that erode at different rates) which appear to erode linearly with atomic oxygen fluence. Comparable atomic oxygen reactivity values, shown in Table 4-22, were generated from both the short-term Space Shuttle STS-5 mission (~40 hrs) and from LDEF (69 months) exposures. Samples on STS-5 were exposed to an atomic oxygen sweeping impingement across the surfaces with a total exposure fluence of $9.9x19^{19}$ atoms/cm^2 for 43.5 hrs. Samples on the LDEF flight experiment were located 38° of the ram direction and exposed to 7.15×10^{21} atoms/cm^2. The reactivity values of Halar from Experiment A0171 (ref. 1) were calculated from thickness decreases or mass loss. Hence, long-term thickness changes due to atomic oxygen attack in this polymer can be predicted from short exposure data for this pure polymer.

Table 4-22. AO Reactivity for Halar LDEF and Space Shuttle

Polymer	AO Reactivity 10^{-24} cm^3/atom		Comments
	LDEF AO171	STS-5	
Halar	2.1	2.0	See also Brower et al.[46]

4.10 KEVLAR

4.10.1 Composition

Poly Para-Phenyleneterephthalamide (Aramid)

4.10.2 Manufacturing Source

DuPont

4.10.3 Effects of the Space Environment

4.10.3.1 Atomic Oxygen Reactivity

Comparative atomic oxygen reactivity values for Kevlar were generated from both short term space exposures (STS-8) and long term space exposures (LDEF), and the results are summarized in Table 4-23. Samples on STS-8 were exposed to ram (normal to surface) conditions for 41.75 hrs leading to a total atomic oxygen fluence of 3.5×10^{20} atoms/cm^2. The high fluence on STS-8 was achieved by lowering the vehicle altitude to 225 km and by maintaining the payload bay pointing into the velocity vector, nose to the Earth. Kevlar located on LDEF Experiment A0171 (ref. 1) was exposed to an atomic oxygen fluence of 8.99×10^{21} atoms/cm^2 and to 11,200 equivalent sun hours (esh).

Kevlar 29 and 49 reactivity values on A0171 were based on thickness measurements of woven fabrics, and Kevlar 29 data from shuttle flight STS-8 was based on mass loss sustained from a woven tether. These data show a distinct difference in the response between Kevlar 49 and 29. Variability of sample configuration and method of determination of reactivity in the short term STS-8 exposure and A0171 exposure for Kevlar 29 leave considerable uncertainty in the data. Kevlar 49 whose reactivity is higher is a more stressed material than is Kevlar 29, suggesting a connection between stress and atomic oxygen reactivity.

Table 4-23. AO Reactivity for Kevlar on LDEF and Space Shuttle

Kevlar	Reactivity 10^{-24} cm^3/atom		Comments
	LDEF AO171	STS-8	
Kevlar 29 High Toughness	1.5 ± 0.5	1.1 ± 0.2	Shuttle data based on STS-8 tether mass loss
Kevlar 49 High Modulus	4.0	---	

RELATIONSHIPS OF SPACE ENVIRONMENT - MATERIAL INTERACTIONS

REFERENCES

1 A.F. Whitaker, "Atomic Oxygen Effects on LDEF Experiment AO171," LDEF Second Post-Retrieval Symposium, NASA CP-3194, 1993, pp.1125-1135.

2 L.C. Christl, J.C. Gregory and P.N. Peters, "Measurements of Erosion Characteristics for Metal and Polymer Surfaces Using Profilometry," LDEF First Post-Retrieval Symposium, NASA CP 3134, 1991, pp. 723-735.

3 J.C. Gregory; "On the Linearity of Fast Atomic Oxygen Effects," LDEF Material Results for Spacecraft Applications, NASA CP 3257, 1994, pp. 193-198.

4 P.R. Young and W. S. Slemp, "Chemical Characterization of Selected LDEF Polymeric Materials," LDEF First Post-Retrieval Symposium, NASA CP 3134, 1991, pp.687-703.

5 W.S. Slemp et al., "Effects of LDEF Flight Exposure on Selected Polymer Matrix Resin Composite Materials," LDEF First Post-Retrieval Symposium, NASA CP 3134, 1991, pp. 1149-1162.

6 P.R. Young, W.S. Slemp, and A.C. Chang, "LDEF Polymeric Materials: 10 Months vs. 5.8 Years of Exposure," LDEF Second Post-Retrieval Symposium, NASA CP 3194, 1993, pp. 827-844.

7 C.J. Hurley and M. Jones, "Long Duration Exposure Facility M0003-5 Recent Results on Polymeric Films," LDEF Materials Workshop '91, NASA CP-3162, 1992, pp. 417-447.

8 V.L. Bell and G.F. Pezdirtz, J. Sci. Polym. Chem. Ed., 21, 1983, p. 3083.

9 V.L. Bell, J. Polym. Sci. Polym. Chem. Ed., 14, 1976, p. 225.

10 P.R. Young, A.K. St. Clair, and W.S. Slemp, "Response of Selected High Performance Polymer Films to LEO Exposure," Technical Proceedings of the 38th International SAMPE Symposium, May 1993, pp. 664-678.

11 J.T. Visentine, L.G. Leger, J.F. Kuminecz, and I.K. Spiker, "STS-8 Atomic Oxygen Effects Experiment," AIAA Paper 85-0415, Jan. 1985.

12 B.A. Banks, M.J. Mirtich, S.K. Rutledge, and H.K. Nahra, "Protection of Solar Array Blankets from Attack by Low Earth Orbital Atomic Oxygen," 18th IEEE Photovoltaic Specialists Conference, October, 1985

13 D.R. Coulter, R.H. Liang, S.H. Chung, K.O. Smith, and A. Gupta, "O-Atom Degradation Mechanisms of Materials," in Proceedings of the NASA Workshop on Atomic Oxygen Effects, D.E. Brinza, ed., NASA CR-181163 (NASA, Washington, D.C., 1987) p. 42.

[14] L.G. Leger, B. Santos-Mason, J.T. Visentine, and J.F. Kuminecz, in Proceedings of the NASA Workshop on Atomic Oxygen Effects, D.E. Brinza, ed., NASA CR-181163 (NASA, Washington, D.C., 1987) pp. 1-10.

[15] L.G. Leger, I.K. Spiker, J.F. Kuminecz, T.J. Ballentine, and J.T. Visentine, "STS-5 LEO Effects Experiment - Background Description and Thin Film Results," AIAA Paper 83-2631-CP, Nov. 1983.

[16] L.J. Leger, "Oxygen Atom Reaction with Shuttle Materials at Orbital Altitudes - Data and Experiment Status," AIAA Paper 83-0073, January 1983.

[17] L.J. Leger, J.T. Visentine, and J.F. Kuminecz, "Low Earth Orbit Atomic Oxygen Effects on Surfaces," AIAA Paper 84-0548, January 1984.

[18] J.T. Visentine, L.J. Leger, J.F. Kuminecz and I.K. Spiker, "STS-8 Atomic Oxygen Effects Experiment," AIAA Paper 85-0415, 1985.

[19] G.S. Arnold and D.R. Peplinski, "Reaction of Atomic Oxygen with Polyimide Films," AIAA Journal, June 11, 1984.

[20] J.C. Gregory and P.N. Peters, "Measurement of Reaction Rates and Activation Energies of 5 eV Oxygen Atoms with Graphite and Other Solid Surfaces," AIAA Paper 85-0417, Jan. 1985.

[21] A.F. Whitaker, "LEO Atomic Oxygen Effects on Spacecraft Materials," AIAA Paper 83-2632-CP, Oct. 1983.

[22] J.C. Guillaumon and A. Paillous, "Spacecraft Materials. Comparison Between Flight Results Obtained on LDEF and MIR," LDEF Materials Results for Spacecraft Applications, NASA CP-3257, 1994, pp. 485-498.

[23] J.C. Guillaumon et al., "Spacecraft Thermal Control Coatings," LDEF First Post-Retrieval Symposium, NASA CP 3194, 1991, pp. 945-960.

[24] B.A. Banks et al., "Sputtered Coatings for Protection of Spacecraft Polymers," NASA TM-83706, 1984.

[25] B.A Banks, M.J. Mirtich, S.K. Rutledge, and H.K. Nahra, "Protection of Solar Array Blankets from Attack by Low Earth Orbital Atomic Oxygen," Proceedings of the 18th IEEE Photovoltaic Specialists Conference, IEEE, 1985, pp. 381-386.

[26] P.W. Knopf, R.J. Martin, R.E. Damman, and M. McCargo, "Correlation of Laboratory and Flight Data for the Effects of Atomic Oxygen on Polymeric Materials," AIAA 20th Thermophysics Conference, Williamsburg, VA, June 19-21, 1985.

[27] B.A. Banks, M.J. Mirtich, S.K. Rutledge, D.M. Swec, and H.K. Nahra, "Ion Beam Sputter-Deposited Thin Film Coatings for the Protection of Spacecraft Polymers in Low Earth Orbit," NASA TM-87051, paper presented at the 23rd Aerospace Sciences Meeting, Reno, Nevada, January, 1985.

[28] S.K. Rutledge and R.M. Olle, "Durability Evaluation of Photovoltaic Blanket Materials Exposed on LDEF Tray S1003," LDEF First Post-Retrieval Symposium, NASA CP-3134, 1991, pp.1379-1394.

[29] B.A. Banks, S.K. Rutledge and L. Gebauer, "SiO_X Coatings for Atomic Oxygen Protection of Polyimide Kapton in Low Earth Orbit," AIAA Materials Specialist Conference, AIAA-92-2151-CP, Dallas, TX, April, 1992.

[30] B.A. Banks and C. LaMoreaux, "Performance and Properties of Atomic Oxygen Protective Coatings for Polymeric Materials," Proceedings of 24th International SAMPE Technical Conference, October 1992, pp. T165-T173.

[31] C.K. Purvis, H.B. Garrett, A.C. Whittlesey, and N.J. Stevens, "Design Guidelines for Assessing and Controlling Spacecraft Charging Effects," NASA Technical Paper 2361, September 1984.

[32] B.A. Banks, S.K. Rutledge and L. Gebauer, "SiO_X Coatings for Atomic Oxygen Protection of Polyimide Kapton in Low Earth Orbit," AIAA Materials Specialist Conference, AIAA-92-2151-CP, Dallas, TX, April, 1992.

[33] B.A. Banks, B.M. Auer, S.K. Rutledge, and C.M. Hill, "Atomic Oxygen Interaction With Solar Array Blankets at Protective Coating Defect Sites", Fourth Annual Workshop on Space Operations Applications and Research (SOAR 90), R.T. Savely, ed., NASA CP-3103-VOL-2, 1990, pp. 726-732.

[34] B.A. Banks, et al., "The Use of Plasma Ashers and Monte Carlo Modeling for the Projection of Atomic Oxygen Durability of Protected Polymers in Low Earth Orbit," 17th Space Simulation Conference, Baltimore, MD, November 1992.

[35] S.K. Rutledge and R.M. Olle, "Space Station Freedom Solar Array Blanket Coverlay Atomic Oxygen Durability Testing Results," Technical Proceedings of the 38th International SAMPE Symposium and Exhibition, May 1993, pp. 679-693.

[36] A. Freeland, J. Fink, G. Meinke, J. Grieser M. Berendt, and H. Takeo, "Atomic Oxygen Resistant SiOx Coated Kapton For Space Station Freedom and Alternate Coatings.

[37] K. Rousslang, R. Crutcher, and G. Pippin, "Results of Examination of Silvered Teflon From the Long Duration Exposure Facility," LDEF First Post-Retrieval Symposium., NASA CP-3134, 1991, pp.847-859.

[38] F. Levadou and G. Pippin, "Effects of the LDEF Environment on the Ag/FEP Thermal Blankets," LDEF Materials Workshop '91, NASA CP 3162, 1992, pp. 311-344.

[39] J.M. Zweiner et al., "Unusual Material Effects Observed on the Thermal Control Surfaces Experiment (S0069)," LDEF First Post-Retrieval Symposium, NASA CP-3134, 1991, pp. 919-934.

[40] B.A. Banks et al., "Atomic Oxygen Interactions with FEP Teflon and Silicones on LDEF," LDEF First Post-Retrieval Symposium, NASA CP-3134, 1991, pp.801-815.

[41] B.A. Stein, "LDEF Materials: An Overview of the Interim Findings," LDEF Materials Workshop '91, NASA CP 3162, 1992, p. 1-58.

[42] S. Koontz, L. Leger, K. Albyn and J. Cross, "Vacuum Ultraviolet Radiation/Atomic Oxygen Synergism in Materials Reactivity," Journal of Spacecraft and Rockets, vol. 27, no.3, May-June 1990, pp. 346-348.

[43] G. Pippin and R. Crutcher, "LDEF Materials Data Analysis: Representative Examples," LDEF Second Post-Retrieval Symposium, NASA CP-3194, 1993, pp. 1187-1199.

[44] W.S. Slemp, "Ultraviolet Radiation Effects," NASA/SDIO Space Environmental Effects Workshop, NASA CP 3035, 1988, pp. 425-446.

[45] D.R. Wilkes et al., "Initial Materials Evaluation of the Thermal Control Surfaces Experiment (S0069)," LDEF First Post-Retrieval Symposium, NASA CP-3134, 1991, pp. 899-917.

[46] W.E. Brower, Jr., H. Harish and R.A. Bauer, "Effects of Orbital Exposure on Halar During the LDEF Mission," LDEF Materials Workshop '91, NASA CP 3162, 1992, pp.391-415.

5.0 ADHESIVES

5.1 INTRODUCTION

Composite components are frequently assembled into larger structures through adhesive bonding. Finished components that are damaged during assembly or service can also be repaired with bonding techniques. Similar to fiber reinforced composite material adhesive can be tailored to meet specific engineering and manufacturing process requirements. Adhesive-bonding techniques are used only if subsequent disassembly of the subcomponents is unlikely. Adhesives are produced in both film (with and with out scrim perforated and non-perforated) and paste form.. Table 5-1 presents some of the adhesive being used in the aerospace industry.

Heat-resistant epoxy adhesives, which meet the qualifications of Federal Specification MMM-A-132, are used in bonding primary and secondary structural and external metallic aerospace parts and for applications which require similar properties. These adhesives are used in bonding aluminum alloys for long exposures (192 hours) to temperatures from -55°C (-67°F) to 149°C (300°F) and for use in bonding corrosion-resisting steel alloys for long exposures (192 hours) to temperatures from from -55°C (-67°F) to 149°C (300°F) and short exposures (10 minutes) to temperatures from 149°C (300°F) to 260°C (500°F). A two-part epoxy paste adhesive, such as 3M Scotch-Weld EC1614, is recommended for bonding electronic parts to printed wiring boards. These type of adhesives are not recommended for service above 85°C (185°F). Epoxy film adhesives, such as Ablefilm 501, are used for bonding aluminum and magnesium heat sinks to printed wiring boards. These adhesives are not recommended for use in excess of 93°C (200°F).

A one component silicone elastomer adhesive/sealant is used primarily for bonding wires, electronic parts and threaded fasteners on RF assemblies. This adhesive has good adhesion to glass, ceramic, metals and most plastics without a primer. A silicone pressure-sensitive adhesive is used for non-structural bonding of silicone materials to themselves and to other material.

Table 5-1. Adhesives for Bonding Spacecraft Components

Type	Form	Cure Temperature °C (°F)	Max. Use Temperature °C (°F)	Advantages	Disadvantages
Epoxy	Two-part paste	Room or accelerated at 93-178 (200-350)	Generally below 82 (180)	Ease of storage at room temperature; ease of mixing and use; long shelf life; gap filling when filled	Not generally as strong of environmentally resistant as typical heat-cured epoxies
	One-part film	121(250)	To 82 (180)	Covers large areas; bondline thickness control; wide variety of formulas; higher-temperature curing materials; better environmental properties	Store at 18°C (0°F), short shelf life; high temperature cure; brittle and low peel strength
Acrylic	Two-part liquid or pastes	Room to 100 (212)	105 (221)	Fast setting; easy to mix and use; good moisture resistance; tolerant of surface contamination	Strong, objectionable odor; limited pot life
Polyurethane	One or two parts	Room or heat cure		Good peel; good for cryogenic use	Moisture sensitive before and after cure
Silicone	One- and two-part pastes	Room to 260 (500)	To 260 (500)	High peel and impact resistance; easy to use; good heat and moisture resistance	High cost, low strength
Hot melt	One-part	Melt at 190-232 (375-450)	18-171 (120-340)	Rapid application; fast setting; low cost; indefinite shelf life; nontoxic; no mixing	Poor heat resistance; special equipment required; poor creep resistance, low strength; high melt temperature
Bismaleimide	One-part paste or film	>178 (350) and 246 (475) postcure	232 (450)	Structural bonds with bismaleimide composites; higher temperature than epoxies; no volatile; good shelf life	Brittle and low peel; limited formulas available
Polyimide	Thermoplastic liquids; one- and two-part pastes	260 (500) and postcure	204-260 (400-500)	High-temperature resistance; structural strength	High cost; low peel strength; high cure and postcure temperatures; volatiles for some forms
Phenolic-based	One-part films	163-177 (325-350)	To 177 (350)	High-temperature use	Low peel strength

5.2 LDEF SPACE ENVIRONMENTAL EFFECTS

A variety of adhesives and adhesive-like materials were flown on LDEF. These included epoxies and silicones, conformal coatings and potting compounds, and several tapes and transfer films. Six different adhesive systems were evaluated using lap shear specimens exposed to leading and trailing edge experiments. All other materials were used in assembly of the various experiments flown on LDEF. Typically, these adhesives were shielded from exposure to the external spacecraft environment. The various materials are listed in Tables 5-2 through 5-7.

In most experiments, the adhesive were of secondary interest and were only investigated by visual examination and a "Did they fail?" criteria. Because of this role, most adhesive applications had only a few specimens, not enough for statistical data generation. Often, no control samples were kept, and documentation of what was used was occasionally sketchy. With few exceptions, the adhesives performed as expected, that is they held the hardware together. Several experimenters noted that the adhesives had darkened in areas that were exposed to UV. The following sections will document the additional information available on the performance of these materials along with the status of their evaluation.

One of the two primary conclusions of this investigation was that if the material was shielded from direct or indirect exposure to atomic oxygen and/or UV radiation, the materials returned in nominal condition. The only exception to this was outgassing of the material. While the outgassing proved to have no effect on the material's ability to function as design, in several cases it did contribute to the overall molecular contamination that was throughout LDEF. The other primary conclusion was that if the material is exposed to the exterior spacecraft environment, a thorough knowledge of both the microenvironment that the material will see and how that material will interact with that microenvironment is essential.

5.2.1 Silicone Adhesives

A discussion of the performance of the silicone adhesives flown on the LDEF is provided below and summarized in Table 5-2.

Table 5-2. Silicone Adhesives[1,2]

Vendor	Product	Experiment	Substrates	Comments[a]
Dennison	Densil Silicone PSA	A0076		1
Dow Corning	6-1104	A0178	Velcro to Silver Teflon Blankets	1,3
	43-117	A0171		1
	93-500	A0171 M0003-5	Polymeric Film	1 1,3
	RTV 3140	S1001		1
General Electric	RTV 560 + 12% graphite	M0003-5	Silver Teflon to Aluminized Kapton[b]	2,3
	RTV 566	A0076 A0171 S0014		1 1 1
	RTV 567	A0054		1
	RTV 655	A0171		1
	SR 585 PSA	A0076		1

(a) 1 Performed as expected
2 Adhesive failure
3 Discussed in this section

(b) Adherends were Inconel on the back side of the Teflon Blanket and the Kapton side.

RTV DC6-1104 Silicone Adhesive. Dow Corning 6-1104 silicone adhesive was used to bond velcro to the thermal blankets on the sixteen trays that comprised experiment LDEF AO178[3] "A High Resolution Study of Ultra-Heavy Cosmic Ray Nuclei." The bond between the velcro and the blanket performed very well. No degradation of the adhesive was noted. This adhesive was observed to outgas over a long period of time as noted in Table 5-3.

Table 5-3. Outgassing Properties of DC6-1104 Silicone Adhesive.

Material	Conditions	TML	CVCM
DC 6-1104(a)	Post-Flight	0.343	0.033
	Pre-Flight	0.14	0.03

(a) 16 specimens

RTV 560 plus 12% Graphite. RTV 560 is a two part room temperature cure silicone and the graphite is used to increase the electrical conductivity through the bond. This adhesive was used to bond silver Teflon to aluminized Kapton on Experiment M0003-5. The adherend was the Inconel on the backside of the silver Teflon and the Kapton. Four specimens were located on the leading edge and four specimens were located on the trailing edge. All eight lap shear specimens had become debonded during the mission. Visual examination showed that it was an adhesive failure.

DC 93-500. Experiment M0003-5 included the exposure of 32 - 1"x6" polymeric film strips. The ends of all 32 strips were wrapped around and then bonded to the backside of the mounting plate using a clear RTV silicone (though to be Dow Corning DC 93-500). All 64 of these shielded bonds survived the mission intact.

5.2.2 Epoxy Adhesives

A discussion of the performance of the epoxy adhesives flown on the LDEF (Reference 1) is provided below and summarized in Table 5-4.

Table 5-4. Epoxy Adhesives

Vendor	Product	Experiment	Substrate	Comments[a]
Ciba Ceigy	Araldite AV 100/HV 100	A0056,A0139		
	Araldite AV 138/HV 998	A0023,A0056 A0138-1,S1002		
	Araldite AV 138/HW 998	A0138-1		
	Araldite AW 136/HY 994	M0002		
	Araldite AW 2101/HW 2951	A0138-1		
	Araldite MY 750/HY 956	A0056		
Creat	3135/7111	A0180		1, 2A
Emerson & Cuming	Eccobond 55	A0147 S1004		1 1, 2A
	Eccobond 55 + 10% Ecosil	S1002		
	Eccobond 56C	A0076 ,A0171 ,S0069		1
	Eccobond 55C + Ag powder	S1002		
	Eccobond 57C	M0003-5	Silver Teflon to Aluminized Kapton(b)	1, 3
Epoxy Technology	Epo-Tec 301	A0147 S0014		1 1
	Epo-Tec 331	M0004		1
Furane	Epi-Bond 104	S0014		1
Hysol	EA 934	A0180 M0004 S1001		1, 2A 1 1
	EA 956	A0054		1
	EA 9210/109519	M0004		1
	EA 9628	M0003-8	T300/934 Composites	1, 2B, 3
Micromeasurements	MBond 600	M0003	Strain gauges to Composites	1, 2C, 3
Rome & Haas	K-14	A0171		1
	N-580	A0171		1
Shell	Epon 828	A0180 P0003 S1001 M0003-8	Solar Cells to Alumina	1, 2A 1 2D, 3
3M	AF-143	M0003-8	Ti to T300/934 Composite T300/934 to T300/934 Composite	1, 2A, 3
	EC 2216	M0003-3 S1005 Viscous Damper		1, 2A, 3 1 11
Varian	Torrseal	M0006		

(a) 1: Performed as expected
2A Discolored where exposed to UV
2B Decrease in Shear Strength
2C Four out of 40 gauges debonded
2D Bond failed at the solar cell interface

(b) Adherends were Inconel on the back side of the Teflon Blanket and the Kapton side

EC 57C. EC 57C is a two part conductive epoxy. This adhesive was used to bond silver Teflon to aluminized Kapton on Experiment M0003-5. The adherend was the Inconel on the backside of the silver Teflon and the Kapton. One specimen was located on the leading edge and one specimen was on the trailing edge. Both bonds were intact.

Shell Epon 828. Shell Epon 828, an unfilled low viscosity epoxy, was used to bond four solar cells deposited onto an alumina substrate to an aluminum mounting plate as part of the LDEF Experiment M0003. On-orbit photographs showed that all four solar cells were no longer bonded to LDEF. No adhesive remained on the cell mounting plates on the leading edge tray but some remained on the mounting plates located on the trailing edge. This indicated that the bond failed at the solar cell interface, and then the adhesive was attacked by atomic oxygen. Epon 828 was used successfully on other experiments so no conclusions have been drawn as to the failure mode. Possibilities include surface contamination prior to bonding, excessive thermal cycling and high loads due to different thermal expansion coefficients between the solar cell substrate and the aluminum mounting plate.

MBond 600. MBond 600 epoxy was used to bond strain gauges, made by Micromeasurements, to composites, and were cured at 200°F. Four out of 40 strain gauges bonded to composite parts on the LDEF Experiment M0003 debonded. The substrates were carbon-epoxy (1), carbon-polyimide (1), and carbon-polysulfone (2). The strain gauges which were mounted on the shielded side of the specimens saw no atomic oxygen or UV. The specimens saw thermal cycles of -40 to 176°F. The composite substrate had the rough texture of the bleeder cloth used to lay up the specimens. No sanding was done to smooth the surfaces prior to bonding. It is thought that the failures were due to a combination of the thermal cycling and poor surface preparation.

EC 2216 (BMS 5-92) and AF 143 (BMS 5-104). EC 2216, a room temperature epoxy cure system, and AF 143, a 350°F epoxy cure system, were used to prepare epoxy adhesive lap shear specimens, and were flown on the trailing edge of the LDEF satellite. Both titanium-composite and composite-composite adherends were evaluated. Composite adherends were T300/934 carbon/epoxy. The lap shear specimens were mounted such that one surface was facing out towards space. Visual examination of the specimens showed the exposed bondline to have become dark brown when compared to the shielded bondline on the backside of the specimens. Five specimens for each of the two epoxy systems were flown (three Ti-composite and two composite-composite specimens for the AF 143 and two Ti-composite and three composite-composite specimens for the EC 2216). The results of post-flight testing indicated that the shear stress values increased 6.8 to 27.8 percent over preflight values (see Table 5-5 and Figure 5-1).[4]

The preflight specimens were tested in 1978. No control specimens existed. The reason for the increase in strength compared to pre-flight values is speculated to be related to continued cure advancement.

Table 5-5. Adhesive Lap Shear Test Results for Epoxy Adhesives

Adhesive	Adherend	Preflight Shear Stress Psi	Post Flight Shear Stress	# Tested
AF 143 Epoxy (BMS 5-104)	Ti - Composite Composite-Composite	4515 3640	4821 4273	3 2
EC 2216 Epoxy (BMS 5-92)	Ti - Composite Composite-Composite	3750 3145	4479 4019	2 3

Hysol EA 9628. Hysol EA 9628, a 250°F epoxy cure system, was evaluated on LDEF using T300/934 composite lap shear specimens. Three specimens were located on the leading edge and three specimens were on the trailing edge. All six specimens were mounted so one flat surface was facing towards space. The pre-flight measurements were made in 1978 and no control samples existed. Post-flight lap shear testing results indicated a decrease in shear strength for all flight specimens when compared to pre-flight measurements and a decrease for the trailing edge specimens (UV only) compared to the leading edge specimens (UV and atomic oxygen). The reason for the difference between leading and trailing edges is unknown as the vast majority of the adhesive is between the mating surfaces and, therefore, shielded from the detrimental effects of the atomic oxygen and UV.

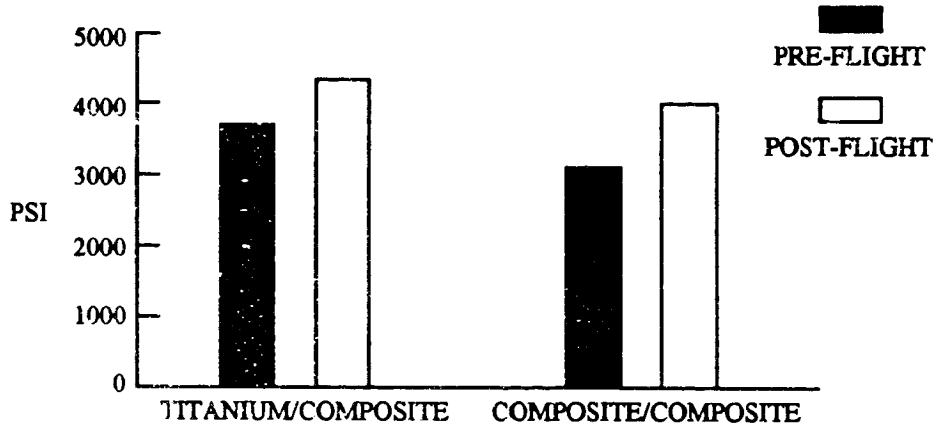

- 3M EC 2216 R.T. cure epoxy adhesive (BMS 5-109)
- Trailing edge

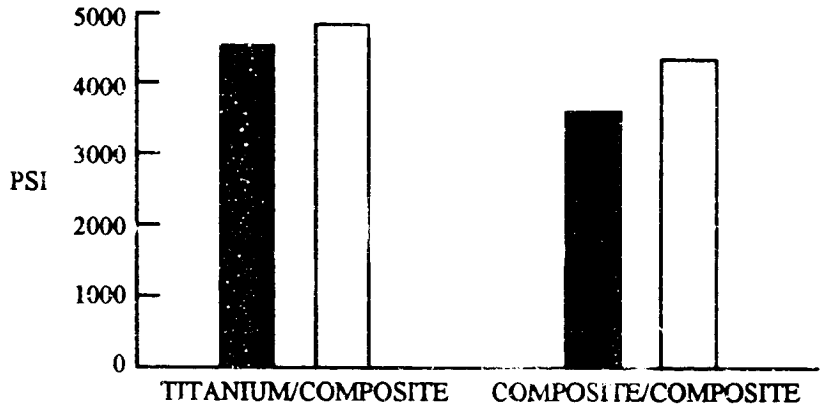

- 3M AF 143 350° F cure epoxy adhesive (BMS 5-109)
- Trailing edge

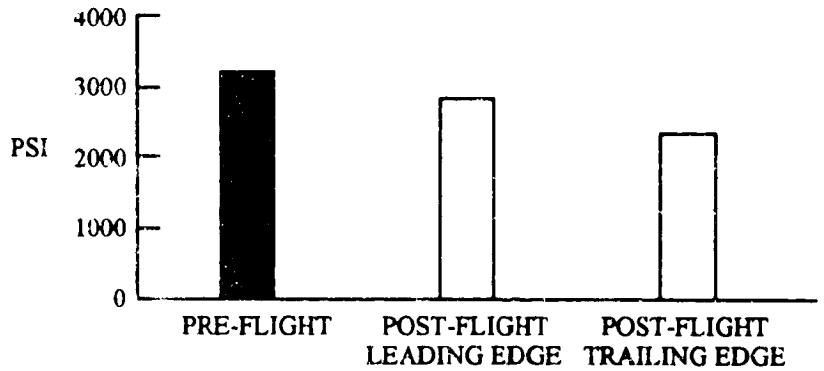

- T300/934 Composite lap shear specimens
- Hysol EA 9628 250° F Cure epoxy tape adhesive

OIM 94.013.118

Figure 5-1. Lap Shear Testing of Epoxy Adhesives Flown on LDEF

5.2.3 Conformal Coatings and Potting Compounds

A summary of the conformal coatings and potting compounds flown on the LDEF (Reference 1) is presented in Table 5-6.

Table 5-6. Conformal Coatings and Potting Compounds

Vendor	Product	Experiment	Comments[a]
Conap	CE-1155	A0201 P0005	1
Emerson & Cuming	Sylgard 182 Sylgard 186	S1001 S1001	1
General Electric	Stycast 1090 Stycast 2850 Stycast 3050	A0056 P0003 S0069	 1 1
	RTV 411/511	S0014	1
Products Research	PR 1535 PR 1568	A0038 A0201	
Thiokol	Solithane 112 Solithane 113	A0178 A0038, A0178, A0187-2, S0001, S1001, S1002	
3M	Scotchcast 280	A0139	

(a) Performed as expected

5.2.4 Adhesive Tapes

A discussion of the performance of the adhesive tapes flown on the LDEF (Reference 1) is presented below and summarized in Table 5-7.

Y966. 3M Y966 is a pressure sensitive acrylic adhesive. This adhesive was used to bond silver Teflon to aluminized Kapton on the LDEF Experiment M0003-5. The adherend was the Inconel on the backside of the silver Teflon and the Kapton. One specimen was located on the leading edge and one specimen was on the trailing edge. Both bonds were intact.

3M tape Y966 was also used in LDEF Experiment A0054. The tape was used to bond vapor deposited aluminum (VDA) Kapton film to the aluminum trays. The tape was tested using a 90 degree peel test similar to ASTM D1000 except that tape width was 0.4 inches. Tape from the leading edge tray had a 4.5 pound peel strength while tape from the trailing edge tray had a 3.5 pound peel strength. A ground control specimen made from a different lot of material had a peel strength of 1.4 pounds. The differences may be attributable to tape variations from batch to batch, additional "cure" of the space exposed tape, and experimental variation. Comparison of the failure mode of the tapes from the leading and trailing edge trays showed significant variation. On the trailing edge tray approximately 75 percent of the adhesive stuck to the VDA Kapton while on the leading edge, 85 percent of the adhesive stuck to the aluminum tray and pulled the VDA from the Kapton film

3M tape Y966 on a silver FEP film was also used to hold the thermal blankets to the tray frame on LDEF experiment M0001. The blankets apparently shrunk in flight causing the blankets to detach from the frame. Portions of the tape were attached to both the blanket and to the frame, having failed across the width of the tape in tension. The film and Y966 remained pliable. Attempts to fail the tape to frame joint in shear were unsuccessful even through a load of roughly 100 pounds was applied to a piece of tape less than a quarter inch wide. The tape was then tested in peel. The Y966 bonded to the aluminum and to the silver on the film well enough to cause delamination of the silver from the film.

3M Y8437 Tape. 3M tape Y8437, a VDA Mylar tape, was used as a coating on the viscous damper shroud, a fiberglass epoxy structure. The tape used on LDEF had a 90 degree peel strength of approximately 7 pounds per inch. After the LDEF tape had been removed, a new piece of the same type of tape (different batch and manufacture time) was applied to the shroud. This tape had a peel strength of only 0.5 pounds per inch. Apparently, the adhesive on the tape sets up with time to give increased adhesion. Space did not appear to have any adverse effect on the tape.

3M Tape 92 ST. 3M tape 92 ST, a Kapton tape with a silicone adhesive, was flown on LDEF Experiment A0054, Space Plasma High Voltage Drainage. Peel strength of tape 0.787 inch wide bonded to aluminum was 1.3 pounds on a leading edge tray, 1.2 pounds on a trailing edge tray, and 0.9 pounds for a fresh, unflown tape.

3M Tape X-1181. 3M tape X-1181, a copper foil tape with a conductive adhesive, was used as grounding straps for the silver/Teflon blankets. The grounding straps were constructed by plying two layers of tape, the adhesives together, with an area of adhesive remaining on each end. A peel test was performed on a sample of the ground strap and compared to a control sample of a freshly constructed strap made from the same roll of tape. All samples had a peel strength of 3.5 to 3.9 pounds per inch. No difference was found between space hardware and ground hardware.

Table 5-7. Tapes and Other Materials

Vendor	Product	Experiment	Substrate	Comments[a]
Emerson & Cuming	Eccoshield PST-C	M0003		
Loctite		A0119 A0138-1		
Mystic Tapes	7355	M0001 P0003		1 1
3M	5	A0139		
3M	56	S0069		1
3M	74	S0069		1
3M	92 ST - Kapton Foil	A0054	Aluminum	1,3
3M	433	A0076		1
3M	X-1181 - Copper Foil	A0178 M0001	Grounding Straps for the Silver Teflon Blankets	1,3
3M	Y966 - Acrylic	A0054 M0003-5 S0069 M0001	VDA Kapton to Al trays Silver Teflon/Kapton Silver Teflon to Trays	1,3 1,3 1 2, 3
3M	Y8437 - VDA Mylar	A0076 Viscous Damper	Fiberglass Epoxy	1 1,3
	Polyester Hot Melt Adhesive	A0133		1

(a) 1: Performed as expected
2: Blankets detached from trays
3: Results discussed in this chapter

REFERENCES

1 H. Dursch, B. Keough, G. Pippin, "Evaluation of Seals, Lubricants, and Adhesives Used on LDEF," LDEF Second Post-Retrieval Symposium, NASA CP 3194, 1993, pp. 1041-1060.

2 Meshishnek, M.J., S.R. Gyetvay, and C.H. Jaggers, "Long Duration Exposure Facility Experiment M0003 Deintegration/Findings and Impacts," LDEF First Post-Retrieval Symposium, NASA CP 3134, 1991, p. 1073-1108.

3 A.F. Whitaker and L.E. Young, "An Overview of the First Results on the Solar Array Materials Passive LDEF Experiment (AO171)," LDEF First Post-Retrieval Symposium, NASA CP 3134, 1991, pp. 1241-1254.

4 P.E. George and S.G. Hill, "Results from Analysis of Boeing Composite Specimens Flown on LDEF Experiment M0003," LDEF Second Post-Flight Symposium, NASA CP 3194, 1993, pp. 1115-1141.

6.0 METALS

6.1 INTRODUCTION

6.1.1 Mechanical and Thermal Properties

Aluminum is the most commonly used metal for the spacecraft structure. It has good strength/weight capability, easy workability in various shapes and forms, and its availability. For lighter weight structures, magnesium is often used. To meet even more stringent requirements for light weight, high stiffness and minimum thermal distortion, advanced materials such as beryllium are used. Titanium and stainless steel are most commonly used for such applications as pressure vessels. A summary of the commonly used metals are provided in Table 6-1. Comparative properties are summarized in Table 6-2.

Table 6- 1. Characteristics of Spacecraft Metals

Material	General Property	Applications	Environment Limitations
Aluminum Alloys • 2024 alloy • 6061 alloy • 7075 alloy	• Light weight; ρ=0.1 lb/in^3 • Corrosion resistance • Excellent electrical and thermal conductivity	• Electronic Housings • Cryogenic • Structural assemblies	• Coatings required for industrial and seacoast exposures
Magnesium Alloys • AZ31B • AZ92A	• Lightweight • High damping • Dimensional stability	• Hardware requiring high strength with transverse toughness	• Susceptible to galvanic corrosion
Titanium Alloys • Ti-6Al-4V • Ti-5Al-2.5Sn • Ti-3Al-2.5V	• Lightweight • Corrosion resistance • High strength-to-weight ratio • Low CTE • High toughness	• Pressure vessels • Cryogenic • Pressurized tubing	• Susceptible to galvanic corrosion and stress-corrosion cracking
Structural Steels Carbon steels • A366, A36 Low Alloy Steels • HSLA, 4130	• Low Cost • High strength	• Used in structural applications where minimum cost materials are desired, and where adequate corrosion resistance can be obtained with paint coatings	
Corrosion Resistant Steel • Type 316L • Type 17-7PH • Type 15-5pH			
Heat Resistant Alloys • A-286 • Inconel 600 • Hastelloy X		• Structural applications in 1200 to 1800°F temperature range	
Refractory Metals • Columbium • Molybdenum • Tantalum • Tungsten		• Structural applications over 1800°F	• Lack of oxidation resistance • Joining and machining problems • Brittle at RT
Copper • Oxygen-Free High Conductivity 102 • Beryllium copper	• High electrical conductivity • High thermal conductivity	• Electrical circuitry wiring • Waveguides • Heat exchangers	
Beryllium	• High elastic modulus • High thermal conductivity • Dimensional stability	• Structural shells • Tubular struts • housings and shafts • heat sinks components	
Kovar • Ni-Co-Fe Alloy	• Low CTE • High toughness	• Glass-to-metal seals in electronics	
Invar • iron base alloy containing 36% Ni	• Low CTE	• Precision instruments • Optical equipment	• Limited to below 400°F use

Table 6- 2. Comparative Mechanical Properties of Spacecraft Metals

Material	Reference	Density lb/in^3	Tensile Strength ksi	Young's Modulus ksi	Elongation %	Coefficient of Thermal Expansion 10^{-6} in/in-°F	Thermal Conductivity Btu/hr-ft-°F
Aluminum Alloy Sheet (2024-T36) Sheet (7075-T6)	Mil-Hndbk-5 Section 3.2.3	0.100	 67 67		 5 7	 11.0 (-200-68°F) 12.1 (0-70°F	 90 (RT) 89 (RT)
Ti6Al-4V solution treated and aged	Mil-Hndbk-5 Section 5.4.3	0.160	160			4.9 (32-212°F)	43 (200°F)
Magnesium (AZ31B-H24)	Mil-Hndbk-5 Section 4.5	0.0642	39		4	12.4 (-200-68°F)	44 (RT)
Steel 17-7PH	Mil-Hndbk-5 Section 3.2.3	0.280	240			6.1 (70-200°F)	8.6 (200°F)
Inconel 600 nickel alloy	Mil-Hndbk-5 Section 3.2.3	0.304	80		30	6.0 (-250-70°F)	8 (70°F)
Invar 36 annealed	Mil-Hndbk-5 Section 3.2.3	0.291	85			0.65 (86-212°F)	9.2 (200°F)
Kovar annealed	Mil-Hndbk-5 Section 3.2.3	0.302	75	20		4.9 (86-752°F)	9.6 (86°F)
Beryllium (Be-38% Al)	Mil-Hndbk-5 Section 3.2.3	0.660	70	44	10	4.8 (-300-70°F)	103 (70°F)
Copper OFHC	Mil-Hndbk-5 Section 3.2.3	0.323	32			9.4 (68-212°F)	226 (61°F)

6.2 LEO ENVIRONMENTAL EFFECTS ON METALS

6.2.1 Silver

A considerable number of silver specimens, including interconnects, disk-type, and vapor-deposited films, were flown on STS-8 to determine quantitative effects resulting from exposure to the orbital atomic oxygen environment. The STS-8 Atomic Oxygen Effects Experiment provided an atomic oxygen fluence of 3.5×10^{20} atoms/cm^2 incident perpendicular to the experiment material surfaces over a period of 41.17 hr at 120 nautical miles. These silver specimens are identified in Table 6-3, and their exposure configurations are noted.[1]

Silver is utilized as solar cell interconnect material. The silver-plated and clad Invar specimens are candidate interconnect substitutes. Lead/tin solder and chromate conversion coating were evaluated for their effectiveness in protecting the silver. The vapor-deposited films were designed for two purposes: (1) to evaluate the atomic oxygen fluence/cosine law degradation dependency in silver, and (2) to assess as far as possible the concept of utilizing the resistance changes induced in a thin film due to atomic oxygen exposure as an environmental monitor.

Table 6- 3. STS-8 Property Data On Silver

Silver Types/Configurations	Exposure Conditions
Cold-rolled (solar cell-interconnects)	(1) Atomic oxygen (AO) normal, and at 45° angle to specimens, temperature controlled at 99 ±8°C (210 ±15°F), 61 ±8°C (142±15°F) (2) AO normal to specimens, temperature uncontrolled ~ 10°C (50°F)
Silver-plated and clad Invar. Pb/Sn solder-clad silver	AO from reflected oxygen only, temperature uncontrolled
Bare and chromate-conversion-coated silver	AO normal to specimen, temperature uncontrolled
Vapor-deposited films, 0.85 μm, 1.70 μm, 3.05 μm	AO incident to films normal, at 45° angle and at 65° angle, temperature uncontrolled

All exposed silver specimens were affected, including those which had no direct exposure but were subject only to reflected atomic oxygen atoms. However, the attack was less severe on those specimens with no direct exposure than on the directly exposed surfaces. The exposed surfaces were converted through oxidation processes to gray/black/brown loose scale or to thin interference films depending on the temperature of the specimen. As expected according to established oxidation theory, considerably more silver was converted to scale on the higher temperature surfaces. The vapor-deposited silver films ranging in thickness from 0.8 to 3.0 μm showed scale formation of definite area and thickness dependent on the initial film thickness.

An activation energy of 0.61±0.9 ev over the temperatures range from +10°C to 99°C (+50° to +210°F) was generated for the conversion to scale of the cold-rolled silver interconnect material. Although the thickness of converted silver at the high temperature varied by about a factor of 2, the variation from the high temperature to the low was as great as a factor of 26, thereby providing well-resolved data. The lead/tin solder protected the low temperature silver, as would be expected since it was thick (~2.4μm) and nonreactive, whereas the chromate conversion coating failed, probably because it was thin and porous. No strong dependency of the conversion process was noted on total incident atomic oxygen, and no conclusion could be reached concerning the role of the angle of incidence of atomic oxygen.

Following silver, the most reactive metal examined was copper with a measurable mass increase. When initial examinations of the metals revealed little reactivity, more sensitive evaluation techniques were attempted, and in many instances the sample preparation was not adequate for good resolutions under these evaluations. These metals generally showed low reactivity, possibly as a result of: (1) low exposure temperature, (2) low oxygen flux, and (3) limited exposure time.

6.2.2 Aluminum

Bare aluminum and anodized aluminum clamps were flown on LDEF to determine quantitative effects resulting from exposure to the orbital atomic oxygen environment and solar ultraviolet radiation.[2] Comparison of the thermal-optical properties indicated minimum property changes caused by flight exposure as discussed below and summarized in Table 6-4.

Table 6- 4. Thermal-Optical Properties of Bare and Anodized Aluminum Clamps

Sample	LDEF Location	Exposure	Surface Treatment	Average Solar Absorptance	Average Thermal Emittance
C03-5	Trailing Edge Back Surface	No Direct Exposure	Bare	0.71	0.13
C03-5	Trailing Edge	2.66×10^3 AO/cm^2 11,00 ESH Solar	Bare	0.74	0.08
C09-7	Leading Edge Back Surface	No Direct Exposure	Bare	0.72	0.09
C09-7	Leading Edge	9.02×10^{21} AO/cm^2 11,200 ESH Solar	Bare	0.69	0.06
Control#4	Ground Control	No Space Exposure	CAA	0.32	0.18
C03-6	Trailing Edge	2.66×10^3 AO/cm^2 11,00 ESH Solar	CAA	0.35	0.14
C09-2	Leading Edge	9.02×10^{21} AO/cm^2 11,200 ESH Solar	CAA	0.33	0.17

The retaining clamps on LDEF Experiment Trays C9 and C3 offered an opportunity to compare the behavior of bare and chromic acid anodized (CAA) aluminum when exposed to space in Low-Earth-orbit. The four corner clamps that held this tray in place on the vehicle are bare 6061-T6 aluminum. The remaining four clamps on Tray C9 are anodized aluminum. Two bare aluminum clamps (C09-7, leading edge and C03-5, trailing edge) and two CAA clamps (C09-2, leading edge and C03-6, trailing edge) were selected for laboratory testing of post-flight measurements and comparison of thermal-optical properties. The thermal-optical properties of exposed surfaces of CAA flight clamps were compared with those of a ground control clamp (data for control clamp #4 were taken after the clamp was removed from storage). The thermal-optical properties of exposed surfaces of the bare aluminum flight clamps were compared with those of the unexposed surfaces (back surfaces) of the same clamps. Solar absorptance and thermal emittance properties are shown in Table 6-4 along with the solar radiation and atomic oxygen exposure data for these clamps. Solar absorptance was measured in accordance with ASTM E903-82 and ASTM E424-17. Thermal emittance was measured in accordance with ASTM E408-71.

Flight exposure caused little change in the thermal-optical properties of either bare or CAA clamp surfaces. The thermal-optical properties of bare clamp surfaces and CAA clamp surface differ significantly. Average solar absorptance for bare flight clamp surfaces (leading edge and trailing edge) is 210 percent that of CAA flight clamp surfaces. Average thermal emittance for bare flight clamp surfaces (leading edge and trailing edge) is 45 percent that of CAA flight clamp surfaces.

6.2.2 Copper

Thin films and solid forms of copper samples were flown on the leading edge C9 tray of the LDEF experiment A0114 with matching trailing edge samples in the C3 tray.[3,4] Thin films of copper were prepared at the Space Sciences Laboratory, NASA Marshall Space Flight Center. Substrates were fused silica optical flats, obtained from Acton Research Corporation. These were coated with ca. 69±1 nm copper using an RF sputtering system. The solid copper sample was cut from OFHC copper rod of one inch diameter and polished with 1 μm diamond powder.

Leading Edge Samples. X-ray diffraction (XRD) analysis of the leading edge 68 nm thin film detected a mixture of mainly Cu_2O and metallic Cu with some CuO being present. These surfaces on row 9 received a total fluence of 8.72×10^{21} oxygen atoms per s re cm. This result, combined with thickness measurement of the exposed region of 105.3 ±1 nm using a stylus profilometry technique,[5] indicated that 55 nm of Cu were oxidized to Cu_2O during the full LDEF exposure. ESCA analysis of both the thin film and the bulk copper verified the conversion of metallic Cu to Cu_2O.

Trailing Edge Samples. The trailing C3 samples showed little effect of atomic oxygen.

6.2.3 Refractory Metals For Rocket Nozzles

Table 6-5 lists six classes of refractory metals used for rocket nozzles along with their melting temperatures. Table 6-6 lists the expected natural environmental effects on these refractory metals. No effects are expected except for object (micrometeoroids and space debris) impacts (which can damage a rocket nozzle, especially when the rocket is firing) and atomic oxygen erosion and glow. The geomagnetic field will only have a small effect because the rocket nozzles are heated beyond the Curie temperatures of any ferromagnetic material present when they are operating.[6]

Table 6- 5. Properties of Refractory Metals

Material	Melt Temperature (°C)
Haynes (Co)	~1,495
Inconels (Ni)	~1,453
Nb Alloys	~2,468
Mo Alloys	~2,610
Ta Alloys	~2,996
W Alloys	~3,387

Table 6- 6. Natural Environmental Effects on Refractory Metals

Environment / Material	UV	Magnetic Field	Vacuum	Van Allen Belts	Objects	Iono-sphere	Hot Plasma	Gases
Haynes (Co)	-	Torques	-	-	Possible Damage	-	-	Erosion, Glow
INCONELS (Ni)	-	Torques	-	-	Possible Damage	-	-	Erosion, Glow
Nb Alloys	-	-	-	-	Possible Damage	-	-	Erosion, Glow
Mo Alloys	-	-	-	-	Possible Damage	-	-	Erosion, Glow
Ta Alloys	-	-	-	-	Possible Damage	-	-	Erosion, Glow
W Alloys	-	-	-	-	Possible Damage	-	-	Erosion, Glow
Primary Concern: Possible Damage Due to Debris Object Impact in LEO								

6.2.4 Metals on the LDEF Mission

6.2.4.1 Experiment AO171

Several metal samples were flown on the LDEF A0171 Experiment.[7] These consisted of various copper and silver ribbon materials, miscellaneous metallic specimens, and 1" diameter bulk metals including materials which readily oxidize and which resist oxidation in the atomic oxygen environment. A series of alloys containing various ratios of aluminum, chromium and nickel in the as-received and preoxidized condition were also flown. Cold rolled silver ribbon both thermally heat sunk to the experiment base and thermally isolated configured with and without a stress loop completed the metal samples reported in this section.

All the metals reported gained weight as a result of being exposed to orbital atomic oxygen. Reactivity values based on linear effects were reported for these materials even though it is known that metals oxidize nonlinearly. This was done in order to give a comparative measure of the observed effects. With the exception of silver, the magnitude of reactivity numbers was less than 1 x 10^{-26} cm^3/atom for the conditions experienced on AO171 (see Table 6-7). Accommodation numbers presented are given in terms of atomic oxygen atoms reacted ratioed to the incident atoms. These calculations based on the mass increase show that, with the exception of stressed, thermally isolated silver, less than 10 atoms per 10^4 incident are reacted. The basic assumption for these accommodation numbers is that the mass increase resulted from the formation of the most thermodynamically favorable oxide. The presence of some of these oxides is yet to be confirmed. The reactivity and accommodation values for the cold rolled, stressed, and thermally isolated silver are an order of magnitude greater than that of the same material which had no additionally applied stares and was heat sunk to the structure. These results suggest that the atomic oxygen effects are more dependent on temperature and microstructure than on total incident atomic oxygen.

Table 6- 7. LDEF AO171 Metals Atomic Oxygen Erosion Data

METAL	AO Reactivity (10^{-26} cm^3 /atom)	Accommodation of AO per 10^4 Incident Atoms	Comments
Copper	0.87	3.6	Accommodation strongly dependent on temperature and stress, numbers are tentative pending confirmation of oxide identity.
Molybdenum	0.14	2.8	
Tungsten	0.044	~1.0	
HOS 875	0.29	2.5	
Pre-Ox HOS 875	TBD	TBD	
Tophet 30	0.55	5.0	
Ni-Cr-Al-Zr Alloy	TBD	TBD	
Pre-Ox Ni-Cr-Al-Zr	---	---	
Tantalum	0.60	8.3	
Titanium 75A	0.39	4.4	
Mg AZ31B	0.45	2.0	
Niobium	0.14	2.0	
Silver disk-fine grain	2.9	8.4	
Silver-cold rolled ribbon in stress loop	27.5	80.0	

6.2.4.2 Ion Beam Textured Surfaces Experiment (IBEX)

Titanium, copper, Inconel, and stainless steel metals were textured[8] using Ta as a seed material with an ion source of 1500 eV argon ions to obtain high thermal emittance surfaces. These samples were part of the LDEF Experiment S1003 located in Row 6. These samples were exposed to 6500 ESH as well as 33,700 thermal cycles.

Results of optical property measurements, shown in Table 6-8, indicated no changes in solar absorptance for all the metals. Table 6-8 shows an increase in thermal emittance only for textured copper (from .50 to .69). This change was probably due to an oxide formation on the surface, which could cause an increase in thermal emittance. SEM analysis indicated no change in surface morphology for the ion beam textured materials flown on LDEF.

Table 6- 8. Ion Beam Textured High Absorptance Metals Flown on LDEF.

Sample	Solar Absorptance		Thermal Emittance (325 K)	
	Pre-flight 1982	Post-flight 1990	Pre-flight 1982	Post-flight 1990
Ti (6% Al, 4%V)	.88	.88	.21	.18
Cu	.94	.94	.50	.69
Inconel	.92	.92	.25	.25
Stainless Steel type 304	.91	.93	.26	.28

6.2.4.3 LDEF Metal Samples

The surface films of six different metals (Al, Cu, Ni, Ta, W, and Zr) exposed to the space environment on the LDEF were studied by variable angle spectroscopic ellipsometry[9]. Thickness and surface composition measurements, carried out on portions of each sample exposed and shielded to the space environment, are summarized in Table 6-9. The analysis revealed that exposed portions of the Cu, Ni, Ta and Zr samples are covered with porous oxide films ranging in thickness from 500 to 1000 Å. The 410 Å thick film of Al_2O_3 on the exposed Al sample is practically free of voids. Except for Cu, the shielded portions of these metals are covered by thin non-porous oxide films characteristic of exposure to air. The shielded part of the Cu sample has a much thicker porous coating of Cu_2O. The tungsten data cold not be analyzed.

Table 6- 9. Thickness and Surface Composition of LDEF Metals

Sample	LDEF Location	Space Conditions	Oxide	Thickness of Oxide	Proportion of Voids
Al	D3 Trailing Edge	1.32×10^{17} atoms/cm^2 11,100 esh	Al_2O_3	395	0
		Shielded	Al_2O_3	68	0
Cu	G12 Earth End	3.33×10^{20} atoms/cm^2 4,500 esh	Cu_2O	1039	0.71
		Shielded	Cu_2O	449	0.69
Ni	D3 Trailing Edge	1.32×10^{17} atoms/cm^2 11,100 esh	NiO	687	0.65
		Shielded	NiO	60	0
Tantalum	D9 Leading Edge	8.99×10^{21} atoms/cm^2 11,200 esh	Ta_2O_5	505	0.73
		Shielded	Ta_2O_5	31.5	0
Tungsten	D9 Leading Edge	8.99×10^{21} atoms/cm^2 11,200 esh	?	not known	not known
		Shielded	?	not known	not known
Zirconium	D9 Leading Edge	8.99×10^{21} atoms/cm^2 11,200 esh	ZrO_2	688	0.81
		Shielded	ZrO_2	42	0

6.2.5 Metals on the Space Shuttle Missions

6.2.5.1 STS-8 Mission

The STS-8 Atomic Oxygen Effects Experiment, a follow-on experiment to that flown on STS-5, was configured to expose a large number of disk-type material specimens for reactivity assessment.[10] The experiment provided an atomic oxygen fluence of 3.5×10^{20} atoms/cm^2 incident perpendicular to the experiment material surfaces over a period of 41.17 hr at 120 n. mi.

Ten metals were exposed on STS-8: silver, copper, lead, magnesium, molybdenum, nickel, platinum, tungsten, HOS-875 (FeCrAl alloy) in the bare and preoxidized condition, and Tophet-30 (NiCr alloy) in the bare and preoxidized condition. These metals are of interest for a variety of reasons. Silver is utilized as solar cell interconnect material on the solar array. High electrical conductivity is required to maintain adequate spacecraft power. Copper and molybdenum are alternate solar cell interconnect materials, and, further, all of these metals have well-known high temperature oxidation characteristics. Under high temperature oxidation conditions, the HOS-875 and the Tophet-30 form their own protective oxide films of Al_2O_3 and Cr_2O_3, respectively. With the exception of some of the silver specimens, these metals were exposed on surfaces that were in the low temperature region, estimated to be about 50°F. The data regarding the results of the metals' exposure are shown in Table 6-10.

Table 6- 10. STS-8 Metals Data Summary

Metal	Exposure Results
Silver	Well-defined visual changes, severe oxidation on all specimens, dilute penetration of oxygen in bulk, increases in refractive index, and decrease in electrical conductivity.
Copper	Visual difference, tarnished appearance, mass increase: 0.5 mg/cm^2 or 1.4×10^{-23} mg/atom, dilute penetration of oxygen into bulk, increased oxidation to CuO.
Lead	No visual change, no mass change
Magnesium	No visual change, no mass change.
Molybdenum	No visual change, no mass change, dilute penetration of oxygen into bulk, increased oxidation to MoO_3.
Nickel	No visual change, no mass change.
Platinum	No visual change, no mass change.
Tungsten	No visual change, no mass change, decrease in refractive index, no trend in absorption coefficient.
HOS-875 -Bare - Preoxidized	No visual change, no mass change, no other changes discernible by SEM/x-ray diffraction.
Tophet 30 -Bare - Preoxidized	No visual change, no mass change, no other changes discernible by SEM/x-ray diffraction.

6.2.5.2 STS-41-G Mission

The effects of the space environment on metals which have applications to space telescope were measured by ellipsometry before and after flight.[11] The metals included Cu, Ag, Au, Ni, Cr, Al, Pt, and Pd on flight 41-G (STS-17). Optical constant data consisting of refractive index n and absorption coefficient k were obtained for each metal specimens and their control. The specimens were evaporated layers of silver, gold, palladium, platinum, nickel, copper, aluminum, and chromium on metal substrates. The nominal thickness of the layers ranged from 500 to 5000 Å.

The results showed that by far the greatest changes which can be attributed to exposure to the space environment occurred for silver. The changes were very large for both the refractive index and the absorption coefficient. Changes in both optical constants due to space exposure were found also for palladium, copper, and chromium, although the effects are not as large as for silver, and likewise (but to a somewhat lesser extent) in gold and aluminum. There was also a change in the refractive index of platinum, but this was of the same order as the sample to sample variation in the absorption coefficient of platinum prior to flight.

6.3 DESIGN CONSIDERATIONS FOR SPACE ENVIRONMENTAL EFFECTS

A number of observations concerning the effects of the LEO environment on metals can be summarized as follows;

- Metals are highly variable in their response to the LEO environment.
- Gold and platinum are nonreactive.
- Osmium, which forms a volatile oxide, is rapidly eroded.
- Silver, which forms a nonprotective oxide, is rapidly eroded.
- Other metals (Al, Cu, Ga, Ge, Ir, Mo, Ni, Ti, and Sn) show some level of reaction unless protected.
- Contamination is a major contributor to exposure effects on metal surfaces.

Table 6-11 provides a summary of the space environment effects on metals.

Table 6- 11. Summary of Performance of Metals in the Space Environment

Observations	Principal Exposures	Engineering Significance
Ram-exposed copper straps darkened	Function of AO dose and possibly temperature	Surface oxidation, copper would survive as interconnect material, but possibly operate at a higher temperature
Bare 6061-T6 aluminum discolored relative to anodized aluminum	High AO exposure	Anodized aluminum maintained desires optical properties
Thin aluminum film on aluminized Mylar and Kapton disintegrated after Kapton and Mylar eroded away	High AO exposure	Significant particulate contamination

Most of the data related to the behavior of materials in the atomic oxygen environment involves the rates of surface erosion. Most of the data obtained are reported in terms of a parameter used to quantify the susceptibility of a material to erosion by atomic oxygen, known as the "erosion yield" or the "reaction efficiency" (R_e). This parameter is defined as

$$R_e = \frac{\text{Volume of Material Lost}}{\text{Total No. of Incident O Atoms}} \quad (cm^3/atom)$$

R_e can be calculated using the relation:

$$R_e = \frac{\Delta m/\rho}{\phi t A}$$

where Δm = mass loss (g)

ρ = material density (g/cm^3)

ϕ = incident AO Flux ($atoms/cm^2$-s)

t = exposure time (s)

A = exposed surface area (cm^2)

Note that the product $\phi t = F$, where F is the total fluence of oxygen atoms which is obtained from atmospheric models, spacecraft velocity, and exposure history.

Consequently, the reaction efficiencies derived from previous Space Shuttle flights (see below) can be used in computing surface recession for materials subject to the orbital environment with the following equation:

$$\Delta x = F_T \times R_e$$

where F_T is accumulated fluence, R_e is reaction efficiency, and Δx is surface recession.

A summary of data obtained from space flight experiments conducted to date are shown quantitatively in Table 6-12.[12] Metals, except for silver and osmium, do not show macroscopic changes. Microscopic changes have, however, been observed and should be investigated for systems very sensitive to surface properties. Silver and osmium react rapidly and are generally considered unacceptable for use in uncoated applications. Copper forms a protective oxide which adversely affects optical and thermal properties.

The major limitation of the current reaction rate data base is that atomic oxygen fluence to which the recession rates are normalized are not precisely known. Atomic oxygen number densities used to compute fluence for previous space flight missions were obtained using thermospheric models to predict atmospheric constituent concentrations as functions of altitude, time of year, Earth latitude and longitude, local solar time, and solar activity conditions. Typically, errors of as much as 25 percent or more can be expected for the density estimations, and since they are used to compute fluence, these errors also appear in the surface recession rates for satellite materials. To improve the database, ambient density measurements need to be made simultaneously with recession measurements during future flight experiments.

Table 6- 12. AO Reaction Efficiencies of Selected Metals in Low Earth Orbit

Material	Reaction Efficiency, $x10^{-24}$ cm^3/atom	Reference
Aluminum (150 Å)	0	13
Chromium (123 Å)	partially eroded	14
Copper (bulk)	0	15
Copper (1,000 Å) on sapphire	0.007	16 ,17
Copper (1,000 Å)	0.0064	14
Gold (bulk)	0	15
Gold	appears resistant	18
Iridium Film	0.0007	15
Lead	0	13,10
Magnesium	0	13,10
Molybdenum (1,000 Å)	0.0056	19
Molybdenum (1,000 Å)	0.006	17,20
Molybdenum	0	10,13
Nichrome (100Å)	0	13
Nickel film	0	15
Nickel	0	21 ,10
Niobium film	0	15,13
Osmium	0.026	22
Osmium	heavily attacked	18
Osmium (bulk)	0.314	15
Platinum	0	10,13
Platinum	appears resistant	18
Platinum film	0	15
Silver	10.5	23
Tantalum	appears resistant	18
Tungsten	0	10,21

REFERENCES

1 A.F. Whitaker, S.A. Little, R.J. Harwell, D.B. Griner, and R.F. DeHaye, "Orbital Atomic Oxygen Effects on Thermal Control and Optical Materials: STS-8 Results," NASA TM 100459, Atomic Oxygen Effects Measurements for Shuttle Missions STS-8 and 41-G, Volume I, pp. 4-1 to 4-11.

2 H.G. Pippin and R.J. Bourassa, "Performance of Metals Flown on the Long Duration Exposure Facility," NASA CR xxxx.

3 P.N. Peters, J.C. Gregory, L.C. Christl and G.N. Raikar, "Effects on LDEF Exposed Copper Film and Bulk," LDEF First Post-Retrieval Symposium, NASA CP-3134, 1991, pp. 755-762.

4 G.N. Raikar, J.C. Gregory, Ligia C. Christl, and P.N. Peters, "The Interaction of Atomic Oxygen with Copper: An XPS, AES, XRD, Optical Transmission and Stylus Profilometry Study," LDEF Second Post-Retrieval Symposium, NASA CP 3194, 1993, pp. 1169-1186.

5 L.C. Christl and J.C. Gregory, "Measurements of Erosion Characteristics for Metal and Polymer Surfaces Using Profilometry," LDEF First Post-Retrieval Symposium, NASA CP-3134, 1991, pp. 723-735.

6 J.W. Haffner et al., "Natural Environmental Effects on SDI Spacecraft Surface Materials," Rockwell International, Report No. AFGL-TR-89-0084, Air Force Geophysical Laboratory, May 20, 1989.

7 A.F. Whitaker et al., "Atomic Oxygen Effects on LDEF Experiment A0171," LDEF Second Post-Retrieval Symposium, NASA CP 3194, 1993, pp. 1125-1134.

8 M.J. Mirtich and S.K. Rutledge, "Ion Beam Textured and Coated Surfaces Experiment (IBEX)," LDEF First Post-Retrieval Symposium, NASA CP-3134, 1991, pp. 989-1004.

9 W. Franzen, J.S. Brodkin, L.C. Sengupta, and P.L. Sagalyn, "Ellipsometric Study of Oxide Films Formed on LDEF Metal Samples," LDEF First Post-Retrieval Symposium, NASA CP-3134, 1991, pp. 1005-1021.

10 A.F. Whitaker, S.A. Little, R.J. Harwell, D.B. Griner, and R.F. DeHaye, "Orbital Atomic Oxygen Effects on Thermal Control and Optical Materials: STS-8 Results," AIAA Paper 85-01415 presented at the 23rd Aerospace Sciences Meeting, January 14-17, 1985.

[11] A.T. Fromhold, Jr. and K. Daneshvar, "Reaction of Metals in Lower Earth Orbit During Space Shuttle Flight 41-G," NASA TM 100459, Atomic Oxygen Effects Measurements for Shuttle Missions STS-8 and 41-G, Volume I, pp. 9-1 to 9-6.

[12] J.T. Visentine and A.F. Whitaker, "Material Selection Guidelines to Limit Atomic Oxygen Effects on Spacecraft Surfaces," NASA TM-100351, February 1989.

[13] Marshall Space Flight Center

[14] Lewis Research Center

[15] J.C. Gregory, "Interaction of Hyperthermal Atoms on Surfaces in Orbit: The University of Alabama Experiment," Proceedings of the NASA Workshop on Atomic Oxygen Effect, November 1986, p. 31.

[16] L.J. Leger, I.K. Spiker, J.F. Kuminecz, T.J. Ballentine, and J.T. Visentine, "STS Flight 5 LEO Effects Experiment - Background Description and Thin Film Results," AIAA-83-2631-CP, October 1983.

[17] Jet Propulsion Laboratory

[18] Goddard Space Flight Center

[19] B.A. Banks, M.J. Mirtich, S.K. Rutledge, and H.K. Nahra, "Protection of Solar Array Blankets from Attack by Low Earth Orbital Atomic Oxygen," 18th IEEE Photovoltaic Specialists Conference, October 1985.

[20] L.J. Leger, I.K. Spiker, J.F. Kuminecz, T.J. Ballentine, and J.T. Visentine, "STS Flight 5 LEO Effects Experiment - Background Description and Thin Film Results," AIAA-83-2631-CP, October 1983.

[21] University of Alabama at Huntsville

[22] L.G. Leger, B. Santos-Mason, J.T. Visentine, and J.F. Kumineca, "Review of LEO Flight Experiments," Proceedings on the NASA Workshop on Atomic Oxygen Effects, November 1986, p. 6.

[23] C.K. Purvis, D.C. Ferguson, D.B. Snyder, N.T. Grier, J.V. Staskus and J.C. Roche, "Environmental Interaction Considerations for Space Station and Solar Array Design," December 1986.

7.0 CERAMICS

Approximately thirty silver and aluminum solar reflectors with thin coatings of various glassy ceramics were flown on the LDEF A0171 experiment.[1] A large group of these reflector samples were configured with one-half of the sample exposed and the other half covered. Small decreases in reflectivity were noted in these samples but no contamination was present to account for these reflectivity decreases.

7.1 ATOMIC OXYGEN EFFECTS

Precision angstrometer traces were made on all the coated silver and aluminum solar reflectors samples, and it was noted that a decrease in film height occurred in the exposed areas. Selected samples were examined with low energy Rutherford backscattering which revealed that a densification of the film materials had occurred in the exposed region. A conversion of SiO to SiO_2 was identified. The results of these measurements are presented below under atomic oxygen erosion effects. However, several factors can bring about the densification of these materials and it remains to be proven that the effects noted rare the result of atomic oxygen attack.

Table 7-1 provides a listing of these effects for the various solar reflectors. Decreases in thickness of these materials range up to 160 angstroms. For applications of these materials where the total coating thickness is 1000 to 1300 angstroms, the percentage change is considerable and the effect can be substantial for space optics. Reactivity values for these materials rare based on the assumption that the observed effects result from atomic oxygen attack range from 0.4 to 2.3 x 10^{-28} cm^3/atom.

Table 7-1. Property Changes in A0171 Glassy Ceramics

Coating/Solar Reflector	Change in Solar Reflectance (%)	Decrease in Film Thickness (Å)
SiO_2/Ag	-<1	40
SiO_2/Al	-<1	50
SiO-SiO_2/Enhanced Al	-2	125
SiO/Al	-1.5	150
MgF_2-Sapphire/Enhanced Al	-1.5	25
MgF_2-Sapphire/Ag	-5 to -10	150
Dielectric/Ag Alloy	-1 to -5	160
No changes observed for shuttle flight exposures. On LDEF SiO-SiO_2, increase in film density noted. Defect observed on all reflectors except SiO_2/Al, small decreases in Rs measured. Reactivity ranges from 0.4 to 2.3 x 10^{-28} cm^3/atom for these materials.		

REFERENCES

[1] A.F. Whitaker et al., "Atomic Oxygen Effects on LDEF Experiment A0171," LDEF Second Post-Retrieval Symposium, NASA CP 3194, pp. 1125-1134.

8.0 PROTECTIVE COATINGS

8.1 SILICON OXIDE (SiO_X)

8.1.1 Introduction

Polycrystalline ceramic films, such as SiO_x (where $1.9 < X < 2.0$), SiO_2, fluoropolymer-filled SiO_2, and Al_2O_3 (see below) have been demonstrated in both ground and space tests (i.e., LDEF) to be effective in protecting polyimide Kapton from oxidation by LEO atomic oxygen.[1,2] These films are often used as an environmental protective coating due to its resistant to atomic oxygen exposure, and provides improved radiative properties during space environment exposure.

8.1.2 Source

Manufacturer: Sheldahl Inc.
Northfield, MN 55057
Tel: 507/663-8000

Sheldahl's SiO_x coating is applied in a roll-to-roll R.F. sputtering process. The vacuum chamber is a 5,000 liter stainless steel vessel with a thirty-two inch diffusion pump. The SiO_x is sputtered from two 5-in x 30-in magnetron cathodes with SiO_2 targets. Power is supplied by a pair of five kilowatt Radio Frequency (R.F.) operating at 13.56 megahertz. Nominal film thickness is 1300 Å on each side of the polyimide. Gas control is separate for each cathode and limited only to the cathode area, which allows the chamber background pressure to remain in the low 10-5 torr range. Maximum film width is 25 inches with a maximum roll diameter of 14 inches. The entire deposition system is monitored by a computer controlled data acquisition system capable of monitoring over 300 separate points (e.g., web tension, speed, power, etc.). This allows a constant log of all important parameters versus time and web footage and helps maintain coating quality and integrity. Because particulate contamination of the Kapton film before coating would be detrimental to its AO resistance, special handling techniques are employed and the entire chamber carriage is enclosed in a hood capable of class 10,000 cleanroom performance.

8.1.2 Properties

Table 8-1 compares the thermo-optical properties of SiO_x coated aluminum/Kapton to that of aluminum/Kapton thermal control material.[3]

Table 8-1. Typical Thermo-Optical Properties of SiO_x-Coated Aluminum/Kapton

Material Description	α_s (1)	ε_H (2)	α_s / ε_H	Temp. Range Continuous °C (°F)
Vacuum deposited Silicon Oxide x vacuum deposited aluminum x 1.0 mil Kapton x 1.0 mil Silicone pressure sensitive adhesive tape	≤0.14	~0.12	~1.0	-184 to 150 (-300 to 300)
Vacuum deposited aluminum x 1.0 mil Kapton x 966 acrylic pressure sensitive adhesive tape	≤0.14	≤0.05	~4.0	-184 to 150 (-300 to 300)

(1) Solar absorptance testing was done with a dual beam, ratio recording Beckman DK-2A UV-VIS-NIR spectrophotometer. Solar absorptance was computed based on 25 equal energy intervals centered on wavelengths from 314 nanometers to 2191 nanometers. These wavelengths are computed from tables of spectra in NASA SP-8005 and ASTM E490-73a.

(2) An approximation to total hemispherical emittance was obtained from a Lion Research Corporation emissometer. This instrument responds to the IR energy emitted from a sample through a potassium bromide window into the detector. The wavelength range is 3-30 microns. This method equates to ASTM E408, Method B.

8.1.2 Effects of the Space Environment

8.1.2.1 1000 Å SiO_x on VDA/Kapton

A 1000 Å SiO_x coating on vacuum deposited aluminized (VDA)/Kapton was flown on the LDEF to determine its ability to perform in the harsh environment.[4] This sample was composed of 1000 Å of SiO_x deposited on VDA face of Kapton, which was attached to the aluminum support disk with 3M Corporation's Y-966 transfer adhesive. Figure 8-1 shows the side view of this specimen. The weight of the assembled components was 4.34883 g and its total thickness was 0.1294 in. (0.3287 cm). The weight of the support disk was 4.25987 g and its thickness was 0.1148 in. (0.2916 cm).

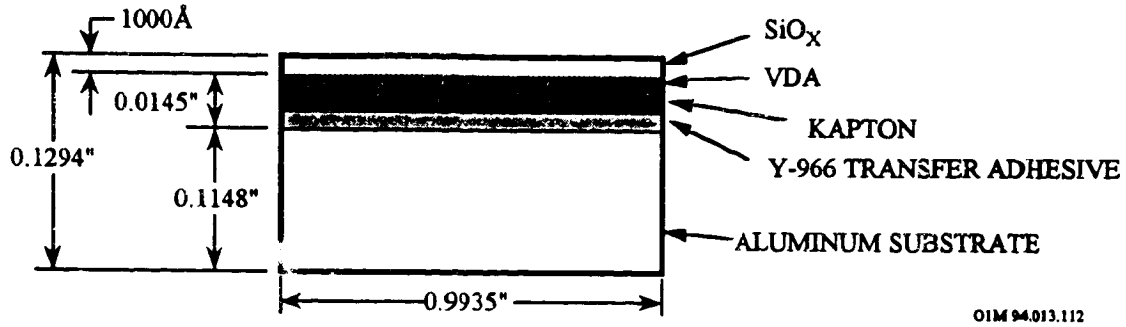

Figure 8-1. Side View of Kapton/VDA with 1000 Å SiO_X Coating

The sample was mounted in the Experiment Environmental Control Canister (EECC), identified as Experiment No. S0010, and was located in Tray B9, which was situated at an angle of 8° from the ram vector. The coated specimen was located in the ram direction of the spacecraft, exposed for 10 months to the low-Earth orbit environment at an orbit of 260 nautical miles. For the 10-month exposure at an altitude of 260 nautical miles, the oxygen fluence is estimated to have been 8.99×10^{21} atoms/cm^2. The UV radiation exposure was 11,200 esh.

Mass Loss. The sample of SiO_x was uniformly eroded. The mass loss of the flight sample was 3.3×10^{-5} g or about 8.9×10^{-6} g cm^{-2} of the exposed area. The thickness change amounted to 3.032×10^{-3} cm, corresponding to about 0.994% of the total sample thickness. The concentrations of O and Si remained constant. The change in thickness, 3.032×10^{-3} cm, is considerably more than the SiO_2 thickness of 1000 Å (1×10^{-5} cm). Some of the VDA Kapton was eroded. One cannot establish a reaction rate constant because the measured mass loss and thickness may include changes due to the sample's outgassing losses.

Optical Properties. Some improved reflectance occurred below 450 nm and above 700 nm. The integrated properties are $\alpha = 0.127$ and $\varepsilon = 0.023$ for the flight sample, and $\alpha = 0.155$ and $\varepsilon = 0.025$ for the reference sample.

8.1.2.2 1300 Å SiO_X on Kapton

NASA Lewis Research Center conducted AO plasma asher testing for a SiO_x coated Kapton.[5] The SiO_x coated Kapton samples used for the ground simulation experiment were 0.00254 cm (1 mil) thick Kapton H samples, which were coated with 1300 Å SiO_x (where $1.9 < X < 2.0$) films on both sides of Kapton by means of RF magnetron sputter deposition. The coatings were deposited by Sheldahl Corporation. The atomic oxygen durability for the SiO_x protected Kapton samples and unprotected Kapton samples was evaluated with an RF plasma

asher (SPI Plasma Prep II). The plasma asher discharge creates a mix of atomic, molecular, ionic, excited-state species, as well as vacuum ultraviolet (VUV) and ultraviolet (UV) radiation.

Mass Loss Degradation. Based on the plasma exposure to both sides of SiO_x -protected Kapton, the erosion rate of SiO_x coated Kapton is reduced to less than 1% of the erosion rate of unprotected Kapton (ref. 5). Figure 8-2 compares the mass loss per unit area as a function of effective atomic oxygen fluence for the atomic oxygen SiO_x protective coated Kapton and the uncoated Kapton. Also included are the effectiveness of electrically conducted atomic oxygen protective coatings, germanium and indium tin oxide.

The mass loss of the ground simulated SiOx coated Kapton sample was ~1 x 10^{-5} g cm^{-2} at an atomic oxygen fluence of 7.10 x 10^{21} atoms/cm^2. This erosion is similar to that observed for a 1000 Å SiO_x on VDA/Kapton in which the mass loss of the flight sample was 3.3 x 10^{-5} g or about 8.9 x 10^{-6} g cm^{-2} of the exposed area for an atomic oxygen fluence of 8.99 x 10^{21} atoms/cm^2 (see above).

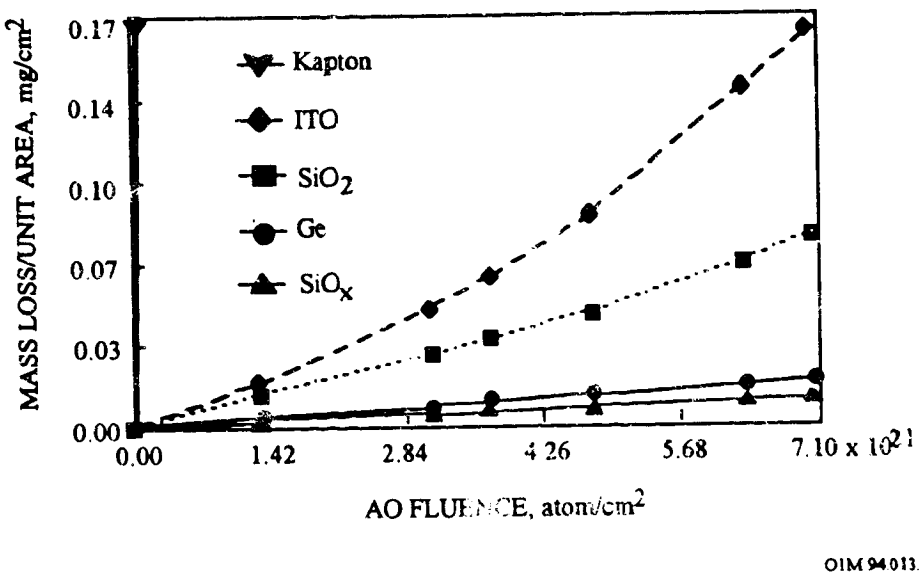

Figure 8-2. Mass Loss Dependence Upon AO Fluence for Silicon Dioxide Coated Kapton and Unprotected Kapton

8.1.2.3 650 Å SiO_2 and 650 Å PTFE/SiO_2 on Kapton

Several candidate protective coatings on Kapton and uncoated Kapton were exposed to the LEO environment on LDEF Tray S1003 to determine if these coatings could be used to protect polymeric substrates from degradation in the LEO environment (ref. 2). Coatings evaluated included 650 Å of silicon dioxide and 650 Å of a 4% polytetrafluoroethylene - 96% silicon dioxide mixed coating. All of the coatings evaluated were ion beam sputter deposited. These materials were exposed to a very low atomic oxygen fluence (4.8×10^{19} atoms/cm^2) as a result of the experiment tray being located 98 degrees from the ram direction. Comparison of the optical properties of coated and uncoated Kapton exposed to the low-Earth space environment to a control uncoated Kapton sample is presented in Table 8-2.

Table 8-2. Effects of SiO_2 Coating on the Optical Properties of Kapton on LDEF (S1003)

Material and Sample Designation	Total Reflectance	Total Transmittance	Solar Absorptance	Thermal Emittance
Uncoated Kapton (not flown)	0.135	0.576	0.289	0.70
Uncoated Kapton (LDEF no.6)	0.136	0.580	0.285	0.72
Uncoated Kapton (LDEF no.34)	0.130	0.583	0.286	0.71
SiO_2 on Kapton(not flown)	0.116	0.573	0.311	0.72
SiO_2 on Kapton (LDEF no.9)	0.105	0.561	0.334	0.72
4% PTFE-96 SiO_2 on Kapton (not flown)	0.109	0.584	0.307	0.72
4% PTFE-96 SiO_2 on Kapton (LDEF no.7)	0.103	0.578	0.319	0.72
4% PTFE-96 SiO_2 on Kapton (LDEF no.14)	0.103	0.576	0.321	0.71

Solar absorptance increased between 7 to 8 % for the SiO_x coated Kapton and only 4 % for the mixed coating. Apparently, the addition of a small amount of fluoropolymer reduced the magnitude of absorptance increase due to environmental exposure. Thermal emittance did not change significantly for any of the exposed samples. Scanning electron microscopy revealed few micrometeoroid or debris impacts, where the extent of damage or cracking of the coating around the defect site did not extend beyond a factor of 3 of the impact crater diameter. This limiting of impact damage is of great significance for the durability of thin film coatings used for protection against the LEO environment. Determination of a mass change was not possible for any of the samples including the uncoated Kapton due to the low AO fluence. There was no evidence of spalling of any of the coatings after the approximately 34,000 thermal cycles recorded for LDEF. The surface of the uncoated Kapton, however, did show evidence of grazing incidence texturing.

8.2 ALUMINUM OXIDE (Al_2O_3)

8.2.1 Introduction

Polycrystalline ceramic films, such as SiO_X (where $1.9 < X < 2.0$), SiO_2, fluoropolymer-filled SiO_2, and Al_2O_3 (see below) have been demonstrated in both ground and space tests (i.e., LDEF) to be effective in protecting polyimide Kapton from oxidation by LEO atomic oxygen.[1,2] These films are often used as an environmental protective coating due to its resistant to atomic oxygen exposure, and provides improved radiative properties during space environment exposure.

8.2.2 Effects of the Space Environment

8.2.2.1 700 Å Al_2O_3 on Kapton

Samples of 700 Å of aluminum oxide protective coated Kapton and uncoated Kapton were exposed to the LEO environment on the LDEF to determine if the coatings could be used to protect polymeric substrates from degradation in the LEO environment (ref. 2). The coating evaluated was ion beam sputter deposited. These materials were exposed to a very low atomic oxygen fluence (4.8×10^{19} atoms/cm^2) as a result of the experiment tray being located 98 degrees from the ram direction.

As a result of the low AO fluence, determination of a change in mass was not possible for any of the samples including the uncoated Kapton. There was no evidence of spalling of any of the coatings after the approximately 33,600 thermal cycles recorded for LDEF. The surface of the uncoated Kapton, however, did show evidence of grazing incidence texturing. There was a 7 to 8 percent increase in solar absorptance for the aluminum oxide coated Kapton (see Table 8-3). Thermal emittance did not change significantly for any of the exposed samples. Scanning electron microscopy revealed few micrometeoroid or debris impacts, but the impact sites found indicated that the extent of damage or cracking of the coating around the defect site did not extend beyond a factor of 3 of the impact crater diameter. This limiting of impact damage is of great significance for the durability of thin film coatings used for protection against the LEO environment.

Table 8-3. Optical Properties of Al_2O_3 Coated and Uncoated Kapton Exposed on LDEF Tray S1003

Material and Sample Designation	Total Reflectance	Total Transmittance	Solar Absorptance	Thermal Emittance
Uncoated Kapton (not flown)	0.135	0.576	0.289	0.70
Uncoated Kapton (LDEF no.6)	0.136	0.580	0.285	0.72
Uncoated Kapton (LDEF no.34)	0.130	0.583	0.286	0.71
Al_2O_3 on Kapton (not flown)	0.120	0.571	0.309	0.72
Al_2O_3 on Kapton (LDEF no. 12)	0 118	0.545	0.337	0.71
Al_2O_3 on Kapton (LDEF no 26)	0.119	0.551	0.330	0.72

8.3 INDIUM OXIDE (In_2O_3)

8.3.1 Introduction

Indium oxide coating provides sufficient electrical conductivity, has little effect on substrate solar absorption and emissivity, and remains stable during long exposure in space to UV radiation and particle bombardment.

8.3.2 Effects of the Space Environment

8.3.2.1 100 Å In_2O_3 on Kapton/VDA

100 Å In_2O_3 coating on Kapton/VDA was flown on the LDEF to determine its ability to perform in the harsh environment (ref. 4). 100 Å of indium oxide was deposited on Kapton. The Kapton was attached with its vacuum-deposited Al face to the aluminum support disk with 3M's Y-966 adhesive. Figure 8-3 shows a side view of the sample. The assembled sample weight was .328355 g and its thickness was 0.1271 in. (0.3228 cm). The support disk weight was approximately 4.259878 g and its thickness was 0.1160 in. (0.2946 cm). The surface was described as "yellow" and "shinny."

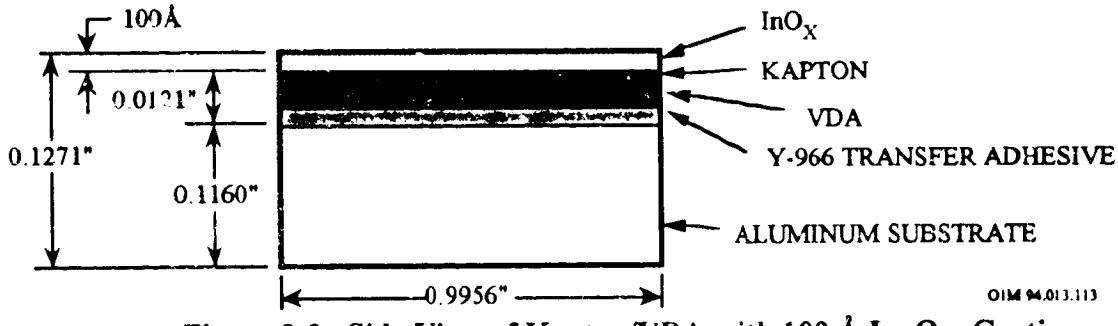

Figure 8-3. Side View of Kapton/VDA with 100 Å In_2O_3 Coating

The sample was mounted in the Experiment Environmental Control Canister (EECC), identified as Experiment No. S0010, and was located in Tray B9, which was situated at an angle of 8.1° from the ram vector. The coated specimen was located in the ram direction of the spacecraft, exposed for 10 months to the low-Earth orbit environment at an orbit of 260 nautical miles. For the 10-month exposure at an altitude of 260 nautical miles, the oxygen fluence is estimated to have been 2.6×10^{20} atoms/cm^2. The UV radiation exposure was 16,000 hours.

The sample was severely eroded, with the indium reduced to less than 0.95 atomic % in comparison to the unexposed sample at 7 atomic %. The color changed from yellow to gray.

Kapton was exposed to the environment through erosion of the InO_x in some areas and the Kapton exhibited substantial erosion.

The mass loss for the sample was 0.001867 g, or about 5.37×10^{-4} g cm^{-2} of exposed area. The thickness change amounted to about 5.08×10^{-3} cm, corresponding to about 1.538% of the total thickness.

The 100 Å (10^{-6} cm) of In_2O_3 and a considerable amount of the VDA/Kapton were eroded. In addition, considerable material and thickness must have been lost by outgassing in space. Not knowing if bakeout in vacuum was performed on the material before launch, it is not possible to estimate the reaction efficiency of the indium. However, the various analyses have indicated that the indium was completely eroded. The reaction rate for the Kapton is known to be about 3×10^{-24} cm^3/atom from other orbital tests.

Losses of 5% to 10% in reflectance resulted below 450 nm and between 600 and 1600 nm, respectively. The integrated values are 0.391 absorption and 0.547 emittance for the flown sample and are 0.363 and 0.564, respectively, for the reference sample.

8.4 CLEAR RTV SILICONE

8.4.1 Introduction

This type of coating is an environmental protective coating used as a sealant and is particularly resistant to atomic oxygen.

8.4.2 Effects of the Space Environment

8.4.2.1 Atomic Oxygen Reaction Efficiency Data

A summary of the AO reaction efficiencies of various silicones flown in low Earth orbit on the Space Shuttle flights is provided in Table 8-4.

Table 8-4. AO Reaction Efficiencies of Silicones in Low Earth Orbit

Material	Mfg.	Reaction Efficiency, $x10^{-24}$ cm^3/atom	Flight Experiment	Reference
DC1-2577	Dow Corning	0.055		6
DC1-2577	Dow Corning	0.02[a]	STS-8	7
DC1-2755-coated Kapton	Dow Corning	0.05	STS-5	8
DC1-2775-coated Kapton	Dow Corning	<.5	STS-5	14
DC6-1104	Dow Corning	0.515		8
DC6-1104	Dow Corning	0.02[a]	STS-8	9
RTV-615 (black, conductive)	GE	0.0		10
RTV-615 (clear)	GE	0.0625		11
RTV-560	GE	0.02[a]	STS-8	16
RTV-670	GE	0.0		12
RTV-S695	GE	1.48		13
RTV-3145	GE	0.128		20
T-650		0.02[a]	STS-8	16
CV-1144-0	McGhan NuSil	0.00	STS-46	14

(a)Units of mg/cm^2 for STS-8 mission. Loss is assumed to occur in early part of exposure; therefore, no assessment of efficiency can be made.

8.4.2.2 Devolatized RTV-615 Bonded on Al with SS 4155 Primer

RTV-615 Silicone on aluminum was flown on the LDEF to determine its ability to perform in the harsh environment. A sample consisting of devolatized General Electric Corporation (GE) RTV-615 two-part silicone with an A/B parts-by-weight mix ratio of 10/1 was bonded to an aluminum disk via GE primer SS4155. The total thickness of the assembly was 0.1253 in. (0.3183 cm). The weight of the support disk was 4.25987 g and its thickness was 0.1127 in. (0.2862 cm). Figure 8-4 shows a side view of the sample (ref. 4).

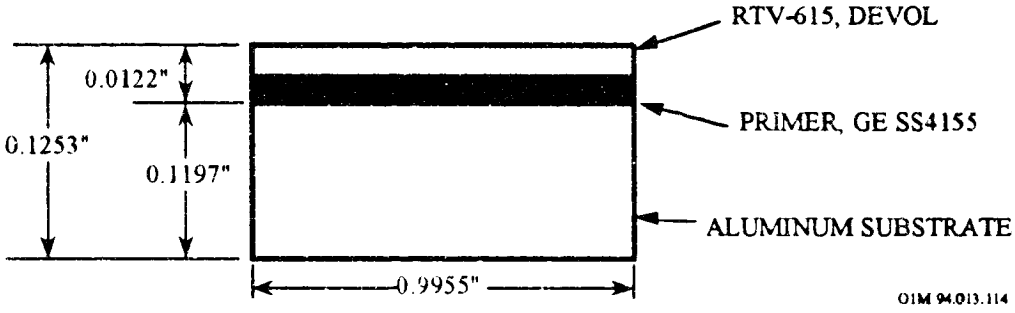

Figure 8-4. Side View of RTV-615 Silicone on Aluminum

The sample was mounted in the Experiment Environmental Control Canister (EECC), identified as Experiment No. S0010, and was located in Tray B9, which was situated at an angle of 8.1° from the ram vector. The coated specimen was located in the ram direction of the spacecraft, exposed for 10 months to the low-Earth orbit environment at an orbit of 260 nautical miles. For the 10-month exposure at an altitude of 260 nautical miles, the oxygen fluence is estimated to have been 2.6×10^{20} atoms/cm^2. The UV radiation exposure was 16,000 hours.

The sample experienced a mass loss of 0.0037 g, or about 8.983×10^{-3} g cm^{-2} of the exposed area. The thickness change amounted to about 8.63×10^{-3} cm, corresponding to about 2.617% of the total thickness.

The change in thickness, 0.0034 in. (8.63×10^{-3} cm), is considerably less than the thickness of the RTV and primer 0.0167 in. (4.24×10^{-2} cm). Under the assumptions that the loss was the result of the oxygen erosion, one could calculate the reaction efficiency. However, calculations to estimate the reaction efficiency using the above data indicate a considerable oxygen erosion, much larger than the value of 6.25×10^{-26} cm^3/atom reported by B.A. Banks et al.[15] The discrepancy in order of magnitude must be assumed to have been produced by loss of material from outgassing.

The flight sample experienced a loss of about 5% in reflectance throughout the measured range of wavelength with respect to that of the reference sample. The integrated properties are: α = 0.489 and ε = 0.819 for the flight sample, and α = 0.432 and ε = 0.824 for the reference sample.

8.4.2.3 McGhan NuSil CV-1144-0 RTV Silicone

McGhan NuSil CV-1144-0 is a one-part, silicone dispersion specially designed and processed for applications requiring extreme low temperature, low outgassing and minimal volatile condensables under extreme operating conditions. CV-1144-0 is based on a dimethyl diphenyl silicone copolymer with a service temperature range of -115°C to 232°C.

This silicone coating was applied to the original Hubble Space Telescope Solar Arrays. It was applied to carbon/epoxy composites, Kapton, Dacron and Chemglaze paint. This coating was recently flight tested on the STS-46 LDCE-3 experiment.[16] No correlation was observed between the flight weight loss of 0.491 percent and the ASTM E-595 CVCM and TML values of 0.00 and 0.31 percent, respectively. Possible mechanisms for the reaction of the silicone elastomer with oxygen atoms are:

- $SiCH_3 + 4\ O$----------$SiOSi + 3H_2O + 2C$
- $SiCH_3 + 4\ O$----------$SiC + SiOH + H_2O + CO_2$

This silicone coating was also applied to a carbon/PEEK thermoplastic composite and flown on the STS-46 LDCE-3 experiment. No measurable erosion was observed in the protected layer (ref. 14).

8.5 SILICONE WITH SILICATE-TREATED ZINC OXIDE (ZnO)

8.5.1 Introduction

This combination is a thermal control coating and is used as a white paint for spacecraft and other structures. It is resistant to UV radiation exposure.

8.5.2 Effects of the Space Environment

8.5.2.1 RTV-615/Silicate-Treated ZnO

RTV-615/silicate-treated ZnO on aluminum was flown on the LDEF to determine its ability to perform in the harsh environment. This sample consisted of GE's devolatized RTV-615 two-part silicone with 68% of IITRI's K_2SiO_3 coated and buffered SP-500 ZnO pigment. The RTV-615 silicone had an A/B parts-by-weight mix ratio of 10:1. The material was bonded to the aluminum disk via GE primer, SS4155. The total weight was 4.55060 g and the total thickness was 0.1343 in. (0.3411 cm). The weight of the support disk was 4.25987 g and its thickness was 0.1197 in. (0.3040 cm). Figure 8-5 shows a side view of the sample (ref. 4).

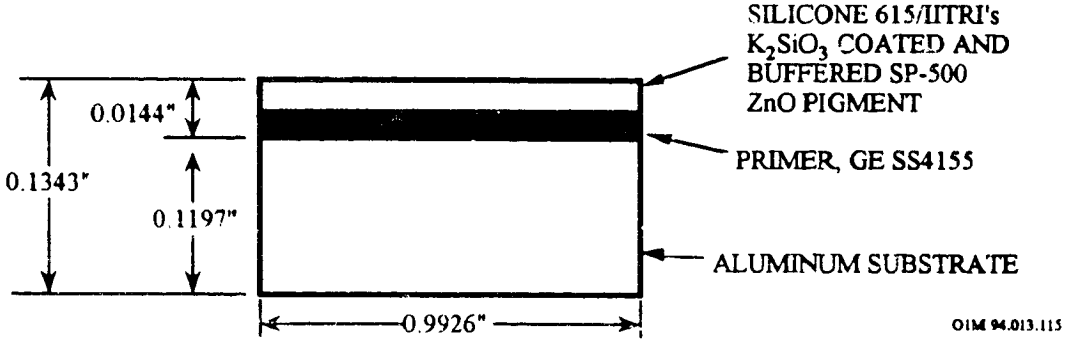

Figure 8-5. Side View of RTV-615 Silicone Treated ZnO

The sample experienced a mass loss of 8.27×10^{-4} g, or about 2.332×10^{-4} g cm^{-2} of exposed surface. The thickness change amounted to 3×10^{-3} in. (7.78×10^{-3} cm), corresponding to about 2.142% of the total thickness.

Both the RTV and the silicate were eroded. The actual erosion and mass thickness are not known because of the possible loss by outgassing, and the calculation for the reaction efficiency could be erroneous. But, as indicated, erosion did occur.

The reflectance versus wavelength, not shown, revealed some loss between 400 and 700 nm and between 1800 and 2100 nm. The integrated absorption is 0.201 and the emittance is 0.891 for the flown sample, and 0.190 and 0.907, respectively, for the reference sample.

8.6 GERMANIUM-COATED KAPTON

8.6.1 Introduction

Germanium is an opaque conductive coating that is applied to the front surface of second-surface mirrors to provide a means of draining static electricity induced by Van Allen radiation belts. Without a conductive coating it is possible to build up charges of 20,000 to 30,000 volts on the surface of a second-surface mirror. When discharge takes place, it can result in erosion of thermal control coatings and electronic systems can be turned on, of, or burned out. Draining of surface charging for geosynchronous spacecraft can be achieved with surface resistivities less than 10^9 ohms per square. Draining of surface charge for LEO polar spacecraft applications requires lower surface resistivity, 10^8 ohms per square because of higher auroral charging current densities.[17] The germanium coating has an adequate surface electrical conductivity for use in LEO polar applications where draining of electrically charged surfaces is desirable to prevent the occurrence of electrical breakdowns and arcs.

A coating of germanium is applied to Kapton blanket material to achieve required thermo-optical properties as well as to protect the polymer from the space environment, in particular erosion caused by atomic oxygen. Germanium/Kapton is used in blanket and closeout applications, and as an interstitial layer between the photovoltaic cells and the facesheet on solar array panels.

The germanium is applied to the Kapton by sputter deposition in a batch process to produce coated material which may then be cut to size. The coating may also be applied to pre-cut pieces of blanket if necessary. The coated blanket is installed in the usual manner with the germanium side typically facing outward. Coating thickness may be varied to tailor thermal the properties of the blanket, but nominal germanium thickness is 1500 Å. The coating has good abrasion resistance and is readily cleaned by wiping with standard solvents.

8.6.2 Effects of the Space Environment

8.6.2.1 STS-46 Flight Experiment

Germanium coated Kapton is a possible material for advanced photovoltaic solar arrays. There are limited short-term environmental exposure data available for germanium/Kapton. Specimens were integrated into the heated trays and passive tray of the JPL EOIM-3 experiments on the STS-46 Space Shuttle flight.[i] Thermal property data for germanium/Kapton are summarized in Table 8-5 below. The material evaluated was 1500 Å germanium on 2 mil Kapton.

Table 8-5. Space Exposure Data for Germanium/Kapton

Specimen Condition	IR Reflectance ρ_{IR}	Solar Absorptance α_s	Emittance ε_h	α_s/ε_h
Preflight	0.384	0.483	0.617	0.78
Control	0.384	0.482	0.616	0.78
Flight	0.386	0.485	0.614	0.79

Estimated Germanium Oxide layer thicknesses were determined by ESCA as shown in Table 8-6.[18] Possible formation of volatile GeO (direct reaction and/or disproportionation).

Table 8-6. GeO_x thicknesses for Coated Kapton Specimens

Specimen Location	GeO_x Thickness (Å)
Passive (10° - 40°C)	60
60°C Strip	40
200°C Strip	20

[i] Flight exposure of germanium/Kapton took place on the Evaluation of Oxygen Interactions with Materials, Mission 3 (EOIM-3) flight experiment sponsored by NASA/BMDO Space Environmental Effects program. Results documented in TRW Advanced Interceptor Technologies Program report No. 57888.93.440-003; total atomic oxygen fluence of 2×10^{21} atoms/cm^2 over 42 hours.

8.6.2.2 Ground-Based Space Simulation Experiment

NASA Lewis Research Center conducted AO plasma asher testing for an electrically conductive germanium coated Kapton.[19] The coated Kapton specimen used for the ground simulation experiment consisted of a 0.00508 cm (2 mil) thick Kapton H substrate coated with 1500 Å germanium films on both sides of Kapton by means of RF magnetron sputter deposition. The coating was deposited by TRW. The atomic oxygen durability for the germanium protected Kapton samples and unprotected Kapton samples was evaluated with an RF plasma asher (SPI Plasma Prep II). The plasma asher discharge creates a mix of atomic, molecular, ionic, excited-state species, as well as vacuum ultraviolet (VUV) and ultraviolet (UV) radiation.

Mass Loss Degradation. Based on the plasma exposure to both sides of the germanium-protected Kapton, the erosion rate of germanium coated Kapton is considerably reduced compared to the erosion rate of unprotected Kapton (ref. 19). Figure 8-6 compares the mass loss per unit area as a function of effective atomic oxygen fluence for several atomic oxygen protective coatings to that of unprotected Kapton. From Figure 8-6, silicon dioxide and germanium coated Kapton samples were found to have the lowest mass loss per unit area. Since germanium is inherently atomic oxygen durable, or develops durable oxides, the range of protection afforded by this coating is a measure of the defect area for this coating.

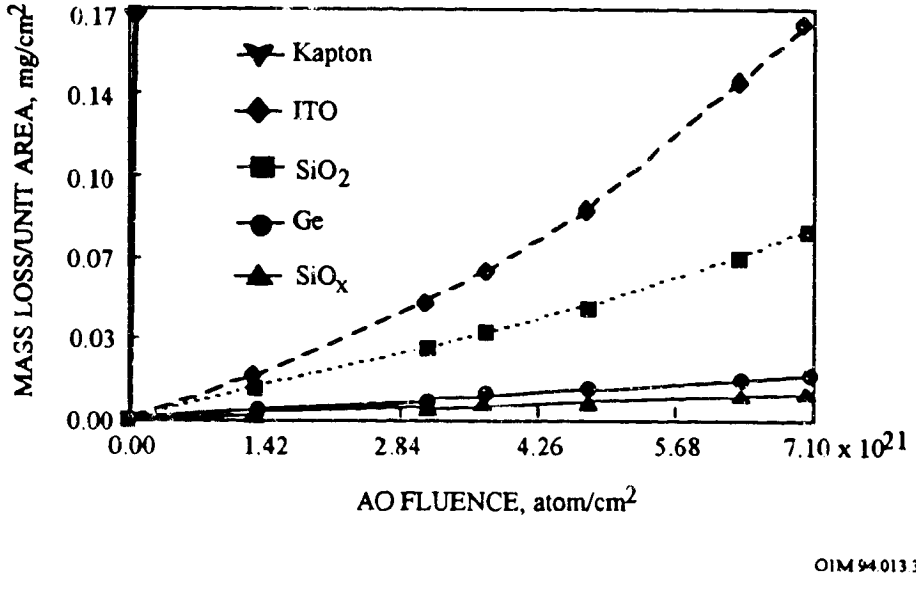

Figure 8-6. Mass Loss Dependence Upon AO Fluence for Germanium-Coated Kapton and Unprotected Kapton

Optical Transmittance. The optical transmittance of the opaque germanium-coated Kapton was not noticeably altered by plasma asher atomic oxygen exposure.

Surface Resistance. The conductive germanium coating was observed to be sufficient to meet polar LEO charging requirements. The surface resistance of germanium coated Kapton was found to stabilize at atomic oxygen fluence of 7×10^{20} atoms/cm^2.

8.6.3 Design Consideration

Germanium/Kapton is stable in the LEO space environment, exhibiting no quantitatively significant degradation in thermal properties from short term space exposure. However, pin-holes in the coating characteristic of the coating process may allow atomic oxygen to erode the Kapton, thus undermining the structural integrity of the blanket. This phenomenon should not significantly affect the thermal performance of the blanket until undercutting has progressed to the point where fragments of the material come free from the body of the blanket. The dislocated fragments may also present a contamination hazard to other systems on a spacecraft. There are no definitive measures of the rate at which this phenomenon occurs, but a conservative estimate would take the erosion rate of uncoated Kapton at the orbit of interest and multiply by a factor of one-half. There are no long-term data on the space-stability of germanium/Kapton, but the germanium coating is expected to be stable in the space environment

Hence, germanium films many find use where conductivity and atomic oxygen protection are required provided visible light transparency is not required.

8.7 INDIUM TIN OXIDE-COATED KAPTON

8.7.1 Introduction

Indium tin oxide is a transparent conductive coating that is applied to the front surface of second-surface mirrors to provide a means of draining static electricity induced by Van Allen radiation belts. Without a transparent conductive coating it is possible to build up charges of 20,000 to 30,000 volts on the surface of a second-surface mirror. When discharge takes place, it can result in erosion of thermal control coatings and electronic systems can be turned on, of, or burned out. Draining of surface charging for geosynchronous spacecraft can be achieved with surface resistivities less than 10^9 ohms per square. Draining of surface charge for LEO polar spacecraft applications requires lower surface resistivity, 10^8 ohms per square because of higher auroral charging current densities (ref. 17).

The ITO coating has an adequate surface electrical conductivity for use in LEO polar applications where draining of electrically charged surfaces is desirable to prevent the occurrence of electrical breakdowns and arcs. Indium tin oxide, as manufactured, has a surface resistivity of approximately 10,000 ohms per square. This coating increases the solar absorptance 3 percent and the emittance is unaffected. It has excellent adhesion. However, care in handling must be exercised because the coating is sensitive to high humidity, abrasion, flexing and thermal cycling.

8.7.2 Source

Manufacturer: Sheldahl Inc.
Northfield, MN 55057
Tel: 507/663-8000

8.7.3 Properties

Table 8-7 compares the typical thermo-optical properties of transparent ITO conductive coating/Kapton/aluminum thermal control material to that of Kapton/aluminum thermal control material.[20] The absorptance and emittance values are measured through the Kapton surface.

Table 8-7. Typical Thermo-Optical Properties of ITO-Coated Kapton/Aluminum

Material Description	α_s (1)	ε_H (2)	α_s / ε_H	Temp. Range Continuous °C (°F)
ITO x 1.0 mil Kapton x vacuum deposited aluminum	≤0.44	≥0.62	~0.50	-184 to 150 (-300 to 300)
ITO x 2.0 mil Kapton x vacuum deposited aluminum	≤0.49	≥0.71	~0.50	-184 to 150 (-300 to 300)
1.0 mil Kapton x vacuum deposited aluminum	≤0.39	≥0.62	~0.50	-184 to 150 (-300 to 300)
2.0 mil Kapton x vacuum deposited aluminum	≤0.44	≥0.71	~0.50	-184 to 150 (-300 to 300)

(1) Solar absorptance testing was done with a dual beam, ratio recording Beckman DK-2A UV-VIS-NIR spectrophotometer. Solar absorptance was computed based on 25 equal energy intervals centered on wavelengths from 314 nanometers to 2191 nanometers. These wavelengths are computed from tables of spectra in NASA SP-8005 and ASTM E490-73a.

(2) An approximation to total hemispherical emittance was obtained from a Lion Research Corporation emissometer. This instrument responds to the IR energy emitted from a sample through a potassium bromide window into the detector. The wavelength range is 3-30 microns. This method equates to ASTM E408, Method B.

8.7.4 Effects of the Space Environment

NASA Lewis Research Center conducted AO plasma asher testing for an electrically conductive indium tin oxide (ITO) coated Kapton (ref. 19). The ITO coated Kapton specimen used for the ground simulation experiment consisted of a 0.00508 cm (2 mil) thick Kapton H substrate coated with 2000 Å ITO films on both sides of Kapton by means of RF magnetron sputter deposition. The coating was deposited by TRW. The atomic oxygen durability for the ITO protected Kapton samples and unprotected Kapton samples was evaluated with an RF plasma asher (SPI Plasma Prep II). The plasma asher discharge creates a mix of atomic, molecular, ionic, excited-state species, as well as vacuum ultraviolet (VUV) and ultraviolet (UV) radiation.

Mass Loss Degradation. Based on the plasma exposure to both sides of the ITO-protected Kapton, the erosion rate of ITO coated Kapton is considerably reduced compared to the erosion rate of unprotected Kapton (ref. 19). Figure 8-7 compares the mass loss per unit area

as a function of effective atomic oxygen fluence for several atomic oxygen protective coatings to that of unprotected Kapton.

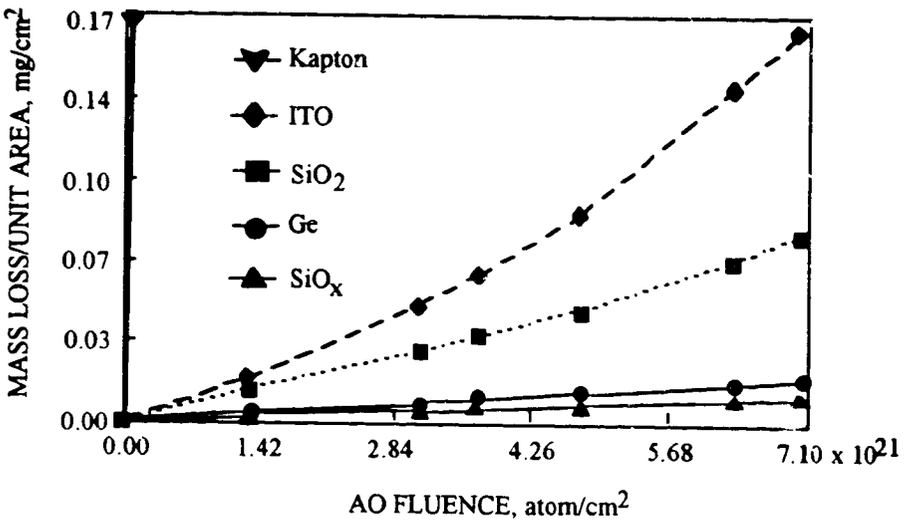

Figure 8-7. Mass Loss Dependence Upon AO Fluence for ITO-Coated Kapton and Unprotected Kapton

From Figure 8-7, the worst performing protection coating was indium tin oxide, which exhibited an increase in the slope of mass loss per unit area with fluence. This increase is typically due to atomic oxygen defects which grow in size with atomic oxygen fluence. Since indium tin oxide is inherently atomic oxygen durable, or develop an durable oxide, the range of protection afforded by the coating is a measure of the defect area of the coating. If the indium tin oxide film is sufficiently stressed, or if the stress increases with atomic oxygen fluence, tearing of the coating at defect sites can allow a gradual increase in exposure of the underlying unprotected Kapton, thus giving rise to an increasing rate of mass loss per unit area with fluence. In contrast, the most protective coating (SiO_x coated by Sheldahl), has very little intrinsic stress and does not tear with atomic oxygen fluence when undercut cavities become large. This is probably why the plot of mass loss per unit area for the SiO_x Sheldahl coated Kapton has a rather constant slope.

Optical Transmittance. The optical transmittance of the transparent indium tin oxide film was noticeably altered by plasma asher atomic oxygen exposure. The film developed a more metallic appearance with increasing atomic oxygen fluence. Figure 8-8 shows the comparative plots of changes in the total spectral transmittance versus fluence for uncoated Kapton and indium tin oxide coated Kapton specimens before and after exposure to an atomic oxygen fluence of 3.48

x 10^{21} atoms/cm^2. The total spectral transmittance of the indium tin oxide film alone can be found by dividing the total spectral transmittance of the coated Kapton by the total spectral transmittance of the uncoated Kapton at each wavelength. As can be seen from Figure 8-8, a significant reduction in total transmittance occurs over a broad wavelength region as a result of atomic oxygen exposure. Such optical degradation may inhibit the use of indium tin oxide for coatings on radiator paints, photovoltaic cover glasses, or on photovoltaic concentrator surfaces.

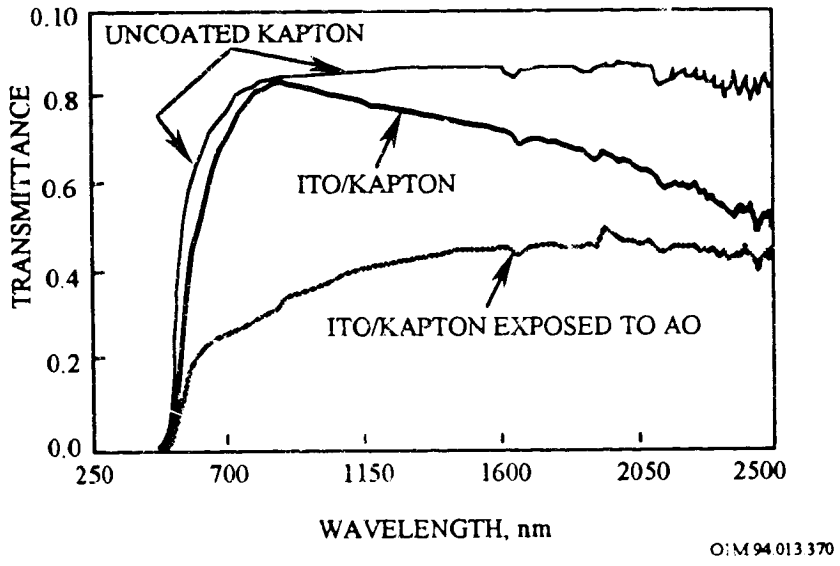

Figure 8-8. Indium Tin Oxide Coated Kapton Prior to and After Exposure to an AO Fluence of 3.48x10^{21} atoms/cm^2

REFERENCES

1 B.A. Banks, M.J. Mirtich, S.K. Rutledge, D.M. Swec, and H.K. Nahra, "Ion Beam Sputter-Deposited Thin Film Coatings for the Protection of Spacecraft Polymers in Low Earth Orbit," NASA TM-87051, paper presented at the 23rd Aerospace Sciences Meeting, Reno, Nevada, January, 1985.

2 S.K. Rutledge and R.M. Olle, "Durability Evaluation of Photovoltaic Blanket Materials Exposed on LDEF Tray S1003," LDEF First Post-Retrieval Symposium, NASA CP-3134, 1991, pp.1379-1394.

3 Sheldahl Data, "Thermal Control Material & Metalized Films."

4 J.J. Scialdone and C.H. Clatterbuck, "Four Space Application Material Coatings on the Long-Duration Exposure Flight (LDEF)", NASA TM 104574, 1992.

5 B.A. Banks, S.K. Rutledge and L. Gebauer, "SiO_x Coatings for Atomic Oxygen Protection of Polyimide Kapton in Low Earth Orbit," AIAA Materials Specialist Conference, AIAA-92-2151-CP, Dallas, TX, April, 1992.

6 Johnson Space Center

7 J.T. Visentine and A.F. Whitaker, "Material Selection Guidelines to Limit Atomic Oxygen Effects on Spacecraft Surfaces," NASA TM-100351, February 1989.

8 L.J. Leger, I.K. Spiker, J.F. Kuminecz, T.J. Ballentine, and J.T. Visentine, "STS-5 LEO Effects Experiment - Background Description and Thin Film Results," AIAA Paper 83-2631-CP, AIAA Shuttle Environment and Operations Meeting, Washington, D.C., October - November, 1983.

9 P. George, "Space Environmental Effects on LDEF Low Earth Orbit Exposed Graphite Reinforced Polymer Matrix Composites," LDEF Materials Workshops '91, NASA CP-3162, 1992, pp. 543-570.

10 Marshall Space Flight Center

11 C.K. Purvis, D.C. Ferguson, D.B. Synder, N.T. Grier, J.V. Staskus, and J.C. Roche, "Environmental Interactions Considerations for Space Station and Solar Array Design," Dec. 1986.

12 A.F. Whitaker, "Atomic Oxygen Effects on LDEF Experiment AO171," LDEF Second Post-Retrieval Symposium, NASA CP-3194, 1993, pp. 1125-1135.

13 British Aerospace

[14] E. Silverman, NASA/CWRU Report on LDCE 1,2 & 3 to TRW, December 1992.

[15] B.A. Banks, S. Rutledge, J.A. Brady, and J.E. Merrow, "Atomic Oxygen Effects on Materials", NASA/SDIO Space Environmental Effects on Materials Workshop, NASA CP 3035, Part I, 1988, pp. 197-239.

[16] D. Petraitis, "The Effects of Atomic Oxygen on NuSil Silicone Elastomers and Coatings," presented at the CSRU/NASA 1993 Materials in Space Meeting, Cleveland Ohio, May 25, 1993.

[17] C.K. Purvis, H.B. Garrett, A.C. Whittlesey, and N.J. Stevens, "Design Guidelines for Assissing and Controlling Spacecraft Charging Effects," NASA Technical Paper 2361, September 1984.

[18] D.E. Brinza, "Early Results from the JPL Experiments on the Evaluation of Oxygen Interactions with Materials (EOIM-3) Experiment Aboard STS-46", Presented at the EOIM-3 BMDO Flight Experiment Workshop, June 22, 1993.

[19] B.A. Banks and C. LaMoreaux, "Performance and Properties of Atomic Oxygen Protective Coatings for Polymeric Materials," Proceedings of 24th International SAMPE Technical Conference, October 1992, pp. T165-T173.

[20] Sheldahl Data, "Thermal Control Material & Metalized Films."

9.0 LUBRICANTS, GREASES, AND SEALS

9.1 LUBRICANTS AND GREASES

9.1.1 Introduction

Lubrication is primarily concerned with reducing the friction which occurs at the interacting surfaces of two solid parts when one is moved relative to the other. Any material introduced between two such surfaces to accomplish a reduction in friction is called a lubricant. Oils, greases, anti-seize compounds, bonded or unbonded solid films, compact and composite materials are some of the kinds of materials which satisfy the definition of a lubricant. Some of the functions of lubricants are to reduce friction, dissipate heat, protect surfaces from corrosion, prevent the entrance of foreign matter, cushion against shock, and distribute loads. Solid-film lubricants have less tendency to perform the same function of removing heat as fluid-film lubricants.

Oils are generally used where lubricant retention is not necessary or where a means of providing a continuous supply of oil is provided as part of the design of a component. Retainer materials which are porous can be impregnated with oil to provide a continuous supply of oil.

Greases are generally used where retention of the lubricant is a requirement. Normally a bearing is partially filled (10-15% of the total void volume), depending upon the operational requirements, to provide for long life operation.

Solid-film lubrication involves a material such as molybdenum disulfide powder, which is normally burnished or bonded onto a part surface. Solid-film lubricants also include compact and composite materials.

9.1.2 Space Environment Effects

A variety of lubricants and greases were flown on LDEF. With the exception of three lubricant systems flown as specimens in experiment M0003, all lubricants were components of functioning hardware, not the primary item of the experimenter's investigation. Table 9-1 identifies the lubricants flown on LDEF, where they were located, and a brief summary of their performances. The majority of the lubricants were shielded from direct exposure to space and performed their design function as anticipated. A detailed review of the investigations into the lubricants and greases flown on the LDEF can be found in the NASA Contractor Report by Harry Dursch et al.[1] The following paragraphs are exerpted from this report.

MoS_2 Dry Film Lubricant. A MoS_2 dry film lubricant and cetyl alcohol were used on nut plate assemblies on the LDEF experiment A0175. Nut plates were coated with either MoS_2 or cetyl alcohol. During post-flight disassembly, severe difficulties were encountered with seizure and thread stripping of the nut plates Post-flight inspection of the fasteners installed into nut plates with MoS_2 dry film lubricant showed no damage to the threads and nominal removal torques. Fasteners installed into nut plates using only cetyl alcohol sustained substantial damage to the fasteners and nut plates. Post-flight FTIR examination of the nut plates found no remaining traces of cetyl alcohol.

MIL-L-23398 air-cured MoS_2 lubricant was used on several components on each of the five NASA provided Environmental Exposure Control Canisters (EECC). The EECC's were located on rows 9 (leading edge), 8,4,3 (trailing edge), and 2. The lubricant was applied to the Bellevile washers, drive shafts, and linkages. Portions of the Bellevile washers and drive shafts were exposed to the external environment. Visual examination of the EECC located on the trailing edge revealed no evidence of abnormal wear or coating degradation on the surfaces not exposed to UV. Portions of the drive shaft exposed to UV exhibited slight discoloration.

Table 9-1. Lubricants and Greases on the LDEF Satellite

Material - Description	LDEF Location	Findings
Cetyl Alcohol	A1 & A7	Used on nut plates, no traces remain
MoS_2	A1 & A7	Used on nut plates, appears to be nominal
MoS_2 - air cured dry film lubricant (MIL-L-23398)	EECCs (shielded and exposed)	No apparent visual change, further testing required
MoS_2 - chemically deposited	B3	Degraded
Ball Aerospace 21207 - MoS_2	A9 (shielded)	System test results nominal, lubricant not evaluated
Ball Aerospace VacKote 18.07 - MoS_2 with polyimide binder	A9 (shielded)	System test results nominal, lubricant not evaluated
Molykote Z - MoS_2	B3 (shielded)	Not tested
WS_2 (tungsten disulfide)	Grapples	Bulk properties unchanged, no difference between leading and trailing edge
Apiezon H - petroleum based thermal grease	F9 (shielded)	Outgassing tests showed no change
Apiezon L - petroleum based thermal grease	D12	Not tested
Apiezon T - petroleum based thermal grease	H3 & H12 (space end)	Slight separation of oil from filler, some migration
Ball Brothers 44177 - Hydrocarbon oil with lead naphthanate and clay thickener	EECCs (shielded)	Not tested, extensive outgassing
Castrol Braycote 601 - PTFE filled perfluoronated polyether lubricant	A3	Extensive testing, to date results show no change
Dow Corning 3440 - Silicone heat sink compound	Shielded	IR spectra unchanged
Dow Corning 1102 - Mineral oil based heat sink compound	Shielded	Appearance unchanged
Exxon Andok C - Petroleum grease	Shielded	System test results nominal, lubricant not evaluated
Mobil Grease 28 - Silicone grease	MTMs (shielded)	System test results nominal, lubricant not evaluated
DuPont Vespel bushings - polyimide	Various	Appearance unchanged
DuPont Vespel 21 - Graphite filled polyimide	D3	Optical, EDX, and friction tests showed no change
E/M Lubricants Everlube 620C - MoS_2 with modified phenolic binder	D3	Complete binder failure, only minimal traces remained
Rod end bearings with PTFE cc Nomex liner	D3	Extensive testing showed no changes

VacKote 18.07 and 21207. VacKote 18.07 and 21207, both made by Ball Aerospace, were used on carousel components of experiment S0069. VacKote 18.07 is a polyimide bonded MoS_2 that is sprayed on to the substrate and then cured at elevated temperatures (1 hour at 310°C or 50 hours at 149°C). This lubricant meets NASA outgassing requirements. The 21207 is thin pure MoS_2 that contains no binder or glue. It is applied by high velocity impingement. Its primary use is in reduction of rolling friction (it possesses poor properties for sliding friction applications). The only post-flight evaluation of either lubricant has been a system functional test of the overall experiment. The system performance was unchanged. No post-flight examination of either lubricant has been performed.

Tungsten Disulfide. Tungsten disulfide WS_2 dry film lubricant was used as the lubricant on both the rigidize sensing and flight-releasable grapple shafts. This lubricant was used to ensure successful release of the grapple from the RMS during initiation of the active experiments, deployment, and retrieval of LDEF. The grapples performed as designed. The tray containing the grapple used for deployment and retrieval was located 122 degrees to ram and saw an atomic oxygen exposure of 22×10^{17} atoms/cm^2. However, because the shaft extended 3 to 4 inches beyond the LDEF surface, portions of the shaft (and the Teflon tip) were exposed to a much greater fluence. During post-flight analysis at JSC, samples of WS_2 were removed from both grapple shafts for SEM and EDX analysis. This analysis showed the bulk lubricant to be intact with no discernible difference between the lubricant exposed on the ram surfaces of the shafts and the lubricant exposed on the trailing edges. No surface analysis was performed. The tribological properties of the WS_2 have not been determined.

Apiezon H. Apiezon H was used as a heat sink grease on experiment A0076, Cascade Variable Conductance Heat Pipe. The grease was not exposed to atomic oxygen or UV. To determine the effect of extended vacuum on the grease, a sample was tested for outgassing in accordance with NASA SP-R-0022A. The LDEF sample had considerably higher total mass loss than the control sample, but the volatile condensable material was similar. It was postulated that this was due to the LDEF sample picking up moisture between satellite retrieval and sample test. Therefore, a series of tests were performed to determine the propensity of Apiezon H to absorb atmospheric moisture. A thin film of the grease was exposed to 100% humidity at room temperature prior to testing. The absorbed moisture caused a total mass loss similar to the difference between the LDEF sample and the control sample. Chemical analysis of the grease indicates that

both the grease and the condensable material from the volatility test match those of a control sample. This implies that changes noted in the LDEF material were caused by storage on Earth, not by exposure to LEO.

Apiezon L. Apiezon L was used on Experiment A0180, as a lubricant during fastener installation. It has not been examined.

Apiezon T. Apiezon T was used on experiment M0001 as a lubricant for installation of a large O-ring in a flange seal. Examination of the lubricant/O-ring by optical microscopy revealed some slight separation of the oil from the filler. Infrared spectroscopy of the lubricant showed no changes from the control. The O-ring was entirely wetted with the oil and showed no evidence of attack. Post-flight examination of the flange revealed migration of the Apiezon T onto the flange. This migration was not quantified.

Ball Brothers 44177 Lubricant. Ball Brothers lubricant 44177 was used to lubricate the thrust washer on the five EECC's. A nearby bracket was found to have a diffraction pattern due to the outgassing of the volatile component of the lubricant. Although the 44177 is still used on previously designed spacecraft, Ball Brothers no longer recommends it for new design.

Castrol Braycote 601. Castrol Braycote 601 was used to lubricate the four drive shafts which opened and closed the clam shells (canisters) of experiment A0187-1, Chemistry of Micrometeoroids. The drive shafts were located on the exterior surface of tray A3 (trailing edge) but saw minimal direct exposure to UV as the clam shells shielded the drive shafts. Due to the trailing edge location, the 601 saw very minimal atomic oxygen. The lubricant had picked up a black color, as yet not identified, but thought to be some form of contamination. Castrol (manufacturer of Braycote) examined the Braycote 601 with the following results. Infrared and thermogravimetric analysis did not indicate any degradation of the base oil or thickener. Differential infrared analysis of the LDEF Braycote 601 showed it to be virtually identical to new 601. Thermal gravimetric analysis results of the flight sample are very similar to those of a control sample. A slight difference was observed but is likely due to traces of moisture and contamination. No significant change in the temperature at which decomposition begins or in the relative levels of base oil to thickener was observed, indicating that the Braycote was unchanged.

Dow Corning 340. Dow Corning 340 heat sink compound was used on two LDEF experiments, A0133 and M0001. The heat sink compound in both experiments performed as expected, transferring heat from one surface to another. Neither application exposed the Dow Corning 340 to UV or to atomic oxygen. The infrared spectra of a sample of Dow Corning 340 from experiment M0001 were unchanged compared to that of a control sample.

Dow Corning 1102. Dow Corning 1102, used on Experiment S1001, Low Temperature Heat Pipe, is an obsolete heat sink compound that was composed of 85% mineral oil, 10% Bentonite, 3% MoS_2, and 3 percent acetone. Post-flight visual examination of the material showed no change from the initial condition.

Exxon Andok C. Exxon Andok C was used in Experiment S0069, Thermal Control Surfaces Experiment. No results have been reported.

Mobil Grease 28. Mobil Grease 28 was used on the NASA provided magnetic tape modules (MTM). The MTMs contained the cassette tape that recorded on-orbit data. The MTMs were tested and compared to pre-flight measurements. No significant changes were noted. The MTMs were not disassembled so no grease analysis has been performed. No change in the grease was expected as it was in a sealed enclosure backfilled with an inert atmosphere.

Vespel Bushings. Vespel bushings were used in experiments A0147, A0187, and S1002. None of the bushings were exposed to UV or to atomic oxygen. All Vespel bushings performed as expected.

9.2 SEALS

9.2.1 Introduction

A variety of seals were used on LDEF, all of them as components of various experiments. These were generally O-rings, although sheet rubber was also used as a seal. In addition, materials that are commonly used for seals were used as cushioning pads. A detailed review of the investigations into the seal materials used on the LDEF can be found in the NASA Contractor Report by Harry Dursch et al. (Reference 1). The following paragraphs are exerpted from this report.

9.2.2 Space Environment Effects

The performances of the elastomeric seal materials flow on LDEF are listed in Table 9-2. These materials performed as designed, sustaining little or no degradation caused by long term exposure to LEO. The only failure was the ethylene propylene O-rings on Experiment S0069 used to seal the lithium carbon monofluoride (LiCF) batteries. This failure was caused by long term exposure to the LiCF electrolyte (dimethyl sulfite) which caused a compression set to occur in the O-ring. This same phenomenon occurred on ground stored batteries; therefore, this failure is not attributed to space exposure.

Table 9-2. Seals on the LDEF Satellite.

Elastomeric Parts	Experiment	Comments[a]
Butyl O-ring	P0004	1, 3
Butyl rubber seal	A0138	1
EP O-ring	S0069	2A, 3
EPDM rubber	P0005	1, 3
NBR rubber	P0005	1, 3
Neoprene gasket	A0139	
Nitrile O-ring	M0006	
Silicone gasket	S0050	1, 2B, 3
Silicone pad	M0004	1, 2B, 3
Viton O-ring	A0015, A0134, A0138-2, A0139, A0180, M0001, M0002, P0005, S0010, S0069	1, 3
Viton washer	A0189	1, 3
Metal "V" washer	EECC's	1, 3

(a) 1: Performed as expected
2A: Failure due to attack by dimethyl sulfite
2B: Discolored where exposed to UV
3: Results discussed in this section.

The effects of the space environment on specific materials flown on the LDEF are discussed in the following paragraphs.

Butyl O-Rings. Butyl O-rings were used in face seals on Experiment P0004, Seeds in Space Experiment. Because the O-rings were sandwiched between metal surfaces, their exposure was limited to vacuum and thermal cycling. The O-rings were apparently installed without lubricant and sustained some scuff marks and pinching upon installation. Accurate post-flight weights of each seed container were taken and compared to preflight values. The results showed no change in weight. This means that the O-rings performed as designed by preventing any desorption of moisture in space (7% of a seed's weight is moisture). There was no evidence of space-induced degradation and the performance of the O-ring seal was as predicted.

Ethylene Propylene (EP) O-Rings. Ethylene propylene O-rings were used to seal the lithium batteries on LDEF Experiment S0069, Thermal Control Surfaces Experiment. These seals failed due to excessive compression set of the O-rings. The temperatures seen by the batteries, 13 to 27°C, were well within the limits of EP O-ring

capabilities. Therefore, failure has been attributed to attack of the O-ring by the battery electrolyte, dimethyl sulfite.

Ethylene Propylene Diene Monomer Rubber (EPDM). EPDM rubber was tested in Experiment P0005, Space Aging of Solid Rocket Materials, which was located on the interior of LDEF. This elastomer exhibited slight changes in strength, modulus and ultimate elongation, as shown in Figure 9-1.

Acrylonitrile Butadiene Rubber (NBR). NBR rubber was tested in Experiment P0005, Space Aging of Solid Rocket Materials, which was located on the interior of LDEF. This elastomer exhibited slight changes in strength, modulus and ultimate elongation, as shown in Figure 9-1.

Silicone Rubber. Silicone rubber was used as a cushioning gasket between the sunscreen and the tray in Experiment S0050, Investigation of the Effects on Active Optical System Components. Portions of the gasket were exposed through holes in the sunscreen. Since the experiment was on the trailing side of LDEF (row 5), the gasket saw UV, but not atomic oxygen. The exposed areas of the gasket were slightly darkened but did not show any other signs of degradation. The hardness of the gasket was the same in exposed and unexposed areas, and all material was very pliable. Although control specimens were not available, tensile strength and elongation were determined and found to be within the range of other silicone elastomers.

Silicone rubber was also used as a cushioning pad between a metal clamp and some optical fibers in Experiment M0004, Space Environment Effects on Fiber Optics Systems. The rubber was mostly shielded, but some edges were exposed to UV and atomic oxygen. The rubber remained pliable and free of cracks. Some darkening of the rubber was observed in the exposed areas.

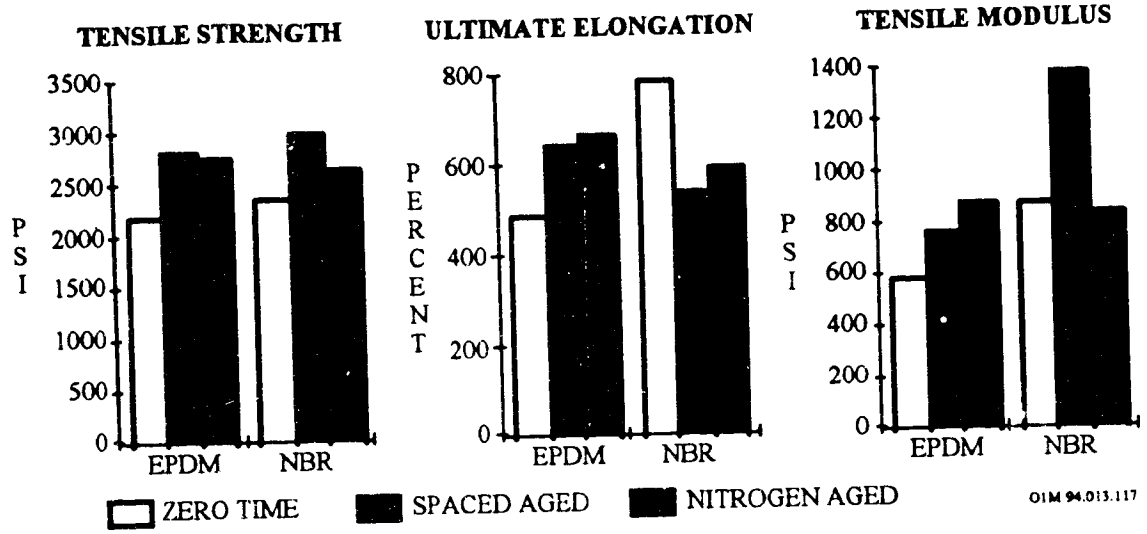

Figure 9-1. Mechanical Properties of EPDM and NBR

Viton O-Rings. A large number of Viton O-rings were used on LDEF. Post flight examination showed that the ones examined were in nominal condition. All Viton O-ring seals maintained a seal. None of the Viton O-rings were exposed to UV or to atomic oxygen.

A group of Viton washers was used to pad the quartz crystal oscillators in Experiment A0189. The washers were apparently taken out of sheet stock as a fabric texture was apparent on the flat surfaces. Many of the washers had indentations on one or both of the contacting surface, indicating compression set. No further analysis is planned because the original compression is unknown.

Metal "V" Seal. A metal "V" seal was used to seal the pressure valve in the EECC's. The seal was made of Inconel 750 and had a currently unknown finish. It was sealing the stainless steel valve to an aluminum surface. There was no evidence of cold welding between the valve, the seal, and the mating aluminum surface contacting an aluminum surface.

REFERENCES

[1] H. Dursch, B. Keough, and G. Pippin, "Evaluation of Seals, Lubricants, and Adhesives Used On LDEF," LDEF Second Post-Retrieval Symposium, NASA CP 3194, 1992, pp. 1041-1060.

REPORT DOCUMENTATION PAGE

Form Approved
OMB No. 0704-0188

1. AGENCY USE ONLY (*Leave blank*)	2. REPORT DATE	3. REPORT TYPE AND DATES COVERED
	August 1995	Contractor Report(April 1993 - March 1995)

4. TITLE AND SUBTITLE
Space Environmental Effects on Spacecraft: LEO Materials Selection Guide

5. FUNDING NUMBERS
C NAS1-19291
TA 12
WU 233-01-01-02

6. AUTHOR(S)
Edward M. Silverman

7. PERFORMING ORGANIZATION NAME(S) AND ADDRESS(ES)
TRW Space & Electronics Group
One Space Park
Redondo Beach, CA 90278

8. PERFORMING ORGANIZATION REPORT NUMBER

9. SPONSORING / MONITORING AGENCY NAME(S) AND ADDRESS(ES)
National Aeronautics and Space Administration
Langley Research Center
Hampton, VA 23681-0001

10. SPONSORING / MONITORING AGENCY REPORT NUMBER
NASA CR-4661, Part 1

11. SUPPLEMENTARY NOTES
Langley Technical Monitors: Joan G. Funk and Stephen S. Tompkins

12a. DISTRIBUTION / AVAILABILITY STATEMENT
Unclassified--Unlimited

Subject Category 18

12b. DISTRIBUTION CODE

13. ABSTRACT (*Maximum 200 words*)

This document provides performance properties on major spacecraft materials and subsystems that have been exposed to the low-Earth (LEO) space environment. Spacecraft materials include metals, polymers, composites, white and black paints, thermal-control blankets, adhesives, and lubricants. Spacecraft subsystems include optical components, solar cells, and electronics. Information has been compiled from LEO short-term spaceflight experiments (e.g., Space Shuttle) and from retrieved satellites of longer mission durations (e.g., Long Duration Exposure Facility). Major space environment effects include atomix oxygen, ultraviolet radiation, micrometeoroids and debris, contamination, and particle radiation.

The main objective of this document is to provide a decision tool to designers for designing spacecraft and structures. This document identifies the space environments that will affect the performance of materials and components, e.g., thermal-optical property changes of paints due to UV exposures, AO-induced surface erosion of composites, dimensional changes due to thermal cycling, vacuum-induced moisture outgassing, and surface optical changes due to AO/UV exposures. Where appropriate, relationships between the space environment and the attendant material/system effects are identified.

14. SUBJECT TERMS
Space environmental effects; Atomic oxygen; Micrometeoroids and debris; Low-Earth orbit; Space Shuttle; Long Duration Exposure Facility (LDEF)

15. NUMBER OF PAGES
502

16. PRICE CODE
A22

17. SECURITY CLASSIFICATION OF REPORT	18. SECURITY CLASSIFICATION OF THIS PAGE	19. SECURITY CLASSIFICATION OF ABSTRACT	20. LIMITATION OF ABSTRACT
Unclassified	Unclassified		